Polishing the Lenses

Refined Modelling of Gravitational Lensing and Delensing of the Cosmic Microwave Background

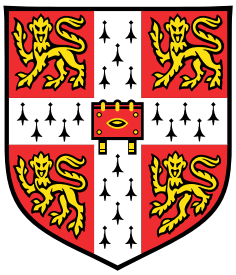

Antón Baleato Lizancos

Institute of Astronomy
University of Cambridge

This dissertation is submitted for the degree of
Doctor of Philosophy

Trinity College October 2021

A Avi e Avoiño, con todo o meu amor.

Declaration

I hereby declare that except where specific reference is made to the work of others, the contents of this dissertation are original and have not been submitted in whole or in part for consideration for any other degree or qualification in this, or any other university. This dissertation is my own work (the use of 'we' instead of 'I' is merely a stylistic choice) and contains nothing which is the outcome of work done in collaboration with others, except as declared below and specified in the text.

- Chapter 2 has been published as:

  A. Baleato Lizancos, A. Challinor and J. Carron (2020), Limitations of CMB B-mode template delensing. Physical Review D 103, 023518 (2021)

- Chapter 4 has been published as:

  A. Baleato Lizancos, A. Challinor and J. Carron (2020), Impact of internal-delensing biases on searches for primordial B-modes of CMB polarisation. Journal of Cosmology and Astroparticle Physics 03(2021)016

- Chapter 3 is based, in part, on work that has been submitted for publication in Monthly Notices of the Royal Astronomical Society as:

  A. Baleato Lizancos, A. Challinor, B. Sherwin & T. Namikawa (2020), Delensing the CMB with the cosmic infrared background: the impact of foregrounds.

- Other parts of chapter 3 will soon be submitted for publications as:

  T. Namikawa, A. Baleato Lizancos, N. Robertson, A. Challinor, B. Sherwin and the Simons Observatory Collaboration (2021), The Simons Observatory: Constraining inflationary gravitational waves with multi-tracer B-mode delensing.

- The work in chapter 5 was done in conversation with W. Coulton, A. Challinor and B. Sherwin, and led by myself.

This dissertation contains fewer than 60,000 words including abstract, tables, footnotes and appendices.

Antón Baleato Lizancos
October 2021

Summary

The cosmic microwave background (CMB) is made up of photons, the majority of which last scattered with electrons during the era of cosmic recombination, at redshift $z \approx 1100$. They have been travelling, virtually undisturbed, ever since. Along their journey, however, the photons' paths are deflected by the gravitational influence of the matter distribution of the Universe — an effect known as 'gravitational lensing'. Though the deflections are small, they can affect the statistical properties of the ensemble in crucial ways.

Lensing converts part of the E-mode polarisation of the CMB into B-modes, thus introducing a source of noise when searching for a primordial B-mode signal associated with primordial gravitational waves (PGWs) generated during cosmic inflation. Fortunately, constraints on PWGs can be improved by partially removing lensing B-modes — i.e., 'delensing' them.

The core of this thesis consists of work towards an improved understanding of the process of B-mode delensing. We dedicate a chapter to exploring the benefits and limitations of delensing B-modes using templates constructed by combining high-resolution measurements of E-modes with proxies of the matter distribution responsible for the lensing deflections. We prove the counter-intuitive result that a gradient-order template is more effective when constructed from lensed E-modes, instead of their delensed or unlensed version. Furthermore, we show that, given lensed E-modes, a gradient-order template is to be preferred over a non-perturbative one. A gradient-order template built from lensed E-modes will be effectively optimal for all planned CMB experiments, with the added benefit of being analytically transparent and computationally efficient.

In another chapter, we consider the case where B-modes are delensed using external tracers of the matter distribution of the Universe. We discuss how uncertainties in measurements of the tracer spectra might translate to biased constraints on PGWs, and show that this effect will be negligible for the upcoming Simons Observatory (SO). Then, we focus on the problem of foreground residuals when the cosmic infrared background (CIB) is used to delens B-modes. Significant biases can arise if the largest angular scales are included in analyses, because of non-Gaussian galactic dust residuals

remaining after foreground cleaning. However, we propose mitigation techniques, and show that they will be highly effective.

We also revisit internal delensing biases arising when B-modes are delensed using a lensing reconstruction obtained from a quadratic combination of E- and B-modes. We learn that these biases necessarily lead to degraded constraints on PGWs, despite appearing to reduce the variance of the estimators we use to constrain them. We derive an analytic model for the bias, but show that it is generally advantageous to exclude the overlapping modes rather than model or renormalise the bias.

In the final original chapter, we address the issue of extragalactic foreground contamination to temperature-based lensing reconstructions. We present an analytic framework for calculating the biases associated with the thermal Sunyaev-Zeldovich effect and the CIB using the halo model. Our predictions can be evaluated very efficiently (at least for the dominant set of terms) and are in reasonable agreement with simulations.

Supervisor and Examiners

Supervisor: Prof. Anthony Challinor

Internal examiner: Prof. George Efstathiou

External examiner: Prof. Antony Lewis

Acknowledgements

I would like to begin by thanking my supervisor, Anthony Challinor, for his mentorship throughout these years. It has been a pleasure to work with him and learn from his outstanding wisdom and creativity. I particularly appreciate the kindness in our every interaction, and I strive to reproduce it in my career as a scientist.

Special thanks also to Blake Sherwin, my second supervisor, who has been an invaluable source of ideas and advice, always looking after my scientific development. I am indebted to my collaborators, Toshiya Namikawa, Will Coulton, Julien Carron, Naomi Robertson and Byeonghee Yu; and the cosmologists on either side of Madingley Road for many enriching interactions. Several results in this thesis rely on products that Colin Hill, Mathieu Remazeilles, Mat Madhavacheril and Yogesh Mehta kindly shared with me; to them, thank you. Many thanks as well to Antony Lewis and George Efstathiou, who thoroughly read through this thesis and provided insightful comments.

The Institute of Astronomy has been the ideal place for me to work and learn during these years: within its walls (or from 1170 km away[1], in times of a pandemic) a student can feel supported, inspired and appreciated, all in equal measure. I am grateful to all the members of the IoA community for enabling that. I will, however, single out Debbie Peterson, Paul Hewett, Martin Haehnelt, Steve Gratton, Max Pettini, Monica Gamboa, Aneesh Naik, Björn Sörgel, Pablo Lemos, Lukas Hergt, George Hawker, Roger de Belsunce, Lewis Weinberger and my good friend and office mate Íñigo Zubeldia. I also would like to express my gratitude to Trinity College, the Isaac Newton Trust and, especially, the British tax-payer, for their material support of my research.

I would like to end by thanking my family. In particular, I would not be who I am without the sacrifices and commitment of Rosario and Manolo, who fought for the Spanish Republic, endured forty years of exile, and had enough energy left to be my wonderful great-grandparents. I am endlessly grateful to my parents, Laura and Eugenio, for the love with which they raised me and continue to give, and for supporting every step I ever took. Thank you to my admired Julia, my bedrock, for the beautiful life we have built together. And a final thought for my grandparents, Avi and Avoiño, whose memory I carry with me every day: this thesis, which I know you would have been proud to see completed, is dedicated to you.

[1] 1170 km is the geodesic distance between A Coruña and Cambridge.

Table of contents

List of figures **xvii**

List of tables **xxi**

1 Introduction **1**

1.1 The concordance cosmological model 1
1.2 Homogeneous and isotropic spacetimes 4
1.3 Inflation and the generation of perturbations 7
1.3.1 Background evolution during inflation 7
1.3.2 Characterising perturbations 10
1.3.3 Primordial power spectra 13
1.3.4 Implications of a detection of tensor modes 14
1.4 Evolution of perturbations in the linear regime 16
1.5 The cosmic microwave background 18
1.5.1 The primary CMB 18
1.5.1.1 Polarisation formalism 25
1.5.1.2 CMB polarisation anisotropies 27
1.5.1.3 Generation of a primordial B-mode 28
1.5.2 CMB lensing 31
1.5.2.1 The deflection angle 32
1.5.2.2 The lensed CMB fields 36
1.5.2.3 The need to delens B-modes 42
1.5.2.4 Lensing reconstructions 45
1.5.3 Other components of the microwave sky 51
1.5.3.1 Galactic foregrounds 52
1.5.3.2 The thermal Sunyaev-Zeldovich effect 54
1.5.3.3 The cosmic infrared background 58
1.6 The formation of cosmic structures 62
1.6.1 Motivation 62
1.6.2 The halo mass function 62
1.6.3 The bias of dark matter halos 67

1.6.4 The density profile of dark matter halos . . . 71
1.6.5 The halo model . . . 74
1.6.6 Populating dark matter halos with galaxies . . . 80
1.6.7 A halo model of the CIB . . . 87

2 Limitations of CMB B-mode template delensing 93
2.1 Introduction . . . 93
2.2 Template delensing . . . 95
2.3 Delensing with a gradient-order template . . . 97
2.4 Delensing with a non-perturbative template . . . 106
2.5 Conclusions . . . 111

3 Delensing B-modes with external tracers 113
3.1 Introduction . . . 113
3.2 Building a template using external tracers . . . 115
3.3 Modelling externally-delensed spectra . . . 118
3.4 The impact of uncertainties in external tracer spectra . . . 121
3.5 The impact of residual foregrounds on CIB delensing . . . 124
3.5.1 Methods . . . 129
3.5.1.1 Simulations of Galactic dust . . . 129
3.5.1.2 Simulations of the CIB . . . 131
3.5.1.3 Estimating dust residuals in the data . . . 132
3.5.1.4 Masking . . . 138
3.5.1.5 Summary of simulation-based procedure for estimating delensing biases . . . 142
3.5.2 Results . . . 143
3.5.2.1 Bias from residual Galactic dust . . . 143
3.5.2.2 Intrinsic bias from non-Gaussianity of the CIB . . . 146
3.5.3 Validation . . . 152
3.5.3.1 Validation against Gaussian simulations . . . 152
3.5.3.2 Validation against Planck data . . . 154
3.6 Conclusions . . . 156

4 Internal delensing of B-modes 161
4.1 Introduction . . . 161
4.2 The quadratic estimators of lensing . . . 162
4.3 Template delensing of the B-mode . . . 164

4.4 Angular power spectrum of delensed B-modes . . . 166
4.4.1 The unbiased case: reconstruction errors statistically independent of the lensed CMB . . . 167
4.4.2 The biased case: $\hat{\phi}$ obtained from an EB quadratic estimator . 168
4.5 Covariances of delensed power spectra . . . 178
4.6 Maximum-likelihood inference of r . . . 182
4.7 The $B^{\rm obs}(B^{\rm obs} - B^{\rm temp})$ estimator . . . 186
4.8 Discussion . . . 192

5 Modelling CMB lensing biases due to extragalactic foregrounds 195
5.1 Introduction . . . 195
5.2 Biases to lensing reconstruction from extragalactic foregrounds . . . 200
5.2.1 Primary bispectrum bias . . . 203
5.2.2 Secondary bispectrum bias . . . 204
5.2.3 Trispectrum bias . . . 205
5.3 Analytic calculation of the biases . . . 206
5.4 Comparison to simulations . . . 210
5.5 Conclusions . . . 214

6 General conclusions and outlook 217

Appendix A Calculations for Chapter 4 221
A.1 Internally-delensed B-mode power spectrum . . . 221
A.1.1 Contributions to the unbiased delensed power spectrum . . . 222
A.1.2 Additional corrections from internal delensing . . . 225
A.2 Simulations . . . 229

Appendix B Calculations for Chapter 3 233
B.1 The BEI bispectrum of the CIB . . . 233
B.2 Modelling the equal-redshift 3D bispectrum . . . 236
B.3 Toy model for CIB higher-point functions . . . 240
B.4 Toy-model CIB bispectrum: one-source term . . . 241
B.5 Toy-model CIB trispectrum: one-source term . . . 244
B.6 Simulating Gaussian LSS tracers correlated with CMB lensing . . . 244
B.7 Constructing curved-sky lensing template . . . 246
B.7.1 Constructing a curved-sky, first-order, lensing B-mode template 246
B.7.2 Constructing a curved-sky, first-order, lensed T template . . . 248
B.8 Analytic Power Spectrum Covariances . . . 249

B.8.1 Delensed B-mode PS covariance 249
B.8.2 Spectrum-based delensing 250
B.8.2.1 Covariance of cross-spectrum 250
B.8.2.2 Covariance of template auto-spectrum 252
B.8.2.3 Cross-covariance of lensing and template auto-spectra . 253
B.8.2.4 Cross-covariance of lensing auto- and template cross-spectra 253
B.8.2.5 Cross-covariance of template auto- and cross-spectra . 253

Appendix C Calculations for Chapter 5 **255**
C.1 Factorial moments of the halo occupation distribution 255
C.2 Fast lensing reconstructions using Hankel transforms 256
C.2.1 Alternative evaluation 258
C.3 Evaluating the secondary bispectrum bias 259
C.4 Halo model of projected higher-point functions 259
C.5 Halo model for the primary bispectrum bias 263
C.6 Halo model for the trispectrum bias 264

References **269**

List of figures

1.1 Evolution of the comoving Hubble horizon during and after inflation . . 8
1.2 Current limits and forecasted constraints on the tensor-to-scalar ratio as a function of n_s. 9
1.3 Present-day, linear-theory matter power spectrum as inferred from a number of cosmological probes 19
1.4 Full sky intensity maps at 30, 100 and 353 GHz as observed by Planck . 21
1.5 Planck measurements of CMB angular spectra 23
1.6 CMB angular power spectra, including lensing and primordial B-modes 30
1.7 Cumulative contribution of different redshifts to the power spectrum of the CMB lensing potential 36
1.8 Fractional difference between lensed and unlensed CMB power spectra . 39
1.9 Map of the lensing deflection angle as reconstructed by Planck 49
1.10 Rms fluctuations, as a function of frequency, of the main components of the microwave sky in polarisation 54
1.11 Comparison of projected pressure maps of simulated clusters to projected, pasted profile maps 59
1.12 A map of the CIB anisotropies overlaid on a map of the CMB lensing potential, covering approximately 456 sq. deg. of the sky 61
1.13 Normalised Fourier transforms of NFW profiles for different halo masses at $z = 0$ 74
1.14 Mean number of galaxies as a function of host halo mass 82

2.1 Corrections to the leading-order calculation of the lensing B-mode spectrum 98
2.2 Real-space scalar fields derived from $\tilde{B}^{(2)}(\mathbf{l})$ and the contribution to the gradient-order B-mode template from the linear lensing correction to E-modes, $\Delta\tilde{B}^{\rm temp}(\mathbf{l})$ 102
2.3 Analytic versus simulated lensing B-mode residual spectra after delensing with various templates 104
2.4 Residual B-mode maps after delensing in the limit of noiseless CMB fields and access to the true ϕ, using various templates 107

2.5 Comparison of template performance as a function of experiment noise 110

3.1 Correlation coefficient of the true CMB lensing field with several tracers of the large-scale structure, and with a co-added tracer 119
3.2 Impact of uncertainties in the tracer spectra on the power spectrum of B-mode lensing residuals after delensing 125
3.3 Bias on the inferred tensor-to-scalar ratio, as a function of input signal, due to deviations from the fiducial model of the spectra of the external tracers used for delensing 126
3.4 Distribution of the bias on r from 5000 realisations (with input $r = 0$), arising from uncertainties in the spectra of the external tracers used to delens SO B-modes, in the case where Planck CIB maps alone are used, or when these CIB maps are co-added with SO internal reconstructions and VRO LSST galaxies 127
3.5 Estimated map-level percentage of residual dust emission after foreground cleaning relative to the unmitigated dust emission in either the 145 GHz channel of the SO LAT, the 145 GHz channel of the SO SAT or different CIB maps at 353 GHz 134
3.6 Impact of dust deprojection on delensing efficiency 137
3.7 Masks used in our analysis. 139
3.8 Stokes Q parameter associated with B-mode templates generated from residual dust intensity and E-modes, for different extents of Galactic masking applied to the input fields prior to Wiener filtering 140
3.9 Power spectra, measured on the SO SAT patch, of the dust-only B-mode templates shown in figure 3.8 141
3.10 Fractional bias on the angular power spectrum of residual lensing B-modes due to residual Galactic dust, plotted for several scenarios with differing residual dust levels 147
3.11 Bias on the inferred tensor-to-scalar ratio due to unmodelled contributions from residual non-Gaussian Galactic dust to the power spectrum of B-modes delensed with the CIB 148
3.12 Delensing biases from angular bispectra of the CIB in a minimal model with uncorrelated source polarisation angles 151
3.13 Comparison of power spectrum amplitudes and biases for a number of fields involved in the delensing procedure 153

3.14 Delensing bias associated with the bispectrum of Galactic dust as calculated from a single realisation of the VS simulation, compared to that measured from a Gaussian simulation of the dust with the same power spectra 154
3.15 Delensing bias associated with the bispectrum of Galactic dust arising from a restricted range of multipoles of the VS Galactic dust simulation or the Planck data, after both are filtered and scaled to emulate levels of residual dust expected after foreground cleaning 157

4.1 Noise power spectra of quadratic estimator lensing reconstructions . . . 165
4.2 Evaluation of D_l, defined in equation (4.17) 171
4.3 Impact of internal delensing biases on B-mode power spectra after delensing 174
4.4 Impact on delensing performance of high-pass filtering the B-modes used for lensing reconstruction 175
4.5 Signal-to-noise of various spectrum-based primordial B-mode estimators 177
4.6 Correlation coefficient of B-mode bandpowers before and after delensing 180
4.7 Cross-sections of the correlation coefficients of B-mode bandpowers before and after delensing 181
4.8 Typical likelihood functions for the tensor-to-scalar ratio r with and without delensing 184
4.9 Distributions of $\hat{r}_{\rm ML}$ and $\sigma(\hat{r}_{\rm ML})$ across simulations comparing the use of analytic or simulated power spectrum covariances in the cases of no delensing and unbiased delensing 185
4.10 Distributions of $\hat{r}_{\rm ML}$ and $\sigma(\hat{r}_{\rm ML})$ across simulations for different delensing analyses, for input $r = 0.01$ 187
4.11 Same as figure 4.10, but in the null scenario of $r_{\rm input} = 0$. 188
4.12 Variances of different spectral estimators from which primordial power is to be extracted 191
4.13 Cross-correlation coefficients of different spectral estimators 191

5.1 Analytic calculation of the primary bispectrum and trispectrum biases to lensing 208
5.2 Lensing reconstruction biases from extragalactic foregrounds as measured from the WebSky simulations 213

A.1 Break-down of contributions to the model, biased, delensed power spectrum of equation (A.18) in the case where $r_{\rm input} = 0.01$ 228

A.2 Break-down of contributions to the difference between the power spectrum of the B-modes observed with the SAT and the power spectrum of the delensed B-modes, as a fraction of the original B-mode lensing power 230

B.1 Delensing biases from the BEI bispectrum and $EIEI$ trispectrum of the CIB, including only 1-source contributions, for point-source masking schemes typical of current and upcoming CMB experiments 242

List of tables

1.1 Non-perturbative CMB lensing response functions in the flat-sky limits 47
1.2 Mass and redshift fit parameters for the pressure profile of Ref. [26] . . 58
1.3 Best-fit parameters for the halo mass function 66
1.4 Best-fit parameters for the large-scale halo bias 70
1.5 Best-fit parameters for the median halo concentration of NFW halos in the model of Ref. [119] 73
1.6 Best-fit CIB halo model parameters from Planck data 91

3.1 Dust parameters used in this work, obtained from Ref. [364]. 129

B.1 Weights for a fast separable implementation of the lensed B-mode template. 248
B.2 Weights for a fast separable calculation of the first-order lensing correction to the CMB temperature anisotropies 249

Chapter 1

Introduction

1.1 The concordance cosmological model

Less than a century ago, in 1924, Hubble found conclusive evidence that M31 and M33 — the great spiral nebulae in the Andromeda and Triangulum constellations — were too distant to be part of our own Galactic system [207].[1] With this breakthrough came the era of extragalactic astronomy, in which humanity has become increasingly aware of the vast scale of the Universe, and has set out to explore it.

It is safe to say that the class of extragalactic astronomy that we refer to as cosmology came to being in 1929, when Hubble (once again) combined estimates of the distance to 24 nearby galaxies with Slipher's spectrographic determination of their velocities, to find the now-famous 'Hubble law': that galaxies in the nearby Universe recede from our own with a velocity, v, that is proportional to their distance, r. The law reads $v = H_0 r$, where the proportionality constant, H_0, is now known as Hubble's constant [206].

In parallel, the early decades of the twentieth century saw a theoretical revolution in the form of Einstein's general theory of relativity (GR [130]). It was soon realised that homogeneous and isotropic solutions to Einstein's field equations — the Friedmann–Lemaître–Robertson–Walker (FLRW) models — generically predict a relationship between velocity and distance, in the context of which Hubble's observations could be explained [248, 400]. Remarkably, our Universe followed mathematical laws we humans could understand.

Since the Universe is expanding at present, it must have been denser and hotter in the past. Extrapolating this argument to the initial conditions, it suggests that the Universe might have begun with an initial 'Big Bang'. It was Gamow and his collaborators who first realised, in the late 1940s, that a hot, dense primeval phase could lead to the formation of the lightest chemical elements [145, 11]. This picture was subsequently

[1] Further details about the history of cosmology can be found in Ref. [270].

refined, and found to predict the observed abundances of helium, deuterium and other elements [194, 496]. The stage was set for the definitive proof of the hot Big Bang model: the discovery, in 1967, of the cosmic microwave background (CMB), the relic radiation from the hot primordial plasma, released at the time of 'recombination' of electrons and protons, approximately 380,000 years after the Big Bang [348]. Precise measurements over the course of subsequent decades have determined the CMB to be remarkably uniform, although tiny deviations from homogeneity (as small as 1 part in 10^4) exist across the sky [454]. These deviations — the CMB *anisotropies* — are related to fluctuations in the energy density of the primordial plasma at the time of recombination, and constitute the seeds of the structures we observe in the Universe at later times.

The extreme homogeneity of the CMB was a puzzle to cosmologists until 1981, when the idea of cosmic *inflation* was introduced [156]. If the Universe underwent a period of accelerated expansion at very early times, the model postulated, then the observed homogeneity (as well as other fundamental problems) could be explained. More importantly, it was soon realised that a period of inflation would also have produced a spectrum of fluctuations in the energy density and spacetime geometry [180, 157, 462, 22]; in the simplest models, these fluctuations had precisely the statistical properties known to be needed for structure formation to proceed in a way that was consistent with observations (a nearly-scale-invariant, or Harrison-Zeldovich, spectrum of perturbations [177, 523]). Crucially, inflation also predicted that the Universe should be spatially flat, or very nearly so, on large scales.

In parallel to these developments, the 1970s and 80s saw the birth of a consensus around the existence of a form of matter that is impervious to electromagnetic interactions, as first suggested by Zwicky in the 1930s to explain the velocities of galaxies in the Coma cluster [527]. Compelling evidence for this dark matter now came from the motions of satellite galaxies around our own and other nearby galaxies [336, 129], and from galaxy rotation curves [399, 405]. Later on, it would also become apparent — from precise observations of the CMB anisotropies — that a dark matter component is required in order to explain the small-scale structure we see in the Universe, as fluctuations of any baryonic form of matter on the relevant scales are washed away before recombination due to their being coupled to the fast-moving photons. In the 1980s, the observational implications of different dark matter candidates were worked out in detail, and it was found that only a cold dark matter (CDM) component moving non-relativistically could explain the clustering properties of observed structures [104]. The standard cosmological model in the late 1980s was thus one which had a Harrison-

Zeldovich spectrum of primordial perturbations, and where dark matter provided most of the energy density needed to make the Universe flat, as required by inflation (the baryon abundance was known to be insufficient).

However, with the new decade came measurements of the clustering of galaxies which proved to be inconsistent with the standard CDM prediction on large angular scales; rather, these pointed to an alternative scenario were most of the energy density needed to make the Universe flat is in the form of a cosmological constant, which would dominate the energy budget of the Universe at late times [127, 279]. The evidence in favour of this cosmological model, ΛCDM, mounted over the years [337, 260, 236], until it was definitively backed, in 1998, by direct determinations of the cosmic acceleration induced by Λ based on observations of distant supernovae [398, 349]. Around the same time, the first measurements of the acoustic features of the CMB anisotropy spectrum were made; in combination with the supernovae data, these established spatial flatness [106, 165, 301]. Since then, the ΛCDM model has passed myriad tests — most notably WMAP's [231] and Planck's [371] precise measurements of the CMB anisotropies — and continues to be in superb agreement with observations (except, perhaps, for the Hubble tension [397, 492]).

Arguably, the only generic prediction of inflationary models that remains to be validated is the generation of a stochastic background of primordial gravitational waves. In addition to serving as a test of the theory and its competitors, a detection would shed light on physics at energy scales many orders of magnitude higher than what can be achieved by particle accelerators on Earth. Efforts towards a detection are now focused on the B-mode of CMB polarisation, which is known to be an unrivalled probe of primordial gravitational waves. There are, however, a number of important complications that the measurements need to account for. In this thesis, we consider one such effect: the B-modes produced by gravitational lensing. This will be the focus of chapters 2–4, where we address several modelling issues involved in the removal of lensing B-modes. The basic notions on which our work relies are introduced in the rest of this chapter.

Despite being a nuisance to searches for primordial B-modes, the lensing effect is also a rich source of information, as it allows for the (projected) distribution of matter in the Universe to be reconstructed internally from the CMB anisotropies. Recent analyses by Planck, ACT and SPT have marked a watershed moment for the field of CMB lensing, which is now a first-rate cosmological probe, and only stands to gain in relevance in the coming era of high-resolution, ground-based CMB experiments spearheaded by SPT-3G, the Simons Observatory and CMB-S4. In chapter 5, we

address the impact that extragalactic contamination from galaxies and galaxy clusters can have on such reconstructions of lensing.

1.2 Homogeneous and isotropic spacetimes

The base assumption of our mathematical understanding of the Universe is the 'cosmological principle': that to all observers comoving with the cosmological fluid, the Universe will appear as homogeneous and isotropic on large scales.

Any homogeneous and isotropic, four-dimensional Riemannian manifold can be described by the FLRW metric

$$ds^2 = g_{\mu\nu}\mathrm{d}x^\mu \mathrm{d}x^\nu = c^2dt^2 - a^2(t)\left[d\chi^2 + f_K^2(\chi)\left(d\theta^2 + \sin^2 d\phi^2\right)\right] . \tag{1.1}$$

Here, the coordinates $\{\chi, \theta, \phi\}$ are comoving, meaning that they are unvarying for comoving observers; comoving distances (which are unobservable) can be related to physical distances via the scale factor, $a(t)$, as $d_{\text{physical}} = a(t)d_{\text{comoving}}$. The geometry of hypersurfaces of constant time is determined by the curvature, K, an intrinsic property of the metric which is related to the 3D Ricci scalar (${}^{(3)}R = 6K/a^2$) — often, we will make reference to its sign, $k \equiv K/|K|$. The three possibilities are that the Universe is globally closed/spherical ($K > 0$), flat ($K = 0$) or open/hyperbolic ($K < 0$); to accommodate these, it is customary to define

$$f_K(\chi) = \begin{cases} K^{-1/2}\sin(K^{1/2}\chi) & \text{for } K > 0 \\ \chi & \text{for } K = 0 \\ |K|^{-1/2}\sinh(|K|^{1/2}\chi) & \text{for } K < 0\,. \end{cases} \tag{1.2}$$

From now on, we will work in units where $c = 1$, unless otherwise stated.

It can be shown from the line element in equation (1.1) that the frequency of a light signal emitted at some time, t_1, is related to that observed at a later time, t_0, by $\nu(t_0)/\nu(t_1) = a(t_1)/a(t_0)$. Hence, in an expanding Universe, observed frequencies are lower (shifted red-wards) than they were at emission. It is conventional to define the cosmological *redshift* as $z \equiv [\nu(t_1) - \nu(t_0)]/\nu(t_0)$, so that

$$1 + z = \frac{a(t_0)}{a(t_1)}\,. \tag{1.3}$$

This is a very important quantity connecting observables, such as the frequency shift of absorption or emission spectral lines, to the dynamics of the underlying spacetime.

The evolution of the spacetime described by the metric above is dictated by Einstein's field equations

$$G_{\mu\nu} + \Lambda g_{\mu\nu} = 8\pi G T_{\mu\nu} \,, \tag{1.4}$$

where $G_{\mu\nu}$ is the Einstein tensor, G is Newton's Gravitational constant and Λ is a cosmological constant. The right-hand side describes the contents of the Universe via the stress-energy tensor, $T_{\mu\nu}$. Solving the Einstein field equations for a perfect fluid fully characterised by its energy density, ρ, and isotropic pressure, p, that is distributed in a homogeneous and isotropic way across an FLRW spacetime yields the Friedmann equations:

$$H^2 = \frac{8\pi G}{3}\rho - \frac{K}{a^2} + \frac{\Lambda}{3} \,, \tag{1.5}$$

$$\frac{\ddot{a}}{a} = -\frac{4\pi G}{3}\left(\rho + 3p\right) + \frac{\Lambda}{3} \,, \tag{1.6}$$

where $H = H(t) \equiv \dot{a}/a$ is the Hubble parameter, whose present-day value is $H(t_0) \equiv H_0$ (overdots denote derivatives with respect to cosmic time, t).

We can derive another constraint on the evolution of the components of the Universe from energy conservation[2], which requires that $\nabla_\mu T^{\mu\nu} = 0$, where ∇ denotes the covariant derivate. For the perfect fluid described above, this gives the continuity equation

$$\dot{\rho} + 3H\left(\rho + p\right) = 0 \,, \tag{1.7}$$

so the energy density and pressure of the fluid are coupled to the global dynamics via the expansion rate, H. Since energy density and pressure are generally related through an equation of state, $p = w\rho$, the continuity equation tells us that the energy density of a particular species evolves with the scale factor as $\rho \propto a^{-3(1+w)}$ — all from energy conservation. We now describe the value that w takes for different components of our Universe.

As anticipated in the previous section, observations demand that approximately 25% of the matter/energy density of the Universe be in the form of cold dark matter, which interacts only gravitationally (as far as we can tell) and behaves like non-relativistic, pressure-less dust. This is accompanied in the matter budget by the matter components of the Standard Model of particle physics — electrons, protons, neutrons, etc. — the ensemble of which cosmologists refer to as 'baryons'. The pressure of both of these

[2]Note that the continuity equation can also be obtained by combining the two Friedmann equations.

flavours of matter, dark and luminous, is negligible compared to their energy density, and we can safely set $w = 0$. Hence, the energy density in matter scales as $\rho_{\rm m} \propto a^{-3}$. On the other hand, isotropic radiation — for our purposes, photons, neutrinos and any relativistic species — produces pressure with $w = 1/3$; hence, the radiation energy density scales as $\rho_{\rm r} \propto a^{-4}$. Finally, we can also regard the phenomenology of a cosmological constant, Λ, as being produced by a fluid with negative pressure, such that it does not dilute; in that case, $w = -1$, and $\rho_\Lambda = \Lambda/(8\pi G)$ is a constant. More general models of dark energy can in principle have $w(z)$ vary with redshift; however, there is currently no observational evidence in their favour [208].

Once we know these scalings, it becomes possible to fully specify the global dynamics of the Universe in terms of the present-day abundance of each component. When doing this, it is convenient to define the energy density required to make the Universe flat today,

$$\rho_{\rm crit,0} \equiv \frac{3H_0^2}{8\pi G} \approx 1.88 \times 10^{-26}\, h^2\, {\rm kg\, m^{-3}}\,, \tag{1.8}$$

where h is the Hubble constant in units of $100\,{\rm km\,s^{-1}\,Mpc^{-1}}$, and use this to normalise the abundances of all components by defining

$$\Omega_{\rm r} \equiv \frac{\rho_{\rm r,0}}{\rho_{\rm crit,0}}, \quad \Omega_{\rm m} \equiv \frac{\rho_{\rm m,0}}{\rho_{\rm crit,0}}, \quad \Omega_\Lambda \equiv \frac{\Lambda}{3H_0} \quad \text{and} \quad \Omega_K \equiv \frac{-K}{a_0^2 H_0^2}\,. \tag{1.9}$$

Here, a_0 is the value of the scale factor today, which we will set to unity from now on, $a_0 = 1$. Frequently, we will split the matter budget into baryons and cold dark matter, with abundances $\Omega_{\rm b}$ and $\Omega_{\rm c}$, respectively, whereas we will continue to denote their joint abundance as $\Omega_{\rm m}$. By definition, these quantities satisfy the relation $\Omega_{\rm m} + \Omega_{\rm r} + \Omega_\Lambda + \Omega_K = 1$. We can use them to cast the first Friedmann equation in a simpler form[3]

$$H = H_0 \left[\Omega_{\rm r}(1+z)^4 + \Omega_{\rm m}(1+z)^3 + \Omega_K(1+z)^2 + \Omega_\Lambda\right]^{\frac{1}{2}} \equiv H_0 E(z)\,. \tag{1.10}$$

This expression tells us that, in a homogeneous and isotropic FLRW model, the evolution at all times is determined by the present-day abundances of the different components. For reference, a combination of Planck's measurements with baryon acoustic oscillation (BAO) data, and the assumption of zero curvature, yield [371]: $\Omega_{\rm b}h^2 = 0.02242 \pm 0.00015$, $\Omega_{\rm c}h^2 = 0.11933 \pm 0.00091$ and $\Omega_\Lambda = 0.6889 \pm 0.0056$, with $h = 0.6766 \pm 0.0042$. If curvature is included in the constraints, the combination of Planck anisotropy spectra, lensing, BAO and supernovae data give $\Omega_K = 0.0004 \pm 0.0018$ [126].

[3]Equation (1.10) assumes the neutrinos are massless.

On the other hand, for a CMB temperature of $T_{\rm CMB} = 2.7260 \pm 0.0013\,\mathrm{K}$ [143], the present-day total energy density in photons and massless neutrinos and antineutrinos is as small as $\Omega_{\rm r} h^2 \approx 4.2 \times 10^{-5}$ (e.g., [507]).

These numbers mean that approximately 69% of the present-day energy density of the Universe is in the form of a cosmological constant, 5% in visible matter and 26% in dark matter, with negligible contributions from the radiation. The ΛCDM model forecasts that, in the future, the cosmological constant will overwhelm contributions from other components and the scale factor will tend to an exponential.

1.3 Inflation and the generation of perturbations

The hot Big Bang model was a success in that it explained the generation and abundances of the light elements, and predicted the existence of the CMB. However, it also raised a number of puzzles. Why was the CMB so homogeneous, if only regions of about 1° could have been in causal contact by the time that it was released? Why did the Universe appear to be spatially flat on large scales, if this was known to be an unstable solution to Einstein's equations? And why haven't any magnetic monopoles or other kinds topological defects been observed, if they are an expected consequence of the breaking of gauge symmetries at the very high energies of the hot Big Bang? These puzzles seemed to call for an extreme level of fine-tuning in the initial conditions of the Universe.

In 1981, an idea was proposed, inflation [156, 263, 264, 5], in the context of which a resolution to those puzzles comes naturally. Moreover — and perhaps more importantly — it was soon realised that during a phase of inflation, the primordial seeds of the structures seen in the Universe would have been established, in the form of small perturbations to the energy density and the geometry of spacetime. Much of the work in this thesis is ultimately geared towards finding evidence of those metric fluctuations, so let us now review the basic theory of inflation.

1.3.1 Background evolution during inflation

Inflation is postulated as a period of accelerated expansion of spacetime, very early on. This would enable the physical size of any comoving distance, including fluctuation wavelengths, to grow faster than the Hubble horizon, H^{-1}, a measure of the distance over which causal contact can be established within an expansion time[4] — in the

[4]We take an expansion time to mean roughly the time it takes for the scale factor to double [115].

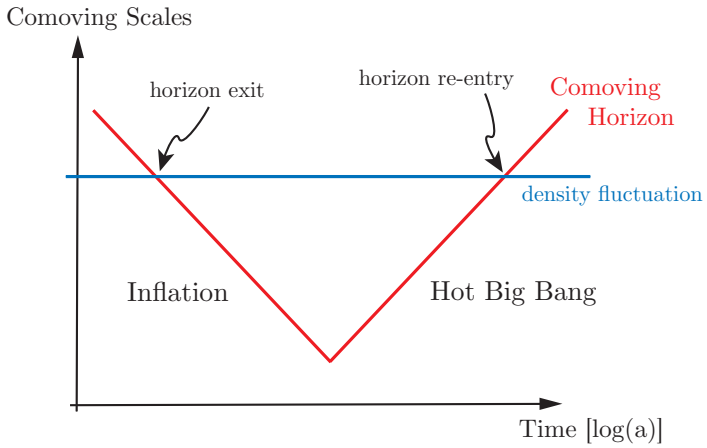

Fig. 1.1 Schematic depiction of the evolution of the comoving Hubble horizon, $(aH)^{-1}$, during and after inflation. For comparison, a constant comoving scale is shown (corresponding, for example, to a density perturbation). Figure from [27].

standard Big Bang evolution, the converse always holds. (Equivalently, the comoving Hubble horizon, $(aH)^{-1}$, decreases during inflation, as pictured in figure 1.1.) In this way, distance scales that were smaller than the horizon *before* inflation, ended up larger than the horizon *after* inflation. The accelerated expansion ought to have lasted long enough that comoving scales as large as the comoving size of the observable Universe were in causal contact (i.e., smaller than the comoving size of the horizon) before inflation. This requires the scale factor to have grown by at least ~ 55 e-folds, but the expansion is so fast that this figure can be attained in a mere $10^{-34}\,\mathrm{s}$ [115]. Inflation would also explain the dearth of exotic relics and curvature, as both would get diluted to insignificant levels with the expansion.

There are several equivalent ways of describing the inflationary period. From the definition of $H \equiv \dot{a}/a$, it follows that $\ddot{a} = (1-\varepsilon)\dot{a}^2/a$, where $\varepsilon \equiv -\dot{H}/H^2$; hence, $\ddot{a} > 0 \iff \varepsilon < 1$. If we define the number of e-folds of inflationary expansion as N, and we note that $\mathrm{d}N \equiv \mathrm{d}\ln a = H\mathrm{d}t$, we can recast the previous requirement as $\varepsilon = -d\ln H/dN < 1$; in other words, during inflation, H must be changing slowly. In the limit that H is constant, the spacetime is pure de Sitter with $a \propto e^{Ht}$; we know this is not the metric of the Universe we live in, for inflation came to an end, so it must have been a period of *quasi*-de Sitter expansion. Finally, it is straightforward to show, from the Friedmann equations, that $\ddot{a} > 0$ requires the Universe be permeated by a substance with negative pressure ($\rho + 3p < 0$) and slowly-diluting energy density.

In the simplest models of inflation, this substance is modelled as a homogeneous scalar field, $\phi(t)$, called the 'inflaton', with potential energy $V(\phi)$. As we will see shortly,

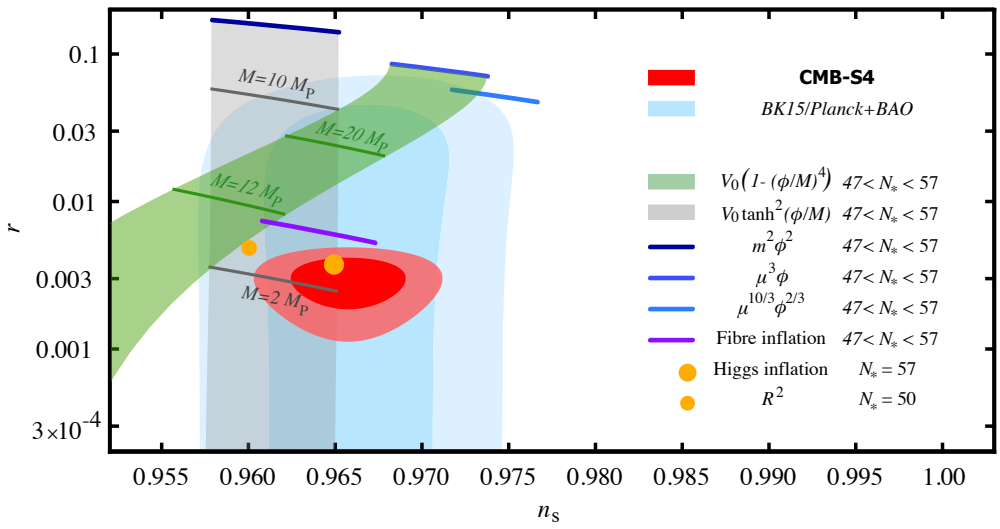

Fig. 1.2 Current limits and forecasted constraints on the tensor-to-scalar ratio, r, as a function of the scalar spectral index n_s, in a ΛCDM model. The blue shaded region shows constraints from a combination of Planck, BICEP2/Keck Array and baryon acoustic oscillation (BAO) data [49]. Also shown (red) are forecasted constraints by the planned CMB-S4 [90] experiment for a fiducial model with $r = 0.003$. Lines show predictions from a number of models as a function of the number of e-folds, N_*, after modes at cosmological scales exited the Hubble radius. Of special note are the Starobinsky model and Higgs inflation, shown as small and large filled circles, respectively. Figure from [366].

some additional mechanism is needed to guarantee that $V(\phi)$ remains almost constant, and that it does so over a wide enough range of $\Delta\phi$. The two simplest frameworks entail either postulating that the field finds itself in a region of phase-space where the potential is approximately flat, or requiring that the potential be convex and steep. The latter class, which includes historically popular models such as the monomial potentials $m^2\phi^2$ or $\lambda\phi^4$, has been severely limited by Planck [373]; see figure 1.2. We now provide a brief introduction to the simplest viable family of models[5]: single-field, 'slow-roll' inflation with Lagrangian $\mathcal{L}(\phi) = \frac{1}{2}(\partial\phi)^2 - V(\phi)$.

It is straightforward to show (see, e.g., [27]) that a scalar field with this Lagrangian evolving in a background FLRW cosmology must follow the equation of motion

$$\ddot{\phi} + 3H\dot{\phi} + V'(\phi) = 0\,, \tag{1.11}$$

where dots and primes denote derivatives with respect to coordinate time and ϕ, respectively. The stress-energy tensor associated with the inflaton can also be calculated

[5] See, e.g., [28] for a generalisation to non-canonical kinetic terms and multiple fields.

from $\mathcal{L}(\phi)$, and the pressure and energy density extracted from it; using these in the Friedmann equations yields

$$H^2 = \frac{1}{3M_{\rm Pl}^2}\left(\frac{1}{2}\dot{\phi}^2 + V(\phi)\right) \tag{1.12}$$

$$\frac{\ddot{a}}{a} = -\frac{1}{3M_{\rm Pl}^2}\left(\dot{\phi}^2 - V(\phi)\right)\,, \tag{1.13}$$

where we have defined the (reduced) Planck mass[6] $M_{\rm Pl} = (8\pi G)^{-1/2}$. Equation (1.13) reveals that inflation happens if $V(\phi) > \dot{\phi}^2$.

It takes two further simplifications — the *slow-roll approximations* — to relate conditions for inflation to happen and persist to the shape of the inflationary potential. Assuming that the potential energy strongly dominates over the kinetic contribution ($\dot{\phi} \ll V$), and neglecting the acceleration in the equation of motion compared to the friction term ($|\ddot{\phi}| \ll |H\dot{\phi}|$), the criteria for sustained inflation become

$$\varepsilon \approx \frac{M_{\rm Pl}^2}{2}\left(\frac{V'}{V}\right)^2 \ll 1 \quad \text{and} \quad |\eta_{\rm inf}| \equiv M_{\rm Pl}^2\frac{|V''|}{V} \ll 1\,. \tag{1.14}$$

Here, $\eta_{\rm inf}$ is a new parameter controlling how fast ε evolves; it must be small if inflation is to last long enough that a grows by at least ~ 55 e-folds (for inflation near the GUT scale $\sim 10^{16}\,$GeV; e.g., [115]).

Granted these requirements are met, inflation will proceed and persist. For a broad class of models, it is also guaranteed to eventually come to an end, as the inflaton rolls down the slope of the potential and finds the true vacuum. However, before it finds a stable equilibrium at the bottom, it will oscillate, while being damped by the Hubble expansion (c.f. equation 1.11). The energy drained away during these oscillations is expected to be transferred to radiation — a process known as 'reheating' (see [272] for a review) — thus kick-starting the hot Big Bang evolution of the Universe.

1.3.2 Characterising perturbations

So far, we have only considered the evolution of perfectly homogeneous and isotropic universes. This is, of course, not the type of universe we inhabit. In order to describe the generation of fluctuations during inflation, let us first introduce a basic framework for studying small perturbations.

[6]Restoring units of c and $\hbar$, $M_{\rm Pl} = [8\pi G/(\hbar c)]^{-1/2} \approx 2.4 \times 10^{18} c^{-2}\,$GeV.

The most general way of perturbing a (spatially-flat) FLRW metric is[7]:

$$\begin{aligned} ds^2 = a^2(\eta)\Big\{&(1+2A)d\eta^2 - 2(\partial_i B + \hat{B}_i)dx^i d\eta + \\ &- [(1+2C)\delta_{ij} + 2\partial_{\langle i}\partial_{j\rangle}E + 2\partial_{(i}\hat{E}_{j)} + h_{ij}]dx^i dx^j \Big\}. \end{aligned} \tag{1.15}$$

Here, we have used conformal time $\mathrm{d}\eta \equiv \mathrm{d}t/a(t)$, and introduced a number of perturbations: A, B, C, E are scalars, $\hat{B}_i, \hat{E}_i$ are divergenceless 3-vectors, and h_{ij} is a divergenceless and traceless 3-tensor; though not denoted explicitly, they are all functions of space and time. This formulation might appear unorthodox at first, but the number of independent perturbations matches the functional degrees of freedom of the metric. More importantly, the decomposition into scalar, vector and tensor components is powerful because, in linear theory, perturbations of different types do not mix [261, 465]. This means the clumping of matter described by scalar perturbations, the vorticity associated with vector modes[8], and the gravitational waves described by tensor perturbations, can all be treated separately when studying the early Universe.

Before we can start thinking about characterising these perturbations observationally, we need to deal with the issue of *gauge freedom*, whereby the value of certain perturbations can change under coordinate transformations. The tensor perturbations, h_{ij}, are gauge-invariant in linear theory, and correspond to physical, transverse and traceless gravitational waves with two polarisation states; they are conserved on super-horizon scales, and quickly oscillate and decay once they enter the horizon [404]. On the other hand, the scalar modes are not gauge invariant. It is therefore worth introducing gauge-invariant quantities on which all observers will agree[9]. One example we will use is the comoving curvature perturbation $\mathcal{R} \equiv C - \nabla^2 E/3 + aH(B+v)$, where $v_i \equiv \partial_i v$ and v_i is the coordinate velocity of the cosmological fluid, $v_i \equiv \mathrm{d}x^i/\mathrm{d}\eta$.[10] This is the perturbation to the intrinsic curvature scalar of hypersurfaces that are orthogonal to worldlines that comove with the total matter, and it has the crucial property of being conserved on super-horizon scales for adiabatic pertubations[11] [20, 275]; taking into

[7]Here, we introduce the notation $\partial_{\langle i}\partial_{j\rangle}E \equiv \partial_i\partial_j E - \delta_{ij}\nabla^2 E/3$ and $\partial_{(i}\hat{E}_{j)} \equiv (\partial_i\hat{E}_j + \partial_j\hat{E}_i)/2$.

[8]We will not consider vector perturbations any further, since any vorticity is expected to rapidly fade away in an expanding Universe.

[9]An alternative is to 'fix the gauge': in this thesis, we will encounter the *spatially-flat gauge* ($C = E = 0$), the *Newtonian gauge* ($B = E = 0$), and the *comoving gauge* ($B = v = 0$, where v is the velocity potential to be defined imminently).

[10]The fluid velocity arises from perturbing the stress-energy tensor, in addition to the metric (see, e.g., [115]). We will skip the details as they are not essential to the rest of this discussion.

[11]Scalar perturbations are 'adiabatic' when, at a given point in spacetime, all fields (matter, radiation, etc.) have the same overdensity relative to their abundance in the background. All observations so far are consistent with adiabatic perturbations (e.g., [366]).

account the appropriate transfer function for evolution inside the Hubble radius (we will discuss this briefly in section 1.4), it can be used to relate perturbations generated during inflation to their observational imprints in the CMB or the large-scale structure (LSS).

The goal of any theoretical model is to give a statistical description of gauge-invariant quantities that can be contrasted with observations. If $f(\boldsymbol{x})$ is a statistically-homogeneous and isotropic function of space — such as the distribution of galaxies, or dark matter — with Fourier transform $f(\boldsymbol{k})$, its two-point correlator can be expressed as

$$\langle f(\boldsymbol{k})f(\boldsymbol{k}')\rangle = \delta(\boldsymbol{k}+\boldsymbol{k}')P(k) \tag{1.16}$$

$$= 2\pi^2\delta(\boldsymbol{k}+\boldsymbol{k}')k^{-3}\mathcal{P}(k)\,. \tag{1.17}$$

In the first line, we have defined the *power spectrum*, $P(k)$, and in the second, we have introduced its *dimensionless* version, $\mathcal{P}(k)$, which speaks more directly to the contribution of each logarithmic interval in k to the real-space variance[12]. (Note that for scale-invariance, $\mathcal{P}(k)$ must be constant, whereas $P(k) \propto k^{-3}$). It is also possible to build higher-point correlators of stochastic fields (the 3-point depends on the 'bispectrum', the 4-point on the 'trispectrum', etc.). However, for zero-mean Gaussian random fields, the statistics are fully described by the power spectrum, since all non-vanishing higher-point correlators can be expressed in terms of it.

In the next section, we will quote predictions from the simplest inflation models for the two-point functions of scalar modes,

$$\langle \mathcal{R}(\boldsymbol{k})\mathcal{R}(\boldsymbol{k}')\rangle = 2\pi^2\delta(\boldsymbol{k}+\boldsymbol{k}')k^{-3}\mathcal{P}_{\mathcal{R}}(k)\,. \tag{1.20}$$

[12] To see this explicitly:

$$\langle f(\boldsymbol{x})^2\rangle = \int \frac{d^3\boldsymbol{k}}{(2\pi)^3}P(k) = \int d\ln k\left[\frac{4\pi}{(2\pi)^3}k^3P(k)\right] \equiv \int d\ln k\mathcal{P}(k)\,. \tag{1.18}$$

Note that other definitions of the power spectrum, differing by factors of 2π, can be found in the literature. This is due to variations in Fourier convention; in this chapter, we work with the symmetric convention, where, in n dimensions,

$$f(\boldsymbol{k}) = \int \frac{d^n\boldsymbol{x}}{(2\pi)^{n/2}}f(\boldsymbol{x})e^{-i\boldsymbol{k}\cdot\boldsymbol{x}} \quad \text{and} \quad f(\boldsymbol{x}) = \int \frac{d^n\boldsymbol{k}}{(2\pi)^{n/2}}f(\boldsymbol{k})e^{i\boldsymbol{k}\cdot\boldsymbol{x}}\,. \tag{1.19}$$

and tensor modes,

$$\langle h^{(p)}(\boldsymbol{k}) h^{(p')}(\boldsymbol{k}') \rangle = 2\pi^2 \delta(\boldsymbol{k}+\boldsymbol{k}') \delta_{pp'} k^{-3} \mathcal{P}_t(k)\,, \tag{1.21}$$

where $h^{(p)}$ is the gravitational wave amplitude in the polarisation state labelled by p.

1.3.3 Primordial power spectra

During a phase of inflation, the scalar and tensor components of the spacetime metric fluctuate as quantum simple-harmonic oscillators with non-zero variance on small scales, on top of a quasi-de Sitter background [180, 157, 462, 22]. As inflation proceeds, these quantum, sub-horizon fluctuations get stretched out to super-horizon scales, where they can be interpreted as classical perturbations to the curvature (in the spatially-flat gauge, inflaton fluctuations are related to curvature perturbations as $\mathcal{R} = -H\delta\phi/\dot{\phi}$) or gravitational waves [154, 460, 404]; see Ref. [27] for a pedagogical review. Their amplitude is then conserved[13] until the Hubble radius — which grows monotonically in the hot Big Bang phase — catches up to their wavelength once again, at which point they 're-enter the horizon' and evolve as prescribed by gravitational and hydrodynamical physics.

In single-field *slow-roll* models, the dimensionless power spectra of primordial scalar and tensor perturbations take the form[14]

$$\mathcal{P}_{\mathcal{R}}(k) = \frac{1}{2M_{\rm Pl}^2}\frac{1}{\varepsilon}\left(\frac{H_k}{2\pi}\right)^2\Bigg|_{k=aH}, \quad \text{and} \tag{1.22}$$

$$\mathcal{P}_t(k) = \frac{8}{M_{\rm Pl}^2}\left(\frac{H_k}{2\pi}\right)^2\Bigg|_{k=aH}. \tag{1.23}$$

The right-hand sides of the expressions are evaluated at the time when modes with wavenumber k exited the horizon. Since H and ε vary slowly during inflation, they change little with k, and the primordial power spectra are almost scale-invariant.

This is a remarkable result. It had been known for several years before the idea of inflation was developed that the spectrum of initial perturbations had to be scale-invariant if it were to eventually give rise to the structures observed in the Universe; such a scale-invariant spectrum came to be known as *Harrison-Zeldovich*, after its first proponents [177, 523]. Inflation generically *predicts* that spectrum.

[13] The quantity $\mathcal{R}$ is only conserved on super-horizon for adiabatic perturbations.

[14] See, e.g., [28] for the results for more general single-field models.

In addition, the simplest models of inflation — including single-field slow-roll — indicate that the perturbations will be adiabatic and very nearly Gaussian (e.g., [276]), in perfect consistency with observations so far [366]. More involved models can produce significant deviations from this behaviour, and indeed searches for non-Gaussianity are a topic of active research; see [25] for a review.

1.3.4 Implications of a detection of tensor modes

In order to connect with observations, it is convenient to parametrise the primordial power spectra as

$$\mathcal{P}_{\mathcal{R}}(k) = A_{\rm s}\left(\frac{k}{k_*}\right)^{n_{\rm s}-1}, \quad \mathcal{P}_t(k) = A_{\rm t}\left(\frac{k}{k_*}\right)^{n_{\rm t}}, \tag{1.24}$$

where k_* is an arbitrary pivot scale (e.g., $k_* = 0.05\,\mathrm{Mpc}^{-1}$). Note the (historical) difference in conventions for scale-invariance: $n_{\rm s} = 1$ vs. $n_{\rm t} = 0$.

The parameters governing the scalar spectrum have been measured from both CMB and LSS surveys and found to be in excellent agreement with expectations: spectra are nearly scale-invariant, with the slight red tilt required for inflation to eventually come to an end, $n_{\rm s} = 0.9652 \pm 0.0042$, and an amplitude $\ln(10^{10} A_{\rm s}) = 3.043 \pm 0.0014$ [371].[15]

Having characterised the scalar perturbations with notable precision, a major next goal in cosmology is to measure the primordial spectrum of tensor perturbations. Unlike $\mathcal{P}_{\mathcal{R}}$, which depends on the detailed inflationary dynamics via ε, $\mathcal{P}_t$ is a direct probe of the energy scale of inflation[16]:

$$\mathcal{P}_t(k) = \frac{128}{3}\left(\frac{E_{\rm inf}}{\sqrt{8\pi}\,\mathrm{M_{Pl}}}\right)^4 = 1.93\times10^{-11}\left(\frac{E_{\rm inf}}{10^{16}\,\mathrm{GeV}}\right)^4 = 2.44\times10^{-11}\left(\frac{r}{0.01}\right). \tag{1.25}$$

In the last line, we have introduced the *tensor-to-scalar ratio*, r, which will be a quantity of unique importance in this thesis. As the name suggests, it is defined as the ratio of tensor-to-scalar power,

$$r \equiv \frac{\mathcal{P}_t(k_*)}{\mathcal{P}_{\mathcal{R}}(k_*)}, \tag{1.26}$$

As we will see shortly, r is best constrained from observations of CMB anisotropies. At the time of writing, the tightest limits come from combining observations by

[15] Remarkably, both the spectral index and the amplitude of fluctuations are comparable to what was originally inferred by Harrison and Zeldovich [305].

[16] It is conventional to define the energy scale of inflation as $E_{\rm inf} \equiv \rho^{1/4}$. Equation (1.25) then follows from combining the Friedman equation, $H^2 = E_{\rm inf}^4/(3M_{\rm Pl}^2)$, with equation (1.23).

BICEP/Keck Array, Planck and WMAP [48]; these place $r < 0.06$ (95 % C.L., at a pivot scale of $0.05\,\mathrm{Mpc}^{-1}$). Planned experiments are expected to dramatically improve on this bound and test popular models such as 'Higgs inflation' [409] or the Starobinsky model [461]; see figure 1.2. There is a vast number of inflationary models in the literature, some predicting values of r so low as to be inaccessible to observations. While upper bounds can still be useful (see below) a detection would be exceedingly important, as the main alternatives to inflation predict vanishing amounts of tensor perturbations (see [90] for an extensive discussion).

Constraints on phenomenological parameters such as r, n_s or n_t can be translated to physical insights if a model is assumed. In the rest of this section, we focus on slow-roll models as an example. To leading order in the slow-roll parameters,

$$r \approx 16\varepsilon\,, \tag{1.27}$$

so the tensor-to-scalar ratio probes the inflationary dynamics at the time when modes with wavenumber k_* (used to define r) exited the horizon. More explicitly, $r(N) = 8(d\phi/dN)^2/M_\mathrm{Pl}^2$. From this, a bound can be derived on the inflaton field range in Planck units [274]:

$$\frac{\Delta\phi}{M_\mathrm{Pl}} = \int_0^{N_*} dN_* \left(\frac{r}{8}\right)^{1/2}\,, \tag{1.28}$$

where N_* is the number of e-folds between the end of inflation and the time when modes with wavenumber k_*, observable in the CMB, exited the horizon. The N_* parameter is poorly constrained, but $N_* \gtrsim 30$ can be used as a conservative estimate [90]. In single-field slow-roll inflation (as in many other models), r increases monotonically, so

$$\frac{\Delta\phi}{M_\mathrm{Pl}} \gtrsim N_* \left(\frac{r_*}{8}\right)^{1/2} \gtrsim \left(\frac{r}{0.01}\right)^{1/2}\,, \tag{1.29}$$

where r_* is defined at the pivot scale k_*. Slow-roll can only proceed as long as it is not 'disturbed' by higher-energy corrections associated with the coupling of gravity to the inflaton. Hence, the inflaton field range is a measure of the energy scale over which quantum gravity corrections are negligible — typically, these are expected to enter below the Planck scale (see, e.g., [90]).

At leading order, one also finds

$$\begin{aligned} &n_\mathrm{s} - 1 \approx 2\eta_\mathrm{inf} - 6\varepsilon\,, \quad \text{and} \\ &n_\mathrm{t} \approx -2\varepsilon\,. \end{aligned} \tag{1.30}$$

The second of these implies a consistency relation for slow-roll inflation, $r = -8n_{\rm t}$, that could in principle be tested observationally. Additional motivations for measuring the tensor spectral index exist: for example, it has been suggested that the frequency spectrum of primordial gravitational waves can be used to map out in detail the thermal history of the Universe [501]. However, gravitational waves quickly decay once they enter the horizon, so that the CMB is likely to be the only viable measurement window for all but the most futuristic proposals; in section 1.5.1.3, we will see how their imprint on CMB polarisation can be identified.

Finally, we note that, as already suggested by equation (1.14), measurements of the slow-roll parameters can be used (at least in principle) to reconstruct the shape of the inflationary potential; see, e.g., [28] for details. More immediately, establishing a hierarchy between parameters can be of importance, especially to inform model-building (e.g., [339]).

1.4 Evolution of perturbations in the linear regime

The early-time behaviour of small perturbations — such as those that inflation might have seeded — can be determined by solving the linearised Einstein and Boltzmann equations for the evolution of all the different perturbed fields, subject to gravity and interactions amongst themselves. Indeed, solutions have been found for a wide range of cosmological models (e.g., [261, 439, 346, 20, 55, 344, 228, 204]). Though a detailed discussion of these is beyond the scope of this thesis (we refer the reader to Ref. [115] for a pedagogical review), our discussion of structure formation in section 1.6 will benefit from an understanding of certain key features that we highlight below.

The fractional excess in density of a certain component of the Universe — matter, radiation, etc. — at some point in space and time (characterising the latter by its redshift in the background cosmology, z) can be denoted as

$$\delta(\boldsymbol{x}, z) \equiv \frac{\rho(\boldsymbol{x}, z) - \bar{\rho}(\boldsymbol{x}, z)}{\bar{\rho}(\boldsymbol{x}, z)}\,, \tag{1.31}$$

where $\bar{\rho}$ is the background density of the component in question. In this thesis, we will only explicitly consider fluctuations in the matter, so we will refer to δ as the matter *overdensity*.

The growth of matter perturbations is sourced by gravity, but damped by cosmic expansion and, below the Jeans scale[17], by pressure gradients. (The latter effect is

[17]The Jeans scale is $c_s[\pi/(G\rho_{\rm m})]^{1/2}$, where c_s is the sound speed of the cosmological fluid [211].

negligible for cold dark matter, but not for baryons, as we will see shortly.) During radiation domination, fluctuations in the radiation density undergo fast oscillations on sub-horizon scales, and the gravitational potential is sourced only by the (subdominant) matter component [297, 506]. In parallel, the background is expanding fast, driven by the dominant radiation density. As a result, gravitational potential modes undergo damped oscillations with an amplitude that decays as a^{-2}, and matter fluctuations grow very slowly, scaling as $\delta \propto \ln a$. Once the Universe transitions to matter domination, sub-horizon matter perturbations grow faster, with $\delta \propto a$, since the timescale for gravitational collapse ($t_{\rm grav} \sim [G\rho]^{-1/2}$) and the timescale for expansion of the background ($t_{\rm exp} \sim [G\bar{\rho}]^{-1/2}$) are almost equal [123]. As soon as Λ comes to dominate, growth stalls.

It is convenient to harness the fact that all sub-horizon perturbations of the cold dark matter density field evolve the same way after matter-radiation equality — the era that we primarily get to observe — to define a linear-theory *growth function*, $D(z)$, such that $\delta(z) \propto D(z)$. For ΛCDM cosmologies, it takes the form [345]

$$D(z) \equiv \frac{5}{2}\Omega_{\rm m} E(z) \int_{\frac{1}{1+z}}^{\infty} \frac{(1+z')}{E^3(z')} dz' \,, \tag{1.32}$$

with $E(z)$ as defined in equation (1.10). This expression is normalised such that, in the matter-dominated era, $D(z) \approx (1+z)^{-1} = a$.

In order to fully describe the amplitude of (linearised) matter fluctuations, it is essential to take into account the fact that modes that enter the horizon during radiation-domination see their growth suppressed until matter-radiation equality. This is conventionally done by defining a wavenumber-dependent *transfer function*, $T(k)$, relating the late-time matter power spectrum after recombination to the primordial curvature perturbation seeded during inflation. In this way, the k-dependence of the power spectrum can be captured as $P(k) \propto T^2(k) P_{\mathcal{R}}(k)$, and the full linear-theory matter power spectrum written as

$$P(k, z) \propto D^2(z) T^2(k) P_{\mathcal{R}}(k) \,. \tag{1.33}$$

Several recent measurements of the matter power spectrum are shown in figure 1.3 (in this discussion, we focus on the comoving-gauge δ). The data are very well described by a ΛCDM model with an almost-scale-invariant spectrum of primordial perturbations. In the context of such a model, the shape of the power spectrum can be understood from first principles.

Consider, first, modes that remain super-horizon for the entirety of the radiation era; i.e., those with $k < k_{\rm eq}$, where $k_{\rm eq}^{-1}$ is the comoving size of the horizon at matter-radiation equality. Matter perturbations are related to the gravitational potential by the Poisson equation, $\delta \propto k^2\Phi$. During the matter- and Λ-dominated eras, Φ is linearly-related to the curvature perturbation $\mathcal{R}$, and independent of scale. It follows that $P(k < k_{\rm eq}) \propto k^4 P_{\mathcal{R}}(k)$, or $T(k < k_{\rm eq}) \propto k^2$. On the other hand, the decay of sub-horizon modes of the gravitational potential during the radiation era causes sub-horizon matter fluctuations to grow only logarithmically (with the scale factor) until matter-radiation equality. Modes with different wavenumbers enter the horizon at different times, and therefore experience varying amounts of logarithmic growth. This imprints a scale-dependence on the power spectrum of the form $P(k > k_{\rm eq}) \propto \ln^2(k/k_{\rm eq}) P_{\mathcal{R}}(k)$ (equivalently, $T[k > k_{\rm eq}] \propto \ln[k/k_{\rm eq}]$) which is preserved after matter-radiation equality when all modes grow by the same amount (in linear theory). Together, these insights mean that, for a scale-invariant spectrum of primordial perturbations — $P_{\mathcal{R}}(k) \propto k^{n_{\rm s}-4}$ with $n_{\rm s} = 1$ — $P(k)$ grows linearly with k for $k < k_{\rm eq}$, and drops approximately as k^{-3} for $k > k_{\rm eq}$; the turnover between the two regimes corresponds to $k \approx k_{\rm eq}$, the comoving scale of matter-radiation equality.

These arguments are, in fact, very crude, as there are important scale-dependent effects. Most notably, baryons and photons are tightly coupled by Thomson scattering prior to recombination ($z \approx 1100$). The baryons thus join the photons in their oscillations, leaving an imprint on the matter distribution after decoupling — the baryon acoustic oscillations (BAO). These oscillations manifest themselves as distinct features in the correlation function of galaxies at around $150\,h^{-1}\,$Mpc, or wiggles in the matter power spectrum. These effects were first detected by [131], and now constitute a powerful cosmological probe (see, e.g., [504] for a review).

1.5 The cosmic microwave background

1.5.1 The primary CMB

The cosmic microwave background (CMB) is the highly isotropic radiation bathing Earth with a blackbody frequency spectrum characterised by a temperature of approximately 3 K. Though there might have been earlier theoretical predictions [11, 145, 118] and even accidental detections (see, e.g., [270]), the first recognised measurement of the CMB was made at millimetre frequencies by Penzias and Wilson in 1967 [348].

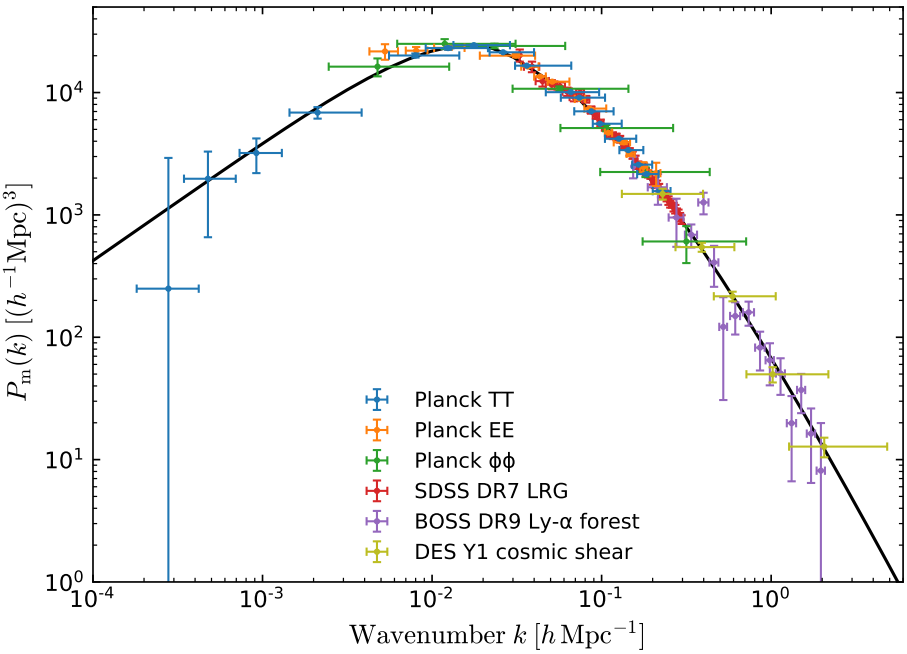

Fig. 1.3 Present-day, linear-theory matter power as inferred from a number of cosmological probes. The black line is a theoretical prediction based on the ΛCDM model best fitting the Planck CMB data. The model provides a remarkably accurate description of data spanning many billions of years of cosmic evolution. Figure from [366].

Immediately, Dicke, Peebles, Roll and Wilkison interpreted it to be the afterglow of an earlier, high-density, high-temperature and ionised phase [110] — the Big Bang.

The reason a 'hot' Big Bang is expected to have produced blackbody radiation is that there ought to have been a time, sufficiently early on, when temperatures and densities were so high that the timescale of thermal processes was shorter than the timescale of expansion. For baryon abundances consistent with observations, this happens at approximately $z \sim 2 \times 10^6$ [70] — about a month after the beginning of time. In section 1.1, we saw that energy conservation requires $\rho_r \propto a^{-4}$ for radiation; at the same time, the Stefan-Boltzmann law tells us that radiation in thermal equilibrium has $\rho_r \propto T_\mathrm{r}^4$, so $T_\mathrm{r} \propto a^{-1}$. This means the radiation temperature evolves the same way as its frequency, which gets redshifted as $\nu \propto a^{-1}$. Since the shape of the blackbody depends (exponentially) on the combination ν/T_r, it must be unchanged through the expansion [505]. Precise determinations of the CMB spectrum had to wait until the 1990s, when the FIRAS instrument aboard COBE could overcome the challenges posed by atmospheric absorption by observing from space; the result was a measurement of the characteristic temperature $T_\mathrm{CMB} = 2.7260 \pm 0.0013\,\mathrm{K}$ [143], and deviations from a perfect blackbody smaller than 0.03% of the maximum intensity over a waveband covering (2.5–0.5) mm.

The remarkable isotropy of the CMB is a result of how homogeneous the early Universe was. However, a small degree of anisotropy is expected — at the level of 1 part in 10^5 — and has indeed been detected; first by COBE's DMR instrument [454] and subsequently with higer precision by other experiments, most notably WMAP [231] and Planck [366]; maps of the microwave sky as seen by the latter are shown in figure 1.4. The expectation of anisotropy can be understood by noticing that the CMB offers a snapshot of the Universe at redshift $z \approx 1100$, when the temperature became low enough for electrons to combine with protons and form hydrogen — the era of cosmic 'recombination'. Prior to this, electrons and photons were coupled together by Thomson scattering; afterwards, the optical depth to Thomson scattering becomes negligibly small, and photons free-stream[18].

The photon phase-space distribution is conserved during free-streaming, so observations of their angular distribution on the sky can be used to probe perturbations in the photon-baryon fluid around the time of recombination. Since the CMB is a two-dimensional field on a sphere, it is useful to express the anisotropies in terms of

[18]With the exception of a small fraction of photons, which do undergo scattering process during cosmic reionisation, or as part of other 'secondary' processes that we will be discussing, to some extent, in section 1.5.3.

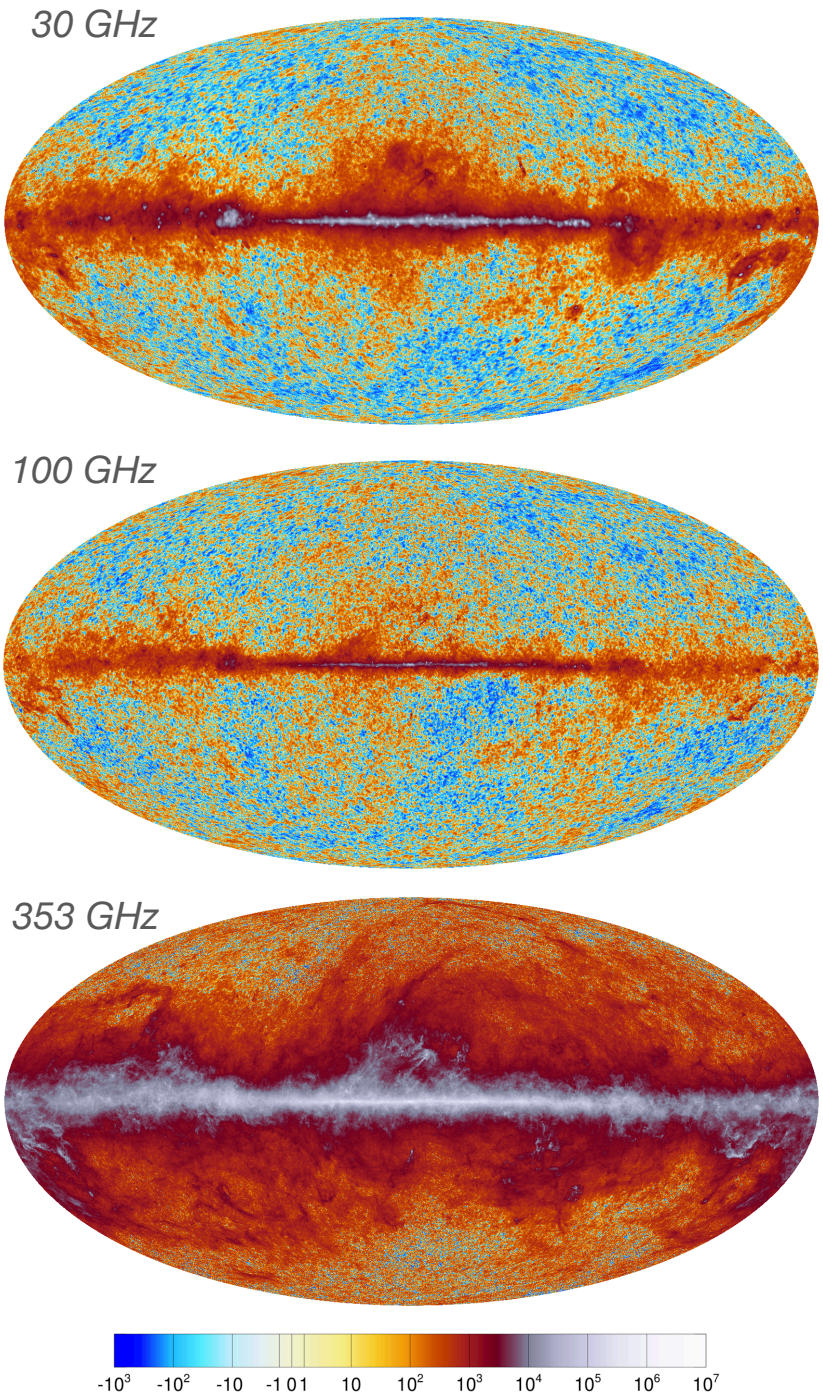

Fig. 1.4 Mollweide projection (in Galactic coordinates and in units of μK) of full-sky intensity maps at 30, 100 and 353 GHz as observed by Planck. Contamination from synchrotron emission is readily apparent in the 30 GHz map near the Galactic plane, while themal dust dominates the 353 GHz channel. Of the three frequencies shown, the CMB is brightest relative to the foregrounds at 100 GHz, particularly away from the Galactic plane. These are just three of Planck's nine frequency channels, which span the frequency range 30–857 GHz. Adapted from `https://www.cosmos.esa.int/web/planck/picture-gallery`.

spherical harmonics as

$$\Delta T(\hat{\boldsymbol{n}}) = \sum_l \sum_{m=-l}^{m=l} a_{lm} Y_{lm}(\hat{\boldsymbol{n}})\,, \tag{1.34}$$

where $\Delta T(\hat{\boldsymbol{n}}) \equiv T(\hat{\boldsymbol{n}}) - T_{\rm CMB}$ is the temperature difference at angular position $\hat{\boldsymbol{n}}$ (we will drop the Δ from now on and refer to the temperature anisotropy as T), and $Y_{lm}(\hat{\boldsymbol{n}})$ are the spherical harmonics. The multipole, l, can be approximately related to the angular scale of anisotropy captured by Y_{lm}: $\theta \sim \pi/l$.

The coefficients, a_{lm}, contain the information about the field; it is through their statistics that observations can be connected with theory. As we have already discussed, the simplest inflationary models predict Gaussian initial perturbations. Linear evolution of these primordial fluctuations up until the time of recombination preserves this Gaussian character, so the CMB fluctuations are expected to be highly Gaussian [62]. Indeed, at the time of writing, no primordial non-Gaussianity has been observed [370]. In the Gaussian limit, all the information in the CMB anisotropies is captured by the angular power spectrum

$$\langle T^*_{lm} T_{l'm'} \rangle = \delta_{ll'} \delta_{mm'} C_l^{TT}\,, \tag{1.35}$$

where the Kronecker delta functions are a consequence of statistical isotropy.

Note that, at angular scale l, there are only $2l+1$ m-modes — that is, $2l+1$ independent pieces of information — that we can hope to measure. Since the CMB anisotropies are stochastic, this fact, which goes by the name of 'cosmic variance', can severely hinder our ability to constrain the physical theories underlying our observations (particularly on large scales, or low l).

Measurements of the angular power spectrum of CMB anisotropies have played a key role in the consolidation of the ΛCDM cosmological model (e.g., [106, 165, 456, 371]). Planck's measurement, shown in figure 1.5, is limited only by cosmic variance for $l \lesssim 1800$; it contains a wealth of information that can be summarised as follows.

On angular scales larger than the Hubble horizon at recombination ($l \lesssim 100$), fluctuations are associated either with super-horizon (and thus primordial) fluctuations at the last-scattering surface, or with modes that entered the horizon after recombination. The contribution from last scattering — the Sachs-Wolfe effect [407] — is produced by super-horizon variations in the gravitational potential, or the primordial curvature perturbation; the amplitude $A_{\rm s}$ and spectral index $n_{\rm s}$ of the primordial power spectrum can be therefore be constrained from it. The measured angular spectrum scales approximately as $C_l^{TT} \propto [l(l+1)]^{-1}$, indicating that the primordial power spectrum

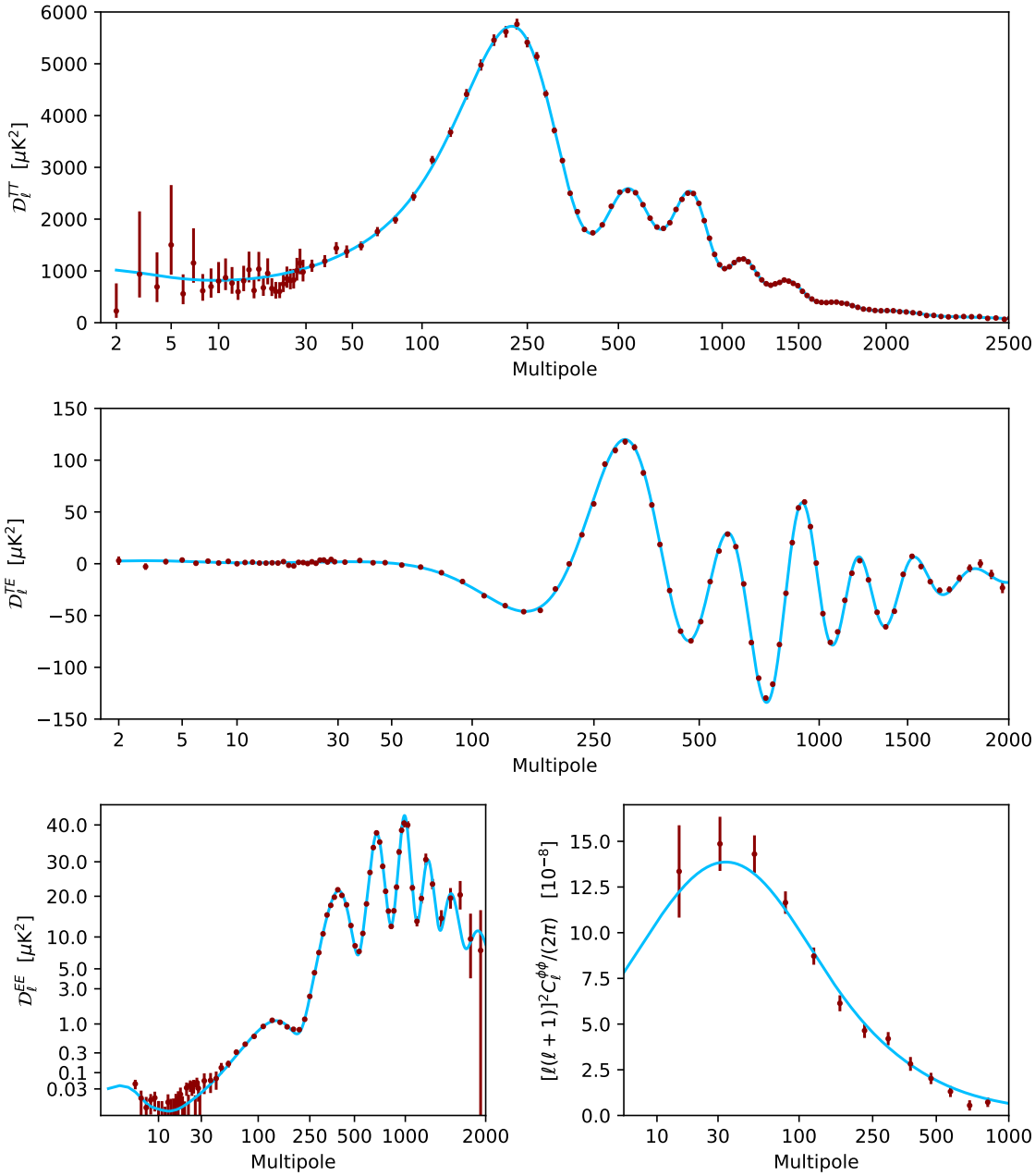

Fig. 1.5 Planck measurements of the CMB temperature angular power spectrum (top panel), T–E correlation (middle panel), E-mode polarisation power spectrum (bottom left) and lensing power spectrum (bottom right). Within each panel, data points are shown as red dots with error bars (below $l \approx 1800$, in TT, uncertainty is due to cosmic variance) and the ΛCDM spectra best fitting the TT, TE and EE spectra are shown as light blue curves. The quantities plotted convey the contribution to the variance of the CMB fluctuations (or fluctuations in the deflection angle, in the case of lensing) per log interval in angular scale: $\mathcal{D}_l^{XY} \equiv l(l+1)C_l^{XY}/(2\pi)$. Figure from [366].

is close to scale-invariant. There is also an 'integrated' Sachs-Wolfe effect (ISW), a frequency shift experienced by photons when the gravitational potential wells they traverse evolve, driven by a component of energy density other than matter (radiation soon after decoupling, or dark energy at low redshift).

The challenge, when it comes to constraining A_s, comes from the fact that a fraction of CMB photons re-scattered after the era of cosmic reionisation ($z \approx 8$ [371]). On scales corresponding to modes that entered the horizon prior to reionisation ($l \gtrsim 10$), the power spectrum is suppressed by a factor of $e^{-2\tau}$, where τ is the optical depth to reionisation; the τ and A_s parameters are therefore degenerate (e.g., [371]). CMB lensing, which we will introduce in the next section, can help get around this issue by providing an independent determination of A_s; and so can measurements of the large-angle polarisation, which are highly constraining of τ (e.g., [105]).

In section 1.4, we briefly mentioned that photons and baryons oscillate jointly on sub-horizon scales before recombination. This results in oscillatory features — 'acoustic' peaks and troughs — at intermediate scales, $250 \lesssim l \lesssim 1000$ (e.g., [203]). The relative heights of the peaks depend on the abundance of baryons and dark matter, and their locations on the sound horizon at recombination and the distance to the last-scattering surface. Hence, peak locations can be used to constrain parameters[19] such as Ω_K [106, 165] or H_0 (see [371]).

Finally, on small angular scales, we see the effects of *Silk damping*, the erasure of perturbations due to photon diffusion [439]. The coupling between photons and baryons is eased progressively, such that the last-scattering surface has non-negligible width. In this regime, photons random walk out of perturbations, over a rather large distance of approximately 30 Mpc, corresponding to $l \sim 1000$; on smaller scales, the perturbations are damped. Measurements of the damping tail can be used to constrain, for example, the effective number of relativistic species — this is one of the main scientific motivations for current and upcoming ground-based, high-resolution measurements of CMB temperature (and polarisation).

The measured angular power spectrum of temperature anisotropies is consistent with having been produced exclusively by scalar perturbations. There can, in principle, be a contribution from tensors, but this falls rapidly for $l > 40$, and measurements on scales larger than that are hindered by the cosmic variance of the scalar perturbations — constraining power is limited to $\sigma(r) \approx 0.08$ because of it [80]. Fortunately, we shall see shortly that there is an observable — the B-mode of CMB polarisation — that bypasses this limitation by having no variance from the primary anisotropies (with

[19] Though note the 'angular-diameter-distance' degeneracy explained in [124].

caveats that we will explore in detail in later chapters). But first, let us introduce a formalism for describing CMB polarisation.

1.5.1.1 Polarisation formalism

Any polarisation field — including diffuse ones, like the CMB — can be described locally in terms of Stokes parameters. The polarisation state of radiation with electric field $\boldsymbol{E}$ in the plane transverse to the propagation can be fully captured by the matrix $\langle E_i(\hat{\boldsymbol{n}}) E_j^*(\hat{\boldsymbol{n}})\rangle$, where the brackets denote zero-lag time averages over an interval that is long compared to the period, but short compared to the timescale of evolution of the field. Like any other 2×2 Hermitian matrix, this can be written in terms of Pauli matrices

$$\begin{aligned}\boldsymbol{P} &= C\langle \boldsymbol{E}(\hat{\boldsymbol{n}})\boldsymbol{E}^\dagger(\hat{\boldsymbol{n}})\rangle \\ &= T(\hat{\boldsymbol{n}})\boldsymbol{\sigma}_0 + Q(\hat{\boldsymbol{n}})\boldsymbol{\sigma}_3 + U(\hat{\boldsymbol{n}})\boldsymbol{\sigma}_1 + V(\hat{\boldsymbol{n}})\boldsymbol{\sigma}_2\,,\end{aligned} \tag{1.36}$$

where

$$\boldsymbol{\sigma}_0 = \begin{pmatrix}1 & 0\\ 0 & 1\end{pmatrix}, \quad \boldsymbol{\sigma}_1 = \begin{pmatrix}0 & 1\\ 1 & 0\end{pmatrix}, \quad \boldsymbol{\sigma}_2 = \begin{pmatrix}0 & -1\\ 1 & 0\end{pmatrix} i\,, \quad \boldsymbol{\sigma}_3 = \begin{pmatrix}1 & 0\\ 0 & -1\end{pmatrix}, \tag{1.37}$$

and we have chosen the constant of proportionality, C, such that the total intensity is equal to the measured CMB temperature, and thus all the Stokes parameters are in temperature units. The Q and U parameters describe the magnitude and direction of linear polarisation, and V parametrises the circular component of polarisation. By symmetry, Thomson scattering cannot source circular polarisation, so we will set $V = 0$ from here on.

From the above, it is clear that the polarisation described by Q is aligned with the axes of our transverse coordinate system, whereas U describes polarisation pointing 45° away from those axes. It is also evident that Q and U depend on the coordinate system of choice. This is a symptom of a more general problem: the impossibility of finding a rotationally-invariant basis of orthogonal vectors on the sphere. If we represent the polarisation as a complex number $Q \pm iU$, this number will transform, under a left-handed rotation of the basis by an angle Ψ, as

$$(Q' \pm iU') \to e^{\pm 2i\Psi}(Q \pm iU). \tag{1.38}$$

Objects that transforms as ${}_s\eta \to e^{is\Psi}{}_s\eta$ under rotations are classified as *spin-s*; hence, polarisation is a spin-2 field on the sphere.

This means that the natural way to describe polarisation is in terms of the tensor eigenfunctions of the Laplace operator on the sphere: the spin-2 spherical harmonics[20] ${}_{\pm2}Y_{lm}(\hat{\boldsymbol{n}})$. Expanding in terms of these,

$$(Q \pm iU)(\hat{\boldsymbol{n}}) = \sum_{lm} (E_{lm} \pm iB_{lm})\,{}_{\pm2}Y_{lm}(\hat{\boldsymbol{n}})\,. \tag{1.39}$$

Conveniently, the E- and B-mode fields are scalars, and thus do not depend on coordinates. This nomenclature appropriately captures the electric or magnetic behaviour of each type of coefficient under parity inversion: E is parity-even, with $E'_{lm} \to (-1)^l E_{lm}$, while B is parity-odd, with $B'_{lm} \to (-1)^{l+1} B_{lm}$. This property is invariant under rotations, so it is preserved when contributions from many different modes are added together.

As in the case of temperature, statistical isotropy requires

$$\begin{aligned}
\langle E^*_{lm} E_{l'm'} \rangle &= \delta_{ll'}\delta_{mm'} C_l^{EE}\,, \\
\langle B^*_{lm} B_{l'm'} \rangle &= \delta_{ll'}\delta_{mm'} C_l^{BB}\,, &(1.40)\\
\langle T^*_{lm} E_{l'm'} \rangle &= \delta_{ll'}\delta_{mm'} C_l^{TE}\,. &(1.41)
\end{aligned}$$

On the other hand, TB and EB correlations vanish if the physical mechanisms that produce and process the fluctuations respect parity.

In the majority of this work, we will strive for simplicity and work in the flat-sky approximation, rather than make explicit use of the spin-weighted spherical harmonics introduced above. It can be shown that, on small patches of sky, spherical harmonic transforms reduce to Fourier transforms. Alternatively, we can use our knowledge regarding the transformation properties of Q and U (equation 1.38) to write [423]

$$\begin{aligned}
E(\mathbf{l}) \pm iB(\mathbf{l}) &= -\int \frac{d^2\mathbf{x}}{2\pi}\, [Q'(\mathbf{x}) \pm iU'(\mathbf{x})]\, e^{-i\mathbf{l}\cdot\mathbf{x}} \\
&= -\int \frac{d^2\mathbf{x}}{2\pi}\, [Q(\mathbf{x}) \pm iU(\mathbf{x})]\, e^{\mp 2i\psi_{\mathbf{l}}} e^{-i\mathbf{l}\cdot\mathbf{x}}\,,
\end{aligned} \tag{1.42}$$

where in the last line we have introduced the factor $e^{\mp 2i\psi_{\mathbf{l}}}$ to rotate the measured $Q(\mathbf{x})$ and $U(\mathbf{x})$ to a more natural basis defined by the wavevector itself ($\psi_{\mathbf{l}}$ is the angle

[20] These are a special case of the Newman-Penrose spin-weighted spherical harmonics, which can be obtained from the standard (spin-0) spherical harmonics via spin-raising and lowering operators [327].

between $\mathbf{l}$ and the x-axis used to define the Stokes parameters). It follows that

$$(Q \pm iU)(\mathbf{x}) = -\int \frac{d^2\mathbf{l}}{2\pi} \left[E(\mathbf{l}) \pm iB(\mathbf{l})\right] e^{\pm 2i\psi_{\mathbf{l}}} e^{i\mathbf{l}\cdot\mathbf{x}} \,. \tag{1.43}$$

Of course, the parity properties of the scalar modes are also manifest in the flat-sky formulation, now in the form of $E(\boldsymbol{l}) \to E(-\boldsymbol{l})$ and $B(\boldsymbol{l}) \to -B(-\boldsymbol{l})$. It is also worth pointing out a more local characterisation of E- and B-modes, which becomes apparent after Fourier-transforming equation (1.43): for a pure E-mode in the $\hat{x}$-direction, $Q(\boldsymbol{l}) = E(\boldsymbol{l})$ and $U(\boldsymbol{l}) = 0$, while for a pure B-mode in the $\hat{x}$-direction, $Q(\boldsymbol{l}) = 0$ and $U(\boldsymbol{l}) = B(\boldsymbol{l})$. Hence, E-modes describe polarisation that varies in directions parallel or perpendicular to the polarisation direction, whereas B-modes capture polarisation that varies at 45° to it (see, e.g., [205]).

For completeness, we give also the flat-sky approximation of the temperature anisotropies, which is simply given by the two-dimensional Fourier transform

$$T(\mathbf{x}) = \int \frac{d^2\mathbf{l}}{2\pi} T(\mathbf{l}) e^{i\mathbf{l}\cdot\mathbf{x}} \,. \tag{1.44}$$

In the flat-sky approximation, the non-vanishing, statistically-isotropic correlators in equation (1.40) become

$$\langle E^*(\boldsymbol{l}) E(\boldsymbol{l}')\rangle = \delta(\boldsymbol{l} - \boldsymbol{l}') C_l^{EE} \,,$$
$$\langle B^*(\boldsymbol{l}) B(\boldsymbol{l}')\rangle = \delta(\boldsymbol{l} - \boldsymbol{l}') C_l^{BB} \,, \tag{1.45}$$
$$\langle T^*(\boldsymbol{l}) E(\boldsymbol{l}')\rangle = \delta(\boldsymbol{l} - \boldsymbol{l}') C_l^{TE} \,. \tag{1.46}$$

1.5.1.2 CMB polarisation anisotropies

Thomson scattering of CMB photons off electrons gives rise to linear polarisation if the incident radiation possesses a quadrupole of anisotropy in the rest frame of the electrons [389]. Both scalar and tensor perturbations can produce this [215, 61, 381]: heuristically, the shear of gravitational waves red/blueshifts the wavelengths of photons in a quadrupolar fashion along the plane perpendicular to the wave's propagation direction, while the temperature and gravitational potential gradients associated with scalar perturbations induce bulk motions of photons parallel to the perturbation direction (e.g., [205]). Polarisation of the CMB was first detected by DASI in 2002 [234] and it has been measured by a number of experiments since; to date, all of them showed consistency with expectations for scalar perturbations, with no contribution from tensors [366].

Any anisotropy in the photon distribution induced prior to recombination is readily quenched by subsequent scattering events. Consequently, all that is needed to understand CMB polarisation is the state of the plasma at the time, and shortly before, the CMB is released; it is only then that a significant quadrupole can build up. The largest source of polarisation is the Doppler shift associated with the velocity of the plasma [519]. As we will see heuristically in the next section, this produces E-mode polarisation. Planck's measurements of the E-mode spectrum are shown in the bottom, left panel of figure 1.5, and they can be understood as follows. Since the baryon-photon fluid is undergoing oscillations on sub-horizon scales, the polarisation has acoustic features on scales smaller than the sound horizon at recombination. However, the velocity is 90° out of phase with the density, so the E-mode spectrum has peaks where the temperature has troughs, and vice versa. This TE correlation has indeed been measured (see the central panel of figure 1.5) and interpreted as evidence of the pre-recombination origin of perturbations. (Moreover, it has been noted that the anti-correlation for multipoles $50 \lesssim l \lesssim 200$ is a sign of adiabatic perturbations [457, 114].) Finally, the power spectrum of E-modes produced at recombination peaks at the scale subtended by the mean free path to Thomson scattering around that time ($l \sim 1000$), and has little power on small scales because of diffusion damping, and large scales due to the fact that no significant quadrupole can build up by free-streaming on scales larger than the mean free path.

Measurements of E-modes have been used to improve constraints on r beyond what can be done with temperature only (e.g., [371]) but, like temperature, they are ultimately limited by the cosmic variance of scalar perturbations. In the next section, we explain the crucial result that B-modes have no variance from scalar fluctuations (at leading order), and thus constitute a powerful probe of primordial tensor perturbations.

1.5.1.3 Generation of a primordial B-mode

We now know that scalar perturbations do not source a B-mode of polarisation (at leading order), while tensors do [219, 426]. The reasons, in broad brush, are the following.

In order to preserve parity, Thomson scattering of a quadrupole of anisotropy can only produce polarisation that locally looks like an E-mode. However, what we actually observe is the local pattern *modulated* across the last-scattering surface. This changes the amplitude, sign and angular dependence of the polarisation, though it preserves the Q or U character. There is then a critical difference between the pattern produced by scalar perturbations and that produced by tensors, which becomes apparent when

we consider a plane wave perturbation travelling along the $\hat{z}$-direction at the time of last scattering.

A scalar plane wave perturbation generates a sinusoidal succession of temperature troughs and crests along the direction of propagation. This results in a polarisation pattern that is locally-Q, and which, upon projection, points either along, or perpendicular to, the direction of propagation/variation; hence it will be seen as an E-mode by an observer at the origin. (The visualisations in Ref. [205] are useful to build intuition.)

On the other hand, the temperature anisotropy induced by a tensor perturbation travelling along $\hat{z}$ is restricted to the plane perpendicular to the propagation direction, so locally, it contains both Q and U components. This is crucial because, upon modulation, the U-part will be at 45° to the direction of variation (the $\hat{z}$-direction), so it will result in a B-mode. For reasons of parity conservation, this B-mode nature will survive integration over all possible propagation directions. Hence, at leading order, *scalar perturbations only give rise to E-modes, while tensor perturbations produce both E- and B-modes.*

A numerical calculation of the primordial B-mode spectrum is shown in figure 1.6, as blue curves. A quadrupole of anisotropy can only arise once gravitational waves enter the horizon and begin to evolve, shearing the photon distribution. We thus expect there to be power only on angular scales smaller than the angle subtended by the horizon at last scattering; i.e., multipoles $l \gtrsim 100$. (In reality, projection effects cause there to be small but non-vanishing amounts of power on large scales.) Since the amplitude of gravitational waves decays most rapidly (shear is largest) immediately after they enter the horizon, the primordial B-mode spectrum peaks at $l \approx 100$. Modes that entered the horizon earlier on are more damped by the time of recombination, so their shearing effect is smaller; hence, power falls for $l \gtrsim 100$. On scales smaller than the mean-free path to Thomson scattering at recombination, the finite width of the last scattering surface becomes important, and oscillations are damped because of phase cancellations between different modes (Landau damping) [386]. Note, finally, the increase in primordial B-mode power at the very largest scales, $l < 10$. This is due to re-scattering at reionisation, and so peaks around the angular size of the horizon at $z \approx 8$. The amplitude of this 'reionisation bump' is proportional to the square of the optical depth to reionisation[21].

To summarise the important point of this section: to leading order, the primordial B-mode polarisation of the CMB is only sourced by tensor perturbations, and is thus a

[21] According to current contraints, $\tau \approx 0.063 \pm 0.006$ [105], so approximately 6% of photons scattered again after recombination.

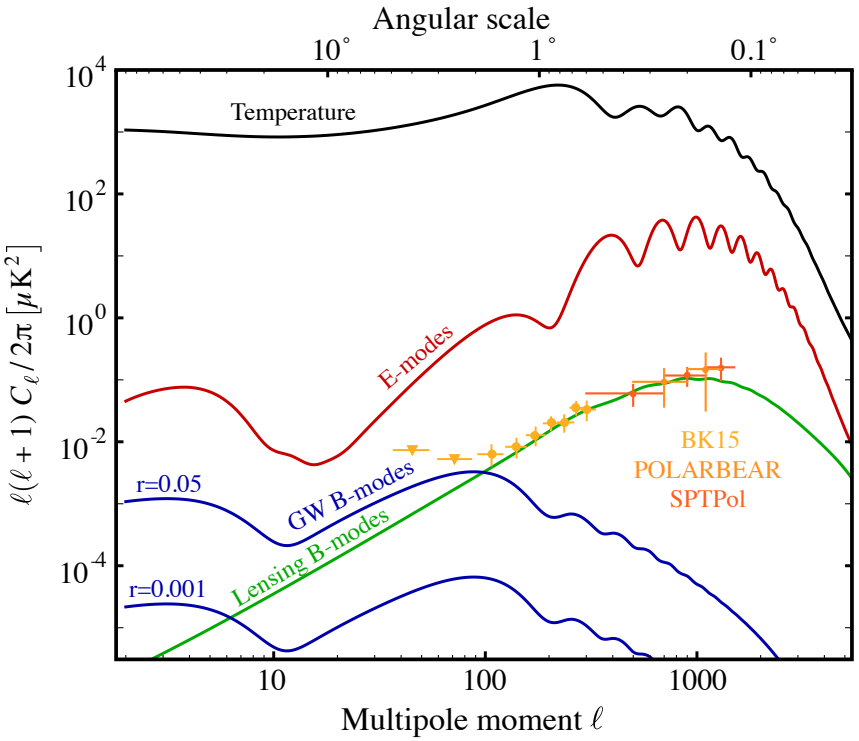

Fig. 1.6 Theoretical calculations of the temperature (black), E-mode (red), and primordial B-mode (blue) angular power spectra (the latter shown for values of the tensor-to-scalar ratio of $r = 0.05$ and $r = 0.001$). Predictions for the lensing B-mode spectrum are shown in green, and measurements from different experiments are overlaid: those from BICEP2/Keck [48] (yellow), POLARBEAR [379] (light orange) and SPTpol [459] (dark orange). Figure from [1]. The lensing signal can be partially removed by delensing.

rather clean probe of inflation (or whatever mechanism set up the initial perturbations). Observations on degree-scales ($l \approx 100$), are expected to be most discerning, since those are the scales where the power spectrum of primordial B-modes peaks. There is also a sizeable 'reionisation bump' at $l < 10$ but, as we shall discuss shortly, measurements of the polarisation on those angular scales are likely to only be attainable from space. In addition to the importance of a measurement of, or even an upper bound on, the tensor mode spectrum (see section 1.3.4), constraining r from B-modes has the added benefit of breaking the degeneracy between r and $n_{\rm s}$ that is present when both are inferred from the temperature and E-mode polarisation (e.g., [28]); in this way, constraints are less model-dependent. Hence, these measurements also indirectly improve our understanding of the scalar perturbations.

The caveat at the beginning of the previous paragraph is an important one: at second order, gravitational lensing can produce B-modes from scalar perturbations, and in amounts that seriously complicate measurements of a primordial signal. We now turn to explaining this issue in detail.

1.5.2 CMB lensing

Gravity can bend the path of light. It was Eddington and his collaborators' observation of this fact — by measuring the shift in the apparent positions of stars in the Hyades cluster due to their angular proximity to the eclipsing sun — together with their confirmation that the size of the deflection was a factor of two larger than the Newtonian prediction, that famously vindicated Einstein's general theory of relativity [122]. Since those early days, gravitational lensing has grown to become one of the most fruitful tools in modern astrophysics and cosmology. There are excellent reviews that the reader might wish to consult for a general introduction to the topic, such as Refs. [24, 116].

Here, we will focus on gravitational lensing of CMB photons [52, 92, 265, 422], which affects the statistical properties of the ensemble in crucial ways. Below, we highlight some key concepts, following Ref. [252]. We first characterise the deflection of photon paths in section 1.5.2.1. Then, in section 1.5.2.2, we show what impact lensing has at the map and power spectrum level. Crucially, we explain that lensing produces B-modes from scalar perturbations already at leading order. This needs to be 'delensed' if we are to detect primordial B-modes with small values of r, as explained in section 1.5.2.3. A critical ingredient of the delensing program is being able to reconstruct the lensing potential from the CMB itself. We describe how this can be done in section 1.5.2.4.

1.5.2.1 The deflection angle

The starting point for an understanding of CMB lensing is the perturbed FLRW metric of equation (1.15). In Newtonian gauge, and considering only scalar perturbations[22], it gives

$$\mathrm{d}s^2 = a^2(\eta)(1+2\Psi_\mathrm{N})\mathrm{d}\eta^2 - a^2(\eta)(1+2\Phi_\mathrm{N})\left[\mathrm{d}\chi^2 + f_K^2(\chi)\left(\mathrm{d}\theta^2 + \sin^2\theta\mathrm{d}\phi^2\right)\right] , \quad (1.47)$$

where we have introduced the gauge-invariant scalar potentials Ψ_N and Φ_N; in linear theory, these are related to the primordial curvature perturbation, $\mathcal{R}$, through simple transfer functions. For the purposes of lensing, it turns out that we only need to worry about the combination $\Psi \equiv (\Psi_\mathrm{N} - \Phi_\mathrm{N})/2$ — the 'Weyl potential'. The Poisson equation describes how this is sourced by the matter fluctuations[23]:

$$\left(\nabla^2 + \frac{3K}{a^2}\right)\Psi = 4\pi G\bar{\delta\rho} \quad (1.48)$$

where $\bar{\delta\rho}$ is the total (comoving) perturbation to the energy density.

The trajectories of CMB photons in an inhomogeneous Universe can be determined by solving the geodesic equation for null geodesics in the spacetime described by equation (1.47). It turns out that the deflections are small and can be treated perturbatively (at least on scales $\gtrsim 1\,\mathrm{arcmin}$, corresponding to the typical size of the deflections).

To see why, let us follow the explanation in Refs. [252, 171]. Consider, first of all, what size structures are most responsible for the deflections experienced by a photon on its journey from the last-scattering surface to Earth. Naturally, the smaller the structures, the more of them there ought to be along any line of sight. On the other hand, the gravitational potential of modes that enter the horizon during radiation domination decay rather quickly (see, e.g., Ref. [115]), while it is conserved for those that enter later on, during matter domination. Hence, for a scale-invariant primordial spectrum of fluctuations, lensing will be dominated by the smallest structures (shortest-wavelength modes) that entered during matter domination. There are approximately $14000/300 \approx 50$ of those along a given line of sight, since the comoving distance to last scattering is approximately $14000\,\mathrm{Mpc}$, and the scale of matter-radiation equality is $\sim 300\,\mathrm{Mpc}$. Let us, on the other hand, model each deflection event as being

[22] Tensor modes can also give rise to lensing, though the effect is expected to be much smaller [218, 117], so we ignore it here.

[23] Rigorously speaking, there should be a term proportional to the anisotropic stress on the RHS of equation (1.48). However, its effect is negligible during matter and dark energy domination — when lensing happens — so we ignore it here. Note also that, in the absence of anisotropic stress, $\Psi_\mathrm{N} = -\Phi_\mathrm{N} = \Psi$.

produced by a point source mass with potential $\Psi_{\rm ps}$; GR predicts the deflection to be $4\Psi_{\rm ps}$ (up to geometric factors of order unity, and in units of $c = 1$). The depth of the Newtonian potentials is typically 2×10^{-5}, so the deflection from each lens is of $O(10^{-4})$. The total deflection angle is the accumulation of all the individual deflections along the line of sight; assuming the deflections are all independent[24], its size is approximately $|\alpha| \sim 50^{1/2}\, 10^{-4} \approx 2\,\mathrm{arcmin}$. (Larger deflections, which in principle could lead to multiple images such as those first detected by Ref. [497] for quasars, are certainly common on sub-arcminute scales in association with cluster substructure and galaxies [193, 132]; however, their effect is unobservable because on those scales the primordial CMB has few features due to Silk damping.) Finally, note that the structures responsible for the largest share of the lensing effect subtend angular scales of approximately $300/7000 \approx 2\,\mathrm{degrees}$ (7000 Mpc is half the comoving distance to the last-scattering surface, the distance at which lensing is most efficient for geometric reasons). Consequently, the arcminute-scale deflections are coherent on degree scales.

Detailed solutions to the geodesic equation in the perturbed background are provided in Ref. [252] and references therein. Here, we will simply highlight the fact that, to leading-order in Ψ, it suffices to evaluate the resulting integrals along the unperturbed photon path — the well-known 'Born approximation'. Although in principle there is an $O(\Psi)$ radial effect in the form of a Shapiro time delay [199], its impact is negligible compared to that of tangential deflections. The latter are encapsulated by the deflection angle,

$$\boldsymbol{\alpha}(\hat{\boldsymbol{n}}) = -2 \int_0^{\chi_*} d\chi \frac{f_K(\chi_* - \chi)}{f_K(\chi_*) f_K(\chi)} \boldsymbol{\nabla}_{\hat{\boldsymbol{n}}} \Psi(\chi \hat{\boldsymbol{n}}; \eta_0 - \chi)\,, \tag{1.49}$$

where $\hat{\boldsymbol{n}}$ is a unit vector along the line of sight, and $\boldsymbol{\nabla}_{\hat{\boldsymbol{n}}}$ denotes the covariant derivative on the sphere; this detail will be implicit in our notation from here on.

The deflection angle relates the observed angular position of an image, $\hat{\boldsymbol{n}}$, to its true position, $\hat{\boldsymbol{n}}'$, via the lens equation

$$\hat{\boldsymbol{n}} = \hat{\boldsymbol{n}}' - \boldsymbol{\alpha}(\hat{\boldsymbol{n}})\,. \tag{1.50}$$

[24] The independence of lensing events is also embedded in the Born approximation, to be defined shortly.

To linear order, the effects of lensing are fully described by the magnification matrix[25]

$$\frac{\partial \hat{n}_i'}{\partial \hat{n}_j} = \begin{bmatrix} 1-\kappa-\gamma_1 & -\gamma_2+\omega \\ -\gamma_2-\omega & 1-\kappa+\gamma_1 \end{bmatrix} \tag{1.52}$$

(we have chosen to work in a locally-Cartesian frame on the sphere). Here, κ is the convergence, $\gamma = \gamma_1 + i\gamma_2$ is the complex shear and ω is the image rotation.

An image is rotated every time the deflection from a given lens is affected by that from another, higher-redshift lens [199]. (Or, possibly, by the presence of vector or tensor modes [258, 33, 516].) This effect has been shown to be small, with ω vanishing to leading order in Ψ [199, 190]. Note, however, that field rotation constitutes one of the leading corrections to the standard calculation of the lensing B-mode power (to be described in the following section) on the scales of interest to searches for a primordial component [384, 256]. Although its power is four orders of magnitude smaller that sourced by convergence, some authors have suggested that rotation B-modes might pose a fundamental limit to our ability to delens [190]; recent discussions have been more optimistic, as it appears that estimators for the rotation can in fact be derived [94, 321].

A shearing of background images by a foreground distribution of matter, the cornerstone of galaxy weak lensing studies, is also manifested in the CMB as an induced ellipticity of the hot and cold spots of its anisotropy pattern. In particular, the γ_1 shear compresses a spot along its x-axis and stretches it along the y-axis, causing an image on the last-scattering surface with infinitesimal angular size $\mathrm{d}\theta$ to appear as $(1-\gamma_1)\mathrm{d}\theta_x$ and $(1+\gamma_1)\mathrm{d}\theta_y$ along each of the axes. The γ_2 shear, on the other hand, compresses along the $y = x$ axis and stretches along $y = -x$. These effect are detectable [40, 489], and can be harnessed to reconstruct lensing maps (more on this in section 1.5.2.4) in a way that is robust to contamination from extragalactic foregrounds [67, 412].

There is a significant difference with galaxy weak lensing, however, in that CMB lensing can be used to extract information from the convergence, not just the shear. This is because the distribution of sizes of the hot and cold spots of the unlensed CMB is very well understood, whereas the intrinsic sizes of galaxies are unknown. At lowest

[25] The name comes from the fact that, since lensing conserves surface brightness, the overall magnification of an image, μ, can be obtained as

$$\mu = \left| \frac{\partial \hat{n}_i'}{\partial \hat{n}_j} \right|^{-1} . \tag{1.51}$$

order, $\mathrm{d}\theta \to (1+\kappa)\mathrm{d}\theta$, so the convergence causes a magnification (or demagnification) of the background image.

Since both the convergence and the shear can be obtained from the deflection angle, it is convenient to work directly with the latter. If we ignore the effect of rotations[26], the deflection angle is fully determined by $\boldsymbol{\alpha}(\hat{\boldsymbol{n}}) = \boldsymbol{\nabla}\phi(\hat{\boldsymbol{n}})$, where we have defined a scalar lensing potential,

$$\phi(\hat{\boldsymbol{n}}) = -2\int_0^{\chi_*} d\chi \frac{f_K(\chi_* - \chi)}{f_K(\chi_*) f_K(\chi)} \Psi(\chi\hat{\boldsymbol{n}}; \eta_0 - \chi)\,. \tag{1.53}$$

It follows from equation (1.52) that the convergence can be obtained from this lensing potential as

$$\kappa = -\frac{1}{2}\nabla^2\phi\,, \tag{1.54}$$

and similarly for the shear components,

$$\gamma_1 = -\frac{1}{2}\left[\frac{\partial^2\phi}{\partial\theta_x\partial\theta_x} - \frac{\partial^2\phi}{\partial\theta_y\partial\theta_y}\right] \quad \text{and} \quad \gamma_2 = \frac{1}{2}\frac{\partial^2\phi}{\partial\theta_x\partial\theta_y}\,. \tag{1.55}$$

We can use equation (1.53) to gain an understanding of how different redshifts contribute to lensing. A numerical calculation of the lensing potential power spectrum, using `CAMB` [254] and `Halofit` [450] to account for non-linear fluctuations of the matter, is shown in Figure 1.7. The lensing kernel is wide, with contributions ranging from the local Universe all the way to $z \approx 1100$, but peaking at $z \sim 2$; this can be understood from our reasoning earlier that the lensing effect must be dominated by structures of comoving size $\sim 300\,\mathrm{Mpc}$ located half way to the last-scattering surface (that is, $z \sim 2$). Those structures project to $\sim 2\,^\circ$, or equivalently $l \sim 60$, thus setting the peak of the lensing power spectrum.

In principle, to improve on the accuracy of equation (1.49), one must simultaneously include higher-order contributions to the Newtonian potentials and relax the Born approximation; instructions on how to do this rigorously are provided in Refs [257] and [384]. In practice, post-Born corrections are small, and non-Gaussianities from the non-linear evolution of matter are reduced extensively by both the predominance of high-redshift contributions to lensing, and the fact that many different modes are projected together along the line of sight (thus 'Gaussianising' the distribution by the central limit theorem). The principal non-linear effect is then an increase of the variance

[26]Note that, though the deflection angle is a two-component vector, the lensing potential in equation (1.53) represents only one degree of freedom. The other one, which is associated with rotations, can be similarly described by a curl potential; see, e.g., Refs. [190, 384].

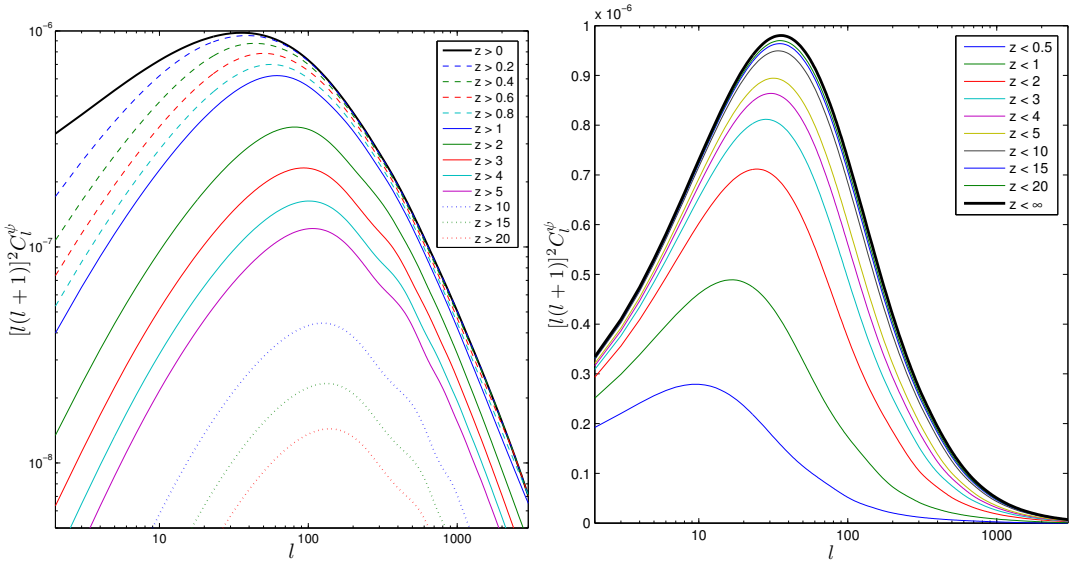

Fig. 1.7 Cumulative contribution of different redshifts to the power spectrum of the CMB lensing potential in a ΛCDM cosmology. (Note that ψ in the figures corresponds to ϕ in our notation.) The $[l(l+1)]^2$ scaling is to connect with the contribution per logarithmic interval to the variance of the deflection angle (c.f. equation 1.62); at the same time, this makes the plotted quantity be proportional to the convergence power spectrum. These curves, which were calculated using `CAMB` [254], take into account non-linear fluctuations of the matter by using the `Halofit` code [450]. From Ref. [252].

of the matter fluctuations on small scales, which is routinely incorporated into lensing calculations — still under the assumption of Gaussian ϕ — by means of a mixture of perturbative models and simulation-based techniques (e.g., using `Halofit` [450]). However, note that non-Gaussianities can have significant impact on small scales [257].

1.5.2.2 The lensed CMB fields

The discussion in the previous section suggests that the lensed and unlensed CMB temperature anisotropies can be related as[27]

$$\tilde{T}(\boldsymbol{x}) = T(\boldsymbol{x}') = T(\boldsymbol{x} + \boldsymbol{\alpha}(\boldsymbol{x}))\,. \tag{1.56}$$

[27] Rigorously speaking, the deflection is by a distance $|\boldsymbol{\alpha}(\boldsymbol{x})|$ along the spherical geodesic through $\boldsymbol{x}$ that has initial unit tangent vector $\hat{\boldsymbol{\alpha}}(\boldsymbol{x})$ [81]. In the case of polarisation, the linear polarisation tensor ought to be parallel transported along this geodesic. Hence, equations (1.56) and (1.57) implicitly rely on the flat-sky approximation, to be introduced shortly.

Throughout this work, tildes will identify lensed fields.

The case of polarisation is slightly more nuanced, as the polarisation tensor must be parallel-transported along the deflected photon path. At lowest order, the observed polarisation angle is the same as that at the un-deflected emission position (when both are defined with respect to the photon's geodesic) [252], so we can also write

$$\tilde{P}(\boldsymbol{x}) = P(\boldsymbol{x}') = P(\boldsymbol{x} + \boldsymbol{\alpha}(\boldsymbol{x}))\,, \tag{1.57}$$

where P denotes the real-space polarisation field $P = Q + iU$, and Q and U are defined on a fixed basis. At higher order, the assumption that the deflected photon path is normal to the unperturbed last-scattering surface breaks down, and this induces a net rotation of the polarisation angle that cannot be captured by the remapping operation above. We ignore this small effect here, and refer the reader to Ref. [256] for details.

We can gain an understanding of how lensing affects the CMB fields by performing a series expansion in terms of the small deflection angles, as in Ref. [196], for example. This gives

$$\tilde{T}(\boldsymbol{x}) = T(\boldsymbol{x} + \boldsymbol{\alpha}(\boldsymbol{x})) = T(\boldsymbol{x}) + \alpha^i \nabla_i T(\boldsymbol{x}) + \frac{1}{2}\alpha^i \alpha^j \nabla_i \nabla_j T(\boldsymbol{x}) + \cdots \tag{1.58}$$

for temperature, and

$$\tilde{P}(\boldsymbol{x}) = P(\boldsymbol{x} + \boldsymbol{\alpha}(\boldsymbol{x})) = P(\boldsymbol{x}) + \alpha^i \nabla_i P(\boldsymbol{x}) + \frac{1}{2}\alpha^i \alpha^j \nabla_i \nabla_j P(\boldsymbol{x}) + \cdots \tag{1.59}$$

for polarisation. This approach is valid when considering the remapping of CMB modes with wavelengths much larger than the typical scale of the deflections, or $l \lesssim 2000$. Interestingly, correlators calculated to leading order in lensing become accurate again on very small scales, $l \gtrsim 5000$, where there is very little power in the unlensed CMB because of diffusion damping, and it can regarded as a pure gradient [200, 252]. The same range of validity holds for polarisation, which is similarly damped on small scales. On intermediate scales between those two regimes, where the series expansion incurs an error of $O(5\%)$, non-perturbative calculations using correlation functions prove much more accurate [422, 84] — they are valid on all scales.

In this work, we will frequently use the flat-sky approximation, where harmonic transforms become two-dimensional Fourier transforms. This route is transparent and actually quite accurate, particularly for experiments covering only a fraction of the sky. Note, however, that lensing couples long and short CMB modes, so the benefits

of using a harmonic approach, as in Ref [196], can manifest themselves across a wide range of scales [84].

Working in this flat-sky limit, and assuming that the deflection angle is fully described by $\boldsymbol{\alpha} = \boldsymbol{\nabla}\phi$, equation (1.58) can be Fourier-transformed to give

$$\begin{aligned}\tilde{T}(\boldsymbol{l}) = \quad & T(\boldsymbol{l}) - \int \frac{\mathrm{d}^2\boldsymbol{l}'}{2\pi} \boldsymbol{l}' \cdot (\boldsymbol{l} - \boldsymbol{l}') T(\boldsymbol{l}') \phi(\boldsymbol{l} - \boldsymbol{l}') \\ & - \frac{1}{2} \int \frac{\mathrm{d}^2\boldsymbol{l}'}{2\pi} \frac{\mathrm{d}^2\boldsymbol{l}''}{2\pi} \boldsymbol{l}' \cdot [\boldsymbol{l}' + \boldsymbol{l}'' - \boldsymbol{l}] \boldsymbol{l}' \cdot \boldsymbol{l}'' T(\boldsymbol{l}') \phi(\boldsymbol{l}'') \phi^*(\boldsymbol{l}' + \boldsymbol{l}'' - \boldsymbol{l}) + O(\phi^3) \,. \quad (1.60)\end{aligned}$$

Already at $O(\phi)$, in the second term, we can see that lensing causes $\tilde{T}$ on a given scale, $\boldsymbol{l}$, to depend on T at a wide range of scales, $\boldsymbol{l}'$; i.e., it induces mode-coupling. We will now see what impact this has on the CMB spectrum, and in section 1.5.2.4, we will discuss how that can be used to reconstruct the particular realisation of the lenses on the sky.

The angular power spectrum of the lensed temperature anisotropies can be readily obtained[28] from the expression above, giving [196]

$$\tilde{C}_l^{TT} \approx (1 - l^2 \langle \boldsymbol{\alpha}^2 \rangle / 2) C_l^{TT} + \int \frac{\mathrm{d}^2\boldsymbol{l}'}{(2\pi)^2} \left[\boldsymbol{l}' \cdot (\boldsymbol{l} - \boldsymbol{l}') \right]^2 C_{|\boldsymbol{l} - \boldsymbol{l}'|}^{\phi\phi} C_{|\boldsymbol{l}'|}^{TT} \,, \quad (1.61)$$

where we have introduced the variance of the deflection angle,

$$\langle \boldsymbol{\alpha}^2 \rangle = \int \frac{d^2\mathbf{l}}{(2\pi)^2} \, l^2 C_l^{\phi\phi} \sim 5 \times 10^{-7} \,. \quad (1.62)$$

The impact of lensing on the temperature spectrum can be visualised from the top panel of figure 1.8. The right-most term in equation (1.61) is a convolution of the unlensed CMB spectrum with the lensing potential power spectrum. It implies that the acoustic peaks and troughs of the primary CMB spectrum will be blurred out by lensing, as if smoothed with a kernel of characteristic width $|\boldsymbol{l} - \boldsymbol{l}'| \sim 60$, corresponding to the scale of the peak of the lensing power spectrum. Furthermore, equation (1.61) predicts that lensing will transfer power from a range of relatively large CMB scales to small scales, where there is very little unlensed power due to diffusion damping: on those small scales,

$$\tilde{C}_l^{TT} \to l^2 C_l^{\phi\phi} R^T \,. \quad (1.63)$$

[28] This ignores the correlation between T and ϕ induced by the integrated Sachs-Wolfe [407] and Rees-Sciama effects [390].

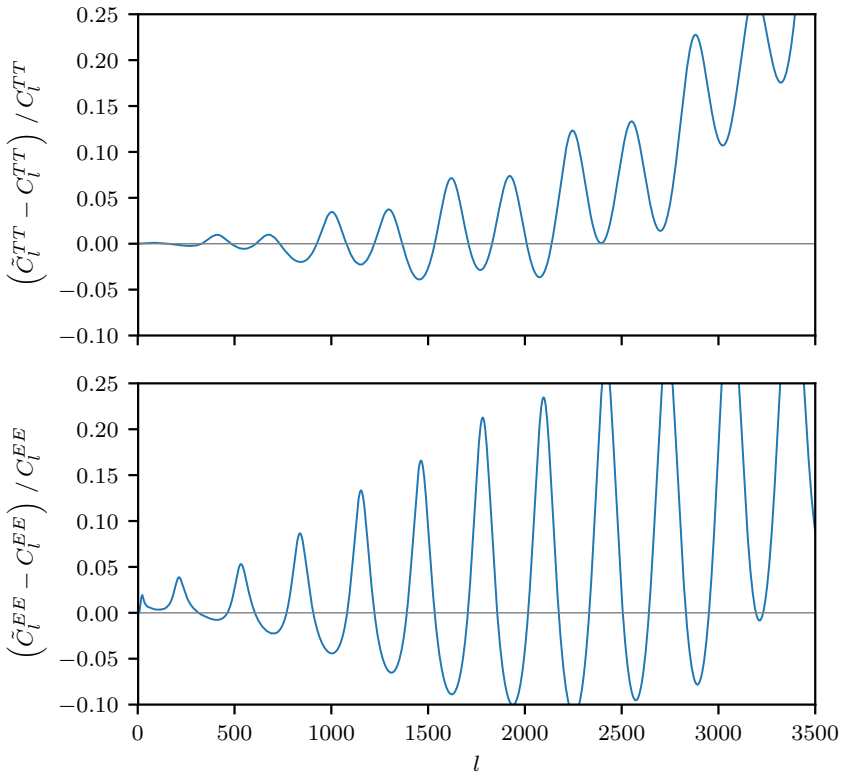

Fig. 1.8 Fractional difference between the angular power spectra of lensed and unlensed CMB temperature (top) and E-mode polarisation (bottom). Lensing smooths out the acoustic peaks in the power spectrum and transfers power from large to small scales. This plot was generated using `CAMB` [254].

Here, we have defined the variance of the gradient of a CMB field, X, as

$$R^X \equiv \frac{1}{2}\langle|\boldsymbol{\nabla} X|^2\rangle = \frac{1}{2}\int \frac{d^2\mathbf{l}}{(2\pi)^2}\, l^2 C_l^{XX}\,. \tag{1.64}$$

For temperature, $R^T = \langle|\boldsymbol{\nabla} T|^2\rangle/2 \sim 10^9\,\mu\mathrm{K}^2$, and for polarisation $R^E = \langle|\boldsymbol{\nabla} Q|^2\rangle/2 = \langle|\boldsymbol{\nabla} U|^2\rangle/2 \sim 2\times 10^7\,\mu\mathrm{K}^2$ [252].

We can also extract E- and B-modes from the lensed, real-space polarisation fields of equation (1.59). We get

$$\begin{aligned}\tilde{E}(\boldsymbol{l}) \pm i\tilde{B}(\boldsymbol{l}) = \quad & E(\boldsymbol{l}) - \int \frac{\mathrm{d}^2\boldsymbol{l}'}{2\pi}\boldsymbol{l}'\cdot(\boldsymbol{l}-\boldsymbol{l}')\phi(\boldsymbol{l}-\boldsymbol{l}')E(\boldsymbol{l}')e^{\pm 2i\psi_{\boldsymbol{l}',\boldsymbol{l}}} \\ & - \frac{1}{2}\int \frac{\mathrm{d}^2\boldsymbol{l}'}{2\pi}\frac{d^2\boldsymbol{l}''}{2\pi}\boldsymbol{l}'\cdot[\boldsymbol{l}'+\boldsymbol{l}''-\boldsymbol{l}]\boldsymbol{l}'\cdot\boldsymbol{l}''E(\boldsymbol{l}')\phi(\boldsymbol{l}'')\phi^*(\boldsymbol{l}'+\boldsymbol{l}''-\boldsymbol{l})e^{\pm 2i\psi_{\boldsymbol{l}',\boldsymbol{l}}} \\ & + O(\phi^3)\,,\end{aligned} \tag{1.65}$$

where $\psi_{\boldsymbol{l}',\boldsymbol{l}}$ is the angle between wavevectors $\boldsymbol{l}'$ and $\boldsymbol{l}$. Note that we have assumed that there are no B-modes in the unlensed CMB, since scalar perturbations do not produce them at linear order, and the lensing of tensor-sourced B-modes is expected to be negligible.

The angular power spectrum of lensed E-modes is

$$\tilde{C}_l^{EE} \approx (1 - l^2\langle\boldsymbol{\alpha}^2\rangle/2)C_l^{EE} + \int \frac{\mathrm{d}^2\boldsymbol{l}'}{(2\pi)^2}\,[\boldsymbol{l}'\cdot(\boldsymbol{l}-\boldsymbol{l}')]\cos^2 2\psi_{\boldsymbol{l}',\boldsymbol{l}} C^{\phi\phi}_{|\boldsymbol{l}-\boldsymbol{l}'|} C^{EE}_{|\boldsymbol{l}'|}\,. \tag{1.66}$$

As for temperature, lensing transfers power to small scales (where the unlensed polarisation is similarly damped),

$$\tilde{C}_l^{EE} \to \frac{1}{2} l^2 C_l^{\phi\phi} R^E\,. \tag{1.67}$$

and smooths out the acoustic features of the E-mode spectrum; since the peaks and troughs in the unlensed E-mode spectrum are sharper than those in temperature, the change is even more acute. These effects are shown in the bottom panel of figure 1.8. See Ref. [252] for the impact on the TE spectrum, which is qualitatively similar.

The lensing-induced smoothing of the acoustic features was first detected in temperature by the ACBAR Collaboration [391], and has now been measured by a number of other CMB experiments in both temperature and polarisation (e.g., [487, 86]), most notably, by Planck [366]. These effects can be modelled and used to constrain post-recombination physics, although their statistical power is hindered by the cosmic variance associated with the unlensed fields, and so they are not competitive with direct reconstructions of map-level realisations of the lensing potential (described in section 1.5.2.4). It has recently been suggested that more cosmological information can be extracted from T and E spectra if the peaks are sharpened by 'delensing' (a technique we will have plenty to say about shortly), as long as information about the lensing potential estimate used to delens is also included in the analysis [153, 164].

The amplitude of the smoothing effect relative to expectations in the cosmology best-fitting other observables is often quantified by the phenomenological parameter $A_{\rm L}$ [71]. At the time of writing, Planck appears to have seen slightly more lensing at the power spectrum level than expected (at approximately $\sim 2\sigma$ significance [371]). As we will see in section 1.5.2.4, lensing can also be measured directly from the four-point function of the CMB, in which case the amplitude of the effect appears to be consistent with ΛCDM [372]. Understanding this behaviour is currently a topic of active research, but we will not be discussing it any further here.

Having addressed the impact of lensing on the T and E spectra, we now move on to describing the production of B-modes by lensing. This is a far more critical aspect, for reasons that will become apparent immediately.

From equation (1.65), it is clear that lensing produces B-modes, even if there were none from recombination [520]. Their angular power spectrum, shown in figure 1.6, is very well approximated as[29]

$$\tilde{C}_l^{BB} \approx \int \frac{\mathrm{d}^2\boldsymbol{l}'}{(2\pi)^2} \left[\boldsymbol{l}' \cdot (\boldsymbol{l} - \boldsymbol{l}')\right]^2 \sin^2 2\psi_{\boldsymbol{l}',\boldsymbol{l}} C^{\phi\phi}_{|\boldsymbol{l}-\boldsymbol{l}'|} C^{EE}_{|\boldsymbol{l}'|} \,. \tag{1.68}$$

This peaks approximately where the E-mode spectrum peaks, and it asymptotes to the same small-scale power as the E-modes:

$$\tilde{C}_l^{BB} \to \frac{1}{2} l^2 C_l^{\phi\phi} R^E \,. \tag{1.69}$$

Crucially, lensing also transfers E-mode power to large scales of the B-mode field[30], where searches for a primordial component are focused. On those scales ($l \ll 1000$) there is relatively little E-mode power, and equation (1.68) can be approximated as

$$\tilde{C}_l^{BB} \sim \frac{1}{4\pi} \int \frac{\mathrm{d}l'}{l'} (l')^6 C^{\phi\phi}_{l'} C^{EE}_{l'} \sim 2 \times 10^{-6}\, \mu\mathrm{K}^2 \,, \tag{1.70}$$

which is independent of l, and hence behaves like white noise. For reference, this is comparable to the power spectrum of isotropic instrument noise[31] with $\Delta_\mathrm{P} \sim 5\,\mu$K-arcmin, or to a tensor signal with $r \sim 0.01$ on scales $10 \lesssim l \lesssim 100$.

[29] In Chapter 2 we explain why this expression is accurate to the 1% level, despite being $O(\phi^2)$. Differences between flat- and full-sky calculations are also $O(1\%)$ [84].

[30] This effect is also present for E-modes, but it is unobservable there due the cosmic variance of the unlensed field.

[31] This way of quoting noise levels is convenient because it is independent of the size of pixels. To see why, let $\delta Q_i^\mathrm{noise}$ denote the polarisation noise in the ith pixel. If we assume that the noise is homogeneous and uncorrelated between pixels, then $\langle \delta Q_i^\mathrm{noise} \delta Q_j^\mathrm{noise} \rangle = \sigma^2_\mathrm{pix} \delta_{ij}$. The variance per pixel, σ^2_pix, is inversely proportional to the pixel area (because the time, t, spent observing a pixel is proportional to the pixel area, and integration time determines the variance as $\sigma^2_\mathrm{pix} = s^2/t$, where s is the detector sensitivity, a fixed number in units of $\mu\mathrm{K}\sqrt{\mathrm{sec}}$). Hence, it is convenient to normalise the pixel's variance by its solid angle, $\Omega_\mathrm{pix} = \theta_\mathrm{FWHM} \times \theta_\mathrm{FWHM}$, and define $\Delta_P^2 \equiv \sigma^2_\mathrm{pix} \Omega_\mathrm{pix}$. The power spectrum of the noise, after deconvolution of a symmetric Gaussian beam with full width at half maximum θ_FWHM (in radians), is then well described by [225]

$$N_l = \Delta^2_\mathrm{P} e^{l(l+1)\theta^2_\mathrm{FWHM}/8\ln 2} \,. \tag{1.71}$$

The white noise character of large-scale lensing B-modes can be understood from equation (1.70), which tells us two things: first, that there will be contributions from all scales on which there is non-zero power in *both* $C_l^{\phi\phi}$ and C_l^{EE}; and second, that it is the action of lenses on E-modes *of their same angular scale* that gives rise to the effect. Since the unlensed E-modes are dominated by fairly small scales (they peak at $l \sim 1000$), the pairs of lenses and E-modes that contribute will have a short coherence length. The large-scale B-mode power will therefore be the sum of contributions from many different, uncorrelated patches, and this can only produce white noise [252].

A first detection of lensing B-modes was recently achieved by the SPTPol Collaboration [172] and soon followed by BICEP2 [47], POLARBEAR [377], ACTpol [488] and Planck [359]. As experimental noise levels improve, and large-scale experimental and foreground systematics are increasingly better understood, lensing is bound to become the main limiting factor in detecting primordial B-modes. In the next section, we motivate why that is the case.

1.5.2.3 The need to delens B-modes

In recent years, observations of temperature and polarisation CMB spectra have placed increasingly stringent upper bounds on the amplitude of tensor perturbations. At the time of writing, the tightest constraints are from the combination of BICEP/Keck Array measurements and Planck and WMAP [48]; these place $r < 0.06$ (95 % C.L., at a pivot scale of $0.05\,\mathrm{Mpc}^{-1}$). For r values this small, it is not possible to distinguish the tensor contribution to the temperature and E-mode polarisation, which are dominated by the much larger contribution from scalar perturbations, and only observations of B-modes can bring further progress.

Although the B-modes have no cosmic variance from scalar perturbations (at leading order) in the unlensed sky, we saw in the previous section that lensing 'rotates' primordial E-modes into B-modes, inducing a potential source of confusion when searching for a primordial component. The situation is illustrated in figure 1.6, where primordial B-modes with plausible values of r are compared to the lensing contribution. A naïve attempt at extracting the tensor component ($C_l^{BB,\mathrm{t}}$), might involve fitting the measured spectrum ($\hat{C}_l^{BB}$) with a model involving tensors, foreground, lensing ($\tilde{C}_l^{BB}$), and experimental noise (N_l^{BB}). However, the sample variance associated with the lensing power would degrade constraints on the relatively small primordial contribution. For low enough r, a detection would be impossible, in fact, no matter how extensive the foreground cleaning or how good the sensitivity.

To see this more explicitly, we will consider a toy model for the Bayesian inference of r from $\hat{C}_l^{BB}$, a simplified version of the machinery often used in the field to forecast constraints on cosmological parameters; see, e.g., [445, 513]. We will be ignoring many important effects, including foregrounds[32], to focus on the error on r arising strictly from lensing.

Let us first Taylor expand a general log-likelihood function $\mathcal{L}(r|\hat{C}_l^{BB})$ around the maximum likelihood (ML) point, $r_{\rm ML}$, obtaining

$$\ln \mathcal{L}(r|\hat{C}_l^{BB}) \approx \ln \mathcal{L}(r_{\rm ML}|\hat{C}_l^{BB}) + \frac{1}{2}\frac{\partial^2 \ln \mathcal{L}(r|\hat{C}_l^{BB})}{\partial r^2}\bigg|_{r_{\rm ML}} (r - r_{\rm ML})^2 \,. \tag{1.72}$$

(Note that the first-order term vanishes at the ML point.) Near the ML point, the likelihood is therefore well approximated as a Gaussian

$$\mathcal{L}(r|\hat{C}_l^{BB}) \approx \mathcal{L}(r_{\rm ML}|\hat{C}_l^{BB}) \exp\left(- \frac{1}{2}\frac{(r - r_{\rm ML})^2}{\sigma_r^2}\right), \tag{1.73}$$

with width

$$\sigma_r = \left|\frac{\partial^2 \ln \mathcal{L}(r|\hat{C}_l^{BB})}{\partial r^2}\right|^{-1/2}_{r_{\rm ML}} . \tag{1.74}$$

This width will translate, via Bayes' theorem[33], to the width of the posterior probability distribution $P(r|\hat{C}_l^{BB})$, and thus to the precision with which we can estimate r. For simplicity, we will set $r_{\rm ML} = 0$, and assume that the likelihood function of r given the data is Gaussian[34].

[32]For simplicity, this pedagogical treatment ignores foregrounds. In reality, their impact must be taken into account, in the form of both additional B-mode power (see, e.g., Ref. [235]) and non-trivial couplings in the delensing process that can bias results (Ref. [30] and Chapter 3).

[33]Bayes' theorem states that the 'posterior' probability distribution, $P(\theta|D)$, of a set of parameters, θ, given some observed data, D, is related to the 'likelihood' of the data given the parameters, $P(D|\theta)$ [though often denoted as $\mathcal{L}(\theta|D)$], by

$$P(\theta|D) = \frac{P(D|\theta)P(\theta)}{P(D)} \,, \tag{1.75}$$

where $P(\theta)$ encodes our 'prior' knowledge about the parameters, and $P(D)$ is a normalisation factor known as the 'evidence'. See, e.g., Ref. [278] for details and applications.

[34]The latter is often not a good approximation in real applications with partial sky coverage (see, e.g., Refs. [163, 148]), but it shall suffice for the purposes of illustration.

In the case where no effort is made to remove lensing B-modes at the map level, the uncertainty on an estimate of r is (e.g., [445])

$$\sigma_0(r) = \left[\frac{f_{\rm sky}}{2}\sum_{l>l_{\rm min}}(2l+1)\left(\frac{\partial C_l^{BB}/\partial r}{\tilde{C}_l^{BB}+N_l^{BB}}\right)^2\right]^{-1/2}, \tag{1.76}$$

where $f_{\rm sky}$ is the fraction of sky under scrutiny, $l_{\rm min}$ is the minimum multipole used in the inference, and $\partial C_l^{BB}/\partial r = C_l^{BB,{\rm t}}(r=1)$. Below a certain level of experimental noise power (the exact figure depending on whether or not the reionisation bump can be accessed), this expression is dominated by the lensing noise, $\tilde{C}_l^{BB}$.

If, on the other hand, the B-modes are partially removed from the maps — that is, they are *delensed* — a derivation analogous to that above will show that the error can be reduced [227, 425]. Let $C_l^{BB,{\rm res}}$ be the power spectrum of residual lensing B-modes after delensing, and $\sigma(r)$ be the new uncertainty. The improvement factor on the error thanks to delensing is then [445]:

$$\alpha \equiv \frac{\sigma_0(r)}{\sigma(r)} = \frac{\tilde{C}_l^{BB}+N_l^{BB}}{C_l^{BB,{\rm res}}+N_l^{BB}}\,. \tag{1.77}$$

In deriving this expression, we have set $C_l^{BB,t}=0$ and used the fact that $\tilde{C}_l^{BB}$, $C_l^{BB,{\rm res}}$ and N_l^{BB} all resemble white noise on large scales. As an example of the sort of impact that delensing can have on $\sigma(r)$, consider an experiment with $\Delta_P = 2\,\mu$K-arcmin and $l_{\rm min}=30$, similar to the intended noise levels of the Simons Observatory's small-aperture telescopes (SATs) at 145 GHz [441]. If half of the lensing B-mode power can be removed by delensing, then $\alpha \approx 1.7$, and the error will be reduced to approximately 60% of its value before delensing. More realistic forecasts for SO predict $\sigma(r)\approx 0.0015$ for the null scenario, a factor of 2 better than in the case of no delensing; barring a detection, this will make it possible to rule with 5σ confidence values of the tensor-to-scalar ratio as low as $r=0.0075$ [313].

In the expression above, we introduced (without explanation) an $l_{\rm min}$ cut, below which observations are discarded. As we will see in section 1.5.3, this must be done in order to avoid biases associated with foreground contamination, primarily from the Earth's atmosphere. The ability, or lack thereof, to observe the largest-angular-scale B-modes has critical consequences when searching for a primordial signal. We have already seen (figure 1.6) that the primodial B-mode spectrum has a bump below $l\lesssim 10$ associated with scattering during reionisation. If those scales can be accessed, signals as small as $r\gtrsim O(10^{-3})$ could, in principle, be detected without delensing [255, 90] (though

delensing would still help characterise the signal). Carrying out those observations would likely require putting a satellite in orbit, as will be done with LiteBird [266] and hopefully PICO [166], or the development of new technologies to enable stable observations from the ground (see the pioneering work by the CLASS team [176]).

Barring difficulties with the removal of foregrounds (see section 1.5.3), the limits to delensing may ultimately lie with non-remapping effects, such as polarisation rotation or time delays, which cannot be removed by the standard delensing techniques described in chapter 2. Fortunately, these effects are small, only entering the lensing B-mode spectrum at the level of 10^{-4} of the standard calculation on scales $l \sim 100$; they would therefore only hinder searches for a primordial signal with $r \ll 10^{-5}$ [256].

Much of the work in this thesis revolves around issues concerning practical implementations of delensing. Since lensing is achromatic, it will not be possible to separate the lensing contribution using frequency information. Instead, delensing will require estimating the actual realisation of the matter distribution on the sky and using it to undo the lensing deflections. In chapter 2, we explain how those deflections can be reversed given some proxy of the lensing potential. For the latter, it is possible to use tracers of the large-scale structure (see chapter 3) or reconstructions obtained from the CMB itself (see chapter 4). The next section is dedicated to those internal reconstructions.

1.5.2.4 Lensing reconstructions

It is clear from equations (1.60) and (1.65) that lensing couples modes of CMB anisotropy that would otherwise be uncorrelated. We will now show that the statistical anisotropy this induces makes it possible to estimate — or 'reconstruct' — the distribution of the lenses across the sky, as first proposed by Ref. [521].

The optimal way to do this entails writing down a likelihood function for the lensing potential given the data[35], and either maximising this likelihood directly [189, 190, 168], or using it to construct a posterior distribution, which can then be maximised [74]. In theory, it should also be possible to sample the joint posterior of unlensed fields and lensing potential [14, 298, 299].

Though promising steps have recently been taken towards obtaining optimal reconstructions from real data [380, 300], the reality is that, until experimental noise levels drop below $\Delta_P \sim 1\,\mu$K-arcmin, these approaches will be indistinguishable in their results from the much simpler 'quadratic estimators' of Ref. [202] — in fact, the

[35]In practice, it is assumed that the lensing potential, the noise and the unlensed CMB are all Gaussian.

latter can be shown to arise as the first step in an iterative approach to maximising the likelihood [189, 171].

The quadratic estimators have been the workhorse of CMB lensing studies for over a decade, having featured in numerous and ground-breaking analyses; see section 5.1 for a brief overview of particularly salient results. In addition to being practically optimal for the time being, they are also highly transparent to analytic explorations, a vital feature for the novel field of CMB lensing, which is still learning how to grapple with systematic effects. In chapters 4 and 5, we will be making use of this simplicity to understand a number of effects affecting lensing reconstruction and delensing analyses; but first let us lay out some basic notions about the quadratic estimators that we will use later on. We will follow Ref. [287], and work in the flat-sky limit, but the results can be easily generalised to harmonic space; see, e.g., [331].

In section 1.5.2.2, we explained that lensing correlates different scales of the CMB power spectra. The coupling is, in fact, more general, and extends also to off-diagonal elements of the covariance. If $\tilde{X}$ and $\tilde{Y}$ are two observed, lensed and noisy CMB fields (either T, E or B), the response of their off-diagonal correlations to changes in a specific lensing mode, $\phi(\boldsymbol{L})$, is

$$\left\langle \frac{\delta}{\delta\phi(\boldsymbol{L})} \left(\tilde{X}(\boldsymbol{l})\tilde{Y}(\boldsymbol{l}') \right) \right\rangle = \delta(\boldsymbol{l}+\boldsymbol{l}'-\boldsymbol{L}) f_{XY}(\boldsymbol{l},\boldsymbol{l}')\,, \tag{1.78}$$

where the average is over Gaussian realisations of the primary CMB, lenses and noise. The weights, f_{XY}, are given in table 1.1. Note that the weights we provide are those calculated by Ref. [253], who generalised the perturbative calculation of Ref. [202] to be valid to all orders.

The expression above suggests that the effect of lensing mode $\phi(\boldsymbol{L})$ is to introduce statistical anisotropy (when lenses are fixed) into the observed CMB. Regarded a different way, it puts forward the possibility of estimating the lensing potential — to leading order — from off-diagonal correlations between pairs of observed CMB fields. In practice, we cannot average over realisations of the CMB, but we can mimic that as a weighted sum over all possible off-diagonal correlations between a pair of observed CMB fields, separated in multipole space by the lensing mode we intend to reconstruct [202]:

$$\hat{\phi}_{XY}(\boldsymbol{L}) \equiv \frac{1}{2\pi} \int d^2\boldsymbol{l} d^2\boldsymbol{l}' \delta(\boldsymbol{l}+\boldsymbol{l}'-\boldsymbol{L}) \tilde{X}(\boldsymbol{l})\tilde{Y}(\boldsymbol{l}') F_{XY}(\boldsymbol{l},\boldsymbol{l}')\,, \tag{1.79}$$

β	$f_\beta(\boldsymbol{l}_1, \boldsymbol{l}_2)$
TT	$\tilde{C}_{l_1}^{T\nabla T}(\boldsymbol{L}\cdot\boldsymbol{l}_1) + \tilde{C}_{l_2}^{T\nabla T}(\boldsymbol{L}\cdot\boldsymbol{l}_2)$
TE	$\tilde{C}_{l_1}^{T\nabla E}\cos 2\psi_{\boldsymbol{l}_1\boldsymbol{l}_2}(\boldsymbol{L}\cdot\boldsymbol{l}_1) + \tilde{C}_{l_2}^{T\nabla E}(\boldsymbol{L}\cdot\boldsymbol{l}_2)$
EE	$[\tilde{C}_{l_1}^{E\nabla E}(\boldsymbol{L}\cdot\boldsymbol{l}_1) + \tilde{C}_{l_2}^{E\nabla E}(\boldsymbol{L}\cdot\boldsymbol{l}_2)]\cos 2\psi_{\boldsymbol{l}_1\boldsymbol{l}_2}$
TB	$\tilde{C}_{l_1}^{T\nabla E}\sin 2\psi_{\boldsymbol{l}_1\boldsymbol{l}_2}(\boldsymbol{L}\cdot\boldsymbol{l}_1)$
EB	$[\tilde{C}_{l_1}^{E\nabla E}(\boldsymbol{L}\cdot\boldsymbol{l}_1) + \tilde{C}_{l_2}^{B\nabla B}(\boldsymbol{L}\cdot\boldsymbol{l}_2)]\sin 2\psi_{\boldsymbol{l}_1\boldsymbol{l}_2}$

Table 1.1 Non-perturbative CMB lensing response functions in the flat-sky limit. The quantity $\tilde{C}^{X\nabla Y}$ is the lensed gradient spectrum defined in Ref. [253], and $\psi_{\boldsymbol{l}_1\boldsymbol{l}_2}$ is the angle between $\boldsymbol{l}_1$ and $\boldsymbol{l}_2$. Note that $\boldsymbol{L} = \boldsymbol{l}_1 + \boldsymbol{l}_2$. We assume there are no primordial B-modes, and ignore also curl-like polarisation terms, which are subdominant to $\tilde{C}_{l_1}^{E\nabla E}$ to the 0.5% level [136]. On scales $l \lesssim 2000$, it is a very good approximation to set $\tilde{C}_{l_1}^{X\nabla Y} \approx \tilde{C}_{l_1}^{XY}$ [169, 136]. Note that the weights quoted here are the generalisation of the leading-order weights of Refs. [202, 331]. The BB estimator is not included because it is higher order in lensing.

where $F_{XY}(\boldsymbol{l}, \boldsymbol{l}')$ is an arbitrary function to be chosen in a way that optimises the estimator's performance. Requiring that the estimator be unbiased at leading order[36] imposes the condition

$$1 = \int \frac{d^2\boldsymbol{l}}{2\pi} f_{XY}(\boldsymbol{l}, \boldsymbol{L}-\boldsymbol{l}) F_{XY}(\boldsymbol{l}, \boldsymbol{L}-\boldsymbol{l})\,. \tag{1.80}$$

The noise properties of such an estimator can be investigated by calculating its variance[37],

$$\langle(\hat{\phi}_{XY}-\phi)(\boldsymbol{L})(\hat{\phi}_{XY}-\phi)(\boldsymbol{L}')\rangle = \delta(\boldsymbol{L}+\boldsymbol{L}')\left(N^{(0),XY}(L) + \cdots + N^{(n),XY}(L) + \cdots\right), \tag{1.81}$$

where the superscript, n, in $N^{(n),XY}(L)$ denotes the order at which $C_L^{\phi\phi}$ explicitly appears in that term. In this way, $N^{(0),XY}(L)$ is the Gaussian contribution, which can be calculated rather accurately from simulations, or from the data using realisation-dependent methods (see [314] and references therein). On the other hand, lensing

[36]The estimator is unbiased at lowest order if $\langle\hat{\phi}_{XY}(\boldsymbol{L})\rangle_{\boldsymbol{L}'\neq\boldsymbol{L}} = \phi(\boldsymbol{L})$, where the average is now over realisation of the unlensed CMB and lensing potential modes $\phi(\boldsymbol{L}')$ with $\boldsymbol{L}' \neq \boldsymbol{L}$.

[37]Note that the variance is a function of the fraction of sky covered by the observations, $f_{\rm sky}$: this enters via the delta function, which gives $\delta(\boldsymbol{0}) = f_{\rm sky}/\pi$.

produces higher-order, connected moments of the CMB trispectrum[38]. While part of those will constitute the signal of interest, other couplings will not have a response to lensing that lends itself to reconstructing $C_L^{\phi\phi}$; those terms will contribute to $N^{(n),XY}(L)$ with $n > 0$ [95, 223, 169].

We can choose the form of the weight function F_{XY} that minimises the $N^{(0),XY}(L)$ variance subject to the constraint in equation (1.80). For all XY except $XY = TE$, the minimum-variance weights are

$$F_{XY}(\boldsymbol{l}, \boldsymbol{l}') = A_L^{XY} \frac{f_{XY}(\boldsymbol{l}, \boldsymbol{l}')}{(1+\delta_{XY}) C_{\boldsymbol{l}}^{XX,\mathrm{tot}} C_{\boldsymbol{l}'}^{YY,\mathrm{tot}}}, \tag{1.82}$$

where $C_{\boldsymbol{l}}^{XX,\mathrm{tot}}$ and $C_{\boldsymbol{l}}^{YY,\mathrm{tot}}$ include all contributions to the power, and

$$A_L^{XY} \equiv \left[\int \frac{d^2\boldsymbol{l}}{(2\pi)^2} \frac{[f_{XY}(\boldsymbol{l}, \boldsymbol{L}-\boldsymbol{l})]^2}{(1+\delta_{XY}) C_{\boldsymbol{l}}^{XX,\mathrm{tot}} C_{|\boldsymbol{L}-\boldsymbol{l}|}^{YY,\mathrm{tot}}} \right]^{-1} . \tag{1.83}$$

The resulting variance is then $N_{XY}^{(0)}(L) = A_L^{XY}$; for an isotropic survey (the idealised limit we will consider in the rest of this work), $N_{XY}^{(0)}(L)$ can be calculated directly from measured spectra using equation (1.83). We refer the reader to, e.g., Ref. [287] for the explicit form of the weights in the case where $XY = TE$; we shall not be needing them in this work, which is only concerned with the EB (chapter 4) and TT combinations (chapter 5). Explicit expressions for the EB and TT estimators are provided in equations (4.2) and (5.1), respectively.

The information extracted from individual quadratic estimators can be combined in a way that minimises the variance of the joint estimate. To date, this has been done in the manner first suggested by Refs. [202, 331]: by determining, at each scale, the linear combination of individual quadratic estimator reconstructions that minimises the variance[39]. However, it has recently been pointed out that this could be improved upon by deriving a new estimator that is explicitly the minimum-variance estimator of a given lensing mode, $\phi(\boldsymbol{L})$, that can be built from a linear combination of pairs of CMB fields [287] (thus accounting for correlations between different pairs). Rigorously speaking, it is only this estimator that can be described as the first step in the iterative reconstruction procedure of [190].

[38] As we will discuss in chapter 5, foregrounds can also introduce lensing reconstruction biases of this type.

[39] The implementations in [359, 372, 514] were, in fact, only approximations to the method suggested by Refs. [202, 331]: TE correlations were ignored in the filtering step for reasons of computational efficiency, which led to slight sub-optimalities [287].

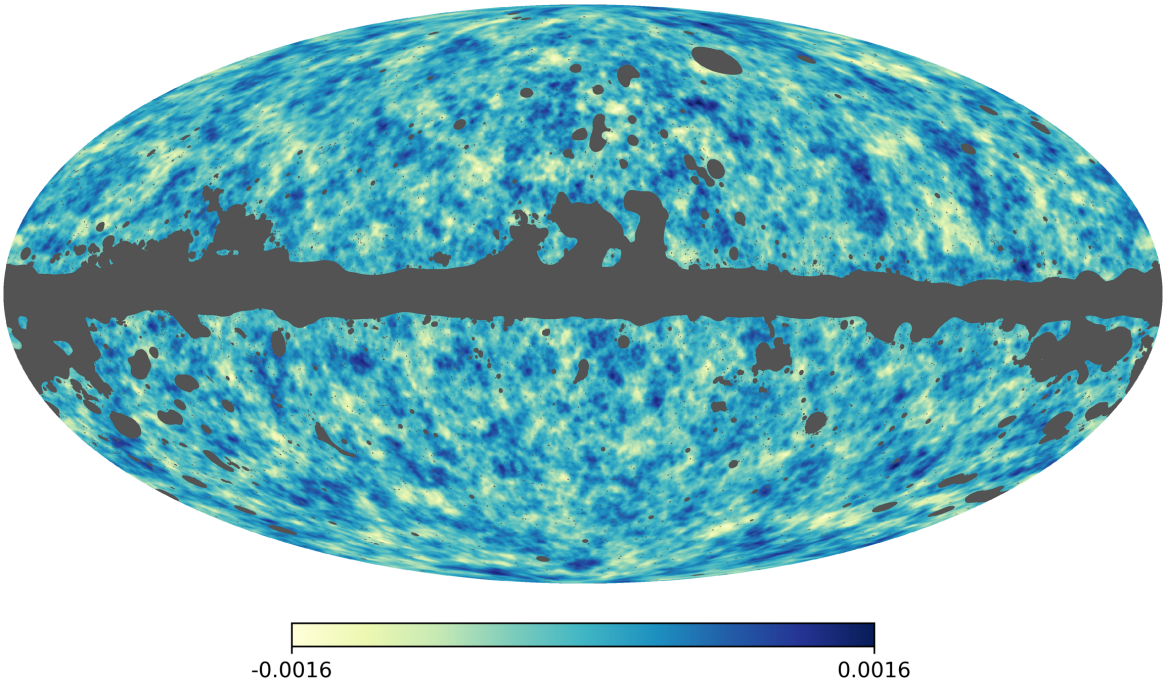

Fig. 1.9 Mollweide projection in Galactic coordinates of $\sqrt{L(L+1)}\hat{\phi}_{LM}$ (a proxy for the gradient mode of the lensing deflection angle) as reconstructed from Planck data using a minimum-variance combination of quadratic estimators. The grey regions were excluded from the analysis to mitigate contamination from our galaxy. Note also that modes with $L < 8$ have been removed. Figure from Ref. [372].

A beautiful example of a lensing reconstruction is shown in figure 1.9, which shows the minimum-variance[40] quadratic estimator reconstruction derived from Planck data [372]. The map covers almost the entire sky (regions that were too contaminated by galactic foregrounds, bright clusters or point sources were masked), so it has great statistical power: it enabled a detection of the lensing effect at 40σ confidence, the highest significance to date. The lensing power spectrum measured from this map is shown in the bottom right panel of figure 1.5.

Most of the signal-to-noise in Planck's lensing reconstructions comes from the TT quadratic estimator. However, once experimental sensitivities and resolutions improve sufficiently (Planck was barely able to detect the lensing contribution to B-mode polarisation), it should be possible to reconstruct lensing with much greater fidelity from the polarisation than from the temperature. The reason for this can be appreciated from equation (1.83), which says that the variance of a quadratic estimator reconstruction scales with the total power in each of the observed maps; there is a

[40] Again, in the general sense of Refs. [202, 331], though neglecting TE correlations in the filtering step.

lot more power in the lensed temperature anisotropies than there is polarisation. In particular, once experimental sensitivities reach $5\,\mu$K-arcmin — the level of power of the lensing B-modes below $l < 1000$ — the EB estimator will dominate; see figure 4.1 for the noise levels of different estimators in an intermediate regime, appropriate for the upcoming Simons Observatory [441].

The dependence of the reconstruction variance on the lensed spectra is only a feature of the quadratic estimators. Bayesian techniques are instead sensitive to the variance of the unlensed fields [189, 190, 74, 299]. The unlensed B-mode power is likely to be negligible in all but the largest angular scales (if at all present), and the TB and EB correlations are guaranteed to vanish on the grounds of parity [252]. Hence, future implementations of those more optimal approaches will be able to take advantage of improvements in sensitivity and resolution to extract exquisite reconstructions from observations of the small-scale polarisation. Two further factors work in favour of polarisation-based reconstructions: first, there is the fact that extragalactic foregrounds are less polarised than the CMB is (see, e.g., [369] and the discussions in chapter 5); and second, the fact that, unlike the case of temperature, lensing B-modes are produced by lenses of a wide range of scales, which it might therefore be possible to reconstruct.

The latter point is important from the perspective of delensing. The lensing B-mode spectrum peaks at $l \approx 1000$, whereas the primordial signal is only significant at $l \approx 100$; one could then imagine using the large number of B-modes available on small scales to reconstruct the relatively-fewer, large-scale lensing modes (recall that $C_L^{\phi\phi}$ peaks at $L \sim 60$), and in turn using those to delens the large-scale B-modes. This approach is expected to enable very extensive delensing, but it will be hindered by the fact that approximately 10% of $\tilde{C}_{l<100}^{BB}$ comes from lensing modes with $L \gtrsim 800$ (see, e.g., figure 1 of [445]). For reference, SO reconstructions will be signal dominated for $L \lesssim 250$ [441] on 40% of the sky, while CMB-S4 [23] and SPT-3G [458] are expected to extend the signal-dominated regime to $L \lesssim 1000$ (though the latter will only cover a few percent of the sky). Though it is possible to improve delensing performance by complementing internal reconstructions with external tracers (see chapter 3), a large fraction of the small-scale lenses we need come from high redshift (see figure 1.7). Delensing is therefore a formidable challenge.

To conclude this section, we note that statistical anisotropy can also be induced by sources other than lensing, such as masks, inhomogeneous experimental noise, or asymmetric beams. The literature is rich with efforts to mitigate these important issues; for brevity, we do not address them here, and instead refer the reader to Refs. [171, 314, 35, 372] and references therein.

1.5.3 Other components of the microwave sky

So far, we have motivated the scientific interest driving measurements of the primary CMB, and introduced an important secondary effect, CMB lensing, which also contains valuable cosmological information. Unfortunately, the sensitivity required to measure these small signals makes the instruments sensitive to a variety of other 'foreground' contaminants, which are generally more local and often regarded as a nuisance in cosmological analyses. As we will see, this characterisation is not really fair, as the foregrounds are themselves rich probes of baryonic physics in our Galaxy and beyond.

Closest to home, the impact of observing through the Earth's atmosphere is a cause of particular concern for ground-based telescopes. Though the atmosphere is not polarised *per se*, spatial and temporal fluctuations in the water vapour content can couple to instrumental effects and cause leakage of T or E into B-modes on large angular scales (e.g., [201, 330, 438]). This is the reason why ground-based CMB observatories are to be found in some of the highest, driest locations on Earth, such as the Atacama desert or the South Pole. Several techniques have been proposed to mitigate these effects, including the modulation of the observed polarisation using a half-wave plate (e.g., [241, 184]). Since it is generally more cost-effective to implement these on small-aperture telescopes (SATs) in the style of BICEP, the CMB community has opted to build SATs to pursue its low-l goals of the coming decade; see, e.g., Refs. [90, 441].

Working our way outwards from Earth, the next foreground worth worrying about is zodiacal light associated with the interplanetary dust cloud. Much more important, however, are diffuse foregrounds associated with emission processes happening within our Galaxy, but outside the Solar System. These produce significant contributions to the microwave sky, to go alongside the CMB, as can be seen from figure 1.4. In intensity, and at frequencies above 100 GHz, there is emission from thermal dust; at lower frequencies, there is free-free emission (brehmsstrahlung radiation associated with electron-ion collisions), synchrotron radiation and spinning-dust emission. From these components, only dust and synchrotron are significantly polarised. Since an accurate characterisation of polarised Galactic foregrounds is essential to searches for primordial B-modes — the main topic of this thesis — we summarise the state-of-the-art understanding of these in section 1.5.3.1, deferring the reader to, e.g. [406], for a more general review of CMB foregrounds.

In addition to Galactic emission, the are contributions from extragalactic foregrounds, which dominate on small angular scales away from the Galactic plane. These are statistically isotropic, owing to their extragalactic origin, and can usually be mod-

elled at the level of the angular power spectrum. Extragalactic foregrounds include 'radio' sources — quasars, blazars, and radio galaxies (see, e.g., [368]) — and the cosmic infrared background (CIB; to be described shortly). Extragalactic foregrounds are expected to have a lesser impact than Galactic foregrounds on searches for primordial B-modes, due to their low polarisation fractions and distinct angular and frequency spectra. However, their effect will need to be taken into account by small- and medium-aperture telescopes targeting a recombination signal with $r < 0.01$ [245]; this will likely entail an aggressive removal of point sources, alongside multi-frequency cleaning techniques such as those used for Galactic foregrounds.

It is also known that B-modes can be produced post-recombination if reionisation proceeded in a patchy, inhomogeneous way. There are two mechanisms for this: either scattering of the CMB quadrupole off electrons which are distributed in an inhomogeneous way [508, 267, 195], or an anisotropic screening of the primary polarisation pattern by those electrons [121]. These effects have been shown to be small, only relevant if degree-scale primordial B-modes with $r \leq 10^{-4}$ are targeted [309, 403].

Though usually considered a secondary source of CMB anisotropy, rather than a foreground, the Sunyaev-Zeldovich (SZ) effect is also associated with extragalactic structures, and can be a nuisance when trying to constrain the primary CMB anisotropies. It is produced by inverse-Compton-scattering of CMB photons off free electrons along the line of sight, and it can be divided into two types: a contribution from thermal motions of hot electrons (thermal SZ, or tSZ) [470] and a kinematic component due to bulk motions of electrons (kSZ) [470, 471, 338]. While the tSZ has a characteristic frequency dependence, the kSZ preserves the blackbody spectrum of the primary CMB to a very high degree, and so it cannot be isolated using multi-frequency observations.

In chapter 5, we will explain that the tSZ and the CIB are the two main extragalactic contaminants to CMB lensing reconstructions, and we will aim to model their effects analytically. In preparation for that, we describe, in sections 1.5.3.3 and 1.5.3.2, the key features of the tSZ and the CIB, respectively.

1.5.3.1 Galactic foregrounds

Figure 1.10 shows the main components of the microwave sky in polarisation. At frequencies above 100 GHz, the dominant polarised foreground is thermal emission from asymmetric dust grains in the interstellar medium (ISM). These grains, which behave like electric dipoles, tend to align themselves with their long axis pointing in the direction of the local magnetic field, thus imprinting a net polarisation on the observed

light (see, e.g., [15]). Our understanding of dust has been revolutionised in recent decades by space-based observations: those of WMAP, Herschel and, especially, Planck. Planck's High Frequency Instrument (HFI) produced full-sky, relatively-high resolution measurements of temperature and polarisation in the frequency range 100–353 GHz, and of temperature only at 545 and 857 GHz. These confirmed that the spectral energy distribution (SED) of dust can be accurately described across CMB frequencies as a modified blackbody with temperature $T_{\rm dust} \approx 19.6\,{\rm K}$ and emissivity $\epsilon \propto \nu^{\beta_{\rm dust}}$, where the spectral index for total intensity is $\beta_{\rm dust} = 1.51 \pm 0.01$, and $\beta_{\rm dust} = 1.53 \pm 0.02$ for polarisation [367]. Planck also showed that the angular power spectra of dust E- and B-modes could both be modelled as power-laws, with $C_l^{EE,{\rm dust}} \propto l^{-2.42\pm0.02}$ and $C_l^{BB,{\rm dust}} \propto l^{-2.54\pm0.02}$ for the largest subdivision of the sky they considered; though the normalisation of these angular spectra were found to vary considerably with sky region, the spectral indices changed much more mildly [367]. Several other interesting features were observed, such as the relation $C_l^{BB,{\rm dust}} \approx 0.5 C_l^{EE,{\rm dust}}$, or TE and TB correlations; understanding these features is currently at the forefront of Galactic science (e.g., [88]).

At frequencies below 100 GHz, the polarised microwave sky is dominated by synchrotron emission associated with cosmic rays interacting with the Galactic magnetic field and radiating. This component is strongly polarised, at the level of up to 20% (e.g., [229]). For a long time, the only all-sky template of synchrotron emission was that of Ref. [178]. This changed dramatically with the low-frequency observations of WMAP [229] and Planck's LFI (Low Frequency Instrument). Planck found that the angular power spectrum of the synchrotron component is well described by a power law with $C_l^{BB,{\rm sync}} \propto l^{-3.1\pm0.1}$ [369].

Notice that the angular power spectra of dust and synchrotron E- and B-modes are both very red, a cause of concern when searching for primordial B-modes (as well as reionisation signals) on large scales. Indeed, at their minimum frequency of 70–90 GHz, polarised foregrounds are at a level comparable to a polarised signal with $r = 0.01$–0.1, depending on sky region [235]. Thanks to the all-sky foreground maps produced by Planck, regions with relatively-lower levels of foreground contamination can be identified and used in analyses.

However, as upper bounds on r approach the aforementioned foreground 'floor', the case for active mitigation of the foregrounds becomes stronger. Current high-sensitivity analyses in fact already rely on foreground cleaning (e.g., [49]). Several mitigation techniques have been developed in recent years to separate the CMB from the foregrounds using multi-frequency observations and, in certain cases, spatial information (see, e.g., Ref. [369], and references therein). These can be broadly classified as 'blind',

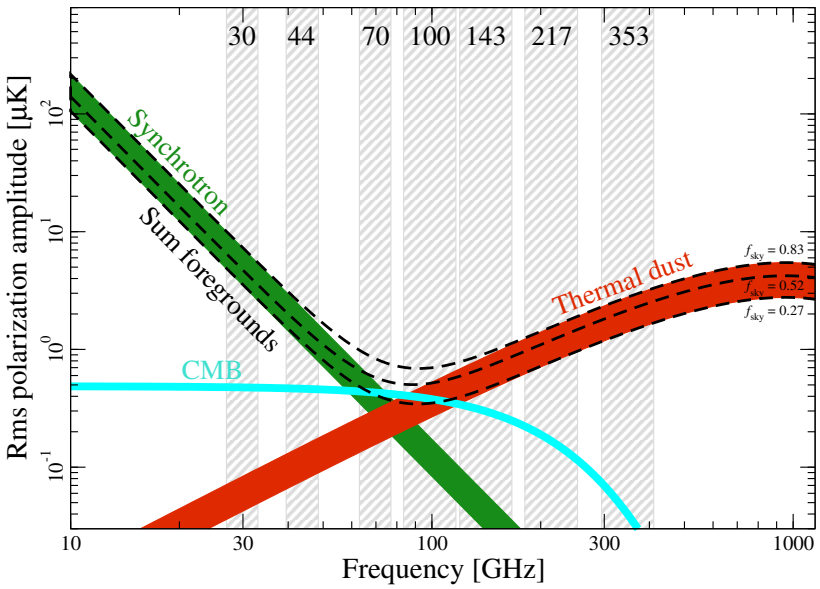

Fig. 1.10 Root-mean-squared fluctuations, as a function of frequency, of the main components of the microwave sky in polarisation ($P = \sqrt{Q^2 + U^2}$). The vertical bands show the seven polarisation-sensitive channels of Planck. The coloured bands denote the range of the foreground rms for different masks with 73–93% sky coverage: green for synchrotron, red for thermal dust. These curves are obtained by smoothing the polarisation to 40′. Since both dust and synchrotron have very red *angular* power spectra, the behaviour shown in this plot is driven by the largest angular scales. Sufficiently far from the Galactic plane, and on small scales, the CMB is not as subdominant as this plot may suggest. The curves are in units of Rayleigh-Jeans temperature, so the CMB falls off with frequency. Figure from [366].

where the only requirement is that the variance of the blackbody component (the CMB) be minimised (e.g., [34, 476, 108]), or 'parametric', where contributions to the observed signal are assumed to follow a spectral model of a certain parametric form, with parameters that are then determined using Bayesian techniques (e.g., [133, 467, 72]). We will have more to say about foreground cleaning in chapter 5, where we estimate the expected level of foreground residuals in SO polarisation data after cleaning.

1.5.3.2 The thermal Sunyaev-Zeldovich effect

A fraction of the CMB photons we observe will have followed trajectories that took them through galaxy clusters — massive, gravitationally-bound regions with many dozens of galaxies in a volume only a few megaparsecs in diameter. These objects have masses ranging from the $10^{10}\,M_\odot$ of "galaxy groups" to the $10^{15}\,M_\odot$ of the most massive

clusters. In addition to galaxies, these clusters contain dark matter, and, crucially for our purposes, gas.

This gas is mostly hydrogen and helium, with traces of metals, and it is smoothly distributed across the intra-cluster medium (ICM). X-ray measurements have determined it to be very hot, with temperatures of order $10^8\,\mathrm{K}$, consistent with the temperature expected if the gas particles are in virial equilibrium in the gravitational potential of the cluster [238].

At such high temperatures, the gas is largely ionised, and the hot, free electrons inverse-Compton-scatter with CMB photons, which are comparatively much colder (around 0.3 meV at $z = 0$, compared to electron energies of a few keV in the ICM of clusters). On average, photons receive an energy boost, which results in a y-type distortion of the CMB frequency spectrum; the *thermal Sunyaev-Zeldovich effect*, or tSZ [470] (for reviews, see, e.g., [396, 73, 308]). Photons are thus systematically shifted from the Rayleigh–Jeans side to the Wien side of the spectrum, which translates to a temperature decrement at frequencies below 217 GHz, and an increment at frequencies higher than this threshold. It is thanks to this effect that clusters can be easily identified in observations of the CMB temperature anisotropies on arcminute scales, appearing as shadows at low frequencies, or as bright spots at high frequencies. Though in principle there can also be a signature in polarisation, the effect is expected to be small, of $O(1\%)$ of the amplitude in intensity [411, 73].

The resulting CMB temperature deviation due to a cluster of mass M and redshift z in the direction of $\boldsymbol{\theta}$ is[41]

$$\frac{\Delta T(\boldsymbol{\theta}, M, z)}{T} = g(\nu) y(\boldsymbol{\theta}, M, z)\,. \tag{1.84}$$

Here, we have split the effect into a characteristic frequency signature, $g(\nu) = x/\tanh(x/2) - 4$, with $x = h\nu/k_\mathrm{B}T$ (k_B is Boltzmann's constant), multiplied by the Compton-y parameter,

$$y(\boldsymbol{\theta}, M, z) = \frac{\sigma_\mathrm{T}}{m_\mathrm{e}c^2} \int_\mathrm{l.o.s.} P_\mathrm{e}\left(\sqrt{l^2 + d_\mathrm{A}^2 |\boldsymbol{\theta}|^2}, M, z\right) \mathrm{d}l\,, \tag{1.85}$$

[41] Equation (1.84) ignores relativistic corrections, which could only be relevant for the most massive clusters in the Universe, with masses in excess of $10^{15} M_\odot$ and able to support electron energies of $k_\mathrm{B}T_\mathrm{e} \gtrsim 10\,\mathrm{keV}$ [209, 83, 329]. We do not include relativistic corrections in our analytic treatment for two reasons: first, because these objects are likely to be masked in actual analyses, and second, because the 'Battaglia' profile, the cornerstone of our calculation, was fit to simulations which ignored such corrections. The Websky simulations, against which we validate our calculations in section 5.4, do not feature them either.

which is an integral of the electron pressure, P_e, along the line of sight (d_A is the angular diameter distance). In a fully-ionised medium with primordial hydrogen fraction $X_\mathrm{H} = 0.76$, the electron pressure is related to the gas pressure, P_th, by $P_\mathrm{th} = P_\mathrm{e}(5X_\mathrm{H} + 3)/[2(X_\mathrm{H} + 1)] = 1.932P_\mathrm{e}$. Typical values for the y-parameter associated with clusters are $y \sim 10^{-4}$, so the tSZ effect can produce anisotropy of order 1 mK in the Rayleigh-Jeans part of the CMB spectrum; this is comparable in amplitude to the primary CMB anisotropies [308].

It is worth noting that free electrons residing outside clusters, in filaments of the cosmic web, can also produce tSZ emission (their contribution has in fact recently been detected at moderate significance [107]). However, since electron pressure is proportional to the product of electron number density and temperature, the tSZ contribution from the 'field' is tiny compared to that originating from clusters, the densest and hottest large-scale structures in the Universe. The predominance of the most massive clusters is captured by the scaling relation $\Delta T \propto M^{5/3}$, where M is the mass of the cluster (see, e.g., [238]).

Measurements of the tSZ effect can be used to extract valuable cosmological information. As we will see in section 1.6.2, the mean number of clusters can be predicted as a function of redshift and mass in different cosmologies; this can then be contrasted with the abundance of clusters detected via their tSZ signature. The comparison requires relating the tSZ amplitude to cluster mass — for instance by calibrating against X-ray observations (e.g., [361]) or CMB lensing (e.g., [526]) — and obtaining cluster redshifts by means of follow-up observations. Since the temperature decrement they induce is independent of their distance to us, clusters can be identified out to high redshifts, granted the angular resolution is sufficient. In principle, this could enable the detection of clusters out to the highest redshifts where they exist; in practice, the numbers are indeed growing rapidly, with SPT, Planck and ACT each having catalogued upwards of 600 [53], 1200 [363] and 4000 [187] SZ-detected clusters, respectively. These have enabled tight constraints on the growth of structure as function of time; see Ref. [526] and references therein.

In chapter 5 we will be concerned with the tSZ effect not as the signal of interest, but as a source of bias to CMB lensing reconstructions. We will strive to model those biases analytically, using the halo model described in section 1.6. Our ability to do so will hinge on being able to accurately parametrise the pressure profile of clusters as a function of cluster mass and redshift. This is a complicated task, because the profile is sensitive to the rich gastrophysics of the ICM: AGN and supernova feedback, radiative cooling and star formation are but a few of the phenomena that affect it.

Analytic efforts to characterise the pressure profile have been popular in the literature. These approaches necessitate several assumptions: spherical symmetry, some type of hydrostatic equilibrium[42] possibly allowing non-thermal pressure terms[43], and a relationship between pressure and density to populate halos with baryons given an underlying dark matter profile [233, 429]. Semi-analytic models share with analytic ones the underlying assumptions of hydrostatic equilibrium and some pressure–density relation, but they replace mass functions with simulations of the dark matter distribution onto which baryons are then pasted [419, 483].

However, there is growing evidence that these fundamental assumptions do not accurately describe real clusters: hydrostatic equilibrium is violated in clusters that have undergone mergers and in the outskirts of all clusters; and fixing a pressure–density relation is also inaccurate, as this relation is in fact a function of radius, and it is affected by non-thermalised bulk flows which provide pressure support in the outer parts of the cluster but do not contribute to the tSZ [26].

These factors are naturally taken into account in both empirical and simulation-based characterisations of the pressure profile. Observational constraints have been important in recent times (see, e.g., [16, 376]), revealing an apparent universality of pressure profiles in mass and redshift. However, it is difficult to obtain data extending to large cluster radii. For this reason, simulations enjoy a particularly prominent position in the literature. Here, we harness the work of Ref. [26], who fit the average, normalised thermal pressure profile, $P_{\rm th}/P_{200}$,[44] in hydrodynamical simulations — featuring AGN and supernova feedback, radiative cooling and star formation processes — with a generalised NFW profile of the form

$$\bar{P}_{\rm fit} = P_0\,(x/x_c)^{\gamma}\,[1+(x/x_c)^{\alpha}]^{-\beta} \quad , \quad x \equiv r/R_{200}\,. \tag{1.86}$$

In addition to the parameters of the standard NFW profile, α and γ, this functional form introduces a core scale parameter, x_c, an amplitude, P_0, and a power-law index, β, which parametrises the fall-off of the profile. Reference [26] found that the parametric form above sufficed to fit the simulations with better than 5% accuracy, out to a

[42]Hydrostatic equilibrium occurs when pressure gradients exactly balance the inward gravitational pull.

[43]Thermal pressure is the dominant type of pressure in the majority of clusters, especially those that have not undergone any recent merges [383] (and the only type, in fact, if the ICM gas is completely thermalised); but non-thermal contributions are also possible. There is growing evidence, coming from hydrodynamical simulations, that the main source of non-thermal pressure in clusters is turbulence, accounting for 10-30% of the total pressure at R_{500} [325, 437].

[44]Here, $P_{200} = 200GM_{200}\rho_{\rm crit}(z)f_{\rm b}/(2R_{200})$, with $f_{\rm b} = \Omega_{\rm b}/\Omega_{\rm m}$, is the self-similar amplitude for pressure [217, 495, 42, 142]

Parameter	A_0	α_m	α_z
P_0	18.1	0.154	-0.758
x_c	0.497	-0.00865	0.731
β	4.35	0.0393	0.415

Table 1.2 Mass and redshift fit parameters for the pressure profile parametrisation of equations (1.86) and (1.87), as obtained by Ref. [26].

radius $R \lesssim 2R_{200}$, and over a wide range of cluster masses and redshifts; performing better than the naïve profile prediction associated with the self-similar solution to the equations of gravitational collapse (which ignore the radiative gas physics).

However, they also noticed a significant dependence of the best-fit parameters on mass and redshift. This dependence can be incorporated into the model by fixing $\alpha = 1.0$ and $\gamma = -0.3$, and casting the remaining parameters as separable functions of mass and redshift,

$$A = A_0 \left(\frac{M_{200}}{10^{14} M_\odot} \right)^{\alpha_\mathrm{m}} (1+z)^{\alpha_z} \,, \tag{1.87}$$

where A can be any of P_0, β or x_c. The best-fit parameters determined by Ref. [26] are shown in table 1.2. We will refer to this combination of fitting form and parameters as the 'Bataglia profile'.

With these parameter values, the predicted pressure profiles were found to deviate from the simulated ones by less than 10% over a wide range of redshifts and masses; some examples are shown in figure 1.11. There was also good agreement at the level of the tSZ power spectrum between analytic calculations based on the Battaglia profile and simulations (see figure 5 of [26]). Recently, the Battaglia profile has also passed several observational tests: X-ray observations of low-z clusters [16], observations of massive clusters with Bolocam [410] and Planck [352], and explorations of less massive galaxy groups using the stacked SZ signal from locally brightest galaxies (LBGs) [152]. Given its ongoing success, we will use the Battaglia profile to model the pressure profile of clusters in chapter 5, where we use an extension of the halo model to calculate biases to CMB lensing reconstrucions due to the tSZ effect.

1.5.3.3 The cosmic infrared background

Stars in actively-star-forming galaxies emit UV light. This radiation can be absorbed by dust grains in the intragalactic medium of those very galaxies, which in turn re-emit the energy in the infrared. The ensemble of infrared radiation produced in this way by galaxies across the redshift range where star formation takes place is called the cosmic

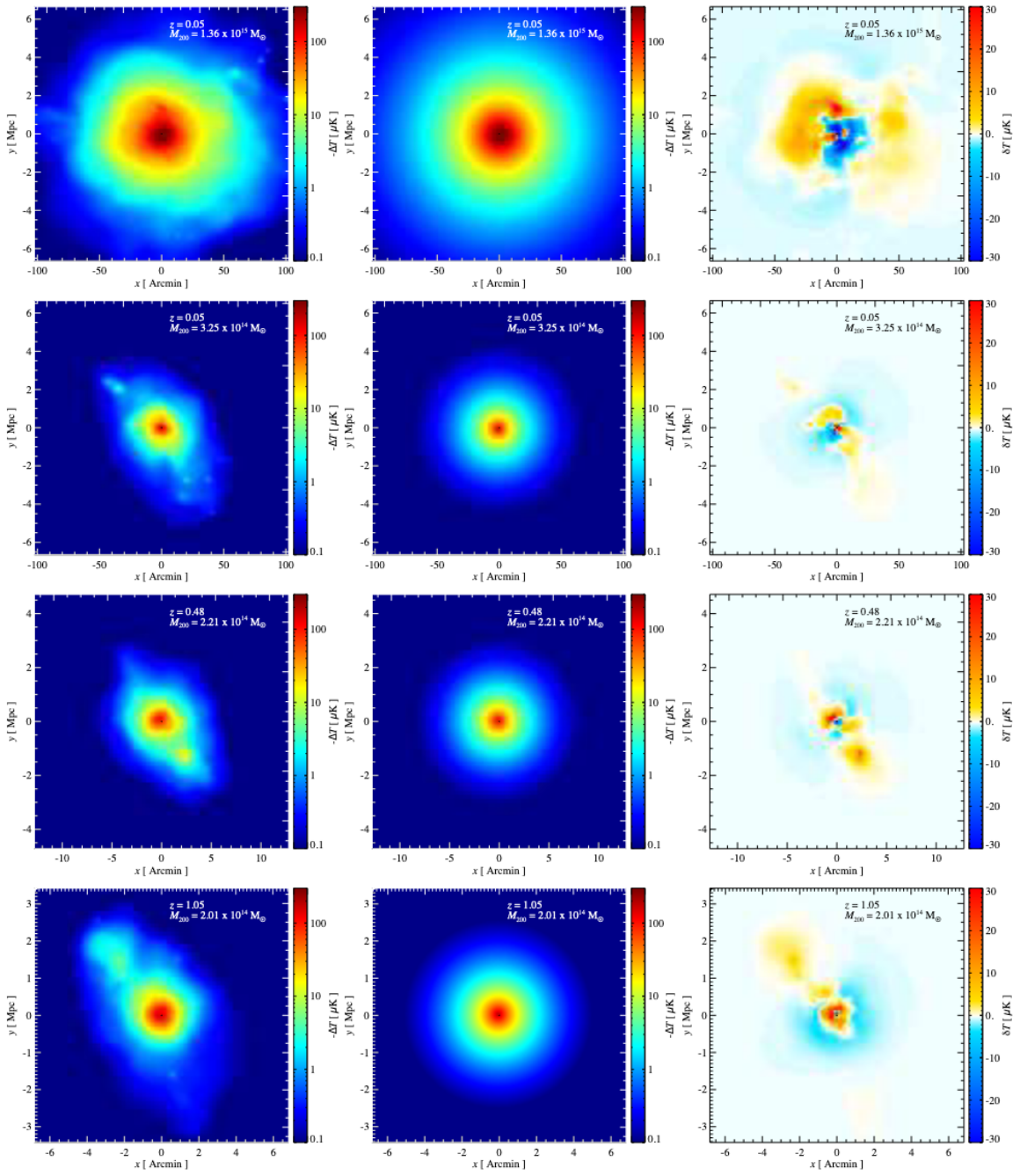

Fig. 1.11 Comparison of four projected pressure maps of simulated clusters to maps of projected, pasted 'Battaglia' profiles. From left to right, the panels show the simulated clusters (truncated at a spherical radius of $6R_{500}$); the projected, pasted profiles from the constrained fit of equations (1.86) and (1.87), using the best-fit parameter values of table 1.2; and the difference between the two. All maps are at 30 GHz. The colour scale is linear for the rightmost column, and logarithmic for the other two. Figure from Ref. [26].

infrared background (CIB). Since the dust is at a temperature of a few tens of Kelvin, CIB emission peaks in the sub-millimetre sector of the electromagnetic spectrum, and can be measured at CMB frequencies. Though theoretical predictions of its existence can be found as early as the 1950s (see [179] for a historical review), the challenges posed by atmospheric absorption of infrared light, together with the faintness of the CIB relative to foreground emission from our Galaxy and the Solar System, meant that a direct detection [387] was not possible until the era of COBE [454] and IRTS [310].

The CIB is highly isotropic on large scales, owing to its extragalactic origin, but some degree of anisotropy was always expected. Since the CIB originates from sources which are intrinsically discrete (though most of them are unresolved), any fluctuations in the number of galaxies along different lines of sight will result in angular fluctuations in the measured brightness on small scales. Moreover, galaxies trace the underlying matter distribution, so the CIB will display large-scale correlations, to the extent that they exist in the matter field [160, 226]. These anisotropies have indeed been detected at high Galactic latitudes [246, 221, 294], and mapped with precision by a number of experiments, most notably, by Planck [357, 365, 283], using its 353, 545 and 857 GHz channels.

The CIB anisotropies depend upon, and thus constrain, the redshift–dependent SEDs of star-forming galaxies, the relationship between the luminosity of a galaxy and the mass of its host halo, and the clustering properties of galaxies relative to those of the dark matter (the galaxy 'bias' we will address in section 1.6.3). By studying the CIB fluctuations, these interesting variables can be investigated much more extensively, and out to higher redshift, than would be possible using only resolved galaxies (see, e.g., [288, 357, 493]).

In order to derive constraints, a theoretical model for the CIB emission must be written down and contrasted with observations. In section 1.6.7, we describe a state-of-the-art CIB halo model which has featured in a number of recent investigations [428, 494, 357]. Then, in chapter 5, we extend it to model bispectra and trispectra of the CIB, and calculate the biases that these induce on CMB lensing reconstructions.

The reason the CIB is a cause of concern when reconstructing CMB lensing has to do (in part[45]) with the fact that the two are highly correlated. Star formation happens in a fairly broad range of redshifts, peaking at approximately $z \sim 2$, but extending as far back as $z \sim 4$ [44, 493, 494]. This overlaps extensively with the distribution of structures responsible for the CMB lensing deflections, to the point that the CIB and

[45] As we will see in chapter 5, a non-Gaussian CIB with a non-vanishing trispectrum would bias CMB lensing reconstructions even if it were not correlated with lensing.

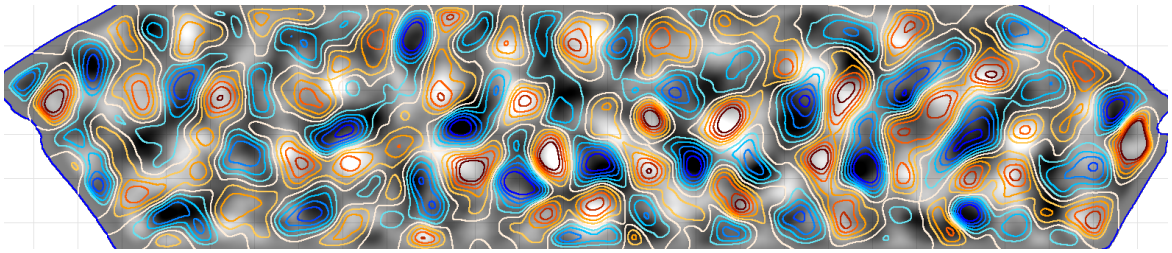

Fig. 1.12 A map of the CIB anisotropies (contours) overlaid on a map of the CMB lensing potential (greyscale), covering approximately 456 sq. deg. of the sky. The CIB is extracted from Planck data at 545 GHz using the GNILC algorithm [365], while lensing is reconstructed internally from ACT data [101]; both fields are Wiener-filtered. The high degree of correlation between CMB lensing and the CIB is readily apparent. Figure from [101].

CMB lensing are up to 80 % correlated [455, 192, 355]. (The similarity between the two can be appreciated by eye from figure 1.12.) For this reason, the CIB has played a key role in early implementations of delensing, as we will discuss in greater detail in chapter 3. In that chapter, we will also explain that separating the CIB from Galactic dust is a challenging task, since both are forms of dust emission with similar SEDs. This difficulty motivates the work in section 3.5, where we investigate how foreground residuals can affect the delensing of B-modes when the CIB is used as a proxy of the matter distribution.

The same mechanisms introduced in section 1.5.3.1 to explain the polarisation of dust emission in our own galaxy suggest that the light from the individual galaxies comprising the CIB should also be polarised. Theoretical predictions put the polarisation fraction at a level of around 1% (e.g., [183]), though recent measurement by Planck indicate a higher value of approximately 10% [367]. The CIB will be less polarised than individual galaxies are due to misalignments of galaxy polarisation directions along the line of sight, which lead to partial cancellations. Recent calculations have shown that clustering contributions to CIB angular spectra — possibly arising from the alignment of galaxies with the local tidal field — are negligibly small [140]. In chapter 3, we consider shot-noise terms, and show that they can give rise to higher-point functions of CIB polarisation even if galaxy polarisation angles are completely random.

1.6 The formation of cosmic structures

1.6.1 Motivation

In section 1.4, the evolution of linearised matter perturbations was laid out. Linear theory is a powerful framework to understand the Universe at early times (including the CMB) but it breaks down once perturbations grow to a certain level and modes stop evolving independently. The relevance of non-linear evolution is a function of scale and time, but a rough measure is that it cannot be ignored when the dimensionless matter power spectrum approaches unity, $\mathcal{P}_{\rm m}(k_{\rm nl}, z) \approx 1$; for the concordance cosmological model, $k_{\rm nl} \approx 0.3h\,{\rm Mpc}^{-1}$ today. In this section, we describe ways in which the evolution of matter fluctuations can be followed well into the non-linear regime, and translated to the abundance of observable tracers such as galaxies or clusters. Our goal will be to introduce the halo model of dark matter clustering, which will be an essential ingredient of our work in chapter 5.

The fundamental assumption underlying the halo model of dark matter clustering (based on the pioneering work of Ref. [328]; see, e.g., [96] for a review) is that all the matter in the Universe is enclosed in bound objects, which have come to be known as halos. The model then posits that the distribution of matter can be described by combining an understanding of the internal structure of the halos, relevant chiefly on small scales, with a characterisation of how the halos are clustered, the dominant factor on large scales. This separation of scales is an essential ingredient of the model: the claim is that the clustering can be described using the tools of perturbation theory (see [41]), while more sophisticated treatments (invoking possibly hydrodynamical simulations) are needed to comprehend the structure of individual halos.

Ever since the seminal work of Ref. [510], the idea that galaxy formation is determined by the characteristics of their host halo has become widely accepted. This suggests that the statistical properties of the galaxy distribution can begin to be understood by studying the statistics of the halo population, including prescriptions for how galaxies occupy halos which depend on the galaxy type under scrutiny. We introduce this extension of the halo model to galaxies in section 1.6.6, and apply it to the CIB in section 1.6.7.

1.6.2 The halo mass function

An essential ingredient of the halo model is a prediction for the number of bound objects of a given mass that are to be found at different redshifts: the halo mass

function. In this section, we outline the analytic derivation of the Press–Schechter mass function, a particularly important one that will also shed light on the physics at play. Despite proving surprisingly accurate, analytically-derived mass functions no longer live up to the precision afforded by observational probes. Therefore, we conclude this subsection by reviewing efforts to obtain halo mass functions from simulations.

Before we can study the properties of the ensemble of collapsed objects, we must understand the dynamics of collapse at the level of individual halos. Unfortunately, keeping track of this process once the perturbations have gone non-linear is only possible in a few, highly-idealised scenarios. The simplest case is that of the spherical collapse of a top-hat overdensity, first calculated by Ref. [155]. In this model, perturbations behave like closed FLRW universes decoupled from their environment: they initially expand; then they stop, turn around, and collapse. Ultimately, the fate of the collapsed object deviates from the closed FLRW prediction and, rather than ending up in a singularity, it forms a virialised halo with a density approximately 178 times that of the background. A crucial feature of the spherical collapse model is that it provides a relationship between the non-linear overdensity of the object and that which it would have had, had it evolved according to linear theory: a virialised object (a halo) which forms at redshift z must have originated from a region of the primordial density field whose overdensity, $\delta_{\rm i}(\boldsymbol{x})$, if evolved using the linear-theory growth rate ($D(z)$, defined in section 1.4, but normalised to unity at present), reaches the threshold $\delta_{\rm i}(\boldsymbol{x})D(z) = \delta_{\rm c} \approx 1.69$.[46] Since general relativity — which governs the dark matter interactions — is a scale-free theory, this number is independent of mass and redshift[47].

Being able to relate the non-linear density of the collapsed object to the density of the perturbations evolved using linear theory is very useful: given the statistics of the primordial density field, one can predict which regions will have collapsed into bound structures at any later time. Moreover, it has the added benefit that a linear transformation preserves the simple, Gaussian character of the primordial fluctuations, greatly simplifying calculations.

The formalism that paved the way for our modern understanding of the mass function was developed by Press and Schechter in [385]. Their ansatz was that the fraction of mass which is in the form of halos of mass M or greater at any specified

[46]This value of $\delta_{\rm c}$ is specific to spherical collapse in an Einstein–de Sitter cosmology (with $\Omega_{\rm m} = 1$, $\Omega_K = 0$ and $\Omega_\Lambda = 0$)

[47]In principle, the critical threshold for collapse could become a function of mass and redshift if we considered baryons, which introduce a physical scale (the sound horizon); or if collapse was in fact not spherical (see, e.g., [434]). We ignore these and other realistic effects in this succint exposition. Note, however, that the formation time *is* a function of the initial conditions and the cosmological model (e.g., [65]).

time is given by the probability that the primordial density field, smoothed over a volume[48] $V_\mathrm{f} = M/\bar{\rho}$ (where $\bar{\rho}$ is the comoving matter density of the background) and linearly-evolved to the time in question, exceeds the critical threshold for collapse, δ_c. For Gaussian primordial fluctuations, they found that the comoving number density of collapsed objects in the range $M \to M + \mathrm{d}M$ is

$$n(M,t)\mathrm{d}M = \frac{\bar{\rho}}{M^2} f_\mathrm{PS}(\nu) \left| \frac{\mathrm{d}\ln\nu}{\mathrm{d}\ln M} \right| \mathrm{d}M\,, \tag{1.88}$$

where

$$f_\mathrm{PS}(\nu) \equiv \sqrt{\frac{2}{\pi}} \nu e^{-\nu^2/2} \tag{1.89}$$

is known as the 'multiplicity function', and we have defined $\nu \equiv \delta_c(t)/\sigma(M)$. Note that, in this formulation, the threshold for collapse, $\delta_c(t) = \delta_c/D(t)$, is time-dependent; while the density field is linearly extrapolated to the present time, $\delta_0(\boldsymbol{x})$, and smoothed as

$$\delta_\mathrm{s}(\boldsymbol{x}, R) \equiv \int \mathrm{d}^3\boldsymbol{x}' \delta_0(\boldsymbol{x}') W(\boldsymbol{x} - \boldsymbol{x}', R), \tag{1.90}$$

where $W(\boldsymbol{x}, R)$ is a window function picking out a comoving volume $V_\mathrm{f}(R) = M/\bar{\rho}$. The mass variance of the smoothed density field is, therefore,

$$\sigma^2(M) = \langle \delta_\mathrm{s}^2(\boldsymbol{x}, R) \rangle = \frac{1}{2\pi^2} \int_0^\infty \mathrm{d}k P(k) \widetilde{W}^2(\boldsymbol{k}R) k^2\,, \tag{1.91}$$

where $\widetilde{W}(\boldsymbol{k}R)$ is the Fourier transform of $W(\boldsymbol{x}, R)$, and $P(k)$ is the linear-theory matter power spectrum at the present day.

Equation (1.88) suggests that halos of mass M cannot become abundant until $\sigma(M) \gtrsim \delta_c/D(t)$. At $z = 0$, $\sigma(M_*) = \delta_\mathrm{c}$ for a characteristic mass scale $M_* = 2{\times}10^{13}\,\mathrm{M}_\odot$; halos more massive than this are indeed rare. More generally, this mass scale of non-linearity increases with time as $M_*(t) \propto [D(t)]^{6/(n+3)}$ for a matter power spectrum of the form $P(k) \propto k^n$ [305]; since CDM spectra generically have $n > -3$ on all relevant scales, structure formation in these models proceeds *hierarchically*, with lower-mass halos typically forming first.

In hierarchical models of structure formation, all matter should collapse into halos at some point in time. This was in fact not guaranteed from the initial derivation in [385], which had to be corrected by a 'fudge factor' of 2 to ensure it. The inaccuracy arises from an internal inconsistency of the formalism: a mass cell which has $\delta_1 > \delta_\mathrm{c}$

[48] The seminal Press–Schechter paper [385] studied the case of smoothing with a top-hat filter — this is, in fact, the only choice that lends itself to an analytic treatment.

when smoothed on scale M_1 and $\delta_2 < \delta_c$ when smoothed on scale M_2 will only count towards the fraction of halos with masses greater than M_1, even if $M_1 > M_2$.

A correct derivation was presented in [60] by studying the excursion set of a Gaussian density field, iteratively filtered with sharp band-passes narrowly-separated in k-space. The resulting trajectory in $(\sigma(M), \delta_s(R))$-space can be shown to be a Markovian random walk with simple, Gaussian statistics. This approach makes it clear that it is a trajectory's *first* crossing of δ_c that matters when counting halos, irrespective of whether the overdensity might fluctuate back below the threshold when smaller-scale modes are taken into account. The resulting picture is that the fraction of random walks which first impinge the barrier on scale $R(M)$ corresponds to the fraction of the total mass contained in halos of mass M.

The assumption of spherical collapse is engrained in the Press–Schechter mass function — specifically, through the value and time-independence of the density threshold for collapse. Alternative models of the mass function exist which are valid in the more realistic limit of ellipsoidal collapse; in this case, the critical threshold for collapse depends on the ellipticity and prolateness of the tidal field (the second derivatives of the gravitational potential). The excursion set approach can be extended to incorporate these effects [434, 436], producing a mass function that can be written as equation (1.88), but replacing $f_{\rm PS}$ with

$$f_{\rm ST}(\nu) \equiv A\left(1 + \frac{1}{\tilde{\nu}^{2q}}\right) f_{\rm PS}(\tilde{\nu})\,. \tag{1.92}$$

Here, $\tilde{\nu} = 0.84\nu$, $q = 0.3$ and $A \approx 0.322$. This is the 'Sheth–Tormen' mass function, which provides a better fit to simulations than the Press–Schechter prediction; in particular, it alleviates a dearth of high-mass halos and an excess of low-mass ones which started to become apparent in the high-resolution cosmological simulations coming online around the turn of the millenium; see, e.g., [212]. Overall, the Sheth–Tormen mass function agrees with state-of-the art simulations to approximately 20% accuracy [500].

Finally, the mass function can also be calibrated to simulations for improved agreement; see, e.g., [212, 135, 388, 500, 479, 57, 56]. Even then, care must be taken that one's definition of the mass of virialised objects in the simulations does not bias the calibration. In particular, Ref. [479] showed that the 'spherical overdensity' halo finder of Ref. [243] is a better choice than the popular 'Friends-of-friends' algorithm: the former correlates more tightly with actual observables, and it offers greater self-

X	X_0	α_X
A	0.368	–
β	0.589	0.20
γ	0.864	-0.01
ϕ	-0.729	-0.08
η	-0.243	0.27

Table 1.3 Best-fit parameters for the Tinker halo mass function parametrisation [479], equation (1.93), in the case where $r_\mathrm{h} = r_{200}$. The redshift evolution of a given parameter, X, is modelled as $X(z) = X_0(1+z)^{\alpha_X}$, where X_0 is the value of the parameter at $z = 0$. Values obtained from Ref. [480].

consistency when used in analytic halo model calculations, which for the most part assume that halos are spherical.

Reference [479] used a suite of N-body cosmological simulations of various ΛCDM cosmologies to calibrate the mass function of halos at redshifts $z \sim 0$–2 and with masses in the range $(10^{11}$–$10^{15})\ h^{-1}\,\mathrm{M}_\odot$. Their fitting form of choice was

$$f_\mathrm{T}(\nu) \equiv A\left[1 + (\beta\nu)^{-2\phi}\right]\nu^{2\nu}e^{-\gamma\nu^2/2}\,, \tag{1.93}$$

where β, ϕ, η and γ are parameters determined from simulations, and A is set by the normalisation constraint that the mass function integrate to unity at $z = 0$ (that is, that all the matter in the Universe resides in halos at present). They found that the mass function deviated significantly from 'universality'[49], as halos of a fixed smoothing scale became less abundant at higher redshifts[50]. This redshift evolution is captured rather well by $X(z) = X_0(1+z)^{\alpha_X}$, where X_0 is the value of parameter X at redshift $z = 0$, and α_X is a new parameter to be fit for; values are shown in table 1.3. The combination of fitting formula and best-fit parameters has come to be known as the 'Tinker' mass function. It agrees with simulations at the level of 5% up to $z \lesssim 2.5$.

All in all, simulations constitute the most promising route to more accurate characterisations of the mass function. However, the work ahead will be arduous, owing to the large dynamic range that is required: from large volumes to track the highest-mass objects, all the way down to fine resolutions to reproduce the insides of halos and their substructure. Furthermore, N-body simulations are unlikely to be able to reproduce the

[49] In this context, universality refers to the shape of $f(\nu)$ being approximately independent of cosmology and redshift.

[50] This is likely due to the evolution of Ω_m with redshift, and the impact this has on the halo concentration, which in turn affects any observables defined over a fixed aperture [479]. See [78], and references therein, for further discussions on the universality of halo abundances and halo clustering.

true halo mass function with percent-level accuracy until they can properly take into account baryonic effects such as AGN and supernova feedback, which significantly alter the distribution of matter within halos relative to the dark-matter-only scenario [238].

1.6.3 The bias of dark matter halos

The halo mass function we introduced in the previous section lets us predict the mean number density of halos of a certain mass that we should expect to find at some redshift in a given cosmology — one might think that, so far, we have learnt nothing about how these halos will be arranged in space. However, note that these halos form once the uncollapsed regions from which they originate have become more overdense than some critical value, and that this is more likely to happen in denser-than-average environments. This implies that the spatial distribution of halos ought to be correlated with their mass: higher-mass halos preferentially form in denser regions, so they are more clustered; on the other hand, halos with low masses can only form and avoid significant accretion or mergers if they form in under-dense regions, so their clustering is penalised relative to that of the linear field (or that of the dark matter that is not yet bound in halos). Halos are therefore said to be *biased* tracers of the underlying dark matter distribution [216]. In this section, we briefly review the formalism for relating the statistics of the halo population to those of the dark matter, in some highly idealised scenarios.

Consider a spherical region of comoving radius R_0 and comoving volume V_0, containing mass $M_0 = V_0\bar{\rho}(z_0)$ at z_0. Denote the overdensity of this region, linearly extrapolated to z_0, as δ_0. We are interested in the overdensity of halos of mass M_1, which were formed at $z_1 > z_0$, and are found in this region; that is,

$$\delta_{\rm h}\left(M_1, z_1|M_0, R_0, z_0\right) = \frac{N\left(M_1, z_1|M_0, R_0, z_0\right)}{n\left(M_1, z_1\right)V_0}\left[1+\delta(z)\right] - 1\,. \tag{1.94}$$

Here, $n\left(M_1, z_1\right)$ is the usual halo mass function, $N\left(M_1, z_1|M_0, R_0, z_0\right)$ is the average number of halos of mass M_1 which formed at z_1 and are found in the patch, and $\delta(z)$ is the non-linear matter overdensity within our region at some redshift $z < z_1$ — the redshift at which we will later ask questions about halo bias. The factor of $[1+\delta(z)]$ is there to account for the change in volume of the region as it contracts or expands by virtue of being over- or under-dense[51].

[51] Equation (1.94) thus leads to the halo bias in the *Eulerian* picture. For its *Lagrangian* equivalent, one must drop the factor of $[1+\delta(z)]$.

One of the advantages of the excursion-set approach to calculating mass functions [60] is that it can be used to calculate quantities such as $N\left(M_1, z_1|M_0, R_0, z_0\right)$: this is just the average number of halos with mass M_1, identified at z_1, that merge to form a more massive halo with mass M_0 at z_0. The formalism can be applied irrespective of whether the region characterised by R_0 has actually collapsed into a halo by z_0 (only the volume of the region and its impact on the background density matter). It gives [307]

$$N\left(M_1, z_1|M_0, R_0, z_0\right) \mathrm{d}M_1 = \frac{M_0}{M_1} f(1|0) \left|\frac{\mathrm{d}\sigma^2(M_1)}{\mathrm{d}M_1}\right| \mathrm{d}M_1 \,, \tag{1.95}$$

where

$$f(1|0)\,\mathrm{d}\sigma^2(M_1) = \frac{1}{\sqrt{2\pi}} \frac{\delta_\mathrm{c}(z_1) - \delta_0}{\left[\sigma^2(M_1) - \sigma^2(M_0)\right]^{3/2}} \exp\left[-\frac{\left(\delta_\mathrm{c}(z_1) - \delta_0\right)^2}{2\left[\sigma^2(M_1) - \sigma^2(M_0)\right]}\right] \mathrm{d}\sigma^2(M_1) \,. \tag{1.96}$$

Consider the limit where R_0 is large, so that $M_0 \gg M_1$ and $\sigma(M_1) \gg \sigma(M_0)$. Equation (1.96) then tells us that the number of halos in our region of choice grows with δ_0. Heuristically, δ_0 can be intepreted as a long-wavelength background modulating shorter-wavelength fluctuations[52], and causing the critical density for collapse at z_1 to be replaced with $\delta_\mathrm{c}(z_1) \to \delta_\mathrm{c}(z_1) - \delta_0$; hence, collapse is easier in denser regions.

In the limit of large R_0, the halo overdensity of equation (1.94) is

$$\begin{aligned}\delta_\mathrm{h}\left(M_1, z_1|M_0, R_0, z_0\right) &\approx \left(1 - \frac{\delta_0}{\delta_\mathrm{c}(z_1)}\right) \exp\left[\frac{\delta_0}{2\sigma^2(M_1)}(2\delta_0 - \delta_\mathrm{c}(z_1))\right] [1 + \delta(z)] - 1 \\ &= \delta(z) + \delta_0 \frac{\nu_1^2 - 1}{\delta_\mathrm{c}(z_1)} + \delta(z)\delta_0 \frac{\nu_1^2 - 1}{\delta_\mathrm{c}(z_1)} + O(\delta_0^2) \,, \end{aligned} \tag{1.97}$$

where $\nu_1 \equiv \delta_\mathrm{c}(z_1)/\sigma(M_1)$. In the linear regime, $\delta(z) \approx \delta_0 D(z) \ll 1$, so we can drop the third term in the last line and replace $\delta_0 \approx \delta(z)/D(z)$. Thus, in this limit, fluctuations in the halo abundance can be related to those of the dark matter rather accurately as

$$\delta_\mathrm{h}\left(M_1, z_1|M_0, R_0, z_0\right) = b(M_1, z_1, z)\delta(z) \,, \tag{1.98}$$

where

$$b(M_1, z_1, z) \equiv 1 + \frac{1}{D(z)}\left(\frac{\nu_1^2 - 1}{\delta_\mathrm{c}(z_1)}\right) \,. \tag{1.99}$$

[52]This idea of decomposing the density field into short and long wavelength modes was first introduced by Ref. [216], and it has been referred to as the 'peak-background' split since [21]; see [109] for a review of the uses of this powerful tool.

is the 'linear bias'[53], at redshift z, of halos of mass M_1, formed at z_1. These expressions reflect the tendency for massive halos to cluster more extensively than the matter field, since $\nu_1 > 1$ implies $b > 1$; while low-mass halos are anti-biased, because $\nu_1 < 1$ means that $b < 1$. The high-mass behaviour might remind the reader of the results in Ref. [216]: massive halos form at high peaks of the density field, which have a higher probability of existing in dense, compact environments. Low-mass halos, on the other hand, can only escape mergers and accrete only moderately if they formed in underdense, sparse environments. Note also that halos of a given mass were more strongly biased at higher redshifts.

In deriving the linear bias relation of (1.99) from equation (1.97), we ignored terms beyond first order in $\delta(z)$, arguing that they were small when considering perturbations in the linear regime. Though this is a good approximation on large scales, halo bias is, in general, non-linear — particularly on small scales. If we Taylor-expand $\delta_{\rm h}(\delta)$ as

$$\delta_{\rm h}\left(M_1, z_1 | M_0, R_0, z_0\right) = \sum_{k>0} b_k(M_1, z_1, z)\delta^k \,, \tag{1.100}$$

we can then define b_k, the k-th order bias coefficients. In certain analytic models — such as spherical or ellipsoidal collapse — $\delta(z)$ is fully determined by δ_0 and R_0, so higher-order bias terms can be calculated analytically [306, 418, 79].

Halo bias must satisfy the 'consistency relation' that

$$\int \mathrm{d}M \frac{M}{\bar{\rho}(z)} n(M, z) b(M, z) = 1 \,, \tag{1.101}$$

at all redshifts and to all orders. As will become clearer from the discussion around equation (1.123), the consistency relation is needed for the halo power spectrum to equal the matter power spectrum on large scales — and hence, for dark matter to be unbiased against itself, once we assume that all of it resides in halos.

If the spread around the mean number of halos predicted by equation (1.95) were negligible, then the (possibly non-perturbative) halo bias extracted from equation (1.97) would be all that is needed to relate the halo population to the matter field. In reality, however, halo formation is affected by peculiarities of the environment other than its mass and redshift, so the relationship is stochastic rather than deterministic [307, 433, 77]. Since the physical processes that source this stochasticity tend to be rather local, the bias can be treated as being deterministic on large scales.

[53] As was the case with the mass function, more accurate results can be obtained analytically if the derivation of the bias relation is carried out based on the physics of ellipsoidal collapse, as opposed to spherical [213, 435].

Parameter	Value
A	$1.0 + 0.24y \exp\left[-(4/\epsilon)^4\right]$
a	$0.44\epsilon - 0.88$
B	0.183
b	1.5
C	$0.019 + 0.107\epsilon + 0.19 \exp\left[-(4/\epsilon)^4\right]$
d	2.4

Table 1.4 Best-fit parameters for the large-scale halo bias parametrisation of equation (1.102), in the case where $r_{\rm h} = r_{200}$. Here, $\epsilon \equiv \log_{10} 200$. Values were obtained from Ref. [480]. These parameter choices ensure that the constraint of equation (1.101) is satisfied to better than percent-level precision when used in conjunction with the mass function of equation (1.93) (and its associated best-fit parameter values given in table 1.3).

In addition, the halo bias can also depend on the smoothing scale, R_0, in which case it is known as 'scale-dependent' bias; this effect is small on large scales[54], so we ignore it here.

Improved characterisations of the halo bias can be obtained from simulations. In chapter 5, we will use the description put forth by [480], who studied the large-scale bias of halos ranging from masses of $10^{10}\,h^{-1}\,{\rm M}_\odot$, to the most massive clusters found in their simulated, cosmological volumes. They introduced the functional form

$$b(\nu) = 1 - {\rm A}\frac{\nu^{\rm a}}{\nu^{\rm a} + \delta_c^{\rm a}} + {\rm B}\nu^{\rm b} + {\rm C}\nu^{\rm d}\,, \tag{1.102}$$

and fit for the parameters A,a,b,B,C and d, subject to the consistency relation of equation (1.101). The best-fit parameters for the case where the mass function is that from Ref. [479] are shown in table 1.4. These fit the bias measured from individual simulations with a typical scatter of approximately 6%. Interestingly, Ref. [480] find that the form of $b(\nu)$ changes by less than 5% (if at all) in the redshift range $0 < z < 2.5$.

To conclude this section, we emphasise that, in the limit where the halo bias is deterministic, the halo mass function is all that is needed to relate the halo population to the matter field. The bias can then be calculated (to all orders) from it.

[54]Note that we are not referring to the effect identified in [100], which is associated with primordial non-Gaussianity.

1.6.4 The density profile of dark matter halos

To lowest order, we can treat dark matter halos as being spherical[55], in which case they are characterised by their density profile, $\rho(r)$. Further analytic insights into the internal structure of these halos can only be derived in the context of highly-idealised scenarios of gravitational collapse. For example, the self-similar solution for the spherical collapse of dark matter perturbations with a spectrum compatible with current constraints predicts a density run scaling as $\rho(r) \propto r^{-2}$ — similar to that of an isothermal sphere (see, e.g., [305]).

Early explorations using N-body simulations yielded dark matter density profiles that indeed resembled this isothermal solution [144]. However, with the advent of higher-resolution simulations in the late 1990s, it became clear that the slopes of simulated profiles were actually shallower than in the isothermal case near the centre, $\rho(r) \propto r^{-1}$, but steeper in the outskirts, $\rho(r) \propto r^{-3}$. The NFW profile — after Navarro, Frenk and White — of Ref. [322] proved to be a particularly good fit to halos of a wide range of masses in CDM cosmologies [323], so it became widely adopted. In chapter 5, it will be our parametrisation of choice to model the distribution of dark matter inside halos. It has the form

$$\rho(r) = \frac{\rho_{\rm crit}\delta_{\rm char}}{(r/r_{\rm s})\,(1+r/r_{\rm s})^2}\,, \tag{1.103}$$

where $\rho_{\rm crit}$ is the critical density to make the Universe flat at the redshift of interest (though we omit this dependence for notational compactness), $\delta_{\rm char}$ is a characteristic overdensity of the halos, and $r_{\rm s}$ is a scale radius parametrising the transition from the $\rho(r) \propto r^{-1}$ to the $\rho(r) \propto r^{-3}$ scaling, where the profile agrees with the isothermal prediction of $\rho(r) \propto r^{-2}$ (in the sense that $d\ln\rho/d\ln r = -2$).

The mass enclosed in the halo, out to radius r, is therefore

$$M(r) = 4\pi\rho_{\rm crit}\delta_{\rm char}r_{\rm s}^3\left[\ln(1+r/r_{\rm s}) - \frac{r}{r_{\rm s}+r}\right]. \tag{1.104}$$

This expression does not converge when integrated out to an infinite radius, so a halo radius, $r_{\rm h}$, must be defined. Conventionally, it is chosen to be the radius within which the mean matter density is some number, $\Delta_{\rm h}$, times the background matter density or the critical density at the redshift in question. In this work, we adopt the former definition, and use $\rho_{\rm h} = \Delta_{\rm h}\rho_{\rm m} = \Delta_{\rm h}\rho_{\rm crit}\Omega_{\rm m}(z)$, where $\Omega_{\rm m}(z) \equiv \rho_{\rm m}/\rho_{\rm crit}$ is now redshift-dependent (unlike in equation (1.9)). Two of the most popular choices are

[55] It has been known since the earliest simulations of structure formation in CDM cosmologies [104] that this unlikely to be strictly true in nature; see [6] and references therein for details.

$\Delta_{\rm h} = 200$ and $\Delta_{\rm h} = \Delta_{\rm vir} \approx 176$. Note that the latter choice[56] is more consistent with the definition of halos used to derive the halo mass function, so it will be the one we preferentially use in our halo model calculations.

Notice, from equation (1.104), that $\delta_{\rm char}$ can be directly calculated from the mass of the halo once $r_{\rm h}$ is defined and $r_{\rm s}$ is specified[57]. This means that, in a given cosmology, the NFW profile is fully determined by the mass and the scale radius of the halo; or, equivalently, by the mass and the concentration, defined as $c \equiv r_{\rm h}/r_{\rm s}$.

The concentration parameter is useful because it highlights interesting trends seen in the simulations. Typical concentration values range between 4–40, with the Milky way halo sitting at roughly $c \approx 10$–15 (see, e.g., Ref. [32] and references therein). In general, it is closely related to the formation history of a halo [323]; as such, it depends on halo mass, redshift and cosmology. Much effort has been devoted to modelling the evolution of the mean concentration of NFW halos, $\bar{c}(M, z)$, in simulations of ΛCDM cosmologies; see, e.g. [323, 68, 119, 113]. This evolution is captured rather well by power laws in mass and redshift[58],

$$\bar{c}(M, z) = {\rm A} \left(\frac{M}{M_{\rm pivot}} \right)^{\rm B} (1+z)^{\rm C} \,, \tag{1.106}$$

where A, B and C are parameters to be fit for. In chapter 5, we will use the parameter values shown in table 1.5, which were obtained by Ref. [119] (though note that more recent constraints exist; see, e.g., [112]). These reflect a trend of decreasing concentration with halo mass and redshift: higher-mass halos typically form later, so they are more likely to have experienced recent mergers and have an abundance of material orbiting far from their central regions. At a fixed halo mass, there is significant scatter around the mean concentration owing to the diversity of halo formation histories;

[56] See the discussion of spherical collapse of dark matter into virialised halos in section 1.6.2.

[57] From the definition of the halo radius, $M(r_{\rm h}) \equiv (\Delta_{\rm h} \rho_{\rm crit} \Omega_{\rm m}(z))(4\pi r_{\rm h}^3/3)$, we learn that

$$\delta_{\rm char} = \frac{\Delta_{\rm h} \Omega_{\rm m}(z)}{3} \frac{c^3}{\ln(1+c) - c/(1+c)} \,, \tag{1.105}$$

where c is the concentration parameter, to be introduced shortly.

[58] Note that power-law parametrisations of $\bar{c}(M, z)$ do not extrapolate well to redshifts, masses and cosmologies different from those on which the model was calibrated — for applications requiring this, a calibration based on ν might be more appropriate, as there is evidence that $\bar{c}(\nu)$ is more universal than $\bar{c}(M, z)$ [524, 382, 45, 113].

Convention	Redshift	A	B	C
$r_{\rm h} = r_{200}$	0–2	5.71 ± 0.12	-0.084 ± 0.006	-0.47 ± 0.04
$r_{\rm h} = r_{\rm vir}$	0–2	$7.85^{\pm 0.17}_{\pm 0.18}$	-0.081 ± 0.006	-0.71 ± 0.04

Table 1.5 Best-fit parameters for the median halo concentration of NFW halos in the model of Ref. [119]. The parameters we quote are calibrated to the full sample of simulated halos on redshifts $z < 2$, with a background cosmology as in [230]. In all cases, $M_{\rm pivot} = 2 \times 10^{12}\, h^{-1}\, {\rm M}_\odot$.

the relation can be approximated as a log-normal distribution,

$$p(c|M,z){\rm d}c = \frac{{\rm d}\ln {\rm c}}{\sqrt{2\pi\sigma^2_{\ln c}}} \exp\left[-\frac{\ln^2\left[c/\bar{c}(M,z)\right]}{2\sigma^2_{\ln c}}\right], \tag{1.107}$$

the width of which, $\sigma_{\ln c} \approx 0.11$–$0.27$ (for relaxed halos, using $r_{\rm h} = r_{\rm vir}$), is largely independent of halo mass; see, e.g., [214, 68, 502, 326].

In this work, we will frequently invoke the normalised Fourier transform of the dark matter distribution within halos[59]. For a halo of mass M, this is

$$u(\boldsymbol{k}|M) \equiv \frac{\int {\rm d}^3\boldsymbol{x}\, \rho(\boldsymbol{x}|M) e^{-i\boldsymbol{k}\cdot\boldsymbol{x}}}{\int {\rm d}^3\boldsymbol{x}\, \rho(\boldsymbol{x}|M)}, \tag{1.109}$$

which, for a spherically-symmetric profile, simplifies to

$$u(\boldsymbol{k}|M) = \int_0^{r_{\rm h}} {\rm d}r\, 4\pi r^2 \frac{\sin(kr)}{kr} \frac{\rho(r|M)}{M}. \tag{1.110}$$

Mathematically, this is just the statement that the Fourier transform of a spherically-symmetric function is a Hankel transform. Figure 1.13 shows the normalised Fourier transform of NFW profiles of different masses, and with their approximate mean concentration today. This figure shows that smaller-mass halos have Fourier transforms extending to smaller scales. Note also that, on scales much larger than their typical spatial extent, halos can be regarded as point masses; i.e., $u(|\boldsymbol{k}| \to 0\,|M) \to 1$.

The reason why density profiles of dark matter halos are nearly universal is not yet understood. However, this is a feature that emerges for a very broad range of

[59] For consistency with the literature, we use the asymmetric Fourier convention in this section. In three dimensions, this is:

$$f(\boldsymbol{x}) = \int \frac{d^3\boldsymbol{l}}{(2\pi)^{3/2}} f(\boldsymbol{l}) e^{i\boldsymbol{l}\cdot\boldsymbol{x}} \quad \text{and} \quad f(\boldsymbol{l}) = \int d^3\boldsymbol{x} f(\boldsymbol{x}) e^{-i\boldsymbol{l}\cdot\boldsymbol{x}}. \tag{1.108}$$

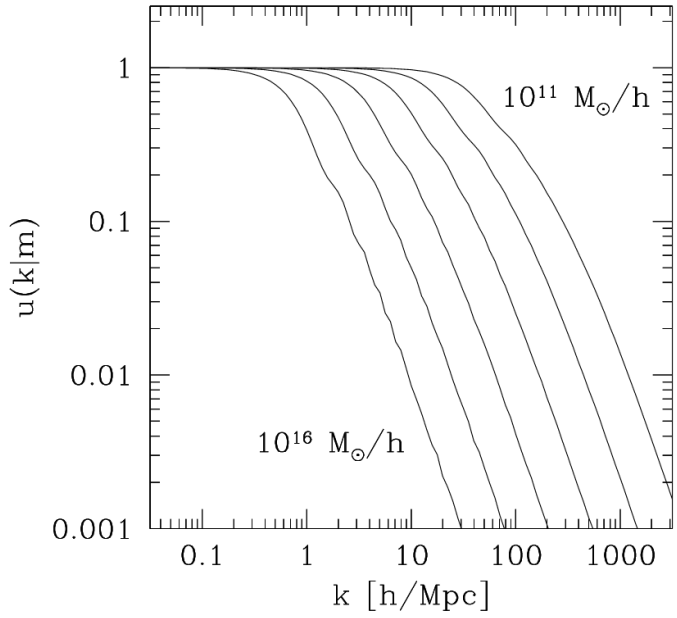

Fig. 1.13 Normalised Fourier transforms of NFW profiles for different halo masses at $z = 0$. Halo concentrations are calculated as $\bar{c}(M) = 9[M/M_*(z = 0)]^{-0.13}$. Notice that small-scale power comes chiefly from low-mass halos, whereas large scales receive contributions from a wide range of masses. Figure from Ref. [96].

initial conditions, so it is likely a product of the relaxation processes driving the halo to equilibrium after the messy stages of formation through mergers[60].

Though in this work we will only be using the NFW profile, it is worth mentioning that other profiles exist in the literature that provide a better fit to modern simulations. One notable contender is the Einasto profile [128, 324], which outperforms NFW even when one of its three parameters is fixed and both fitting forms have the same number of degrees of freedom [305].

1.6.5 The halo model

There is compelling evidence that the dark matter component of our Universe is 'cold'. As discussed in section 1.6.2, cold dark matter is expected to all end up eventually bound in virialised halos. In this section, we combine the infrastructure developed in previous sections — the halo mass function, bias and internal structure — into a formalism

[60]In dynamics, a relaxed system is one which is found in an equilibrium state. There are several pathways for a system to achieve this from a non-relaxed configuration; but for collisionless systems like dark matter halos, the only one available is violent relaxation due to a changing gravitational potential [305]. One plausible explanation for the universality of dark matter halo profiles is that violent relaxation might have erased virtually all dependence on the initial conditions.

describing the clustering properties of the matter: the 'halo model'(e.g., [424, 277, 96]). This will be the main tool we use in chapter 5 to model extragalactic CMB foregrounds, and in section 3.5.2.2, we will use similar techniques to calculate the equal-time bispectrum and trispectrum of the cosmic infrared background. For this reason, we will go thorough the derivation in detail.

The total matter density at a point can be calculated by adding the contributions from all individual halos,

$$\rho(\boldsymbol{x}) = \sum_i M_i u\left(\boldsymbol{x} - \boldsymbol{x}_i | M_i\right) , \tag{1.111}$$

where each halo is located at position $\boldsymbol{x}_i$, and has mass M_i. In a statistical sense, the normalised density profile of halos is fully determined by their mass and redshift: the halo concentration can be obtained statistically from these two using, for example, equations (1.106) and (1.107). For the purpose of this introduction, we consider halos at a fixed redshift, so that the normalised density profile, $u\left(\boldsymbol{x}|M\right)$, depends only on mass.

The mean matter density at this redshift, $\bar{\rho}$, can then be calculated as

$$\begin{aligned} \bar{\rho} = \langle\rho(\boldsymbol{x})\rangle &= \langle\sum_i M_i u\left(\boldsymbol{x} - \boldsymbol{x}_i | M_i\right)\rangle \\ &= \int \mathrm{d}M n(M) M \underbrace{\int \mathrm{d}^3\boldsymbol{x}' u\left(\boldsymbol{x} - \boldsymbol{x}' | M_i\right)}_{=1} . \end{aligned} \tag{1.112}$$

In the second line, we have used the definition of the mass function to replace the ensemble average of sums over halo masses and positions with mass-function-weigthed integrals over mass and volume.

This formalism also enables calculation of the clustering properties of the matter. The two-point function of the density is given by

$$\langle\rho(\boldsymbol{x}_1)\rho(\boldsymbol{x}_2)\rangle = \langle\sum_{i,j} M_i u\left(\boldsymbol{x}_1 - \boldsymbol{x}_i | M_i\right) M_j u\left(\boldsymbol{x}_2 - \boldsymbol{x}_j | M_j\right)\rangle . \tag{1.113}$$

This received two types of contributions: those where both legs of the correlator come from the same halo ($i = j$), and those stemming from two different halos ($i \neq j$). The

one-halo contribution is

$$\langle\sum_{i=j} M_i^2 u\left(\boldsymbol{x}_1-\boldsymbol{x}_i|M_i\right) u\left(\boldsymbol{x}_2-\boldsymbol{x}_i|M_i\right)\rangle = \int \mathrm{d}M M^2 n(M) \times \int \mathrm{d}^3\boldsymbol{x}' u\left(\boldsymbol{x}_1-\boldsymbol{x}'|M\right) u\left(\boldsymbol{x}_2-\boldsymbol{x}'|M\right) , \tag{1.114}$$

while the two-halo terms are

$$\begin{aligned}
&\langle\sum_{i\neq j} M_i u\left(\boldsymbol{x}_1-\boldsymbol{x}_i|M_i\right) M_j u\left(\boldsymbol{x}_2-\boldsymbol{x}_j|M_j\right)\rangle \\
&= \int \mathrm{d}M_1 M_1 n(M_1) \int \mathrm{d}M_2 M_2 n(M_2) \\
&\quad \times \int \mathrm{d}^3\boldsymbol{x}' \mathrm{d}^3\boldsymbol{x}'' \left[1+\xi_{\mathrm{hh}}\left(\boldsymbol{x}'-\boldsymbol{x}''|M_1,M_2\right)\right] u\left(\boldsymbol{x}_1-\boldsymbol{x}'|M_1\right) u\left(\boldsymbol{x}_2-\boldsymbol{x}''|M_2\right) \\
&= (\bar{\rho})^2 + \int \mathrm{d}M_1 M_1 n(M_1) \int \mathrm{d}M_2 M_2 n(M_2) \\
&\qquad \times \int \mathrm{d}^3\boldsymbol{x}' \mathrm{d}^3\boldsymbol{x}'' \xi_{\mathrm{hh}}\left(\boldsymbol{x}'-\boldsymbol{x}''|M_1,M_2\right) u\left(\boldsymbol{x}_1-\boldsymbol{x}'|M_1\right) u\left(\boldsymbol{x}_2-\boldsymbol{x}''|M_2\right) .
\end{aligned} \tag{1.115}$$

In the first equality, we have defined the halo correlation function, $\xi_{\mathrm{hh}}\left(r|M_1,M_2\right)$, which describes the excess clustering probability, over a random distribution in space, of a pair of halos of masses M_1 and M_2 separated by a distance r.

We are now in a position to compute the covariance of the dark matter overdensity,

$$\begin{aligned}
\langle\delta(\boldsymbol{x}_1)\delta(\boldsymbol{x}_2)\rangle &= \frac{1}{\bar{\rho}^2}\langle\rho(\boldsymbol{x}_1)\rho(\boldsymbol{x}_2)\rangle - 1 \\
&\equiv \xi^{1\mathrm{h}}\left(|\boldsymbol{x}_1-\boldsymbol{x}_2|\right) + \xi^{2\mathrm{h}}\left(|\boldsymbol{x}_1-\boldsymbol{x}_2|\right) ,
\end{aligned} \tag{1.116}$$

where we have defined a one-halo contribution,

$$\xi^{1\mathrm{h}}\left(|\boldsymbol{x}_1-\boldsymbol{x}_2|\right) = \frac{1}{\bar{\rho}^2}\int \mathrm{d}M M^2 n(M) \int \mathrm{d}^3\boldsymbol{x}' u\left(\boldsymbol{x}_1-\boldsymbol{x}'|M\right) u\left(\boldsymbol{x}_2-\boldsymbol{x}'|M\right) , \tag{1.117}$$

and a two-halo term,

$$\begin{aligned}
\xi^{2\mathrm{h}}\left(|\boldsymbol{x}_1-\boldsymbol{x}_2|\right) =& \frac{1}{\bar{\rho}^2}\int \mathrm{d}M_1 M_1 n(M_1) \int \mathrm{d}M_2 M_2 n(M_2) \\
&\times \int \mathrm{d}^3\boldsymbol{x}' \mathrm{d}^3\boldsymbol{x}'' \xi_{\mathrm{hh}}\left(\boldsymbol{x}'-\boldsymbol{x}''|M_1,M_2\right) u\left(\boldsymbol{x}_1-\boldsymbol{x}''|M_1\right) u\left(\boldsymbol{x}_2-\boldsymbol{x}''|M_2\right) .
\end{aligned} \tag{1.118}$$

We have assumed that the halo distribution is a stationary point process, so that the correlation function depends on the distance between halos but not on their global location or orientation.

Notice that these expressions involve convolutions of density profiles; they are ubiquitous in halo model calculations. Since convolutions in real space become multiplications in Fourier space, it shall prove convenient to work in the latter. The Fourier space equivalent of the correlation function is the power spectrum,

$$P(k) = P^{1h}(k) + P^{2h}(k). \tag{1.119}$$

The first term on the right-hand side is the one-halo contribution,

$$P^{1h}(k) = \int \mathrm{d}M \left(\frac{M}{\bar{\rho}}\right)^2 n(M)|u\left(k|M\right)|^2\,, \tag{1.120}$$

which only depends on the halo profile and mass function. On the other hand, the two-halo term,

$$P^{2h}(k) = \int \mathrm{d}M_1 \left(\frac{M_1}{\bar{\rho}}\right) n(M_1) u\left(k|M_1\right) \int \mathrm{d}M_2 \left(\frac{M_2}{\bar{\rho}}\right) n(M_2) u\left(k|M_2\right) P_{\rm hh}(k|M_1, M_2)\,, \tag{1.121}$$

depends also on $P_{\rm hh}(k|M_1, M_2)$, the cross-power spectrum of halos with masses M_1 and M_2; in fact, on scales much larger than the size of individual halos, the two-halo term is insensitive to the the shape of the individual halos.

On large scales, the halo overdensity is simply related to that of the matter via deterministic halo bias (see section 1.6.3); hence,

$$P_{\rm hh}\left(k_{\rm long}|M_1, M_2\right) \approx b(M_1) b(M_2) P(k_{\rm long})\,, \tag{1.122}$$

where $P(k)$ is the matter power spectrum (for now, we ignore all redshift dependence). Notice that, on scales much larger than the typical size of a halo (call them $k_{\rm long}^{-1}$), $u\left(k_{\rm long}|M\right) \to 1$; this, together with the consistency relations of equation (1.101), implies that

$$P^{2h}(k_{\rm long}) \approx P(k_{\rm long}) \approx P_{\rm lin}(k_{\rm long})\,. \tag{1.123}$$

The last equality follows from the fact that, on large scales, the matter power spectrum is very well approximated by the linear-theory calculation, $P_{\rm lin}$. Hence, in the regime

where the two-halo term is important,

$$P^{\rm 2h}(k) \approx P_{\rm lin}(k) \int {\rm d}M_1 \left(\frac{M_1}{\bar{\rho}}\right) b(M_1) n(M_1) u\left(k|M_1\right) \\ \times \int {\rm d}M_2 \left(\frac{M_2}{\bar{\rho}}\right) b(M_2) n(M_2) u\left(k|M_2\right) \, . \tag{1.124}$$

Rigorously speaking, this expression only holds insofar as we are probing scales where both the assumption of deterministic halo bias and our neglect of halo exclusion effects hold. In practice, we shall not need to refine the expression any further, for the one-halo term dominates on scales small enough that these assumptions break.

To conclude, note that, as $k \to 0$, the two-halo term goes as $P^{\rm 2h}(k_{\rm long}) \propto P_{\rm lin}(k_{\rm long}) \propto k$ (for CDM spectra), while the one-halo term is constant. At large enough scales, the unphysical happens: the one-halo term dominates the power spectrum. One way to avoid this is to consider 'compensated' halo profiles built from combinations of positive and negative overdensities [96, 85], but these have problems of their own, such as a lack of power on large scales. Instead, in the halo model calculations of chapter 5, we introduce an *ad hoc* factor in the style proposed by Ref. [295] that damps the density profiles on large scales when calculating the one-halo contribution:

$$u(k|M) \to u(k|M) \left(1 - e^{-k/k_*}\right) \, , \tag{1.125}$$

where k_* is a damping scale for which we choose the value $k_* \equiv 0.01\,{\rm Mpc}^{-1}$. Physically, this is motivated by the fact that halos cannot exist within each other, by definition [451].

The framework can be extended to calculate the higher-point correlations of the matter fluctuations. We quote now some results that will be useful later; and refer the reader to [96] for details. The matter bispectrum is

$$B(\boldsymbol{k}_1, \boldsymbol{k}_2, \boldsymbol{k}_3 | M_1, M_2, M_3) = B^{\rm 1h} + B^{\rm 2h} + B^{\rm 3h} \, , \tag{1.126}$$

where,

$$
\begin{aligned}
B^{\rm 1h} &= \int dM\, n(M) \left(\frac{M}{\bar{\rho}}\right)^3 \prod_{i=1}^{3} u(k_i|M)\,, \\
B^{\rm 2h} &= \int dM_1\, n(M_1) \left(\frac{M_1}{\bar{\rho}}\right) u(k_1|M_1) \int dM_2\, n(M_2) \left(\frac{M_2}{\bar{\rho}}\right)^2 u(k_2|M_2) u(k_3|M_2) \\
&\quad \times P_{\rm hh}(k_1|M_1, M_2) + \text{perms.}\,, \\
B^{\rm 3h} &= \left[\prod_{i=1}^{3} \int dM_i\, u(k_i|M_i) n(M_i) \left(\frac{M_i}{\bar{\rho}}\right)\right] B_{\rm hhh}(\boldsymbol{k}_1, \boldsymbol{k}_2, \boldsymbol{k}_3|M_1, M_2, M_3)\,.
\end{aligned}
\tag{1.127}
$$

The three-halo term depends on the halo bispectrum,

$$
B_{\rm hhh}(\mathbf{k}_1, \mathbf{k}_2, \mathbf{k}_3; M_1, M_2, M_3) = \prod_{i=1}^{3} b_i(M_i) \left[B^{\rm lin}(\mathbf{k}_1, \mathbf{k}_2, \mathbf{k}_3) + \frac{b_2(M_3)}{b_1(M_3)} P^{\rm lin}(k_1) P^{\rm lin}(k_2)\right],
\tag{1.128}
$$

where b_i is the ith order halo bias (for convenience, we have denoted the linear halo bias as b_1, though in earlier discussions we used b), and $B^{\rm lin}$ is obtained from tree-level perturbation theory; see, e.g. [96].

The same ideas can be used to calculate the matter trispectrum,

$$
T(\boldsymbol{k}_1, \boldsymbol{k}_2, \boldsymbol{k}_3, \boldsymbol{k}_4|M_1, M_2, M_3, M_4) = T^{\rm 1h} + T^{\rm 2h} + T^{\rm 3h} + T^{\rm 4h}\,,
\tag{1.129}
$$

where

$$
\begin{aligned}
T^{\rm 1h} &= \int dM\, n(M) \left(\frac{M}{\bar{\rho}}\right)^4 \prod_{i=1}^{4} u(k_i|M)\,, \\
T^{\rm 2h} &= \Big[\int dM_1\, n(M_1) \left(\frac{m_1}{\bar{\rho}}\right) u(k_1|M_1) \int dM_2\, n(M_2) \left(\frac{M_2}{\bar{\rho}}\right)^3 \\
&\quad \times u(k_2|M_2) u(k_3|M_2) u(k_4|M_2) P_{\rm hh}(k_1|M_1, M_2) + \text{perms.} \Big] \\
&+ \Big[\int dM_1\, n(M_1) \left(\frac{M_1}{\bar{\rho}}\right)^2 u(k_1|M_1) u(k_2|M_2) \int dM_2\, n(M_2) \left(\frac{M_2}{\bar{\rho}}\right)^2 u(k_3|M_2) u(k_4|M_2) \\
&\quad \times P_{\rm hh}(|\mathbf{k}_1 + \mathbf{k}_2||M_1, M_2) + \text{perms.} \Big]\,, \\
T^{\rm 3h} &= \int dM_1\, n(M_1) \left(\frac{M_1}{\bar{\rho}}\right) u(k_1|M_1) \int dM_2\, n(M_2) \left(\frac{M_2}{\bar{\rho}}\right) u(k_2|M_2) \\
&\quad \times \int dM_3\, n(M_3) \left(\frac{M_3}{\bar{\rho}}\right)^2 u(k_3|M_3) u(k_4|M_3) B_{\rm hhh}(\mathbf{k}_1, \mathbf{k}_2, \mathbf{k}_3 + \mathbf{k}_4|M_1, M_2, M_3)\,, \\
T^{\rm 4h} &= \left[\prod_{i=1}^{4} \int dM_i\, u(k_i|M_i) n(M_i) \left(\frac{M_i}{\bar{\rho}}\right) \right] \\
&\quad \times T_{\rm hhhh}(\mathbf{k}_1, \mathbf{k}_2, \mathbf{k}_3, \mathbf{k}_4; M_1, M_2, M_3, M_4). \qquad (1.130)
\end{aligned}
$$

Notice that the four-halo contribution depends on the halo trispectrum,

$$
\begin{aligned}
T_{\rm hhhh}(\mathbf{k}_1, \mathbf{k}_2, \mathbf{k}_3, \mathbf{k}_4|M_1, M_2, M_3, M_4) = \prod_{i=1}^{4} b_i(M_i) \Bigg[& T^{\rm lin}(\mathbf{k}_1, \mathbf{k}_2, \mathbf{k}_3, \mathbf{k}_4) \\
& + \frac{b_2(M_4)}{b_1(M_4)} P^{\rm lin}(k_1) P^{\rm lin}(k_2) P^{\rm lin}(k_3) \Bigg]\,, \qquad (1.131)
\end{aligned}
$$

which is a function of the tree-level matter trispectrum, $T^{\rm lin}$.

1.6.6 Populating dark matter halos with galaxies

In a seminal paper from the late 70s, White and Rees [510] realised that, for gas to cool efficiently and form stars, it must inhabit potential wells such as those provided by dark matter halos. In the decades since, increasingly sophisticated hydrodynamical simulations have consolidated a picture of galaxy formation within which dark matter halos have retained their early importance: whilst some halos are devoid of galaxies,

every galaxy forms in a halo — the most massive halos can, in fact, contain many galaxies; each one forming in a subhalo.

This understanding might, at first, appear to be in conflict with observations. The galaxy correlation function, $w(\theta)$ — which measures the clustering of galaxies as a function of the angular separation on the sky, θ — has been determined empirically to follow a power-law with approximately $w(\theta) \propto \theta^{-0.7}$ (e.g., figure 1 of [279]; see also [343, 522]). This implies, in turn, that the three-dimensional correlation function of galaxies must also be a power law [343]. Contrast this, however, with the shape of the dark matter power spectrum as measured from simulations (e.g., figure 4 of [125]) or predicted by the halo model: galaxies appear to cluster very differently from the dark matter on small scales ($\leq$ 1–2 Mpc).

In this section, we shall see how our understanding of the clustering of dark matter can be extended to model the clustering of galaxies. In doing so, we will make contact with the complex 'gastrophysics' at play, which ultimately determines the way in which galaxies populate halos (see, e.g. [509]). Two extra pieces need to be added to the halo model in order to capture this richness [342, 418]: the probability distribution, $P(N|M)$, that a halo of mass M contains N galaxies; and some knowledge of how those galaxies are distributed in the halos. These two elements constitute the 'halo occupation distribution' (HOD), and they can be calibrated to simulations and/or observations.

Simulations have provided an increasingly accurate characterisation of $P(N|M)$ in recent years; e.g. [38, 237]. The first moment of the distribution — the mean number of galaxies per halo, $\langle N_{\rm gal} \rangle$ — is particularly important for our purposes, for if the distribution is Poissonian, the mean specifies all the higher-order factorial moments, $\langle N_{\rm gal}(N_{\rm gal}-1)\dots(N_{\rm gal}-j)\rangle = \langle N_{\rm gal}\rangle^{1+j}$. As can be seen from figure 1.14, $\langle N_{\rm gal} \rangle$ scales as a power law at high halo masses ($M \geq 10^{13}\,h^{-1}\,{\rm M}_\odot$), plateaus to values of order unity at intermediate masses, and drops to zero for masses below some threshold. This behaviour is also consistent with theoretical predictions (e.g., [38]) and fits to observations (e.g., [418]). No single probability distribution — be it Poissonian, binomial, or a nearest-integer distribution — can adequately describe the population statistics across the entire range of halo masses that host galaxies [38, 237].

However, progress can be made by splitting the galaxy population into two classes [158, 237]: centrals, which occupy the centre of their parent halos; and satellites, which form in the substructure of those host halos. There is reason to expect that galaxy formation will not proceed below a certain mass threshold — supernova explosions of stars formed early on are expected to readily disperse baryons away from

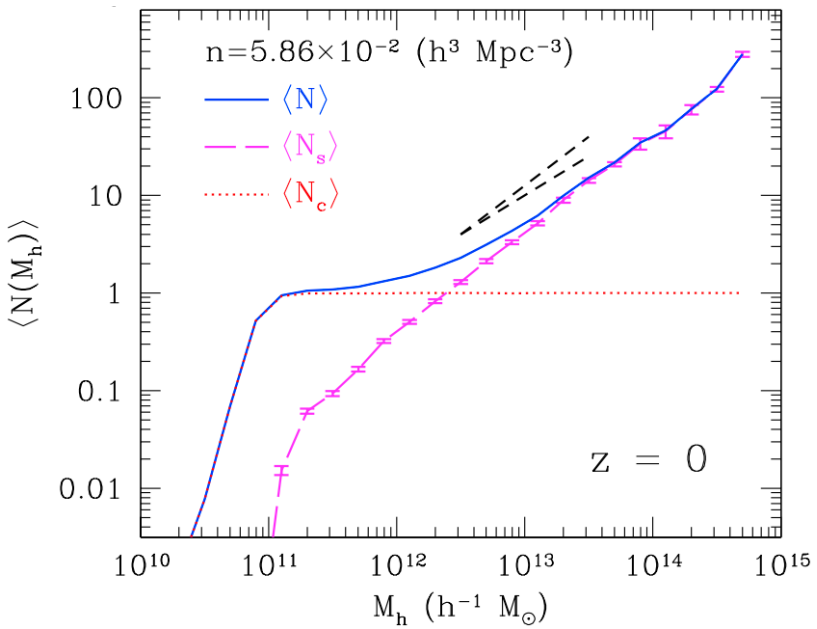

Fig. 1.14 Mean number of subhalos as a function of host halo mass at $z = 0$ in simulations of ΛCDM cosmology with a halo number density of $n = 5.86 \times 10^{-2}\, h^3\, \mathrm{Mpc}^{-3}$. Contributions from satellite (magenta dashed) and central (red dotted) halos to the total halo population (blue solid) are plotted separately. Uncertainties in the mean number of satellites is shown by the magenta error bars. Black, dashed lines show scalings of the form $N \propto M^{\alpha}$, where $\alpha = \{1, 0.8\}$. Under the assumption that dark matter halos in N-body simulations correspond to galaxies, these curves can be used as the first moment of a HOD. Adapted from Ref. [237].

low-mass halos with not enough gravitational pull to bind them. The number of central galaxies within a halo, $N_{\rm cen}$, can therefore be described as a step function

$$N_{\rm cen} = \begin{cases} 0, & \text{if } M \leq M_{\rm min}; \quad \text{and} \\ 1, & \text{if } M \geq M_{\rm min}. \end{cases} \tag{1.132}$$

If the host halos are massive enough, they will comprise a number of subhalos large enough for 'satellite' galaxies to form within them. To a first approximation, we expect the number of satellites per halo, $N_{\rm sat}$, to scale approximately as $N_{\rm sat} \propto M$ — galaxies are made up of baryons, so their number should be proportional to the baryon abundance, which in turn is a fixed fraction of the dark matter abundance. By studying the subhalo mass function in N-body simulations (and assuming that it corresponds to the abundance of satellite galaxies[61]), Ref. [237] found that, at sufficiently high masses, the population of satellite galaxies is well described[62] by a Poissonian distribution whose mean is given by a power law in mass,

$$\langle N_{\rm sat} \rangle_{N_{\rm cen}=1} = \left(\frac{M}{M_{\rm sat}} \right)^{\alpha} , \tag{1.133}$$

where, indeed, $\alpha \approx 0.87 \pm 0.01$, and $M_{\rm sat}$ is defined to be the mass of halos which (on average) host a single satellite galaxy. These parametrisations of satellites and centrals can be extended to accommodate non-zero scatter in the relation between host halo mass and number of galaxies; see, e.g., [525].

Notice that, in the equation above, we have made a distinction between the mean number of satellites across halos of any type, $\langle N_{\rm sat} \rangle$, and the mean number in halos that already have a central galaxy, $\langle N_{\rm sat} \rangle_{N_{\rm cen}=1}$. Rigorously speaking, it is only in the latter set of halos that the distribution of satellites can be considered Poissonian. The

[61] This assumption — often referred to as 'abundance matching' — is generally in good agreement with semi-analytic techniques (see, e.g., [150, 96, 237]), although the exact choice of which property of the dark matter halo best correlates with galaxy abundance is a topic of active research [503]. Note, however, that abundance matching is not guaranteed to capture potentially important baryonic effects, such as the fact that the cooling efficiency of the gas — and hence, the efficiency of galaxy formation — diminishes with the mass of the host halo, as its virial temperature grows.

[62] The satellite HOD only begins to deviate significantly from the Poissonian approximation in the mass range where the HOD of centrals dominates the overall behaviour; see figure 1.14.

two definitions can be related as

$$\begin{aligned}\langle N_{\rm sat}\rangle &= \sum_{N_{\rm cen}}\sum_{N_{\rm sat}} N_{\rm sat}P(N_{\rm sat}|N_{\rm cen},M)P(N_{\rm cen}|M)\\ &= P(N_{\rm cen}=1|M)\sum_{N_{\rm sat}} N_{\rm sat}P(N_{\rm sat}|N_{\rm cen}=1,M)\\ &= \langle N_{\rm cen}\rangle\langle N_{\rm sat}\rangle_{N_{\rm cen}=1}\,. \end{aligned} \tag{1.134}$$

In going to the second line, we have assumed that satellite galaxies only form once there is a central galaxy in the host halo; and in going to the last, we have used the fact that $P(N_{\rm cen}=1|M)=\langle N_{\rm cen}\rangle$, since $N_{\rm cen}\in\{0,1\}$. Note also that $N_{\rm gal}=N_{\rm cen}+N_{\rm sat}$.

In equations (1.120) and (1.121), we weighted the normalised halo profiles by mass in order to draw conclusions about the density distribution. How should this weighting be modified if we were instead interested in the statistics of galaxy number density? We will now address this question in detail; the understanding we develop along the way will be useful to our discussions in chapter 5 of extensions of the halo model to higher-point functions of the CIB.

Consider, first, the one-halo term. In particular, let us calculate the contribution to the galaxy power spectrum coming from pairs of galaxies[63] within a halo of mass M, a quantity we will call Q. One important ingredient we will need is the spatial distribution of galaxies across the halo, $u_{\rm gal}\,(r|M)$; this is radial, by assumption, and has Fourier transform $u_{\rm gal}\,(k|M)$. In general, it is a very good approximation to replace $u_{\rm gal}\,(k|M)$ with an NFW profile [96]; however, we will keep the $u_{\rm gal}$ notation here to retain generality. We will use the fact that central galaxies sit at the centre of halos, where $u_{\rm gal}\,(k|M)\to 1$. Hence, we can sum over all possible pairs of galaxies in the halo as

$$\begin{aligned}\mathcal{Q} &= \sum_{N_{\rm gal}=2} P(N_{\rm gal}|M)\left[N_{\rm sat}u_{\rm gal}\,(k|M)+\frac{1}{2}N_{\rm sat}(N_{\rm sat}-1)u_{\rm gal}\,(k|M)^2\right]\\ &= \langle N_{\rm cen}\rangle\sum_{N_{\rm sat}=0} P(N_{\rm sat}|M)\left[N_{\rm sat}u_{\rm gal}\,(k|M)+\frac{1}{2}N_{\rm sat}(N_{\rm sat}-1)u_{\rm gal}\,(k|M)^2\right]\\ &= \frac{1}{2}\langle N_{\rm cen}\rangle\left[2\langle N_{\rm sat}\rangle_{N_{\rm cen}=1}u_{\rm gal}\,(k|M)+\langle N_{\rm sat}\rangle^2_{N_{\rm cen}=1}u_{\rm gal}\,(k|M)^2\right]\\ &= \frac{1}{2\langle N_{\rm cen}\rangle}\left[2\langle N_{\rm cen}\rangle\langle N_{\rm sat}\rangle u_{\rm gal}\,(k|M)+\langle N_{\rm sat}\rangle^2 u_{\rm gal}\,(k|M)^2\right]\,. \end{aligned} \tag{1.135}$$

[63] Contributions from individual galaxies are also possible, but these are part of the 'shot-noise' budget.

In the third line, we have used the fact that $N_{\rm sat}$ follows a Poisson distribution when conditioned to $N_{\rm cen} = 1$, so $\langle N_{\rm sat}(N_{\rm sat} - 1)\rangle_{N_{\rm cen}=1} = \langle N_{\rm sat}\rangle^2_{N_{\rm cen}=1}$. Finally, in the last line, we have restored the unconditional averages, expressed in terms of the entire halo population. Note that $M_{\rm sat}$ is significantly larger than $M_{\rm min}$ (see, e.g., Ref. [237]), so $\langle N_{\rm cen}\rangle \approx 1$ for the mass of halos that can host at least a pair of galaxies; for this reason the $\langle N_{\rm cen}\rangle$ factor in the denominator is usually dropped. It can be shown that $\mathcal{Q} \approx \langle N_{\rm gal}(N_{\rm gal} - 1)\rangle$, and indeed this formulation is more common in the literature — we will encounter it shortly, when discussing generalisations to higher-point functions of the galaxy field.

Inspired by this weighting, we can modify equation (1.120) to obtain the one-halo contribution to the galaxy power spectrum [96]:

$$P^{\rm 1h}_{\rm gal}(k) = \int {\rm d}M n(M) \frac{1}{\bar{n}^2_{\rm gal}} \left[2\langle N_{\rm cen}\rangle\langle N_{\rm sat}\rangle u_{\rm gal}\left(k|M\right) + \langle N_{\rm sat}\rangle^2 u_{\rm gal}\left(k|M\right)^2\right] , \quad (1.136)$$

where

$$\bar{n}_{\rm gal} = \int {\rm d}M n(M) \left(\langle N_{\rm cen}\rangle + \langle N_{\rm sat}\rangle\right) \quad (1.137)$$

and the averages are to be evaluated at mass M. Note also that, in a magnitude-limited sample, the integration would be restricted to the mass range accessible given the depth of the survey (once a relationship between halo mass and galaxy luminosity has been asserted).

The two-halo term depends only on the mean number of galaxies per halo; it is given by

$$\begin{aligned} P^{\rm 2h}_{\rm gal}(k) = P_{\rm hh}(k) &\int {\rm d}M_1 \left(\frac{\langle N_{\rm gal}\rangle(M_1)}{\bar{n}_{\rm gal}}\right) b(M_1) n(M_1) u_{\rm gal}\left(k|M_1\right) \\ &\times \int {\rm d}M_2 \left(\frac{\langle N_{\rm gal}\rangle(M_2)}{\bar{n}_{\rm gal}}\right) b(M_2) n(M_2) u_{\rm gal}\left(k|M_2\right) . \end{aligned} \quad (1.138)$$

Finally, the total power in galaxy clustering is

$$P_{\rm gal}(k) = P^{\rm 1h}_{\rm gal}(k) + P^{\rm 2h}_{\rm gal}(k) + P^{\rm shot}_{\rm gal}(k), \quad (1.139)$$

where $P^{\rm shot}_{\rm gal}(k)$ is a shot-noise contribution where both legs come from the same galaxy. We will not consider shot-noise terms in detail here; instead, we refer the reader to, e.g., [428], for details.

If we compare equations (1.136) and (1.138) to their dark-matter-only counterparts, equations (1.120) and (1.138), we can immediately see that the clustering of galaxies will

differ from that of the dark matter to the extent that $\langle N_{\rm gal}\rangle$ and $2\langle N_{\rm sat}\rangle\langle N_{\rm cen}\rangle + \langle N_{\rm sat}\rangle^2$ are not exactly proportional to M and M^2, respectively. Thanks to this flexibility, the combination of halo model for dark matter clustering and a HOD has been used to successfully fit the two-point function of galaxies (e.g. [481, 97]), which has helped constrain possible models of galaxy formation.

Higher-order statistics of the galaxy population can be obtained by generalising the ideas in this section to higher-point functions of the matter field, such as equations (1.126) or (1.129). In the literature, one can find extensions of this kind to calculate, for example, the three-point function of galaxies [499], the redshift-space bispectrum [452] or the CIB bispectrum[64] [242].

This last reference provides a convenient set of rules to build higher-point functions of the 3D galaxy field. The n-order polyspectrum of galaxies (that is, the Fourier transform of the galaxy n-point function) will be a sum over all possible ways of arranging n galaxies in halos (including shot-noise-type terms where the same galaxy is featured several times). Each of these terms can be written down as follows:

- Start with an overall factor of $(1/\bar{n}_{\rm gal})^n$.
- For each one of p halos (with $p \leq n$) labelled by α_i, where $i \in \{1, \ldots, p\}$, put in a factor of $\int \mathrm{d}M_{\alpha_i}$; a halo mass function $n(M_{\alpha_i})$; and a factorial moment $\langle N_{\rm gal}(N_{\rm gal}-1)\ldots(N_{\rm gal}-j)\rangle(M_{\alpha_i})$, where $j+1$ is the number of different galaxies in that halo.
- For each galaxy in halo i, include a density profile $u_{\rm gal}\left(k_i|M_{\alpha_i}\right)$. If the term at hand has the same galaxy contracted several times (hence contributing to the shot-noise), k_i is the magnitude of the sum over the momenta of all the legs associated with that galaxy.
- Include the p-th order halo polyspectrum[65] evaluated at the masses (and redshifts) of the halos, $\mathcal{P}_{\rm h}^{(p)}\left(\sum_{r\in\alpha_1}\boldsymbol{k}_r, \ldots, \sum_{r\in\alpha_p}\boldsymbol{k}_r|M_i, \ldots, M_p\right)$, where the sum $\sum_{r\in\alpha_i}\boldsymbol{k}_r$ is over the wavevectors associated with galaxies in halo α_i. The first few halo polyspectra — with $p = 2$, $p = 3$ and $p = 4$ — are the halo power spectrum, bispectrum and trispectrum of equations (1.122), (1.128) and (1.131), respectively.

The total contribution is then the sum over all possible arrangements of the n galaxies in the halos which produce different diagrams/expressions, weighted by the appropriate permutation factors.

[64] We will see more on CIB halo models in section 1.6.7.
[65] See [242] for a rigorous definition.

The factorial moment in the second point can be cast in a form that makes more transparent the connection with equation (1.136), and with the mass-dependent-luminosity models we will introduce in section 1.6.7. In appendix C.1, we show that

$$\langle N_{\rm gal}(N_{\rm gal}-1)\dots(N_{\rm gal}-j)\rangle = \left(\frac{\langle N_{\rm sat}\rangle}{\langle N_{\rm cen}\rangle}\right)^j \left[(1+j)\langle N_{\rm cen}\rangle + \langle N_{\rm sat}\rangle\right] , \tag{1.140}$$

where we have once again omitted the mass and redshift dependences of the averages. This relation only holds insofar as the distribution of satellites can be approximated as Poissonian in the regime where $P(N_{\rm cen} = 1|M) \approx 1$. Though this is a very good approximation, higher-order factorial moments in principle require knowledge of higher-order moments of the full probability distribution, $P(N_{\rm gal}|M)$.

To conclude this section, note that this exposition has assumed that galaxies at different redshifts, and of different spectral types, all respond to the same HOD — this is, of course, not strictly true in nature. It is, in principle, possible to incorporate a variable HOD into the model, though at the risk of increasing degeneracies between the new model parameters.

1.6.7 A halo model of the CIB

As described in section 1.5.3.3, the CIB is helping further our understanding of key areas of astrophysics, such as star formation or CMB lensing. These promising use-cases have prompted numerous efforts to model the CIB. Given the existing evidence for clustering contributions to its power spectrum [161, 120, 351] and bispectrum [98, 357], a framework that can accommodate clustering is evidently preferred over simpler treatments that assume the sources are uncorrelated. The halo model is a natural candidate for this; here, we briefly review how it can be extended to understand the CIB.

Let I_ν denote the specific intensity of the CIB at frequency ν. This is given by

$$\begin{aligned} I_\nu &= \int {\rm d}z \frac{{\rm d}\chi}{{\rm d}z} a(z) j_\nu(z) \\ &= \int {\rm d}z \frac{{\rm d}\chi}{{\rm d}z} a(z) \bar{j}_\nu(z) \left[1 + \frac{\delta j_\nu(z)}{\bar{j}_\nu(z)}\right] , \end{aligned} \tag{1.141}$$

where a is the scale factor of the Universe, and χ is the comoving distance to redshift z; note also that we have assumed a spatially-flat Universe. The expression above is an integral along the line of sight of the comoving infrared emissivity, j_ν, which is sourced

by the luminosity of galaxies:

$$j_\nu(z) = \frac{1}{4\pi}\int \mathrm{d}L\, n(L,z) L_{(1+z)\nu}\,. \tag{1.142}$$

Here, $n(L,z)$ is the IR galaxy luminosity function.

Early attempts to apply the halo model to the CIB (e.g., [351, 12]) assumed that the emissivity traces the galaxy number density, so that $\delta j_\nu/\bar{j}_\nu = \delta n_{\rm gal}/\bar{n}_{\rm gal}$. This is equivalent to assuming that the luminosity function above is flat; that is, that all galaxies have the same luminosity. Though conveniently simple, these models failed to fit simultaneously the CIB power spectra across the range of frequencies observed by Planck [351].

An improved model was introduced by Ref. [428], who let galaxy luminosity be a function of halo mass. This fix is important: the assumption that all galaxies have the same luminosity leads to over-estimation of the number of satellites in massive halos when fitting the CIB power spectrum on small scales. It is for this reason that previous studies, such as [12], returned values of α — the power law exponent in equation (1.133), which governs the high-mass scaling of the mean number of galaxies per halo — sigificantly higher than the theoretical prediction of $\alpha \leq 1$. The model of Ref. [428] resolves this by having fewer, but more luminous, satellite galaxies in massive halos. Slightly modified versions of this model were subsequently used to fit successfully Planck [357] and Herschel [493] measurements of the power spectra of CIB anisotropies. This is also the model that we will use in chapter 5 to describe the CIB. We explain it, in detail, below.

If we allow galaxy luminosity to depend on the mass of the host halo, we can rewrite equation (1.142) as

$$j_\nu(z) = \int \mathrm{d}M\, n(M,z)\left[f_\nu^{\rm cen}(M,z) + f_\nu^{\rm sat}(M,z)\right]\,, \tag{1.143}$$

where we have separated the contributions from centrals,

$$f_\nu^{\rm cen}(M,z) = \frac{1}{4\pi} N_{\rm cen} L_{{\rm cen},\,(1+z)\nu}(M,z)\,, \tag{1.144}$$

and from satellite galaxies,

$$f_\nu^{\rm sat}(M,z) = \frac{1}{4\pi}\int \mathrm{d}m\, n_{\rm sub}(m,z|M) L_{{\rm sat},\,(1+z)\nu}(m,z)\,. \tag{1.145}$$

In these expressions, $n(M,z)$ and $n_{\rm sub}(m,z)$ are the halo and subhalo mass functions, respectively. The latter element can be obtained from the fitting functions of Ref. [482], for example.

Note now the similarity between equation (1.143) and the galaxy number density of equation (1.137); this suggests that the power spectrum of the emissivity can be obtained by simply replacing $\bar{n}_{\rm gal} \to \bar{j}$, $N_{\rm cen} \to f^{\rm cen}$ and $N_{\rm sat} \to f^{\rm sat}$ in the expressions for the galaxy power spectrum, equations (1.136) and (1.138). (This can also be shown rigorously by following a derivation analogous to the one in section 1.6.6.) The same will be true for higher-point functions of the emissivity.

The key ingredient in this model is a description of how luminosity depends on halo mass, frequency and redshift. Neglecting any scatter in the relation, we can write

$$L_{(1+z)\nu}(M,z) = L_0 \Phi(z) \Sigma(M) \Theta\left((1+z)\nu, z\right) \,. \tag{1.146}$$

Here, L_0 is a normalisation constant, and the other functions will be defined shortly.

The function $\Phi(z)$ attempts to capture how the IR luminosity of the galaxies comprising the CIB evolves with redshift. For this class of galaxies, luminosity is known to correlate with star formation rate (SFR) [222]. The SFR grows with redshift because of higher accretion and merger rates, higher gas fractions and objects being more compact at earlier times (see, e.g., [498] and references therein). Reference [428] argues that, theoretically, this evolution should be well approximated as a power law,

$$\Phi(z) = (1+z)^{\delta} \,, \tag{1.147}$$

though they also warn that the data, albeit still uncertain, seem to favour more flexible models with a plateau at high redshifts $z > 2$; e.g., [473].

The luminosity–mass, or $L-M$ relation is modelled by the function $\Sigma(M)$. It is well known that the stars driving this luminosity only form efficiently in a range of halo masses, since at lower and higher masses their formation is suppresed by feedback processes associated with supernovae and AGN activity, photoionisation heating, or virial shocks; see, e.g., [37, 99]. Denoting as $M_{\rm eff}$ the mass at which star formation peaks, the dependence of galaxy luminosity on halo mass can be modelled as a log-normal distribution,

$$\Sigma(M) = M \frac{1}{\left(2\pi\sigma^2_{L/M}\right)^{1/2}} e^{-(\log_{10} M - \log_{10} M_{\rm eff})^2/(2\sigma^2_{L/M})} \,, \tag{1.148}$$

where $\sigma_{L/M}$ parametrises the characteristic width of the distribution. In order to account for the quenching of gas accretion at low masses [63], the distribution is

truncated by setting $L = 0$ below $M < M_{\rm min}$, where $M_{\rm min}$ is an additional parameter to be fit for in the range $10^{10} - 10^{11}\,{\rm M}_\odot$.

Finally, $\Theta(\nu, z)$ reflects the frequency-dependence of the IR luminosity of dusty, star-forming galaxies. Inspired by the CIB SED of Ref. [161], Ref. [428] models it as

$$\Theta(\nu, z) = \begin{cases} \nu^\beta B_\nu(T_{\rm d}), & \text{if } \nu < \nu_0; \quad \text{and} \\ \nu^{-\gamma}, & \text{if } \nu > \nu_0\,, \end{cases} \tag{1.149}$$

where B_ν is the Planck function; and β, γ and $T_{\rm d}(z)$ are parameters to be fit for. The temperature of the dust within the galaxies sourcing the CIB, $T_{\rm d}(z)$, is presumed to be a function of redshift and parametrised as [357]

$$T_{\rm d}(z) = T_0(1+z)^\alpha\,. \tag{1.150}$$

See [357] for a discussion of the physical interpretation and appropriate prior ranges for these parameters. To ensure a smooth transition between the two regimes in equation (1.149), the free parameters are fit for subject to the constraint that $\mathrm{d}\ln\left[\nu^\beta B_\nu(T_{\rm d})\right]/\mathrm{d}\ln\nu = -\gamma$ at ν_0.

In order to keep the complexity of the model to a minimum, it is standard to assume that both satellites and centrals have the same luminosity if they inhabit halos of equal mass, at the same redshift[66]; hence, we drop the subscripts and set $L_{{\rm sat},\nu}(m, z) = L_{{\rm cen},\nu}(m, z) = L_\nu(m, z)$.

Reference [357] used the framework described above to model the 15 possible combinations of auto- and cross-spectra measured by Planck at 217, 353, 545, 857 GHz, and by IRAS[67] at 3000 GHz, on angular scales $187 \leq \ell \leq 2649$. They constrained eight halo model parameters, $\{\alpha, T_0, \beta, \gamma, \delta, M_{\rm eff}, M_{\rm min}, L_0\}$ (the width of the $L-M$ distribution was held fixed at a value of $\sigma^2_{L/M} = 0.5$), along with 15 other ones corresponding to the shot-noise in each channel. Best-fit values for the former set are shown in table 1.6; we refer the reader to Ref. [357] for a discussion of the physical implications of these constraints, as well as for the best-fit values of the shot-noise parameters. The model not only provides a very good fit to the data, but it also predicts with notable accuracy the cross-correlation between CMB lensing reconstructions and CIB observations made by Planck at various frequencies. Reference [493] fit a slightly-

[66] This appears to be a rather good approximation when the mass of the subhalo is measured at the time of accretion [357].

[67] The measurements were made on the reprocessed IRAS maps of [303], which go by the name of IRIS.

Parameter	Mean value
α	0.36 ± 0.05
T_0 [K]	24.4 ± 1.9
β	1.75 ± 0.06
γ	1.7 ± 0.2
δ	3.6 ± 0.2
$\log(M_{\rm eff})$ [$\mathrm{M}_\odot$]	12.6 ± 0.1
$M_{\rm min}$ [$\mathrm{M}_\odot$]	unconstrained

Table 1.6 Mean values and marginalised 68% confidence intervals for the CIB halo model parameters constrained by Ref [357]. They belong to a model, based on that of Ref. [428], which allows for mass-dependent galaxy luminosities. These parameters were fit (jointly with parametrisations of the shot-noise amplitude) to all possible auto- and cross- spectra of Planck data at frequencies of 217, 353, 545, 857 GHz and IRAS data at 3000 GHz for angular scales of $187 \leq \ell \leq 2649$. The normalisation parameter, L_0, is then obtained by fitting the model CIB power spectrum calculated from the parameter values above to the Planck data. From table 9 of Ref. [357].

modified version of the model to Herschel data, obtaining results that were qualitatively similar.

Chapter 2

Limitations of CMB B-mode template delensing

This chapter is based on [18].

2.1 Introduction

As discussed in chapter 1, the wealth of cosmological data gathered in recent decades favours models where a period of accelerated expansion of space took place at very early times: *cosmic inflation*. As a general and rather unique feature, inflationary models predict that a background of primordial gravitational waves would have been generated during that period along with fluctuations in the density. These primordial perturbations would have been present 380,000 years later, when the cosmic microwave background (CMB) was emitted, hence they are expected to have left an imprint in the temperature and polarisation patterns of this relic light [381, 219, 426]. In fact, one can form a curl-like, B-mode component of polarisation which, during recombination and in linear theory, is generated only by tensor fluctuations. Consequently, a detection of large-scale primordial B-modes would widely be considered direct evidence for cosmic inflation.

Unfortunately, we also explained in the introductory chapter that the faint, primordial signal is obscured by B-modes generated from primordial E-modes by the process of gravitational lensing of the CMB as it propagates through the large-scale matter distribution of the Universe [520]. On large angular scales, where the power spectrum of primordial B-modes peaks ($l < 200$), the lensing power spectrum resembles that of white noise, comparable in amplitude to the noise power of an experiment with a sensitivity of $\Delta_P = 5\,\mu\mathrm{K}\,\mathrm{arcmin}$, approximately that of experiments coming online at the time of writing; see section 1.5.2.2. Lensing-induced B-modes are now routinely observed in high-precision polarisation surveys, following the first detection (with data

from the South Pole Telescope) by Ref. [172]. In order to be able to detect any small, primordial B-mode signal, the variance associated with the lensing contribution ought to be mitigated — a procedure known as *delensing*, which several groups have already applied to real data [76, 290, 372, 380, 164].

Since the effect of lensing on the CMB is very well approximated as a re-mapping of the unlensed anisotropies by the gradient of the lensing potential, extensive delensing can be achieved by reversing these deflections. For B-modes, this re-mapping approximation should be valid until polarisation sensitivities become better than $O(0.01)\,\mu$K arcmin, corresponding to lensing residuals $O(10^{-4})$ of the original power, at which point non-remapping effects such as rotation of the emission-angle [256], apparent warping of the last-scattering surface due to Shapiro time-delays [199, 256] and post-Born field rotation [190, 384] (dominant only on small angular scales) will present a source of B-mode noise not reducible by standard delensing. We shall neglect non-remapping corrections throughout this thesis.

For B-mode delensing, the information that is needed to delens the large angular scales of interest is contained in the intermediate and small-scale fluctuations [445]. Given that it is challenging to make stable large-scale measurements with the large-aperture telescopes needed to access the small-scale fluctuations, upcoming ground-based observatories will feature one or more large-aperture telescopes (for lensing and other CMB science needing high angular resolution) and a set of small-aperture telescopes targeting the primordial B-mode signal on large angular scales [1, 441]. The two surveys will have different footprints, with the small-aperture survey contained within the wider large-aperture one.

In this set-up, a convenient way to perform delensing is to form a "template" estimating the particular realisation of lensing B-modes present on the sky by combining high-resolution E-mode observations with some proxy of the lensing potential, and to subtract this template from the B-modes observed by the small-aperture telescopes. The template may be constructed using a linear expansion in the lensing deflections (which we refer to as a gradient-order template) or using a non-perturbative remapping scheme. Both approaches have already been successfully applied to real data: Ref. [290] used a leading-order template for a first demonstration of B-mode delensing, while Refs [372, 380] used non-perturbative templates for their similarly successful analyses. The gradient-order method has been particularly popular in the literature for forecasts of performance (e.g., Refs [292, 444, 445, 316, 317, 440, 432, 23, 134, 320, 517, 82, 289, 220]) and characterisations of systematic effects (e.g., Refs [312, 319, 30, 17, 19]) owing, perhaps, to its analytic transparency and ease of computation. A further reason for

the ubiquity of the gradient-order template method is that it is assumed to track the true lensing B-modes very accurately.

In this chapter, we put the last statement to the test, aiming to quantify and understand the intrinsic limitations on the residual B-mode power after delensing with gradient-order and non-perturbative templates. We begin, in Sec. 2.2, with a brief introduction to template delensing. Then, in Secs. 2.3 and 2.4 we calculate the power spectrum of delensed B-modes to $O(\phi^4)$ (i.e., two-loop order in the power spectrum of the lensing potential, ϕ) for the gradient-order and non-perturbative templates, respectively. We demonstrate that the former has better performance due to cancellations between the lensing corrections to the E-modes used in the template, and the $O(\phi^2)$ contributions to the lensed B-modes, which do not arise in the non-perturbative case. We also point out similar calculations in the lensed B-mode power spectrum itself at $O(\phi^4)$ in Sec. 2.3. Much of our discussion concerns the fundamental limitations of template methods, which we illustrate by considering the idealised case of noise-free E-mode measurements and access to the true lensing potential. However, we show in Sec. 2.4 that our conclusion regarding the relative performance of gradient-order and non-perturbative templates still holds, albeit with more marginal differences, in the practical case of noisy observations and an imperfectly correlated lensing proxy.

2.2 Template delensing

We work in the flat-sky limit throughout for simplicity. While differences do exist at the percent level between flat-sky and spherical results, for example, in the lensed B-mode power spectrum [84], our findings on the limitations of template delensing should hold similarly in the spherical case. We follow the notation of Ref. [252], so that the Stokes parameters defined on the global x–y basis are related to the E- and B-modes in Fourier space as

$$(Q \pm iU)(\mathbf{x}) = -\int \frac{d^2\mathbf{l}}{2\pi}\, [E(\mathbf{l}) \pm iB(\mathbf{l})]\, e^{\pm 2i\psi_{\mathbf{l}}} e^{i\mathbf{l}\cdot\mathbf{x}}\,, \tag{2.1}$$

where $\psi_{\mathbf{l}}$ is the angle between $\mathbf{l}$ and the x-direction. Ignoring primordial B-modes, the B-modes generated from E-modes by lensing are, up to second order in lensing

displacements,

$$\tilde{B}(\mathbf{l}) = -\int \frac{d^2\mathbf{l}_1}{2\pi} \sin 2(\psi_{\mathbf{l}_1} - \psi_{\mathbf{l}})\mathbf{l}_1 \cdot (\mathbf{l}-\mathbf{l}_1)E(\mathbf{l}_1)\phi(\mathbf{l}-\mathbf{l}_1)$$
$$+ \frac{1}{2}\int \frac{d^2\mathbf{l}_1}{2\pi}\int \frac{d^2\mathbf{l}_2}{2\pi} \sin 2(\psi_{\mathbf{l}_1} - \psi_{\mathbf{l}})\mathbf{l}_1 \cdot \mathbf{l}_2\mathbf{l}_1 \cdot (\mathbf{l}-\mathbf{l}_1-\mathbf{l}_2)E(\mathbf{l}_1)\phi(\mathbf{l}_2)\phi(\mathbf{l}-\mathbf{l}_1-\mathbf{l}_2) + \cdots . \tag{2.2}$$

Here, ϕ is the lensing potential so the lensing displacements are $\boldsymbol{\alpha} = \boldsymbol{\nabla}\phi$. We denote lensed fields with a tilde. In particular, we write the contribution to the lensed B-mode at nth order in ϕ as $\tilde{B}^{(n)}$. Further introducing the linear functional $\mathcal{B}_{\mathbf{l}}[P]$, which extracts the B-modes at $\mathbf{l}$ from the real-space polarisation field $P = Q + iU$, we can write

$$\tilde{B}^{(n)}(\mathbf{l}) = \frac{1}{n!}\mathcal{B}_{\mathbf{l}}[\alpha^{i_1}\ldots\alpha^{i_n}\nabla_{i_1}\ldots\nabla_{i_n}P^E]\,, \tag{2.3}$$

where P^E is the unlensed polarisation field constructed from $E(\mathbf{l})$.

Given the observed, noisy E-mode polarisation after beam-deconvolution, $E^{\rm obs}(\mathbf{l})$, and some proxy for the lensing potential $\phi^{\rm proxy}$, we can form a leading-order template (which we shall refer to as the gradient-order template) for the lens-induced B-modes:

$$\tilde{B}^{\rm temp}(\mathbf{l}) = -\int \frac{d^2\mathbf{l}_1}{2\pi} \sin 2(\psi_{\mathbf{l}_1} - \psi_{\mathbf{l}})\mathbf{l}_1 \cdot (\mathbf{l}-\mathbf{l}_1)\mathcal{W}^E_{l_1}E^{\rm obs}(\mathbf{l}_1)\mathcal{W}^{\phi}_{|\mathbf{l}-\mathbf{l}_1|}\phi^{\rm proxy}(\mathbf{l}-\mathbf{l}_1)\,. \tag{2.4}$$

Here, the Wiener filters

$$\mathcal{W}^E_l \equiv \frac{\tilde{C}^{EE}_l}{C^{EE,{\rm tot}}_l} \quad \text{and} \quad \mathcal{W}^{\phi}_l \equiv \frac{C^{\phi\phi_{\rm proxy}}_l}{C^{\phi_{\rm proxy}\phi_{\rm proxy}}_l}\,, \tag{2.5}$$

are chosen to minimise the residual power in $\tilde{B}(\mathbf{l}) - \tilde{B}^{\rm temp}(\mathbf{l})$ at leading order (note that $C^{EE,{\rm tot}}_l$ includes noise). A template that is non-perturbative in the lens remapping can also be constructed:

$$\tilde{B}^{\rm temp}_{\text{non-pert}}(\mathbf{l}) = \mathcal{B}_{\mathbf{l}}\left(P^{\mathcal{W}^E * E^{\rm obs}}\left[\mathbf{x} + \boldsymbol{\nabla}\left(\mathcal{W}^{\phi} * \phi^{\rm proxy}\right)\right]\right)\,, \tag{2.6}$$

where, for example, $\mathcal{W}^E * E^{\rm obs}$ are the Wiener-filtered E-modes. Taylor expanding at gradient order recovers the gradient-order template in equation (2.4).

For most of this work, we shall assume that the polarisation measurements are noise-free and that we have access to the true lensing potential, in which case both Wiener filters in equation (2.5) equal one. However, we relax these assumptions in

Sec. 2.4, where we compare the performance of gradient-order and non-perturbative templates in a more practical context.

2.3 Delensing with a gradient-order template

It is sometimes argued, e.g., Ref. [290], that delensing with a gradient-order template constructed from ideal (lensed) E-modes and the true ϕ is very accurate since the non-perturbative lensed B-mode power differs only at the percent level from the power spectrum of $\tilde{B}^{(1)}$ [84]. As we shall see, the conclusion is correct that the residual power after template delensing can be at the percent level. However, the logic above is somewhat flawed since:

1. the template is constructed from the lensed E-modes, not the unobservable unlensed ones; and

2. the power spectrum of the residuals after template delensing is not simply related to the difference between the power spectra of the template and $\tilde{B}(\mathbf{l})$.

To see some of the subtleties, consider forming a gradient-order template with the unlensed E-modes, which might seem a desirable thing to be able to do. Of course, if we made a non-perturbative template this would be perfect, but we are interested in this section in a gradient-order template of the form in equation (2.4). If we subtract this template, the residual B-modes are $\tilde{B}^{(2)}(\mathbf{l}) + \tilde{B}^{(3)}(\mathbf{l}) + \cdots$. *The power spectrum of these residuals is much larger than the percent-level difference between the power spectra of the template and* $\tilde{B}(\mathbf{l})$.

The difference between the power spectra of the template (constructed at gradient order with the unlensed E-modes) and of $\tilde{B}(\mathbf{l})$ at second order in $C_l^{\phi\phi}$ is of the form

$$\Delta C_l^{BB} = 2\langle \tilde{B}^{(1)}(\mathbf{l})\tilde{B}^{(3)}(\mathbf{l}')\rangle' + \langle \tilde{B}^{(2)}(\mathbf{l})\tilde{B}^{(2)}(\mathbf{l}')\rangle' \,, \tag{2.7}$$

where the primes on the expectation values denote that the delta-functions $\delta^{(2)}(\mathbf{l}+\mathbf{l}')$ are removed. This is simply the contribution to the lensed B-mode power at second order in $C_l^{\phi\phi}$. However, the power spectrum of the residual B-modes after gradient-order template delensing with the unlensed E-modes is

$$C_l^{BB,\mathrm{resid}} = \langle \tilde{B}^{(2)}(\mathbf{l})\tilde{B}^{(2)}(\mathbf{l}')\rangle' \tag{2.8}$$

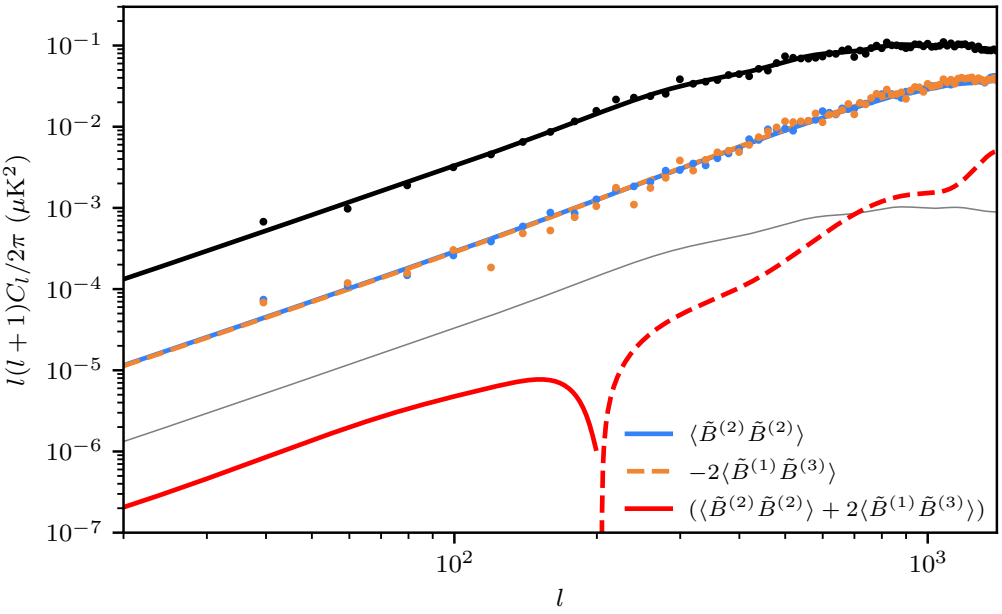

Fig. 2.1 Power spectrum of $\tilde{B}^{(1)}(\mathbf{l})$ estimated from a single flat-sky simulation (black points) compared to the non-perturbative, spherical calculation of the lens-induced B-mode power from CAMB [84, 254] (black solid). The leading-order difference between these spectra involves the sum of $\langle \tilde{B}^{(2)}(\mathbf{l})\tilde{B}^{(2)}(\mathbf{l}')\rangle'$ (blue) and $2\langle \tilde{B}^{(1)}(\mathbf{l})\tilde{B}^{(3)}(\mathbf{l}')\rangle'$ (with minus this shown in dashed, orange). Separately, these two spectra are large in magnitude, of $O(10)\,\%$ of the lensed B-mode spectrum on large scales, but they cancel rather precisely to leave only sub-percent-level corrections to the lensed B-mode power spectrum (red solid for positive values, red dashed for negative). For reference, the thin gray line shows the non-perturbative lensing power spectrum, scaled to 1% of its original amplitude. Analytic evaluations are shown as solid lines, and estimates derived from a single flat-sky simulation as points.

to the same order in $C_l^{\phi\phi}$. There turns out to be a strong cancellation between the two terms on the right-hand side of equation (2.7), each of which are separately at the $O(10)\,\%$ level of the lensed B-mode power; see figure 2.1.

We first calculate $\langle \tilde{B}^{(2)}(\mathbf{l})\tilde{B}^{(2)}(\mathbf{l}')\rangle'$ from equation (2.2); we find

$$\langle \tilde{B}^{(2)}(\mathbf{l})\tilde{B}^{(2)}(\mathbf{l}')\rangle' = \frac{1}{2}\int \frac{d^2\mathbf{l}_1}{(2\pi)^2}\frac{d^2\mathbf{l}_2}{(2\pi)^2}\,\sin^2 2(\psi_{\mathbf{l}_1}-\psi_{\mathbf{l}}) \times (\mathbf{l}_1\cdot\mathbf{l}_2)^2\,[\mathbf{l}_1\cdot(\mathbf{l}-\mathbf{l}_1-\mathbf{l}_2)]^2\,C_{l_1}^{EE}C_{l_2}^{\phi\phi}C_{|\mathbf{l}-\mathbf{l}_1-\mathbf{l}_2|}^{\phi\phi}\,. \tag{2.9}$$

For $\langle\tilde{B}^{(1)}(\mathbf{l})\tilde{B}^{(3)}(\mathbf{l}')\rangle'$, it is simplest to make use of equation (2.3), so that

$$\begin{aligned}\langle\tilde{B}^{(1)}(\mathbf{l})\tilde{B}^{(3)}(\mathbf{l}')\rangle' &= \frac{1}{3!}\langle\mathcal{B}_{\mathbf{l}}[\boldsymbol{\alpha}\cdot\boldsymbol{\nabla}P^E]\mathcal{B}_{\mathbf{l}'}[\alpha^{i_1}\alpha^{i_2}\alpha^{i_3}\nabla_{i_1}\nabla_{i_2}\nabla_{i_3}P^E]\rangle' \\ &= \frac{3}{2\times 3!}\langle\boldsymbol{\alpha}^2\rangle\langle\mathcal{B}_{\mathbf{l}}[\boldsymbol{\alpha}\cdot\boldsymbol{\nabla}P^E]\mathcal{B}_{\mathbf{l}'}[\boldsymbol{\alpha}\cdot\boldsymbol{\nabla}\nabla^2P^E]\rangle'\,, \end{aligned} \tag{2.10}$$

where we have used $\langle\alpha_i\alpha_j\rangle = \delta_{ij}\langle\boldsymbol{\alpha}^2\rangle/2$ at a point. It follows that the calculation of this "1–3" term is simply related to the power spectrum of $\tilde{B}^{(1)}$, and we have

$$2\langle\tilde{B}^{(1)}(\mathbf{l})\tilde{B}^{(3)}(\mathbf{l}')\rangle' = -\frac{\langle\boldsymbol{\alpha}^2\rangle}{2}\int\frac{d^2\mathbf{l}_1}{(2\pi)^2}\,\sin^2 2(\psi_{\mathbf{l}_1}-\psi_{\mathbf{l}})\,[\mathbf{l}_1\cdot(\mathbf{l}-\mathbf{l}_1)]^2\,l_1^2C_{l_1}^{EE}C_{|\mathbf{l}-\mathbf{l}_1|}^{\phi\phi}\,. \tag{2.11}$$

On large scales, the integral on the right of equation (2.11) is dominated by small-scale E-modes and similarly small-scale lenses, as for the power spectrum of $\tilde{B}^{(1)}(\mathbf{l})$, making $\langle\tilde{B}^{(1)}(\mathbf{l})\tilde{B}^{(3)}(\mathbf{l}')\rangle$ approximately constant. (Indeed, the additional factor of l_1^2 in the integrand compared to the power spectrum of $\tilde{B}^{(1)}(\mathbf{l})$ accentuates this coupling to smaller-scale lenses and E-modes.) On the other hand, the mean-squared deflection angle $\langle\boldsymbol{\alpha}^2\rangle$ preferentially receives contributions from degree-scale lenses (i.e., the coherence length of the deflections). Physically, the large-scale modes of $\tilde{B}^{(3)}$ that correlate with the large-scale modes of $\tilde{B}^{(1)}$ are mostly sourced by the action of one small-scale lens and two larger-scale lenses on the small-scale (unlensed) E-modes. Roughly, this can be thought of as the small-scale lens linearly producing B-modes from the small-scale E-modes, and then these being displaced rigidly by lenses on larger scales, preserving the B-mode character.

A similar thing happens for $\tilde{B}^{(2)}$: the dominant contribution on large scales is from one small-scale lens acting on small-scale unlensed E-modes, followed by displacement by one large-scale lens. Equivalently, the integral in equation (2.9) is dominated on large scales by modes with $l \ll l_1$ and $l_2 \ll l_1$, with an equal contribution (by symmetry of the integrand) from the disjoint region with $\mathbf{l}_2 \to \mathbf{l}-\mathbf{l}_1-\mathbf{l}_2$. The two contributions correspond to the two orderings of the large- and small-scale lenses in $\tilde{B}^{(2)}(\mathbf{l}) = \mathcal{B}_{\mathbf{l}}[\alpha^i\alpha^j\nabla_i\nabla_jP^E]/2$. Evaluating the integral in these limits, we find

$$\begin{aligned}\langle\tilde{B}^{(2)}(\mathbf{l})\tilde{B}^{(2)}(\mathbf{l}')\rangle' &\approx \frac{1}{2}\left(\int\frac{d^2\mathbf{l}_2}{(2\pi)^2}\,l_2^2C_{l_2}^{\phi\phi}\right)\int\frac{d^2\mathbf{l}_1}{(2\pi)^2}\,\sin^2 2(\psi_{\mathbf{l}_1}-\psi_{\mathbf{l}})l_1^6C_{l_1}^{EE}C_{l_1}^{\phi\phi}\,, \\ &\approx \frac{\langle\boldsymbol{\alpha}^2\rangle}{2}\frac{1}{4\pi}\int\frac{dl_1}{l_1}l_1^4C_{l_1}^{\phi\phi}l_1^4C_{l_1}^{EE}\,, \end{aligned} \tag{2.12}$$

which is independent of l. Here, we have used

$$\langle \boldsymbol{\alpha}^2 \rangle = \int \frac{d^2\mathbf{l}}{(2\pi)^2}\, l^2 C_l^{\phi\phi}\,. \tag{2.13}$$

Evaluating equation (2.11) in the large-scale limit, we see that

$$\langle \tilde{B}^{(2)}(\mathbf{l})\tilde{B}^{(2)}(\mathbf{l}')\rangle' \approx -2\langle \tilde{B}^{(1)}(\mathbf{l})\tilde{B}^{(3)}(\mathbf{l}')\rangle'\,, \tag{2.14}$$

and so the two terms approximately cancel in equation (2.7). This result is validated numerically in figure 2.1, showing that the $O(\phi^4)$ contribution to the lensed B-mode spectrum is below 1 % of the total lensing power, despite the power spectrum of $\tilde{B}^{(2)}$ being around 10 % of the lensing power.

The approximate cancellation between the "1–3" and "2–2" terms arises since displacing the B-modes, which are produced by the action of the small-scale lens on the small-scale unlensed E-modes, with large-scale lensing deflections has a relatively minor effect on their power spectrum due to statistical isotropy (only relative displacements matter). However, there can still be significant changes in the B-mode fields themselves if the size of the displacements are comparable to the coherence scale of the field being displaced. In this way, $\tilde{B}^{(2)}$ can have power that is a sizable fraction of $\tilde{B}^{(1)}$ (i.e., around 10 % here), but the correction to the total lensed B-mode power at second order in $C_l^{\phi\phi}$ remains small (around 1 %). Similar cancellations are also the reason why the lensing correction to the temperature power spectrum remains small on the intermediate scales of the acoustic peaks.

We now consider the physically more relevant case of delensing with a gradient-order template constructed with the *lensed* E-modes. Fortunately, cancellations also occur in this case, leaving the power spectrum of the delensed B-modes at the 1 % level of the lensed B-mode power. Here, the dominant cancellation is between $\tilde{B}^{(2)}$ and the contribution to the template of the leading-order change in the E-modes due to lensing (although we verify using simulations that similar cancellations also occur at higher orders). In Ref. [340], it was argued that this cancellation is responsible for the lack of bias seen in their recovery of the tensor-to-scalar ratio r across simulations of the delensing process, but no quantitative details were given. Here, we fill in these details.

If we construct the B-mode lensing template at gradient order using the lensed E-modes, the leading-order correction to the template is

$$\Delta\tilde{B}^{\rm temp}(\mathbf{l}) = -\int \frac{d^2\mathbf{l}_1}{2\pi}\, \sin 2(\psi_{\mathbf{l}_1} - \psi_{\mathbf{l}})\mathbf{l}_1\cdot(\mathbf{l}-\mathbf{l}_1)\tilde{E}^{(1)}(\mathbf{l}_1)\phi(\mathbf{l}-\mathbf{l}_1)\,, \tag{2.15}$$

where $\tilde{E}^{(1)}(\mathbf{l})$ is the first-order change in E-modes due to lensing:

$$\begin{aligned}\tilde{E}^{(1)}(\mathbf{l}) &= \mathcal{E}_{\mathbf{l}}[\boldsymbol{\alpha}\cdot\boldsymbol{\nabla}P^E] \\ &= -\int \frac{d^2\mathbf{l}_1}{2\pi}\,\cos 2(\psi_{\mathbf{l}_1}-\psi_{\mathbf{l}})\mathbf{l}_1\cdot(\mathbf{l}-\mathbf{l}_1)E(\mathbf{l}_1)\phi(\mathbf{l}-\mathbf{l}_1)\,,\end{aligned} \tag{2.16}$$

where $\mathcal{E}_{\mathbf{l}}[P]$ extracts the E-modes at wavevector $\mathbf{l}$ from P. The residual B-modes after delensing with such a template become $\tilde{B}^{(2)}(\mathbf{l}) - \Delta\tilde{B}^{\rm temp}(\mathbf{l})$ to second order in ϕ. A simulated realisation of the fields $\tilde{B}^{(2)}(\mathbf{l})$ and $\Delta\tilde{B}^{\rm temp}(\mathbf{l})$ are shown in figure 2.2. The fields are clearly very similar and so we expect the residual B-mode power after delensing to be much smaller than the power of either field alone (which, recall, for $\tilde{B}^{(2)}(\mathbf{l})$ is $O(10)\,\%$ of the power of $\tilde{B}^{(1)}(\mathbf{l})$ on large scales). To understand the similarity of $\tilde{B}^{(2)}(\mathbf{l})$ and $\Delta\tilde{B}^{\rm temp}(\mathbf{l})$, we note that

$$\begin{aligned}B^{(2)}(\mathbf{l}) &= \frac{1}{2}\mathcal{B}_{\mathbf{l}}[\alpha^i\alpha^j\nabla_i\nabla_j P^E] \\ &\approx \mathcal{B}_{\mathbf{l}}[\alpha^i_{\rm short}\alpha^j_{\rm long}\nabla_i\nabla_j P^E] \quad \text{(large scales)}\,,\end{aligned} \tag{2.17}$$

where the approximation, valid on large scales, is that $\tilde{B}^{(2)}$ is dominated by a large-scale deflection, $\boldsymbol{\alpha}_{\rm long}$, and a small-scale deflection, $\boldsymbol{\alpha}_{\rm short}$, as discussed above. For the leading-order correction to the template from the lensed E-modes, we have

$$\begin{aligned}\Delta B^{\rm temp}(\mathbf{l}) &= \mathcal{B}_{\mathbf{l}}\left[\alpha^i\nabla_i P^{\tilde{E}^{(1)}}\right] \\ &\approx \mathcal{B}_{\mathbf{l}}\left[\alpha^i\nabla_i\left(\alpha^j_{\rm long}\nabla_j P^E\right)\right] \\ &\approx \mathcal{B}_{\mathbf{l}}\left[\alpha^i_{\rm short}\nabla_i\left(\alpha^j_{\rm long}\nabla_j P^E\right)\right] \quad \text{(large scales)} \\ &\approx \mathcal{B}_{\mathbf{l}}\left[\alpha^i_{\rm short}\alpha^j_{\rm long}\nabla_i\nabla_j P^E\right]\,.\end{aligned} \tag{2.18}$$

Here, the approximation in the second line ignores the B-modes in $\boldsymbol{\alpha}\cdot\boldsymbol{\nabla}P^E$, i.e.,

$$P^{\tilde{E}^{(1)}} = \boldsymbol{\alpha}\cdot\boldsymbol{\nabla}P^E - P^{\tilde{B}^{(1)}} \approx \boldsymbol{\alpha}\cdot\boldsymbol{\nabla}P^E\,, \tag{2.19}$$

which is valid since the power spectrum of $\tilde{B}^{(1)}$ is only $O(1)\,\%$ of the power spectrum of $\tilde{E}^{(1)}$ on the small scales ($l\sim 1500$) where the power in the latter peaks. In the second and third lines of equation (2.18), we have used the fact that it is mostly large-scale (i.e., degree-scale) lenses that contribute to $\tilde{E}^{(1)}$ while smaller-scale lenses displace this to produce large-scale B-modes. In the final line, we have ignored the derivative of $\boldsymbol{\alpha}_{\rm long}$ compared to that of the small-scale $\boldsymbol{\nabla}P^E$. With these approximations, we see that $\Delta B^{\rm temp}(\mathbf{l}) \approx \tilde{B}^{(2)}(\mathbf{l})$.

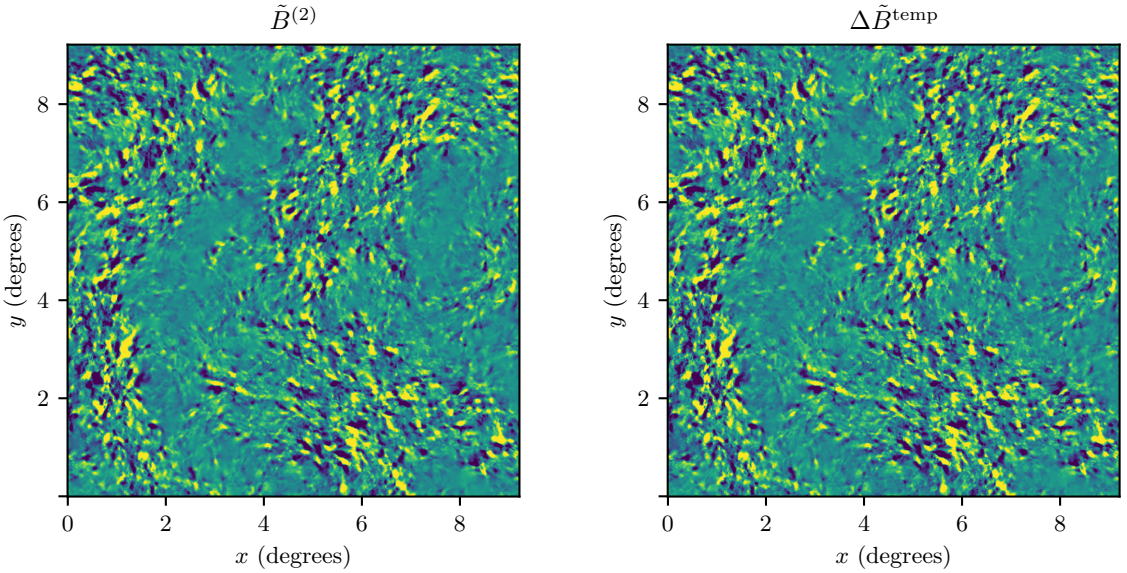

Fig. 2.2 Real-space scalar fields derived from $\tilde{B}^{(2)}(\mathbf{l})$ (left) and the contribution to the gradient-order B-mode template from the linear lensing correction to E-modes, $\Delta\tilde{B}^{\rm temp}(\mathbf{l})$ (right). The plotted intensity ranges from $-0.5\,\mu$K (dark blue) to $0.5\,\mu$K (yellow). The similarity of these fields and their non-Gaussian nature are clearly apparent.

We now calculate the power spectrum of residual B-modes after delensing, with a gradient-order template formed using lensed E-modes, correct to second order in $C_l^{\phi\phi}$:

$$C_l^{BB,\rm resid} = \langle\tilde{B}^{(2)}(\mathbf{l})\tilde{B}^{(2)}(\mathbf{l}')\rangle' - 2\langle\tilde{B}^{(2)}(\mathbf{l})\Delta\tilde{B}^{\rm temp}(\mathbf{l}')\rangle' + \langle\Delta\tilde{B}^{\rm temp}(\mathbf{l})\Delta\tilde{B}^{\rm temp}(\mathbf{l}')\rangle' \,. \quad (2.20)$$

The first of these terms was already calculated in equation (2.9). On the other hand, the cross-term is given by

$$\langle\tilde{B}^{(2)}(\mathbf{l})\Delta\tilde{B}^{\rm temp}(\mathbf{l}')\rangle' = \int \frac{d^2\mathbf{l}_1}{(2\pi)^2}\frac{d^2\mathbf{l}_2}{(2\pi)^2}\sin 2\left(\psi_{\mathbf{l}_2}-\psi_{\mathbf{l}}\right)\sin 2\left(\psi_{\mathbf{l}_1}-\psi_{\mathbf{l}}\right)\cos 2\left(\psi_{\mathbf{l}_1}-\psi_{\mathbf{l}_2}\right)$$
$$\times\left[(\mathbf{l}_2-\mathbf{l})\cdot\mathbf{l}_1\right]\left[(\mathbf{l}_2-\mathbf{l})\cdot\mathbf{l}_2\right]\left[(\mathbf{l}_2-\mathbf{l}_1)\cdot\mathbf{l}_1\right]^2 C_{l_1}^{EE}C_{|\mathbf{l}-\mathbf{l}_2|}^{\phi\phi}C_{|\mathbf{l}_2-\mathbf{l}_1|}^{\phi\phi}, \quad (2.21)$$

and the last term, $\langle \Delta\tilde{B}^{\rm temp}(\mathbf{l})\Delta\tilde{B}^{\rm temp}(\mathbf{l}')\rangle'$, receives contributions from the following two couplings:

$$U_l = \int \frac{d^2\mathbf{l}_1}{(2\pi)^2}\frac{d^2\mathbf{l}_2}{(2\pi)^2}\sin^2 2\left(\psi_{\mathbf{l}_2}-\psi_{\mathbf{l}}\right)\cos^2 2\left(\psi_{\mathbf{l}_1}-\psi_{\mathbf{l}_2}\right) \times [\mathbf{l}_2\cdot(\mathbf{l}-\mathbf{l}_2)\mathbf{l}_1\cdot(\mathbf{l}_2-\mathbf{l}_1)]^2 C^{EE}_{l_1} C^{\phi\phi}_{|\mathbf{l}-\mathbf{l}_2|} C^{\phi\phi}_{|\mathbf{l}_2-\mathbf{l}_1|}\,; \tag{2.22}$$

and

$$\begin{aligned} V_l = \int \frac{d^2\mathbf{l}_1}{(2\pi)^2}\frac{d^2\mathbf{l}_2}{(2\pi)^2} &\sin 2\left(\psi_{\mathbf{l}_2}-\psi_{\mathbf{l}}\right)\cos 2\left(\psi_{\mathbf{l}_1}-\psi_{\mathbf{l}_2}\right) \\ &\times \sin 2\left(\psi_{\mathbf{l}-\mathbf{l}_2+\mathbf{l}_1}-\psi_{\mathbf{l}}\right)\cos 2\left(\psi_{\mathbf{l}_1}-\psi_{\mathbf{l}-\mathbf{l}_2+\mathbf{l}_1}\right) \\ &\times \mathbf{l}_2\cdot(\mathbf{l}-\mathbf{l}_2)\mathbf{l}_1\cdot(\mathbf{l}_2-\mathbf{l}_1)(\mathbf{l}-\mathbf{l}_2+\mathbf{l}_1)\cdot(\mathbf{l}_2-\mathbf{l}_1)\mathbf{l}_1\cdot(\mathbf{l}-\mathbf{l}_2) C^{EE}_{l_1} C^{\phi\phi}_{|\mathbf{l}-\mathbf{l}_2|} C^{\phi\phi}_{|\mathbf{l}_2-\mathbf{l}_1|}\,. \end{aligned} \tag{2.23}$$

The first, U_l, arises from correlating the (large-scale) lenses in each $\tilde{E}^{(1)}$; it is expected to dominate over V_l, which arises from correlations between the large- and small-scale lenses.

As expected from the similarity of the two fields highlighted in figure 2.2, an explicit numerical evaluation of all these terms[1] reveals that $\langle \Delta\tilde{B}^{\rm temp}(\mathbf{l})\Delta\tilde{B}^{\rm temp}(\mathbf{l}')\rangle' \approx \langle \tilde{B}^{(2)}(\mathbf{l})\tilde{B}^{(2)}(\mathbf{l}')\rangle' \approx \langle \tilde{B}^{(2)}(\mathbf{l})\Delta\tilde{B}^{\rm temp}(\mathbf{l}')\rangle'$ (with $V_l \ll U_l$ by approximately two orders of magnitude). Consequently, there is extensive cancellation between leading-order contributions, and *the residual lensing B-mode power spectrum after delensing with a gradient-order template built from lensed E-modes has an amplitude of* $O(1)\,\%$ *of the lensing B-mode power spectrum*; see figure 2.3. This is in good agreement with simulations[2] on large angular scales up to the accuracy afforded by our numerical integration and field remapping codes. On small scales, $l > 1000$, the simulated and analytic spectra diverge somewhat, likely due to the significance of higher-order contributions missing from the analytic expressions.

We can also recover the approximate cancellation between the terms in equation (2.20) by approximating the integrands in Eqs. (2.21–2.22). The first of these

[1] In order to deal appropriately with the highly oscillating, multi-dimensional integrands at hand, we employ a Monte-Carlo approach combining importance sampling with globally-adaptive subdivision of the integration domain, as implemented in the code `Suave`, part of the publicly-available `Cuba` library [159].

[2] We use 200 flat-sky simulations on a square grid with 1024 pixels per side and a pixel width of 1 arcmin. To do this, we use the publicly-available code `QuickLens` (`https://github.com/dhanson/quicklens`, though an amended and extended version can be found at `https://github.com/abaleato/Quicklens-with-fixes`).

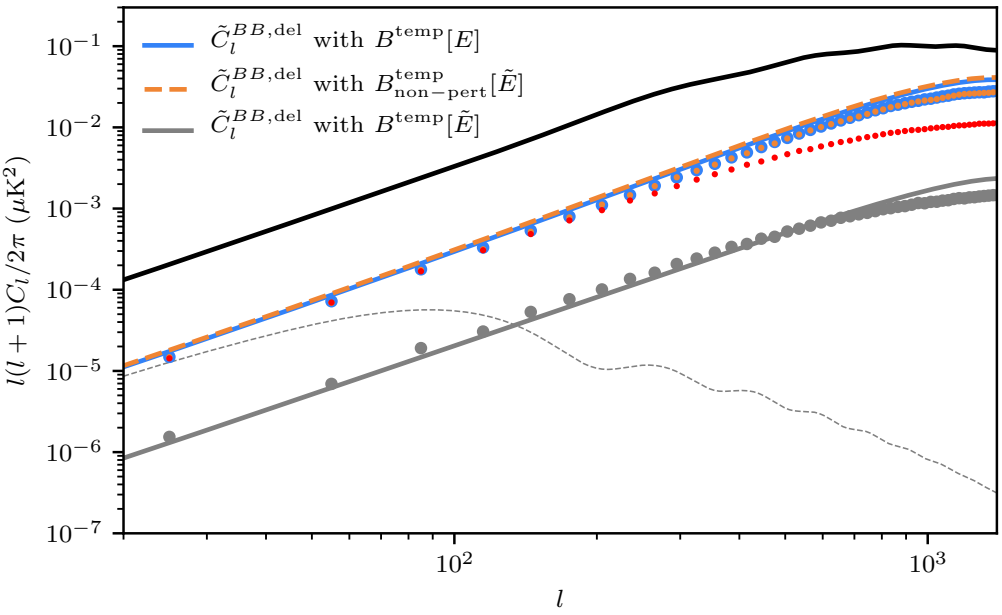

Fig. 2.3 Analytic (solid lines) versus simulated (dots) lensing B-mode residual spectra after delensing by: (i) building a gradient-order template from unlensed (blue) or lensed (gray) E-modes; and (ii) forming a non-perturbative template involving lensed E-modes (orange). We also show the simulated residual B-mode power after anti-lensing polarisation fields containing lensed E- and B-modes (red dots). Noiseless polarisation fields and perfect ϕ are used in all cases. Also shown is the lensing B-mode power spectrum (black, solid line) and a primordial B-mode spectrum for $r = 0.001$ (dashed) generated using `CAMB` [254].

is dominated by large-scale lenses in the construction of $\tilde{E}^{(1)}$ correlating with the large-scale lens in $\tilde{B}^{(2)}$, and the smaller-scale lens remapping $\tilde{E}^{(1)}$ to the large-scale $\Delta\tilde{B}^{\rm temp}$ correlating with the small-scale lens in $\tilde{B}^{(2)}$. This corresponds to $|\mathbf{l}_2 - \mathbf{l}_1| \ll l_1$ in the integrand of equation (2.21). In the large-scale limit, we therefore have

$$\begin{aligned}\langle\tilde{B}^{(2)}(\mathbf{l})\Delta\tilde{B}^{\rm temp}(\mathbf{l}')\rangle' &\approx \int \frac{d^2\mathbf{l}_1}{(2\pi)^2}\,\sin^2 2\,(\psi_{\mathbf{l}_1} - \psi_{\mathbf{l}})\,[\mathbf{l}_1\cdot(\mathbf{l}_1-\mathbf{l})]^2\,C^{EE}_{l_1}C^{\phi\phi}_{|\mathbf{l}-\mathbf{l}_1|}\\ &\quad\times\int\frac{d^2\mathbf{l}_2}{(2\pi)^2}\,[\mathbf{l}_1\cdot(\mathbf{l}_2-\mathbf{l}_1)]^2\,C^{\phi\phi}_{|\mathbf{l}_2-\mathbf{l}_1|}\\ &\approx \frac{1}{2}\langle\boldsymbol{\alpha}^2\rangle\int\frac{d^2\mathbf{l}_1}{(2\pi)^2}\,\sin^2 2\,(\psi_{\mathbf{l}_1}-\psi_{\mathbf{l}})\,l_1^6 C^{EE}_{l_1}C^{\phi\phi}_{l_1}\\ &\approx \langle\tilde{B}^{(2)}(\mathbf{l})\tilde{B}^{(2)}(\mathbf{l}')\rangle'\,. \end{aligned}\tag{2.24}$$

Similarly, U_l is dominated by $|\mathbf{l}_2 - \mathbf{l}_1| \ll l_1$, and in the large-scale limit it is straightforward to show that $U_l \approx \langle\tilde{B}^{(2)}(\mathbf{l})\tilde{B}^{(2)}(\mathbf{l}')\rangle'$.

For reference, the residual power obtained after delensing with a gradient-order template constructed from the lensed E-modes is one order of magnitude smaller than what can be attained by anti-lensing in the idealised case of perfect polarisation observations and access to the true ϕ; see figure 2.3 and Ref. [111]. Anti-lensing attempts to remap the observed (possibly filtered) polarisation field directly, approximating the inverse-remapping operation $P(\mathbf{x}) = \tilde{P}(\mathbf{x} + \boldsymbol{\alpha}^{-1})$ with $P^{\rm del}(\mathbf{x}) = \tilde{P}(\mathbf{x} - \boldsymbol{\alpha})$, where $\boldsymbol{\alpha}$ is evaluated at $\mathbf{x}$. This incurs an error of $O(\boldsymbol{\alpha}\cdot\boldsymbol{\nabla}\boldsymbol{\alpha})$ [14] since

$$\begin{aligned}P^{\rm del}(\mathbf{x}) &= P^E\Big(\mathbf{x} - \boldsymbol{\alpha} + \boldsymbol{\alpha}(\mathbf{x}-\boldsymbol{\alpha})\Big)\\ &\approx P^E(\mathbf{x} - \boldsymbol{\alpha}\cdot\boldsymbol{\nabla}\boldsymbol{\alpha})\\ &\approx P^E(\mathbf{x}) - (\boldsymbol{\alpha}\cdot\boldsymbol{\nabla}\boldsymbol{\alpha})\cdot\boldsymbol{\nabla}P^E(\mathbf{x}),\end{aligned}\tag{2.25}$$

where, in the first line, $\boldsymbol{\alpha}(\mathbf{x}-\boldsymbol{\alpha})$ denotes $\boldsymbol{\alpha}$ evaluated at $\mathbf{x} - \boldsymbol{\alpha}(\mathbf{x})$. Extracting the B-modes gives

$$B^{\rm del}(\mathbf{l}) \approx -\mathcal{B}_{\mathbf{l}}\left[(\boldsymbol{\alpha}\cdot\boldsymbol{\nabla}\boldsymbol{\alpha})\cdot\boldsymbol{\nabla}P\right] = -\frac{1}{2}\mathcal{B}_{\mathbf{l}}\left[\left(\boldsymbol{\nabla}\boldsymbol{\alpha}^2\right)\cdot\boldsymbol{\nabla}P^E\right],\tag{2.26}$$

where the relation $\boldsymbol{\alpha}\cdot\boldsymbol{\nabla}\boldsymbol{\alpha} = \boldsymbol{\nabla}\boldsymbol{\alpha}^2/2$ follows from $\boldsymbol{\alpha}$ being a gradient. We see that the leading-order B-mode residuals after anti-lensing are the same as the B-modes produced by lensing E with a lensing potential $-\boldsymbol{\alpha}^2/2$. Simulated residuals after anti-lensing noise-free polarisation with the true ϕ are shown in figure 2.4, along with the residuals for template delensing. The power spectrum of the anti-lensing residuals

on large scales is very similar to the power spectrum after gradient-order template delensing with the unlensed E-modes (i.e., approximately the power spectrum of $\tilde{B}^{(2)}$); see figure 2.3. This is because

$$-\frac{1}{2}\left(\boldsymbol{\nabla}\boldsymbol{\alpha}^2\right)\cdot\boldsymbol{\nabla}P^E = -\frac{1}{2}\boldsymbol{\nabla}\cdot\left(\boldsymbol{\alpha}^2\boldsymbol{\nabla}P^E\right) + \frac{1}{2}\boldsymbol{\alpha}^2\nabla^2 P^E, \tag{2.27}$$

and the first term on the right is a total divergence, which is suppressed on large scales compared to the second term. The power spectrum of $\mathcal{B}_{\mathbf{l}}[\boldsymbol{\alpha}^2\nabla^2 P^E]/2$ evaluates to

$$\frac{1}{4}\langle\mathcal{B}_{\mathbf{l}}[\boldsymbol{\alpha}^2\nabla^2 P^E]\mathcal{B}_{\mathbf{l}'}[\boldsymbol{\alpha}^2\nabla^2 P^E]\rangle' = \frac{1}{2}\int\frac{d^2\mathbf{l}_1}{(2\pi)^2}\frac{d^2\mathbf{l}_2}{(2\pi)^2}\,\sin^2 2(\psi_{\mathbf{l}_1}-\psi_{\mathbf{l}})l_1^4\,[\mathbf{l}_2\cdot(\mathbf{l}-\mathbf{l}_1-\mathbf{l}_2)]^2 \times C_{l_1}^{EE}C_{l_2}^{\phi\phi}C_{|\mathbf{l}-\mathbf{l}_1-\mathbf{l}_2|}^{\phi\phi}\,, \tag{2.28}$$

the same as for $\tilde{B}^{(2)}$, equation (2.9), but with $(\mathbf{l}_1\cdot\mathbf{l}_2)^2[\mathbf{l}_1\cdot(\mathbf{l}-\mathbf{l}_1-\mathbf{l}_2)]^2$ replaced by $l_1^4[\mathbf{l}_2\cdot(\mathbf{l}-\mathbf{l}_1-\mathbf{l}_2)]^2$. However, both of these geometric couplings become equal in the limit $l \ll l_1$ and $l_2 \ll l_1$ (and the disjoint region with $\mathbf{l}_2 \to \mathbf{l}-\mathbf{l}_1-\mathbf{l}_2$), which dominate the integral on large scales.

We end this section by noting a further apparent benefit of delensing with a gradient-order template constructed from the lensed E-modes. When adjusted to an appropriate colour scale, the residuals shown in figure 2.4 for the noise-free case appear to the eye to be significantly more Gaussian than for either anti-lensing, a gradient-order template made from the unlensed E-modes, or a non-perturbative template with the lensed E-modes (which we discuss in detail in the next section). In the future, when noise levels permit very aggressive delensing, having more Gaussian residuals may simplify the subsequent likelihood analysis, e.g., by reducing the covariance between power spectrum estimates at different scales. We defer a more quantitative analysis of the statistics of these residuals to future work.

2.4 Delensing with a non-perturbative template

We now consider the case of B-mode delensing with a template constructed from the lensed E-modes but with the lens remapping handled non-perturbatively (equation 2.6). This was the approach adopted in Refs. [372, 380], for example. As we shall see, this case performs similarly badly in the noise-free limit to the gradient-order template constructed from unlensed E-modes.

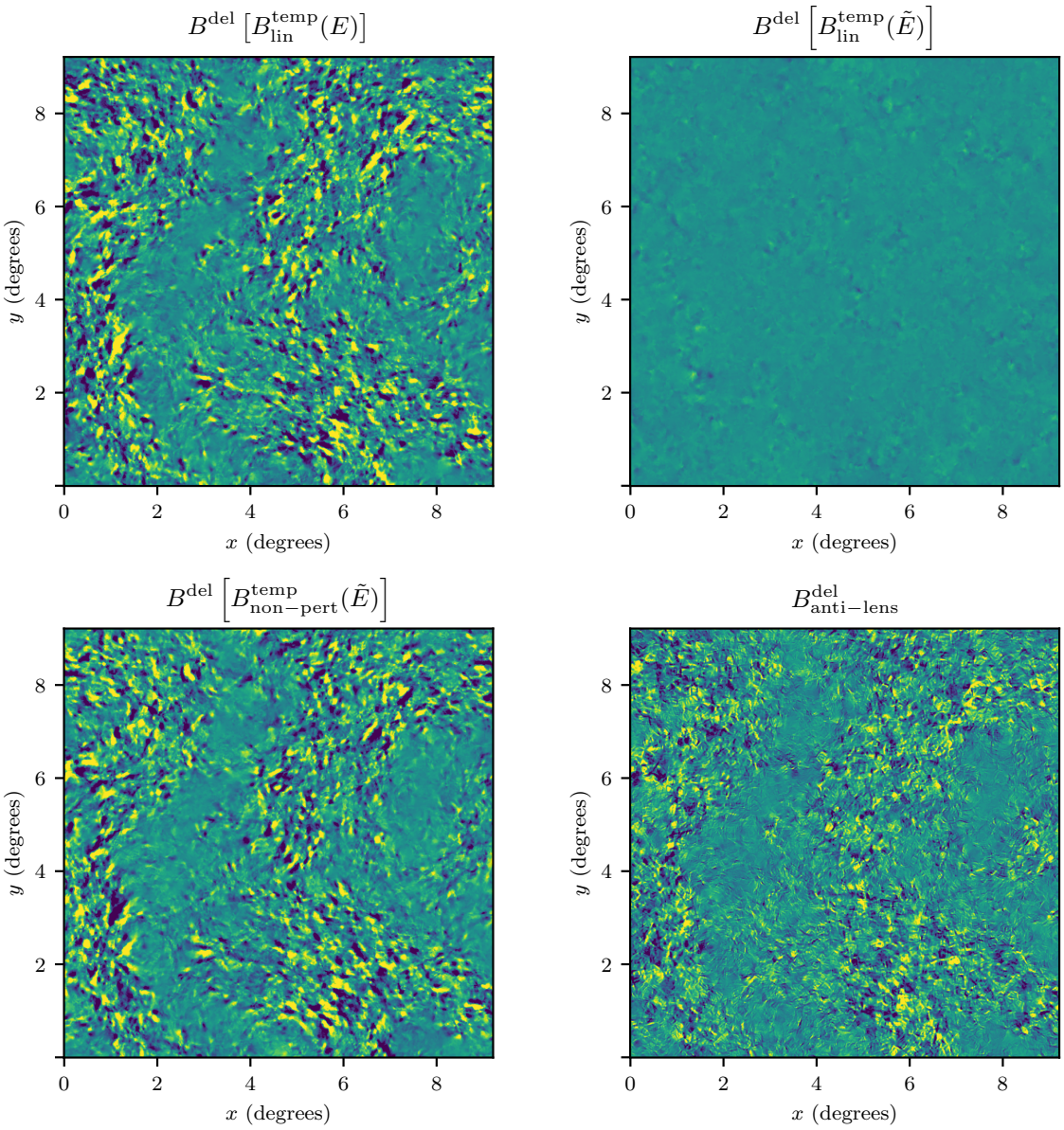

Fig. 2.4 Residual B-mode maps after delensing in the limit of noiseless CMB fields and access to the true ϕ, and using either a gradient-order template built from unlensed E-modes (*top left*), a gradient-order template built from lensed E-modes (*top right*), a non-perturbative template built from lensed E-modes (*bottom left*) or by anti-lensing polarisation maps containing both E- and B-modes (*bottom right*).The plotted intensity ranges from $-0.5\,\mu$K (dark blue) to $0.5\,\mu$K (yellow).

Expanding the non-perturbative template to second order in ϕ, we have

$$\begin{aligned}\tilde{B}^{\rm temp}_{\rm non\text{-}pert}(\mathbf{l}) &= \mathcal{B}_{\mathbf{l}}\left(\alpha^i\nabla_i P^E\right) + \mathcal{B}_{\mathbf{l}}\left(\alpha^i\nabla_i P^{\tilde{E}^{(1)}}\right) + \frac{1}{2}\mathcal{B}_{\mathbf{l}}\left(\alpha^i\alpha^j\nabla_i\nabla_j P^E\right) + O(\phi^3) \\ &= \tilde{B}^{(1)}(\mathbf{l}) + \Delta\tilde{B}^{\rm temp}(\mathbf{l}) + \tilde{B}^{(2)}(\mathbf{l}) + O(\phi^3)\,. \end{aligned} \tag{2.29}$$

It follows that the leading-order residuals after delensing with such a template are $-\Delta\tilde{B}^{\rm temp}(\mathbf{l})$. Notice now how the term $\tilde{B}^{(2)}(\mathbf{l})$ is absent from the residuals, in contrast to the case of the gradient-order template. It follows that the residual power after delensing with the non-perturbative template is $O(10)\,\%$ of the original lensing power in the noise-free limit, reintroducing this delensing floor; see figure 2.3. Furthermore, the residuals, a simulation of which are shown in figure 2.4, appear to the eye to be less Gaussian for the non-perturbative template than those obtained for the gradient-order template. *We see that for templates constructed directly from the observed E-modes, it is preferable to construct the template at gradient order rather than with non-perturbative remapping.* In the case of non-perturbative templates built from anti-lensed E-modes, there would be no delensing floor of this nature, since anti-lensing removes $\tilde{E}^{(1)}$ and consequently $\Delta\tilde{B}^{\rm temp}(\mathbf{l})$ would be absent from equation (2.29)[3].

So far we have considered the idealised case of noiseless E-modes and access to the true ϕ. We now demonstrate that the conclusion that a gradient-order template is preferable over a non-perturbative one still holds in the practical case of noisy E-modes and a lensing proxy $\phi^{\rm proxy}$ that is only partially correlated with the true ϕ, albeit with more marginal benefits. The residuals after delensing are more complicated in this case, in part because the term that is first-order in ϕ no longer vanishes. The gradient-order and non-perturbative templates share the same $O(\phi)$ residuals

$$\begin{aligned}\tilde{B}^{\rm temp}_{\rm res}(\mathbf{l}) = -\int\frac{d^2\mathbf{l}_1}{2\pi}\,&\sin 2(\psi_{\mathbf{l}_1}-\psi_{\mathbf{l}})\mathbf{l}_1\cdot(\mathbf{l}-\mathbf{l}_1) \\ &\times\left(E(\mathbf{l}_1)\phi(\mathbf{l}-\mathbf{l}_1) - \mathcal{W}^E_{l_1}[E(\mathbf{l}_1)+n^E(\mathbf{l}_1)]\mathcal{W}^{\psi}_{|\mathbf{l}-\mathbf{l}_1|}\phi^{\rm proxy}(\mathbf{l}-\mathbf{l}_1)\right),\end{aligned} \tag{2.30}$$

where n^E is the noise on the observed E-modes. Indeed, it is the power spectrum of this term that is usually assumed to dominate the B-mode signal power after delensing:

$$\tilde{C}^{BB,{\rm res}}_l = \int\frac{d^2\mathbf{l}_1}{(2\pi)^2}\left[\mathbf{l}_1\cdot(\mathbf{l}-\mathbf{l}_1)\,\sin 2(\psi_{\mathbf{l}_1}-\psi_{\mathbf{l}})\right]^2 C^{EE}_{l_1}C^{\phi\phi}_{|\mathbf{l}-\mathbf{l}_1|}\left(1-\mathcal{W}^E_{l_1}\mathcal{W}^{\phi}_{|\mathbf{l}-\mathbf{l}_1|}\right). \tag{2.31}$$

[3]This is in agreement with what was seen in simulations by Ref. [111].

For sufficiently-low E-mode noise levels and a highly-correlated lensing proxy, the residual power after delensing may instead be dominated by terms that are second order in $C_l^{\phi\phi}$, particularly for the case of a non-perturbative template. Now, there will be contributions from both "2–2" and "1–3" terms (which may partially cancel, as for the lensed B-mode spectrum), although as the ideal limit is approached the former will dominate.

Although the residual power at second order in $C_l^{\phi\phi}$ could be calculated along similar lines to the calculations for the ideal cases in Sec. 2.3, instead we shall estimate the residual power from simulations. We simulate the observed, lensed E-modes by remapping a realisation of unlensed E-modes with a Gaussian realisation of ϕ, and subsequently add white noise with variance Δ_P^2. For the lensing proxy, we add white noise to the lensing convergence ($\kappa = -\nabla^2\phi/2$), with variance Δ_κ^2. This mimics the statistical noise that arises when reconstructing ϕ internally from the CMB[4] (e.g., Ref. [198]). Such reconstruction noise is approximately white on large scales, and generally remains so on all scales where the reconstruction is signal dominated. For reference, white noise with (constant) power equal to the peak power in the convergence power spectrum, $C_l^{\kappa\kappa} \approx 2.2 \times 10^{-7}$ at $l \approx 30$, corresponds to $\Delta_\kappa = 1\,\text{arcmin}$ (i.e., the standard deviation of the white noise averaged in a pixel of side 1.6 arcmin is 1.6). In addition, the large-scale white noise level for a (non-iterative) reconstruction from a CMB survey with $\Delta_P = 1\,\mu\text{K}\,\text{arcmin}$ (and using multipoles up to $l = 3000$) is 0.26 arcmin. Gradient-order and non-perturbative templates are constructed from the Wiener-filtered observed E-modes and lensing proxy, and delensed fields are obtained by subtracting these from simulated, noiseless lensed B-modes. In this way, we can isolate the change in B-mode power due to delensing.

The results of these simulations are given in figure 2.5. The left panel shows the ratio of the delensed power using the non-perturbative template to the original lensing B-mode power. For sufficiently low noise levels (top-left corner), we recover the $O(10)\,\%$ floor in the delensed power that we uncovered in the idealised case. The right panel shows the ratio of the residual powers after delensing with the gradient-order template and the non-perturbative template. The former gives lower residual power for all noise levels. As the ideal limit is approached, we recover the ratio of $O(0.1)$

[4]We choose not to use the usual quadratic estimator noise power because this would detract from the pedagogical value of this exercise without necessarily making it more realistic. The reason is that quadratic estimators will be superseded by iterative delensing before the lower range of κ sensitivities considered here — those that unveil the delensing floors — can be reached. For higher noise levels and instrument resolutions of $O(1)$ arcmin, we find the quadratic estimator noise power for κ to be quite well approximated as white noise on the relevant scales, such that the different treatments produce only percent-level differences on the spectrum of delensed B-modes on scales $l < 300$.

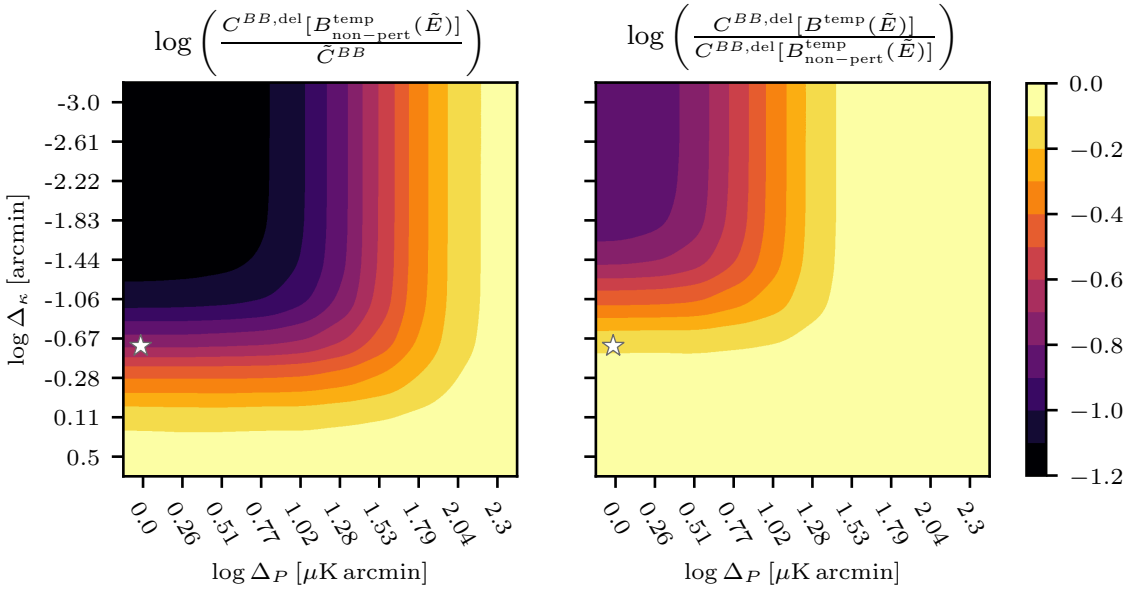

Fig. 2.5 *Left*: Fraction of lensing power remaining after delensing noiseless B-modes with a non-perturbative template built from (Wiener-filtered) noisy, lensed E-modes and noisy ϕ. *Right*: Ratio of residual power after delensing with a gradient-order template to that after delensing with a non-perturbative template, in both cases using filtered, noisy, lensed E-modes and ϕ to delens noiseless B-modes. When computing the ratios, we first average spectra over the multipole range $l \in [25, 325]$, and over 20 simulations. In all cases, we add white noise to the simulated lensed E-modes used to construct the templates with variance Δ_P^2 (and ignore the effects of finite instrumental angular resolution). For the lensing proxy, we add white noise to the true lensing convergence ($\kappa = -\nabla^2\phi/2$) with variance Δ_κ^2 per arcmin^2 pixel. Note the $O(10)\,\%$ floor in delensed power when using the non-perturbative template in the ideal limit (top-left corner), and how the gradient-order template consistently outperforms the non-perturbative one, even before the latter has hit its delensing floor. The improvement will start to be significant for non-iterative lensing reconstructions in the era of CMB-S4 [90] (marked with stars).

seen earlier for the ideal case. In the opposite limit, where noise is significant in either the observed E-modes or the lensing proxy, the ratio tends to one with the delensed power given by equation (2.31) for both templates. For the specifications of a nominal Stage-4 CMB experiment ($\Delta_P = 1\,\mu\mathrm{K}\,\mathrm{arcmin}$ and $\Delta_\kappa = 0.26\,\mathrm{arcmin}$) [90], the residual power after gradient-order delensing is approximately 80 % of that obtained using a non-perturbative template. This translates to the removal of an additional 4.5 % of the lensing power originally in the maps.

2.5 Conclusions

The variance associated with lensing B-modes ought to be mitigated in order to optimise searches for the primordial signal associated with a stochastic background of gravitational waves that may have been produced during cosmic inflation. The partial removal of lensing, known as delensing, is often carried out by combining high-resolution E-mode observations with some proxy of the lensing potential to produce a template-estimate of the lensing B-modes, which can then be subtracted from observations on large angular scales. This was the approach followed by the *Planck* [372], SPT [290] and POLARBEAR [380] Collaborations in their successful demonstrations of delensing on real B-mode data.

In this chapter, we have considered the limitations of this template method that arise from lensing of the E-modes used in the template and the remapping approximations made in its construction. Gradient-order templates, where the lensing action on the E-mode observations is approximated by the gradient term in a Taylor expansion, are often used, particularly in forecasting work given their analytic simplicity. Such templates are usually presumed to be highly accurate in tracking the true lensing B-modes if the polarisation measurements are of sufficient precision and an estimate of the lensing deflections is available that is highly correlated with the true lensing. This accuracy is often assumed to follow from the fact that higher-order corrections to the leading-order calculation of the lensing B-mode spectrum are very small, at the $O(1)$ % level. However, we showed that in the case of the lensed B-mode spectrum, the small contribution from terms beyond gradient order is a result of cancellations between terms that are separately relatively large (around 10 %), and that these cancellations are not necessarily relevant for the delensed spectrum. In particular, a gradient-order template constructed from the unlensed (or, more realistically, the delensed or anti-lensed) E-modes introduces a floor in the residual power of around 10 % of the original lensing B-mode power due to unsubtracted terms in the lensing

B-modes that are second order in the lensing deflections. Fortunately, in the case of a gradient-order template constructed from the lensed E-modes, cancellations appear at higher order which reduce the floor in the residual power to the $O(1)\,\%$ level. The dominant cancellations in this case are between the second-order term in the lensing B-modes and that in the template arising from the first-order lensing correction to the E-modes. The larger $10\,\%$ residual-power floor also arises in anti-lensing, where one displaces the full lensed polarisation field using minus the lensing deflections as an approximation to the true inverse remapping.

Non-perturbative templates are also sometimes considered, in which a template is made by directly deflecting the (filtered) observed E-modes by the lensing proxy, rather than relying on the gradient-order approximation. Importantly, we showed that such templates are also fundamentally limited, reintroducing a floor of $O(10)\,\%$ in the delensed power. This behaviour arises since the first-order lensing correction to the E-modes used in the template are no longer approximately cancelled. We further showed that in practical applications of delensing, where noisy E-modes and a partially-correlated lensing proxy are used, the benefits of the gradient-order template persist, albeit with more marginal gains. Indeed, the better performance of the gradient-order template becomes significant well before the non-perturbative template has hit its delensing floor: for an experiment with characteristics similar to CMB-S4, this would enable the removal of an additional $5\,\%$ of lensing power, reducing the lensing-related uncertainty on the tensor-to-scalar ratio r by a factor of around 1.2 in the limit $r = 0$. We therefore recommend that in practical applications of B-mode template delensing, where the template is constructed directly from the (filtered) observed E-modes, the gradient-order approach should be used rather than a non-perturbative remapping.

Chapter 3

Delensing B-modes with external tracers

This chapter is based on [19] and [313]. Note that the asymmetric convention for Fourier transforms is used throughout it[1]*.*

3.1 Introduction

In previous chapters, we explained the need to delens CMB B-mode polarisation in order to better constrain primordial gravitational waves. The deflections induced by lensing can be undone — at least partially — given an estimate of the projected matter distribution, which determines the lensing convergence κ. In the not-so-distant future, it will be possible to reconstruct lensing from the CMB itself; we have already discussed this in section 1.5.2.4, and will do so in greater depth in chapters 4 and 5.

However, for the sensitivity and resolution of current and near-future CMB experiments, tracers external to the CMB, such as galaxy surveys or the cosmic infrared background [445, 432], play a crucial role: they provide access to intermediate and small-scale lenses at high redshift that internal reconstructions cannot yet extract with sufficient precision.

In recent years, one tracer has emerged as being particularly useful for delensing – the cosmic infrared background (CIB); see section 1.5.3.3 for an introduction. Recent observations at 353, 545 and 857 GHz made by the High-Frequency Instrument (HFI) aboard the *Planck* satellite have led to significant improvements in our understanding of the CIB thanks to the instrument's high sensitivity, fine angular resolution and

[1] In the asymmetric convention for two-dimensional Fourier transforms:

$$f(\boldsymbol{x}) = \int \frac{d^2\boldsymbol{l}}{(2\pi)^2} f(\boldsymbol{l}) e^{i\boldsymbol{l}\cdot\boldsymbol{x}} \quad \text{and} \quad f(\boldsymbol{l}) = \int d^2\boldsymbol{x} f(\boldsymbol{x}) e^{-i\boldsymbol{l}\cdot\boldsymbol{x}} \,. \tag{3.1}$$

large sky coverage. On the one hand, these have allowed for a refinement of models [351, 357, 427, 283, 288], and on the other, high-fidelity maps of the CIB anisotropies over large fractions of the sky have been produced [365, 250]. These maps are some of the best tracers of the large-scale structure of the Universe at high redshift that have been made available to date, and are up to 80 % correlated with CMB lensing [455, 192, 355]. As such, they hold great promise for upcoming implementations of delensing, particularly in combination with other tracers [517]. CIB maps from Planck were used by Ref. [247] in the first demonstration of delensing, and more recently Ref. [51] used them to show the first improvement in r constraints thanks to delensing. Meanwhile, Ref. [291] used *Herschel* CIB data to achieve the first statistically-significant delensing of B-modes.

As discussed previously, the aim of delensing is to reduce the variance on estimates of the B-mode power spectrum by subtracting the specific realisation of lensing B-modes present on the sky. The more effective this procedure, the more attention one must pay to potential systematic errors. In spite of this, the impact of foreground emission on delensing has remained largely unexplored, with the exception of Ref. [30]'s recent study of the impact of residual foregrounds on internal delensing of B-modes. In section 3.5 — the core of this chapter — we focus on the impact of foregrounds when using the CIB to delens B-modes. The principal worry is that, as part of the delensing procedure, residual amounts of dust or CIB emission left over in the CMB maps can couple with residual dust or the CIB in the matter tracer maps. The problem is exacerbated by the fact that both the CIB and Galactic dust emission are the product of radiating dust and therefore display very similar spectral energy distributions, making it difficult to disentangle the two. We show that these couplings are indeed present, even after foreground cleaning, and could be significant on the very largest angular scales. We also discuss mitigation techniques, which fortunately prove very effective.

Another topic that merits attention is that of astrophysical uncertainties in the characterisation of the tracers used as matter proxies when delensing — modelling residuals can, in principle, translate to biases on the inferred values of the tensor-to-scalar ratio. In section 3.4, we study this issue in the context of delensing with the Simons Observatory (SO). We show that the impact will only be small, particularly when delensing is carried out using a combination of external tracers and internal reconstructions of lensing.

The structure of this chapter is as follows. We begin, in section 3.2, with a brief reminder of the basics of B-mode delensing and an explanation of how external tracers can be incorporated into the procedure. That is followed, in section 3.3, by a discussion

of how delensed spectra are to be modelled when using external tracers. Then, in section 3.4, we quantify the impact on the inferred value of r of uncertainties in the spectra of external tracers. Next, in section 3.5, we investigate the ways in which foregrounds can impact delensing when the CIB is used as the matter proxy. Since this section is rather long, let us briefly comment on its substructure. In section 3.5.1, we introduce the simulations of Galactic dust and CIB used in the section, we estimate the levels of dust residuals expected of upcoming experiments, we discuss masking schemes, and we lay out in detail the overall analysis. Then, in section 3.5.2, we present our results for the magnitude of delensing bias that we expect to arise from higher-point functions of both residual Galactic dust and the CIB itself, with details of the latter provided in appendices B.1, B.2, B.3, B.4 and B.5. These results are validated in section 3.5.3 by comparing to data from Planck and to Gaussian simulations. Finally, we summarise our conclusions in section 3.6. Throughout this work, we assume a cosmology with parameters as determined by Ref. [366].

3.2 Building a template using external tracers

The lensing-induced B-modes can be approximated, to leading order in the lensing convergence κ and in the flat-sky approximation, by

$$B^{\rm lens}(\boldsymbol{l}) = \int \frac{d^2\boldsymbol{l}'}{(2\pi)^2} W(\boldsymbol{l},\boldsymbol{l}') E(\boldsymbol{l}') \kappa(\boldsymbol{l}-\boldsymbol{l}') \,, \tag{3.2}$$

where $E(\boldsymbol{l})$ is the unlensed E-mode polarisation. The geometric coupling

$$W(\boldsymbol{l},\boldsymbol{l}') = \frac{2\boldsymbol{l}'\cdot(\boldsymbol{l}-\boldsymbol{l}')}{|\boldsymbol{l}-\boldsymbol{l}'|^2} \sin 2(\psi_{\boldsymbol{l}} - \psi_{\boldsymbol{l}'}) \,, \tag{3.3}$$

where $\psi_{\boldsymbol{l}}$ is the angle that $\boldsymbol{l}$ makes with the x-axis. It was shown by Ref. [84] that the power spectrum of this linear-order approximation is in excellent agreement with the non-perturbative power spectrum at multipoles $l \leq 2000$, which comfortably includes the range we are interested in ($l < 200$) when searching for B-modes from primordial gravitational waves. The reasons behind the accuracy of this leading-order expression were explained in some level of detail in chapter 2.

Given some tracer I of the lensing convergence, the analysis of chapter 2 suggests that we can construct an accurate lensing B-mode template as:

$$\hat{B}^{\rm lens}(\boldsymbol{l}) = \int \frac{d^2\boldsymbol{l}'}{(2\pi)^2} f(\boldsymbol{l},\boldsymbol{l}') W(\boldsymbol{l},\boldsymbol{l}') E^{\rm obs}(\boldsymbol{l}') I(\boldsymbol{l}-\boldsymbol{l}') \,, \tag{3.4}$$

where $E^{\rm obs}$ is the observed (lensed and noisy but beam-deconvolved) E-mode and $f(\boldsymbol{l}, \boldsymbol{l}')$ is a function that can be chosen to minimise the variance of the power spectrum of the delensed B-modes. The delensed B-modes are obtained by subtracting this lensing template from the observed B-modes.

Delensing methods structured around the construction and subtraction of a lensing template provide significant advantages over alternative approaches relying on an inverse deflection of the observed fields. This is particularly true for ground-based experiments, for which it is much more cost-effective to carry out the large-angular-scale B-mode science using arrays of small-aperture telescopes (SATs)[2], while the high-resolution polarisation observations required to delens are made by a large-aperture telescope (LAT). The template formalism provides the necessary framework to combine the data from the different telescopes. In chapter 2, we showed that, in the limit of noiseless E-modes and perfect ϕ, such a template built from lensed E-modes (which turns out to be preferable over using delensed E-modes, or forming a non-perturbative template by remapping lensed E-modes) can be used to reduce the residual lensing power down to around 1 % of its original amplitude. In practical applications, the method will be effectively optimal even beyond the era of CMB-S4.

The matter tracer, I, can be obtained either internally from the observed CMB or externally via observables known to correlate with the distribution of matter in the Universe. Although, ultimately, internal techniques based on quadratic estimators [331], maximum-likelihood [190] or Bayesian/iterative approaches [74, 298] will provide the best means of extracting the information, current and near-future experiments will benefit greatly from combining internal reconstructions with external tracers [445, 432, 517, 289, 51]. The reason for this is that large-scale lensing B-modes are produced from lenses over a wide range of multipoles, with 50 % of the power coming from lenses at $l > 400$ [445, 82]. Internal reconstructions obtained by experiments surveying wide fields at high angular resolution (such as the forthcoming Simons Observatory, SO; [441]) will be noise-dominated on these intermediate and small scales and so will benefit from combining with external tracers. Looking further ahead to experiments such as CMB-S4 [90], the gain in delensing efficiency from adding external tracers is marginal. However, it will be possible to use the CIB in combination with other tracers as a cross-check on internal delensing.

[2]The main challenge for making highly sensitive measurements of CMB polarisation on the largest angular scales ($l < 20$) is control of temperature-to-polarisation leakage of the spatially- and temporally-varying emission from the atmosphere. A leading way to achieve this is by means of devices that modulate the observed polarisation. At the time of writing, it is more cost-effective to increase sensitivity by installing these devices on many SATs rather than on a LAT [90].

For an external tracer, Ref. [432] showed that the choice of $f(\boldsymbol{l}, \boldsymbol{l}')$ in equation (3.4) that minimises the power spectrum of the delensed B-modes is a product of Wiener filters:

$$f(\boldsymbol{l}, \boldsymbol{l}') = \mathcal{W}^E_{l'} \mathcal{W}^I_{|\boldsymbol{l}-\boldsymbol{l}'|}\,, \tag{3.5}$$

with

$$\mathcal{W}^E_l \equiv \frac{\tilde{C}^{EE}_l}{\tilde{C}^{EE}_l + N^{EE}_l} \quad \text{and} \quad \mathcal{W}^I_l \equiv \frac{C^{\kappa I,\text{fid}}_l}{C^{II}_l}\,. \tag{3.6}$$

Here, $\tilde{C}^{EE}_l$ is the lensed E-mode power spectrum, N^{EE}_l is the instrument noise power, $C^{\kappa I}_l$ is the cross-power spectrum between the tracer I and the true CMB lensing convergence κ, and C^{II}_l is the total power spectrum of the tracer including, for example, shot noise. In the remainder of this work, we shall assume that E-mode observations are sample-variance limited up to $l \approx 2000$, so that $\mathcal{W}^E_{l<2000} = 1$. This is a good approximation for current and upcoming experiments with beams of a few arcmin and polarisation sensitivities better than $10\,\mu$K arcmin.

It is worth noting that delensing performance can be further improved by linearly combining many lensing tracers $\{I_i\}$ in a way that maximises the cross-correlation between the emerging, co-added tracer and the true convergence. Reference [432] showed that the weights that achieve this are

$$c^i_l = \sum_j (\rho^{-1})^{ij}_l \rho^{\kappa I_j}_l \sqrt{\frac{C^{\kappa\kappa}_l}{C^{I_i I_i}_l}}\,, \tag{3.7}$$

where $\rho^{\kappa I_i}_l$ is the correlation coefficient, at multipole l, between tracer I_i and the true convergence; $\rho^{I_i I_j}_l$ is the correlation between tracers I_i and I_j, and $C^{I_i I_i}_l$ is the power spectrum of tracer I_i. An optimally co-added tracer can then be obtained as $\kappa^{\text{comb}}_l = \sum_i c^i_l I^i_l$; it can be shown that this is equivalent to combining Wiener-filtered tracers as

$$\mathcal{W}^I_l I(\boldsymbol{l}) \to \sum_{ij} I_i(\boldsymbol{l}) \left(C^{-1}_l\right)^{ij} C^{\kappa I_j}_l\,, \tag{3.8}$$

where $C^{\kappa I_i}_l$ is the cross-power spectrum between the true convergence and the ith tracer, and $\left(C^{-1}_l\right)^{ij}$ is the matrix inverse of the cross-power spectra $C^{I_i I_j}_l$ between the tracers. The correlation coefficient of the linearly-combined tracers with the true convergence can be expressed in terms of measurable properties of each individual tracer as

$$\rho^2_l = \sum_{ij} \left(\rho^{-1}_l\right)^{ij} \rho^{\kappa I_i}_l \rho^{\kappa I_j}_l\,. \tag{3.9}$$

Qualitatively, on a given angular scale, this scheme gives most weight to those tracers that best correlate with the underlying convergence. In practice, this means that internal reconstructions, which accurately reconstruct lensing on the largest angular scales, can be supplemented with external tracers on the small scales where the former are dominated by reconstruction noise. For SO, for example, information from the CIB and photometric galaxy surveys will enable the co-added tracer to maintain a high degree of correlation with the true lensing convergence for multipoles $250 \lesssim l \lesssim 1000$ [313], despite internal reconstructions only being signal-dominated for $L \lesssim 250$ [441]; see figure 3.1. This is of particular importance for delensing, since, as noted above, it is those intermediate and small-scale lenses that are most relevant for this purpose [445]. Since the small-scale lenses are located at high redshift (see figure 3 of [252]), delensing will remain a challenging effort for the foreseeable future.

3.3 Modelling externally-delensed spectra

Once templates of the lensing B-modes have been produced, the inference process can begin. For the purposes of this chapter, we shall only be concerned with the impact of inaccurate modelling either due to uncertainties in the tracer spectra (section 3.4) or to the presence of residual foregrounds trickling through the delensing pipeline (section 3.5). These problems can be isolated by directly contrasting modelled and empirical spectra, and propagating any residuals to biases on r using simplified treatments without ever explicitly writing down a likelihood function. Please refer to chapter 4 for an example of a (slightly) more realistic inference.

The power spectrum of residual lensing B-modes after delensing can be expressed, to leading order and in the flat-sky approximation, as

$$\tilde{C}_l^{BB,\mathrm{res}} = \int \frac{d^2\boldsymbol{l}'}{(2\pi)^2} W^2(\boldsymbol{l},\boldsymbol{l}') C_{l'}^{EE} C_{|\boldsymbol{l}-\boldsymbol{l}'|}^{\kappa\kappa} \left[1 - \mathcal{W}_{l'}^{E} \rho_{|\boldsymbol{l}-\boldsymbol{l}'|}^2\right] , \tag{3.10}$$

where ρ_l is the correlation coefficient between the tracer at hand and the underlying CMB lensing convergence. Much like its fully-lensed precursor, the delensed spectrum above is almost constant (i.e., like white noise) on large angular scales. In section 3.4, we will show that this behaviour is robust to uncertainties in measurements of the auto- and cross-spectra (with CMB lensing) of the tracers when combined with a precise large-scale internal reconstruction. This means that, in actual analyses, it should be possible to deal with any uncertainties in the residual lensing power by marginalising over the amplitude of a constant spectrum.

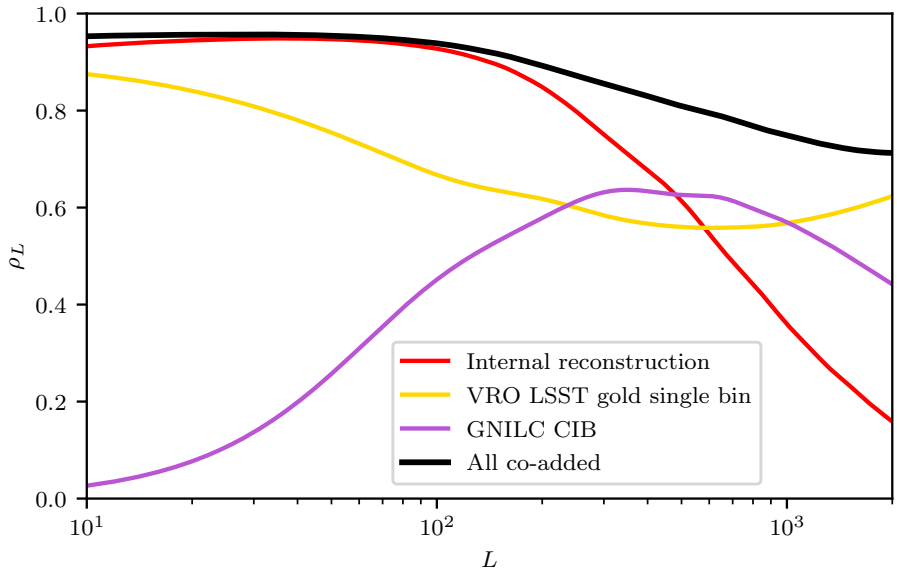

Fig. 3.1 Correlation coefficient of the true CMB lensing field with several tracers of the large-scale structure, and with a co-added tracer. On large angular scales, correlation between the CIB map extracted from Planck data using the GNILC algorithm drops due to the presence of residual CIB in the dust maps (which, in turn, gets filtered out of the CIB maps). Fortunately, on those scales internal techniques can very accurately reconstruct lensing, as shown here for a projected minimum-variance quadratic estimator reconstruction with SO goal noise levels and standard Internal Linear Combination (ILC) foreground cleaning [441]. On the other hand, the relevance of shot noise on small scales means that the correlation with the CIB decreases for large l. For clarity of illustration, the forecasted curves involving VRO LSST galaxies correspond to the case where tomographic observations of galaxies in the "gold" sample (approximately 40 galaxies per squared arcminute) [210] are merged into a single bin, which is only marginally suboptimal for the purpose of delensing. The auto- and cross-spectra shown in this plot are taken from Ref. [517].

The expression above can be used to model the residual lensing power when a lensing template is subtracted from foreground-cleaned maps. However, alternative approaches to incorporating foregrounds are possible, which might require modifications to our modelling; see, e.g., Ref. [441] for the options being explored within SO. One particularly prominent technique — which has already been demonstrated on simulations [2, 313] and real data [49] — involves measuring all the possible auto- and cross-spectra between the frequency maps; modelling those as a combination of parametrised foregrounds, noise and CMB signal; and finally writing down an approximate likelihood which, given some priors on the foregrounds, can be used to constrain the relevant parameters. In this context, the lensing template can be incorporated as an additional channel, requiring us to be able to model its power spectrum and cross-correlations with every frequency map. Although this approach should (in principle) be equivalent to the map-level subtraction described previously, we provide here, for completeness, expressions to model the auto- and cross-spectra of the template with the observed B-modes; this can then be easily generalised to different frequency channels if necessary.

Consider, then, the cross-spectrum between the lensing template and a co-added tracer, $\kappa^{\rm comb}$, constructed from the weights in equation (3.8). To $O(\kappa^2)$, this is

$$\begin{aligned} C_l^{BB,\rm cross} &= \int \frac{\mathrm{d}^2\boldsymbol{l}'}{(2\pi)^2}\, W^2(\boldsymbol{l}',\boldsymbol{l}) W_{l'}^E C_{l'}^{EE} C_{|\boldsymbol{l}'-\boldsymbol{l}|}^{\kappa\kappa^{\rm comb}} \\ &= \int \frac{\mathrm{d}^2\boldsymbol{l}'}{(2\pi)^2}\, W^2(\boldsymbol{l}',\boldsymbol{l}) W_{l'}^E C_{l'}^{EE} C_{|\boldsymbol{l}'-\boldsymbol{l}|}^{\kappa\kappa} \rho^2_{|\boldsymbol{l}'-\boldsymbol{l}|}\,, \end{aligned} \tag{3.11}$$

where $\rho_L = C_L^{\kappa\kappa^{\rm comb}}/\sqrt{C_L^{\kappa\kappa} C_L^{\kappa^{\rm comb}\kappa^{\rm comb}}}$ is now the cross-correlation coefficient of the co-added tracer with lensing; conveniently, this can be calculated from the spectra of the individual tracers using equation (3.9). We also use $C_L^{\kappa\kappa^{\rm comb}} = C_L^{\kappa^{\rm comb}\kappa^{\rm comb}}$ (see equation (B.75) to gain intuition as to why this expression holds).

On the other hand, the auto-spectrum of the template can be modelled as

$$\begin{aligned} C_l^{BB,\rm temp} &= \int \frac{\mathrm{d}^2\boldsymbol{l}'}{(2\pi)^2}\, W^2(\boldsymbol{l}',\boldsymbol{l}) \left(W_{l'}^E\right)^2 C_{l'}^{E^{\rm obs}E^{\rm obs}} C_{|\boldsymbol{l}'-\boldsymbol{l}|}^{\kappa^{\rm comb}\kappa^{\rm comb}} \\ &= \int \frac{\mathrm{d}^2\boldsymbol{l}'}{(2\pi)^2}\, W^2(\boldsymbol{l}',\boldsymbol{l}) W_{l'}^E C_{l'}^{EE} C_{|\boldsymbol{l}'-\boldsymbol{l}|}^{\kappa\kappa} \rho^2_{|\boldsymbol{l}'-\boldsymbol{l}|}\,. \end{aligned} \tag{3.12}$$

The model spectra described above can be tested against simulations, revealing that they are sufficiently accurate for the analyses presented in this chapter, and for validating the SO delensing pipeline [313]. For applications requiring greater accuracy, it might be desirable to relax the flat-sky approximation and work with spherical

harmonics (on the angular scales relevant for SO, flat-sky results are in very good agreement with the exact ones, within $\sim 1\%$ [84]). Perhaps more importantly, the series expansion could be replaced with a non-perturbative treatment as in Refs. [422, 84].

In addition to model spectra, another important ingredient of realistic inferences involving approximate likelihoods — such as that introduced by Hamimeche and Lewis [163] — is a set of fiducial angular power spectra and their covariances. The latter can be obtained either from simulations or analytically. Simulated covariances, which fully capture important effects such as masking and inhomogeouneous noise, are expensive to compute, since a large number of them is needed for the Monte Carlo error to be small enough that the small correlations between bandpowers can be resolved [446, 36, 17] (see the discussion in chapter 4.5). To complement these efforts, we provide, in appendix B.8, analytic calculations of the covariances of the auto- and cross-spectra described above. An implementation of these, based on modifying the publicly-available code `LensCov` [347], was used as part of the effort to validate the SO delensing pipeline in Ref. [313].

In the following sections, we explain the ways in which the models above can prove insufficient. We begin by showing, in the next section, how uncertainties in our knowledge of the spectra of the external tracers used for delensing can propagate to constraints on r. Then, in section 3.5, we explore in detail the ways in which residual foregrounds affect the delensing process when the CIB is used as a proxy of the lensing potential.

3.4 The impact of uncertainties in external tracer spectra

Evaluating the model spectra of the previous section requires knowledge of the auto- and cross-spectra with CMB lensing of each of the tracers involved. In practical applications, the tracer spectra will likely be determined by fitting a smooth curve to measurements, and hence will be uncertain to some degree. It is important, then, to accurately quantify this uncertainty, as otherwise we run the risk of mistaking non-trivially-shaped lensing residuals for a primordial signal, and thus biasing constraints on r [432]. In this section, we explore this possibility quantitatively.

Before proceeding further, we note that this issue will also mean that, in principle, the weighting scheme summarised in equation (3.8) will be sub-optimal whenever the fiducial spectra deviate from the truth. However, we ignore this effect because

the corrections are second-order in the error of the weight function and are therefore small [432].

Consider the angular power spectrum of residual lensing B-modes after map-level delensing with a co-added tracer, $\kappa_l^{\rm comb} = \sum_i c_l^i I_l^i$. To leading order in lensing, this is

$$\tilde{C}_l^{BB,\rm res} = \int \frac{\mathrm{d}^2\boldsymbol{l}'}{(2\pi)^2} W^2\left(\boldsymbol{l},\boldsymbol{l}'\right) \Bigg[C_{l'}^{EE} C_{|\boldsymbol{l}-\boldsymbol{l}'|}^{\kappa\kappa} - 2\, C_{l'}^{EE} \mathcal{W}_{l'}^E \sum_i c_{|\boldsymbol{l}-\boldsymbol{l}'|}^i C_{|\boldsymbol{l}-\boldsymbol{l}'|}^{\kappa I^i} + \left(C_{l'}^{EE} + N_{l'}^{EE}\right) \left(\mathcal{W}_{l'}^E\right)^2 \sum_i \sum_j c_{|\boldsymbol{l}-\boldsymbol{l}'|}^i c_{|\boldsymbol{l}-\boldsymbol{l}'|}^j C_{|\boldsymbol{l}-\boldsymbol{l}'|}^{I^i I^j} \Bigg], \tag{3.13}$$

where the weights, c_l^i, are calculated using fiducial spectra. Equation (3.13) can be further simplified by noticing that $\sum_i \sum_j c_{|\boldsymbol{l}-\boldsymbol{l}'|}^i c_{|\boldsymbol{l}-\boldsymbol{l}'|}^j C_{|\boldsymbol{l}-\boldsymbol{l}'|}^{I^i I^j} = \sum_j c_{|\boldsymbol{l}-\boldsymbol{l}'|}^j C_{|\boldsymbol{l}-\boldsymbol{l}'|}^{\kappa I^j}$, which follows from $c_l^i = \sum_j C_l^{\kappa I^j} \left(C_l^{I^i I^j}\right)^{-1}$.

Now, consider the case where the measured spectra deviate from the fiducial model. We parametrise this as

$$C_l^{\kappa I^i} = C_l^{\kappa I^i,\rm fid} \left(1 + a_l^i\right), \tag{3.14}$$

and

$$C_l^{I^i I^i} = C_l^{I^i I^i,\rm fid} \left(1 + b_l^i\right), \tag{3.15}$$

where a_l^i and b_l^i are random variables drawn from Gaussian distributions centred at zero, and with standard deviation given by the estimated measurement error on the angular power spectrum of tracer i at multipole l. The angular power spectrum of residual lensing B-modes after delensing, allowing for errors in both the auto- and cross-spectra of the tracers, is then

$$\tilde{C}_l^{BB,\rm res} = \int \frac{\mathrm{d}^2\boldsymbol{l}'}{(2\pi)^2} W^2\left(\boldsymbol{l},\boldsymbol{l}'\right) C_{l'}^{EE} C_{|\boldsymbol{l}-\boldsymbol{l}'|}^{\kappa\kappa} \Bigg[1 - \mathcal{W}_{l'}^E \left(\rho_{|\boldsymbol{l}-\boldsymbol{l}'|}^{\rm fid}\right)^2 - \mathcal{W}_{l'}^E \sum_i c_{|\boldsymbol{l}-\boldsymbol{l}'|}^i \frac{C_{|\boldsymbol{l}-\boldsymbol{l}'|}^{\kappa I^i,\rm fid}}{C_{|\boldsymbol{l}-\boldsymbol{l}'|}^{\kappa\kappa}} \left(2\, a_{|\boldsymbol{l}-\boldsymbol{l}'|}^i - b_{|\boldsymbol{l}-\boldsymbol{l}'|}^i\right) \Bigg]. \tag{3.16}$$

where $\rho^{\rm fid}$ is the correlation of the co-added tracer with lensing in the fiducial model.

We can use the above expression to study possible deviations of the true lensing B-mode residual from a model constructed around the fiducial tracer spectra (the one used to calculate the weights). We set $\mathcal{W}_l^E$ to the values appropriate for the SO LAT after foreground cleaning [441], and consider two scenarios: in the first

one, the matter proxy is taken to be the Planck GNILC CIB maps[3] [365]; in the second, the CIB is co-added, using the weights in equation (3.8), with a map of the galaxy distribution and an internal reconstruction of lensing. On the galaxy side, we assume the characteristics expected of the Vera Rubin Observatory Legacy Survey of Space and Time (VRO LSST) "gold" sample (approximately 40 galaxies per squared arcminute) [210]. For the internal reconstruction, on the other hand, we use the forecasted performance on SO data of a minimum-variance combination of quadratic estimator reconstructions using both temperature and polarisation information [441]. We adopt a conservative stance and assign to all bandpowers of all external tracers an uncertainty of $\Delta(2l_iC_i/\sqrt{2}) = 0.02\mu\mathrm{K\,sr}$, roughly equal to that estimated by Planck for their measurement of the CIB auto-spectrum (e.g., Table 2 and Figure 5 of [355]). Since there is relatively little overlap in redshift between the external tracers we use, we ignore any covariance between them. We sample a_l^i and b_l^i in 23 bins with width $\Delta l = 63.5$ and ranging approximately between $60 < l < 1500$.

Several realisations of modelling residuals consistent with the estimated measurement errors are shown in figure 3.2 for the two scenarios described above. We see that the combination of external tracers with internal reconstructions (for which the correlation with lensing on large-scale scales is known very accurately) leads to residuals which are rather flat, significantly more so than in the case where only external tracers are used. This suggests that uncertainties in tracer spectra can be integrated into constraints on r by means of a simple marginalisation procedure involving a single parameter governing the amplitude of the residual. Reference [432] assessed this approach in the case where the CIB was the only tracer, finding that the uncertainty grows only moderately. Given that the residuals we see arise when co-adding multiple tracers are significantly flatter than when the CIB is used by itself, we expect the degradation in constraining power to be even smaller.

The residuals due to improper modelling shown in figure 3.2 can be propagated to biases on estimates of r using the relation (e.g., [403])

$$\Delta\hat{r} = \left(\sum_{l=l_{\mathrm{min}}}^{l_{\mathrm{max}}} \left[C_l^{BB,\mathrm{prim}}(r=1) \right]^2 / \mathrm{Var}\left(\tilde{C}_l^{BB,\mathrm{res}} \right) \right)^{-1} \times \sum_{l=l_{\mathrm{min}}}^{l_{\mathrm{max}}} C_l^{BB,\mathrm{unmodelled}} C_l^{BB,\mathrm{prim}}(r=1) / \mathrm{Var}\left(\tilde{C}_l^{BB,\mathrm{res}} \right) . \tag{3.17}$$

[3]Further details about these maps are provided in the following section.

Here, $C_l^{BB,\mathrm{prim}}(r=1)$ is the angular power spectrum of primordial B-modes with $r=1$, $\mathrm{Var}(\tilde{C}_l^{BB,\mathrm{res}})$ is the variance of the power spectrum of delensed B-modes (which we assume to be Gaussian, free of foregrounds, and to feature a level of experimental noise appropriate for the 93 GHz channel of the SO SATs in the *goal* scenario) and $C_l^{BB,\mathrm{unmodelled}}$ is the part of the delensed B-mode spectrum that we have not modelled — in this case, the bias due to incorrect modelling of the external tracer spectra.

In figure 3.3, we compare the estimated shifts for ten random realisations to the standard deviation on $r=0$ expected of an experiment covering 5 % of the sky, with the noise levels of the SO SAT, and in the limit of no foreground BB power and a removal of lensing as appropriate for delensing with the CIB alone or in the multi-tracer approach described above. We use $l_{\mathrm{min}}=38$ and $l_{\mathrm{max}}=188$. We see that the shifts induced by uncertainty in the tracer spectra are typically small compared to the precision afforded by SO. Figure 3.4 illustrates this by comparing the distribution of r shifts to the SO statistical uncertainty in the null scenario; the biases are not statistically significant. Reference [51], who used the CIB to delens B-modes, reached similar conclusions, having estimated that a misestimation of the CIB-lensing cross-spectrum could bias their inference of r by at most 0.2 standard deviations

3.5 The impact of residual foregrounds on CIB delensing

At high frequencies, Galactic dust emission and CIB radiation both behave as grey-bodies with very similar temperatures and spectral indices. Hence, it is very difficult to separate the two based on multi-frequency information alone, and CIB maps extracted in this way — such as those obtained by Ref. [357] — suffer considerable contamination from Galactic dust, and vice versa.

Several approaches to separating Galactic dust from the CIB have been explored in the literature. In this work, we evaluate two such techniques. First, we consider the GNILC CIB maps of Ref. [365] which several groups have recently used in implementations of delensing [247, 517, 51]. This algorithm makes use of differences in the angular power spectrum of the two components – approximately l^{-1} for the CIB [351] and $l^{-2.7}$ for the dust [357] – to separate them.

Another method to disentangle CIB and Galactic dust emission is by exploiting the correlation between 21-cm emission from neutral Hydrogen, H I, in the inter-stellar medium (ISM) and Galactic dust [351]. Recently, Ref. [250] have harnessed this to clean high-frequency Planck observations using H I data from the H I4PI survey [182],

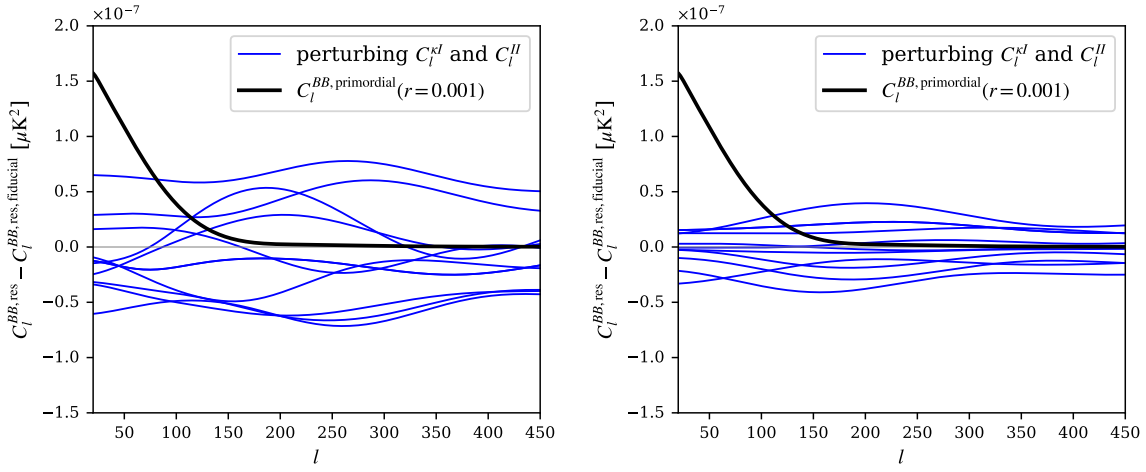

Fig. 3.2 Impact of uncertainties in the tracer spectra on the power spectrum of SO B-mode lensing residuals after delensing. We quantify this by perturbing the fiducial tracer auto- and cross-spectra with errors drawn from a Gaussian distribution consistent with the *Planck* uncertainty on the CIB auto-spectrum bandpowers. *Left:* The case where delensing is performed using *Planck* GNILC CIB maps as the only matter tracer. *Right:* the *Planck* CIB maps are co-added with LSST galaxies (gold sample) and SO internal reconstructions. It is readily apparent that co-adding external tracers with internal reconstructions mitigates possible shapes in the residuals that might be confused with a primordial component. For comparison, a primordial signal with $r = 0.001$ is shown.

producing high-quality CIB maps on a wide range of angular scales. As a side note, H I gas in the ISM tends to form filamentary structures aligned with the local Galactic magnetic field [89, 87], so it correlates with polarised emission from asymmetric dust grains, which also tend to align with their short axes pointing along the local magnetic field. By harnessing this connection, observations of H I have the potential to further our understanding of Galactic foregrounds for CMB polarisation studies.

From the considerations above, it is clear a complete removal of dust from the CIB maps is virtually impossible. Hence, we now seek to identify the ways in which the presence of residual dust could impact the power spectrum of delensed B-modes – the estimator from which we hope to extract information about a primordial component.

Though our analysis will be restricted to the case where delensing is carried out using the CIB as the sole tracer, it will be worth keeping the multi-tracer weights in mind for two reasons. First, it will inform our choice of minimum multipole cutoff, l_{min}, to be applied to the CIB maps — as we will see in later sections, this choice has a significant impact on the expected amplitude of the bias in the delensed spectrum.

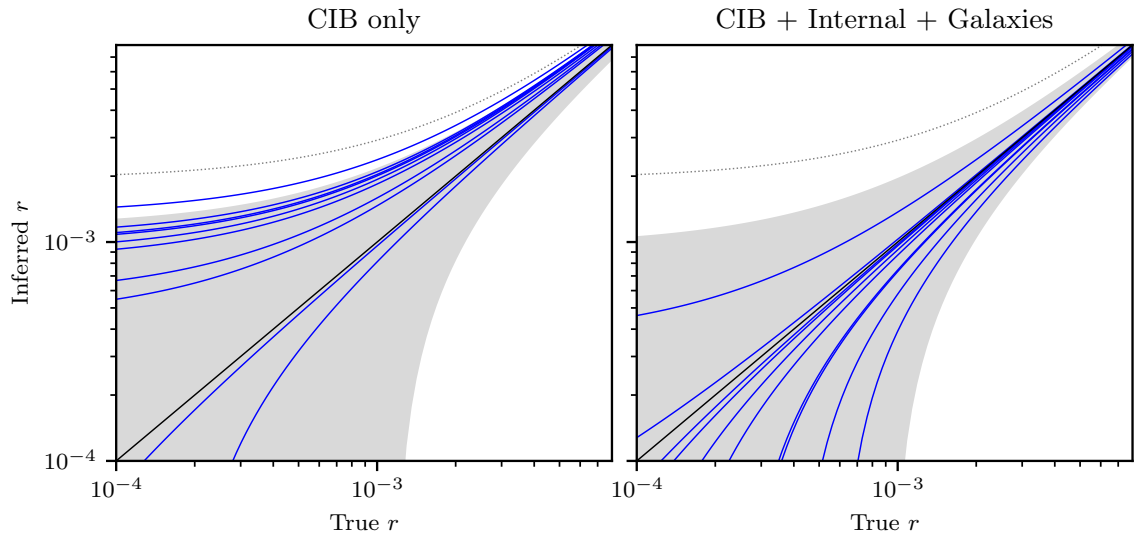

Fig. 3.3 Bias on the inferred tensor-to-scalar ratio, as a function of input signal, due to deviations from the fiducial model of the spectra of the external tracers used for delensing. We show the case of ten different, random fluctuations of the tracer spectra consistent with *Planck* measurement errors (see text). We constrain r using scales $l_{\rm min} = 38$ and $l_{\rm max} = 188$. In general, the bias is small compared to the statistical uncertainty of SO. To show this, we plot as the shaded, grey region the $\pm 1\,\sigma$ uncertainty for $r = 0$ of an experiment covering 5 % of the sky with the noise level of the SO SAT's 93 GHz channel, no foregrounds and delensing as allowed by each of the tracer combinations, in the case where r is constrained over the multipole range described above. For comparison also, the dotted lines show the size of the bias on r if residual dust B-modes in the SO SAT maps (as forecasted by Ref. [441]) are not modelled in the BB power spectrum.

And second, the magnitude of the bias in an analysis involving multiple tracers, one of them being the CIB, can be recovered from that determined in this work once the weight given to the CIB in the linear combination is known. In this sense, the results in this study can be regarded as an upper limit on the amplitude of the bias terms.

The most naïve approach would have us model the power spectrum of delensed B-modes as the residual lensing B-mode power plus some contribution from the auto-spectrum of dust and CIB B-mode polarisation. That is

$$C_l^{BB,\rm del,naive} = \tilde{C}_l^{BB} + N_l^{BB} + C_l^{BB,\rm dust,res} + C_l^{BB,\rm CIB,res} - 2\,g_l \left[\langle \tilde{B}\tilde{E}I^{\rm CIB}\rangle\right] + h_l \left[\langle \tilde{E}I^{\rm tot}\tilde{E}I^{\rm tot}\rangle\right], \tag{3.18}$$

where $I^{\rm tot}$ includes CIB ($I^{\rm CIB}$, composed of correlated signal and shot noise), residual Galactic dust ($I^{\rm dust}$) and experimental noise ($I^{\rm noise}$); and $\tilde{C}_l^{BB}$, N_l^{BB}, $C_l^{BB,\rm dust,res}$ and

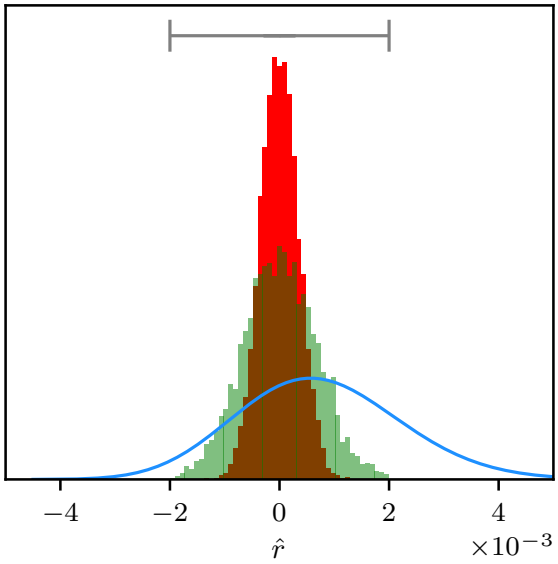

Fig. 3.4 Distribution of the bias on r from 5000 realisations (with input $r = 0$), arising from uncertainties in the spectra of the external tracers used to delens SO B-modes, in the case where *Planck* CIB maps alone are used (green histogram), or when these CIB maps are co-added with SO internal reconstructions and VRO LSST galaxies (red histogram). The bias is small compared to the precision of a typical likelihood curve when the inference is carried out in the presence of residual lensing and experimental noise (blue curve), and even smaller compared to the standard deviation on r expected after foreground-cleaning and delensing SO observations (grey interval). The histograms and curve are all normalized to have unit area.

$C_l^{BB,\mathrm{CIB,res}}$ are, respectively, the angular power spectra of lensing, instrument noise, residual dust and residual CIB B-modes. For economy of notation, we have denoted the convolution integral of equation (3.4) as the functional g_l, written the double integral as the functional h_l, and hidden the multipole-dependence of their arguments[4]. We have also assumed that E-mode instrument noise is negligible, but this can easily be accounted for by replacing the lensed E-modes in the final term on the right of equation (3.18) with their noisy counterparts. The inclusion of the dust and noise components along with the CIB in I^{tot} in this term is in order to take into account the decorrelation between CIB and lensing convergence that comes about as a consequence

[4]The last two terms in equation (3.18) are normally calculated to leading order in κ, which amounts to ignoring lensing in $\tilde{E}$ and replacing $\tilde{B}$ by the leading-order expression $\tilde{B} \sim E\phi$. We showed in chapter 2 that this is actually very accurate (with errors at the 1 % level of $\tilde{C}_l^{BB}$ in the case that $I^{\mathrm{tot}} = \phi$, and presumably even better for a partially-correlated tracer). However, the individual $O(\phi^4)$ contributions to the three- and four-point terms may be larger (at the 10 % level of $\tilde{C}_l^{BB}$), but they cancel rather precisely [18].

of their presence. The four-point function in equation (3.18) can be written in terms of its connected part (denoted $\langle\rangle_c$) and Gaussian contractions as

$$\begin{aligned}\langle\tilde{E}I^{\rm tot}\tilde{E}I^{\rm tot}\rangle &= \langle\tilde{E}I^{\rm tot}\tilde{E}I^{\rm tot}\rangle_c + \tilde{E}\overbrace{I^{\rm tot}\tilde{E}}I^{\rm tot} \\ &= \langle\tilde{E}I^{\rm CIB}\tilde{E}I^{\rm CIB}\rangle_c + \tilde{E}\overbrace{I^{\rm tot}\tilde{E}}I^{\rm tot}\,, \end{aligned} \tag{3.19}$$

where we have assumed that all fields are zero-mean. In the Gaussian contractions we have used the fact that the lensed E-modes are uncorrelated (although not independent) of $I^{\rm tot}$.

In reality, the residual amounts of Galactic dust and CIB emission contained in the data will have non-Gaussian statistics. Consequently, they can, in principle, contribute higher-point functions to the delensed spectrum not captured by equation (3.18). The possible additional terms — which we will be referring to as "biases" — are schematically described by

$$\begin{aligned}\mathcal{B}_l &\equiv \tilde{C}_l^{BB,\rm res} - C_l^{BB,\rm del,naive} \\ &= -2\,g_l\left[\langle B^{\rm dust}E^{\rm dust}I^{\rm dust}\rangle_c + \langle B^{\rm CIB}E^{\rm CIB}I^{\rm CIB}\rangle_c\right] \\ &\quad + h_l\left[\langle E^{\rm dust}I^{\rm dust}E^{\rm dust}I^{\rm dust}\rangle + E^{\rm dust}\overbrace{I^{\rm CIB}E^{\rm dust}}I^{\rm CIB} + E^{\rm dust}\overbrace{I^{\rm noise}E^{\rm dust}}I^{\rm noise}\right] \\ &\quad + h_l\left[\langle E^{\rm CIB}I^{\rm CIB}E^{\rm CIB}I^{\rm CIB}\rangle_c + E^{\rm CIB}\overbrace{I^{\rm tot}E^{\rm CIB}}I^{\rm tot}\right]. \end{aligned} \tag{3.20}$$

Here, we have ignored terms involving the two-point function $\langle E^{\rm CIB}I^{\rm CIB}\rangle$ since this vanishes if we assume, as we shall do, that the polarisation angles of CIB galaxies are uncorrelated (see section 3.5.2.2). Of the three terms with the Gaussian contractions shown explicitly, we shall only consider the first (i.e., that with $I^{\rm CIB}$ shown explicitly), since we can ignore instrument noise in the CIB measurement on the scales relevant for delensing and since CIB polarisation residuals are small relative to the polarised dust residuals [244]. This work estimates the remaining terms.

In section 3.5.2.1, we calculate the biases resulting from $g_l[\langle B^{\rm dust}E^{\rm dust}I^{\rm dust}\rangle_c]$, $h_l[\langle E^{\rm dust}I^{\rm dust}E^{\rm dust}I^{\rm dust}\rangle]$ and $h_l[\langle E^{\rm dust}I^{\rm CIB}E^{\rm dust}I^{\rm CIB}\rangle]$ using simulations. The dust simulations we work with are detailed in section 3.5.1.1, while those of the CIB are explained in section 3.5.1.2. At the time of writing there exist no simulations of the polarised component of the CIB, so an analytic treatment of $\langle B^{\rm CIB}E^{\rm CIB}I^{\rm CIB}\rangle_c$ and $\langle E^{\rm CIB}I^{\rm CIB}E^{\rm CIB}I^{\rm CIB}\rangle_c$ is required. This calculation is presented in section 3.5.2.2.

Symbol	Description	Value
$T_{\rm dust}$	Equilibrium temperature of the thermal dust SED [K]	19.6
$\beta_{\rm dust}$	Spectral index of the thermal dust emission	1.53

Table 3.1 Dust parameters used in this work, obtained from Ref. [364].

In addition to introducing a bias, the presence of residual foregrounds will increase the variance of the delensed power spectrum. Part of this additional variance will be associated with tracer fluctuations which can be described using Gaussian statistics; so when actually doing the analysis, this effect could be simply captured using simulations. However, there will be additional contributions to the variance coming from the non-Gaussian component of the foregrounds. When estimating the impact of CIB non-Gaussianities, progress can be made with existing simulations (see, e.g., [51]); but in the case of polarised Galactic dust, a number of non-Gaussian simulations far greater than the single realisation available at the time of writing would be required. On the other hand, an analytic treatment is likely to be exceedingly difficult given the acutely non-Gaussian distribution of the Galactic dust. Since bias is expected to be a more significant issue than the increase in variance, we defer the study of the latter to future work.

3.5.1 Methods

In this section we introduce much of the machinery used in section 3.5.2.1 to estimate, based on simulations, the delensing bias arising from residual Galactic dust.

3.5.1.1 Simulations of Galactic dust

Given the lack of small-scale polarisation data currently available, we rely on simulations to perform our analysis. In particular, we make use of a single, full-sky, non-Gaussian simulation of the Galactic dust component at 353 GHz produced by Ref. [491, hereafter VS]. We focus on this frequency for two reasons: first, it is the highest frequency for which there is polarisation data from Planck, which will enable the validation process described in section 3.5.3; and second, that, among the high-frequency Planck channels, the one at 353 GHz is where the CIB is brightest relative to Galactic dust (see, e.g., [283]), so that one might *a priori* expect CIB maps at this frequency to be particularly useful for delensing.

The phenomenological model underlying this simulation is an extension of that in Ref. [364], which models the local Galactic magnetic field (GMF) by stacking an ordered

component together with several layers containing Gaussian random realisations of turbulence drawn from a power-law angular power spectrum. The free parameters of the model are determined by fitting the model spectra to the Planck data. VS then builds on this to allow for a level of TE correlation and E/B power asymmetry that matches the observations of Ref. [367]. We emphasise that the total intensity in this simulation is based on dust inferred from Planck observations, and so is representative of (and correlated with) our sky at the map level. In section 3.5.3, we will validate this simulation against Planck data, and also compare it to Gaussian simulations.

Assuming that emission from thermal dust is perfectly correlated across microwave frequencies, the dust intensity in the 145 GHz "science channel" (the one where the CMB is brightest relative to the foregrounds) can be obtained by extrapolating the 353 GHz simulated template down as

$$I_\nu^{\rm dust}(145\,{\rm GHz},\hat{\boldsymbol{n}}) = I_\nu^{\rm dust}(353\,{\rm GHz},\hat{\boldsymbol{n}})\left(\frac{145}{353}\right)^{\beta_{\rm dust}}\frac{B(145\,{\rm GHz},T_{\rm dust})}{B(353\,{\rm GHz},T_{\rm dust})}\,, \tag{3.21}$$

and similarly for Q and U. This scaling assumes that the dust spectral energy distribution (SED) is well modelled as a modified blackbody [478] with temperature $T_{\rm dust}$ and spectral index $\beta_{\rm dust}$ as determined by Ref. [367]. The values of $T_{\rm dust}$ and $\beta_{\rm dust}$ used are detailed in Table 3.1. The Planck function is $B(\nu,T)$. To convert this specific intensity to the corresponding differential CMB temperature at 145 GHz, we apply a multiplicative unit conversion factor appropriate for infinitesimally-narrow frequency bands; this can be calculated using, for example, equation (8) of Ref. [353].

Our approach ignores spatial variations in the dust temperature and spectral index that are known to be present in the data [367]. While important for component separation efforts, we expect this choice to have only a small impact on our analysis given that contributions from regions where extrapolation over-estimates the true level of dust emission should, statistically-speaking, balance out those from regions where emission is under-estimated. In addition to this, we also expect some further decorrelation in polarised dust emission across frequencies for any line of sight that passes through more than one dust cloud. The reason, explained by Ref. [474], is that, in that direction, the total Q and U Stokes parameters arise as a sum of contributions with different polarisation orientations (to the extent that the GMF direction threading the clouds changes along the line of sight) and whose relative strengths vary with frequency if the temperature of the clouds differs (because then their emission would follow different SEDs). However, Ref. [375] have shown that this effect contributes only a small amount to the current extrapolation error budget for Planck data, and

indeed Ref. [367] find no evidence of decorrelation between 150 GHz and 353 GHz at the high Galactic latitudes that we will be restricting our analysis to.

3.5.1.2 Simulations of the CIB

The subset of bias terms described in section 3.5 associated with CIB emission can, in principle, be computed using simulations. However, among these terms are $\langle B^{\rm CIB}E^{\rm CIB}I^{\rm CIB}\rangle_c$ and $\langle E^{\rm CIB}I^{\rm CIB}E^{\rm CIB}I^{\rm CIB}\rangle_c$, and estimating these would require non-Gaussian simulations of the CIB polarisation, which, unfortunately, are not available at the time of writing. We therefore study them analytically in section 3.5.2.2. The remaining CIB-related bias terms can be computed using Gaussian simulations. In this section, we explain how those simulations can be generated. For the sake of wider applicability, our method allows for the resulting CIB realisations to be appropriately correlated with an underlying realisation of the lensing convergence. However, we note that having the CIB correlate with κ is not strictly necessary when calculating the subset of bias terms we are after.

Generating correlated Gaussian simulations is straightforward if all the relevant auto- and cross-spectra are known. Suppose κ_{lm} are the spherical harmonic coefficients of a particular realisation of the lensing convergence. We seek to simulate I_{lm}, the coefficients of a simulation of the CIB. (We drop the superscript CIB here to avoid cluttering the notation.) Given that the two are correlated, we can say that, in general,

$$I_{lm} = A_l^{I\kappa}\kappa_{lm} + u_{lm}, \tag{3.22}$$

where u_{lm} are the harmonic coefficients of the uncorrelated part and $A_l^{I\kappa}$ is a function to be solved for. By requiring the correct auto and cross-spectra, we see that

$$A_l^{I\kappa} = \frac{C_l^{I\kappa}}{C_l^{\kappa\kappa}}, \tag{3.23}$$

and the power spectrum of the uncorrelated part is

$$C_l^{uu} = C_l^{II} - (A_l^{I\kappa})^2 C_l^{\kappa\kappa}. \tag{3.24}$$

We calculate $C_l^{\kappa\kappa}$ for the parameters of the best-fit ΛCDM cosmology of Ref. [366]. On the other hand, C_l^{II} and $C_l^{I\kappa}$ are obtained following Ref. [517]. Briefly, $C_l^{I\kappa}$ is based on fitting the single-SED CIB model of Ref. [161] to the cross-spectrum of the GNILC CIB map (at 353 GHz) and the internal reconstruction of κ from Ref. [359]. The same CIB model, plus a shot noise and power-law Galactic dust contribution, is then used

to fit the auto-spectrum of the GNILC map. We construct C_l^{II} as the sum of the modelled (clustered) CIB spectrum and shot noise.[5]

Finally, we can generate I_{lm} as described in equation (3.22) by drawing the harmonic coefficients u_{lm} from a Gaussian probability distribution with mean zero and variance given by C_l^{uu}, and adding them to a filtered version of the convergence, $A_l^{I\kappa}\kappa_{lm}$.

In appendix B.6, we generalise this approach to an arbitrary number of tracers and make the implementation publicly available[6]. Along with the weighting scheme of equation (3.8) – also implemented – this framework can be used to simulate multi-tracer estimates of the lensing potential with which to test delensing procedures.

3.5.1.3 Estimating dust residuals in the data

In addition to simulating the raw Galactic dust and CIB emission, we must also determine what fraction of that original radiation is left in the CMB maps after foreground cleaning, as well as how much residual dust is present in the CIB maps used as the matter tracers for delensing. In general, these residuals will be a function of angular scale and of telescope type.

In order to identify what residual dust fraction to expect for the CIB maps, we first investigate the GNILC maps. Their construction from the multi-frequency Planck maps is described in detail in Ref. [365]; see also Ref. [395]. For our purposes, the key points are as follows: first, at each frequency, an estimate of the dust component, $m_{\rm dust}$, is extracted by filtering out the CIB, CMB and instrumental noise components; then, another map, $m_{\rm dust+CIB}$, is obtained by removing only the CMB and the noise (this is done by withdrawing the prior on the CIB angular power spectrum from the procedure for obtaining $m_{\rm dust}$). The CIB maps at each frequency are then obtained by subtracting $m_{\rm dust}$ from $m_{\rm dust+CIB}$. Given that the extent of confusion between dust and noise or CMB emission ought to be relatively small, it follows that any dust that $m_{\rm dust}$ fails to capture will make it into $m_{\rm dust+CIB}$, and will therefore appear as a dust residual in the CIB map. If we assume that the multipoles of $m_{\rm dust}$ extracted over the region of interest contain a fraction α_l of the true dust multipoles for that region, while $m_{\rm dust+CIB}$ accurately captures the sum of the dust and CIB, the residual dust in the estimated CIB multipoles will be $1-\alpha_l$ of the raw dust level. We estimate α_l, and hence the fractional dust residual at a given frequency, multipole and sky region, from the cross-correlation, on the patch of choice, between GNILC maps obtained by applying the GNILC algorithm to simulations containing all sky components (specifically, the

[5] All spectra were kindly provided by Byeonghee Yu.

[6] `https://github.com/abaleato/MultitracerSims4Delensing`

FFP8 Planck simulations described in Ref. [358]; the results were kindly provided by Mathieu Remazeilles) and the input dust in these simulations. The resulting estimate for the multipole-dependent, fractional residual at 353 GHz is shown in figure 3.5. We note that the GNILC algorithm is optimised for dust reconstruction, so other methods designed to prioritise the extraction of the CIB might display higher levels of residual dust. We also point out that the GNILC algorithm tends to suppress the true CIB due to residual CIB in $m_{\rm dust}$, which is subtracted from $m_{\rm dust+CIB}$. There is evidence of this in the cross-correlation of the GNILC CIB maps with κ from Planck, as discussed in the appendix of Ref. [286]. However, for the purposes of delensing, provided that correlation coefficients are obtained empirically any suppression of the CIB will not lead to bias but only a reduction in the delensing efficiency.

Another means of mapping dust in our galaxy is via its correlation with the 21 cm emission from the hyperfine transition of neutral hydrogen. This technique was first exploited by Ref. [351] to disentangle Galactic dust from extragalactic CIB emission. Subsequently, Ref. [250] extended the method to larger regions of the sky, and it is those maps that we consider here. In order to estimate the magnitude of dust residuals in them, we focus on the strong correlation observed between higher H I column densities ($N_{\rm H\,I}$) – or, equivalently, larger sky areas – and higher dust residuals. This is the reason why angular power spectra of maps obtained using different column density thresholds converge only for the lowest few values of $N_{\rm H\,I}$, and grow significantly in amplitude for higher ones (see figure 15 of Ref. [250]). If we assume that all that additional auto-power is due to dust contamination, we can make a rough estimate of the residual dust power present in any given CIB map by comparing its power spectrum to that of the map with the lowest column density ($N_{\rm H\,I} = 1.5 \times 10^{20}\,{\rm cm}^{-2}$), and assuming that the latter is free of dust. In order to avoid noise biases, auto-spectra are measured by taking the cross-correlation of maps derived from Planck observations with independent instrumental noise (the half-ring maps), masked with the appropriate apodised windows provided. As the maps from Ref. [250] are provided in intensity units, the resulting absolute residual spectra are converted to temperature units by multiplying by a wide-band unit conversion factor[7] twice and subsequently compared to the raw power of the VS dust simulation at 353 GHz. The fractional residual shown in figure 3.5 is the ratio between these two. Away from the small scales where it increases due to the limited resolution of the H I maps, the residual dust power is approximately

[7]This multiplicative unit correction differs slightly from the one we met in section 3.5.1.1 due to the fact that it takes into account the finite width of the Planck bandpasses – see Ref. [353] for an explanation, and Ref. [367] for values appropriate for the 2018 polarisation data we use.

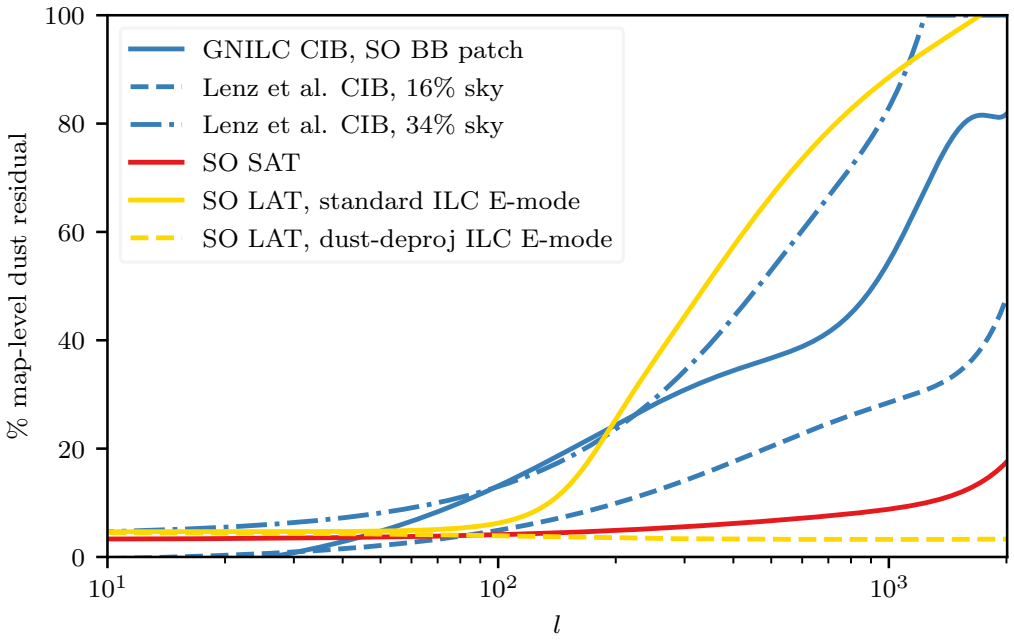

Fig. 3.5 Estimated map-level percentage of residual dust emission after foreground cleaning relative to the unmitigated dust emission in either the 145 GHz channel of the SO LAT (yellow), the 145 GHz channel of the SO SAT (red) or different CIB maps at 353 GHz (blue) — the latter in intensity, the former two in polarisation. These fits to CIB residuals are not to be trusted below $l < 100$; however, this is irrelevant in practical applications, since internal techniques dominate the reconstruction on those scales (see, e.g., Ref. [313]). For the SO, we plot residuals corresponding to the *goal* noise levels. The SO LAT residuals are estimated using a global ILC method and thus represent the fraction by which to scale the unmitigated emission anywhere on the sky. On the other hand, the residuals quoted for the CIB maps are appropriate to the specific regions of the sky on which they are estimated.

scale-independent. On the other hand, the raw dust power is very red, hence the shape of the residual fraction curve shown.

We now consider the removal of dust from small-scale polarisation observations of a survey with the characteristics of the Simons Observatory's (SO) large-aperture telescope survey (LAT; [441]) by means of an internal linear combination of channels (ILC) in harmonic space (see, e.g., Ref. [475]). Though, a priori, one might think this easier than temperature cleaning, owing to the fact that in polarisation there are only two contaminants to the signal of interest (dust and synchrotron), the situation is complicated by the fact that LAT polarisation noise levels are higher than dust emission for all but the largest angular scales [441]. Consequently, in a standard implementation of the ILC method, the most effective way to minimise the variance of the cleaned map while leaving the CMB signal unchanged will be to suppress the noise, with little being done to remove dust. Quantitatively, the fraction, R_l, of the original Galactic dust emission in the 145 GHz channel of SO that remains in the ILC-cleaned map at multipole l is

$$R_l = \sum_\nu w_l(\nu) I^{\rm dust}(\nu)/I^{\rm dust}(145\,{\rm GHz}), \tag{3.25}$$

where $w_l(\nu)$ are the ILC weights[8], $I^{\rm dust}(\nu)$ is the dust SED assumed in the simulations in differential CMB temperature units (such that $\sum_\nu w_l(\nu) = 1$) and the sum is over all 13 of the Planck and SO frequency channels expected to be used for component separation. The unit conversions at all these frequencies are calculated under the assumption of infinitely-narrow passbands. Finally, the residual level of dust after ILC-cleaning (with noise levels corresponding to the SO's *goal*) is shown in figure 3.5.

The LAT E-mode foreground residuals can be further suppressed by "deprojecting" the dust contribution – that is, requiring that the cleaned map have zero response to the SED of the dust component [394]. Though in principle one might expect this method to completely neutralise dust residuals, in practice the removal will not be complete due to differences between the dust model used to compute the ILC weights and the true dust SED (arising, for instance, from spatial variation of the dust spectral index). Our calculated dust-deprojected residual, shown in figure 3.5, illustrates this, as it arises from differences in the dust model used to generate the ILC weights and that which we use to extrapolate the dust template from 353 GHz to other frequencies. This estimate is likely to be rather optimistic given that it appears to be comparable (when measured as a fraction of the unmitigated emission) to that obtained in a parametric foreground cleaning of the SAT – as we shall soon discuss, this is expected to be more

[8]Based on the ILC weights provided by the authors of Ref. [441].

extensive since it allows for a degree of variation of foreground parameters across the sky. However, our estimates will suffice given the number of other approximations we are making. As we will see in section 3.5.2.1, deprojecting the dust can help mitigate the magnitude of delensing biases. However, doing so comes at the cost of increased variance in the maps, which in turn brings about a degradation of delensing efficiency. In order to estimate the extent of the degradation, we use equation (3.10) to forecast the residual lensing B-mode power after delensing with the GNILC CIB maps and E-mode observations after the latter are Wiener-filtered to reflect the polarisation noise level after ILC cleaning. Our forecasts, shown in figure 3.6, predict a small degradation, no greater than one percent, between the dust-deprojected and standard cleaning scenarios. When deciding whether or not to use dust-deprojected maps for delensing, the goal must be to maximise delensing efficiency while keeping the emerging delensing bias to acceptable levels. The newly developed partially-constrained ILC method of Ref. [469] might be particularly useful in this context, allowing optimisation of the tradeoff between post-cleaning noise (and associated delensing efficiency) and bias on r.

Finaly, the cleaning procedure ought to be more extensive (fractionally speaking) for a small-aperture telescope – such as the the SO's SAT – measuring CMB polarisation on large angular scales. It is on those large scales that polarised foregrounds peak and are brighter than the experimental noise (assuming that systematics are under tight enough control that leakage of atmospheric emission into polarisation is small). Hence, they will be preferentially removed in foreground-cleaning procedures. Furthermore, given the importance of mitigating the foreground variance on large angular scales to faciliate searches for primordial B-modes, map-based component separation techniques have been developed that allow for variation of the foreground modelling parameters across the sky (see, e.g., Ref. [466] or Ref. [9] and references therein). This flexibility results in improved cleaning: by simulating the entire foreground-cleaning operation for the SAT, [441] forecast a map-level dust residual of around 10 %, shown also in figure 3.5.

We fit smooth functions to all of these map-level dust residual fractions as a function of multipole and use them to filter the simulated, raw dust maps of section 3.5.1.1. The end result is maps of the expected residual dust in each of the E, B and I fields involved in the delensing analysis.

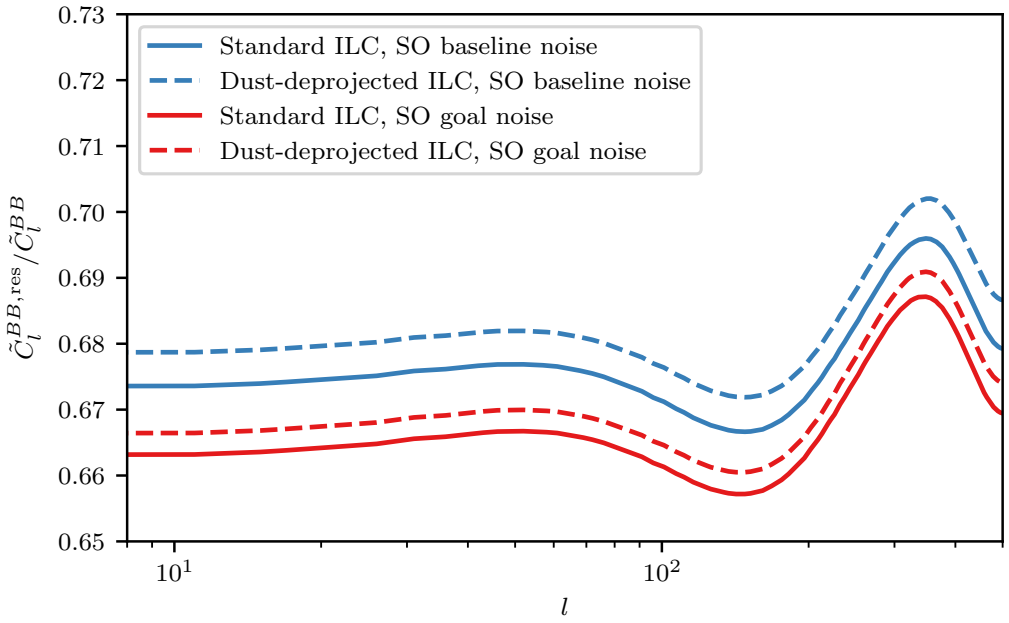

Fig. 3.6 Residual lensing B-mode power after delensing with the GNILC CIB map and E-mode observations from the SO'S LAT. In either the baseline or goal scenarios, there is a small degradation in delensing efficiency relative to the standard cleaning procedure when the dust component is nulled during foreground cleaning. This theoretical estimate is obtained from the leading-order approximation of equation (3.10).

3.5.1.4 Masking

When calculating the delensing biases of section 3.5 from simulations, we must adopt masks that mimic the procedures that would be followed and sky areas that would be covered in actual analyses.

In order to reduce the extent of mode coupling induced by masking and facilitate the deconvolution of mode-coupling matrices for power spectrum estimation, all masks are apodised. We obtain Galactic masks apodised with 2° Gaussian kernels from the Planck Legacy Archive. On the other hand, the mask to be used for large-scale B-mode searches was kindly provided to us (in binary form) by the authors of Ref. [441]. Apodisation of this mask is carried out using procedures built into the publicly-available code `NaMaster` [10], which ensures that regions originally excluded in the binary mask remain so after apodisation. Given that this mask has a relatively small footprint on the sky, we choose a FWHM of 1° for the Gaussian smoothing kernel. The final mask is shown in figure 3.7a. Henceforth, we refer to it as the "SAT mask". This will be the mask used to delineate the patch covered by a ground-based, small-aperture telescope going after large-angular-scale B-modes. We shall also consider the case of a space-based experiment targeting B-mode science, in the style of the upcoming LiteBird satellite [266]. The sky patch covered by such an experiment is approximated by the 60 % sky Galactic mask from Planck shown in figure 3.7c. We will sometimes refer to this as the "LB patch".

Though we expect the lensing B-mode template to be quite local – owing to the fact that it is the product of predominantly intermediate and small-scale E-modes and lenses that give rise to lensed B-modes — we saw in section 3.5 that the delensing bias is sensitive to certain bispectra and trispectra. Since these scale as the third and fourth power of pixel values, they are very sensitive to bright structures in the dust residuals lying outside the footprint that we ultimately make B-mode measurements on. This is indeed what we see, already at the level of the template, when bright regions near the Galactic plane are left unmasked in the E and I fields from which these templates are constructed. Figure 3.8 shows several such templates for which input fields were first masked using Galactic masks of different extents before applying the Wiener filters in equation (3.6). Bright artifacts outside the masked regions are readily apparent in those involving the largest unmasked fractions. Furthermore, these issues translate to increased power and scatter on the largest scales of the resulting templates, as shown by figure 3.9.

These phenomena have the potential to hinder efforts to delens by accentuating the biases described in section 3.5 and therefore should be mitigated by masking the

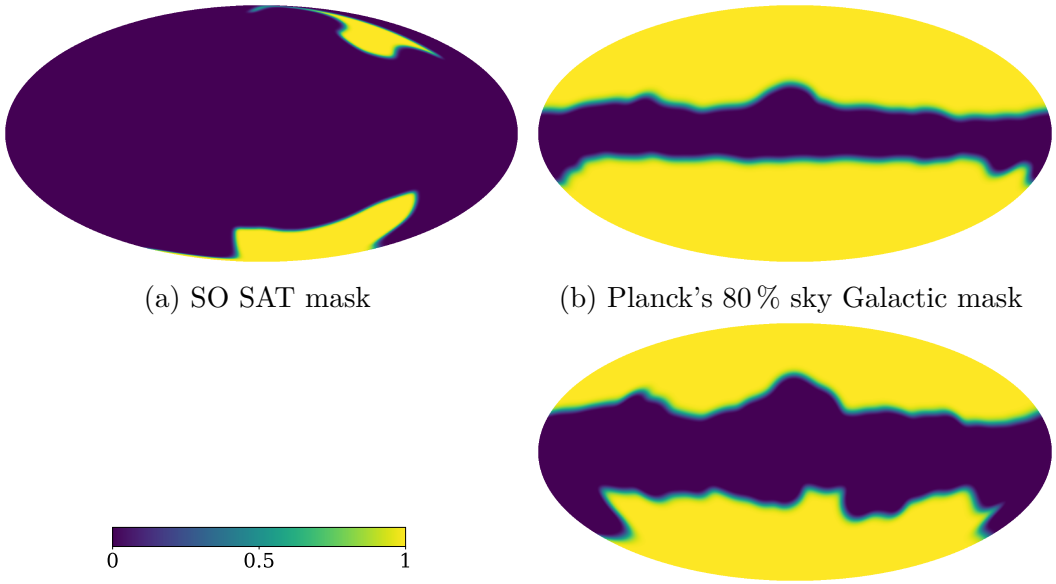

(a) SO SAT mask

(b) Planck's 80 % sky Galactic mask

(c) Planck's 60 % sky Galactic mask ("LB mask")

Fig. 3.7 Masks used in our analysis. They have been apodised using Gaussian kernels with a FWHM of 1° in the case of (a) and 2° in the case of (b) and (c).

Galactic region when constructing templates from wide-area data. We settle on the Planck mask that leaves 80 % of the sky available – shown in figure 3.7b – as the option that minimises the masked fraction (to reduce mode-coupling effects in the construction of the Wiener-filtered fields) while keeping artifacts in the low-l modes of the templates to acceptable levels. This scheme for masking fields going into templates will be implicit in all results quoted in the remainder of this work. Of course, similar masking arrangements are inevitable in practical applications (at least from the ground) due to the telescopes' limited sky coverage. Even for space-based experiments, it will be important to mask away the galaxy – and bright sources – before constructing lensing templates.

To check that the power spectrum amplitudes we are seeing in figure 3.9 are physical in origin, we also show in the figure the results for a statistically-isotropic, Gaussian simulation. In this case, the I and E residual dust fields are simulated on the full sky from power spectra forced to match those of the VS simulation measured over the SO SAT patch. The full-sky Gaussian fields are masked with the 80 % sky mask prior to Wiener filtering in the construction of the lensing template. We verify that the amplitude resulting from the Gaussian simulation is consistent with an analytic calculation in the style of the leading-order lensing B-mode power spectrum where

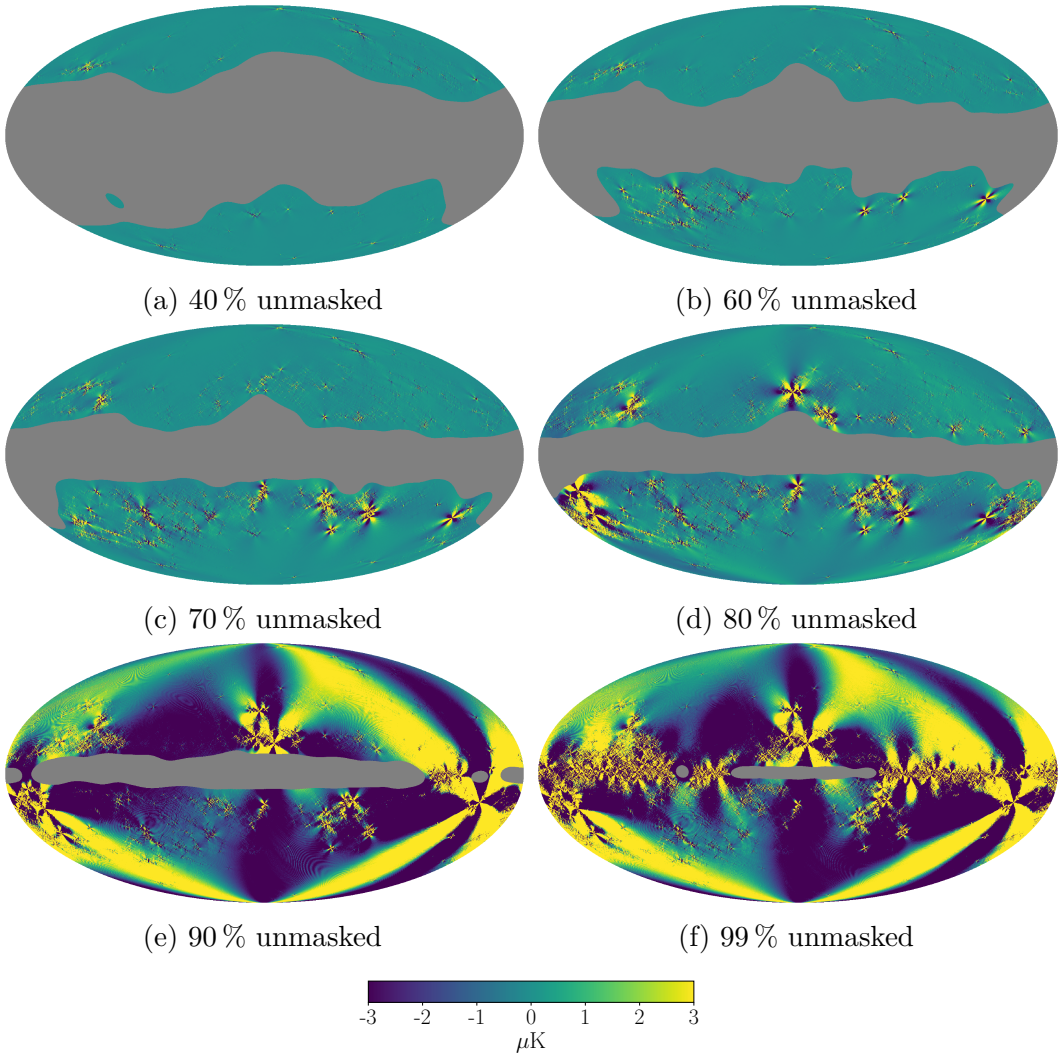

(a) 40 % unmasked (b) 60 % unmasked

(c) 70 % unmasked (d) 80 % unmasked

(e) 90 % unmasked (f) 99 % unmasked

Fig. 3.8 Stokes Q parameter associated with B-mode templates generated from residual dust intensity and E-modes (as determined in section 3.5.1.3), for different extents of Galactic masking applied to the input fields prior to Wiener filtering. Here, X % unmasked is to be interpreted as meaning that X % of the sky is left unmasked in each of the two fields, E and I, from which the template is built (the masked region is shown in grey). The input dust E-modes are scaled to the residual level expected for standard ILC cleaning of the LAT in the *goal* scenario, while dust total-intensity is scaled to levels appropriate for the residuals in the GNILC CIB maps over the SO SAT patch. Intensity modes below $l_{\rm min} = 100$ are removed in all cases.

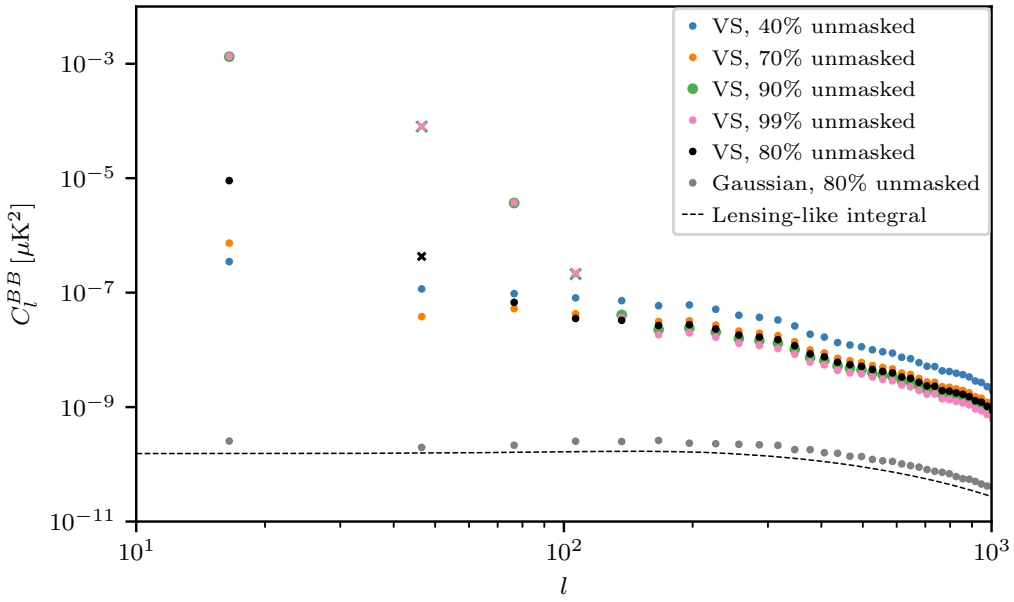

Fig. 3.9 Power spectra, measured on the SO SAT patch of figure 3.7a, of the dust-only B-mode templates shown in figure 3.8. We emphasise the comparison between the VS dust simulation and a Gaussian simulation (whose amplitudes in intensity and polarisation are made to match the power of the VS simulation measured on the SO SAT patch), after both are masked with the same 80 % sky mask of figure 3.7b prior to Wiener filtering in the construction of the lensing template. We verify that the power in the Gaussian case is consistent with that expected from a leading-order lensing-like calculation based on the E and I dust spectra measured from the masked maps. On the other hand, the VS simulation displays more power, likely due to the relevance of the Galactic dust trispectrum. We also note the approximate convergence of template power between different masking fractions on intermediate and small scales. Power spectra, with the effect of the SO SAT mask deconvolved, are extracted with the code `NaMaster`, using bins with $\Delta l = 30$. On large scales, the mask deconvolution sometimes gives rise to negative bandpowers, which we plot as crosses of the appropriate colour. This is particularly the case for those Galactic masks retaining large sky fractions, and is likely due to interactions between the extreme bright features in the templates in these cases and deconvolution of the mask.

C_l^{EE} and $C_l^{\kappa\kappa}$ are replaced with the dust spectra measured from the simulation. The amplitude in this Gaussian limit is significantly lower than that arising from the VS simulations. This is likely due to the power in the non-Gaussian VS simulations being boosted by the $\langle EIEI \rangle_c$ trispectrum of Galactic dust, though, in principle, statistical anisotropy could also be contributing to the difference seen between the VS simulation and the statistically-isotropic Gaussian simulations.

3.5.1.5 Summary of simulation-based procedure for estimating delensing biases

We summarise here the procedure used to calculate the delensing biases of section 3.5 from simulations. The steps are as follows:

1. Load in full-sky I, Q and U simulated dust maps at 353 GHz. Take them to harmonic space to produce $I^{\rm dust}$, $E^{\rm dust}$ and $B^{\rm dust}$.
2. Scale $E^{\rm dust}$ and $B^{\rm dust}$ to 145 GHz as described in section 3.5.1.1.
3. Apply the dust residual transfer functions measured in section 3.5.1.3 to each of $I^{\rm dust}$, $E^{\rm dust}$ and $B^{\rm dust}$.
4. Simulate a CIB map, $I^{\rm CIB}$, in harmonic space using the method of section 3.5.1.2.
5. Take $I^{\rm dust}$, $E^{\rm dust}$, $B^{\rm dust}$ and $I^{\rm CIB}$ to configuration space.
6. Apply the apodised 80 % sky mask of figure 3.7b to all of the maps.
7. Take maps back to harmonic space.
8. Wiener filter $I^{\rm CIB}$ and $I^{\rm dust}$ according to equation (3.6), with the total power spectrum in the denominator appropriate to the appropriate residual dust level under study. Mask modes below the $l_{\rm min}$ cutoff of choice.
9. Using the methods described in appendix B.7.1[9], build template B-modes of the form $\hat{B}\left(E^{\rm dust}, I^{\rm dust}\right)$ and $\hat{B}\left(E^{\rm dust}, I^{\rm CIB}\right)$.
10. Convert these templates, as well as $B^{\rm dust}$ from step 7, to Q and U maps.
11. Apply the apodised SO SAT mask of figure 3.7a to these Q and U maps.

[9]These tools are packaged and made publicly-available under `https://github.com/abaleato/curved_sky_B_template`

12. Use the pseudo-C_l code `NaMaster` [10] to measure the correlations of interest (described in section 3.5) and deconvolve the mode couplings induced by the mask.

13. Fit a power-law to the bandpowers in the range $200 < l < 600$.

Note that, in step 6, we use a Galactic mask from Planck rather than that from the SO LAT. There are two reasons for this: firstly, this mask is less restrictive and hence leads to less E-to-B leakage in polarisation [255, 69]; and secondly, due to the local nature of the templates (see figure 3.8) it should be possible to recover similar results if we were to restrict analysis to the LAT patch. In contrast, in step 12, the SAT mask is used, which restricts analysis to a much smaller patch than that in step 6. However, there is no risk of E-to-B leakage here since the polarisation maps do not contain E-modes by construction. For this reason, we do not bother to use the pure-B-mode formalism [443] when computing power spectra over the SO SAT patch.

As a means of cross-validating our pipeline, we apply the same filtering and masking scheme to lensed simulations of CMB E-modes and combine these with $I^{\rm CIB}$ to build a lensing template. We verify that, when this template is used to delens B-modes, the theoretically-expected level of power (as determined by equation 3.10) is obtained.

Except where noted otherwise, we restrict the fields we work with to multipoles $8 < l < 2008$. This is the Planck GNILC bandwidth and, approximately, includes the full range of scales relevant for delensing the large-scale B-mode polarisation.

3.5.2 Results

3.5.2.1 Bias from residual Galactic dust

With the tools developed in the previous sections, we are now in a position to estimate the delensing bias arising from residual Galactic dust left over in the CMB and CIB maps involved in the delensing analysis. By applying the procedures of section 3.5.1.5 to dust simulations from VS, we shall see that there is indeed a bias dominated by the BEI bispectrum of Galactic dust, that it is negative, and that it has a very red power spectrum, peaking on the largest angular scales.

In figure 3.10, we show this power spectrum bias for several assumptions about the residual dust levels according to the type of CIB maps used, minimum-l-cuts applied to these, sky patch on which the B-mode measurement is carried out and whether or not dust is explicitly deprojected when ILC-cleaning the E-modes. We compare these biases to the power spectrum of residual lensing B-modes after delensing down

to 70% of the original lensing power — this is approximately the expected extent of delensing when using the GNILC CIB maps as the only tracer (c.f., figure 3.6). For reference, we show via shaded regions the Gaussian part of the standard deviation of delensed B-modes when observed on either $\sim 10\%$ or $\sim 60\%$ of the sky, representative of the SO B-mode survey patch or a larger patch observable from space, respectively. We model this delensed B-mode spectrum as comprising 70% of the original lensing power and a white noise component in polarisation similar to that of the SO SAT's 145 GHz channel in the *goal* specifications (a beam $\theta_{\rm FWHM}$=17 arcmin and a sensivity of $\Delta_{\rm P} = \sqrt{2} \times 2.1\,\mu$K arcmin; [441]).

The very 'red' spectral tilt displayed by the dust bias means that it will likely be smaller than the statistical uncertainty on the multipole range and sky regions probed by upcoming ground-based telescopes ($l \gtrsim 30$ and $f_{\rm sky} < 0.1$), as long as modes of the CIB mass-tracer maps are removed for $l \lesssim 100$. From the left panel of figure 3.10, we see that this is true even in the case where dust is not deprojected as part of the foreground-cleaning procedure. However, one might want to be especially careful and work with dust-deprojected E-modes, as this is shown by the right panel of figure 3.10 to mitigate the bias very significantly, while only marginally degrading delensing performance (at least for SO, see figure 3.6).

On the other hand, the bias might pose challenges for space-based experiments (such as LiteBird) for two reasons: first, given their full-sky coverage and immunity to atmospheric noise, satellite missions will be able to probe polarisation down to the lowest multipoles, but it is on those largest scales that the bias is largest; and second, in observing a larger fraction of the sky, they encompass regions where the dust is brighter. These, compounded with the fact that larger sky coverage ($f_{\rm sky} \approx 0.6$) translates to lower statistical uncertainty, means that this bias could potentially confuse searches for primordial B-modes by space-based missions, unless their foreground cleaning capabilities are improved relative to SO. To illustrate this, we consider a scenario where the foreground cleaning is as for SO, but the analysis is performed on the larger 'LiteBird' patch. Figure 3.10 shows that the resulting bias is well in excess of the statistical errors, particularly when dust is not explicitly deprojected from the E-mode maps. The right panel of figure 3.10 shows that doing this deprojection is very effective at reducing the amplitude of the bias, but even then it is large enough to signficantly compromise contraints on r (as we will quantify shortly). Fortunately, space-based experiments targeting large-scale B-mode science will take advantage of their privileged vantage point above the atmosphere to observe in many more frequency channels channels than SO – LiteBird, for instance, is expected to have 15 frequency

bands [266]. Hence, foreground cleaning of, at least, the large-scale B-modes should be more extensive than what is assumed in the figure, which has dust residuals appropriate for SO. Since the bias is dominated by the BEI bispectrum of dust, its amplitude is very sensitive to improved cleaning of the CMB polarisation fields.

For a fixed level of foreground residuals, the bias can be mitigated by filtering out the largest scales of the CIB maps, which tend to be relatively more contaminated by dust (this is particularly acute for the GNILC products, as discussed in section 3.5.1.3). In all likelihood, upcoming implementations of CIB delensing will be complemented with internal reconstructions, which are able to reconstruct the largest-angular-scale lenses very accurately. Even if the largest scales are discarded altogether, the impact is expected to be small since it is scales smaller than that (chiefly $200 < l < 500$) that are most informative for delensing: for instance, Ref. [432] show that delensing efficiency only worsens by 12 % if the CIB fields are high-pass filtered with $l_{\rm min} = 150$ instead of $l_{\rm min} = 60$. Consequently, the recommendation we issue here of removing those largest scales from the CIB maps should come at very little cost in terms of delensing efficiency.

In figure 3.11, we quantify how the power spectrum biases of figure 3.10 propagate to biases on the inferred value of the tensor-to-scalar ratio, r. As we did in section 3.4, we use (e.g., Ref. [403])

$$\Delta\hat{r} = \left(\sum_{l=l_{\rm min}}^{l_{\rm max}} \left[C_l^{BB,\rm prim}(r=1) \right]^2 / \mathrm{Var}\left(\tilde{C}_l^{BB,\rm res} \right) \right)^{-1} \times \sum_{l=l_{\rm min}}^{l_{\rm max}} C_l^{BB,\rm unmodelled} C_l^{BB,\rm prim}(r=1) / \mathrm{Var}\left(\tilde{C}_l^{BB,\rm res} \right) \tag{3.26}$$

to translate an improper modelling of the B-mode power spectrum to a shift in r. Here, $C_l^{BB,\rm prim}(r=1)$ is the angular power spectrum of primordial B-modes with $r = 1$, $\mathrm{Var}(\tilde{C}_l^{BB,\rm res})$ is the variance of the power spectrum of delensed B-modes and $C_l^{BB,\rm unmodelled}$ is the part of the delensed B-mode spectrum that we have failed to model. We compute $\mathrm{Var}(\tilde{C}_l^{BB,\rm res})$ assuming the delensed B-modes to be Gaussian, and to feature only experimental noise (at a level appropriate for the SO SAT's 145 GHz *goal* specifications), primordial signal and 70 % of the original lensing power. For constraints on the SO SAT patch, we use $l_{\rm min} = 20$ and $l_{\rm max} = 200$, and for the larger 'LB' patch we set $l_{\rm min} = 2$ and $l_{\rm max} = 200$. We compare the estimated shifts to the standard deviation on inferences of r in the limit $r = 0$ expected of experiments covering either 10 % or 60 % of the sky, with the noise levels of the SO SAT, and in the limit of no

foreground BB power and residual lensing power of 70 % of the original. Figure 3.11 shows that the bias discussed here results in inferences of r that are systematically lower that the truth, although for ground-based experiments this is still within the bounds of statistical errors. This is in contrast with the impact of failing to model dust residuals on large angular scales of the B-mode power spectrum, in which case one tends to over-estimate the true value of r. As we show in the figure, failing to model dust B-mode residuals with a level of power as estimated in figure 3.5 for the SO SAT could result in a bias larger than those considered in this section, but in the opposite direction.

By combining the mitigation techniques described here, we ultimately expect the delensing bias from residual Galactic dust to be contained to levels where it does not compromise constraints on r, for virtually any application of CIB delensing. In particular, deprojection of dust from the E-modes proves to be particularly effective, while incurring only a small degradation in delensing efficiency, as shown in figure 3.6. However, this work highlights that, if we are to exploit the full power of the CIB for delensing, realistic simulations of Galactic dust, extending to small angular scales, ought to be developed so that they can be used to model and properly account for the expected amplitude and shape of the bias.

3.5.2.2 Intrinsic bias from non-Gaussianity of the CIB

Emission from UV-heated dust in star-forming galaxies – the diffuse component of which constitutes the CIB – is linearly polarised. This is thought to arise from the alignment of asymmetric dust grains in the inter-stellar medium of these galaxies with the local magnetic field direction. For observations along a particular line of sight, the stacking of emission from a large number of sources, each with incoherent, randomly-orientated polarisation directions, gives rise to depolarisation of the observed, integrated radiation. This depolarisation is practically complete for low-flux sources, of which there are very many. On the other hand, the number of bright sources is more modest, and their incomplete averaging gives rise to a net polarisation of the observed light. Experimental applications are able to mitigate this effect somewhat by removing the bright sources that they are able to resolve (e.g., Ref. [362]), but the contribution from those that are not resolved ought to be modelled.

We determined in section 3.5 that, if the CIB itself has non-vanishing $\langle BEI\rangle_c$ and $\langle EIEI\rangle_c$ correlations, the power spectrum of delensed B-modes will be biased by the

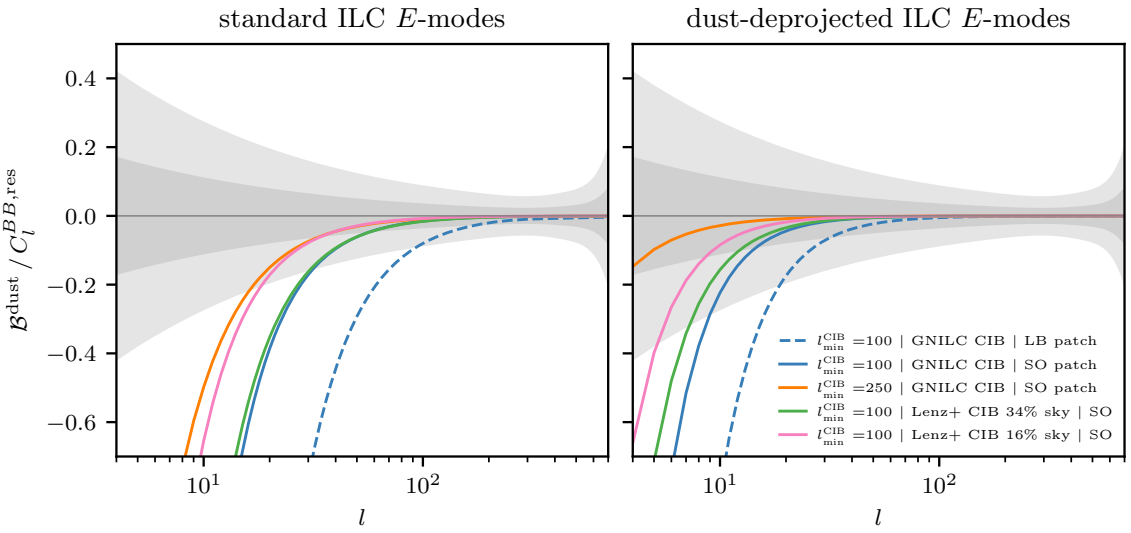

Fig. 3.10 Fractional bias on the angular power spectrum of residual lensing B-modes due to residual Galactic dust, plotted for several scenarios with differing residual dust levels. We model the residual lensing power as $C_l^{BB,\rm res} = 0.7\tilde{C}_l^{BB}$, as expected after delensing with the CIB as the only tracer. *Left panel:* E-mode residual for a standard ILC cleaning of SO's LAT (no dust deprojection and *goal* noise levels assumed). *Right panel:* E-mode residual as for SO's LAT (*goal* noise levels), with deprojection of dust in the ILC cleaning. Foreground cleaning of B-modes is everywhere as for the SO SAT. Dashed lines are for measurements on the large 'LB patch', while solid ones are on the smaller SO SAT patch. The shaded regions show the $\pm 1\,\sigma$ uncertainty on the power spectrum of delensed B-modes $\tilde{C}_l^{BB,\rm res} = 0.7\tilde{C}_l^{BB} + N_l^{BB}$, where N_l^{BB} is the (*goal*) noise power spectrum of the SO SAT. We calculate this uncertainty by assuming the delensed field is Gaussian, and that the experiment covers either 10 % (light grey) or 60 % of the sky (dark grey), and uses bins of $\Delta l = 30$. These biases are dominated by the BEI bispectrum of Galactic dust and are negative.

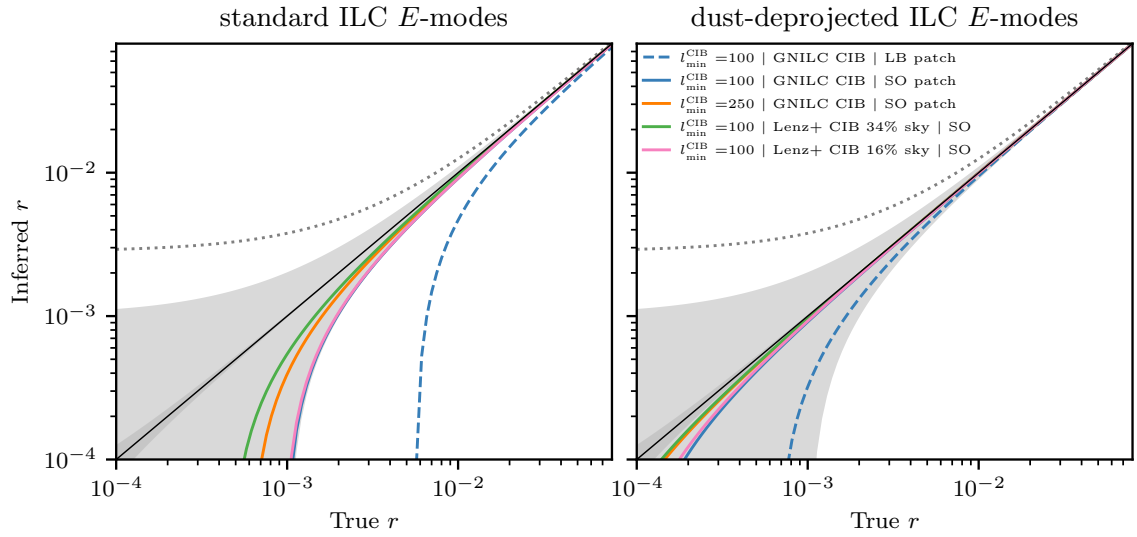

Fig. 3.11 Bias on the inferred tensor-to-scalar ratio due to unmodelled contributions from residual non-Gaussian Galactic dust to the power spectrum of B-modes delensed with the CIB. Dashed lines are for measurements on the 'LB patch' (approximately 60 % of the sky), and solid ones are on the smaller SO SAT patch (approximately 10 % of the sky). Foreground cleaning of B-modes is everywhere as for the SO SAT. Dust residuals in the E-modes are as for a harmonic ILC cleaning of the SO LAT at *goal* noise levels, either in a standard implementation (left panel) or after deprojection of Galactic dust (right panel). We constrain r using scales $l_{\rm min} = 20$ and $l_{\rm max} = 200$ or $l_{\rm min} = 2$ and $l_{\rm max} = 200$ when working with either the SO SAT patch or the 'LB' patch, respectively. For reference, the shaded regions show the approximate $\pm 1\,\sigma$ uncertainty for $r = 0$ of experiments covering either 10 % (light grey) or 60 % (dark grey) of the sky with the noise level of the SO SAT, no foregrounds, delensing down to 70 % of the original lensing BB power and when r is constrained over the multipole ranges described above for each of the sky fractions. For comparison also, the dotted lines show the size of the bias on r if residual dust B-modes in the SO SAT maps are as in figure 3.5 and are not modelled in the BB power spectrum.

following two terms:

$$\mathcal{B}_l^{BEI} = \frac{4}{(2\pi)^2}\int \frac{d^2\boldsymbol{l}'}{(2\pi)^2}\frac{\boldsymbol{l}'\cdot(\boldsymbol{l}-\boldsymbol{l}')}{|\boldsymbol{l}-\boldsymbol{l}'|^2}\mathcal{W}^E_{l'}\mathcal{W}^I_{|\boldsymbol{l}-\boldsymbol{l}'|}\sin 2(\psi_{\boldsymbol{l}'}-\psi_{\boldsymbol{l}})\langle B(-\boldsymbol{l})E(\boldsymbol{l}')I(\boldsymbol{l}-\boldsymbol{l}')\rangle'; \tag{3.27}$$

and

$$\begin{aligned}\mathcal{B}_l^{EIEI} = -\frac{4}{(2\pi)^2}\int \frac{d^2\boldsymbol{l}'d^2\boldsymbol{l}''}{(2\pi)^4}\frac{\boldsymbol{l}'\cdot(\boldsymbol{l}-\boldsymbol{l}')}{|\boldsymbol{l}-\boldsymbol{l}'|^2}\frac{\boldsymbol{l}''\cdot(\boldsymbol{l}+\boldsymbol{l}'')}{|\boldsymbol{l}+\boldsymbol{l}''|^2}\mathcal{W}^E_{l'}\mathcal{W}^E_{l''}\mathcal{W}^I_{|\boldsymbol{l}-\boldsymbol{l}'|}\mathcal{W}^I_{|\boldsymbol{l}+\boldsymbol{l}''|}\\ \times\sin 2(\psi_{\boldsymbol{l}'}-\psi_{\boldsymbol{l}})\sin 2(\psi_{\boldsymbol{l}''}-\psi_{\boldsymbol{l}})\,\langle E(\boldsymbol{l}')I(\boldsymbol{l}-\boldsymbol{l}')E(\boldsymbol{l}'')I(-\boldsymbol{l}-\boldsymbol{l}'')\rangle'_c\,,\end{aligned} \tag{3.28}$$

where the primes on the expectation values denote that the delta-function has been dropped.

In order to obtain an analytic understanding of these biases and be able to calculate higher-point functions of the CIB, we introduce a minimal model where the source polarisation fraction is constant and the polarisation angles of sources are uncorrelated. A detailed derivation of the BEI bispectrum of the CIB in this limit is provided in appendix B.1. Following equation (B.13), we learn that this sources a bias given in CMB temperature units by

$$\begin{aligned}\mathcal{B}_l^{BEI} = 2p^2\int \frac{d^2\boldsymbol{l}'}{(2\pi)^2}\frac{\boldsymbol{l}'\cdot(\boldsymbol{l}-\boldsymbol{l}')}{|\boldsymbol{l}-\boldsymbol{l}'|^2}\mathcal{W}^E(\boldsymbol{l}')\mathcal{W}^I(|\boldsymbol{l}-\boldsymbol{l}'|)\sin^2 2(\psi_{\boldsymbol{l}'}-\psi_{\boldsymbol{l}})\\ \times\int dz\left(\frac{I^{\rm CIB}[145(1+z)\,{\rm GHz}]}{I^{\rm CIB}[353(1+z)\,{\rm GHz}]}\right)^2 G_{353\,{\rm GHz}}G^2_{145\,{\rm GHz}}\\ \times\left[S^{(3)}_{353\,{\rm GHz}}(z)+\frac{H(z)}{cr^2(z)}S^{(2)}_{353\,{\rm GHz}}(z)S^{(1)}_{353\,{\rm GHz}}(z)P_g\left(|\boldsymbol{l}-\boldsymbol{l}'|/r(z);z\right)\right],\end{aligned} \tag{3.29}$$

where $r(z)$ is the comoving distance to redshift z, $I^{\rm CIB}(\nu)$ is the CIB SED at frequency ν, G_ν is a conversion factor[10] to go from specific intensity to differential CMB temperature units at frequency ν, p is the polarisation fraction of CIB galaxies, which we assume to have a constant value of 5 %[11], and $P_g(k;z)$ is the galaxy power spectrum. We have

[10] For narrow frequency bands, this can be calculated using, for example, equation (8) of Ref. [353].

[11] This value is more conservative than what has recently been discussed in the literature: Ref. [244], for example, suggest a smaller $p\approx 1\,\%$. The rationale behind such low figures is that the complex arrangement of magnetic field lines in dusty, star-forming galaxies is expected to bring about extensive depolarisation when integrated over the whole galaxy.

also defined

$$S_\nu^{(n)}(z) \equiv \int_{s_{\min}}^{s_{\max}} dS_\nu S_\nu^n \frac{dN}{dS_\nu dz d\Omega}, \tag{3.30}$$

that is, an integral over the nth power of source flux density, S_ν, weighted by $dN/dS_\nu dz d\Omega$ – the number of sources per steradian, at a given redshift in a certain flux-density range $[s_{\min}, s_{\max}]$ at frequency ν. These number counts can be obtained by fitting a model to sub-mm data. In this work, we use those of Ref. [43].

Since we have assumed that the polarisation angles of different galaxies are uncorrelated, the two polarisation legs of the bispectrum must be sourced by the same galaxy, so there can be no 3-source contribution. Hence, both terms in equation (3.29) can be interpreted as shot-noise contributions where the same galaxy appears in more than one leg – the first term comes from a single galaxy and the second, from two. If a mechanism exists for aligning galaxy spins (and, hence, polarisations) in the filamentary cosmic web (see, e.g., Ref. [350] and Ref. [91]), then there can, in principle, also be a 3-source contribution dependent on the 3D galaxy bispectrum. However, such a mechanism has been shown by Ref. [140] to produce contributions to the CIB power spectrum that are several orders of magnitude smaller than the shot noise, so we will be ignoring it henceforth.

In order to evaluate equation (3.29), we need to compute the power spectrum of the galaxies comprising the CIB emission. Galaxies are known to be biased tracers of the matter distribution [216], so additional prescriptions are needed to relate their clustering statistics to those of the matter. This could be done, for instance, by applying the tools of the halo model to the CIB, as was done by Ref. [242]. However, given the number of approximations we have already made, we pursue a cruder approach and relate the power spectrum of galaxy fluctuations to that of the matter by means of an effective galaxy bias $b_g(k, z)$, relating the over-densities of galaxy number density and matter as $\delta_g(k, z) = b_g(k, z)\delta_m(k, z)$. We use the value measured by Ref. [357], which assumes that the galaxy bias is scale-independent. If, as evidence suggests, galaxy formation is chiefly a local process, then this ought to be a very good approximation on large scales [93], where the two-halo term dominates the galaxy power spectrum. Those are precisely the scales of the power spectrum that we probe in the bispectrum configuration we are dealing with here. To see why, notice that, given $\mathcal{W}_l^E$ decreases quickly below $l > 2000$ due to limited sensitivity, the multipole in the argument of the galaxy power spectrum in equation (3.29) is at most that large, which in turns forces the wavenumber $k = l/r(z)$ (where $r(z)$ is the comoving distance out to a redshift of a few, i.e., a few 1000 Mpc) to be small enough that we are probing a regime where the linear bias approximation roughly holds.

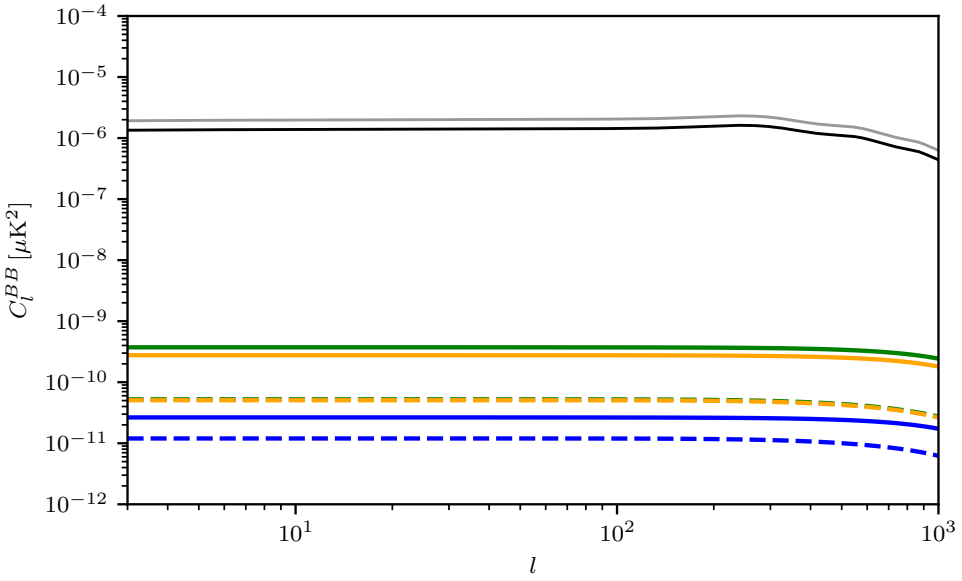

Fig. 3.12 Delensing biases from angular bispectra of the CIB in our minimal model with uncorrelated source polarisation angles. Solid (dashed) lines show the one(two)-source contribution from different point-source masking schemes with $s_{\mathrm{max}} = \{200, 20, 2\}\,\mathrm{mJy}$ (in green, orange and blue, respectively). We evaluate our predictions using $0.2 < z < 6$, $s_{\mathrm{min}} = 10^{-5}\,\mathrm{mJy}$, a fixed galaxy polarisation fraction of 5 %, and the number counts of Ref. [43]. For comparison, we show also the fiducial power spectrum of lensed B-modes before (grey) and after (black) delensing with the CIB such that the power is reduced by 30 %. We note that the two-source contribution is virtually unchanged if the flux cut is lowered from 200 mJy to 20 mJy, so the orange and green dashed lines lie on top of each other.

Finally, we evaluate the delensing bias of equation (3.29) for different flux cuts typical of current and upcoming experiments, and show the results in figure 3.12. We see that the one-source contribution dominates over the two-source, but it is everywhere negligible compared to the amplitude of the delensed B-mode spectrum. This is the case even though we have assumed that, beyond masking the brightest sources, no attempt is made to mitigate the CIB contribution to the CMB polarisation maps using, for example, multi-frequency cleaning techniques.

On the other hand, the bias of equation (3.28), sourced by the $EIEI$ trispectrum of the CIB, can, in principle, receive contributions of one-, two- and three-source type; where in all cases, the two polarisation modes are sourced by the same galaxy. As before, these can be evaluated in the framework of the halo model, this time requiring

computation of the 3D halo bispectrum to obtain the three-source term. However, we argue that the trispectrum ought to be subdominant to the bispectrum (which we have shown is negligible) for the level of point-source removal expected of upcoming experiments, since the former scales as the fourth power of the flux density while the latter goes as the third. In appendix B.3, we motivate this claim by comparing the 1-source contributions to both higher-point functions, showing that, indeed, the relevant trispectrum is smaller than the bispectrum in this even simpler model (see figure B.1).

Our conclusion is that biases sourced by higher-point functions of the CIB are negligible for the levels of point-source masking and delensing expected of any foreseen applications of the CIB-based method considered in this work.

3.5.3 Validation

In this section, we aim to validate the results of section 3.5.2.1, where we used simulations to quantify the delensing bias associated with residual Galactic dust. For reference, the power spectra of all the fields involved in the delensing procedure are shown in figure 3.13.

Of course, the results of section 3.5.2.1 are only valid in as much as the simulations on which they rely faithfully reproduce the true behaviour of dust on the sky. Given the dearth of small-scale polarisation data at the time of writing, it is not possible to gauge the accuracy of simulations by comparing them to observations. We can, however, test the results in two critical ways: firstly, we can ensure that the delensing bias (which, as we have already established, is dominated by the $\langle BEI\rangle_c$ bispectrum of dust) does not appear when our pipeline is applied to Gaussian simulations with the same power spectra; and secondly, we can verify that the biases that ensue after either dust data from Planck or the VS dust simulations are used in the analysis display similar characteristics after both inputs are restricted to the same scales.

3.5.3.1 Validation against Gaussian simulations

In order to guarantee that the delensing bias we identified in section 3.5.2.1 – associated, recall, with the $\langle BEI\rangle_c$ bispectrum of Galactic dust – is physical in origin and not some artifact of our analysis, we re-run on Gaussian simulations of Galactic dust with the same power spectra as their non-Gaussian counterparts from VS.

We work with full-sky simulations of Galactic dust at 145 GHz. First, we fit smooth curves to the ratios of TT, EE and BB power in these simulations to those measured

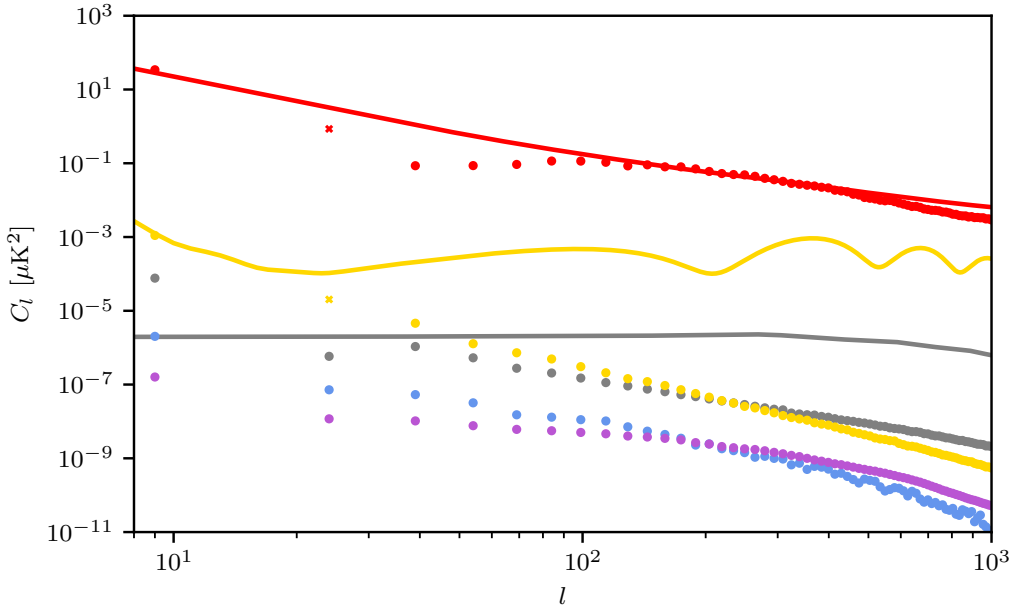

Fig. 3.13 Comparison of power spectrum amplitudes and biases for a number of fields involved in the delensing procedure. *Red dots*: residual dust intensity after filtering the VS simulation at 353 GHz with the GNILC CIB residual transfer function of figure 3.5. *Red line*: theoretical CIB intensity at 353 GHz. *Yellow dots*: VS dust E-mode power scaled to the residual dust amplitude expected for the SO LAT at 145 GHz after ILC-cleaning with dust deprojection. *Yellow line*: theoretical, lensed CMB E-mode. *Grey dots*: VS dust B-mode power at 145 GHz, scaled to the residual dust amplitude expected for the SO SAT. *Grey line*: theoretical, lensed CMB B-modes. *Purple dots*: power spectrum of a $\hat{B}(E^{\rm dust}, I^{\rm dust})$ template constructed with $E^{\rm dust}$ and $I^{\rm dust}$ with amplitudes as shown in this plot. *Blue dots*: delensing bias associated with the $\langle B^{\rm dust} E^{\rm dust} I^{\rm dust}\rangle_c$ bispectrum for residual levels as shown in this plot (note that this bias is negative, though here we plot it as a positive quantity). Comparison of the blue and purple dots shows that the bispectrum term dominates on the scales relevant for primordial B-mode searches. All empirical measurements are carried out on the LB patch, using `NaMaster` and a binning scheme with $\Delta l = 15$. On the largest scales, the uncertainty introduced by mask deconvolution can give rise to negative values, which we plot as crosses. Nevertheless, the deconvolved pseudo-C_l estimator should be unbiased in the mean.

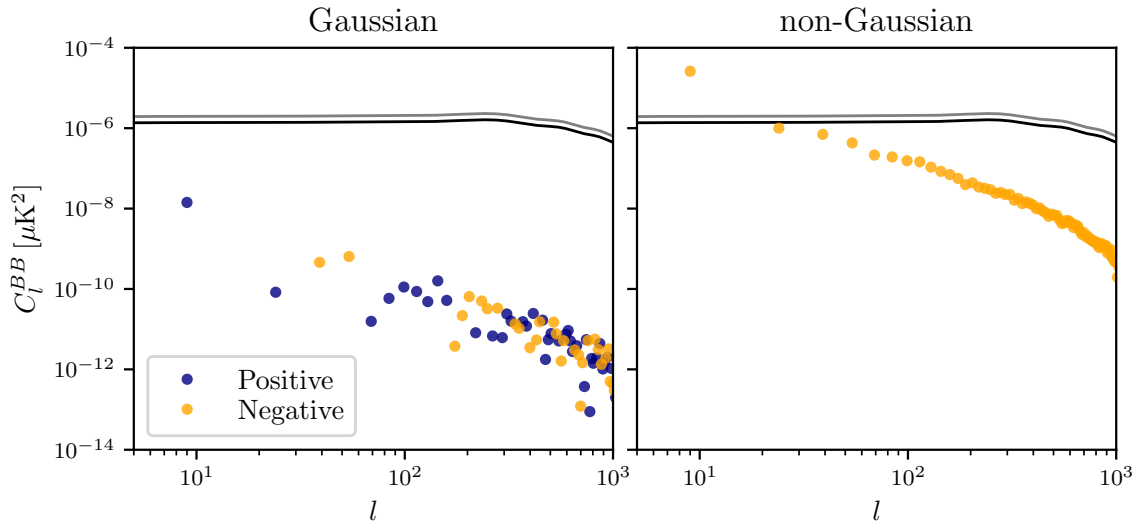

Fig. 3.14 Delensing bias associated with the bispectrum of Galactic dust as calculated from a single realisation of the VS simulation (right panel), compared to that measured from a Gaussian simulation of the dust (left panel) with the same power spectra. The same transfer functions are applied in both cases to induce the scale-dependent dust residuals estimated in section 3.5.1.3. Spectra are measured on the "LB patch" shown in figure 3.7c and binned with $\Delta l = 15$. For comparison, the amplitude of the lensing B-mode spectrum is plotted before (grey) and after (black) delensing using the CIB as the only matter tracer. While the measurement on Gaussian simulations is consistent with scatter around zero, the non-Gaussian case shows a distinct bias-like behaviour.

in the VS simulations on scales $60 < l < 2000$, after the latter have been scaled to the appropriate frequency and residual amplitude, and restricted to the region allowed by the SAT mask of figure 3.7a. The square root of these smooth transfer functions are then used to filter the Gaussian simulations, obtaining Gaussian maps with the same power spectra as the VS simulations.

Next, we use these re-scaled Gaussian simulations in the analysis steps described in section 3.5.1.5. As shown in figure 3.14, the output is consistent with pure scatter, in contrast with the distinct bias arising from the non-Gaussian simulations.

3.5.3.2 Validation against Planck data

Given that the results of section 3.5.2.1 are only as accurate as the simulations on which they rely, we set out now to validate those findings against Planck data on the scales where the latter has sufficient signal-to-noise. More specifically, we compare the output of our analysis procedure (detailed in section 3.5.1.5) when applied to

the VS simulations to the case where the temperature and polarisation maps we use are instead the Planck 2018 full-mission or GNILC products, both at 353 GHz. (The Planck products we use are available on the Planck Legacy Archive.)

The idea is that the dust component of the observations is to be processed in the same ways as the dust in the simulations. For this reason, we apply the same filtering protocol to both, aiming to retrieve the same residual dust fractions. In addition to this, we extrapolate the polarisation observations at 353 GHz to 145 GHz with an SED appropriate for dust, to estimate the dust at this frequency before foreground cleaning. This is done by assuming that the dust behaves as a modified blackbody with parameters given in table 3.1 and applying the relevant wide-band unit-conversions for the 143 and 353 GHz channels of Planck. Furthermore, specific intensity measurements made by broad-band instruments are necessarily related to a reference frequency and calibration SED profile. In the Planck 353 GHz band, this is the CMB dipole. In order to relate measurements on that band to a thermal dust SED, we apply a multiplicative colour correction as given by Ref. [367]. An explanation of the philosophy of such corrections can be found in Ref. [353].

As is the case with all astronomical observations, the Planck data are convolved with the instrument's beam. In order to ensure that the observed and simulated modes we are comparing have the same normalisation, we filter the VS simulation with approximate beam transfer functions derived by fitting the window function of a symmetric Gaussian beam to the ratios of EE, BB and TT power measured from the Planck data to those measured from the simulations, on scales of $20 < l < 100$ (below the multipoles where experimental noise becomes significant in the Planck polarisation data). This correction enables a like-for-like comparison on scales of approximately $l < 200$, in the case of the GNILC dust data (for which the maps are convolved with a beam with FWHM of 80 arcmin to ensure they have the same resolution everywhere), and $l < 500$ in the case of the raw 353 GHz frequency data (approximately the angular scale where polarisation noise in the 353 GHz channel begins to dominate). The latter is an important range for our purposes, since it encompasses most of the multipole range where Galactic dust dominates over CIB emission in total intensity (see, e.g., Ref. [365]). Furthermore, we verify that, in the 353 GHz channel, the effects of beam convolution at $l = 500$ are still relatively limited and signal power is only suppressed by approximately 10 %.

When using the raw 353 GHz maps, which include significant amounts of CIB emission, our validation could potentially be confused by its sensitivity to the bispectrum of CIB fields. However, from the calculations in section 3.5.2.2, we expect this to be

small for the expected extent of point-source removal. In order to ensure this is the case, we apply a mask – also obtained from the Planck Legacy Archive – which removes point sources detected with $S/N > 5$ at 353 GHz . We do, however, see increased scatter in the bispectrum measurements from the CIB (and the CMB and instumental noise) as discussed below.

The results of the delensing bias from the bispectrum of dust computed from the re-scaled VS simulations or the Planck data are shown in figure 3.15. The bias that appears when using the raw data as input is approximately two orders of magnitude larger than that produced by the GNILC dust maps, owing to the much restricted multipole range going into the latter.

For a given type of input map, the level of agreement between data and simulations is remarkable. The bias calculation based on the raw Planck frequency maps shows higher scatter than seen in the simulation (particularly on smaller scales), which can be explained as the added variance from the other components present in those maps such as the CIB, the CMB or experimental noise. This explanation is consistent with the fact that such increase in scatter is not seen when the GNILC dust products are used. On that note, it is worth pointing out that the similar amplitude and shape of the biases arising from the raw channel data and the pure-dust simulations is consistent with the claim made in section 3.5.2.2 that the BEI bispectrum of the CIB is small once point-sources are masked.

3.6 Conclusions

In this chapter, we have addressed several topics relevant to B-mode delensing when performed using external tracers. We began, in section 3.3, by showing how the relevant auto- and cross- spectra can be modelled in the case where the matter proxy consists of a combination of multiple tracers; then, in appendix B.8, we provided analytic expressions for the covariance between all those spectra. These results were used to validate the SO delensing pipeline, Ref. [313].

In section 3.4, we studied possible biases to SO's contraints on the tensor-to-scalar ration, r, arising from uncertainties in our knowledge of the power spectrum and cross-correlation with lensing of the different tracers involved. We found that such biases will be much smaller than the statistical uncertainty, particularly when external tracers are co-added with internal reconstructions.

The rest of the chapter was dedicated to a lengthy discussion of ways in which residual foregrounds can impact the power spectrum of CMB B-modes after they are

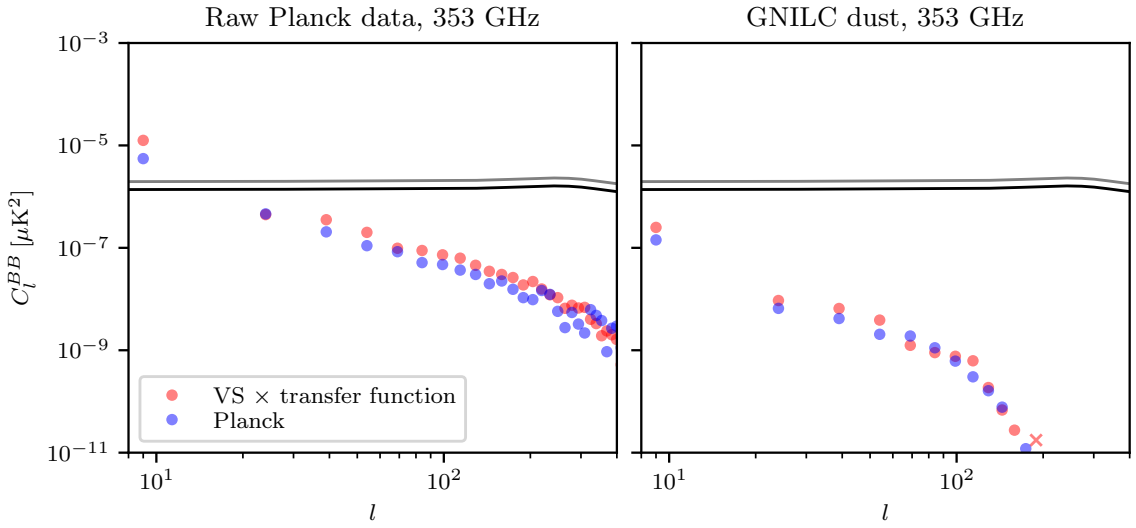

Fig. 3.15 Delensing bias associated with the bispectrum of Galactic dust arising from a restricted range of multipoles of the VS Galactic dust simulation or the Planck data, after both are filtered and scaled to emulate levels of residual dust expected after foreground cleaning. In order to incorporate the effect of beam convolution, the VS simulation is filtered with a smooth transfer function fit to the power spectra of the data. This enables a comparison in the range $l < 200$ when the Planck 353 GHz GNILC dust data is used to model residuals (right panel) and for $l < 500$ when the raw 353 GHz channel data is used for this purpose instead (left panel). In the latter case, we ensure point-sources are masked. For comparison, the lensing B-mode spectrum is plotted before (grey) and after (black) being delensed with the CIB. The amplitude of the dust in each map is scaled down to the level appropriate for the residuals expected in the GNILC estimate of the CIB and the SO LAT and SAT polarisation maps (both after standard ILC-cleaning), as estimated in section 3.5.1.3. Furthermore, an $l_{\rm min} = 100$ cut is applied to the fields. Spectra are measured on the "LB patch" shown in figure 3.7c and binned with $\Delta l = 15$. In both cases, negative values are plotted as circles and positive ones as crosses.

delensed using the CIB as a proxy for the lensing potential. We identified two sources of bias which could, in principle, affect constraints on the tensor-to-scalar ratio: residual Galactic dust and residual CIB emission left over in the CMB maps after foreground cleaning.

Given that, at the time of writing, no simulations of polarised CIB emission exist, we calculated the delensing bias arising from higher-point functions of the CIB analytically, in the context of a model where source polarisation angles are uncorrelated. We found that the dominant contribution to this bias ought to be the $\langle BEI \rangle$ bispectrum of the CIB. Our calculation shows that, given the extent of point source masking expected of upcoming experiments, this bias ought to be negligible. As a side note, our model shows that certain bispectra involving CIB polarisation fields can be non-vanishing even if galaxy polarisation angles are uncorrelated, namely those containing two polarisation legs sourced by the same galaxy.

We also presented a first attempt to characterise the delensing bias arising from residual Galactic dust left over in CMB and CIB maps used for delensing. We simulated the delensing procedure as applied to these dust residuals, using a non-Gaussian simulation of Galactic dust from Ref. [491] filtered to model the expected levels of residuals after foreground cleaning appropriate for CMB E- and B-mode polarisation and CIB observations in the coming era of CMB experiments. In particular, we estimated residual dust levels for the Simons Observatory's (SO) measurements of E-modes with its large-aperture telescope (LAT) and B-modes with its small-aperture telescopes, and for the CIB maps of Ref. [365] and Ref. [250]. We also validated our results directly against the Planck data on large and intermediate scales.

We found that the bias from residual Galactic dust is dominated by the $\langle BEI \rangle_c$ bispectrum of Galactic dust, and that it is negative. It is also very red, peaking on the very largest angular scales. Given the extent of foreground cleaning expected of upcoming ground-based experiments (we focus on the specifications of SO), the bias only becomes relevant for multipoles $l \lesssim 20$, scales likely too large to be probed from the ground. Hence, we find that a failure to model this bias at the level of the power spectrum translates to an inference on r that is systematically lower than the truth, but only by an amount smaller than the 1σ statistical uncertainty. To err on the side of caution, however, we recommend explicitly deprojecting dust from the high-resolution E-mode fields – e.g., with a constrained internal-linear combination approach applied to multi-frequency data [394] – used in delensing if the delensed B-modes on scales larger than $l < 30$ are to be considered. Although this might come at the cost of degraded delensing efficiency, we show that for an experiment with the characteristics

of the SO LAT this is a small effect (with only a percent-level increase in the residual lensing power).

On the other hand, the bias could be large enough to be a cause of concern for space-based experiments, such as LiteBird, targeting the reionisation peak of the primary CMB in addition to the recombination peak targeted by ground-based experiments. By covering larger sky areas, space-based experiments are prone to including regions where the dust is very bright, causing the bias to grow and become significant on scales that the telescope is sensitive to. Furthermore, their situation above the atmosphere allows them to probe the large-scale signal from reionisation, scales where the bias is largest. In spite of this, we show that a combination of dust deprojection in the foreground cleaning of E-modes and removal of large-scale CIB modes in the construction of the lensing B-mode template is effective in reducing this bias. The latter can always be implemented at little cost in terms of delensing efficiency (at least for $l_{\rm min}^{\rm CIB} \lesssim 250$), since internal lensing reconstruction techniques can estimate these large-scale lenses very accurately. Furthermore, the bias is very sensitive to the removal of dust from the CMB polarisation fields involved, so we expect the situation to be less concerning for future satellite missions, for which foreground cleaning will be much improved relative to the levels considered in this work. Altogether, we are confident that the bias can be kept in check and CIB delensing can remain a valuable tool.

We note also that, in addition to the biases described above, residual foregrounds ought also to impact the variance of the power spectrum of delensed B-modes. However, we defer the study of that problem to future work, given the difficulty of studying it analytically and the lack of realistic simulations to assist a computational treatment.

The results presented in this work illustrate the community's need for non-Gaussian simulations of Galactic dust extending to small angular scales on which to test the robustness of delensing analyses against the systematic effects identified in this work. Such simulations are also necessary to assess the level of contamination in CMB lensing power spectrum reconstruction from polarisation-based estimators [82, 30]. We emphasise that the approach followed to date of testing against Gaussian simulations (see, e.g., Ref. [291] or Ref. [51]) will not suffice, as validation experiments based on those will be insensitive to the non-Gaussian biases discussed here, which can be significant on the largest angular scales.

Chapter 4

Impact of internal-delensing biases on searches for primordial B-modes

This chapter is based on [17]. Note that the asymmetric convention for Fourier transforms is used throughout it[1]*.*

4.1 Introduction

The extent to which lensing B-modes can be removed depends on the fidelity with which the lensing potential can be estimated. For sufficiently low experimental noise levels, the lensing potential, ϕ, can be reconstructed internally from the CMB maps themselves by employing either the quadratic estimators of Ref. [331] — introduced in section 1.5.2.4 — or the more powerful, albeit analytically and computationally complex, maximum-likelihood [190] or Bayesian methods [75, 298]. For experimental noise levels available already in the next generation of CMB observatories, a quadratic combination involving E- and B-fields will provide a sizeable fraction of the signal-to-noise, dominating over other estimators in the regime where $\Delta_P < 5\,\mu\mathrm{K}\,\mathrm{arcmin}$.

However, Ref. [477] showed that whenever there is an overlap in modes between the field we wish to delens and the fields from which a lensing reconstruction is derived, the delensed power is subject to a bias that leads to a suppression in power going beyond that which can be attributed to a mitigation of the lensing effects. More importantly, the variance associated with this delensed spectrum is also reduced, posing the question of whether the bias could help better constrain the tensor-to-scalar ratio, r.

[1] In the asymmetric convention for two-dimensional Fourier transforms:

$$f(\boldsymbol{x}) = \int \frac{d^2\boldsymbol{l}}{(2\pi)^2} f(\boldsymbol{l}) e^{i\boldsymbol{l}\cdot\boldsymbol{x}} \quad \text{and} \quad f(\boldsymbol{l}) = \int d^2\boldsymbol{x} f(\boldsymbol{x}) e^{-i\boldsymbol{l}\cdot\boldsymbol{x}}\,. \tag{4.1}$$

In this chapter, we set out to understand the angular power spectrum of B-modes after internal delensing with an EB quadratic estimator, as a function of experimental characteristics and, importantly, primordial B-mode power, assuming no foreground or survey non-idealities. In section 4.2, we review the quadratic estimators of lensing reconstruction, focusing on the EB combination. In section 4.3, we build a lensing B-mode template (of the style described in chapter 2) from observations of E and estimates of ϕ. Then, in section 4.4, we introduce analytic models for the angular power spectrum of delensed B-modes in both the cases with and without overlapping modes, and compare them to simulations. (These models are derived carefully in appendix A.1, and the simulations are described in appendix A.2.) In section 4.5, we consider simple models for the covariance of the delensed B-mode power spectrum. We combine the power spectrum models and covariances in a maximum-likelihood framework in section 4.6, where we simulate inferences of r to compare quantitatively the different ways in which the bias can be dealt with. Finally, in section 4.7, we briefly study the impact of the bias on an alternative estimator which correlates observed and delensed B-modes.

The results in this chapter will often refer to the experimental specifications of the upcoming Simons Observatory (SO)[441], which will feature a large-aperture telescope (LAT) responsible, among other scientific targets, for lensing reconstruction; and separate small-aperture telescopes (SATs) for observations of B-modes on large angular scales. However, the insights developed here apply more widely, and will likely be relevant to any application of internal delensing that uses information from the B-modes for the purpose of lensing reconstruction.

4.2 The quadratic estimators of lensing

In order to undo the deflections induced by lensing, an estimate of the projected matter distribution on the sky – which determines the lensing potential – is required. For the sensitivities and resolution of current CMB experiments, the best possible estimate is obtained from tracers external to the CMB such as the cosmic infrared background (CIB) or very deep galaxy surveys [445, 432, 247, 416]; see chapter 3. The CIB retains a high degree of correlation with the smaller-scale lenses at high redshift that are important for converting E-modes into B-modes, something that is not yet possible with internal lensing reconstruction, which is very noisy on the relevant angular scales. However, this situation will change with planned CMB polarisation surveys, which can provide high signal-to-noise lensing reconstructions on nearly all scales relevant

for B-mode delensing [90]. Consequently, reconstructions of ϕ derived from the CMB fields themselves will ultimately provide the best delensing performance.

Internal reconstruction techniques use the fact that, if we could average over realisations of the CMB while keeping the lensing potential fixed, lensing would break statistical isotropy by inducing correlations between fluctuations on different scales; consequently, the lensing potential can be reconstructed by combining many off-diagonal correlations. In general, the optimal internal reconstruction of ϕ will be obtained from studying the likelihood function of the lensed CMB temperature and polarisation anisotropies [189, 190, 75, 298]. However, for the noise levels attainable in the near future, the optimal lensing reconstruction has been shown (see, e.g., Ref. [82]) to be equivalent to that from the more tractable and computationally efficient "quadratic estimators" of Refs. [202, 331]. In fact, in the upcoming era of high-resolution CMB experiments such as the Simons Observatory [441] and SPT3G [458], which feature experimental noise levels $1\,\mu\mathrm{K\,arcmin} < \Delta_P < 10\,\mu\mathrm{K\,arcmin}$, the optimal reconstruction will arise from a combination of external tracers and internal reconstructions involving quadratic estimators [432].

A minimum-variance internal reconstruction of the lensing potential can be obtained from combining different quadratic estimators, as seen in figure 4.1. For low enough noise levels, the quadratic estimator involving E and B fields is expected to provide the highest signal-to-noise reconstruction – the reason being that, in this case, the dominant source of reconstruction noise involves the Gaussian contraction $\langle EE\rangle\langle BB\rangle$, and the lensing and primordial contributions to $\langle BB\rangle$ are small [82]. It is because of its relevance in upcoming efforts to delens the CMB that we focus on the EB estimator in this work. It takes the form

$$\hat{\phi}_{EB}(\boldsymbol{L}) = A_L^{EB} \int \frac{d^2\boldsymbol{l}}{(2\pi)^2} W(\boldsymbol{L}-\boldsymbol{l},-\boldsymbol{l}) \frac{\tilde{C}_l^{EE,\,\mathrm{fid}}}{C_l^{EE,\,\mathrm{obs,\,fid,\,LAT}} C_{|\boldsymbol{l}-\boldsymbol{L}|}^{BB,\,\mathrm{obs,\,fid,\,LAT}}} \times E^{\mathrm{obs,LAT}}(\boldsymbol{l}) B^{\mathrm{obs,LAT}}(\boldsymbol{L}-\boldsymbol{l}), \tag{4.2}$$

where $E^{\mathrm{obs,LAT}}$ and $B^{\mathrm{obs,LAT}}$ are beam-deconvolved observed fields[2], A_L^{EB} is a normalisation factor, $C_l^{XX,\,\mathrm{obs,\,fid,\,LAT}}$ is the fiducial, total power observed by the LAT which is

[2]In the case where an observatory consists of separate telescopes with different characteristics and mapping strategies, the one with the larger aperture – labeled here as LAT, in contrast with the SAT, or small aperture telescope – will provide the superior lensing reconstruction as it can more finely resolve the small scales where lensing dominates.

used to inverse-variance filter[3] the field X, and the geometric coupling

$$W(\boldsymbol{l},\boldsymbol{l}') \equiv \boldsymbol{l}'\cdot(\boldsymbol{l}-\boldsymbol{l}')\sin 2\left(\psi_{\boldsymbol{l}}-\psi_{\boldsymbol{l}'}\right). \tag{4.3}$$

Here, $\psi_{\boldsymbol{l}}$ is the angle between $\boldsymbol{l}$ and the x-axis used to define positive Stokes parameter Q, and similarly for $\psi_{\boldsymbol{l}'}$. Notice the use of the fiducial lensed $\tilde{C}_l^{EE,\mathrm{fid}}$ instead of its unlensed counterpart, since this has been shown to optimise the correlation of estimates of the lensing potential with the underlying truth[4] [169, 253]. If equation (4.2) were to minimise exactly the variance of $\hat{\phi}_{EB}$, it would include an additional term proportional to the primordial B-mode spectrum[5], $C_l^{BB,t}$, like the one shown but replacing $W(\boldsymbol{L}-\boldsymbol{l},-\boldsymbol{l})\tilde{C}_l^{EE,\mathrm{fid}} \to -W(-\boldsymbol{l},\boldsymbol{L}-\boldsymbol{l})C_{|\boldsymbol{L}-\boldsymbol{l}|}^{BB,\mathrm{t,fid}}$. We ignore it here, however, as its effect is negligible for values of r compatible with experimental bounds.

4.3 Template delensing of the B-mode

Once we have an estimate for the lensing potential, delensing can be performed by using it to build a template approximating the lensing B-modes, B^{temp}, which can then be subtracted from the observed B-modes[6], $B^{\mathrm{obs,\,SAT}}$, to yield a delensed field

$$B^{\mathrm{del}} = B^{\mathrm{obs,\,SAT}} - B^{\mathrm{temp}}. \tag{4.4}$$

To leading order in $\boldsymbol{\nabla}\phi$ (what is usually referred to as the "gradient approximation", and is known to be an excellent approximation to the non-perturbative calculation of the lensed B-mode spectrum on large angular scales [84]), the template can be constructed as

$$B^{\mathrm{temp}}(\boldsymbol{l}) = \int \frac{d^2\boldsymbol{l}'}{(2\pi)^2} f(\boldsymbol{l},\boldsymbol{l}')W(\boldsymbol{l},\boldsymbol{l}')E^{\mathrm{obs,LAT}}(\boldsymbol{l}')\hat{\phi}(\boldsymbol{l}-\boldsymbol{l}'), \tag{4.5}$$

[3]For simplicity, we take this filter to be diagonal. In practical applications with masking and/or inhomogeneous noise, the optimal filtering function will no longer be diagonal.

[4]For the experimental configurations considered in this chapter, the delensing performance obtained by using these weights appears to be indistinguishable from the case where the unlesed spectra are used instead.

[5]While we denote as $\tilde{C}_l^{EE}$ the lensed E-mode spectra (including primordial E-modes), we follow the standard convention that $\tilde{C}_l^{BB}$ comprises only the lensing contribution to the B-mode spectrum, with the primordial part given separately by $C_l^{BB,t}$

[6]In multi-telescope observatories, small aperture telescopes (SATs), which have proven stability to large-scale signals, are being adopted to pursue primordial B-modes.

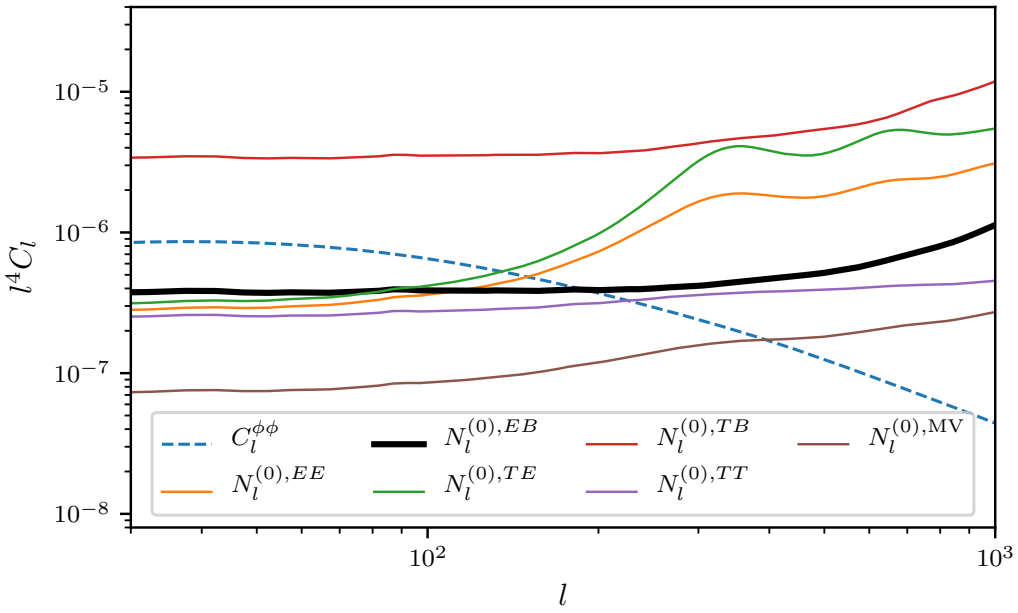

Fig. 4.1 Lensing reconstruction noise levels associated with the five different quadratic estimators, and their minimum-variance combination, for an experiment with resolution $\theta_{\mathrm{FWHM}} = 1.5\,\mathrm{arcmin}$ (full width at half maximum) and isotropic white noise with $\Delta_T = 6\,\mu\mathrm{K}\,\mathrm{arcmin}$ for temperature and $\Delta_P = \sqrt{2}\Delta_T$ for polarisation. The maximum multipole used in the reconstruction is $l_{\mathrm{max}} = 3000$. These specifications are similar to the goals for the SO LAT at 145 GHz. The dashed blue line is the lensing potential power spectrum.

with $W(\boldsymbol{l}, \boldsymbol{l}')$ as defined in equation (4.3). We know, from chapter 2, that a template built this way can be highly effective. The function $f(\boldsymbol{l}, \boldsymbol{l}')$ can be chosen to minimise the power spectrum of the delensed field (4.4), which Ref. [445] shows to be the case when the fields are filtered with

$$f(\boldsymbol{l}, \boldsymbol{l}') = \mathcal{W}^E_{l'} \mathcal{W}^\phi_{|\boldsymbol{l}-\boldsymbol{l}'|}, \tag{4.6}$$

where

$$\mathcal{W}^E_l \equiv \frac{\tilde{C}^{EE,\mathrm{fid}}_l}{C^{EE,\mathrm{obs,fid,\,LAT}}_l} \quad \text{and} \quad \mathcal{W}^\phi_L \equiv \frac{C^{\phi\phi,\mathrm{fid}}_L}{C^{\phi\phi,\mathrm{fid}}_L + N^{\phi\phi}_L}, \tag{4.7}$$

are Wiener filters for the E-modes and the estimate of the lensing potential. Here, $N^{\phi\phi}_L$ is the reconstruction noise on $\hat{\phi}$. In practice, we use $N^{\phi\phi}_L \approx N^{(0),EB}_L$, the disconnected (Gaussian) contribution to the power spectrum of $\hat{\phi}$, and ignore higher-order terms such as $N^{(1),EB}_L$, as the former dominates over the latter by several orders of magnitude on all relevant scales [95]. Notice also that equation (4.5) uses the observed (lensed and noisy) $E^{\mathrm{obs,LAT}}$, rather than unlensed (or delensed) E-modes. This is to be preferred *for template delensing* since an approximate cancellation suppresses higher-order contributions in $C^{\phi\phi}_L$ to the delensed power spectrum, which would otherwise be as big as 30 % on large scales [18].

4.4 Angular power spectrum of delensed B-modes

Most inflationary models predict a spectrum of primordial perturbations that are very nearly Gaussian distributed. This character extends approximately to the fluctuations of the primary CMB, as linear-theory transfer functions are an excellent approximation in the early universe. For such Gaussian fields, the data can be losslessly compressed into a power spectrum, making the latter one of the most powerful tools for studying the CMB. Although the *lensed* CMB is actually non-Gaussian (as a result of the Gaussian primary CMB fields being displaced by the nearly-Gaussian lensing potential), delensing has been shown to mitigate its non-Gaussian character to the point where the delensed B-modes – if delensed in such a way that the EB delensing bias is avoided – deviate only slightly from Gaussianity [317] and the information lost from working with the power spectrum is relatively small.

More importantly, in practical applications involving masked observations and anisotropic noise, any computation of the exact likelihood of the data becomes in-

tractable and one must work instead with approximate forms, most typically involving estimators of the power spectra and their covariance [163].

For these reasons, most efforts to detect primordial B-modes work with the power spectrum of the delensed field of equation (4.4):

$$\begin{aligned}\langle B^{\rm del}(\boldsymbol{l}_1)B^{\rm del}(\boldsymbol{l}_2)\rangle &= \langle B^{\rm obs,\,SAT}(\boldsymbol{l}_1)B^{\rm obs,\,SAT}(\boldsymbol{l}_2)\rangle - 2\langle B^{\rm temp}(\boldsymbol{l}_1)B^{\rm obs,\,SAT}(\boldsymbol{l}_2)\rangle \\ &\quad + \langle B^{\rm temp}(\boldsymbol{l}_1)B^{\rm temp}(\boldsymbol{l}_2)\rangle \\ &\equiv (2\pi)^2\delta^{(2)}(\boldsymbol{l}_1+\boldsymbol{l}_2)C_{l_1}^{BB,{\rm del}},\end{aligned} \tag{4.8}$$

where in the last line we have used the statistical isotropy of the CMB to define $C_l^{BB,{\rm del}}$, the angular power spectrum of the delensed B-modes. In the remainder of this section we examine this expression in detail. In section 4.4.1, we evaluate it in the case where the statistical errors in the estimated lensing potential are independent of the lensed CMB fields, exploring the reduction in power associated with removal of part of the lensing signal. Then, in section 4.4.2, we study equation (4.8) in the case where $\hat{\phi}$ is derived from an EB quadratic estimator; new couplings then appear that further suppress the delensed power spectrum beyond a simple removal of lensing power. We conclude the section by proposing an analytic model to capture the behaviour of such "bias" terms.

4.4.1 The unbiased case: reconstruction errors statistically independent of the lensed CMB

If the noise on $\hat{\phi}$ were independent of the B-mode we would like to delens, as would be the case if an external tracer were used for $\hat{\phi}$, the delensed power spectrum would take the form

$$C_l^{BB,{\rm del,unbiased}} = N_l^{BB,{\rm SAT}} + C_l^{BB,t} + C_l^{BB,{\rm res}}. \tag{4.9}$$

In addition to the instrumental noise, $N_l^{BB,\,{\rm SAT}}$, and primordial component, $C_l^{BB,{\rm t}}$, there is a contribution from residual deflections – imperfect delensing – given to leading order in lensing by [445]

$$\begin{aligned}C_l^{BB,{\rm res}} &\approx \int \frac{d^2\boldsymbol{l}'}{(2\pi)^2} W^2(\boldsymbol{l},\boldsymbol{l}')C_{l'}^{EE}C_{|\boldsymbol{l}-\boldsymbol{l}'|}^{\phi\phi}\Big[1-\mathcal{W}_{l'}^{E}\mathcal{W}_{|\boldsymbol{l}-\boldsymbol{l}'|}^{\phi}\Big] \\ &= \tilde{C}_l^{BB} - C_l^{W},\end{aligned} \tag{4.10}$$

where we have defined

$$C_l^W \equiv \int \frac{d^2\boldsymbol{l}'}{(2\pi)^2} W^2(\boldsymbol{l},\boldsymbol{l}') \left[\mathcal{W}_{l'}^E C_{l'}^{EE,\mathrm{fid}}\right] \left[\mathcal{W}_{|\boldsymbol{l}-\boldsymbol{l}'|}^{\phi} C_{|\boldsymbol{l}-\boldsymbol{l}'|}^{\phi\phi,\mathrm{fid}}\right] \tag{4.11}$$

and assumed that our fiducial model for the lensing power spectrum, $C_l^{\phi\phi,\mathrm{fid}}$, is correct. We note that C_l^W is simply the fiducial power spectrum of the B-mode template. In appendix A.1.1, we explain how equation (4.10) can be recovered in the analytic framework developed in section 4.4.2 to characterise the delensing bias. Notice that, in the limit of no observational noise and a perfect $\hat{\phi}$, we have $\mathcal{W}_l^E \to 1$ and $\mathcal{W}_l^{\phi} \to 1$ and all of the (leading-order) lensing signal is removed. Higher-order terms mean that template delensing can, in fact, be used to reduce the lensing contribution to the power spectrum to approximately 1 % of its original level. This is in the case where lensed E-modes are employed in the construction of the B-mode template – the alternative of using unlensed/delensed E-modes performs worse with a lensing residual of order 30 % as noted above [18]. Were estimates of the lensing potential accurate enough to reduce the delensed power to the 1 % level, template delensing should be replaced with non-perturbative methods whereby the Wiener-filtered $\hat{\phi}$ is used to remap the observed CMB directly (see, e.g., [247, 76, 380, 372] for demonstrations of this method).

Henceforth, we will refer to equation (4.9) as the *unbiased* delensed power spectrum in order to differentiate it from the case where the errors in $\hat{\phi}$ are statistically dependent on the lensed CMB, as is the case when internal delensing with overlapping modes. We now consider the new terms that arise in the delensed power for this latter case.

4.4.2 The biased case: $\hat{\phi}$ obtained from an EB quadratic estimator

We discussed in section 4.2 that, in the upcoming era of low-noise CMB experiments, the highest signal-to-noise reconstruction using quadratic estimators will arise from combining E and B fields. Crucially, Ref. [477] first noticed that, if such a reconstruction is used to delens observations of B-modes, the delensed power spectrum will be biased: while equation (4.10) continues to quantify the power spectrum due to residual deflections, the total delensed spectrum will show an additional suppression of power beyond that which can be attributed to delensing. In this section, we add to the work of [477, 316, 312] by providing a detailed calculation of the biased delensed B-mode power spectrum, including terms neglected by equation (4.10).

In order to isolate the effects of the bias, we assume henceforth that the lensing reconstruction is obtained exclusively from an EB quadratic estimator. Although this is set to be the dominant source of information on lensing for upcoming experiments, in real applications the optimal reconstruction will, in fact, arise as a minimum-variance (MV) combination of several quadratic estimators. In that scenario, the bias arising from EB reconstruction needs to be propagated through the co-adding procedure, and will ultimately be reduced relative to the case where only the EB estimator is used because the other estimators it is combined with do not source a bias. Hence, to obtain the amplitude of the bias on the delensed B-mode spectrum and on r in the MV case, the results quoted in this chapter would need to be scaled appropriately by the MV weight pertaining to the EB estimator.

In this *biased* case, the first term in the delensed B-mode spectrum of equation (4.8) is still

$$\langle B^{\rm obs,\,SAT}(\boldsymbol{l}_1)B^{\rm obs,\,SAT}(\boldsymbol{l}_2)\rangle = (2\pi)^2\delta^{(2)}(\boldsymbol{l}_1+\boldsymbol{l}_2)C_{l_1}^{BB,{\rm obs,\,SAT}}, \tag{4.12}$$

but the other two correlators receive important new contributions. Substituting in eqs. (4.2) and (4.5), the second term becomes

$$\begin{aligned}\langle B^{\rm temp}(\boldsymbol{l}_1)B^{\rm obs,\,SAT}(\boldsymbol{l}_2)\rangle = \int \frac{d^2\boldsymbol{l}_1' d^2\boldsymbol{l}_1''}{(2\pi)^4}\mathcal{W}^E_{l_1'}\mathcal{W}^\phi_{|\boldsymbol{l}_1-\boldsymbol{l}_1'|}\\ \times \frac{A^{EB}_{|\boldsymbol{l}_1-\boldsymbol{l}_1'|}\tilde{C}^{EE,\,\rm fid}_{l_1''}}{C^{EE,\,\rm obs,\,fid,\,LAT}_{l_1''}C^{BB,\,\rm obs,\,fid,\,LAT}_{|\boldsymbol{l}_1-\boldsymbol{l}_1'-\boldsymbol{l}_1''|}}W(\boldsymbol{l}_1,\boldsymbol{l}_1')W(\boldsymbol{l}_1-\boldsymbol{l}_1'-\boldsymbol{l}_1'',-\boldsymbol{l}_1'')\\ \times \langle E^{\rm obs,\,LAT}(\boldsymbol{l}_1')E^{\rm obs,\,LAT}(\boldsymbol{l}_1'')B^{\rm obs,\,LAT}(\boldsymbol{l}_1-\boldsymbol{l}_1'-\boldsymbol{l}_1'')B^{\rm obs,\,SAT}(\boldsymbol{l}_2)\rangle.\end{aligned} \tag{4.13}$$

The last term, which correlates two templates, takes the form

$$\begin{aligned}\langle B^{\rm temp}(\boldsymbol{l}_1)B^{\rm temp}(\boldsymbol{l}_2)\rangle = \int \frac{d^2\boldsymbol{l}_1' d^2\boldsymbol{l}_2' d^2\boldsymbol{l}_1'' d^2\boldsymbol{l}_2''}{(2\pi)^8}\mathcal{W}^E_{l_1'}\mathcal{W}^E_{l_2'}\mathcal{W}^\phi_{|\boldsymbol{l}_1-\boldsymbol{l}_1'|}\mathcal{W}^\phi_{|\boldsymbol{l}_2-\boldsymbol{l}_2'|}\\ \times \frac{A^{EB}_{|\boldsymbol{l}_1-\boldsymbol{l}_1'|}A^{EB}_{|\boldsymbol{l}_2-\boldsymbol{l}_2'|}}{C^{BB,\,\rm obs,\,fid,\,LAT}_{|\boldsymbol{l}_1-\boldsymbol{l}_1'-\boldsymbol{l}_1''|}C^{BB,\,\rm obs,\,fid,\,LAT}_{|\boldsymbol{l}_2-\boldsymbol{l}_2'-\boldsymbol{l}_2''|}}\frac{\tilde{C}^{EE,\,\rm fid}_{l_1''}}{C^{EE,\,\rm obs,\,fid,\,LAT}_{l_1''}}\frac{\tilde{C}^{EE,\,\rm fid}_{l_2''}}{C^{EE,\,\rm obs,\,fid,\,LAT}_{l_2''}}\\ \times W(\boldsymbol{l}_1,\boldsymbol{l}_1')W(\boldsymbol{l}_2,\boldsymbol{l}_2')W(\boldsymbol{l}_1-\boldsymbol{l}_1'-\boldsymbol{l}_1'',-\boldsymbol{l}_1'')W(\boldsymbol{l}_2-\boldsymbol{l}_2'-\boldsymbol{l}_2'',-\boldsymbol{l}_2'')\\ \times \langle E^{\rm obs,\,LAT}(\boldsymbol{l}_1')E^{\rm obs,\,LAT}(\boldsymbol{l}_1'')B^{\rm obs,\,LAT}(\boldsymbol{l}_1-\boldsymbol{l}_1'-\boldsymbol{l}_1'')\\ \times E^{\rm obs,\,LAT}(\boldsymbol{l}_2')E^{\rm obs,\,LAT}(\boldsymbol{l}_2'')B^{\rm obs,\,LAT}(\boldsymbol{l}_2-\boldsymbol{l}_2'-\boldsymbol{l}_2'')\rangle.\end{aligned} \tag{4.14}$$

The evaluation of the four- and six-point functions that appear in eqs (4.12) and (4.14) is discussed in detail in appendix A.1. These are expanded in terms of

connected n-point functions with $n = 2$ and 4 (the connected six-point function is higher order in $C_l^{\phi\phi}$). A subset of these terms combine to give the standard unbiased result (4.10), as shown in appendix A.1.1. The remaining terms introduce corrections, with the most important of these identified and evaluated in appendix A.1.2. Combining these results, we show that the biased delensed B-mode power spectrum can be approximated as

$$C_l^{BB,\mathrm{del}} = (C_l^{BB,\mathrm{res}}+C_l^{BB,t})(D_l-1)^2+D_l^2C_l^W+N_l^{BB,\mathrm{SAT}}+N_l^{BB,\mathrm{LAT}}D_l^2-2D_lN_l^X, \quad (4.15)$$

where the correlation of experimental noise in the SAT and the LAT is denoted as

$$N_l^X = \begin{cases} 0 & \text{if SAT and LAT are separate,} \\ N_l^{BB,\mathrm{LAT}} = N_l^{BB,\mathrm{SAT}} & \text{for a single telescope.} \end{cases} \quad (4.16)$$

We have also defined

$$D_l \equiv \frac{1}{C_l^{BB,\mathrm{obs,fid,LAT}}} \int \frac{d^2\boldsymbol{l}'}{(2\pi)^2} W^2(\boldsymbol{l},\boldsymbol{l}') \left[\mathcal{W}_{l'}^E \tilde{C}_{l'}^{EE}\right] \left[\mathcal{W}_{|\boldsymbol{l}-\boldsymbol{l}'|}^{\phi} A_{|\boldsymbol{l}-\boldsymbol{l}'|}^{EB}\right], \quad (4.17)$$

whose origin and properties are discussed further below.

Equation (4.15) captures the general case where a large-aperture telescope (LAT) focuses on lensing reconstruction while a separate small-aperture telescope (SAT) makes observations of the B-modes on large angular scales. In such a configuration, the experimental noise is uncorrelated between instruments and $N_l^X = 0$. On the other hand, the case where a single telescope is used for both purposes can easily be recovered by letting $N_l^X = N_l^{BB,\mathrm{LAT}} = N_l^{BB,\mathrm{SAT}}$, in which case the biased delensed spectrum reduces to

$$C_l^{BB,\mathrm{del}} = (C_l^{BB,\mathrm{res}} + C_l^{BB,t} + N_l^{BB})(D_l - 1)^2 + D_l^2 C_l^W. \quad (4.18)$$

All of the correction terms in equation (4.15) are proportional to one or two powers of D_l; for $D_l = 0$ it reduces to the unbiased result (4.10). The function D_l arises when one contracts the B-mode template over the pair of observed E-modes that enter explicitly. In detail,

$$\langle B^{\mathrm{temp}}(\boldsymbol{l})\rangle_{E^{\mathrm{obs,LAT}}} = B^{\mathrm{obs,LAT}}(\boldsymbol{l}) D_l \,. \quad (4.19)$$

All of the correction terms retained in equation (4.15) arise from such contractions. For example, since E- and B-modes are uncorrelated, the disconnected contribution to

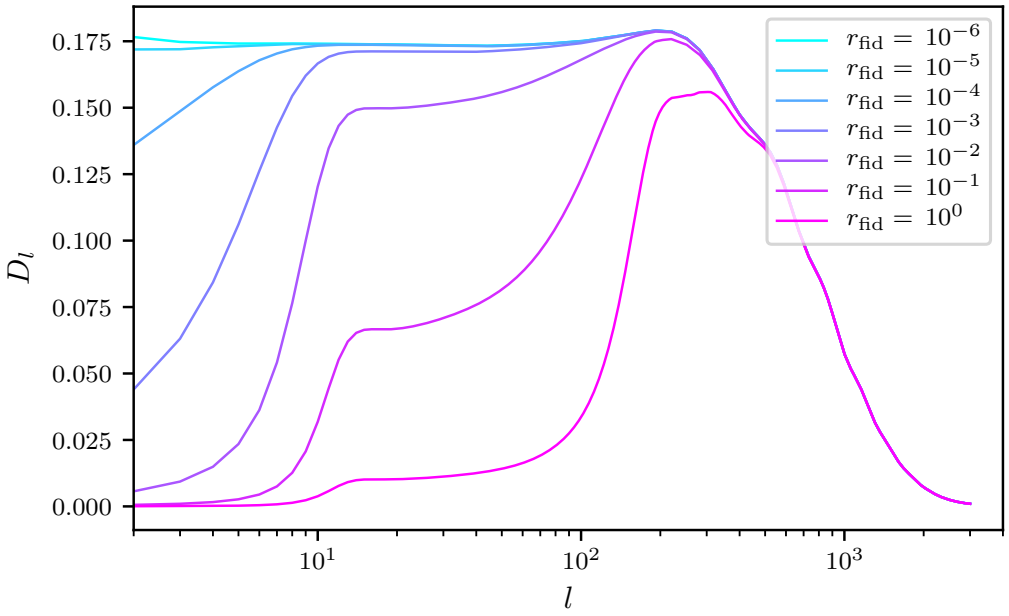

Fig. 4.2 Evaluation of D_l, defined in equation (4.17), for several values of the fiducial $r_{\rm fid}$ in the filter $1/C_l^{BB,\rm obs,fid,LAT}$ applied to the B-modes in lensing reconstruction with the EB quadratic estimator. The experimental set-up is as in figure 4.1.

$\langle B^{\rm temp}(\boldsymbol{l}_1) B^{\rm obs,\,SAT}(\boldsymbol{l}_2)\rangle$ gives a term

$$\begin{aligned}\langle B^{\rm temp}(\boldsymbol{l}_1) B^{\rm obs,\,SAT}(\boldsymbol{l}_2)\rangle &\supset D_{l_1}\langle B^{\rm obs,LAT}(\boldsymbol{l}_1) B^{\rm obs,\,SAT}(\boldsymbol{l}_2)\rangle \\ &= (2\pi)^2\delta^{(2)}(\boldsymbol{l}_1+\boldsymbol{l}_2) D_{l_1}\left(\tilde{C}_{l_1}^{BB} + C_{l_1}^{BB,\rm t} + N_{l_1}^X\right) . \end{aligned} \tag{4.20}$$

Note how this involves the cross-correlation of the experimental noise between the SAT and the LAT, N_l^X, and the tensor B-mode power. It is the main correction term and, given that it enters the delensed power through $-2\langle B^{\rm temp}(\boldsymbol{l}_1) B^{\rm obs,\,SAT}(\boldsymbol{l}_2)\rangle$, *suppresses* the power further. (The other correction terms we retain increase the delensed power.)

We can gain further insight into D_l by noting that in the limit of noiseless E-mode observations, and setting the normalisation of the quadratic estimator to $A_L^{EB} = N_L^{(0),EB}$ (which is correct in the usual limit that the fiducial spectra used to inverse-variance filter the CMB fields in the lensing reconstruction are close to the true total power), $D_l \to C_l^{BB,\rm res}/C_l^{BB,\rm obs,fid,LAT}$ [cf. equation (4.10)]. Consequently, in this limit D_l can be interpreted as the ratio of residual lensing power to fiducial power used to inverse-variance filter the B-modes in the lensing reconstruction. More generally, the Wiener filter $\mathcal{W}_l^E$ will reduce D_l below this value. In all cases $0 < D_l < 1$. In figure 4.2, we see that D_l depends strongly on large scales on the fiducial primordial B-mode power

contained in the inverse-variance filters and parametrised by $r_{\rm fid}$. (The figure includes large values of $r_{\rm fid}$ inconsistent with observations but included for illustration.) To understand this behaviour recall that, for $r \sim 0.01$, $C_l^{BB,{\rm t}}$ becomes comparable to the lensing power on large angular scales between $10 < l < 100$. By raising $r_{\rm fid}$ above this value, we are effectively down-weighting the large-scale lensing B-modes in the fields from which the reconstruction is derived. Although this will not significantly affect the fidelity of the lensing reconstruction – which is derived from information coming chiefly from smaller angular scales – it will give a sizeable reduction in D_l and the bias in the total delensed power on large scales.

The result in equation (4.15) is a generalisation of that in Ref. [316] (equation A16 there), which assumes $r = 0$ and separate LAT and SAT observations ($N_l^X = 0$). An important insight from our result is that the bias term responsible for the additional suppression of power, equation (4.20), is proportional to the *total* observed B-mode power, and not simply its lensing component[7]. Crucially, our result thus predicts a suppression of the primordial signal whenever it is present, as first noted in Ref. [477]. This effect is also hinted at in Ref. [312], though the fact that their simulations have $r = 0$ prevents them from making a quantitative statement.

In order to assess the validity of the model in equation (4.15), we compare it to the output of applying the reconstruction and delensing pipelines to simulations (detailed in appendix A.2) of an experiment with characteristics similar to those of SO [441]. Specifically, the LAT survey has angular resolution $\theta_{\rm FWHM} = 1.5\,{\rm armin}$ and temperature noise level $\Delta_T = 6\,\mu{\rm K\,arcmin}$ (with the polarisation level $\Delta_P = \sqrt{2}\Delta_T$), as in figure 4.1. It is the simulated data from this telescope which we use for the purpose of lensing reconstruction, with $l_{\rm max} = 3000$. The SAT survey has $\theta_{\rm FWMH} = 17\,{\rm arcmin}$, $\Delta_T = 2\,\mu{\rm K\,arcmin}$ and $\Delta_P = \sqrt{2}\Delta_T$. Where needed for calculations of the power spectrum variance, we assume the SAT survey covers approximately 2.8 % of the sky (and is fully contained within the wider LAT survey). The simulations have tensor-to-scalar ratio $r = 0.01$. The results are shown in figure 4.3. The biased delensed power spectrum (yellow curve in the top panel) is seen to be in excellent agreement with equation (4.15), shown as the dashed black curve. The differences are smaller than 0.5 % on all scales. For lower noise levels, the level of agreement is expected to worsen as bias terms neglected by our model play an increasingly significant role. Since the most relevant of those terms (the contribution to the six-point function from the first term on the right of equation A.10) makes a positive contribution to

[7]The model of equation (4.18) (with $N_l^X = 0$) can be obtained from equation (A.16) of Ref. [316] by adding $-2D_l C_l^{BB,{\rm t}}$ and including a primordial component in all the B-mode auto spectra.

the power, equation (4.15) is expected to underestimate the amplitude of the biased delensed power spectrum. Indeed, we simulate a single-telescope experiment with $\theta_{\rm FWHM} = 6\,\text{arcmin}$ and $\Delta_T = 3\,\mu\text{K}\,\text{arcmin}$ and find that the modelled biased spectrum is around 2–3 % lower than its simulated counterpart.

The bias in the delensed spectrum is around 80 % of the signal power, $C_l^{BB,t}+C_l^{BB,\rm res}$, in the unbiased delensed spectrum for the configuration in figure 4.3 (see discussion below). This bias would need to be modelled or otherwise mitigated in a likelihood analysis if inferences on the tensor-to-scalar ratio are not to be biased. One simple way to remove the bias in the delensed spectrum on the scales relevant for searches for primordial B-modes was noted by Ref. [477]: exclude from the reconstruction any B-modes that overlap in scales with the B-modes we wish to delens. This follows from the local character of the bias, whose origin is given in equation (4.19), meaning that it will be avoided at a given multipole as long as *that* multipole is removed from the B-field used for the lensing reconstruction. For the purpose of primordial B-mode searches, we shall remove reconstruction B-modes on the largest angular scales $l \leq l_{\rm cut}$. In this case, equation (4.19) becomes

$$\langle B^{\rm temp}(\boldsymbol{l})\rangle_{E^{\rm obs,LAT}} = B^{\rm obs,LAT}(\boldsymbol{l}) D_l \Theta(l - l_{\rm cut})\,, \tag{4.21}$$

where $\Theta(l)$ is the Heaviside function, and so the bias terms in the delensed power spectrum vanish for $l \leq l_{\rm cut}$. Note that the normalisation and noise of the EB quadratic estimator are changed, albeit by a small amount, on all scales by excising the input B-modes at certain scales, and D_l (for $l > l_{\rm cut}$) needs to be calculated with the modified normalisation and Wiener filter; see equation (4.17). Equivalently, we can think of effectively setting to infinity the noise on the B-modes used *in the reconstruction* on the scales that we wish to exclude. In this case, D_l goes to zero for $l \leq l_{\rm cut}$, and both equation (4.15) and (4.18) reduce to the unbiased spectrum of equation (4.9). Averting the bias in this way comes at the cost of a lower signal-to-noise lensing reconstruction as information is being discarded, although the degradation is expected to be minor since most of the lensing information is obtained from smaller scales of the polarisation fields. In order to take this effect into account when computing the delensed power spectrum below the cutoff using equation (4.10), we must make sure to calculate C_l^W using a Wiener filter that includes the higher reconstruction noise. When this modification is included, the simple unbiased model agrees very well with the simulated spectrum, as shown in figure 4.3 for the case of $l_{\rm cut} = 300$, with differences between the two less than 0.2 % for an SO-like experiment. Imposing a cutoff at $l_{\rm cut} = 300$ leads to a lower signal-to-noise lensing reconstruction and a small decrease in C_l^W which, on

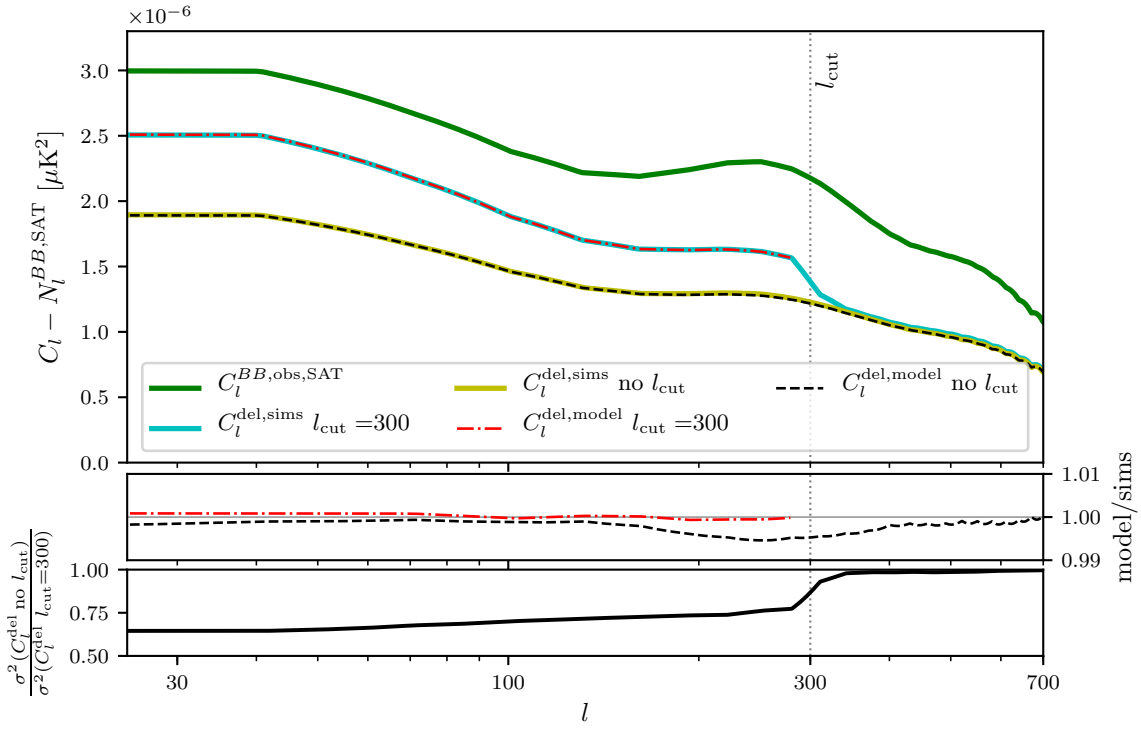

Fig. 4.3 *Upper panel*: noise-subtracted simulated power spectra of the observed B-mode (green), biased residual after delensing with $\hat{\phi}^{EB}$ (yellow) and residual after delensing with a reconstruction cutoff at $l_{\mathrm{cut}} = 300$ (cyan). The shaded regions represent the variance of each of the delensed spectra, obtained from simulations. Notice that the biased spectrum (yellow) has less variance than its unbiased counterpart (cyan). Also plotted are noise-subtracted theoretical curves modelling delensed spectra with (red, dot-dashed) and without (black, dashed) an l_{cut}. *Middle Panel*: ratio of model-to-simulated delensed power spectrum amplitude for the biased (black, dashed) and unbiased (red, dot-dashed) cases. *Lower panel*: ratio of delensed power spectrum variance in the case where no l_{cut} is imposed to that where $l_{\mathrm{cut}} = 300$, obtained from simulations. All curves are for an experiment with characteristics similar to the Simons Observatory, as described in the text.

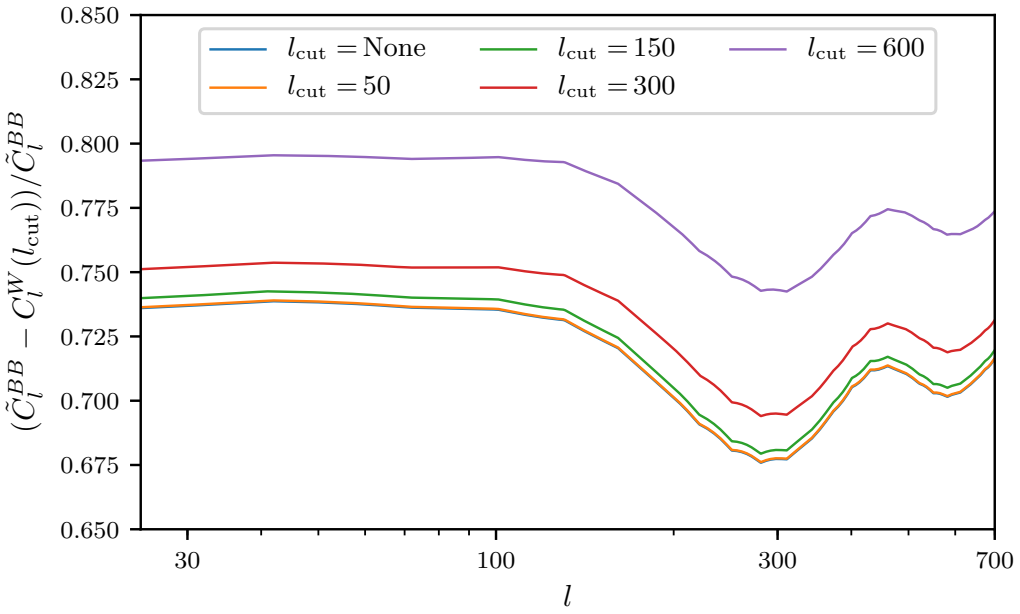

Fig. 4.4 Remaining fraction of lensing B-mode power after delensing with an EB quadratic estimator for different choices of the cutoff, for an experiment with LAT specifications as in figure 4.1. Note that the curves with $l_{\rm cut} = 50$ and no $l_{\rm cut}$ overlap visually.

large angular scales, results in an increase of the residual lensing power spectrum and a degradation of delensing efficiency by approximately 2 %. Several techniques have been suggested to reduce this small degradation, including realisation-dependent methods [312] and an upgrade of the cutoff approach which involves splitting the whole multipole space into "notches" within which the bias can be avoided by excluding modes common to the notch and the reconstruction [477, 420].

Although the bias from internal delensing can be easily removed on large scales with the techniques just discussed, an alternative is to model explicitly the biased delensed spectrum as part of any subsequent likelihood analysis. Figure 4.3 suggests it is worth exploring this approach further since the bias not only suppresses the delensed B-mode spectrum beyond what can be attributed to the (partial) removal of lensing effects, but also reduces its variance. Indeed, in figure 4.3 the variance of the biased delensed spectrum is roughly 65 % of that associated with the unbiased case (the latter with $l_{\rm cut} = 300$). If the power spectrum bias were independent of the primordial B-mode power, this reduction in variance would translate directly into improved constraints on the tensor-to-scalar ratio (assuming there is no significant difference in the non-Gaussian correlations between the power spectra at different

multipoles; see section 4.5). However, part of the bias does depend on the primordial spectrum, suppressing the contribution of $C_l^{BB,t}$ in the biased delensed spectrum by a factor $(D_l - 1)^2$ (see equation 4.15).

The suppression of the primordial signal in the biased delensed spectrum acts as a multiplicative bias. We can remove this by renormalising by $(D_l - 1)^{-2}$, in which case the contribution from $C_l^{BB,t}$ is the same as for unbiased delensing:

$$\frac{C_l^{BB,\mathrm{del}}}{(D_l-1)^2} = C_l^{BB,\mathrm{del,unbiased}} + \left(\frac{D_l}{D_l-1}\right)^2 \left[C_l^W + N_l^{BB,\mathrm{LAT}} + N_l^{BB,\mathrm{SAT}}\left(\frac{2}{D_l}-1\right) - \frac{2}{D_l}N_l^X\right], \quad (4.22)$$

with $C_l^{BB,\mathrm{del,unbiased}}$ as defined in equation (4.9). The last three noise terms on the right-hand side vanish for the case of $B^{\mathrm{obs,LAT}} = B^{\mathrm{obs,SAT}}$, i.e., when the same maps are used in all parts of the analysis, and are positive when $B^{\mathrm{obs,LAT}}$ and $B^{\mathrm{obs,SAT}}$ have independent instrument noise ($N_l^X = 0$) since $0 < D_l < 1$. On the other hand, the term proportional to C_l^W is always positive. Crucially, this means that, in presence of the bias, the renormalised delensed power is generally larger than from the unbiased approach.[8] In other words, the primordial power is always suppressed by a larger fraction than the sources of (lensing and experimental) noise. This is illustrated in figure 4.5 where we see that, for the experimental configuration adopted in figure 4.3, the signal-to-noise noise on a primordial component is lower when the bias is allowed to play a part and modelled than in the alternative approaches where the bias is avoided – worse, even, than in the case of no delensing. In section 4.6, we shall see that this indeed translates to errors on estimates of r from a maximum-likelihood inference pipeline that inevitably increase (in a statistical sense) whenever the bias is modelled instead of avoided. For noise levels lower than those considered here, we expect the approximate expression for the biased delensed spectrum, equation (4.15), to underestimate the true power, as noted above, with the dominant correction coming from the first term on the right of equation (A.10). In this term, B-modes only enter through a connected four-point function of the form $\langle BEEB\rangle_c$, which receives no contribution from tensor modes (ignoring lensing for these). It follows that the additional term adds power but

[8] Mitigating the bias by excluding large-scale B-modes from the reconstruction will increase $C_l^{BB,\mathrm{del,unbiased}}$ a little since the reconstruction is noisier (figure 4.4). For our instrument configuration, this increase is only around 2 % of $\tilde{C}_l^{BB}$ or 8 % of C_l^W on large scales. By way of comparison, for the $N_l^X = 0$ case, the instrument noise terms in square brackets in equation (4.22) are about $25C_l^W$ (taking $\tilde{C}_l^{BB}$ equivalent to 5 μK arcmin white noise and $C_l^W = 0.25\tilde{C}_l^{BB}$), and on multiplying by $D_l^2/(D_l-1)^2 \approx 0.045$, the additional power over $C_l^{BB,\mathrm{del,unbiased}}$ is about $1.1C_l^W$, which is worse than doing no delensing at all.

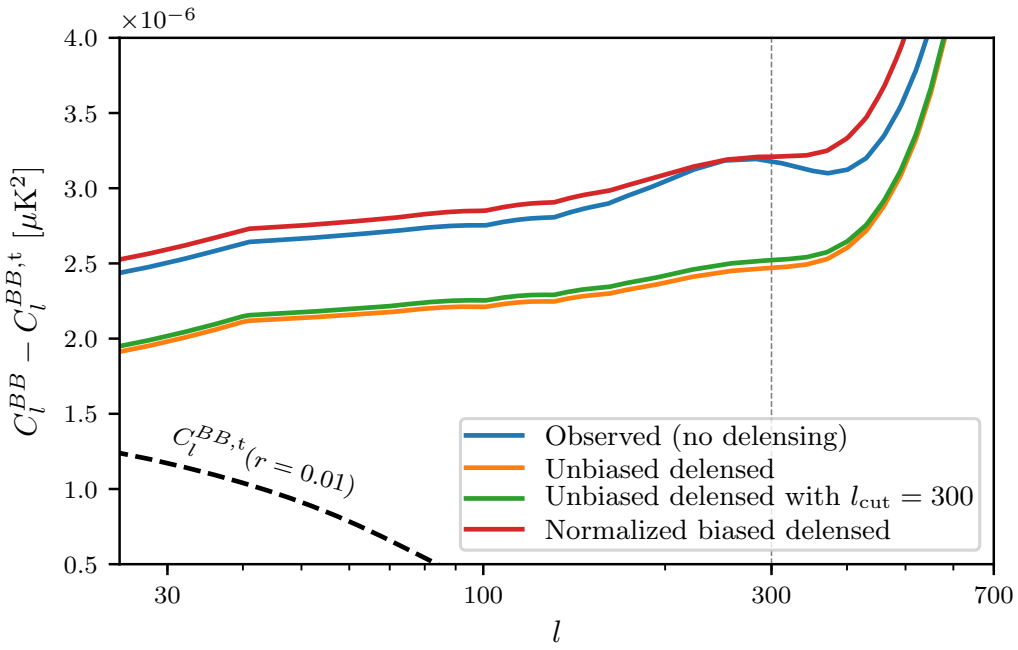

Fig. 4.5 Effective noise power (i.e., the difference between the total delensed power and the primordial contribution) for different estimators from which a primordial B-mode signal (black dashed) is to be extracted. In the biased case, the spectrum is first renormalised so that the amplitude of the primordial power is the same as in the unbiased cases. The experimental set-up is the same as in figure 4.3.

does not couple to $C_l^{BB,t}$, and so further reduces the signal-to-noise on the primordial signal.

The renormalised spectrum of equation (4.22) is lower, all other things being equal, if the same maps are used for all parts of the analysis. The reason is that in this case the experimental noise in the reconstruction and in the B-modes to be delensed are correlated, allowing the disconnected couplings (A.15) and (A.16) to suppress the experimental noise contribution to the delensed power spectrum by the same fraction as for the primordial signal. If, on the contrary, the noise is uncorrelated between the reconstruction and the B-modes to delens, it will not contribute to the disconnected term (A.16) and will consequently be suppressed by a smaller amount than the signal – in fact, it will be amplified relative to the unbiased case by coupling (A.15).

The degradation in signal-to-noise on the primordial B-mode power in the biased case can be understood by noticing that, in the case $N_l^{BB,\mathrm{LAT}} = N_l^{BB,\mathrm{SAT}} = N_l^X$, the disconnected couplings (A.15) and (A.16) combine with the terms retained in the unbiased calculation to yield a suppression of the primordial power and experimental noise by an equal fraction, while for the lensing contribution there is an additional

(positive) term, equation (A.11), which reinstates some lensing power while leaving the primordial signal unaffected. This last contribution arises from the connected coupling of the B-mode in one of the templates and the EEB fields in the other template. This is not the only term that restores lensing power, since the partially-connected six-point function (A.6) coupling the lensing part of $\hat{\phi}$ across templates has a similar effect. However, the latter is already included in the unbiased calculation.

4.5 Covariances of delensed power spectra

The precision with which we can isolate a primordial component from the observed (or delensed) B-mode power spectrum is ultimately determined by the covariance of the latter. The non-Gaussian covariance of lensed CMB spectra is well understood by now [446, 453, 36, 347] and models exist that allow for its numerical evaluation. In this work, we use the publicly-available code `LensCov` [347] to compute the theoretical bandpower covariances for observations corresponding to our choice of cosmology and experimental parameters. We find good agreement between this theoretical computation and results from simulations after applying the appropriate binning and sky fraction corrections, as illustrated by figures 4.6 and 4.7. For visualisation purposes, we plot the cross-correlation coefficient of bandpowers, defined as

$$R_{l_1 l_2}(\tilde{C}_l^{BB}) \equiv \frac{\mathrm{Cov}(\tilde{C}_{l_1}^{BB}, \tilde{C}_{l_2}^{BB})}{\sqrt{\mathrm{Cov}(\tilde{C}_{l_1}^{BB}, \tilde{C}_{l_1}^{BB})\mathrm{Cov}(\tilde{C}_{l_2}^{BB}, \tilde{C}_{l_2}^{BB})}}, \tag{4.23}$$

where $\mathrm{Cov}(\tilde{C}_{l_1}^{BB}, \tilde{C}_{l_2}^{BB})$ is the covariance of the binned angular power spectrum

$$\mathrm{Cov}(\tilde{C}_{l_1}^{BB}, \tilde{C}_{l_2}^{BB}) = \langle \tilde{C}_{l_1}^{BB} \tilde{C}_{l_2}^{BB} \rangle - \langle \tilde{C}_{l_1}^{BB} \rangle \langle \tilde{C}_{l_2}^{BB} \rangle, \tag{4.24}$$

and the angle brackets denote averaging over realisations of either the lensed or delensed CMB and noise.

The delensed bandpower covariance is more complicated, but it can begin to be understood by studying the case where the lensing reconstruction is independent of the CMB. Reference [317] presents the following extension of the lensed B-mode power covariance to this delensed case under the assumptions that the E-modes used in the template are cosmic-variance limited on all relevant scales (i.e., for multipoles $l \lesssim 2000$)

and that ϕ is Gaussian:

$$\begin{aligned}\mathrm{Cov}(\tilde{C}_{l_1}^{BB,\mathrm{del}}, \tilde{C}_{l_2}^{BB,\mathrm{del}}) \approx \quad & \frac{2}{2l_1+1}\left(\tilde{C}_{l_1}^{BB,\mathrm{del}}\right)^2 \delta_{l_1 l_2} \\ & + \sum_l \left(\frac{\partial \tilde{C}_{l_1}^{BB,\mathrm{res}}}{\partial C_l^{EE}} \frac{2}{2l+1} (C_l^{EE})^2 \frac{\partial \tilde{C}_{l_2}^{BB,\mathrm{res}}}{\partial C_l^{EE}} \right) \\ & + \sum_l \left(\frac{\partial \tilde{C}_{l_1}^{BB,\mathrm{res}}}{\partial C_l^{\phi\phi}} \frac{2}{2l+1} (C_l^{\phi\phi})^2 \frac{\partial \tilde{C}_{l_2}^{BB,\mathrm{res}}}{\partial C_l^{\phi\phi}} \right). \end{aligned} \tag{4.25}$$

The assumption that E-modes are limited by cosmic variance on the relevant scales is not strictly true for the specifications adopted here. Although it is not difficult to generalise equation (4.25) to account for noise in the E-modes, Ref. [317] finds that the covariance without E-mode noise still matches well that obtained from simulations of experiments with the noise levels of current and upcoming experiments.

We evaluate equation (4.25) by modifying the `LensCov` code for the calculation of lensed B-mode covariances. Along with a modified Gaussian variance (the first term on the right of equation 4.25), we must also replace the derivative terms with those appearing above. We calculate these analytically from the leading-order expression of equation (4.10). The results are shown in figure 4.6. From this figure, and more acutely from figure 4.7, it is clear that delensing reduces the non-Gaussian correlation between scales introduced by lensing [446], effectively increasing the number of independent pieces of information available. Figures 4.6 and 4.7 also suggest that the simple model of Ref. [317] is consistent – up to Monte-Carlo errors from the finite number (25 000) of simulations[9] – with the simulated covariance of delensed B-mode bandpowers below the cutoff, where $\hat{\phi}$ is effectively independent of B.

[9]It can be shown (assuming that the errors on estimates of individual bandpowers are distributed as Gaussian random variables with appropriate correlations) that the fractional error on an element of the correlation matrix, estimated from N simulations, is

$$\frac{\sigma(R_{ij})}{|R_{ij}|} = \sqrt{\frac{1}{N}\left(1 + \frac{1}{R_{ij}^2}\right)},$$

where R_{ij} are the true correlation coefficients between bandpowers and the mean bandpowers are known in advance. In the more usual case where the angular bandpowers are also estimated from the data, the relation is replaced with

$$\frac{\sigma(R_{ij})}{|R_{ij}|} = \frac{1}{\sqrt{N}} \left| \frac{1}{R_{ij}} - R_{ij} \right|.$$

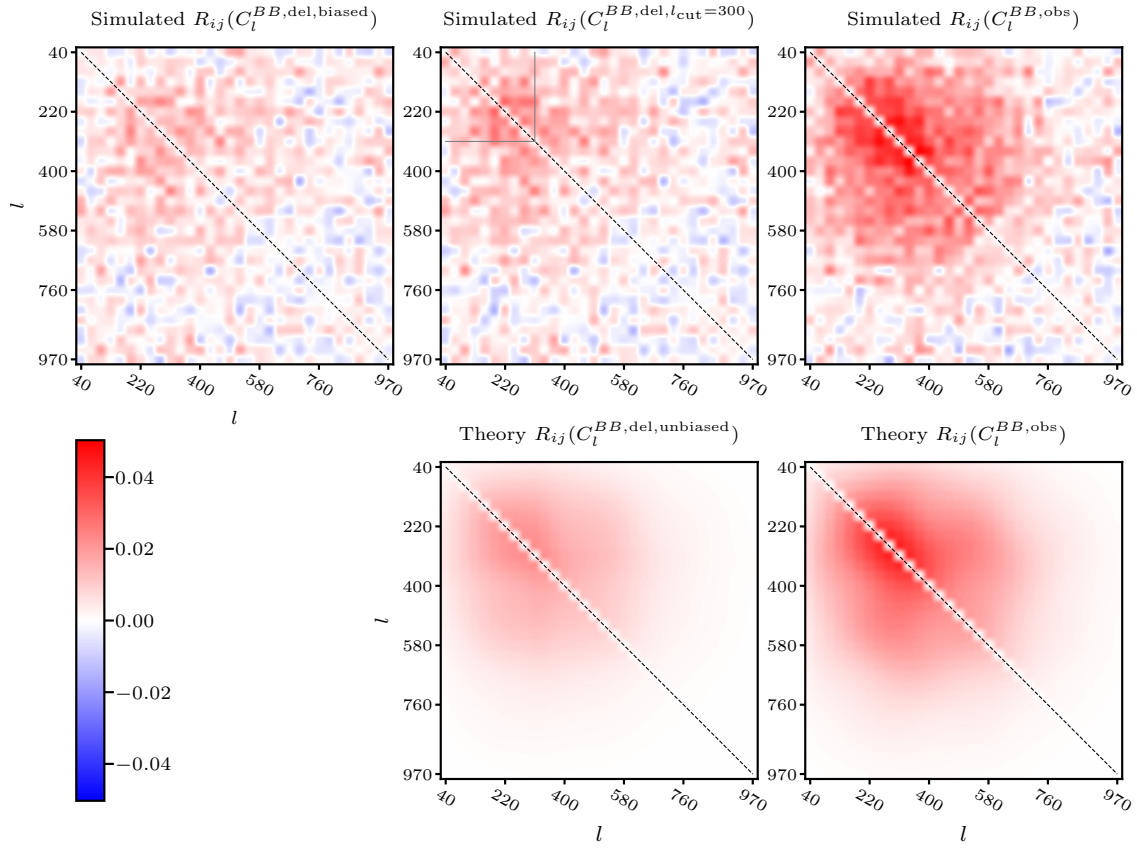

Fig. 4.6 Correlation coefficient of B-mode bandpowers ($\Delta l = 30$) for an experiment with characteristics similar to the Simons Observatory, as described in section 4.4.2, and a SAT sky fraction of 2.8 % (with periodic boundary conditions assumed). The fiducial cosmology includes a primordial B-mode component with $r_{\mathrm{input}} = 0.01$. The top row are obtained from 25 000 simulations and the bottom row are analytic approximations evaluated by modifying `LensCov` [347], as described in the text. *Right column*: observed (lensed and noisy) bandpowers. *Central column*: delensed bandpowers in the case where the bias is avoided by either introducing a cutoff at $l_{\mathrm{cut}} = 300$ (top) – thus avoiding the bias for $l < l_{\mathrm{cut}}$ – or by working with a $\hat{\phi}$ that is independent of B yet just as correlated with the actual ϕ as the reconstructed $\hat{\phi}^{EB}$ employed in the simulated analysis (bottom). *Left column*: biased delensed bandpowers from simulations.

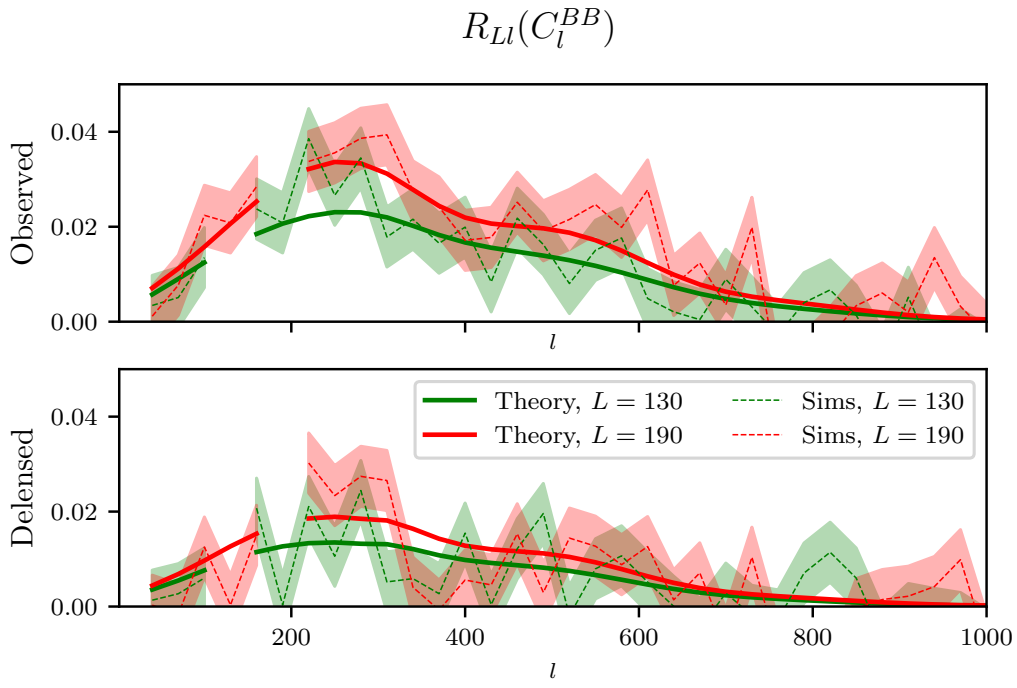

Fig. 4.7 Rows of the correlation matrices of bandpowers of the observed (top) and delensed (bottom) B-modes shown in figure 4.6. Dashed curves correspond to simulated covariances, with the shaded region representing their approximate $1\,\sigma$ simulation error due to the finite number (25 000) of simulations. In the delensed case, the simulations involve a reconstruction $l_{\rm cut} = 300$ so that the delensed power is unbiased below $l < 300$. Theory curves are shown as solid lines, taken from the bottom panels of figure 4.6. Gaps are shown where the correlation coefficient is one.

Finally, we study the bandpower covariance in the case where no $l_{\rm cut}$ is imposed and thus the delensed B-mode spectrum is biased. An analytic exploration of this case is beyond the scope of this work, since the framework of appendix A.1.2 suggests that the covariance receives contributions from 12-point correlators of lensed polarisation fields although some simplifications are likely possible. It can, however, be obtained from simulations, as shown in figure 4.6. Interestingly, at the noise levels considered here, the lower variance induced by the bias does not appear to be accompanied by the larger off-diagonal correlations between bandpowers seen by Ref. [319]. The most likely explanation is that the Gaussian experimental noise dominates the variance on the small angular scales where we would expect the bias to induce strong covariance between delensed bandpowers (cf. figure 9 of [319]). This suppresses the correlation and increases the fractional Monte-Carlo error to the point where the signal gets buried in the noise.

In summary, we have seen that, for an experiment with characteristics similar to SO, the EB lensing reconstruction bias brings about a reduction in the variance of the power spectrum of delensed B-modes while the extent of the correlations between bandpowers remains comparable to the unbiased case. If the primordial signal were not suppressed by the bias, analysis of the biased delensed bandpowers (with appropriate modelling of the bias) would lead to improved constraints on the tensor-to-scalar ratio. However, we have already seen in section 4.4.2, that the bias acts multiplicatively on the primordial power, suppressing the signal more than the Gaussian variance. We thus expect constraints on r to worsen in this case, which we now demonstrate through a simulated maximum-likelihood analysis.

4.6 Maximum-likelihood inference of r

Although the likelihood of CMB temperature and polarisation data can in principle be written down exactly, even accounting for the effects of lensing [189, 75, 298], in practical applications with realistic survey complexities, easily-computable summary statistics (e.g., angular power spectra) and their approximate sampling distributions are typically preferred (see [149] for a review). For power spectra of approximately Gaussian fields, several such likelihood approximations involving the estimated power spectra and their covariance appear in the literature. We choose to work with the approximation developed in Ref. [163], and which was used by the BICEP/Keck Collaboration to analyse their most recent data [48]. For our application here, it takes

the form

$$-2\ln\mathcal{L}(r|\{\hat{C}_i^{BB}\}) = \sum_{ij}[g(\hat{C}_i^{BB}/C_i^{BB})C_i^{BB,\mathrm{fid}}] \times \mathrm{Cov}^{-1}(C_i^{BB,\mathrm{fid}}, C_j^{BB,\mathrm{fid}})[C_j^{BB,\mathrm{fid}} g(\hat{C}_j^{BB}/C_j^{BB})], \quad (4.26)$$

where $g(x) \equiv \mathrm{sign}(x-1)\sqrt{2(x-\ln x-1)}$ and $\hat{C}_i^{BB}$ (C_i^{BB}) denotes the ith empirical (model) bandpower of the delensed B-mode spectrum. Only multipoles below $l_{\mathrm{max}} = 280$ are used in the inferences that follow. An advantage of using this approximate likelihood is that the non-Gaussian character introduced by lensing can be accounted for through the fiducial delensed bandpower covariance, $\mathrm{Cov}(C_i^{BB,\mathrm{fid}}, C_j^{BB,\mathrm{fid}})$, which only needs to be computed (either analytically or via simulations) and inverted once. As long as it matches the fiducial $C_l^{BB,\mathrm{fid}}$, the exact form of this fiducial covariance has a negligible impact on the resulting inferences. Indeed, we verify that there is no appreciable change in the inferences when we vary the fiducial level of primordial B-mode signal. Furthermore, Ref. [163] shows that, even if the fiducial model deviates from the truth, the likelihood is still exact in the full-sky, isotropic limit with Gaussian fields. Hence, all analyses presented henceforth use fiducial bandpower amplitudes and covariances with the same r_{input}.

The question remains whether the bandpower covariances ought to be modelled or whether they could simply be obtained from simulations. In section 4.5 we saw that, while it is possible to write a simple analytic model for the covariance of *unbiased* delensed bandpowers, doing the same for the *biased* case is more difficult. To address this question partially, we compare the distribution across simulations of the maximum-likelihood estimates for the tensor-to-scalar ratio $\hat{r}_{\mathrm{ML}}$ and their associated uncertainties $\sigma(\hat{r}_{\mathrm{ML}})$ – derived from the second derivative of the log-likelihood function at the maximum-likelihood point – in the cases where the bandpower covariance is obtained analytically (using `LensCov`) or from simulations. We do this for the cases of no delensing and unbiased delensing, the latter excluding B-modes below $l_{\mathrm{cut}} = 300$ from the simulated fields used for reconstructing $\hat{\phi}^{EB}$. The simulations used in these comparisons, and for all results presented in this section, assume the experimental set-up described in section 4.4.2. The likelihood curves for these two cases are shown in figure 4.8 for a typical realisation, and the distribution of $\hat{r}_{\mathrm{ML}}$ and $\sigma(\hat{r}_{\mathrm{ML}})$ across 25 000 simulations are given in figure 4.9. We find only a slight degradation in the errors on r when simulated bandpower covariances are employed, justifying our ensuing use of simulated matrices.

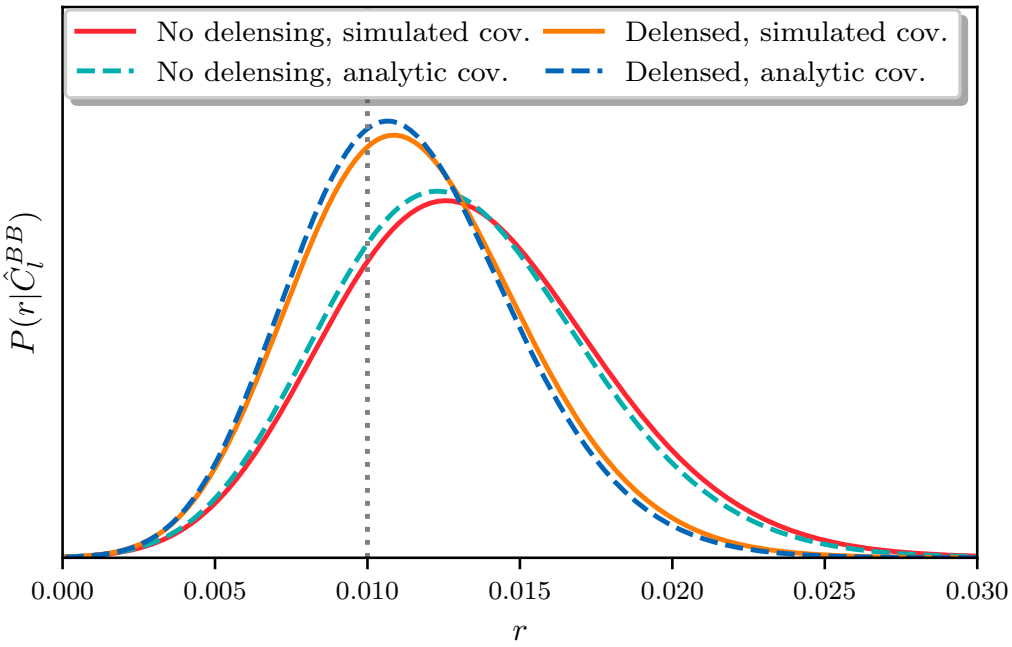

Fig. 4.8 Typical likelihood functions for the tensor-to-scalar ratio r for analyses of simulated data with and without (unbiased) delensing. In both cases, the use of simulated (solid lines) or analytic (dashed lines) power spectrum covariances is compared and found to be in good agreement. All curves are normalised to have unit area. The input value $r_{\mathrm{input}} = 0.01$ is indicated with the dotted line. The simulations are for the experimental set-up described in section 4.4.2.

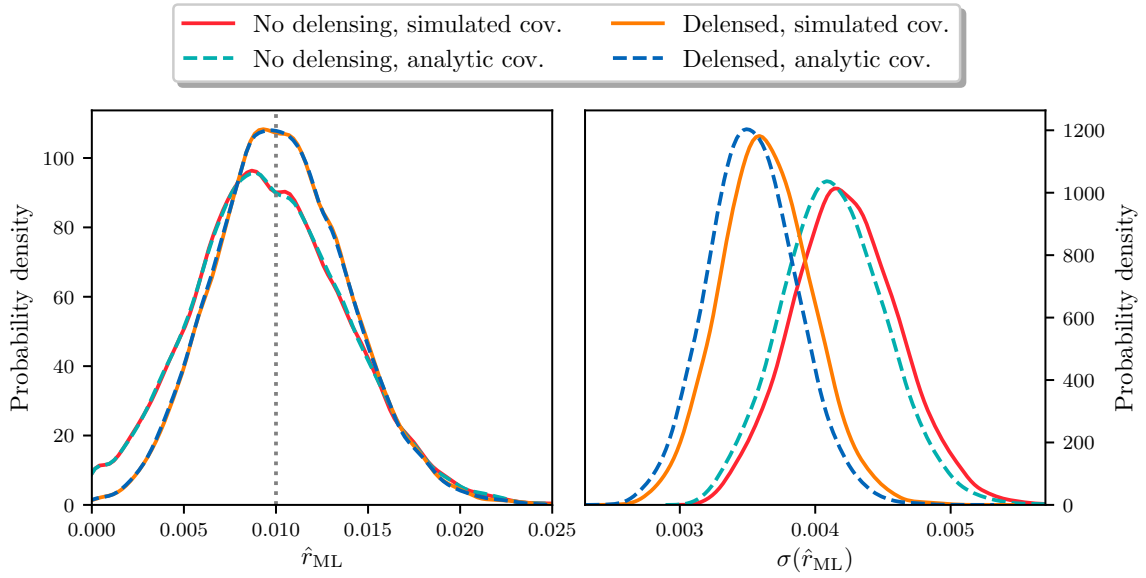

Fig. 4.9 Distributions of $\hat{r}_{\mathrm{ML}}$ (left) and $\sigma(\hat{r}_{\mathrm{ML}})$ (right) across simulations comparing the use of analytic (dashed lines) or simulated (solid lines) power spectrum covariances in the cases of no delensing and unbiased delensing. The distributions have been estimated from 25 000 simulated maximum-likelihood inferences, with a typical likelihood curve as shown in figure 4.8, using a Gaussian kernel density method with a bandwidth of 5×10^{-4} for the left panel and 7×10^{-5} for the right.

We illustrate the need to account for (or mitigate) the bias in the delensed B-mode power spectrum when delensing with $\hat{\phi}^{EB}$ with the following naïve analysis. For the empirical spectrum $\hat{C}_l^{BB}$ used in the likelihood of equation (4.26), we take the simulated biased delensed spectrum, but all other fiducial and model spectra and covariances in the likelihood are unbiased – that is, calculated assuming that $\hat{\phi}$ is independent of the CMB but with the same correlation to ϕ as $\hat{\phi}^{EB}$. In figure 4.10, we verify that ignoring the suppression in the biased empirical spectrum leads to inferences on r that are biased low relative to the input $r_{\rm input} = 0.01$, with a significant number of likelihoods peaking (in the range $r \geq 0$) at $r = 0$, and artificially small typical errors on r. This is also true in the null case where $r_{\rm input} = 0$, as shown in figure 4.11.

We have already discussed, in section 4.4.2, several ways in which the bias can be taken into account: modelling the biased spectrum; renormalizing the biased spectrum to restore unit response to primordial power; or imposing a low-l cutoff on the B fields used for estimating $\hat{\phi}$. The first two approaches should yield equivalent results on r, but are expected to be very non-optimal since the bias reduces the primordial power by a larger fraction than the rest of the power (see figure 4.5). Mitigating the bias with a cut-off is preferred, although there is a small penalty due to the lower signal-to-noise lensing reconstruction in this case. In figure 4.10, we quantitatively compare these methods. For our experimental set-up and input value $r_{\rm input} = 0.01$, we see that modelling the bias inflates the errors on r by typically 15 %[10] compared to when a cutoff at $l_{\rm cut} = 300$ is imposed, translating to a slightly wider distribution of $\hat{r}_{\rm ML}$ and a lower number of detections of non-zero r. The figure also shows that, for our set-up, modelling the bias degrades the sensitivity on r to a level comparable to (or even slightly worse than) the case of no delensing, as suggested by our earlier results for the normalised power in this case (figure 4.5).

4.7 The $B^{\rm obs}(B^{\rm obs} - B^{\rm temp})$ estimator

In section 4.4.2, we saw that the bias from internal delensing with an EB estimator *reduces* the signal-to-noise on a primordial contribution to the power spectrum of delensed B-modes. We attributed this to the coupling in equation (A.11), which arises in the cross-correlation of the B-mode lensing template with itself, and that restores some of the lensing power while leaving the primordial signal unaffected. This

[10]The exact figure depends on the experimental characteristics and $r_{\rm input}$. We remind the reader that our likelihood results assume that lensing reconstruction is done exclusively by an EB quadratic estimator and so underestimate the actual internal-delensing performance.

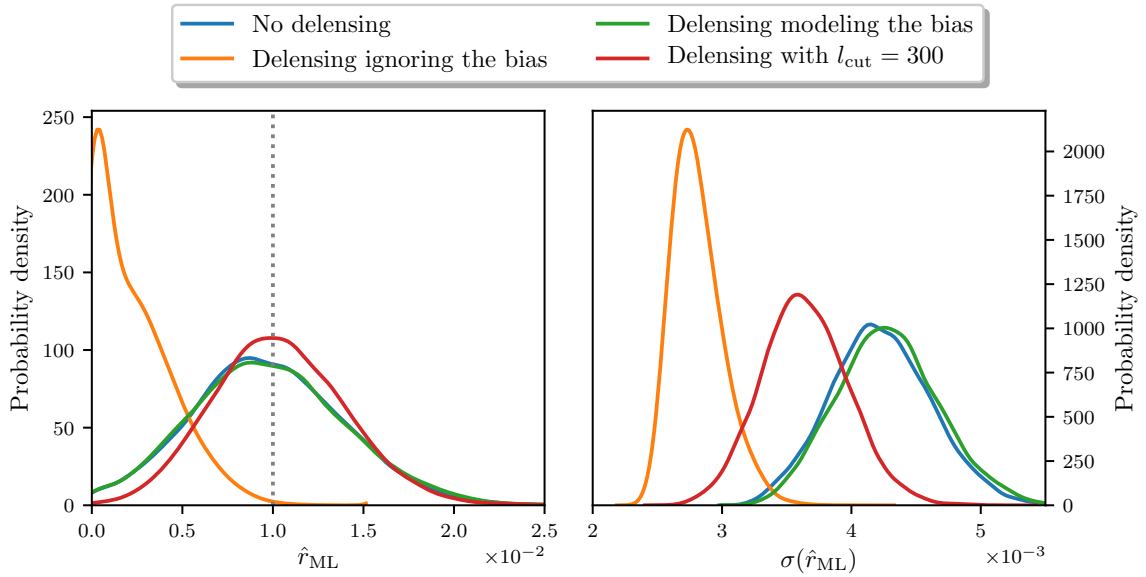

Fig. 4.10 Distributions of $\hat{r}_{\rm ML}$ (left) and $\sigma(\hat{r}_{\rm ML})$ (right) across simulations for different delensing analyses. *Blue*: no delensing. *Orange*: biased delensing, based on a reconstructed $\hat{\phi}^{EB}$ that does not impose a low-l B-mode cutoff, with no attempt to model the resulting power spectrum bias in the likelihood. This results in $\hat{r}_{\rm ML}$ being biased low (and a significant number of simulated likelihoods that peak at $r = 0$) and with artificially small errors. *Green*: biased delensing, but with the power spectrum bias modelled as described in section 4.4.2. This mitigates the bias in r but, for our experimental set-up, has comparable performance to no delensing. *Red*: a cutoff at $l_{\rm cut} = 300$ is imposed on the B-modes used in the reconstruction, avoiding the bias to the delensed B-mode power spectrum below $l_{\rm cut}$. There is no bias in r in this case, and delensing reduces $\sigma(\hat{r}_{\rm ML})$ as intended. All analyses employ simulated bandpower covariances.

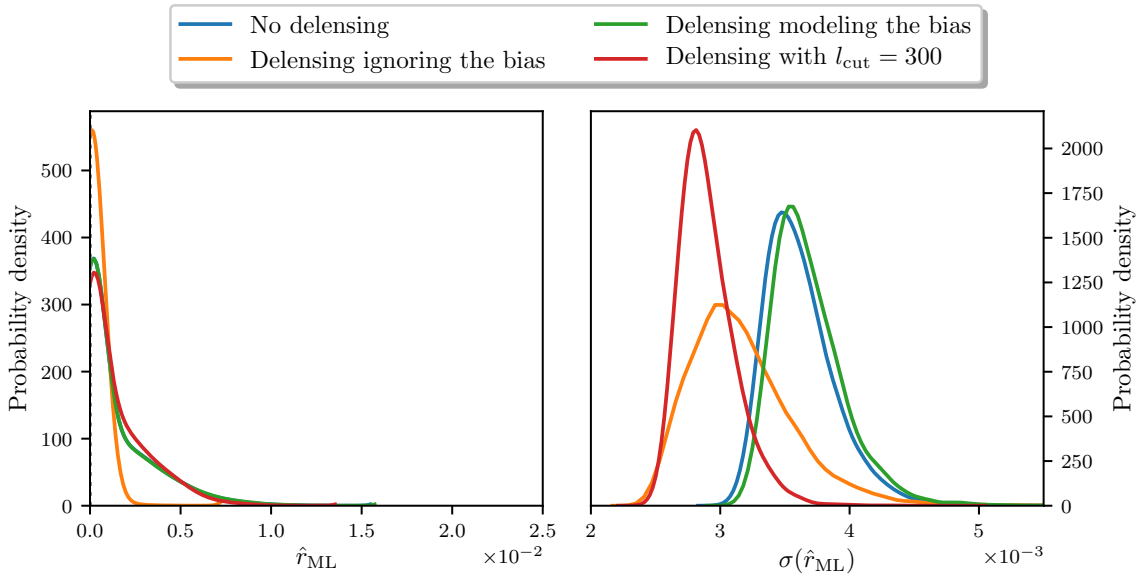

Fig. 4.11 Same as figure 4.10, but in the null scenario of $r_{\rm input} = 0$.

motivates the idea of considering an alternative power spectrum estimator of the form $B^{\rm obs}(B^{\rm obs} - B^{\rm temp})$, i.e., the cross-correlation of the observed B-modes with the delensed B-modes, $B^{\rm del} = B^{\rm obs} - B^{\rm temp}$. This estimator does not involve the cross-correlation of the template with itself, and so avoids couplings such as that in equation (A.11). In the case of no $l_{\rm cut}$ in the lensing reconstruction (such that the B-modes used for reconstruction overlap with those to be delensed on all scales) and two separate surveys, LAT and SAT, the expected value of the cross-correlation is

$$\begin{aligned}\langle B^{\rm obs}(\boldsymbol{l})\left[B^{\rm obs}(\boldsymbol{l}') - B^{\rm temp}(\boldsymbol{l}')\right]\rangle_{\rm biased} \\ = (2\pi)^2\delta^{(2)}(\boldsymbol{l}+\boldsymbol{l}')\Big[(1-D_l)\left(C_l^{BB,\rm res} + C_l^{BB,\rm t} + N_l^{BB,\rm SAT}\right) \\ + D_l\left(N_l^{BB,\rm SAT} - N_l^{X}\right) - D_l C_l^{W}\Big].\end{aligned} \tag{4.27}$$

In the case of a single survey, this reduces to

$$\begin{aligned}\langle B^{\rm obs}(\boldsymbol{l})\left[B^{\rm obs}(\boldsymbol{l}') - B^{\rm temp}(\boldsymbol{l}')\right]\rangle_{\rm biased} \\ = (2\pi)^2\delta^{(2)}(\boldsymbol{l}+\boldsymbol{l}')\Big[(1-D_l)\left(C_l^{BB,\rm res} + C_l^{BB,\rm t} + N_l^{BB}\right) - D_l C_l^{W}\Big].\end{aligned} \tag{4.28}$$

The last term on the right-hand side is always negative. Renormalising the cross-correlation by $(1 - D_l)$ to have unit response to the primordial power, we see that its renormalised value is reduced below the power of the unbiased, delensed spectrum (equation 4.9) by this negative term. While the non-primordial power in both of these spectra decreases monotonically with the experimental noise, the difference between the two is greatest when $C_l^W D_l/(1-D_l)$ peaks. This is the case when the experimental noise level in polarisation is approximately $3\sqrt{2}\,\mu$K arcmin, corresponding to a delensing efficiency of approximately 40 %. For such an experimental configuration, the term $-D_l C_l^W$ reduces the cross-correlation in equation (4.28) by an amount equivalent on large scales to white noise with $\Delta_P \approx 2\,\mu$K arcmin after normalising to have unit response to a primordial signal.

It is instructive to compare the $B^{\rm obs}(B^{\rm obs} - B^{\rm temp})$ estimator above to another defined along similar lines, but which features no overlap between reconstruction B-modes and B-modes to be delensed (for example, by introducing an $l_{\rm cut}$ in the reconstruction, such that $\langle B^{\rm obs}(B^{\rm obs} - B^{\rm temp})\rangle$ is unbiased on scales $l < l_{\rm cut}$). This alternative estimator has expectation value

$$\langle B^{\rm obs}(\boldsymbol{l})(B^{\rm obs}(\boldsymbol{l}') - B^{\rm temp}(\boldsymbol{l}'))\rangle_{\rm unbiased} = (2\pi)^2\delta^{(2)}(\boldsymbol{l}+\boldsymbol{l}')\left(C_l^{BB,{\rm res}} + C_l^{BB,{\rm t}} + N_l^{BB}\right), \tag{4.29}$$

which is the same as the unbiased, delensed power spectrum of equation (4.9). Comparing this to the biased estimator of equation (4.28), we see that, after appropriate renormalisation, the expectation value of the latter is lower than the estimator in equation (4.29), or even the standard power spectrum approach of equation (4.9). Our analytic models for all these different estimators are found to be in excellent agreement with their values in simulations.

In assessing the performance of the cross-correlation estimators for constraining the primordial signal, we remind the reader that, for a cross-correlation, the variance is not determined by the expected value (even in the limit of Gaussian fields). For a single survey, treating both $B^{\rm obs}$ and $B^{\rm del}$ as Gaussian fields, the variances of the

estimators at hand are

$$\frac{1}{(1-D_l)^2}\mathrm{Var}\left(B^{\mathrm{obs}}B^{\mathrm{del}}\right)_{\mathrm{biased}} = \frac{1}{2l+1}\Bigg[2\Big(C_l^{BB,\mathrm{del,unbiased}}\Big)^2 + \Big(\frac{1-2D_l}{1-D_l}\Big)^2 C_l^W C_l^{BB,\mathrm{del,unbiased}} + 2\left(\frac{D_l}{1-D_l}\right)^2\left(C_l^W\right)^2\Bigg], \tag{4.30}$$

$$\mathrm{Var}\left(B^{\mathrm{obs}}B^{\mathrm{del}}\right)_{\mathrm{unbiased}} = \frac{1}{2l+1}\left[2\left(C_l^{BB,\mathrm{del,unbiased}}\right)^2 + C_l^W C_l^{BB,\mathrm{del,unbiased}}\right], \tag{4.31}$$

$$\mathrm{Var}\left(B^{\mathrm{del}}B^{\mathrm{del}}\right)_{\mathrm{unbiased}} = \frac{1}{2l+1}\left[2\left(C_l^{BB,\mathrm{del,unbiased}}\right)^2\right], \tag{4.32}$$

where, recall, $C_l^{BB,\mathrm{del,unbiased}} = C_l^{BB,\mathrm{res}} + C_l^{BB,t} + N_l^{BB}$. Clearly, the Gaussian variance is smallest for the usual $\left(B^{\mathrm{del}}B^{\mathrm{del}}\right)_{\mathrm{unbiased}}$ estimator. Moreover, we will now see that the (co)-variance of both the cross-estimators is dominated by non-Gaussian effects, which further degrade their constraining power.

In figure 4.12, we use simulations of an experiment with $\Delta_P = 3\sqrt{2}\,\mu$K arcmin and $\theta_{\mathrm{FWHM}} = 6$ arcmin to quantify the variance associated with the different estimators. Although the Gaussian variance of equation (4.32) appears to capture correctly the simulated behaviour of the unbiased $\left(B^{\mathrm{del}}B^{\mathrm{del}}\right)$ estimator, the unbiased and renormalised $\left(B^{\mathrm{obs}}B^{\mathrm{del}}\right)$ estimators show variances well in excess of the Gaussian result. This can be attributed to the predominance of non-Gaussian contributions, which also manifest themselves in the strong correlations between bandpowers shown in figure 4.13. Intuitively, the reason why the non-Gaussian character is less acute in $\left(B^{\mathrm{del}}B^{\mathrm{del}}\right)$ than in $\left(B^{\mathrm{obs}}B^{\mathrm{del}}\right)$ is that the former involves two delensed fields and delensing is known to mitigate the correlations between scales introduced by lensing.

Given these considerations, we believe that the estimator of equation (4.28) should lead to inferior constraints on r compared to an analysis involving the usual power spectrum estimator of equation (4.9). A more careful demonstration of this would require working within a maximum-likelihood inference framework, as in section 4.6. Unfortunately, this is not straightforward since standard likelihood approximations are not applicable for a single cross-spectrum. These likelihood approximations are very convenient in the presence of real-world effects such as masking, and for including non-Gaussian power spectrum covariances. Extending these to a single cross-spectrum would require further development.

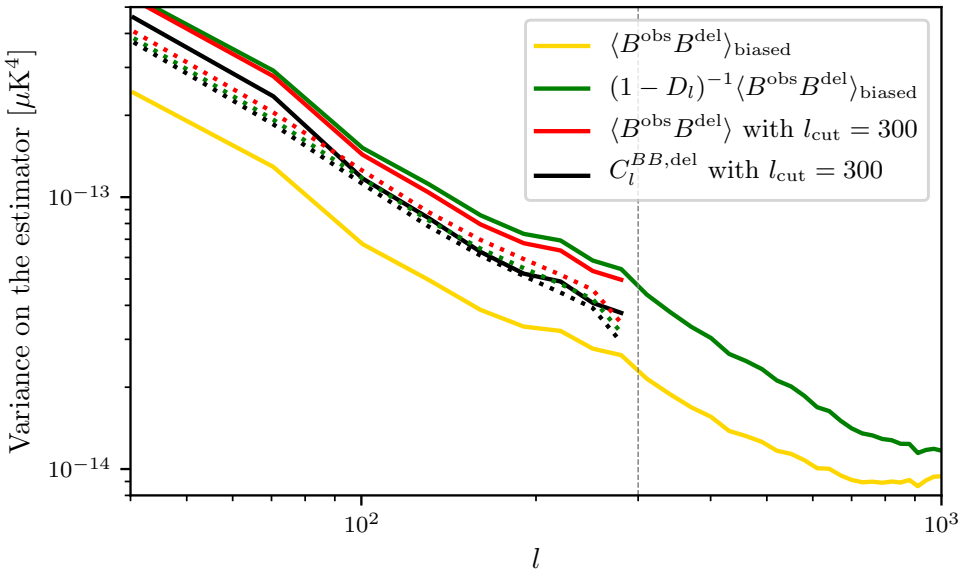

Fig. 4.12 Variances of different spectral estimators from which primordial power is to be extracted, obtained from 25 000 simulations of an experiment consisting of a single survey with $\Delta_P = 3\sqrt{2}\,\mu$K arcmin, $\theta_{\rm FWHM} = 6$ arcmin and covering 2.8 % of the sky. *Yellow*: the biased $(B^{\rm obs}B^{\rm del})_{\rm biased}$ estimator of equation (4.28). *Green*: the same for the case where $(B^{\rm obs}B^{\rm del})_{\rm biased}$ is normalised to have unit response to primordial B-mode power. *Red*: the $(B^{\rm obs}B^{\rm del})_{\rm unbiased}$ estimator of equation (4.28) (only below $l_{\rm cut} = 300$). *Black*: the auto-spectrum of $B^{\rm del}$ in the case where the bias is averted below $l_{\rm cut} = 300$. Dotted lines show the Gaussian variance expected for each estimator, calculated analytically.

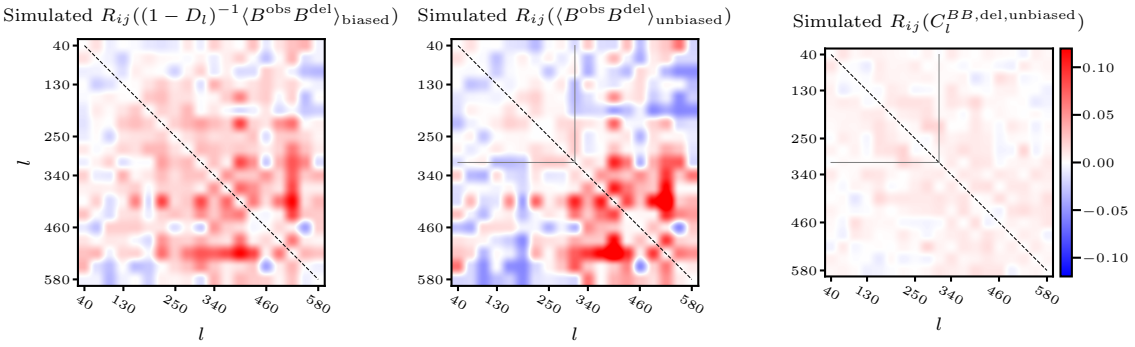

Fig. 4.13 Cross-correlation coefficients of different spectral estimators for the experimental set-up in figure 4.12, estimated from 25 000 simulations. *Right*: delensed B-mode bandpowers in the case where the bias is avoided below $l < l_{\rm cut}$ by introducing a cutoff at $l_{\rm cut} = 300$. *Centre*: $(B^{\rm obs}B^{\rm del})_{\rm unbiased}$ estimator of equation (4.29), unbiased below $l_{\rm cut} = 300$. *Left*: $(B^{\rm obs}B^{\rm del})_{\rm biased}$ estimator of equation (4.28), renormalised to have unit response to any primordial power. All estimators are binned with $\Delta l = 30$.

4.8 Discussion

Searches for primordial B-modes in CMB data already necessarily require the removal of the contamination from gravitational lensing. In the near future, experimental characteristics will be such that the EB quadratic estimator is expected to provide a large fraction of the signal-to-noise on reconstructions of the lensing potential, which is used to perform the delensing procedure. It is well known that any overlap in modes between the B-field to be delensed and the B-field from which the reconstruction is derived biases the amplitude and variance of the delensed power spectrum [477, 312].

In this chapter, we have refined the modelling of this bias, based on a cumulant expansion and identification of the dominant terms, and used simulations to verify its efficacy. Our model is consistent with others in the literature [316, 312] that are valid in the absence of a primordial (gravitational wave) signal, but extends our understanding to include the primordial component. The power spectrum bias acts multiplicatively on the primordial power, suppressing its amplitude. The bias also suppresses lensing and instrument noise power but, crucially, generally less so than for the primordial signal. This leads to a loss of constraining power for primordial B-modes, and this becomes more acute whenever separate surveys (i.e., with independent instrument noise) are used for lensing reconstruction and the study of B-modes on large angular scales.

Fortunately, the bias is completely local in multipole space in the sense that bias to the delensed B-mode power at multipole l originates from B-modes at that same multipole being used in the lensing reconstruction. The bias can therefore be avoided by eliminating overlapping modes in the B-field employed in the reconstruction, and within the context of searches for primordial gravitational waves this can be done with little loss of performance. We have shown that, for any reasonable $l_{\rm cut}$, such elimination of overlapping modes is actually preferable over an approach where the bias is modelled, as it yields improved constraining power. These findings are verified by simulating the reconstruction and delensing procedures and performing maximum-likelihood inferences of the primordial power on the resulting delensed spectra.

Our model for the biased, delensed B-mode power spectrum is in excellent agreement with simulations for experimental noise levels comparable or inferior to those of the Simons Observatory, but we note that the agreement worsens for lower noise levels as new terms that we ignore become relevant. In this limit of low noise, we expect our model to over-estimate the signal-to-noise so that our claim that retaining, but modelling, the bias hinders efforts to constrain the primordial signal continues to hold. We therefore recommend that any attempt to delens large-scale B-modes internally

building on lensing information gleaned from the B-modes themselves – be it via quadratic estimators or likelihood-based techniques – feature the excision of large-scale B-modes from the lensing inference.

Finally, we have considered alternative cross-correlation estimators for the primordial power involving the observed and delensed B-modes, with a view to removing some couplings in the biased spectrum that degrade the signal-to-noise on r. We provided analytic models for the expectation values of these cross-correlations and verified these against simulations. However, we showed that ultimately these estimators have lower signal-to-noise to primordial power than the auto-power spectrum of the (unbiased) delensed fields, due to their cross-correlation character and their increased non-Gaussian covariance between multipoles.

Chapter 5

Modelling CMB lensing biases due to extragalactic foregrounds

5.1 Introduction

We have seen, in previous chapters, that the statistical anisotropy induced by lensing on the CMB can be used to reconstruct maps of the lensing potential — a quantity related to the matter distribution responsible for the deflections, integrated all the way to the last-scattering surface at redshift $z \sim 1100$. Those reconstructions can then be used, for example, to delens B-modes, as we saw in chapter 4. However, there is a wealth of information to be gleaned from the statistics of lensing itself.

Thanks to lensing, CMB observations can be used to investigate phenomena whose imprint only becomes significant after recombination — dark energy, the sum of the neutrino masses, modifications of gravity, and more. If only the information in the primordial CMB was accessible, these models would be highly degenerate with their alternatives; see, e.g., [124, 444], for further details about the angular-diameter-distance degeneracy of the primary CMB.

It is for this reason that a great deal of experimental effort is currently orientated towards reconstructing the lensing potential from observations of the CMB anisotropies, with results pouring in since about a decade ago. The first measurements of the angular power spectrum were obtained using temperature data by the ACT Collaboration [103], followed shortly thereafter by SPT [487] and Planck [374]. A combination of temperature anisotropy observations from the latter two experiments was also used by Ref. [334] to reconstruct lensing maps, which were then cross-correlated with DES measurements of galaxy weak lensing, obtaining a high-significance detection of lensing effects [332]. Ultimately, though, the greatest constraining power will come from the CMB polarisation, particularly from correlations between E- and B-modes. Therefore, as the resolution and sensitivity of polarisation-sensitive observations improved,

this information was steadily incorporated into analyses, and used to improve the reconstruction signal-to-noise in the results of Refs. [468, 431, 372, 514]; in parallel, the POLARBEAR and BICEP2/Keck Array Collaborations measured the lensing power spectrum using only polarisation data [378, 50]. At the time of writing, the highest signal-to-noise measurement is that from Planck — shown in figure 1.5— with a reported 40σ detection of lensing [372]. This is due, in large part, to the full-sky coverage of this space-based mission. However, its relatively large beam meant that the signal-to-noise per reconstructed mode is never greater than unity, and there is great potential in ground-based telescopes probing the microwave sky with arcminute-scale resolution: the Simons Observatory [441] is expected to produce reconstructions that are signal-dominated for multipoles $L \lesssim 250$ over 40% of the sky, and CMB-S4 is aiming to do the same for $L \lesssim 1000$ [90]; SPT-3G will achieve similar lensing depth to CMB-S4, but only over a few percent of the sky [458].

In addition to the information obtained from their auto-spectra, CMB lensing reconstructions are also powerful probes in cross-correlation with lower-redshift tracers of the large-scale structure. This approach benefits from a cancellation of cosmic variance arising when two tracers of the same underlying matter field, each biased in a different way, are cross-correlated [416]. The most obvious application of CMB lensing cross-correlations is, perhaps, in constraining cosmological parameters; for example, by cross-correlating with galaxy lensing [167, 268, 224, 174, 173, 304, 333, 318, 293, 401]. But many other insights are possible: cross-correlations of CMB lensing with the distribution of galaxies [449, 188, 54, 7, 46, 151, 341, 332, 512, 239, 101, 240], quasars [430, 146], galaxy groups [280] and galaxy clusters [29, 281] can be used to study the biasing properties of those tracers and the growth rate of structure (related, of course, to dark energy); cross-correlations with the cosmic infrared background (CIB) [192, 357, 485, 250], or the Sunyaev-Zeldovich effect [490, 186, 191] contain information about the relationship between dark and luminous matter; and cross-correlations of tracers with different bias properties can be used to probe primordial non-Gaussianity via the scale-dependence of halo bias [100]. Furthermore, cross-correlations can partially get around the impairing reliance — see Ref. [8] — on knowledge of the optical depth to reionisation when constraining the sum of the neutrino masses [518].

CMB lensing is sensitive to a set of systematic effects that is — for the most part — different from optical lensing surveys, so another possibility is to use it to calibrate the multiplicative shear bias of galaxy weak-lensing surveys [484, 102, 269, 414, 442, 175, 401]. Though CMB lensing reconstructions can be subject to additive biases (the likes

of $N^{(0)}, N^{(1)}$, etc.), the standard weights employed guarantee that it will be correctly normalised — i.e., that it will have no multiplicative bias. Calibrating multiplicative bias this way promises to be particularly effective at high redshift, where it is also most useful, since it is at high redshift that simulations of the galaxy population are most uncertain, making image-based calibration difficult. At the very least, CMB lensing will be a powerful complementary tool to cross-check other calibration methods; see Ref. [284] for a review.

As discussed in section 1.5.2.4, the quadratic estimator of Ref. [202] is the lowest-order (in the small deflection angles), optimally-weighted lensing estimator. In essence, this tool extracts information from off-diagonal elements of the covariance between pairs of CMB fields. The power spectrum of such a lensing reconstruction is therefore a linear functional of the trispectrum of the lensed CMB anisotropies, which is a particularly sensitive probe of the lensing effect [39]. If sensitive enough observations of the CMB polarisation are available, the statistical power of a temperature-based reconstruction can be expanded by combining it with other quadratic combinations of different pairs of fields, in a way that minimises the variance of the reconstructed map [287, 190].

Much work has recently been devoted to studying how auto- and cross-correlations of lensing reconstructions obtained using quadratic estimators are complicated by systematic effects. Some particularly critical areas are the $N^{(0)}, N^{(1)}$ and higher-order biases of lensing [223, 169]; the coupling to instrumental effects [171, 444, 302, 311, 137]; the challenges posed by limited sky coverage [487, 315, 35]; the impact of non-Gaussianity from Galactic foregrounds [138, 82, 30] or from the very early Universe [251, 296]; and biases due to the non-linear evolution of structure and post-Born lensing [58, 31, 59, 384, 136]. In addition to characterisations of possible biases, these recent efforts have provided a useful set of tools to mitigate them; with those methods in hand, lensing reconstructions are rather clean, particularly when only polarisation data is used, in which case there is effectively no contamination from extragalactic sources.

However, for as long as a significant fraction of the lensing reconstruction signal-to-noise comes from the temperature anisotropies — which is the case for current and soon-upcoming experiments such as AdvACT [181], the Simons Array, or the Simons Observatory [441] — contamination from extragalactic foregrounds will pose a major challenge. At microwave frequencies, there is substantial emission from radio-bright galaxies, from the thermal and kinetic Sunyaev-Zeldovich effects (tSZ and kSZ, respectively) produced by galaxy clusters, and from the cosmic infrared background

(CIB). Since these foregrounds are polarised by a smaller fraction than the CMB is, polarisation-based lensing reconstructions are more robust to their impact that temperature-based ones are [444].

The contributions of extragalactic foregrounds to the observed anisotropies have acutely non-Gaussian statistics — bispectra of both the tSZ [511, 98, 356] and the CIB [98, 357] have been measured — so they can potentially confuse the lensing estimators. Early work by Ref. [13] using simulations suggested that the kSZ alone could bias the power spectrum of lensing reconstructions by 10–200%. Similar warnings were issued in Refs. [449, 54, 487] about biases arising from the CIB. These estimates were subsequently refined and extended using simulations by Refs. [485, 335, 408], who harnessed the improved understanding of the microwave sky enabled by the observations of SPT, ACT, and Planck. They showed that a wide range of extragalactic foregrounds — tSZ, CIB, radio sources — can bias CMB lensing auto- and cross-spectra at the level of several percent, even after detectable point sources have been masked. More recently, Ref. [141] completed the picture by providing a detailed study of biases associated with the kSZ. These extragalactic contaminants — in particular, the tSZ and the CIB — are probably the greatest impediment to extracting lensing information from the small-scale anisotropies of the CMB.

Several techniques have been suggested in the literature to mitigate lensing biases from extragalactic foregrounds. One approach, used in the analyses of Refs. [431, 514], is to subtract from measured spectra the bias templates calculated by Ref. [485] using the simulations of Ref. [419]. If the templates are accurately known, this approach has the benefit of not incurring any loss in signal-to-noise.

Another option, known as bias hardening [335, 314, 408], entails using knowledge of the statistics of the foregrounds (in particular, their power spectrum and bispectrum) to engineer quadratic estimators which optimally extract the foreground contribution at leading order. It is then possible to form a linear combination of this foreground reconstruction and the lensing estimators that extensively reduces the bias. This method is very effective at mitigating the bias while only incurring a small noise penalty; as such, it featured in the analysis of Planck data in Refs. [359, 372]. Strictly-speaking, however, bias-hardening only nulls the 'primary bispectrum' bias (we will explain this nomenclature shortly) if the foregrounds are perfectly correlated with lensing, and the 'trispectrum' bias if the sources are Poisson-distributed with identical profiles; lastly, it is in general not effective at mitigating the 'secondary bispectrum' bias [408].

Multi-frequency cleaning techniques (see, e.g., [476, 475, 395, 394]) will be useful in mitigating these biases, but they will be handicapped by the fact that very high-resolution measurements — which can only be achieved from the ground — will be limited to just a few frequency channels. It has recently been suggested that applying frequency cleaning to only the gradient leg[1] of the quadratic estimator might incur a smaller loss in lensing signal-to-noise than doing it to both legs (at least on the scale of clusters) [282, 101]. The reason for this is that contributions from the primary CMB to the local gradient of CMB anisotropies saturate by $l \approx 2000$ due to Silk damping, so that there is little cost associated with increasing the noise on scales smaller than that.

Finally, it is worth mentioning the foreground-immune estimators of Ref. [412]. By performing a harmonic expansion of the weights of the quadratic estimator, one can show that most of the signal-to-noise is in the first two moments — the monopole and the quadrupole. In the limit of large-scale lenses, these correspond to extracting the convergence and shear, respectively. Importantly, to the extent that the source emission profiles are azimuthally-symmetric, only the monopole is affected by foregrounds. Consequently, the shear-only estimator can be used to obtain lensing reconstructions that are highly robust to foregrounds; and although it has only around 60% of the signal-to-noise of the full quadratic estimator, the statistical power is made up for thanks to being able to use smaller-scale data while keeping biases under control.

In this chapter, we present a tool — complementary to the ones just described — to model the biases to lensing reconstructions due to the tSZ and the CIB. We do so analytically, using the halo model. (The reason we do not study the kSZ for now is that it receives important contributions from material outside halos; radio galaxies, on the other hand, largely behave as Poisson sources, so they can be understood with simpler treatments.) We believe that having a tool that can quickly calculate these biases as a function of experimental sensitivity, resolution, filtering and point-source masking schemes will be useful to the community — for example, when optimising experiment configurations, in order not to rely on expensive simulations that can only be run in a small number of setups. Moreover, by providing an understanding of the intricacies of the clustering configurations, as well as the redshift and mass ranges, that give rise to the biases, this tool can complement existing mitigation techniques such as bias hardening, or shed light on the regime of validity of the shear-only estimators.

Furthermore, in this work we develop techniques that allow for very efficient computation of a subset of the biases. If these techniques can be extended to all

[1]This terminology makes reference to the real-space formulation of the quadratic estimators, equation C.4.

of the dominant terms, it might then become possible to model the lensing biases efficiently at each point in parameter space in a likelihood analysis. One could then (optimistically) imagine marginalising over astrophysical uncertainties associated with, for example, the pressure profile of clusters, or the halo occupation distribution of the dusty, star-forming galaxies that produce the CIB.

This chapter is organised as follows. In section 5.2, we introduce the biases to lensing reconstructions induced by extragalactic foregrounds. Then, in section 5.3, we describe the analytic framework for computing those biases using the halo model, and we present the results of our calculations. We compare these to measurements from simulations in section 5.4. Finally, in section 5.5, we conclude and summarise our findings.

Throughout this chapter, we assume a ΛCDM cosmology with $\Omega_\mathrm{m} = \Omega_\mathrm{b} + \Omega_\mathrm{cdm} = 0.25$, where the baryon density is $\Omega_\mathrm{b} = 0.043$; cosmological constant $\Omega_\Lambda = 0.75$, a power-law primordial spectrum of fluctuations with spectral index $n_\mathrm{s} = 0.96$, fluctuation amplitude $\sigma_8 = 0.8$ and Hubble constant $H_0 = 70\,\mathrm{km\,s^{-1}\,Mpc^{-1}}$. (These are the parameters assumed by Ref. [26] when determining the electron pressure profile we will be using.)

5.2 Biases to lensing reconstruction from extragalactic foregrounds

Recall, from section 1.5.2.4, that the temperature–temperature (TT) quadratic estimator can be written in the flat-sky limit as

$$\hat{\phi}(\mathbf{L}) = A_L^{TT} \int \frac{\mathrm{d}^2\boldsymbol{l}}{2\pi} T^\mathrm{obs}(\boldsymbol{l}) T^\mathrm{obs}(\mathbf{L}-\boldsymbol{l}) g(\boldsymbol{l},\mathbf{L})\,, \tag{5.1}$$

where $T^\mathrm{obs}(\boldsymbol{l})$ is the Fourier transform of the observed CMB temperature, which comprises lensed CMB signal, experimental noise and foreground emission, and has angular power spectrum $C_l^{TT,\mathrm{obs}}$. If we choose the weight function $g(\boldsymbol{l},\mathbf{L})$ to be

$$g(\boldsymbol{l},\mathbf{L}) = \frac{(\mathbf{L}-\mathbf{l})\cdot\mathbf{L}\tilde{C}^{TT}_{|\mathbf{l}-\mathbf{L}|} + \mathbf{l}\cdot\mathbf{L}\tilde{C}^{TT}_{l}}{2C_l^{TT,\mathrm{obs}} C^{TT,\mathrm{obs}}_{|\boldsymbol{l}-\boldsymbol{L}|}}\,, \tag{5.2}$$

and the normalisation A_L^{TT} as

$$A_L^{TT} = \left[2\int \frac{\mathrm{d}^2\boldsymbol{l}}{(2\pi)^2} C_l^{TT,\mathrm{obs}} C_{|\boldsymbol{l}-\boldsymbol{L}|}^{TT,\mathrm{obs}} \left[g(\boldsymbol{l},\mathbf{L})\right]^2\right]^{-1}, \tag{5.3}$$

then the estimator is unbiased at lowest order in lensing, and its leading-order variance is $N_L^{(0),TT} = A_L^{TT}$, which is guaranteed to be the minimum value possible for an estimator of ϕ that is quadratic in T [202]. Note the use of the lensed power spectrum in the numerator of equation (5.2): as described in section 1.5.2.4, this is an approximation to the non-perturbative weights calculated by Ref. [253] and given in table 1.1.

The auto-correlation of such a reconstruction takes the form

$$\begin{aligned}\langle\hat{\phi}(\mathbf{L})\hat{\phi}(\mathbf{L}')\rangle = A_L^{TT}A_{L'}^{TT}\int\frac{\mathrm{d}^2\boldsymbol{l}'}{2\pi}\frac{\mathrm{d}^2\boldsymbol{l}''}{2\pi}g(\boldsymbol{l}',\mathbf{L})g(\boldsymbol{l}'',\mathbf{L}')\\ \times\langle T^{\mathrm{obs}}(\boldsymbol{l}')T^{\mathrm{obs}}(\mathbf{L}-\boldsymbol{l}')T^{\mathrm{obs}}(\boldsymbol{l}'')T^{\mathrm{obs}}(\mathbf{L}'-\boldsymbol{l}'')\rangle\,;\end{aligned} \tag{5.4}$$

from this, it is possible to extract the angular power spectrum of the reconstruction,

$$\langle\hat{\phi}(\mathbf{L})\hat{\phi}(\mathbf{L}')\rangle = \delta^{(2)}(\mathbf{L}'+\mathbf{L})\left(C_L^{\phi\phi}+C_L^{\mathrm{biases}}\right),$$

which is an estimator of the lensing potential angular power spectrum, $C_L^{\phi\phi}$, once the biases denoted as C_L^{biases} have been accounted for.

The 4-point function in equation (5.4) contains both connected and disconnected couplings. The disconnected ones contribute to the $N^{(0),TT}$ bias discussed in section 1.5.2.4; removing these should, ideally, include contributions from the foreground power.

As per the connected ones, there are several possibilities. One of them is a pure lensing component,

$$\langle T^{\mathrm{obs}}(\boldsymbol{l}')T^{\mathrm{obs}}(\mathbf{L}-\boldsymbol{l}')T^{\mathrm{obs}}(\boldsymbol{l}'')T^{\mathrm{obs}}(\mathbf{L}'-\boldsymbol{l}'')\rangle \subset \langle\tilde{T}(\boldsymbol{l}')\tilde{T}(\mathbf{L}-\boldsymbol{l}')\tilde{T}(\boldsymbol{l}'')\tilde{T}(\mathbf{L}'-\boldsymbol{l}'')\rangle_{\mathrm{c}}\,. \tag{5.5}$$

Some of the couplings making up this trispectrum constitute the signal of interest, $C_L^{\phi\phi}$; others, those whose response is not simply related to the lensing potential, will contribute to the $N^{(n),TT}$ biases with $n>0$ (see Ref. [169] and references therein). We will not be concerned with any of these pure-lensing terms.

Instead, we shall be interested in couplings that involve emission from extragalactic foregrounds. These can also give rise to bias, and, to date, are not as well characterised. We describe these schematically now, and leave a careful analysis of each term to the following sections.

Let us denote the TT quadratic estimator, applied to an observed map, $T^{\rm obs}$, as

$$\hat{\phi}[T^{\rm obs}, T^{\rm obs}] = \hat{\phi}[\tilde{T} + n + s, \tilde{T} + n + s] \,. \tag{5.6}$$

Here, $\tilde{T}$ denotes the lensed CMB temperature anisotropies, n is the instrument noise (which we assume to be Gaussian) and s refers to one of possibly several foregrounds, which we take to be correlated with the underlying matter distribution. The connected 4-point function of $T^{\rm obs}$ contributes to the power spectrum of a lensing reconstruction, schematically, as[2]

$$\begin{aligned}\langle \hat{\phi}[T^{\rm obs}, T^{\rm obs}]\, \hat{\phi}[T^{\rm obs}, T^{\rm obs}] \rangle_{\rm c} =& \langle \hat{\phi}[\tilde{T}, \tilde{T}]\, \hat{\phi}[\tilde{T}, \tilde{T}] \rangle_{\rm c} + 2\, \langle \hat{\phi}[\tilde{T}, \tilde{T}]\, \hat{\phi}[s, s] \rangle_{\rm c} \\ &+ 4\, \langle \hat{\phi}[\tilde{T}, s]\, \hat{\phi}[\tilde{T}, s] \rangle_{\rm c} + \langle \hat{\phi}[s, s]\, \hat{\phi}[s, s] \rangle_{\rm c} \,. \end{aligned} \tag{5.7}$$

The first term on the right-hand side arises from the trispectrum in equation (5.5); as we just discussed, it contains the signal of interest, as well as a number of lensing-related bias terms. In addition, there are three other terms on the right, above, that can bias the estimate.

The second and third terms on the right are usually called the primary and secondary bispectrum biases, respectively, for reasons that will become apparent soon. They arise due to the fact that the foregrounds are correlated with lensing (this has been measured directly for the CIB [192, 355, 172] and the tSZ [186]). The last term, on the other hand, comes from the foreground trispectrum, so it would be present even if there was no such correlation.

If the foregrounds are indeed correlated with lensing, they will also bias cross-correlations with other tracers of the matter distribution — for example, galaxy surveys. If we denote such a tracer as $\mathcal{G}[\phi]$, then

$$\langle \mathcal{G}[\phi]\, \hat{\phi}[T^{\rm obs}, T^{\rm obs}] \rangle_{\rm c} = \langle \mathcal{G}[\phi]\, \hat{\phi}[\tilde{T}, \tilde{T}] \rangle_{\rm c} + \langle \mathcal{G}[\phi]\, \hat{\phi}[s, s] \rangle_{\rm c} \,. \tag{5.8}$$

Once again, the second term on the right biases estimates of the true lensing cross-correlation.

Note that, for clarity of exposition, the expressions above omit the possibility of s differing across legs of the quadratic estimators, or between different estimators. In the discussions that follow, we allow for the more general possibility of mixed couplings arising from the fact that different foregrounds are correlated by virtue of tracing

[2]We ignore the small correlation between the unlensed CMB and the lensing potential induced by the integrated Sachs-Wolfe [407] and Rees-Sciama effects [390]. Hence, we need an even number of $\tilde{T}$s in every correlator.

the same underlying matter distribution. Indeed, the tSZ and CIB correlation was measured by Ref. [360] to be at a level of approximately 15% at $l = 3000$ for all-sky Planck data, and indirect evidence for such a positive correlation was also found by Refs. [392, 147, 86, 393]. Physically, a one-halo contribution arises if some of the galaxies comprising the CIB reside in the massive, nearby clusters that produce the tSZ effect; and a two-halo term is also possible — even if there is no star formation in the clusters that produced the tSZ — as long as there is some overlap in the redshift distributions of the tSZ and CIB [4, 285].

Throughout this work, we ignore the fact that the foregrounds are themselves lensed, since this has only a small effect on the tSZ [515] and the CIB [413].

5.2.1 Primary bispectrum bias

Extragalactic foregrounds trace the matter distribution, so they correlate with the lensing potential. This is the defining property of the 'bispectrum' biases affecting CMB lensing measurements.

Because of this correlation, there is a term in the power spectrum of lensing reconstructions that depends on

$$\langle T^{\rm obs}(\boldsymbol{l}')T^{\rm obs}(\mathbf{L}-\boldsymbol{l}')T^{\rm obs}(\boldsymbol{l}'')T^{\rm obs}(\mathbf{L}'-\boldsymbol{l}'')\rangle \subset 2\,\langle \tilde{T}(\boldsymbol{l}')\tilde{T}(\mathbf{L}-\boldsymbol{l}')T^{s_1}(\boldsymbol{l}'')T^{s_2}(\mathbf{L}'-\boldsymbol{l}'')\rangle_{\rm c}\,. \tag{5.9}$$

In this coupling arrangement — the 'primary' one — the two lensed CMB legs are input into one quadratic estimator, and the two foreground legs (T^{s_1} and T^{s_2}) are arranged into the other one. (Notice that, from now on, we allow the foreground components, s_i, to all be different.) By construction, the quadratic estimator produces an estimate of the lensing potential that is unbiased to leading order when averaging over the CMB. Hence, we can replace the quadratic estimator acting on the $\tilde{T}$ fields with ϕ. We then see that couplings of this sort induce a bias on the power spectrum of CMB lensing reconstructions:

$$C_L^{{\rm bias}-\phi s_1 s_2} = 2\,\delta^{(2)}(\boldsymbol{L}'+\boldsymbol{L})A_L^{TT}\int\frac{{\rm d}^2\boldsymbol{l}}{2\pi}g(\boldsymbol{l},\boldsymbol{L})b_{\phi s_1 s_2}(\boldsymbol{L}',\boldsymbol{l},\boldsymbol{L}-\boldsymbol{l})\,, \tag{5.10}$$

where we have defined the angular bispectrum,

$$\langle\phi(\boldsymbol{l}_1)T^{s_1}(\boldsymbol{l}_2)T^{s_2}(\boldsymbol{l}_3)\rangle = \delta^{(2)}(\boldsymbol{l}_1+\boldsymbol{l}_2+\boldsymbol{l}_3)b_{\phi s_1 s_2}(\boldsymbol{l}_1,\boldsymbol{l}_2,\boldsymbol{l}_3)\,. \tag{5.11}$$

Equation (5.10) goes by the name of 'primary bispectrum bias'. As illustrated by equation (5.8), cross-correlations between CMB lensing reconstructions and any observable that traces the matter distribution — which is therefore also a tracer of ϕ — will be affected by the same bias, though the amplitude will be smaller by a permutation factor of 2.

Note that estimates exist for the disconnected version of the 4-point function in equation (5.9) (and for that in the next section, equation 5.12), in the limit that the foregrounds are Gaussian [95]. However, explorations using non-Gaussian simulations of the CIB have shown that the resulting biases greatly exceed predictions relying on the assumption of Gaussianity [486].

5.2.2 Secondary bispectrum bias

Another possible contribution to the trispectrum of observed CMB temperature anisotropies is

$$\langle T^{\rm obs}(\boldsymbol{l}')T^{\rm obs}(\mathbf{L}-\boldsymbol{l}')T^{\rm obs}(\boldsymbol{l}'')T^{\rm obs}(\mathbf{L}'-\boldsymbol{l}'')\rangle \subset 4\,\langle \tilde{T}(\boldsymbol{l}')T^{s_1}(\mathbf{L}-\boldsymbol{l}')\tilde{T}(\boldsymbol{l}'')T^{s_2}(\mathbf{L}'-\boldsymbol{l}'')\rangle_{\rm c}\,. \tag{5.12}$$

Now, each of the two quadratic estimators takes in both a lensed CMB leg and a foreground leg — a 'secondary' coupling that gives the resulting bias the name of 'secondary bispectrum bias'.

To calculate this term, we will expand perturbatively to leading order in lensing, obtaining

$$\langle \hat{\phi}(\mathbf{L})\hat{\phi}(\mathbf{L}')\rangle \subset -\frac{8}{2\pi}\delta^{(2)}(\mathbf{L}+\mathbf{L}')\,A_L^{TT}A_{L'}^{TT}\int\frac{{\rm d}^2\boldsymbol{l}'}{2\pi}\frac{{\rm d}^2\boldsymbol{l}''}{2\pi}g(\boldsymbol{l}',\mathbf{L})g(\boldsymbol{l}'',\mathbf{L}')h(\boldsymbol{l}',-\boldsymbol{l}'')C_{l''}^{TT} \times b_{\phi s_1 s_2}(\mathbf{l}'+\mathbf{l}'',\mathbf{L}-\boldsymbol{l}',\mathbf{L}'-\boldsymbol{l}'')\,, \tag{5.13}$$

where $h(\boldsymbol{l},\boldsymbol{l}')\equiv\boldsymbol{l}'\cdot(\boldsymbol{l}-\boldsymbol{l}')$. Like the primary bispectrum bias, this bias term depends on the lensing amplitude $C_L^{\phi\phi}$.

Note that, in deriving equations (5.10) and (5.13), we have assumed that there is no correlation between the unlensed CMB and the lensing potential or the extragalactic foregrounds. Although this is strictly not true because of the integrated Sachs-Wolfe [407] (ISW) and Rees-Sciama effects [390], we expect corrections to be small (particularly for the ISW, which is a large-scale effect, while it is small-scale modes that are up-weighted in the reconstruction).

5.2.3 Trispectrum bias

Finally, we consider the case where all four quadratic estimator legs in the lensing power spectrum estimator take in foregrounds. This is associated with the coupling

$$\langle T^{\rm obs}(\boldsymbol{l}')T^{\rm obs}(\mathbf{L}-\boldsymbol{l}')T^{\rm obs}(\boldsymbol{l}'')T^{\rm obs}(\mathbf{L}'-\boldsymbol{l}'')\rangle \subset \langle T^{s_1}(\boldsymbol{l}')T^{s_2}(\mathbf{L}-\boldsymbol{l}')T^{s_3}(\boldsymbol{l}'')T^{s_4}(\mathbf{L}'-\boldsymbol{l}'')\rangle_{\rm c}\,, \tag{5.14}$$

which translates to an additive bias on the lensing power spectrum of the form

$$\begin{aligned} C^{{\rm bias}-s_1s_2s_3s_4}(\boldsymbol{L}) =& \delta^{(2)}(\boldsymbol{L}'+\boldsymbol{L})A_L^{TT}A_{L'}^{TT} \\ &\times \int \frac{{\rm d}^2\boldsymbol{l}{\rm d}^2\boldsymbol{l}'}{(2\pi)^2} g(\boldsymbol{l},\boldsymbol{L})g(\boldsymbol{l}',\boldsymbol{L}')t_{s_1s_2s_3s_4}(\boldsymbol{l}',\boldsymbol{L}'-\boldsymbol{l}',\boldsymbol{l},\boldsymbol{L}-\boldsymbol{l})\,, \end{aligned} \tag{5.15}$$

where we have defined the angular trispectrum,

$$\langle T^{s_1}(\boldsymbol{l}_1)T^{s_2}(\boldsymbol{l}_2)T^{s_3}(\boldsymbol{l}_3)T^{s_4}(\boldsymbol{l}_4)\rangle = \delta^{(2)}(\boldsymbol{l}_1+\boldsymbol{l}_2+\boldsymbol{l}_3+\boldsymbol{l}_4)t_{s_1s_2s_3s_4}(\boldsymbol{l}_1,\boldsymbol{l}_2,\boldsymbol{l}_3,\boldsymbol{l}_4)\,. \tag{5.16}$$

We emphasise that this 'trispectrum bias' exists also for foregrounds which are not correlated with the lensing potential — it is relevant, for example, to biases from galactic foregrounds [30].

Reference [486] notes that, in the limit that the sources are Poisson-distributed and sufficiently numerous, their distribution will approach that of a Gaussian random field by the central limit theorem. It is then easy to see, using Wick's theorem, that their 4-point function will only contribute to the $N^{(0)}$ bias, which can be easily and accurately calculated and removed. In reality, this limit does not apply, since the clusters that produce the tSZ are rare, and the galaxies that comprise the CIB reside in dark matter halos which, as we saw in section 1.6, tend to cluster together.

However, galaxies can still appear to follow a Poisson distribution if the emission is dominated by a few, bright sources. This is, indeed, the dominant impact that extragalactic radio sources appear to have had on Planck's lensing analyses [359], which could only resolve — and mask away — sources brighter than 145 mJy at 143 GHz. Since the clustering contributions were estimated to be small given the limited angular resolution ($l_{\rm max} \approx 1800$), the bias was expected to be sourced largely by approximately-Poisson-distributed, bright galaxies just below the flux cut. It was therefore possible to estimate their contribution analytically and account for it in the analyses; it came out to be at around 2% of the lensing power spectrum amplitude.

For higher-resolution experiments, this simple treatment will not do. Hence, in this work we strive to calculate the clustering contributions to the bias. Note that calculations of the shot-noise terms can be found in other works; e.g., Refs [485, 242].

5.3 Analytic calculation of the biases

In the previous section, we saw that computing the biases requires knowledge of $b_{\phi s_1 s_2}$ and $t_{s_1 s_2 s_3 s_4}$. Since both the CIB and the tSZ effect are produced by material that is (for the most part) in halos, we should, in principle, be able to calculate these rather accurately using the halo model. (Note that the same cannot be said about other effects such as the kSZ, which receives significant contributions from the 'field' external to halos.) In appendix C.4, we explain the details of our calculation, but see also section 1.6 for an introduction to the formalism. Our modelling of the tSZ hinges on the 'Battaglia' pressure profile [26], described in section 1.5.3.2. For the CIB, on the other hand, we extend the mass-dependent luminosity halo model of the CIB introduced by Ref. [428], and detailed in section 1.6.7.

For the purposes of this work, we restrict ourselves to contributions where all inputs into a given quadratic estimator originate from the same halo (the reasons are explained in appendix C.4). This means that we will be studying a subset of the one- and two-halo contributions to the relevant angular bispectra and trispectra. As we shall soon see, these terms already provide a rather good description of the primary bispectrum and trispectrum biases when compared to simulations. However, our methodology can be generalised to other terms, and we intend to do so in future.

Calculating the biases in equations (5.10), (5.13) and (5.15) involves evaluating the quadratic estimators of lensing. Several implementations of these can be found in the literature, allowing for their efficient application to CMB maps. In this work, we use the flat-sky version of the `QuickLens`[3] code, which has been extensively tested — for example, in the analysis of Ref. [359].

In spite of the proved performance of publicly available quadratic estimator codes, the lensing reconstructions we are concerned with can be evaluated much faster thanks to the following insight: to the extent that the emission profiles of the foregrounds are azimuthally-symmetric[4] and the filtering is isotropic, the two-dimensional Fourier transforms involved in the lensing reconstruction reduce to one-dimensional Hankel

[3] `QuickLens` can be found at `https://github.com/dhanson/quicklens`, though we provide an amended and extended version in `https://github.com/abaleato/Quicklens-with-fixes`).

[4] Note that this assumption is also often made in the context of bias hardening [314, 335, 408] and shear-only reconstructions [412].

transforms. These can be evaluated very efficently (in their discrete limit) using the FFTlog algorithm[5] [472, 162]; see appendix C.2 for details. When comparing the bias calculations obtained in this way to the output of 2D codes such as `QuickLens`, we indeed find indistinguishable results. (This is perhaps not suprising given that the assumption of spherical symmetry of the halos is implicit in our halo model calculations by virtue of having used the NFW and Battaglia profiles.) However, we find that the 1D approach is up to four orders of magnitude faster, taking $O(10\,\mathrm{ms})$ per reconstruction on a single core of a modern laptop.

In order to harness this vast improvement in computational speed, we evaluate equations (5.10) and (5.15) by performing a lensing reconstruction for every mass and redshift step in the Limber-approximated halo model calculations of the angular bispectrum and trispectrum — that is, the projection, using equation (C.23), of the 3D bi- and trispectra in appendices C.5 and C.6. We find sufficient convergence of the integrals when 30 steps in redshift and 30 in mass are used, for a total computation time (on a single core) of $O(10\,\mathrm{s})$ per foreground. Note that this approach is in contrast to what equation (5.10) might appear to suggest: evaluating the angular bispectrum first, and only carrying out the lensing reconstruction once, at the very end. We make our code, `CosmoBLENDER`, publicly available[6].

Unfortunately, these faster lensing reconstructions cannot be applied to the secondary bispectrum bias, equation (5.13). The reason is that the two reconstructions in the expression are not separable; and when one tries to evaluate them as nested operations, azimuthal symmetry is broken. In principle, equation (5.13) can be evaluated by first computing the angular bispectrum in the integrand, and then carrying out the outer integrals associated with the lensing reconstructions. However, we anticipate there might be an advantage in terms of evaluation speed if we instead perform the nested lensing reconstructions for each mass and redshift step in the halo model integrals, while harnessing the convolution theorem. This approach — which constitutes work in progress — is explained in appendix C.3.

In figure 5.1, we show our calculations of the primary bispectrum bias and the trispectrum bias for an experiment with characteristics similar to SPT and ACTpol (θ_{FWHM}=1 arcmin and $\Delta_{\mathrm{T}} = 18\,\mu\mathrm{K}\,\mathrm{arcmin}$) observing at 143 GHz. We assume that no effort is made to clean the foregrounds (using, perhaps, frequency information) and that only temperature modes up to $l_{\mathrm{max}} = 3000$ are used for the reconstructions.

[5] We use the implementation in the `pyCCL` library [273]: `https://github.com/LSSTDESC/CCL`

[6] The code CosmoBLENDER (Cosmological Biases to LENsing Due to Extragalactic Radiation) can be found at `https://github.com/abaleato/CosmoBLENDER`.

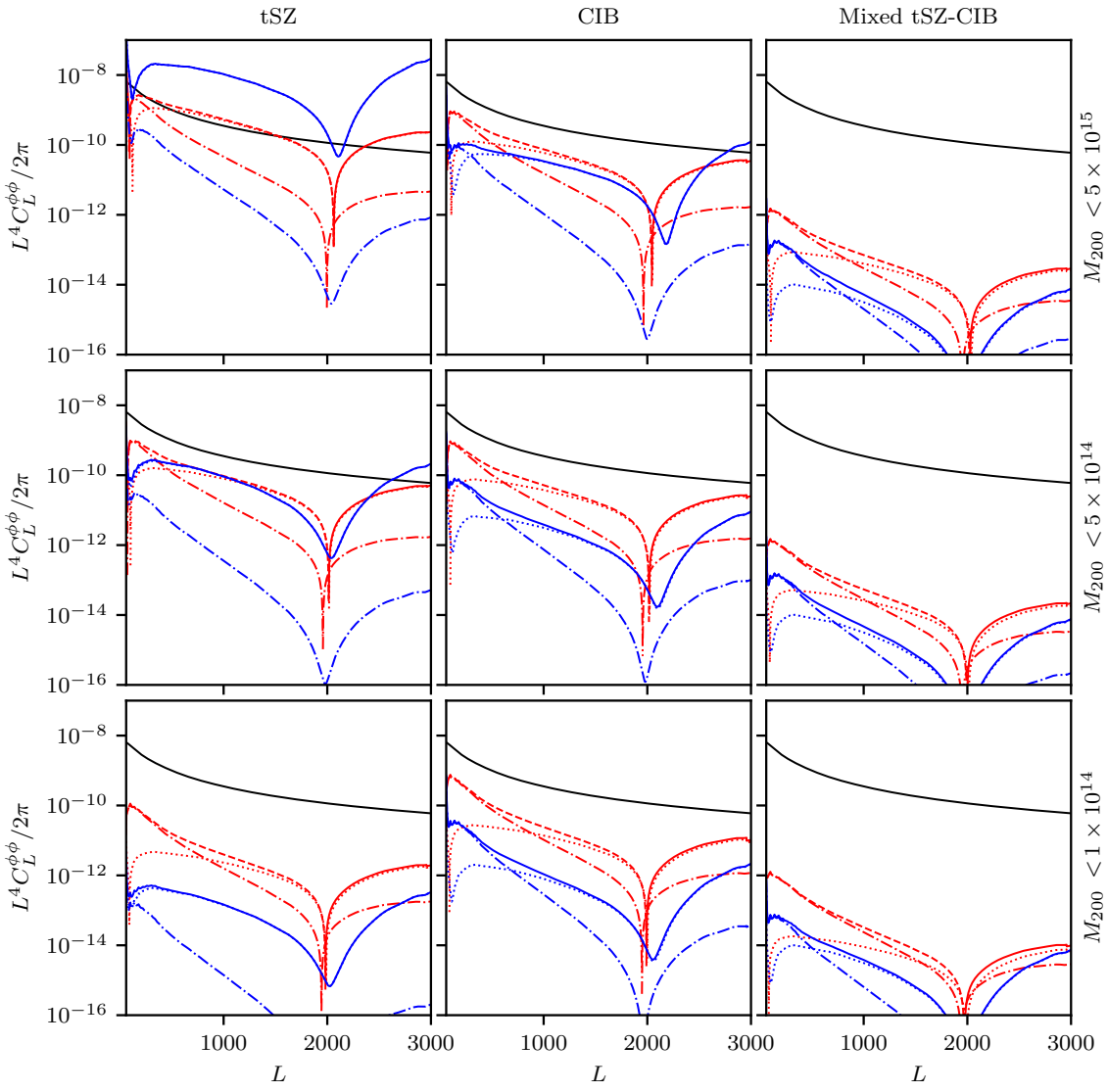

Fig. 5.1 Analytic calculation of the 'primary bispectrum' (red) and 'trispectrum' (blue) biases to the power spectrum of CMB lensing reconstructions obtained using a TT quadratic estimator. The biases arising from the tSZ alone are shown in the left column, those from the CIB alone on the central column, and those from the dependencies between the two in the right column. Different rows show different thresholds for the maximum halo mass in the calculation; from top to bottom: $M_{200} < 5 \times 10^{15}\,\mathrm{M}_\odot$, $M_{200} < 5 \times 10^{14}\,\mathrm{M}_\odot$ and $M_{200} < 10^{14}\,\mathrm{M}_\odot$. Within each panel, the one-halo (two-halo) contributions are shown as dotted (dot-dashed) lines; the total is shown as a solid line where positive, and a dashed line where negative. We assume an experiment with θ_{FWHM}=1 arcmin and $\Delta_\mathrm{T} = 18\,\mu$K arcmin observing at 143 GHz, discarding modes above $l_{\mathrm{max}} = 3000$, and performing no foreground cleaning. We only consider halos with mass above $M_{\mathrm{vir}} > 10^{11}\,\mathrm{M}_\odot$, and in the redshift range $0.07 < z < 3$ (we check that including larger z does not have a significant impact). The black curve shows the lensing power spectrum, scaled to 5% of its amplitude. Though we only calculate the subset of terms where both legs of a quadratic estimator come from the same halo, and ignore shot-noise contributions, our results are in reasonable agreement with the simulation-based measurements of section 5.4 and Refs. [486, 408, 335].

In different rows, we show the outcome of varying the maximum mass of halos included in the calculation; we test the values $M_{200} < \{1 \times 10^{14}, 5 \times 10^{14}, 5 \times 10^{15}\}\,\mathrm{M}_\odot$, where M_{200} is the halo mass contained within the radius at which the density is 200 times that of the background (see section 1.6). For the minimum mass, we set $M_{200} > 10^{11}\,\mathrm{M}_\odot$, as this is likely to encompass the majority of halos contributing to the tSZ and the CIB; see, e.g., Ref. [464] and references therein. Since the tSZ amplitude is directly related to the halo mass, these cuts tell us how the biases respond to our ability to identify and mask bright clusters. In the case of the CIB, on the other hand, more work is required to relate halo mass cuts to the flux limit of CMB experiments.

In the left column of figure 5.1, we show the biases resulting from the tSZ alone. If unmitigated, the trispectrum bias can be several times larger than lensing amplitude at $L \sim 1000$, while the primary bispectrum bias is at around the 10% level. The first thing worth noting is that the primary bispectrum bias is negative below $L \sim 2000$, and positive above. We also see that the tSZ biases are generally dominated by the one-halo term; this was perhaps to be expected, given the known subdominance of the clustering contributions to the tSZ power spectrum[7] [232]. Note also that, since the trispectrum bias scales as the fourth power of the Compton-y parameter (which, in turn, grows with the mass of the halo), it is very sensitive to the upper mass cut, much more so than the primary bispectrum bias. All in all, both can be mitigated substantially by masking: a mass cut of $M_{200} < 5 \times 10^{14}$ will reduce them both to the 2% level at $L \sim 1000$ (and note that the fact that they have opposite signs means they will cancel out to some extent).

In the centre column of figure 5.1, we show the biases resulting from the CIB alone. In the limit of no foreground cleaning and no masking, the trispectrum and primary bispectrum biases are of $O(10\%)$ at $L \sim 1000$. The same sign switch at $L \sim 2000$ observed for the primary bispectrum bias produced by the tSZ is observed for the CIB. Notice that mass cuts have less of an impact here, because we are ignoring shot-noise terms where a very bright galaxy (in all likelihood, sitting at the centre of a massive halo) can feature in several legs of the quadratic estimator; this agrees with the behaviour seen by Ref. [486] in simulations. However, a halo mass cut of $M_{200} < 5 \times 10^{14}$ is sufficient to reduce the primary bispectrum bias to the 5% level, and the trispectrum bias to a negligible 0.05% at $L \sim 1000$.

For completeness, we show, in the right-most column of figure 5.1, a subset of the biases arising from the fact that the CIB and the tSZ are correlated. Though further

[7] Tantalising evidence for a two-halo contribution has only recently been suggested [402].

work is required to implement more possible couplings, it appears that these biases will be negligible.

5.4 Comparison to simulations

Generating mock observations of the microwave sky over the large sky fractions covered by modern CMB experiments, and with a resolution matching the observational standard, is extremely challenging from a computational standpoint. Huge volumes are needed to account for the phenomena affecting our past lightcone, but also to sample appropriately the high-mass tail of the mass function; the latter point is crucial for effects such as the tSZ, which is dominated by the most massive clusters in the Universe. Unfortunately, volumes of this scale are beyond the reach of current hydrodynamical simulations featuring baryonic effects. For this reason, the CMB community relies on mocks based on approximations to the LSS, calibrated to observations and hydrodynamical simulations. The simulations of Refs. [421, 419], which have proven invaluable for over a decade in the analysis of CMB data, are an example of this. In them, astrophysical prescriptions are used to assign emission to halos identified in N-body simulations of the dark matter distribution.

The latest iteration in this lineage of simulations of the microwave sky are the WebSky simulations [464]. This suite uses the efficient peak-patch algorithm [463] — built around the physics of ellipsoidal collapse — to construct halo catalogues at various redshifts, in the cosmology best-fitting the Planck 2018 data [371]. Thanks to their large volumes ($\sim 600\,(\mathrm{Gpc}/h)^3$) and high-resolution ($\sim 10^{12}$ resolution elements) the Websky simulations are able to reproduce all halos more massive than $10^{12}\,\mathrm{M}_\odot$ along our past lightcone. In addition to this, second-order, Lagrangian perturbation theory [64] is used to model the material in the 'field' external to those halos. Mock observations of the microwave sky are then obtained by projecting the emission associated with halos and the field along the line of sight, for each frequency and emission process.

WebSky calculates the tSZ and CIB components by assigning emission properties to halos based on their mass and redshift. Given the fact that all halos above $M > 10^{12}\,\mathrm{M}_\odot$ are represented, this is an excellent approximation for the tSZ, and only misses out on a small fraction of the CIB emission from low-mass halos below the limit. The process of assigning emission to halos is carried out based on prescriptions from astrophysical models, under the assumption that halos are spherically symmetric. The cornerstone of the tSZ model is the 'Battaglia' pressure profile of Ref. [26]; while for the CIB, point-like galaxies are distributed in halos according to the CIB halo model of Ref. [428]

(explained in detail in section 1.6.7) with the best-fit parameters of Ref. [493]. The simulations show a level of correlation between tSZ and CIB that is in good agreement with the observations of Ref. [360], especially at 143 and 353 GHz.

Other astrophysical effects, such as CMB lensing or the kinetic SZ effect, are produced by fluctuations on scales so large that they are not bound in halos. In those cases, WebSky projects the emission from the field in addition to the contribution from halos.

Simulating CMB lensing is also complicated by the fact that a great deal of the effect comes from redshifts beyond what is covered by the WebSky simulation, which only extends to $z = 4.5$. In order to get around this limitation, the low-redshift lensing convergence — associated with halos[8] and the field — is supplemented with an uncorrelated Gaussian random realisation with a power spectrum matching that of the $z > 4.5$ convergence[9]. These stacked lensing convergence maps are then used to remap the primary CMB anisotropies, following the Born approximation[10]. The resulting convergence power spectrum is in reasonable agreement with theoretical expectations, with differences of only a few percent for $l < 4000$; and the cross-correlation with the CIB is also in good agreement with the observations of Refs. [357] and [250].

From the discussion above, it is clear that we can use the WebSky simulations of the lensed CMB and appropriately-correlated extragalactic foregrounds to calculate the lensing reconstruction biases in equations (5.7) and (5.8). We now detail how each of the bias terms in those equations can be estimated.

The primary bispectrum bias could, in principle, be calculated as $2\,\langle\hat{\phi}[\tilde{T},\tilde{T}]\,\hat{\phi}[s,s]\rangle$. However, if computed this way, the estimate would be subject to the sample variance of the quadratic estimator — this would be particularly problematic when, for the time being, we only have access to a single realisation of the WebSky simulations[11]. In order to avoid this issue, we harness the fact that, to leading order, the quadratic estimator is an unbiased estimator of the lensing potential, and we compute instead $2\,\langle\phi\,\hat{\phi}[s,s]\rangle$, where ϕ is the input lensing potential of the simulation — in reality, this would, of course, not be known.

[8] In the Websky simulations, the contribution from halos to CMB lensing is calculated by assuming that they follow an NFW profile with concentration parameter $c = 7$.

[9] The latter is obtained from a Halofit [254] calculation of the matter power spectrum and a projection that involves the Limber approximation [262].

[10] The simulations produced by Ref. [419] might prove more valuable for applications requiring a highly-accurate treatment of the lensing deflections, since they are produced using ray-tracing techniques.

[11] For this reason, the angle brackets in the equations do not have an effect on the results of this section.

The same concerns regarding sample variance apply to the secondary bispectrum bias if it is calculated as $4\,\langle\hat{\phi}[\tilde{T}, s]\,\hat{\phi}[\tilde{T}, s]\rangle_{\rm c}$. We avoid the problem by following Ref. [412] and computing instead $8\,\langle\hat{\phi}[T, s]\,\hat{\phi}[\tilde{T}^{(1)}, s]\rangle$, where T is the unlensed CMB temperature and $\tilde{T}^{(1)}$ is the first-order part of the lensed CMB temperature field; in appendix B.7.2, we explain how $\tilde{T}^{(1)}$ can be calculated in an efficient manner for full-sky maps, and we make our implementation available[12].

Finally, to estimate the trispectrum bias, $\langle\hat{\phi}[s, s]\,\hat{\phi}[s, s]\rangle_{\rm c}$, we first cross-correlate two lensing reconstructions where all input legs are foregrounds. Then, we subtract the Gaussian part of this correlation, which can be calculated analytically by replacing the angular power spectra in equation (5.3) with spectra measured from the foreground simulations. (In actual analyses, this would be part of the $N^{(0)}$ noise bias.)

In figure 5.2, we show the biases measured by applying a TT quadratic estimator to a single, full sky Websky simulation at 143 GHz, when only temperature modes up to $l_{\rm max} = 3000$ are used. In the left panel, we isolate the biases coming from the tSZ alone. We do not apply any masking of point sources.

In the central panel of figure 5.2, the same is done for the CIB. In this case, we first subtract the mean intensity, and then mask point sources brighter than 5 mJy — the approximate 5σ masking threshold for ACT and SPT at 150 GHz. Recall that, in the WebSky simulations, galaxies are only assigned to halos, not the field; at the same time, the non-linear formation of those halos is only recreated for redshifts lower than $z = 4.5$. Consequently, we expect the bispectrum biases measured from the simulations to miss contributions from $z > 4.5$ and from low-mass halos with $M < 10^{12} M_{\odot}$, and hence to underestimate their true amplitude.

In the right panel of figure 5.2, we show the mixed biases containing both tSZ and CIB legs. We do this by applying the estimation procedures described above to a map of the combined tSZ and CIB emission, and subtracting from the result bias estimates obtained from maps of each foreground individually. Note, however, that the noisy results suggest that we cannot draw any conclusions from a single realisation.

Qualitatively, figure 5.2 is in agreement with the analytic modelling of the previous section. However, we defer a more quantitative comparison to future work, once we have implemented a larger number of terms in our model — including shot-noise contributions, which *do* feature in the simulation-based measurements — and defined a rigorous mapping between halo mass cuts in the analytic calculations and masking in the simulations.

[12]The code to compute $\tilde{T}^{(1)}$ on the full, curved sky can be found at `https://github.com/abaleato/curved_sky_B_template`.

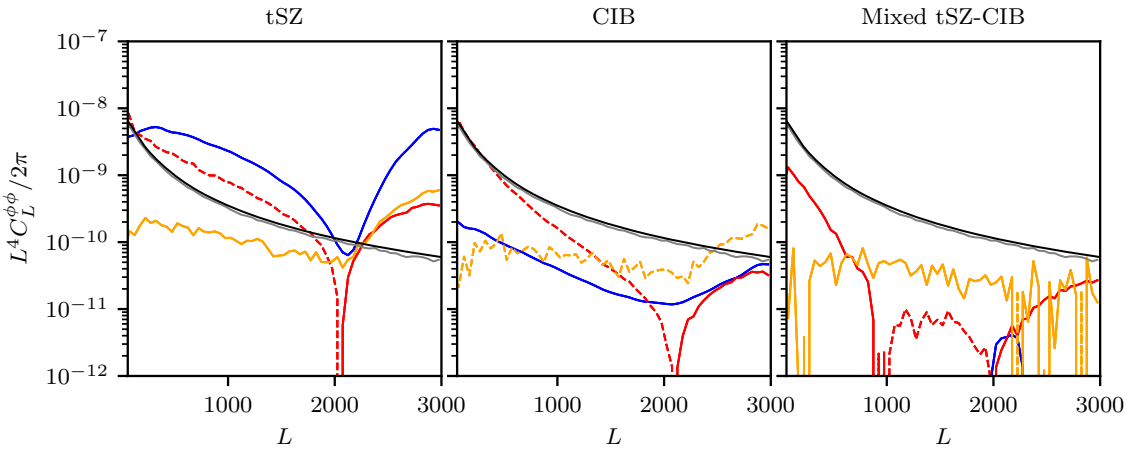

Fig. 5.2 Lensing reconstruction biases from extragalactic foregrounds as measured from a single realisation of the WebSky simulations [464]. We show the biases arising from the tSZ (left), CIB (centre), and the dependencies between the two (right), assuming that no prior attempt is made to remove these foregrounds. In the case of the CIB, we mask point sources 5 mJy brighter than the mean. In each panel, the primary bispectrum bias is shown in red, the secondary bispectrum bias in orange, and the trispectrum bias in blue; positive (negative) values are plotted as solid (dashed) curves. For comparison, we show the theoretical lensing potential power spectrum (black), and the cross-correlation between input and temperature-based lensing reconstruction (grey), both scaled to 5% of their amplitude. Measurements are based on the quadratic estimators as implemented in the code `QuickLens`, with $l_{\rm max} = 3000$. Spectra are binned with width $\Delta L = 50$. Though the simulations are noiseless, we apply to them inverse-variance filters appropriate for an experiment with $\Delta_T = 18\,\mu$K-arcmin and $\theta_{\rm FWHM} = 1\,$arcmin. Note that neither the range of the y-axis, nor the mass cuts, are the same as in figure 5.1.

It is worth emphasising the significance of the secondary bispectrum bias in figure 5.2. This was seen as well by Ref. [408], who also noted that it is not possible to harden against this bias. It would therefore be very interesting to have the ability to model this bias analytically — and this will, indeed, be the focus of future work.

5.5 Conclusions

The angular power spectrum and cross-correlations of CMB lensing reconstructions are powerful cosmological probes, because they are sensitive to physical effects that would be highly degenerate if only unlensed anisotropies could be observed: the sum of the neutrino masses, geometry, dark energy, and more.

For the foreseeable future, lensing reconstructions are going to depend on the temperature anisotropies for a significant fraction of their signal-to-noise. This poses a major challenge: in intensity, the microwave sky is rather complex, with important contributions from extragalactic foregrounds such as the tSZ and the CIB, which have been shown to bias significantly lensing reconstructions. Hence, these contaminants limit our ability to extract information from the small-scale CMB anisotropies.

In this work, we present a tool designed to complement existing bias mitigation techniques. We show that the most important properties of the 'primary bispectrum' and 'trispectrum' biases to lensing spectra can be understood analytically — at least in the case of the tSZ and the CIB. Our modelling is based on the halo model of dark matter clustering, with a prescription for assigning tSZ emission to halos that is based on the Battaglia profile of Ref. [26], and a mass-dependent-luminosity halo model of the CIB that builds on the work of Ref. [428]. Our calculations are in good qualitative agreement with measurements derived from the WebSky simulations.

Harnessing the approximate spherical symmetry of the emission profiles, we speed up the evaluation of the quadratic estimators of lensing by up to four orders of magnitude relative to what is achievable by a naïve application of standard codes; they can now be evaluated in $O(10\,\mathrm{ms})$ on a single laptop core.

Thanks to this, we are able to evaluate the dominant contributions to the primary bispectrum and trispectrum biases — a subset of the one- and two-halo terms — very fast ($O(10\,\mathrm{s})$ per foreground component), and work is ongoing to extend the method to other terms with more complicated coupling structures. In particular, it remains to be seen whether the secondary bispectrum bias can be calculated efficiently.

If these extensions are successful, the computational efficiency of our method could open the door to likelihood-based treatments of the biases to lensing due to extragalactic

foregrounds. According to Ref. [486], the trispectrum bias is highly sensitive to the normalisation of the concentration-mass relation (parameter A in equation 1.106), and also to σ_8 and Ω_m. One could imagine marginalising over these parameters — as well as, for example, pressure profiles or HODs — when analysing measurements of lensing spectra, thus incorporating modelling uncertainties into the estimates. Even more futuristically, methods inspired by our approach could become ingredients of more optimal, more Bayesian constraints of the lensing potential and other parameters, as in Refs. [189, 190, 170, 74, 75, 299, 300]. Potentially, if the modelling is accurate enough, one could consider using smaller-scale modes (higher l_{max}) than would have been previously advisable while still being able to model the biases incurred (similarly to how the $N^{(n)}$-type biases of lensing are corrected for).

More immediately, we believe our tool — which we make publicly available under the name `CosmoBLENDER` — can be of use when optimising experiment designs and filtering choices, as the space of experimental and astrophysical parameters can be explored very efficiently.

Of course, our method has limitations. There is evidence that realistic effects such as cluster asphericity or substructure increase the tSZ power spectrum by as much as 10–20% on small angular scales $l \sim 2000$–8000 [26]; it is reasonable to expect these effects to impact higher-point functions as well, and for their importance to extend to other foregrounds. It would therefore be desirable to validate our analytic method against hydrodynamical simulations, which properly take these effects into account. Unfortunately, hydrodynamical simulations of the size required for our purposes appear to be unattainable in the near term. In the meantime, carefully-selected zoom-in simulations might prove useful for our purposes.

Chapter 6

General conclusions and outlook

In under a century, humanity's understanding of the Universe has evolved from believing that our Galaxy contained all that there is, to a picture where it has no end. In the current consensus cosmological model, ΛCDM, approximately 69% of the present-day energy density of the Universe is in the form of a cosmological constant, 5% in visible matter and 26% in cold dark matter; these component abundances are just enough to make the Universe flat. The model relies on there being a spectrum of primordial perturbations in the energy density with a power spectrum that is very nearly scale-invariant; observations have confirmed this, and further constrained the perturbations to being adiabatic and Gaussian to high precision. ΛCDM is in superb agreement with a wide variety of observations, ranging from abundances of the light elements to the clustering of galaxies and the temperature and polarisation anisotropies of the CMB. The level of consistency with Planck's high-precision tests is especially remarkable.

At present, inflation appears to provide the best explanation for the initial conditions of the Universe. It predicts the generation of initial fluctuations in the energy density at very early times with properties which, in the simplest versions of the model, are perfectly consistent with observations. Moreover, a period of inflation is expected to have produced gravitational waves in addition to density fluctuations. This is the last major prediction of inflation that remains to be tested, and the one that is most discerning between inflation and its leading alternatives. A detection would be doubly important, as it would also open a window into physics at energy scales unattainable from Earth's laboratories.

Primordial gravitational waves quickly decay once they enter the Hubble horizon, so our best bet to detect them is by studying the imprint that they left, right as they were crossing the horizon, on the temperature and polarisation anisotropies of the CMB. However, measurements have constrained a gravitational wave contribution to the temperature and E-mode polarisation to be small compared to that associated with scalar perturbations; the large variance associated with the latter limits our

ability to derive further constraints from T or E. Fortunately, scalar perturbations do not produce B-mode polarisation at leading order, while tensors do. Measuring a primordial B-mode on degree scales — approximately the angle subtended by the Hubble horizon at recombination — has thus become one of the driving goals of modern cosmology. Upcoming experiments, such as the Simons Observatory (SO) and SPT-3G will measure B-modes with sufficient precision to detect a primordial contribution with $r \sim 0.01$, while the more futuristic CMB-S4 is aiming for $r \sim 0.001$. This would probe interesting scenarios such as Higgs inflation or the Starobinsky model.

Though reaching these targets will certainly require impressive technological developments, the two major challenges ahead are likely to come from Galactic foreground contamination (chiefly thermal dust and synchrotron emission) and gravitational lensing. Lensing converts part of the primordial E-mode polarisation produced by scalar perturbations into B-modes, adding a source of variance that can hinder constraints. The partial removal — or delensing — of these lensing B-modes constitutes the main focus of this thesis.

A popular and effective way of removing the lensing noise entails subtracting a template of the lensing B-modes from observations. The template can be built by combining high-resolution observations of E-modes with some proxy of the lensing potential. In chapter 2, we studied in detail the benefits and limitations of such templates. We found that a gradient-order template is more effective when constructed from lensed E-modes, instead of their delensed or unlensed version. Furthermore, we showed that, given lensed E-modes, a gradient-order template is to be preferred over a non-perturbative one. We concluded that a gradient-order template built from lensed E-modes will be effectively optimal for all planned CMB experiments, with the added benefit of being analytically transparent and computationally efficient.

The matter proxy needed to build lensing B-mode templates can either be obtained internally, by reconstructing lensing from the CMB itself, or externally, from tracers of the large-scale structure of the Universe. The latter approach is important for current and soon-upcoming CMB experiments, such as SO. In chapter 3, we studied the process of delensing by combining several tracers (some of them external), focusing on the case of SO. We provided models for the auto- and cross-spectra with observations of the templates (and their covariance) in the case where the matter proxy is made of multiple tracers. We also discussed how uncertainties in measurements of the tracer spectra might translate to biased constraints on r, though we showed that this effect will likely be negligible for SO.

The CIB is known to be highly correlated with lensing, making it an attractive tracer for delensing. Indeed, it has been used in several recent demonstrations of the procedure, and it will be an important element of SO's delensing analysis. As part of the work in chapter 3, we studied delensing biases from foreground residuals when the CIB is used as a proxy of the matter. We found that significant biases can arise if the largest angular scales are included in analyses, because of non-Gaussian galactic dust residuals remaining after foreground cleaning. Fortunately, the mitigation techniques we propose appear to be highly effective. We also calculated certain relevant bispectra and trispectra involving CIB intensity and polarisation, and used them to show that biases from CIB residuals will be negligible for any future application of CIB delensing.

Ultimately, the optimal matter proxy used for delensing will be reconstructed internally from the CMB. In particular, the EB quadratic estimator will soon provide most of the lensing signal-to-noise — certainly for CMB-S4, and already for SPT-3G. The challenge comes whenever there is an overlap in modes between the field that is to be delensed (in this case, the B-modes) and the fields from which the reconstruction is obtained: couplings then appear that can potentially bias a naïve analysis. We explored this bias in detail in chapter 4, and learnt that it necessarily leads to degraded constraints on r, despite appearing to reduce the variance of the estimators used in the inference. We derived an analytic model for the bias, but showed that it is generally advantageous to exclude the overlapping modes rather than model or renormalise the bias.

CMB lensing reconstructions are a topic of much wider interest beyond just delensing. Since lensing is sensitive to any physics that could have affected the growth of structure after the CMB was released, it can be used to probe important late-time phenomena — the sum of the neutrino masses, the growth of structure, curvature, etc. — which are highly degenerate if only the primary CMB is considered. In the coming years, SO will produce maps of the lensing potential over 40% of the sky that are signal-dominated down to angular scales of approximately 40 arcmin; this figure will subsequently improve to 10 arcmin for CMB-S4 and SPT-3G (though for the latter, only over a few percent of the sky). Among many other applications, these precise measurements will be able to weigh in on the apparent discrepancy between the low-redshift lensing amplitude measured by galaxy weak lensing surveys, and the value calculated in the context of ΛCDM from the primary CMB anisotropies (see, e.g., [240]).

An important challenge for SO (and any experiment relying significantly on temperature information for its lensing reconstructions) is contamination from extragalactic foregrounds. The tSZ and CIB alone can bias measurements of the lensing power

spectrum at the level of several percent if not accounted for. In chapter 5, we introduced a framework for calculating these biases analytically, using halo models calibrated to simulations. Though only a subset of all possible terms have been implemented so far, our calculations already show promising agreement with simulations. This tool might be useful to the CMB community when optimising experiment designs or deciding on schemes/thresholds for removal of sources. Furthermore, our implementation is computationally efficient, and could potentially be of interest to optimal lensing analyses where signal and noise are modelled jointly.

Though the abundances and phenomenology of the different components of the Universe appear to be well established, the truth is that the nature of the vast majority of what exists remains a mystery. We do not know what constitutes the dark matter or the dark energy (together, over 95% of the energy density of the Universe), and we do not know why inflation (or whatever mechanism produced the seeds of structure) proceeded the way it did. What we do know is that there is physics beyond the Standard Model — such as massive neutrinos — that cosmology, with gravitational lensing at the forefront, is uniquely positioned to unveil.

Appendix A

Calculations for Chapter 4

A.1 Internally-delensed B-mode power spectrum

In this appendix, we give details of the calculation of the B-mode power spectrum after internal delensing, as given in equation (4.15) in the main text. Specifically, we evaluate the four- and six-point functions of the observed CMB that appear in the cross-correlation of the lensing B-mode template with the observed B-modes, equation (4.13), and the power spectrum of the template, equation (4.14), respectively.

It is convenient to expand these four- and six-point functions in terms of connected n-point functions. In the absence of lensing, the CMB would be Gaussian and all connected n-point functions with $n > 2$ would vanish. As the CMB fields are zero mean, the evaluation of n-point functions would reduce to products of two-point functions. However, in section 4.5 we saw that lensing distorts the Gaussian primordial statistics, introducing significant non-Gaussianities in the form of non-vanishing, higher-order connected n-point functions, which we shall also refer to as "connected correlators". In particular, the connected four-point function, or trispectrum, induced by lensing lies at the heart of any effort to infer $C_L^{\phi\phi}$ from the lensed CMB [197, 95, 223, 169]. Note that Gaussian instrumental noise does not contribute to the connected correlators of the observed CMB fields. Moreover, if we ignore the impact of lensing on the (otherwise Gaussian) gravitational wave contributions to the CMB (which should be a good approximation given their power falls rapidly on intermediate and small scales), these contributions are independent of the lensed, scalar contribution and so do not contribute to the connected correlators either.

We organise the expansion of the n-point functions with the aid of a graphical representation where fields are represented by nodes, drawing those that are observed by the LAT in red, and those observed by the SAT in green. Lines connecting n nodes denote the connected n-point function of the associated fields, which can be evaluated perturbatively to the desired order in lensing. In order to preserve generality, we ensure

that the case where a single telescope is used for both construction of the delensing template and the observation of the large-scale B-modes can be recovered by letting $N_l^X = N_l^{BB,\mathrm{LAT}} = N_l^{BB,\mathrm{SAT}}$, with $N_l^X = 0$ otherwise.

In this way, the four-point function appearing in equation (4.13) can be represented as

$$\langle E^{\mathrm{obs,\,LAT}}(\boldsymbol{l}_1')E^{\mathrm{obs,\,LAT}}(\boldsymbol{l}_1'')B^{\mathrm{obs,\,LAT}}(\boldsymbol{l}_1-\boldsymbol{l}_1'-\boldsymbol{l}_1'')B^{\mathrm{obs,\,SAT}}(\boldsymbol{l}_2)\rangle =$$

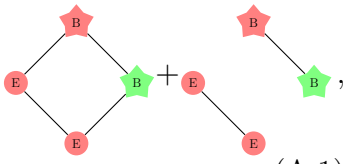

(A.1)

where terms of the form $\langle EB\rangle$ have vanished due to parity invariance. The B- and E-fields involved in the lens reconstruction are at the top and bottom of the diagrams, respectively, and the E-modes used further in the template are at the midpoint on the left. The two diagrams on the right of equation (A.1) correspond to a trispectrum $\langle E^{\mathrm{obs}}E^{\mathrm{obs}}B^{\mathrm{obs}}B^{\mathrm{obs}}\rangle_c$ and a product of two-point functions $\langle E^{\mathrm{obs}}E^{\mathrm{obs}}\rangle\langle B^{\mathrm{obs}}B^{\mathrm{obs}}\rangle$. Similarly, the six-point function appearing in equation (4.14) can be decomposed into

$$\begin{aligned}&\langle E^{\mathrm{obs,\,LAT}}(\boldsymbol{l}_1')E^{\mathrm{obs,\,LAT}}(\boldsymbol{l}_1'')B^{\mathrm{obs,\,LAT}}(\boldsymbol{l}_1-\boldsymbol{l}_1'-\boldsymbol{l}_1'')\\&\quad\times E^{\mathrm{obs,\,LAT}}(\boldsymbol{l}_2')E^{\mathrm{obs,\,LAT}}(\boldsymbol{l}_2'')B^{\mathrm{obs,\,LAT}}(\boldsymbol{l}_2-\boldsymbol{l}_2'-\boldsymbol{l}_2'')\rangle\end{aligned}$$

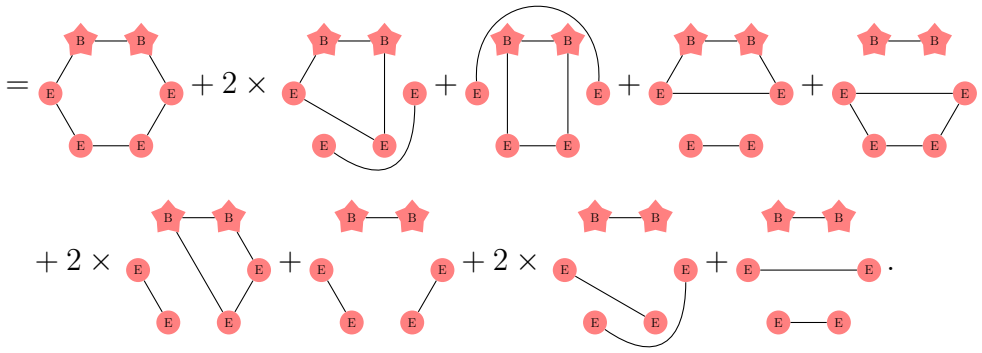

(A.2)

Diagrams shown with multiplicity factors of two correspond to two diagrams related by $\boldsymbol{l}_1 \leftrightarrow \boldsymbol{l}_2$ (and similarly for primed wavevectors).

A.1.1 Contributions to the unbiased delensed power spectrum

The standard calculation of equation (4.10) assumes that the statistical noise in the lensing reconstruction, $\hat{\phi}$, that appears in B^{temp} is independent of the CMB fields. For

this reason, it includes only some of the terms making up eqs. (4.13) and (4.14) or, equivalently, some of the couplings represented by the diagrams of eqs. (A.1) and (A.2). We calculate these here, before assessing the remaining terms in section A.1.2.

We start with the cross-correlation of the template with the observed B-modes, i.e., $-2\langle B^{\rm temp}(\boldsymbol{l}_1)B^{\rm obs}(\boldsymbol{l}_2)\rangle$. Only the part involving the connected four-point function is included in the standard calculation, and then only the "primary coupling" in which there is a contraction over the unlensed E-modes across the two legs of the quadratic estimator $\hat{\phi}$. This yields

$$-2 \times \quad \supset -2\,\langle \tilde{E}[E,\phi]\tilde{E}[E,\phi]\tilde{B}[E,\phi]\tilde{B}[E,\phi]\rangle \tag{A.3}$$

$$\rightarrow -2\,(2\pi)^2\delta^{(2)}(\boldsymbol{l}_1+\boldsymbol{l}_2)C_{l_1}^W,$$

where C_l^W is defined in equation (4.11). Here, we have introduced the notation, for example, $\tilde{E}[E,\phi]$ to show the functional dependence of the field $\tilde{E}$ on the unlensed E-modes and ϕ. Note that the dependence on the unlensed E-modes is linear, and where ϕ is uncontracted, the unlensed field E is implied. The one other possible trispectrum coupling is subdominant. Ultimately, our justification of this is the good agreement between our model for the delensed B-mode power spectrum and our simulation results. However, a plausibility argument can be made based on the volume of wavevector space that terms can accumulate in the integral in equation (4.13), similar to the reasoning why the primary coupling should dominate over other "$N^{(1)}$" couplings in the auto-power spectrum in CMB lensing reconstruction [197]. Generally, terms that couple together two or more of the weights $[W(\boldsymbol{l}_a,\boldsymbol{l}_b)]$ in the integrand, i.e., the least factorisable terms, will be subdominant relative to other terms where the weights are uncoupled and some of the nested integrals can be separated, since the volume of wavevector space is reduced in the former case. In the specific case of equation (A.3), the primary coupling produces the same pattern of weights as appears in the rest of the integrand in equation (4.13), while for the other coupling there is no such factorisation. The primary coupling is responsible for the removal of the lensing signal in $B^{\rm obs}$ that correlates with $B^{\rm temp}$; that is, the actual delensing.

We now consider contributions from the six-point function $\langle B^{\rm temp}(\boldsymbol{l}_1)B^{\rm temp}(\boldsymbol{l}_2)\rangle$. The only fully-disconnected term that appears in the standard calculation is

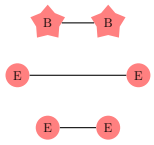

$$\to (2\pi)^2\delta^{(2)}(\boldsymbol{l}_1+\boldsymbol{l}_2)\int\frac{d^2\boldsymbol{l}'_1}{(2\pi)^2}W^2(\boldsymbol{l}_1,\boldsymbol{l}'_1)\left(\mathcal{W}^E_{l'_1}\right)^2 C^{EE,\rm obs,LAT}_{l'_1}\left(\mathcal{W}^\phi_{|\boldsymbol{l}_1-\boldsymbol{l}'_1|}\right)^2$$
$$\times\left(A^{EB}_{|\boldsymbol{l}_1-\boldsymbol{l}'_1|}\right)^2\int\frac{d^2\boldsymbol{l}''_1}{(2\pi)^2}W^2(\boldsymbol{l}_1-\boldsymbol{l}'_1-\boldsymbol{l}''_1,-\boldsymbol{l}''_1)$$
$$\times\frac{\left(\tilde{C}^{EE,\rm fid}_{l''_1}\right)^2 C^{EE,\rm obs,LAT}_{l''_1}C^{BB,\rm obs,LAT}_{|\boldsymbol{l}_1-\boldsymbol{l}'_1-\boldsymbol{l}''_1|}}{\left(C^{EE,\rm obs,fid,LAT}_{l''_1}C^{BB,\rm obs,fid,LAT}_{|\boldsymbol{l}_1-\boldsymbol{l}'_1-\boldsymbol{l}''_1|}\right)^2}. \tag{A.4}$$

Typically, the fiducial observational power spectra used to inverse-variance weight the CMB fields for lensing reconstruction, and in the Wiener filters, will be calibrated from the observed power so to an excellent approximation $C_l^{EE,\rm obs,LAT}\approx C_l^{EE,\rm obs,fid,LAT}$, and similarly for the B-mode spectra. In this case, the integral over $\boldsymbol{l}''_1$, combined with the (fiducial) normalisation $(A^{EB}_{|\boldsymbol{l}_1-\boldsymbol{l}'_1|})^2$, gives the Gaussian reconstruction noise $N^{(0)EB}_{|\boldsymbol{l}_1-\boldsymbol{l}'_1|}$ of the quadratic estimator. Finally, if we substitute $\mathcal{W}^E_l C^{EE,\rm obs,LAT}_l\approx C^{EE,\rm fid}_l$ in equation (A.4), we obtain

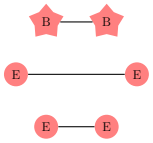

$$\to (2\pi)^2\delta^{(2)}(\boldsymbol{l}_1+\boldsymbol{l}_2)\int\frac{d^2\boldsymbol{l}'_1}{(2\pi)^2}W^2(\boldsymbol{l}_1,\boldsymbol{l}'_1)\left[\mathcal{W}^E_{l'_1}C^{EE,\rm fid}_{l'_1}\right]\left[\left(\mathcal{W}^\phi_{|\boldsymbol{l}_1-\boldsymbol{l}'_1|}\right)^2 N^{(0)EB}_{|\boldsymbol{l}_1-\boldsymbol{l}'_1|}\right]. \tag{A.5}$$

The only other diagram that is retained in the standard calculation involves a Gaussian correlation of E-modes across templates multiplying a trispectrum made up of two quadratic estimators, $\langle\hat{\phi}\hat{\phi}\rangle_c$. This trispectrum has been studied in detail by Ref. [95]. To $\mathcal{O}(C_L^{\phi\phi})$, it evaluates to a sum of the lensing power spectrum, from the primary coupling, and an $N^{(1)}$ term from the other couplings. Only the primary coupling is included in the standard calculation, and arises from contractions of the form

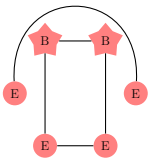

$$\supset\langle\hat{\phi}^{EB}[E,\tilde{B}[E,\phi]]\hat{\phi}^{EB}[E,\tilde{B}[E,\phi]]\rangle. \tag{A.6}$$

However, we include $N^{(1)}$ here for completeness to find

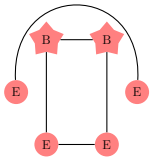

$$\to (2\pi)^2\delta^{(2)}(\boldsymbol{l}_1+\boldsymbol{l}_2)\int\frac{d^2\boldsymbol{l}'_1}{(2\pi)^2}W^2(\boldsymbol{l}_1,\boldsymbol{l}'_1)\left[\mathcal{W}^E_{l'_1}C^{EE,\mathrm{fid}}_{l'_1}\right]$$
$$\times\left[\left(\mathcal{W}^{\phi}_{|\boldsymbol{l}_1-\boldsymbol{l}'_1|}\right)^2\left(C^{\phi\phi,\mathrm{fid}}_{|\boldsymbol{l}_1-\boldsymbol{l}'_1|}+N^{(1)EB}_{|\boldsymbol{l}_1-\boldsymbol{l}'_1|}\right)\right], \quad \text{(A.7)}$$

where we have assumed, again, that $\mathcal{W}^E_l C^{EE,\mathrm{obs,LAT}}_l \approx C^{EE,\mathrm{fid}}_l$. The explicit form of $N^{(1)EB}_{|\boldsymbol{l}_1-\boldsymbol{l}'|}$ is given in equation (57) of Ref. [95]. We find this contribution to be subdominant on the relevant scales to both (A.5) and to the contribution from the primary coupling of the trispectrum, which gives rise to $C^{\phi\phi}_l$ in the integrand of (A.7).

Combining eqs. (A.5) and (A.6) gives

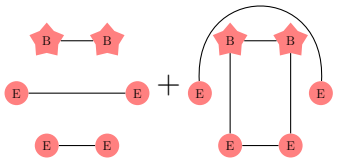

$$\to (2\pi)^2\delta^{(2)}(\boldsymbol{l}_1+\boldsymbol{l}_2)\int\frac{d^2\boldsymbol{l}'_1}{(2\pi)^2}W^2(\boldsymbol{l}_1,\boldsymbol{l}'_1)\mathcal{W}^E_{l'_1}C^{EE,\mathrm{fid}}_{l'_1}(\mathcal{W}^{\phi}_{|\boldsymbol{l}_1-\boldsymbol{l}'_1|})^2$$
$$\times\left(C^{\phi\phi,\mathrm{fid}}_{|\boldsymbol{l}_1-\boldsymbol{l}'_1|}+N^{(0)EB}_{|\boldsymbol{l}_1-\boldsymbol{l}'_1|}+N^{(1)EB}_{|\boldsymbol{l}_1-\boldsymbol{l}'_1|}\right)$$
$$\approx (2\pi)^2\delta^{(2)}(\boldsymbol{l}_1+\boldsymbol{l}_2)C^W_{l_1}, \quad \text{(A.8)}$$

where in the last line we have neglected $N^{(1)EB}_{|\boldsymbol{l}_1-\boldsymbol{l}'|}$ and assumed that $\mathcal{W}^{\phi}_l(C^{\phi\phi}_l+N^{(0)EB}_l)\approx C^{\phi\phi}_l$. Together with equation (4.12) and equation (A.3), we recover the standard result for the residual lensing power spectrum of equation (4.10):

$$\langle B^{\mathrm{del}}(\boldsymbol{l}_1)B^{\mathrm{del}}(\boldsymbol{l}_2)\rangle = (2\pi)^2\delta^{(2)}(\boldsymbol{l}_1+\boldsymbol{l}_2)\left(N^{BB,\mathrm{SAT}}_{l_1}+C^{BB,t}_{l_1}+\tilde{C}^{BB}_{l_1}-C^W_{l_1}\right). \quad \text{(A.9)}$$

A.1.2 Additional corrections from internal delensing

We now consider the remaining couplings, represented by the diagrams of eqs. (A.1) and (A.2), which are not included in the standard calculation and lead to biases if left uncorrected.

We start with the six-point function (equation A.2). The contribution from the connected six-point function (the first diagram on the right) is expected to be negligible compared to the other terms in the six-point function since it is one order higher in $C^{\phi\phi}_l$. For the other terms, we are guided by the argument above about the volume of wavevector space available given the implied couplings between the weights. For

the remaining terms involving the connected four-point function, this suggests that, symbolically,

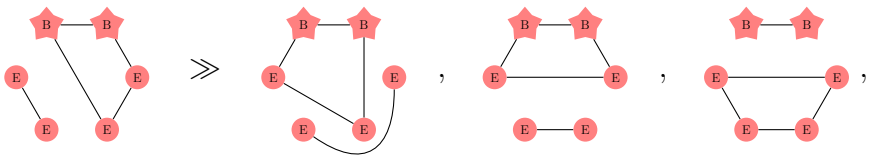

(A.10)

so we retain only the term on the left. The simulations of Ref. [312] indicate that the first term makes the largest contribution of those on the right of equation (A.10), but it is still significantly smaller (on large scales) than that on the left. Retaining only the primary coupling, we find

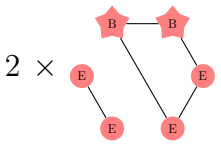

$$\supset \quad 2\,\langle \overbrace{E^{\rm obs}}\, \overbrace{E^{\rm obs}}\, \tilde{B}[E,\phi]\tilde{E}[E,\phi]\tilde{E}[E,\phi]\tilde{B}[E,\phi]\rangle$$

$$\rightarrow \quad 2\,(2\pi)^2\delta^{(2)}(\boldsymbol{l}_1+\boldsymbol{l}_2)C_{l_1}^{W}D_{l_1}\,, \tag{A.11}$$

where we have defined

$$D_l \equiv \frac{1}{C_l^{BB,\rm obs,fid,LAT}}\int\frac{d^2\boldsymbol{l}'}{(2\pi)^2}W^2(\boldsymbol{l},\boldsymbol{l}')\left[\mathcal{W}_{l'}^{E}\tilde{C}_{l'}^{EE}\right]\left[\mathcal{W}_{|\boldsymbol{l}-\boldsymbol{l}'|}^{\phi}A_{|\boldsymbol{l}-\boldsymbol{l}'|}^{EB}\right]\,. \tag{A.12}$$

Note that the spectrum D_l arises when one contracts the two observed E-modes that explicitly appear in the lensing template:

$$\langle B^{\rm temp}(\boldsymbol{l})\rangle_{E^{\rm obs,LAT}} = B^{\rm obs,LAT}(\boldsymbol{l})D_l\,. \tag{A.13}$$

For the remaining terms in equation (A.2) that involve only the two-point functions, we expect, symbolically, that

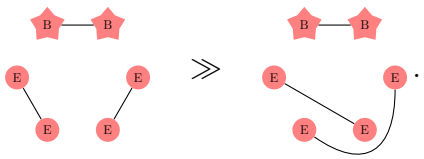

(A.14)

Retaining only the term on the left, we have

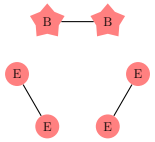

$$\rightarrow \quad (2\pi)^2\delta^{(2)}(\boldsymbol{l}_1+\boldsymbol{l}_2)C_{l_1}^{BB,\mathrm{obs,LAT}}D_{l_1}^2 \quad . \tag{A.15}$$

Note how this involves a contribution from the primordial B-mode power, if present, through $C_{l_1}^{BB,\mathrm{obs,LAT}}$.

Finally, we return to the four-point function, equation (A.1). The term not included in the standard calculation is that involving only the two-point functions, whose contribution to the delensed power spectrum is

$-\ 2\ \times$

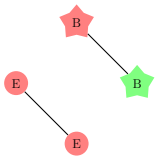

$$\rightarrow \quad -2D_{l_1}\langle B^{\mathrm{obs,LAT}}(\boldsymbol{l}_1)B^{\mathrm{obs,SAT}}(\boldsymbol{l}_2)\rangle\,. \tag{A.16}$$

The term $D_{l_1}B^{\mathrm{obs,LAT}}(\boldsymbol{l}_1)$ arises from contracting the observed E-modes in the template represented by the left-half of the diagram. Allowing for the case where the B-modes used in the lensing reconstruction are from the same survey as those used to measure the large-scale B-modes, with the noise cross-spectrum N_l^X, we have

$$-2D_{l_1}\langle B^{\mathrm{obs,LAT}}(\boldsymbol{l}_1)B^{\mathrm{obs,SAT}}(\boldsymbol{l}_2)\rangle = -2\,(2\pi)^2\delta^{(2)}(\boldsymbol{l}_1+\boldsymbol{l}_2)\left(\tilde{C}_{l_1}^{BB}+C_{l_1}^{BB,\mathrm{t}}+N_{l_1}^X\right)D_{l_1}\,. \tag{A.17}$$

Note how this term also receives a contribution from the primordial B-mode power.

The term (A.17) differs from its equivalent in previous work. In Ref. [316], only the lensing contribution on the right is considered (see the third term on the right of their equation A16), while in Ref. [477] only the tensor and noise contributions are present (see their eqs. 7 and 8). The total correction to the standard delensed power involving the tensor B-mode power is $D_l(D_l-2)C_l^{BB,\mathrm{t}}$, which is negative since $0<D_l<1$ (see the discussion after equation 4.17 in the main text) and so there is a suppression of the primordial power [477].

Putting all the relevant terms together, the biased delensed spectrum can be modelled as

$$\begin{aligned} C_l^{BB,\mathrm{del}} &= C_l^{BB,\mathrm{obs,SAT}} - C_l^W + C_l^{BB,\mathrm{obs,LAT}}D_l^2 - 2D_l(\tilde{C}_l^{BB}+C_l^{BB,t}+N_l^X-C_l^W) \\ &= (C_l^{BB,\mathrm{res}}+C_l^{BB,\mathrm{t}})(D_l-1)^2 + D_l^2C_l^W + N_l^{BB,\mathrm{SAT}} + N_l^{BB,\mathrm{LAT}}D_l^2 - 2D_lN_l^X\,. \end{aligned} \tag{A.18}$$

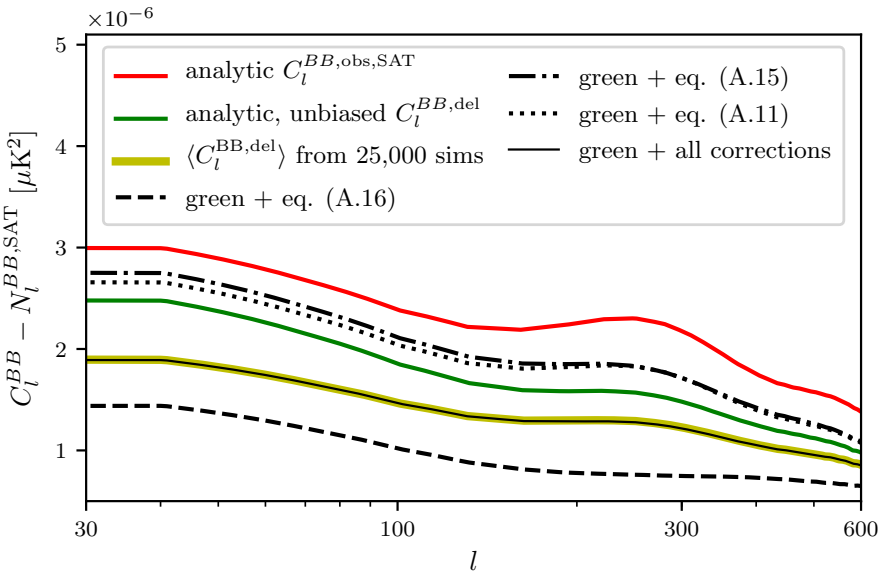

Fig. A.1 Break-down of contributions to the model, biased, delensed power spectrum of equation (A.18) in the case where $r_{\mathrm{input}} = 0.01$. The experimental set-up is a LAT with polarisation noise $\Delta_{\mathrm{P}} = 6\sqrt{2}\,\mu$K arcmin and beam size $\theta_{\mathrm{FWHM}} = 1.5$ arcmin and a SAT with $\Delta_{\mathrm{P}} = 2\sqrt{2}\,\mu$K arcmin and $\theta_{\mathrm{FWHM}} = 17$ arcmin. The average delensed power from 25 000 simulations is also shown.

The contributions from the various terms are shown in figure A.1, along with the total delensed power measured from simulations. The model for the total predicted power agrees very well with the simulation results.

The bias, i.e., the terms in equation (A.18) involving D_l, can be avoided by excluding from the lensing reconstruction any B-modes that overlap in scale with the B-modes we wish to delens [477, 316]. This easily follows from noting that all significant bias terms arise from contracting the pair of observed E-modes in at least one lensing template, that is they involve $\langle B^{\mathrm{temp}}(\boldsymbol{l}) \rangle_{E^{\mathrm{obs,LAT}}}$ when attempting to delens B-modes at wavevector $\boldsymbol{l}$. The result of this contraction is proportional to the observed B-mode at $\boldsymbol{l}$, $B^{\mathrm{obs,LAT}}(\boldsymbol{l})$, used in the lensing reconstruction (see equation A.13). If such modes are excluded from the reconstruction, the bias necessarily vanishes.

In the case of a single survey, the correlated noise between the B-modes used in the lensing reconstruction and the B-modes to delens sources a larger bias on the delensed spectrum than in the case of independent surveys (although, as explained in section 4.4.2, the signal-to-noise on primordial B-mode power is also greater in the former configuration), and acts to emulate an apparent, but spurious, delensing efficiency much greater than expected. This is particularly clear from the cross-spectrum

of the template with the observed B-modes. Combining equation (A.17) with the unbiased result equation (A.3) — after identifying D_l with $C_l^{BB,\mathrm{res}}/C_l^{BB,\mathrm{obs,fid,LAT}}$ in the limit where E-mode noise can be neglected in the template (see section 4.4.2) — we find that this cross-spectrum produces the entire lensing power:

$$\langle B^{\mathrm{obs,\,SAT}}(\boldsymbol{l}_1) B^{\mathrm{templ,\,SAT}}(\boldsymbol{l}_2)\rangle \approx (2\pi)^2 \delta^{(2)}(\boldsymbol{l}_1+\boldsymbol{l}_2)\tilde{C}_{l_1}^{BB} \quad (\text{for } N_l^X = N_l^{BB,\mathrm{LAT}} = N_l^{BB,\mathrm{SAT}}) \tag{A.19}$$

irrespective of the actual fidelity of the lensing reconstruction. In figure A.2, we quantify further this apparent delensing. We show the difference of the power spectrum of the observed SAT B-modes and the power spectrum of their delensed counterparts as a fraction of the B-mode lensing power as the instrument noise level is varied. This apparent delensing efficiency is shown averaged over degree-scale multipoles, for $r_{\mathrm{input}} = 0$, keeping otherwise the same simulation and reconstruction parameters as in figure 4.1. It is shown for the single-survey case in blue, while the black and green curves show the unbiased case ($C_l^W/\tilde{C}_l^{BB}$) and biased case with $N_l^X = 0$, respectively, for comparison. The single-survey apparent efficiency is broken down into the contribution from the four-point function of the observed fields (i.e., twice the cross-correlation between the template and the observed B-modes; shown in orange) and the six-point function (i.e., the auto-power spectrum of the template; red). The latter contribution does not depend on N_l^X and so is the same whether the surveys are independent or not (provided $N_l^{BB,\mathrm{SAT}} = N_l^{BB,\mathrm{LAT}}$), but the contribution of the cross-spectrum is boosted in the single-survey case. In this case, at low noise levels both cross- and auto-spectra are conspicuously close to $\tilde{C}_l^{BB}$, resulting in an apparent delensing efficiency close to 100 %. For higher noise levels, the apparent delensing efficiency is even larger, exceeding 100 %.

A.2 Simulations

We simulate observations of the CMB sky using the publicly-available code `QuickLens`[1] for a fiducial cosmology best fitting the Planck+WP+highL data of Ref. [354]. Inspired by the experimental configurations of the upcoming Simons Observatory, we simulate a reconstruction-oriented large-aperture-telescope (LAT) survey with noise levels $\Delta_P = 6\sqrt{2}\,\mu\mathrm{K\,arcmin} = \sqrt{2}\,\Delta_T$ and beam FWHM of $\theta_{\mathrm{FWHM}} = 1.5\,\mathrm{arcmin}$, together with a small-aperture-telescope (SAT) survey with $\Delta_P = 2\sqrt{2}\,\mu\mathrm{K\,arcmin} = \sqrt{2}\,\Delta_T$ and

[1] `https://github.com/dhanson/quicklens`, though an amended and extended version can be found at `https://github.com/abaleato/Quicklens-with-fixes`.

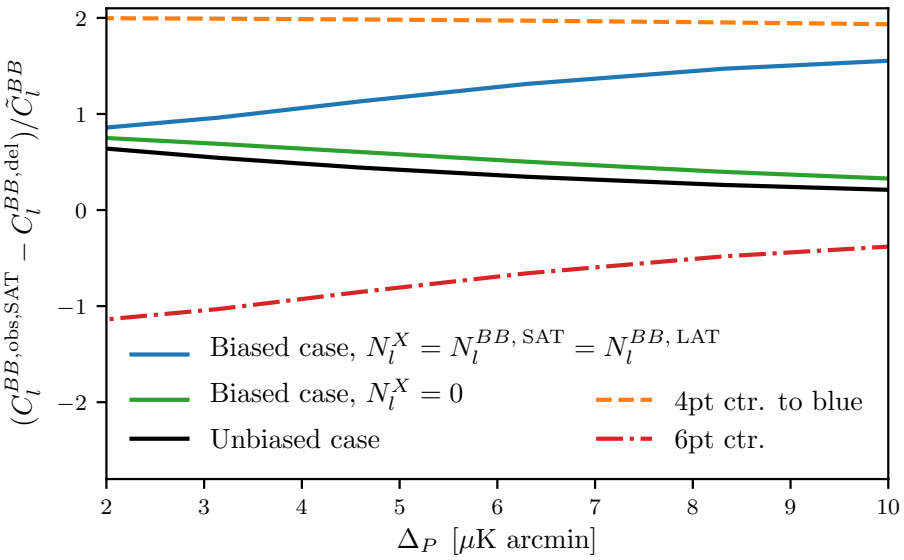

Fig. A.2 Break-down of contributions to the difference between the power spectrum of the B-modes observed with the SAT and the power spectrum of the delensed B-modes, as a fraction of the original B-mode lensing power. This apparent delensing efficiency is shown as a function of the polarisation white-noise level, for vanishing r_{input}, keeping other specifications unchanged with respect to our baseline configuration in figure 4.1. In the case of independent surveys, the same noise level is assumed in each ($N_l^X = 0$ and $N_l^{BB,\mathrm{SAT}} = N_l^{BB,\mathrm{LAT}}$). The internal delensing bias is larger for a single survey (blue) than for independent SAT and LAT noise (green), in both cases artificially inflating the apparent delensing efficiency compared to the unbiased case (black). The orange line shows the contribution to the single-survey case (i.e., the blue line) from the cross-correlation between the template and the observed B-modes, which is almost exactly equal to the full lensing power (see equation A.19). The red line shows the contribution from the auto-power spectrum of the template.

$\theta_{\mathrm{FWHM}} = 17\,\mathrm{arcmin}$. The simulations we generate are on the flat sky with 1024 pixels per side with an inter-pixel separation of 2 arcmin, covering approximately 2.8 % of the sky. Our simulations have periodic boundary conditions and are free of foregrounds. Note that we only simulate the part of the LAT survey that overlaps with the SAT survey.

The procedure for obtaining lensed CMB maps is as follows: first, we generate unlensed T, E, B and ϕ fields in harmonic space by drawing their Fourier coefficients from zero-mean Gaussian distributions with variance at each (interpolated) angular scale given by the theory power spectra (obtained from `CAMB` [254]). At this stage, we choose a pixelisation, which in turn sets the maximum frequency we can adequately sample by the Nyquist–Shannon sampling theorem. Then, the unlensed T, E and B fields are rotated into T, Q and U and remapped according to the deflection field $\boldsymbol{d}(\hat{\boldsymbol{n}}) = \boldsymbol{\nabla}\phi$ as

$$\tilde{T} = T[\hat{\boldsymbol{n}} + \boldsymbol{d}(\hat{\boldsymbol{n}})], \tag{A.20}$$

and analogously for Q and U, using a bivariate spline interpolation over a rectangular mesh. In order to mimic the effect of observations, we convolve the lensed fields with the transfer function for an experimental beam that is assumed to be symmetric and Gaussian with the required FWHM. As a final step, we add uncorrelated, Gaussian-distributed experimental noise at the map level.

Appendix B

Calculations for Chapter 3

B.1 The BEI bispectrum of the CIB

In order to model the BEI bispectrum of the CIB, we begin by considering the specific intensity observed at frequency ν, along a line of sight $\hat{\boldsymbol{n}}$. We shall work in the flat-sky limit, in which case $\hat{\boldsymbol{n}}$ is close to the pole and the 3D comoving position of a source, $\boldsymbol{x}_{\rm 3D}$, can be related to its angular position in the plane of the sky, $\boldsymbol{\theta}$, as $\boldsymbol{x}_{\rm 3D} \approx r(z)(\boldsymbol{\theta} + \hat{\boldsymbol{z}})$, where $r(z)$ is the comoving distance to the redshift where the source is located and $\hat{\boldsymbol{z}}$ is a unit vector along the z-direction. In this limit, the observed temperature is an integral along the line of sight of j_ν, the emissivity per unit comoving volume and per solid angle :

$$I_\nu(\boldsymbol{\theta}) = \int dz \frac{dr}{dz} a(z) j_{\nu(1+z)}(r(z)(\boldsymbol{\theta} + \hat{\boldsymbol{z}}), z). \tag{B.1}$$

Similarly, the Stokes parameters for linear polarisation can be related to $j_\nu^{(\pm)}$, the polarised emissivity per unit comoving volume along the negative z-direction, via

$$(Q \pm iU)_\nu(\boldsymbol{\theta}) = p \int dz \frac{dr}{dz} a(z) j^{(\pm)}_{\nu(1+z)}(r(z)(\boldsymbol{\theta} + \hat{\boldsymbol{z}}), z), \tag{B.2}$$

where p is the polarisation fraction of the sources, which we will take to be a constant. In the flat-sky limit, the Fourier modes of polarisation can be extracted as

$$\begin{aligned}
(Q \pm iU)_\nu(\boldsymbol{l}) &= \int d^2\boldsymbol{\theta} (Q \pm iU)_\nu(\boldsymbol{\theta}) e^{-i\boldsymbol{l}\cdot\boldsymbol{\theta}} \\
&= p \int dz \, \frac{dr}{dz} a(z) \int \frac{d^3\boldsymbol{k}}{(2\pi)^3} \, j^{(\pm)}_{\nu(1+z)}(\boldsymbol{k}, z) \int d^2\boldsymbol{\theta} \, e^{ir(z)\boldsymbol{k}\cdot(\boldsymbol{\theta}+\hat{\boldsymbol{z}})} e^{-i\boldsymbol{l}\cdot\boldsymbol{\theta}} \\
&= p \int dz \, \frac{dr}{dz} a(z) \int \frac{d^3\boldsymbol{k}}{2\pi} \, j^{(\pm)}_{\nu(1+z)}(\boldsymbol{k}, z) \delta^{(2)}_{\rm D}(\boldsymbol{k}_\perp r(z) - \boldsymbol{l}) e^{ik_3 r(z)} \\
&= p \int dz \, \frac{dr}{dz} \frac{a(z)}{r^2(z)} \int \frac{dk_3}{2\pi} \, e^{ik_3 r(z)} j^{(\pm)}_{\nu(1+z)}(\boldsymbol{l}/r(z) + k_3\hat{\boldsymbol{z}}, z),
\end{aligned} \tag{B.3}$$

and, similarly, for the intensity:

$$I_\nu(\boldsymbol{l}) = \int dz \, \frac{dr}{dz} \frac{a(z)}{r^2(z)} \int \frac{dk_3}{(2\pi)} \, e^{ik_3 r(z)} j_{\nu(1+z)}(\boldsymbol{l}/r(z) + k_3 \hat{\boldsymbol{z}}, z). \tag{B.4}$$

Here, $\boldsymbol{k}_\perp$ is the projection of the wavevector $\boldsymbol{k}$ perpendicular to the z-direction. We are now in a position to extract E and B modes. In the flat-sky approximation, these can be constructed as

$$E(\boldsymbol{l}) = Q(\boldsymbol{l}) \cos 2\psi_{\boldsymbol{l}} + U(\boldsymbol{l}) \sin 2\psi_{\boldsymbol{l}} \tag{B.5}$$

and

$$B(\boldsymbol{l}) = U(\boldsymbol{l}) \cos 2\psi_{\boldsymbol{l}} - Q(\boldsymbol{l}) \sin 2\psi_{\boldsymbol{l}}, \tag{B.6}$$

where $\psi_{\boldsymbol{l}}$ is the angle between the Fourier wavevector $\boldsymbol{l}$ and the x-direction. Substituting in from equations (B.3) and (B.4), we obtain

$$\begin{aligned} E_\nu(\boldsymbol{l}) = \frac{p}{2} G_\nu \int dz \frac{dr}{dz} \frac{a(z)}{r^2(z)} \frac{dk_3}{(2\pi)} e^{ik_3 r(z)} \\ \times \left[j^{(+)}_{\nu(1+z)}(\boldsymbol{l}/r(z) + k_3 \hat{\boldsymbol{z}}, z) e^{-2i\psi_{\boldsymbol{l}}} + j^{(-)}_{\nu(1+z)}(\boldsymbol{l}/r(z) + k_3 \hat{\boldsymbol{z}}, z) e^{2i\psi_{\boldsymbol{l}}} \right] \end{aligned} \tag{B.7}$$

and

$$\begin{aligned} B_\nu(\boldsymbol{l}) = \frac{-ip}{2} G_\nu \int dz \frac{dr}{dz} \frac{a(z)}{r^2(z)} \frac{dk_3}{(2\pi)} e^{ik_3 r(z)} \\ \times \left[j^{(+)}_{\nu(1+z)}(\boldsymbol{l}/r(z) + k_3 \hat{\boldsymbol{z}}, z) e^{-2i\psi_{\boldsymbol{l}}} - j^{(-)}_{\nu(1+z)}(\boldsymbol{l}/r(z) + k_3 \hat{\boldsymbol{z}}, z) e^{2i\psi_{\boldsymbol{l}}} \right]. \end{aligned} \tag{B.8}$$

The bispectrum can therefore be constructed as

$$\begin{aligned}\langle B_{\nu_1}(\boldsymbol{l}_1)E_{\nu_2}(\boldsymbol{l}_2)I_{\nu_3}(\boldsymbol{l}_3)\rangle =& \frac{-ip^2}{2(2\pi)^3}\int\prod_{j=1}^{3}dz_j dk_{j,3}\frac{dr(z_j)}{dz_j}\frac{a(z_j)}{r^2(z_j)}e^{ik_{j,3}r(z_j)}\\ &\times\Bigg[e^{-2i(\psi_{\boldsymbol{l}_1}-\psi_{\boldsymbol{l}_2})}\langle j^{(+)}_{\nu_1(1+z_1)}(\boldsymbol{l}_1/r(z_1)+k_{1,3}\hat{\boldsymbol{z}},z_1)\\ &\times j^{(-)}_{\nu_2(1+z_2)}(\boldsymbol{l}_2/r(z_2)+k_{2,3}\hat{\boldsymbol{z}},z_2)j_{\nu_3(1+z_3)}(\boldsymbol{l}_3/r(z_3)+k_{3,3}\hat{\boldsymbol{z}},z_3)\rangle\\ &- e^{2i(\psi_{\boldsymbol{l}_1}-\psi_{\boldsymbol{l}_2})}\langle j^{(-)}_{\nu_1(1+z_1)}(\boldsymbol{l}_1/r(z_1)+k_{1,3}\hat{\boldsymbol{z}},z_1)\\ &\times j^{(+)}_{\nu_2(1+z_2)}(\boldsymbol{l}_2/r(z_2)+k_{2,3}\hat{\boldsymbol{z}},z_2)j_{\nu_3(1+z_3)}(\boldsymbol{l}_3/r(z_3)+k_{3,3}\hat{\boldsymbol{z}},z_3)\rangle\Bigg],\end{aligned} \tag{B.9}$$

where we have only retained those terms that survive averaging over independent polarisation directions (see appendix B.2).

Assuming the 3D bispectrum we have encountered is homogeneous and isotropic, we can write it as

$$\begin{aligned}&\langle\prod_{j=1}^{3}j^{(s_j)}_{\nu_j(1+z_j)}(\boldsymbol{l}_j/r(z_j)+k_{j,3}\hat{\boldsymbol{z}},z_j)\rangle\\ &\quad=(2\pi)^3\delta_{\mathrm{D}}^{(3)}\left(\boldsymbol{l}_1/r(z_1)+\boldsymbol{l}_2/r(z_2)+\boldsymbol{l}_3/r(z_3)+(k_{1,3}+k_{2,3}+k_{3,3})\,\hat{\boldsymbol{z}}\right)\\ &\qquad\times B^{s_1s_2s_3}_{\nu_1'\nu_2'\nu_3'}\Big(|\boldsymbol{l}_1/r(z_1)+k_{1,3}\hat{\boldsymbol{z}}|\,,|\boldsymbol{l}_2/r(z_2)+k_{2,3}\hat{\boldsymbol{z}}|\,,|\boldsymbol{l}_3/r(z_3)+k_{3,3}\hat{\boldsymbol{z}}|\,;\,z_1,z_2,z_3\Big).\end{aligned} \tag{B.10}$$

For the sake of compactness, we have introduced the shorthand s_j to label the $(\pm)$ polarisation and the intensity. Additionally, we have defined $\nu'=\nu(1+z)$.

At this stage, we invoke the Limber approximation (see, e.g., Ref. [66] in the context of the projected bispectrum), whereby the radial integrations enforce $k_{j,3}\ll|\boldsymbol{l}_j|/r(z_j)$ such that the bispectrum is approximately independent of the $k_{j,3}$. Performing the integrals over the $k_{j,3}$ in equation (B.9) gives rise to delta functions in r_j, which in turn require that all contributions come from the same redshifts. After factoring the three-dimensional delta function as

$$\begin{aligned}&\delta_{\mathrm{D}}^{(3)}\left(\boldsymbol{l}_1/r(z)+\boldsymbol{l}_2/r(z)+\boldsymbol{l}_3/r(z)+(k_{1,3}+k_{2,3}+k_{3,3})\,\hat{\boldsymbol{z}}\right)\\ &\qquad=r^2(z)\delta_{\mathrm{D}}^{(2)}\left(\boldsymbol{l}_1+\boldsymbol{l}_2+\boldsymbol{l}_3\right)\delta_{\mathrm{D}}\left(k_{1,3}+k_{2,3}+k_{3,3}\right),\end{aligned} \tag{B.11}$$

we find that

$$\begin{aligned}\langle B_{\nu_1}(\boldsymbol{l}_1)E_{\nu_2}(\boldsymbol{l}_2)I_{\nu_3}(\boldsymbol{l}_3)\rangle =& -\frac{p^2}{2}\sin 2(\psi_{\boldsymbol{l}_1}-\psi_{\boldsymbol{l}_2})(2\pi)^2\delta_{\mathrm{D}}^{(2)}\left(\boldsymbol{l}_1+\boldsymbol{l}_2+\boldsymbol{l}_3\right)\\ &\times\int dr_1dr_2dr_3\,a(z_1)\frac{a(z_2)}{r_2^2}\frac{a(z_3)}{r_3^2}\delta_{\mathrm{D}}\left(r_1-r_2\right)\delta_{\mathrm{D}}\left(r_1-r_3\right)\\ &\times B^{(+)(-)()}_{\nu_1'\nu_2'\nu_3'}\left(\frac{l_1}{r_1},\frac{l_2}{r_2},\frac{l_3}{r_3};z_1,z_2,z_3\right)\\ =& -\frac{p^2}{2}\sin 2(\psi_{\boldsymbol{l}_1}-\psi_{\boldsymbol{l}_2})(2\pi)^2\delta_{\mathrm{D}}^{(2)}\left(\boldsymbol{l}_1+\boldsymbol{l}_2+\boldsymbol{l}_3\right)\\ &\times\int dz\frac{dr}{dz}\frac{a^3(z)}{r^4(z)}B^{(+)(-)()}_{\nu_1'\nu_2'\nu_3'}\left(\frac{l_1}{r(z)},\frac{l_2}{r(z)},\frac{l_3}{r(z)};z\right).\end{aligned}\tag{B.12}$$

The next step is to calculate the equal-redshift 3D galaxy bispectrum. This is done in appendix B.2. Using its explicit form from equation (B.26) and using $dr/dz = c/H(z)$ to simplify, we obtain

$$\begin{aligned}\langle B_{\nu}(\boldsymbol{l}_1)E_{\nu}(\boldsymbol{l}_2)I_{\nu}(\boldsymbol{l}_3)\rangle =& -\frac{p^2}{2}\sin 2(\psi_{\boldsymbol{l}_1}-\psi_{\boldsymbol{l}_2})(2\pi)^2\delta_{\mathrm{D}}^{(2)}\left(\boldsymbol{l}_1+\boldsymbol{l}_2+\boldsymbol{l}_3\right)\\ &\int dz\left[S_{\nu}^{(3)}(z)+\frac{H(z)}{cr^2(z)}S_{\nu}^{(2)}(z)S_{\nu}^{(1)}(z)P_g\left(\frac{l_3}{r(z)};z\right)\right],\end{aligned}\tag{B.13}$$

with $S_{\nu}^{(n)}(z)$ as defined in equation (3.30). This expression was derived by assuming that the SED of all sources is the same at a given redshift. By introducing in the integral over redshift appropriate ratios of the SED of the galaxies' luminosity at the redshifted frequencies, it can be generalised to a scenario where the different fields are observed at different frequencies.

B.2 Modelling the equal-redshift 3D bispectrum

We now calculate the equal-redshift 3D bispectrum of polarised emissivities under the assumption that all sources have the same SED. For convenience, we consider the case of all three frequencies being the same, which we can easily generalise to mixed frequencies later on by scaling with appropriate ratios across frequency of the sources' SED.

The emissivity at position $\boldsymbol{x}$, redshift z and frequency ν is

$$j_{\nu}(\boldsymbol{x},z)=\frac{1}{4\pi}\sum_i L_{\nu,i}\delta_{\mathrm{D}}^{(3)}\left(\boldsymbol{x}-\boldsymbol{y}_i\right)=\frac{1}{4\pi}\sum_i\int dL_{\nu}\,L_{\nu}\delta_{\mathrm{D}}\left(L_{\nu}-L_{\nu,i}\right)\delta_{\mathrm{D}}^{(3)}\left(\boldsymbol{x}-\boldsymbol{y}_i\right),\tag{B.14}$$

where $L_{\nu,i}$ is the spectral luminosity of the source labeled by the subscript i, and $\boldsymbol{y}_i$ its position, both at redshift z. Note that the expectation value

$$\langle \delta_{\rm D}\left(L_\nu - L_{\nu,i}(z)\right) \delta_{\rm D}^{(3)}\left(\boldsymbol{x} - \boldsymbol{y}_i\right)\rangle = n_g(L_\nu, z), \tag{B.15}$$

where $n_g(L_\nu, z) \equiv dN/dV dL_\nu$ is the number density of galaxies per comoving volume and specific luminosity range, at redshift z. Similarly, the polarised emissivity is

$$j_\nu^{(\pm)}(\boldsymbol{x}, z) = \frac{1}{4\pi}\sum_i L_{\nu,i}\delta_{\rm D}^{(3)}\left(\boldsymbol{x} - \boldsymbol{y}_i\right) e^{\pm 2i\theta_i}, \tag{B.16}$$

where θ describes the direction of the linear polarisation in the plane of the sky for emission along the $-z$ direction. As will immediately become apparent, the only possible independent three-point function involving two factors of polarised emissivity is

$$\begin{aligned}
&(4\pi)^3\langle j_\nu^{(+)}(\boldsymbol{x}_1, z) j_\nu^{(-)}(\boldsymbol{x}_2, z) j_\nu(\boldsymbol{x}_3, z)\rangle \\
&\quad = \langle \sum_{ijk}\int dL'_\nu dL''_\nu dL'''_\nu\, L'_\nu L''_\nu L'''_\nu \delta_{\rm D}\left(L'_\nu - L_{\nu,i}\right)\delta_{\rm D}\left(L''_\nu - L_{\nu,j}\right)\delta_{\rm D}\left(L'''_\nu - L_{\nu,k}\right) \\
&\qquad \times \delta_{\rm D}^{(3)}\left(\boldsymbol{x}_1 - \boldsymbol{y}_i\right)\delta_{\rm D}^{(3)}(\boldsymbol{x}_2 - \boldsymbol{y}_j)\delta_{\rm D}^{(3)}\left(\boldsymbol{x}_3 - \boldsymbol{y}_k\right) e^{2i(\theta_i - \theta_j)}\rangle \\
&\quad = \delta_{\rm D}^{(3)}(\boldsymbol{x}_1 - \boldsymbol{x}_2)\int dL'_\nu dL'''_\nu\, \left(L'_\nu\right)^2 L'''_\nu \\
&\qquad \times \langle \sum_i \delta_{\rm D}^{(3)}(\boldsymbol{x}_1 - \boldsymbol{y}_i)\delta_{\rm D}(L'_\nu - L_{\nu,i}) \sum_k \delta_{\rm D}^{(3)}(\boldsymbol{x}_3 - \boldsymbol{y}_k)\delta_{\rm D}(L'''_\nu - L_{\nu,k})\rangle.
\end{aligned} \tag{B.17}$$

In going to the last line, we have used the fact that averaging over the polarisation angles θ_i imposes δ_{ij}. This is to be interpreted as saying that, since the polarisation angle is uncorrelated between sources, the only possible contributions come from terms where a polarisation leg can be matched to another polarisation leg from the same source. This logic has consequences for other interesting bispectra such as $\langle BII\rangle$ or $\langle EII\rangle$, which necessarily vanish. Futhermore, we also learn that any bispectrum with three polarisation legs – which we might have naïvely expected to accept 1-source contributions – vanish upon averaging as they involve first and third powers of sines and cosines. Of course, this all only holds under the assumption that the polarisation angles of galaxies are uncorrelated.

We can relate the expectation value in equation (B.17) to the galaxy density and the two-point correlation function; following Ref. [415], we have

$$\begin{aligned}\langle\sum_i \delta_{\rm D}^{(3)}(\boldsymbol{x}_1-\boldsymbol{y}_i)\delta_{\rm D}(L'_\nu-L_{\nu,i})\sum_k \delta_{\rm D}^{(3)}(\boldsymbol{x}_3-\boldsymbol{y}_k)\delta_{\rm D}(L'''_\nu-L_{\nu,k})\rangle \\ = n_g(L'_\nu,z)\delta_{\rm D}^{(3)}\left(\boldsymbol{x}_1-\boldsymbol{x}_3\right)\delta_{\rm D}\left(L'_\nu-L'''_\nu\right) \\ + n_g(L'_\nu,z)n_g(L'''_\nu,z)\left[1+\xi\left(|\boldsymbol{x}_1-\boldsymbol{x}_3|,L'_\nu,L'''_\nu;z\right)\right]\,.\end{aligned} \tag{B.18}$$

We shall take the galaxy correlation function, ξ, to be independent of the luminosity of the galaxies involved from here on. Using the relation above in equation (B.17), we have that

$$\begin{aligned}&\langle j_\nu^{(+)}(\boldsymbol{x}_1,z)j_\nu^{(-)}(\boldsymbol{x}_2,z)j_\nu(\boldsymbol{x}_3,z)\rangle \\ &= (4\pi)^{-3}\delta_{\rm D}^{(3)}\left(\boldsymbol{x}_1-\boldsymbol{x}_2\right)\left(\delta_{\rm D}^{(3)}\left(\boldsymbol{x}_1-\boldsymbol{x}_3\right)L_\nu^{(3)}(z)+\left[1+\xi\left(|\boldsymbol{x}_1-\boldsymbol{x}_3|;z\right)\right]L_\nu^{(2)}(z)L_\nu^{(1)}(z)\right),\end{aligned} \tag{B.19}$$

where we have defined

$$L_\nu^{(n)}(z)\equiv\int dL_\nu L_\nu^n\frac{dN}{dV\,dL_\nu}. \tag{B.20}$$

The bispectrum can be easily obtained from the three-point function by expressing $j_\nu(\boldsymbol{x},z)$ in terms of its Fourier transform. This yields

$$\begin{aligned}&(4\pi)^3\langle j_\nu^{(+)}(\boldsymbol{k}_1,z)j_\nu^{(-)}(\boldsymbol{k}_2,z)j_\nu(\boldsymbol{k}_3,z)\rangle \\ &\quad=\int d^3\boldsymbol{x}_1d^3\boldsymbol{x}_2d^3\boldsymbol{x}_3\,\langle j_\nu^{(+)}(\boldsymbol{x}_1,z)j_\nu^{(-)}(\boldsymbol{x}_2,z)j_\nu(\boldsymbol{x}_3,z)\rangle e^{-i(\boldsymbol{k}_1\cdot\boldsymbol{x}_1+\boldsymbol{k}_2\cdot\boldsymbol{x}_2+\boldsymbol{k}_3\cdot\boldsymbol{x}_3)} \\ &\quad=L_\nu^{(3)}(z)(2\pi)^3\delta_{\rm D}^{(3)}\left(\boldsymbol{k}_1+\boldsymbol{k}_2+\boldsymbol{k}_3\right)+L_\nu^{(2)}(z)L_\nu^{(1)}(z)\Bigg[(2\pi)^6\delta_{\rm D}^{(3)}\left(\boldsymbol{k}_1+\boldsymbol{k}_2\right)\delta_{\rm D}^{(3)}\left(\boldsymbol{k}_3\right) \\ &\qquad\qquad+\int d^3\boldsymbol{x}_1d^3\boldsymbol{x}_3\,\xi\left(|\boldsymbol{x}_1-\boldsymbol{x}_3|;z\right)e^{-i(\boldsymbol{k}_1+\boldsymbol{k}_2)\cdot\boldsymbol{x}_1-i\boldsymbol{k}_3\cdot\boldsymbol{x}_3}\Bigg].\end{aligned} \tag{B.21}$$

The first term in the last line corresponds to the one-source contribution, and the last term to the two-source. The term involving $\delta^{(3)}(\boldsymbol{k}_3)$ arises from a disconnected contraction; we can ignore this term since it will not contribute to the BEI bispectrum for multipoles of I with $l_3>0$. Recalling that the galaxy correlation function, $\xi(\boldsymbol{x})$, is

the Fourier transform of the galaxy power spectrum, $P_g(k)$, or more explicitly

$$\xi\left(|\boldsymbol{x}_1-\boldsymbol{x}_3|;z\right)=\int\frac{d^3\boldsymbol{k}}{(2\pi)^3}P_g(k;z)e^{i\boldsymbol{k}\cdot(\boldsymbol{x}_1-\boldsymbol{x}_3)}, \tag{B.22}$$

we can finally write

$$\begin{aligned}\langle j^{(+)}_{\nu'}(\boldsymbol{k}_1,z)j^{(-)}_{\nu'}(\boldsymbol{k}_2,z)j_{\nu'}(\boldsymbol{k}_3,z)\rangle =&(4\pi)^{-3}(2\pi)^3\delta_D^{(3)}\left(\boldsymbol{k}_1+\boldsymbol{k}_2+\boldsymbol{k}_3\right)\\ &\times\left[L^{(3)}_{\nu'}(z)+L^{(2)}_{\nu'}(z)L^{(1)}_{\nu'}(z)P_g(|\boldsymbol{k}_3|;z)\right],\end{aligned} \tag{B.23}$$

where $\nu'=\nu(1+z)$. The other non-vanishing term, $\langle j^{(-)}_{\nu'}(\boldsymbol{k}_1,z)j^{(+)}_{\nu'}(\boldsymbol{k}_2,z)j_{\nu'}(\boldsymbol{k}_3,z)\rangle$, has the same value.

It will prove convenient to rewrite this expression in terms of observed flux-densities, S_ν, rather than intrinsic spectral luminosities, $L_{\nu'}$. These are related via the luminosity distance, d_L, as

$$L_{\nu'}=4\pi(1+z)^{-1}d_L^2S_\nu. \tag{B.24}$$

In a flat cosmology, the luminosity distance is very simply related to the comoving distance as $d_L=(1+z)r$. Hence

$$\begin{aligned}L^{(n)}_{\nu'}(z)&=\int dL_{\nu'}L^n_{\nu'}\frac{dN}{dVdL_{\nu'}}\\ &=r^{-2}\left(\frac{dr}{dz}\right)^{-1}\int dS_\nu\left(4\pi(1+z)r^2S_\nu\right)^n\frac{dN}{dS_\nu dzd\Omega}\\ &=(4\pi)^n(1+z)^nr^{2n-2}\left(\frac{dr}{dz}\right)^{-1}S^{(n)}_\nu(z)\,,\end{aligned} \tag{B.25}$$

with $S^{(n)}_\nu(z)$ as defined in equation (3.30) – a quantity that can be evaluated from observed number counts.

Finally, we can cast equation (B.23) in the following, more convenient, form

$$\begin{aligned}\langle j^{(+)}_{\nu'}(\boldsymbol{k}_1,z)j^{(-)}_{\nu'}(\boldsymbol{k}_2,z)j_{\nu'}(\boldsymbol{k}_3,z)\rangle =&(1+z)^3r^4(z)(2\pi)^3\delta_D^{(3)}\left(\boldsymbol{k}_1+\boldsymbol{k}_2+\boldsymbol{k}_3\right)\left(\frac{dr}{dz}\right)^{-1}\\ &\times\left[S^{(3)}_\nu(z)+\frac{1}{r^2(z)}\left(\frac{dr}{dz}\right)^{-1}S^{(2)}_\nu(z)S^{(1)}_\nu(z)P_g(|\boldsymbol{k}_3|;z)\right].\end{aligned} \tag{B.26}$$

B.3 Toy model for CIB higher-point functions

In this section, we aim to motivate the claim that, for the extent of point-source removal expected of upcoming CMB experiments, the $EIEI$ trispectrum of the CIB ought to result in a smaller bias than the BEI bispectrum. We do so by studying the 1-source contribution in a minimal model where sources locations on the sky are assumed to be random and uncorrelated. Similarly, we assume that source flux, polarisation fraction and polarisation angle are all uncorrelated.

If we consider only 1-source contributions where all legs in the correlator come from the same galaxy, the biases of equations (3.27) and (3.28) reduce to

$$\begin{aligned}\mathcal{B}_{1s}^{BEI}(\boldsymbol{l}) = -4\int \frac{d^2\boldsymbol{l}'}{2\pi}\frac{\boldsymbol{l}'\cdot(\boldsymbol{l}-\boldsymbol{l}')}{|\boldsymbol{l}-\boldsymbol{l}'|^2}\mathcal{W}^E(\boldsymbol{l}')\mathcal{W}^I(|\boldsymbol{l}-\boldsymbol{l}'|)\sin^2 2(\phi_{\boldsymbol{l}_2}-\phi_{\boldsymbol{l}_1}) \\ \times G_{145}^2 G_{353} p^2 \sum_i \langle S_i^2(145\text{GHz}) S_i(353\text{GHz})\rangle \end{aligned} \tag{B.27}$$

and

$$\begin{aligned}\mathcal{B}_{1s}^{EIEI}(\boldsymbol{l}) = 2\int \frac{d^2\boldsymbol{l}' d^2\boldsymbol{l}''}{(2\pi)^2}\frac{\boldsymbol{l}'\cdot(\boldsymbol{l}-\boldsymbol{l}')}{|\boldsymbol{l}-\boldsymbol{l}'|^2}\frac{\boldsymbol{l}''\cdot(\boldsymbol{l}-\boldsymbol{l}'')}{|\boldsymbol{l}-\boldsymbol{l}''|^2}\mathcal{W}^E(\boldsymbol{l}')\mathcal{W}^E(\boldsymbol{l}'')\mathcal{W}^I(|\boldsymbol{l}-\boldsymbol{l}'|)\mathcal{W}^I(|\boldsymbol{l}-\boldsymbol{l}''|) \\ \times \sin 2(\phi_{\boldsymbol{l}'}-\phi_{\boldsymbol{l}})\sin 2(\phi_{\boldsymbol{l}''}-\phi_{\boldsymbol{l}})\sin 2(\phi_{\boldsymbol{l}''}-\phi_{\boldsymbol{l}'}) \\ \times G_{145}^2 G_{353}^2 p^2 \sum_i \langle S_i^2(145\text{GHz}) S_i^2(353\text{GHz})\rangle\,, \end{aligned} \tag{B.28}$$

where the flux density at 145 GHz, $S(145\text{GHz})$, is obtained by extrapolating the value at 353 GHz, $S(353\text{GHz})$, according to the SED of a thermal dust emitter with temperature T_{dust} and spectral index β_{dust} as given in table 3.1. Details of the derivations of the relevant bispectrum and trispectrum are provided in appendices B.4 and B.5, respectively.

In practice, it is more convenient to compute the sums over sources as integrals over flux, weighted by the number of sources per steradian per unit flux, dn/ds, in a certain flux range $[s_{\min}, s_{\max}]$. That is

$$\sum_i S_i^n \to \int_{s_{\min}}^{s_{\max}} ds S^n \frac{dn}{ds}. \tag{B.29}$$

The number density dn/ds can be obtained by fitting a model to sub-mm data. Our parametric forms follow those employed by Ref. [283] and are as follows: in the faint

end, a double power-law,

$$\frac{dN}{dS} = A\left(\left(\frac{S}{B}\right)^{n_1} + \left(\frac{S}{B}\right)^{n_2}\right)^{-1}, \tag{B.30}$$

with parameters $A = 2.82 \times 10^8\,\mathrm{Jy}^{-1}\,\mathrm{sr}^{-1}$, $B = 0.007\,\mathrm{Jy}$, $n_1 = 6.5$ and $n_2 = 2.42$; and on the bright end, a single power-law,

$$\frac{dN}{dS} = kS^{-2.5}, \tag{B.31}$$

with $k = 17.24$.

The biases from 1-source are plotted in figure B.1 as a function of the flux cut. Given that $\mathcal{B}_{1s}^{EIEI}$ scales as the fourth power of the flux density, while $\mathcal{B}_{1s}^{BEI}$ goes only as the third power, the former is bigger than the latter if sources brighter than $\sim 1\,\mathrm{Jy}$ are left unmasked. However, for the typical flux cut values expected of the next generation of experiments, the bispectrum term dominates over the trispectrum term by several orders of magnitude.

From figure B.1, it is clear that, on large scales, the full calculation of B_{1s}^{BEI} is exceptionally well described by a squeezed limit in which a large-scale B-mode leg couples to two, small-scale T and a E-mode legs. In this limit, equation B.27 approaches

$$\mathcal{B}_{1s}^{BEI}(\boldsymbol{l}) \approx G_{145}^2 G_{353} p^2 \int \frac{d^2\boldsymbol{l}'}{2\pi} l' \mathcal{W}^E(\boldsymbol{l}')\mathcal{W}^I(\boldsymbol{l}')\sin^2 2\phi_{\boldsymbol{l}'} \sum_i \langle S_i^2(145\mathrm{GHz}) S_i(353\mathrm{GHz})\rangle \tag{B.32}$$

which is independent of l and thus gives rise to the flat, white-noise-like angular power spectrum we see.

B.4 Toy-model CIB bispectrum: one-source term

The one-source contribution to the CIB bispectrum can also be calculated by working directly with the flux densities of the sources. Consider a galaxy at position $\boldsymbol{y}$, with flux density S_ν at frequency ν. This contributes to the specific intensity of the CIB as

$$I_\nu(\boldsymbol{x}) = S_\nu \delta_{\mathrm{D}}(\boldsymbol{x} - \boldsymbol{y})\,. \tag{B.33}$$

In the Fourier domain, this is

$$I_\nu(\boldsymbol{l}) = S_\nu e^{-i\boldsymbol{l}\cdot\boldsymbol{y}}\,. \tag{B.34}$$

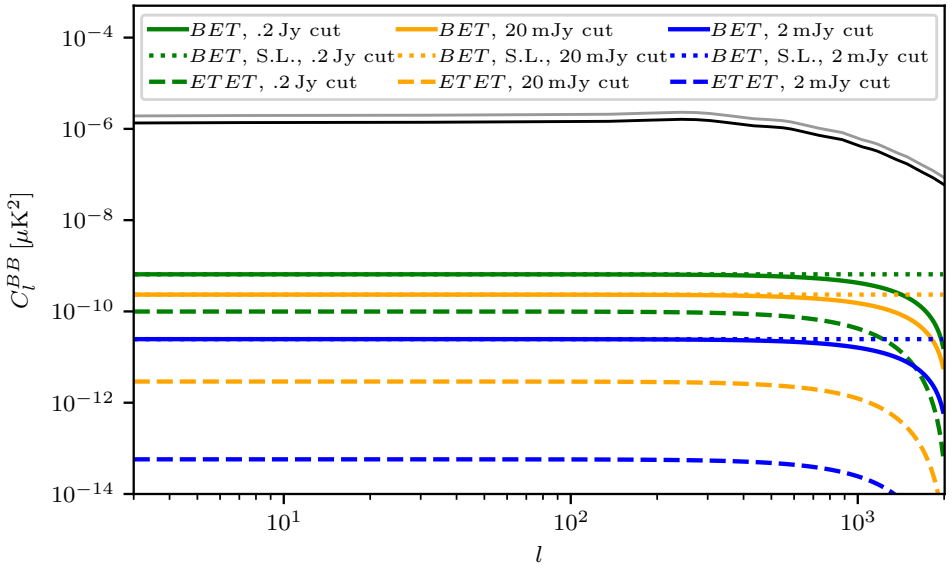

Fig. B.1 Delensing biases from the BEI bispectrum (solid) and $EIEI$ trispectrum (dashed) of the CIB, including only 1-source contributions, for point-source masking schemes typical of current and upcoming CMB experiments. The squeezed limit of the bispectra are shown as dotted lines. For comparison, we show also the fiducial power spectra of lensed B-modes before (grey) and after delensing with the CIB such that the power is reduced by 30 % (black).

For N sources with positions and flux densities labeled as $\boldsymbol{y}_i$ and $S_{\nu,i}$, respectively, this generalises to

$$I_\nu(\boldsymbol{l}) = \sum_i S_{\nu,i} e^{-i\boldsymbol{l}\cdot\boldsymbol{y}_i} \,. \tag{B.35}$$

If we allow the sources to be linearly polarised with a polarisation fraction p – which we shall assume is independent of flux and position – the observed polarisation can be described by the Stokes parameters

$$(Q \pm iU)_\nu(\boldsymbol{l}) = \sum_i p S_{\nu,i} e^{\pm 2i\theta_i} e^{-i\boldsymbol{l}\cdot\boldsymbol{y}_i} \,. \tag{B.36}$$

where θ_i is the angle between the polarisation direction of the source and the x-axis. The E- and B-modes of the observed polarisation follow from

$$(Q \pm iU)(\boldsymbol{l}) = (E \pm iB)(\boldsymbol{l}) e^{\pm 2i\psi_{\boldsymbol{l}}} \,, \tag{B.37}$$

so that

$$E_\nu(\boldsymbol{l}) = p \sum_i S_{\nu,i} e^{-i\boldsymbol{l}\cdot\boldsymbol{y}_i} \cos 2(\psi_{\boldsymbol{l}} - \theta_i) \,, \tag{B.38}$$

$$B_\nu(\boldsymbol{l}) = -p \sum_i S_{\nu,i} e^{-i\boldsymbol{l}\cdot\boldsymbol{y}_i} \sin 2(\psi_{\boldsymbol{l}} - \theta_i) \,. \tag{B.39}$$

The bispectrum at frequency ν can therefore be constructed as

$$\begin{aligned}\langle B_\nu(\boldsymbol{l}_1) E_\nu(\boldsymbol{l}_2) I_\nu(\boldsymbol{l}_3)\rangle = -p^2 \langle \sum_{ijk} S_{\nu,i} S_{\nu,j} S_{\nu,k} e^{-i\boldsymbol{l}_1\cdot\boldsymbol{y}_i} e^{-i\boldsymbol{l}_2\cdot\boldsymbol{y}_j} e^{-i\boldsymbol{l}_3\cdot\boldsymbol{y}_k} \\ \times \sin 2(\psi_{\boldsymbol{l}_1} - \theta_i) \cos 2(\psi_{\boldsymbol{l}_2} - \theta_j)\rangle \,.\end{aligned} \tag{B.40}$$

If we assume that the polarisation angles θ_i are independent of the positions and fluxes of sources, averaging over the angles will cause the bispectrum to vanish unless $i = j$. This implies that either $i = j = k$ or $i = j \neq k$. If we ignore source clustering, so that the positions of the sources are independent of each other, the case $i = j \neq k$ gives a vanishing contribution for $\boldsymbol{l}_3 \neq 0$. Keeping only the one-source term, $i = j = k$, we have

$$\begin{aligned}\langle B_\nu(\boldsymbol{l}_1) E_\nu(\boldsymbol{l}_2) I_\nu(\boldsymbol{l}_3)\rangle &= -p^2 \langle \sum_i S^3_{\nu,i} e^{-i(\boldsymbol{l}_1+\boldsymbol{l}_2+\boldsymbol{l}_3)\cdot\boldsymbol{y}_i} \sin 2(\psi_{\boldsymbol{l}_1} - \theta_i) \cos 2(\psi_{\boldsymbol{l}_2} - \theta_i)\rangle \\ &= -\frac{p^2}{2} \sin 2(\psi_{\boldsymbol{l}_1} - \psi_{\boldsymbol{l}_2}) \langle \sum_i S^3_{\nu,i} e^{-i(\boldsymbol{l}_1+\boldsymbol{l}_2+\boldsymbol{l}_3)\cdot\boldsymbol{y}_i}\rangle \,,\end{aligned} \tag{B.41}$$

where we have averaged over the polarisation angles in passing to the second line. Finally, averaging over the source locations across a sky area $A_{\rm sky}$ gives

$$\langle B_\nu(\boldsymbol{l}_1)E_\nu(\boldsymbol{l}_2)I_\nu(\boldsymbol{l}_3)\rangle = -\frac{p^2}{2}\sin 2(\psi_{\boldsymbol{l}_1}-\psi_{\boldsymbol{l}_2})(2\pi)^2\delta_{\rm D}^{(3)}(\boldsymbol{l}_1+\boldsymbol{l}_2+\boldsymbol{l}_3)\frac{1}{A_{\rm sky}}\langle\sum_i S^3_{\nu,i}\rangle\,. \tag{B.42}$$

It can be shown that this spectrum satisfies all the required symmetries. Note also that it agrees with the one-source component of equation (B.13) on replacing

$$\frac{1}{A_{\rm sky}}\langle\sum_i S^3_{\nu,i}\rangle \to \int dz\int dS_\nu\, S_\nu^3\frac{dN}{dS_\nu dz d\Omega} = \int dz\, S_\nu^{(3)}(z)\,. \tag{B.43}$$

B.5 Toy-model CIB trispectrum: one-source term

Following the calculation of appendix B.4, we calculate here the $EIEI$ trispectrum of the CIB. Assuming once again that flux, position and polarisation are uncorrelated, this trispectrum is given by

$$\begin{aligned}\langle E_\nu(\boldsymbol{l}_1)E_\nu(\boldsymbol{l}_2)I_\nu(\boldsymbol{l}_3)I_\nu(\boldsymbol{l}_4)\rangle_c =& \frac{1}{2}p^2\cos 2(\psi_{\boldsymbol{l}_2}-\psi_{\boldsymbol{l}_1})\\ &\times\langle\sum_{ikm} S^2_{\nu,i}S_{\nu,k}S_{\nu,m}e^{-i(\boldsymbol{l}_1+\boldsymbol{l}_2)\cdot\boldsymbol{y}_i}e^{-i\boldsymbol{l}_3\cdot\boldsymbol{y}_k}e^{-i\boldsymbol{l}_4\cdot\boldsymbol{y}_m}\rangle\,.\end{aligned} \tag{B.44}$$

Once again, we have the restriction that both polarisation legs must come from the same source, though this time there can in principle also be 2-source and 3-source contributions. The one-source contribution to this is

$$\langle E_\nu(\boldsymbol{l}_1)E_\nu(\boldsymbol{l}_2)I_\nu(\boldsymbol{l}_3)I_\nu(\boldsymbol{l}_4)\rangle_c = \frac{(2\pi)^2}{2\,A_{\rm sky}}p^2\cos 2(\psi_{\boldsymbol{l}_1}-\psi_{\boldsymbol{l}_2})\delta_{\rm D}^{(2)}(\boldsymbol{l}_1+\boldsymbol{l}_2+\boldsymbol{l}_3+\boldsymbol{l}_4)\langle\sum_i S^4_{\nu,i}\rangle\,. \tag{B.45}$$

B.6 Simulating Gaussian LSS tracers correlated with CMB lensing

Though in this thesis we are only concerned with the CIB, we present here a more general framework for generating simulations of large-scale-structure tracers which are appropriately correlated with a given simulation of the CMB lensing potential and amongst themselves. The basic idea — which has been studied extensively in the

literature around Cholesky decompositions — is to set up a linear system of equations from which it will be possible to solve for the coefficients involved granted we know the theoretical auto- and cross- spectra of the tracers.

Suppose we are to work with just three tracers: the CIB, a map of the galaxy distribution, and an internal reconstruction, with spherical harmonic coefficients expressed as $I_{lm}, g_{lm}, \kappa^{rec}_{lm}$, respectively. Given a map of the true convergence with spherical harmonic coefficients κ_{lm}, the different tracers are correlated as

$$\kappa^{rec}_{lm} = \kappa_{lm} + n_{lm}\,, \tag{B.46}$$

$$g_{lm} = A^{g\kappa}_l \kappa_{lm} + u_{lm}\,, \tag{B.47}$$

$$I_{lm} = A^{I\kappa}_l \kappa_{lm} + A^{gI}_l u_{lm} + e_{lm}\,, \tag{B.48}$$

$$\tag{B.49}$$

where n_{lm}, u_{lm}, e_{lm} are coefficients of the noise – and as such are presumed to each be uncorrelated with everything else – and κ_{lm} are the coefficients of the true convergence for the particular realisation that we wish to generate correlated tracers for. We can solve for the coefficients

$$A^{g\kappa}_l = \frac{C^{g\kappa}_l}{C^{\kappa\kappa}_l}\,, \tag{B.50}$$

$$A^{I\kappa}_l = \frac{C^{I\kappa}_l}{C^{\kappa\kappa}_l}\,, \tag{B.51}$$

$$A^{gI}_l = \frac{C^{gI}_l - A^{g\kappa}_l A^{I\kappa}_l C^{\kappa\kappa}_l}{C^{uu}_l} \tag{B.52}$$

and the noise spectra

$$C^{nn}_l = N^{\kappa\kappa}_l\,, \tag{B.53}$$

$$C^{uu}_l = C^{gg}_l - (A^{g\kappa}_l)^2 C^{\kappa\kappa}_l\,, \tag{B.54}$$

$$C^{ee}_l = C^{II}_l - (A^{I\kappa}_l)^2 C^{\kappa\kappa}_l - (A^{gI}_l)^2 C^{uu}_l\,, \tag{B.55}$$

where $N^{\kappa\kappa}_l$ is the internal reconstruction noise level.

From the above, it is clear that the problem is soluble if we know all the auto- and cross- spectra, in which case all we have to do is draw the coefficients n_{lm}, u_{lm} and e_{lm} from probability distributions with angular power spectra $N^{\kappa\kappa}_l, C^{uu}_l$ and C^{ee}_l.

The solution above can be generalised to any number of tracers as follows. Consider tracer i with auto- spectrum C^{ii} and cross-spectrum C^{ij} with tracer j. Let it be

described as a linear combination $\sum_p \sum_{lm} A_l^{ij} a^p(l,m)$ of harmonic coefficients a^p with angular power spectra $C_l^{a^p a^p}$ and scaled with weights given by the square, off-diagonal matrix A_l^{ij}. In the case above, $a^p = \{\kappa_{lm}, u_{lm}, e_{lm}\}$, $C_l^{a^p a^p} = \{C_l^{\kappa\kappa}, C_l^{uu}, C_l^{ee}\}$. The general formula for the weights is

$$A_l^{ij} = \frac{1}{C_l^{a^j a^j}} \left(C_l^{ij} - \sum_{p=0}^{j-1} A_l^{jp} A_l^{ip} C_l^{a^p a^p} \right), \tag{B.56}$$

with auxiliary spectra given by:

$$C_l^{a^j a^j} = C_l^{jj} - \sum_{p=0}^{j-1} \left(A_l^{jp} \right)^2 C_l^{a^p a^p} . \tag{B.57}$$

This infrastructure is implemented and made publicly-available on `GitHub`[1].

B.7 Constructing curved-sky lensing template

In this section, we described algorithms for computing the first order lensing corrections to the temperature and B-mode anisotropies.

B.7.1 Constructing a curved-sky, first-order, lensing B-mode template

We describe here the construction of a map-level template for lensing B-modes. We work to leading order in lensing and on the curved-sky formalism, a combination that was shown by Ref. [84] to be a very good approximation to the true B-modes on large angular scales. We arrive at a fast position-space implementation which is made publicly-available on `GitHub`[2]. These lensed B-modes can be approximated in

[1] `https://github.com/abaleato/MultitracerSims4Delensing`
[2] `https://github.com/abaleato/curved_sky_B_template`

harmonic space by[3]

$$\begin{aligned}\tilde{B}_{lm} &= \sum_{(lm)_1}\sum_{(lm)_2}\phi_{(lm)_1}E_{(lm)_2}\frac{1}{2i}\left[{}_2I^{mm_1m_2}_{ll_1l_2} - {}_{-2}I^{mm_1m_2}_{ll_1l_2}\right] \\ &= \sum_{(lm)_1}\sum_{(lm)_2}\frac{-i\,(-1)^m}{4} \\ &\quad\times\sqrt{(2l+1)(2l_1+1)(2l_2+1)/4\pi}[l_1(l_1+1)+l_2(l_2+1)-l(l+1)] \\ &\quad\times\phi_{(lm)_1}E_{(lm)_2}\begin{pmatrix} l_1 & l_2 & l \\ m_1 & m_2 & -m\end{pmatrix}\left[\begin{pmatrix} l_1 & l_2 & l \\ 0 & -2 & 2\end{pmatrix}-\begin{pmatrix} l_1 & l_2 & l \\ 0 & 2 & -2\end{pmatrix}\right]. \end{aligned} \tag{B.58}$$

Inspired by the implementation of the quadratic estimators for lensing reconstruction in the publicly-available code `QuickLens`[4], we write

$$\hat{\tilde{B}}_{lm} = \frac{(-1)^m}{2}\sum_{(lm)_1}\sum_{(lm)_2}\begin{pmatrix} l_1 & l_2 & l \\ m_1 & m_2 & -m\end{pmatrix}W_{l_1l_2l}\hat{\phi}_{(lm)_1}\hat{E}_{(lm)_2}\,, \tag{B.59}$$

where the weights

$$\begin{aligned}W_{l_1l_2l} =& \frac{-i}{2}\sqrt{(2l+1)(2l_1+1)(2l_2+1)/4\pi}[l_1(l_1+1)+l_2(l_2+1)-l(l+1)] \\ &\times\left[\begin{pmatrix} l_1 & l_2 & l \\ 0 & -2 & 2\end{pmatrix}-\begin{pmatrix} l_1 & l_2 & l \\ 0 & 2 & -2\end{pmatrix}\right]\end{aligned} \tag{B.60}$$

can be cast in separable form as

$$W_{l_1l_2l} = \sum_i W^i_{l_1l_2l}\,, \tag{B.61}$$

with

$$W^i_{l_1l_2l} = \sqrt{(2l+1)(2l_1+1)(2l_2+1)/4\pi}\begin{pmatrix} l_1 & l_2 & l \\ -s^i_1 & -s^i_2 & s\end{pmatrix}w^i_{l_1}w^i_{l_2}w^i_l\,. \tag{B.62}$$

The value for the separable weights $w^i_{l_j}$ can be found in Table B.1.

[3] In this notation summation is implicit over matching pairs of indices.

[4] `https://github.com/dhanson/quicklens`, though an amended and extended version can be found at `https://github.com/abaleato/Quicklens-with-fixes`

i	s_1^i	s_2^i	s^i	$w_{l_1}^i$	$w_{l_2}^i$	w_l^i
1	0	2	2	$l_1(l_1+1)$	$-1/2$	i
2	0	2	2	$-1/2$	$l_2(l_2+1)$	i
3	0	2	2	$1/2$	i	$l(l+1)$
4	0	-2	-2	$l_1(l_1+1)$	$1/2$	i
5	0	-2	-2	$1/2$	$l_2(l_2+1)$	i
6	0	-2	-2	$-1/2$	i	$l(l+1)$

Table B.1 Weights for a fast separable implementation of the lensed B-mode template.

B.7.2 Constructing a curved-sky, first-order, lensed temperature template

The first-order lensing correction to the temperature anisotropies is[5]

$$\begin{aligned}\tilde{T}_{lm} &= \sum_{(lm)_1}\sum_{(lm)_2}\phi_{(lm)_1}T_{(lm)_2}I^{mm_1m_2}_{ll_1l_2}\\ &= \sum_{(lm)_1}\sum_{(lm)_2}\frac{(-1)^m}{2}\sqrt{(2l+1)(2l_1+1)(2l_2+1)/4\pi}[l_1(l_1+1)+l_2(l_2+1)-l(l+1)]\\ &\quad\times\phi_{(lm)_1}T_{(lm)_2}\begin{pmatrix}l_1 & l_2 & l\\ m_1 & m_2 & -m\end{pmatrix}\begin{pmatrix}l_1 & l_2 & l\\ 0 & 0 & 0\end{pmatrix}. \end{aligned}\tag{B.63}$$

As in the previous section, we write

$$\hat{\tilde{T}}_{lm} = \frac{(-1)^m}{2}\sum_{(lm)_1}\sum_{(lm)_2}\begin{pmatrix}l_1 & l_2 & l\\ m_1 & m_2 & -m\end{pmatrix}Z_{l_1l_2l}\hat{\phi}_{(lm)_1}\hat{T}_{(lm)_2}\,,\tag{B.64}$$

where the weights

$$\begin{aligned}Z_{l_1l_2l} =&\sqrt{(2l+1)(2l_1+1)(2l_2+1)/4\pi}[l_1(l_1+1)+l_2(l_2+1)-l(l+1)]\\ &\times\begin{pmatrix}l_1 & l_2 & l\\ 0 & 0 & 0\end{pmatrix}\end{aligned}\tag{B.65}$$

can be separated into three terms

$$Z_{l_1l_2l} = \sum_i Z^i_{l_1l_2l}\,,\tag{B.66}$$

[5]In this notation summation is implicit over matching pairs of indices.

i	$z^i_{l_1}$	$z^i_{l_2}$	z^i_l
1	$l_1(l_1+1)$	1	1
2	1	$l_2(l_2+1)$	1
3	-1	1	$l(l+1)$

Table B.2 Weights for a fast separable calculation of the first-order lensing correction to the CMB temperature anisotropies

with

$$Z^i_{l_1 l_2 l} = \sqrt{(2l+1)(2l_1+1)(2l_2+1)/4\pi} \begin{pmatrix} l_1 & l_2 & l \\ 0 & 0 & 0 \end{pmatrix} z^i_{l_1} z^i_{l_2} z^i_l \,. \tag{B.67}$$

The value for the separable weights $z^i_{l_j}$ can be found in Table B.2.

B.8 Analytic Power Spectrum Covariances

In this section, we provide analytic models for the covariances of the different combinations of spectra in section 3.3. These serve as a complement and cross-check of simulated covariances, and are particularly important given that simulating the lensed CMB on the full sky is computationally costly, and that a large number of such simulations is required to reduce Monte Carlo errors to levels which allow one to resolve the small correlations between B-mode bandpowers [36, 446, 453, 447, 259, 417, 317].

B.8.1 Delensed B-mode PS covariance

In order to calculate the power spectrum covariance of delensed B-modes, we employ the following covariance [317], which is an extension of the lensing B-mode covariance by [36]:

$$\mathrm{Cov}\left(\tilde{C}^{BB,\mathrm{res}}_l, \tilde{C}^{BB,\mathrm{res}}_{l'}\right) = \frac{2}{2l+1}\delta_{ll'}\left(\tilde{C}^{BB,\mathrm{res}}_l\right)^2 + \mathrm{Cov}_{\mathrm{NG}}\left(\tilde{C}^{BB,\mathrm{res}}_l, \tilde{C}^{BB,\mathrm{res}}_{l'}\right), \tag{B.68}$$

where

$$\begin{aligned}\mathrm{Cov}_{\mathrm{NG}}\left(\tilde{C}^{BB,\mathrm{res}}_l, \tilde{C}^{BB,\mathrm{res}}_{l'}\right) = \sum_L \frac{2}{2L+1}\Bigg[&\frac{\partial \tilde{C}^{BB,\mathrm{res}}_l}{\partial C^{EE}_L}\left(C^{EE}_L\right)^2 \frac{\partial \tilde{C}^{BB,\mathrm{res}}_{l'}}{\partial C^{EE}_L} \\ &+ \frac{\partial \tilde{C}^{BB,\mathrm{res}}_l}{\partial C^{\kappa\kappa}_L}\left(C^{\kappa\kappa}_L\right)^2 \frac{\partial \tilde{C}^{BB,\mathrm{res}}_{l'}}{\partial C^{\kappa\kappa}_L}\Bigg].\end{aligned} \tag{B.69}$$

is the non-Gaussian part of the covariance. This expression assumes 1) that the E-modes are cosmic-variance limited, 2) that the noise in the matter tracer is uncorrelated with the lensing convergence and the CMB and 3) that $C_l^{EE}, C_l^{\kappa\kappa}$ and the noise spectrum all have Gaussian covariance.

Now, under the assumption that the E-modes are limited by cosmic variance, the power spectrum of delensed B-modes is [432]

$$\tilde{C}_l^{BB,\mathrm{res}} = \int \frac{\mathrm{d}^2\boldsymbol{l}'}{(2\pi)^2} W^2(\boldsymbol{l},\boldsymbol{l}') C_{l'}^{EE} C_{|\boldsymbol{l}-\boldsymbol{l}'|}^{\kappa\kappa} \left(1-\rho^2_{|\boldsymbol{l}-\boldsymbol{l}'|}\right), \tag{B.70}$$

where ρ_L is the cross-correlation coefficients of our co-added tracer with the true CMB lensing. When taking the derivatives of equation (B.69), ρ_L can be regarded as a constant, which means that

$$\frac{\partial \tilde{C}_l^{BB,\mathrm{res}}}{\partial C_L^{\kappa\kappa}} = \left(1-\rho_L^2\right) \frac{\partial \widetilde{C}_l^{BB}}{\partial C_L^{\kappa\kappa}}, \tag{B.71}$$

and

$$\frac{\partial \tilde{C}_l^{BB,\mathrm{res}}}{\partial C_L^{EE}} = \left.\frac{\partial \widetilde{C}_l^{BB}}{\partial C_L^{EE}}\right|_{C^{\kappa\kappa}=(1-\rho^2)C^{\kappa\kappa}}. \tag{B.72}$$

In order to evaluate this last expression, we use an expression in the style of equation (27) of Ref. [417].

With these insights in hand, the covariance of equation (B.68) can be evaluated by modifying existing codes such as `LensCov` [347] which compute the power spectrum covariance of lensed CMB fields.

B.8.2 Spectrum-based delensing

In this section, we calculate the covariance of all auto- and cross-spectra of the observed and template B-modes, which might be needed when writing down a spectrum-based likelihood as in Refs. [49, 2, 313].

B.8.2.1 Covariance of cross-spectrum

In section 3.3, we saw that, to leading order, the cross-spectrum between lensing and template B-modes can be modelled as

$$C_l^{BB,\mathrm{cross}} = \int \frac{\mathrm{d}^2\boldsymbol{l}'}{(2\pi)^2} W^2(\boldsymbol{l}',\boldsymbol{l}) C_{l'}^{EE} C_{|\boldsymbol{l}-\boldsymbol{l}'|}^{\kappa\kappa} \rho^2_{|\boldsymbol{l}-\boldsymbol{l}'|}. \tag{B.73}$$

Proceeding analogously to how the lensing B-mode power spectrum covariance is calculated, we approximate the non-Gaussian part of the covariance as:

$$\mathrm{Cov}_{\mathrm{NG}}\left(C_l^{BB,\mathrm{cross}}, C_{l'}^{BB,\mathrm{cross}}\right) \approx \sum_L \frac{1}{2L+1}\left[\frac{\partial C_l^{BB,\mathrm{cross}}}{\partial C_L^{EE}} 2\left(C_L^{EE}\right)^2 \frac{\partial C_{l'}^{BB,\mathrm{cross}}}{\partial C_L^{EE}} + \frac{\partial \widetilde{C}_l^{BB}}{\partial C_L^{\kappa\kappa}} \mathrm{Var}\left(C_L^{\kappa\kappa^{\mathrm{WF}}}\right) \frac{\partial \widetilde{C}_{l'}^{BB}}{\partial C_L^{\kappa\kappa}}\right]. \quad \text{(B.74)}$$

where κ^{WF} is the wiener-filtered tracer map. As determined in [432], this takes the form $\kappa_l^{\mathrm{WF}} = (C_l^{\kappa I}/C_l^{II})I_l$, where I is the tracer itself, so

$$C_l^{\kappa^{\mathrm{WF}}\kappa^{\mathrm{WF}}} = \left(\frac{C_l^{\kappa I}}{C_l^{II}}\right)^2 C_l^{II} = \left(\frac{C_l^{\kappa I}}{C_l^{II}}\right) C_l^{\kappa I} = C_l^{\kappa\kappa^{\mathrm{WF}}}. \quad \text{(B.75)}$$

We can now use the correlation between the tracer and lensing, defined as $\rho_l = C_l^{\kappa I}/\sqrt{C_l^{\kappa\kappa} C_l^{II}}$, to rewrite $C_l^{\kappa^{\mathrm{WF}}\kappa^{\mathrm{WF}}} = C_l^{\kappa\kappa^{\mathrm{WF}}} = \rho_l^2 C_l^{\kappa\kappa}$. Under the assumption of Gaussianity of the lens power spectrum, the variance we are after can be computed using the usual prescription for Gaussian covariance,

$$\mathrm{Cov}_{ll'}^{G_aG_b,G_cG_d} = \frac{\delta_{ll'}}{2l+1}\left[C_l^{G_aG_c} C_l^{G_bG_d} + C_l^{G_aG_d} C_l^{G_bG_c}\right], \quad \text{(B.76)}$$

yielding

$$\mathrm{Var}\left(C_L^{\kappa\kappa^{\mathrm{WF}}}\right) = \frac{1}{2l+1}\left[C_L^{\kappa\kappa} C_L^{\kappa^{\mathrm{WF}}\kappa^{\mathrm{WF}}} + C_L^{\kappa\kappa^{\mathrm{WF}}} C_L^{\kappa\kappa^{\mathrm{WF}}}\right] \quad \text{(B.77)}$$

$$= \frac{1}{2l+1}\left[\rho^2 C_L^{\kappa\kappa} + \rho^4 C_L^{\kappa\kappa}\right]. \quad \text{(B.78)}$$

Finally,

$$\mathrm{Cov}_{\mathrm{NG}}\left(C_l^{BB,\mathrm{cross}}, C_{l'}^{BB,\mathrm{cross}}\right) \approx \sum_L \frac{1}{2L+1}\left[\left.\frac{\partial \widetilde{C}_l^{BB}}{\partial C_L^{EE}}\right|_{C^{\kappa\kappa}=\rho^2 C^{\kappa\kappa}} 2\left(C_L^{EE}\right)^2 \left.\frac{\partial \widetilde{C}_{l'}^{BB}}{\partial C_L^{EE}}\right|_{C^{\kappa\kappa}=\rho^2 C^{\kappa\kappa}} + \frac{\partial \widetilde{C}_l^{BB}}{\partial C_L^{\kappa\kappa}}\left(\rho_L^2 + \rho_L^4\right)\left(C_L^{\kappa\kappa}\right)^2 \frac{\partial \widetilde{C}_{l'}^{BB}}{\partial C_L^{\kappa\kappa}}\right]. \quad \text{(B.79)}$$

In addition to this, the full covariance receives a purely Gaussian contribution. Including it, we obtain

$$\begin{aligned}\mathrm{Cov}\left(C_l^{BB,\mathrm{cross}}, C_{l'}^{BB,\mathrm{cross}}\right) = \frac{1}{2l+1}\delta_{ll'}\left[\widetilde{C}_l^{BB} C_l^{BB,\mathrm{temp}} + \left(C_l^{BB,\mathrm{cross}}\right)^2\right] \\ + \mathrm{Cov}_{\mathrm{NG}}\left(C_l^{BB,\mathrm{cross}}, C_{l'}^{BB,\mathrm{cross}}\right).\end{aligned} \tag{B.80}$$

B.8.2.2 Covariance of template auto-spectrum

To leading order, the auto- and cross-spectra are equal, $C_l^{BB,\mathrm{temp}} = C_l^{BB,\mathrm{cross}}$. Consequently, the non-Gaussian part of the covariance can be approximated as:

$$\begin{aligned}\mathrm{Cov}_{\mathrm{NG}}\left(C_l^{BB,\mathrm{temp}}, C_{l'}^{BB,\mathrm{temp}}\right) &\approx \sum_L \frac{1}{2L+1}\left[\frac{\partial C_l^{BB,\mathrm{temp}}}{\partial C_L^{EE}} 2\left(C_L^{EE}\right)^2 \frac{\partial C_{l'}^{BB,\mathrm{temp}}}{\partial C_L^{EE}}\right. \\ &\qquad \left. + \frac{\partial \widetilde{C}_l^{BB}}{\partial C_L^{\kappa\kappa}} \mathrm{Var}\left(C_L^{\kappa^{\mathrm{WF}}\kappa^{\mathrm{WF}}}\right) \frac{\partial \widetilde{C}_{l'}^{BB}}{\partial C_L^{\kappa\kappa}}\right] \qquad \text{(B.81)} \\ &\approx \sum_L \frac{2}{2L+1}\left[\frac{\partial C_l^{BB,\mathrm{temp}}}{\partial C_L^{EE}} \left(C_L^{EE}\right)^2 \frac{\partial C_{l'}^{BB,\mathrm{temp}}}{\partial C_L^{EE}}\right. \\ &\qquad \left. + \frac{\partial \widetilde{C}_l^{BB}}{\partial C_L^{\kappa\kappa}} \left(\rho_L^2 C_L^{\kappa\kappa}\right)^2 \frac{\partial \widetilde{C}_{l'}^{BB}}{\partial C_L^{\kappa\kappa}}\right], \qquad \text{(B.82)}\end{aligned}$$

and the full covariance is

$$\mathrm{Cov}\left(C_l^{BB,\mathrm{temp}}, C_{l'}^{BB,\mathrm{temp}}\right) = \frac{2}{2l+1}\left(C_l^{BB,\mathrm{temp}}\right)^2 + \mathrm{Cov}_{\mathrm{NG}}\left(C_l^{BB,\mathrm{temp}}, C_{l'}^{BB,\mathrm{temp}}\right). \tag{B.83}$$

B.8.2.3 Cross-covariance of lensing and template auto-spectra

The non-Gaussian part of the covariance can be approximated as:

$$\begin{aligned}\mathrm{Cov}_{\mathrm{NG}}\left(\widetilde{C}_l^{BB}, C_{l'}^{BB,\mathrm{temp}}\right) \approx \sum_L \frac{1}{2L+1}\Bigg[&\frac{\partial \widetilde{C}_l^{BB}}{\partial C_L^{EE}} 2\left(C_L^{EE}\right)^2 \left.\frac{\partial \widetilde{C}_{l'}^{BB}}{\partial C_L^{EE}}\right|_{C^{\kappa\kappa}=\rho^2 C^{\kappa\kappa}} \\ &+ \frac{\partial \widetilde{C}_l^{BB}}{\partial C_L^{\kappa\kappa}} \mathrm{Cov}\left(C_L^{\kappa\kappa}, C_L^{\kappa^{\mathrm{WF}}\kappa^{\mathrm{WF}}}\right) \frac{\partial \widetilde{C}_{l'}^{BB}}{\partial C_L^{\kappa\kappa}}\Bigg] \quad \text{(B.84)} \\ \approx \sum_L \frac{2}{2L+1}\Bigg[&\frac{\partial \widetilde{C}_l^{BB}}{\partial C_L^{EE}} \left(C_L^{EE}\right)^2 \left.\frac{\partial \widetilde{C}_{l'}^{BB}}{\partial C_L^{EE}}\right|_{C^{\kappa\kappa}=\rho^2 C^{\kappa\kappa}} \\ &+ \frac{\partial \widetilde{C}_l^{BB}}{\partial C_L^{\kappa\kappa}} \left(\rho_L^2 C_L^{\kappa\kappa}\right)^2 \frac{\partial \widetilde{C}_{l'}^{BB}}{\partial C_L^{\kappa\kappa}}\Bigg]. \quad \text{(B.85)}\end{aligned}$$

and the full covariance is

$$\mathrm{Cov}\left(\widetilde{C}_l^{BB}, C_{l'}^{BB,\mathrm{temp}}\right) = \frac{2}{2l+1}\delta_{ll'}\left(C_l^{BB,\mathrm{cross}}\right)^2 + \mathrm{Cov}_{\mathrm{NG}}\left(\widetilde{C}_l^{BB}, C_{l'}^{BB,\mathrm{temp}}\right). \quad \text{(B.86)}$$

B.8.2.4 Cross-covariance of lensing auto- and template cross-spectra

The non-Gaussian part of the covariance can be approximated as:

$$\mathrm{Cov}_{\mathrm{NG}}\left(\widetilde{C}_l^{BB}, C_{l'}^{BB,\mathrm{cross}}\right) \approx \mathrm{Cov}_{\mathrm{NG}}\left(\widetilde{C}_l^{BB}, C_{l'}^{BB,\mathrm{temp}}\right), \quad \text{(B.87)}$$

and the full covariance is

$$\mathrm{Cov}\left(\widetilde{C}_l^{BB}, C_{l'}^{BB,\mathrm{temp}}\right) = \frac{2}{2l+1}\delta_{ll'}\widetilde{C}_l^{BB} C_l^{BB,\mathrm{cross}} + \mathrm{Cov}_{\mathrm{NG}}\left(\widetilde{C}_l^{BB}, C_{l'}^{BB,\mathrm{temp}}\right). \quad \text{(B.88)}$$

B.8.2.5 Cross-covariance of template auto- and cross-spectra

The non-Gaussian part of the covariance can be approximated as

$$\mathrm{Cov}_{\mathrm{NG}}\left(C_l^{BB,\mathrm{temp}}, C_{l'}^{BB,\mathrm{cross}}\right) \approx \mathrm{Cov}_{\mathrm{NG}}\left(C_l^{BB,\mathrm{temp}}, C_{l'}^{BB,\mathrm{temp}}\right), \quad \text{(B.89)}$$

and the full covariance is

$$\mathrm{Cov}\left(C_l^{BB,\mathrm{temp}}, C_{l'}^{BB,\mathrm{cross}}\right) = \frac{2}{2l+1}\delta_{ll'}\tilde{C}_l^{BB,\mathrm{temp}}C_l^{BB,\mathrm{cross}} + \mathrm{Cov}_{\mathrm{NG}}\left(C_l^{BB,\mathrm{temp}}, C_{l'}^{BB,\mathrm{temp}}\right) \tag{B.90}$$

$$= \mathrm{Cov}\left(C_l^{BB,\mathrm{temp}}, C_{l'}^{BB,\mathrm{temp}}\right). \tag{B.91}$$

Appendix C

Calculations for Chapter 5

C.1 Factorial moments of the halo occupation distribution

In this appendix, we relate the factorial moments of the halo occupation distribution when expressed in terms of the total number of galaxies in a halo, $N_{\rm gal}$, to the alternative — and also common — case where they are expressed in terms of the number of satellites, $N_{\rm sat}$, and centrals, $N_{\rm cen}$. In the former formulation, we have

$$\begin{aligned}
&\langle N_{\rm gal}(N_{\rm gal}-1)\dots(N_{\rm gal}-j)\rangle \\
&\quad = \sum_{N_{\rm gal}} P(N_{\rm gal}|M) N_{\rm gal}(N_{\rm gal}-1)\dots(N_{\rm gal}-j) \\
&\quad = \langle N_{\rm cen}\rangle \sum_{N_{\rm sat}} P(N_{\rm sat}|N_{\rm cen}=1,M)(N_{\rm sat}+1)N_{\rm sat}(N_{\rm sat}-1)\dots(N_{\rm sat}+1-j) \\
&\quad = \langle N_{\rm cen}\rangle \langle (N_{\rm sat}+1)N_{\rm sat}(N_{\rm sat}-1)\dots(N_{\rm sat}+1-j)\rangle_{N_{\rm cen}=1}\,. \qquad \text{(C.1)}
\end{aligned}$$

In going to the second line, we have factored $P(N_{\rm gal}|M) = P(N_{\rm sat} = N_{\rm gal}-1|N_{\rm cen} = 1, M)P(N_{\rm cen}=1|M)$ (valid for $N_{\rm gal} > 0$) and used the fact that $P(N_{\rm cen}=1|M) = \langle N_{\rm cen}\rangle$.

When conditioned to $N_{\rm cen} = 1$, the number of satellites follows a Poisson distribution; e.g., [237]. It is straightforward to show that, if a random variable N is drawn from a Poisson distribution, then

$$\langle (N+1)N(N-1)\dots(N+1-j)\rangle = \langle N\rangle^j \left[1 + j + \langle N\rangle\right]\,. \qquad \text{(C.2)}$$

Recall now that the mean number of satellite galaxies in *any* halo, $\langle N_{\rm sat}\rangle$, can be related to the mean *conditioned* on there being a central, $\langle N_{\rm sat}\rangle_{N_{\rm cen}=1}$, as $\langle N_{\rm sat}\rangle =$

$\langle N_{\rm cen}\rangle\langle N_{\rm sat}\rangle_{N_{\rm cen}=1}$. Hence,

$$\langle N_{\rm gal}(N_{\rm gal}-1)\dots(N_{\rm gal}-j)\rangle = \left(\frac{\langle N_{\rm sat}\rangle}{\langle N_{\rm cen}\rangle}\right)^j \left[(1+j)\langle N_{\rm cen}\rangle + \langle N_{\rm sat}\rangle\right] . \tag{C.3}$$

C.2 Fast lensing reconstructions using Hankel transforms

The TT quadratic estimator can be written in real space as

$$\hat{\phi}(\mathbf{L}) = -A_L^{TT}\int \frac{d^2\mathbf{x}}{2\pi}\, e^{-i\mathbf{L}\cdot\mathbf{x}}\nabla\cdot[F_1(\mathbf{x})\nabla F_2(\mathbf{x})], \tag{C.4}$$

where

$$F_1(\mathbf{L}) \equiv \frac{\hat{T}(\mathbf{L})}{\tilde{C}_l^{\rm tot}} \quad \text{and} \quad F_2(\mathbf{L}) \equiv \frac{\tilde{C}_l^{TT}\,\hat{T}(\mathbf{L})}{\tilde{C}_l^{\rm tot}} . \tag{C.5}$$

Here, $\hat{T}$ denotes the observed temperature anisotropies of the CMB, and we assume that the filtering is diagonal in harmonic space. Intuitively, the QE harnesses the fact that, to leading order, lensing introduces a depence on its unlensed gradient into the lensed CMB. Hence, ϕ can be extracted by correlating (filtered) observations of small-scale, lensed anisotropies with their (filtered) gradient.

For the subset of one- and two-halo contributions to the primary bispectrum and trispectrum biases that we consider in this work, it is always possible to evaluate equations (5.10) and (5.15) by performing a lensing reconstruction on the anisotropy produced by each halo, and then summing over the contributions of all halos by integrating over z (equation C.23) and M (equations C.25 through C.28). We can therefore harness the approximate azimuthal symmetry of the (projected) emission profiles — even though the total emission, summed over all halos, is generally *not* azimuthally-symmetric — to approximate $\hat{T}(\mathbf{l}) \approx \hat{T}(l)$, such that $F_1(\boldsymbol{l}) \approx F_1(l)$ and $F_2(\boldsymbol{l}) \approx F_2(l)$. This will enable us to carry out the angular integrals analytically. As expected, the two-dimensional Fourier transform of an isotropic profile reduces to its

Hankel transform (see, e.g., Ref. [139]),

$$\begin{aligned} F(\mathbf{x}) &= \int \frac{d^2\mathbf{l}}{2\pi} F(\mathbf{l}) e^{-i\mathbf{l}\cdot\mathbf{x}} \\ &= \int \frac{dl d\theta}{2\pi} lF(l) e^{-ilr\cos\theta} \\ &= \int dl\, lF(l) J_0(lr), \end{aligned} \tag{C.6}$$

where $r = |\boldsymbol{x}|$, and $J_n(x)$ is the n-th order Bessel function of the first kind. In the last line, we have used the fact that

$$\int_0^{2\pi} d\theta e^{-ilr\cos\theta} = 2\pi J_0(lr). \tag{C.7}$$

Consequently, the quadratic estimator can be rewritten as

$$\begin{aligned} \hat{\phi}(\mathbf{L}) &= -A_L^{TT} \int \frac{dr d\Psi}{2\pi} re^{-iLr\cos(\Psi_{\mathbf{L}}-\Psi)} \boldsymbol{\nabla}\cdot[F_1(r)\boldsymbol{\nabla}F_2(r)] \\ &= -A_L^{TT} \int dr\, rJ_0(lr)\boldsymbol{\nabla}\cdot[F_1(r)\boldsymbol{\nabla}F_2(r)] \\ &= -A_L^{TT} \int dl'\, l'F_1(l') \int dl''\, l''F_2(l'') \int dr\, J_0(Lr)\partial_r\left[rJ_0(l'r)\partial_r J_0(l''r)\right], \end{aligned} \tag{C.8}$$

where, in the first line, we defined $\Psi_{\mathbf{L}}$ as the angle between the vector $\mathbf{L}$ and the x-axis. Although the integral over r in the last line can, in principle, be tabulated in advance, the fact that it is not separable would leave an overall computational complexity of $O(N^2)$, where N is the number of samples needed for the integrals to converge. We detail this approach in appendix C.2.1, as it provides a useful cross-check on other methods.

The expression in equation (C.8) can, in fact, be evaluated much faster as a nested series of Hankel transforms. If we first express the derivatives of J_0 in terms of higher-order Bessel functions [3], the integral over three Bessel functions becomes

$$\begin{aligned} \int dr\, J_0(Lr)\partial_r\left[rJ_0(l'r)\partial_r J_0(l''r)\right] = \int dr\, rJ_0(Lr) \\ \times\Bigg[-\frac{l''}{r}J_0(l'r)J_1(l''r) + l'l''J_1(l'r)J_1(l''r) \\ -\frac{1}{2}(l'')^2 J_0(l'r)J_0(l''r) + \frac{1}{2}(l'')^2 J_0(l'r)J_2(l''r)\Bigg]. \end{aligned} \tag{C.9}$$

Therefore, if we denote as $\mathcal{H}_n[f]$ the n-th order Hankel tranform of function f, the quadratic estimator applied to azimuthally-symmetric profiles can be written as

$$\hat{\phi}(\mathbf{L}) = -A_L^{TT}\mathcal{H}_0\Bigg[-\frac{1}{r}\mathcal{H}_0[F_1(l)]\mathcal{H}_1[lF_2(l)] + \mathcal{H}_1[lF_1(l)]\mathcal{H}_1[lF_2(l)] \\ -\frac{1}{2}\mathcal{H}_0[F_1(l)]\mathcal{H}_0[l^2F_2(l)] + \frac{1}{2}\mathcal{H}_0[F_1(l)]\mathcal{H}_2[l^2F_2(l)]\Bigg]. \tag{C.10}$$

This can be further simplified to

$$\hat{\phi}(\mathbf{L}) = -A_L^{TT}\mathcal{H}_0\Bigg[\mathcal{H}_1[lF_2(l)]\left(-\frac{1}{r}\mathcal{H}_0[F_1(l)] + \mathcal{H}_1[lF_1(l)]\right) \\ + \frac{1}{2}\mathcal{H}_0[F_1(l)]\left(-\mathcal{H}_0[l^2F_2(l)] + \mathcal{H}_2[l^2F_2(l)]\right)\Bigg]. \tag{C.11}$$

Hence, we have reduced the problem to the evaluation of seven continuous Hankel transforms.

These transforms can be approximated in a fast and accurate way using the FFTlog algorithm for computing discrete Hankel transforms with logarithmically-spaced samples. The computational complexity is thus reduced to $O(4N\log N)$, with the added advantage that N can be relatively small (we find $N = 4096$ to be sufficient for our purposes).

C.2.1 Alternative evaluation

Another possible approach to evaluating equation (C.8) entails calculating the product of three J_0 functions analytically. This reduces the expression to

$$\hat{\phi}(\mathbf{L}) = -2A_L^{TT}\int\frac{dl\,dl'}{2\pi}lF_1(l)l'F_2(l')\Delta(l,l',L) \\ \times\left(\frac{L^2+l'^2-l^2}{2Ll'}\right)\left[1-\left(\frac{L^2+l'^2-l^2}{2Ll'}\right)\right]^{-\frac{1}{2}}, \tag{C.12}$$

where $\Delta(l,l',L) = 1$ if the triangle inequality is satified and zero otherwise (note that there is an integrable singularity at the limits of the inequality). Although this approach scales as $O(N^2)$, and is thus significantly slower than that presented above, it will serve as a useful benchmark for comparison.

C.3 Evaluating the secondary bispectrum bias

Harnessing statistical isotropy, which imposes $\mathbf{L} = -\mathbf{L}'$, we can evaluate equation (5.13) at a fixed L as a QE reconstruction

$$\langle\hat{\phi}(\mathbf{L})\hat{\phi}(\mathbf{L}')\rangle \supset -\frac{8}{2\pi}\,A_L^{TT}\int\frac{\mathrm{d}^2\boldsymbol{l}'}{2\pi}g(\boldsymbol{l}',\mathbf{L})\langle G(\mathbf{l}')_L T^s(\mathbf{L}+\boldsymbol{l}')\rangle\,, \tag{C.13}$$

where one of the input legs is itself a QE reconstruction,

$$G(\mathbf{l}')_L \equiv A_L^{TT}\int\frac{\mathrm{d}^2\boldsymbol{l}''}{2\pi}g(\boldsymbol{l}'',\mathbf{L})\left[C_{l''}^{TT}T^s(\mathbf{L}-\mathbf{l}'')\mathbf{l}''\right]\cdot[(\mathbf{l}'+\mathbf{l}'')\phi(\mathbf{l}'+\mathbf{l}'')]\,. \tag{C.14}$$

The outer reconstruction of equation (C.13) has to be carried out by brute force, but the inner one can be computed fast using the convolution theorem, given that $\mathbf{L}$ is a constant for the purpose of each reconstruction.

C.4 Halo model of projected higher-point functions

It is evident from equations (5.10) and (5.15) that calculating these lensing biases requires being able to compute angular bispectra and trispectra involving the foreground contaminants.

In order to do this, consider first a projected quantity of the form

$$q(\hat{\boldsymbol{n}}) = \int\mathrm{d}z\frac{\mathrm{d}\chi}{\mathrm{d}z}W(z)Q(\hat{\boldsymbol{n}}\chi(z),z)\,, \tag{C.15}$$

where $\chi(z)$ is the comoving distance to redshift z, $W(z)$ is some weight function, and $Q(\boldsymbol{x},z)$ is a three-dimensional quantity whose projection onto the celestial sphere we observe in the direction of $\hat{\boldsymbol{n}}$ as $q(\hat{\boldsymbol{n}})$. Some relations of this form that are relevant for our purposes are[1]

$$\kappa^{\mathrm{CMB}}(\hat{\boldsymbol{n}}) = \int\mathrm{d}z\frac{\mathrm{d}\chi}{\mathrm{d}z}W_\kappa(z)\delta_{\mathrm{m}}(\hat{\boldsymbol{n}}\chi(z),z)\,, \tag{C.16}$$

$$\delta I_\nu(\hat{\boldsymbol{n}}) = \int\mathrm{d}z\frac{\mathrm{d}\chi}{\mathrm{d}z}W_{\mathrm{CIB}}\delta j_\nu(\hat{\boldsymbol{n}}\chi(z),z)\,,\quad\text{and} \tag{C.17}$$

$$y(\hat{\boldsymbol{n}}) = \int\mathrm{d}z\frac{\mathrm{d}\chi}{\mathrm{d}z}W_{\mathrm{tSZ}}(z)y_{\mathrm{3D}}(\hat{\boldsymbol{n}}\chi(z),z)\,, \tag{C.18}$$

[1]Note that these relations only hold in flat universes.

with

$$W_\kappa(z) = \frac{3\Omega_m H_0^2 \chi}{2a} \frac{\chi_* - \chi}{\chi_*}\,, \tag{C.19}$$

$$W_{\rm CIB}(z) = a(z)\,, \quad \text{and} \tag{C.20}$$

$$W_{\rm tSZ}(z) = a(z)\,. \tag{C.21}$$

Here, χ_* is the comoving distance to the surface of last scattering.

Note that, in equation (C.18), we have introduced a 3D Compton-y field. Following Ref. [185], this is a rescaled version of the electron pressure profile we encountered in section 1.5.3.2,

$$y_{\rm 3D}(\boldsymbol{x}, z) \equiv \frac{\sigma_{\rm T}}{m_e c^2} P_e(\boldsymbol{x}, z)\,, \tag{C.22}$$

with dimensions of inverse length. In our calculations, we use the fitting form of Ref. [26] for the electron pressure profile and its evolution with mass and redshift; the details are described in section 1.5.3.2.

In order to calculate the 'bispectrum' biases — those arising from the correlation between the CMB lensing potential and the extragalactic foregrounds — we need a model for the dark matter overdensity, $\delta_{\rm m}$, which produces the lensing effect. Following the halo model ansatz, we model the dark matter overdensity as an NFW profile; we let the halo concentration vary with mass and redshift according to the fitting functions of Ref. [119] for the mean concentration seen in simulations. Note that, in assuming that the matter overdensity is entirely associated with halos, we are ignoring possible correlations between material in the field (which actually plays an important role in producing the lensing deflections) and the material that produced the CIB and tSZ emission, which lives mostly in halos.

In the Limber approximation [262, 271, 249], angular polyspectra of these projected quantities are related to the equal-redshift polyspectra of the 3D quantities by

$$\mathcal{P}^{(n)}_{q_1\ldots q_n}(\boldsymbol{l}_1, \ldots, \boldsymbol{l}_n) = \int {\rm d}z \frac{{\rm d}\chi}{{\rm d}z} \chi^{2(1-n)}(z) W_1(z) \ldots W_n(z) \mathcal{P}^{(n)}_{Q_1\ldots Q_n}(\boldsymbol{k}^*_1, \ldots, \boldsymbol{k}^*_n; z)\,, \tag{C.23}$$

where $\boldsymbol{k}^* = \boldsymbol{l}/\chi(z)$. See, e.g., appendix E of [242] for a derivation of this relation.

Note that the expression above depends on the Fourier transform of Q. In this work, we assume that all quantities of the form of Q are spherically-symmetric. It is straightforward to show that (in the asymmetric convention) the Fourier transform of

such spherically-symmetric functions simplifies to[2]

$$Q(\boldsymbol{k}, M, z) = 4\pi \int \mathrm{d}r\, r^2\, \frac{\sin(kr)}{kr}\, Q(r, M, z)\,, \tag{C.24}$$

where $k = |\boldsymbol{k}|$. This is merely the three-dimensional instance of a more general theorem that relates the Fourier transform of a radial function to its Hankel transform; see, e.g., Ref. [139]. In appendix C.2, we use its two-dimensional version to speed up the evaluation of the quadratic estimators of lensing.

Finally, we can use the halo model to calculate the equal-redshift bispectra and trispectra needed to evaluate equation (C.23). For now, we only consider terms where all inputs into a given quadratic estimator come from the same halo. (It is only those terms that lend themselves to fast evaluation, harnessing the fact that the integrals over the mass of each halo remain separable once the lensing reconstruction operations have been 'pushed in'.) This restriction leaves us with a subset of the 1- and two-halo contributions in equations (1.128) and (1.131), namely:

$$B^{\mathrm{1h}}_{Q_1Q_2Q_3}(\boldsymbol{k}_1, \boldsymbol{k}_2, \boldsymbol{k}_3; z) = \int \mathrm{d}M\, n(M, z) Q_1(\boldsymbol{k}_1, M, z) Q_2(\boldsymbol{k}_2, M, z) Q_3(\boldsymbol{k}_3, M, z)\,, \tag{C.25}$$

and

$$\begin{aligned} B^{\mathrm{2h}}_{Q_1Q_2Q_3}(\boldsymbol{k}_1, \boldsymbol{k}_2, \boldsymbol{k}_3; z) = P_{\mathrm{lin}}(|\boldsymbol{k}_1|, z) \int \mathrm{d}M'\, n(M', z) b(M', z) Q_1(\boldsymbol{k}_1, M', z) \\ \times \int \mathrm{d}M\, n(M, z) b(M, z) Q_2(\boldsymbol{k}_2, M, z) Q_3(\boldsymbol{k}_3, M, z) \;+\; \text{perms.}\,, \end{aligned} \tag{C.26}$$

while the subset of trispectra are

$$\begin{aligned} &T^{\mathrm{1h}}_{Q_1Q_2Q_3Q_4}(\boldsymbol{k}_1, \boldsymbol{k}_2, \boldsymbol{k}_3, \boldsymbol{k}_4; z) \\ &\qquad = \int \mathrm{d}M\, n(M, z) Q_1(\boldsymbol{k}_1, M, z) Q_2(\boldsymbol{k}_2, M, z) Q_3(\boldsymbol{k}_3, M, z) Q_4(\boldsymbol{k}_4, M, z)\,, \end{aligned} \tag{C.27}$$

[2]We give equation (C.24) in the asymmetric Fourier convention to make contact with earlier discussions involving the normalised NFW profile (c.f. equation (1.110)); to convert to the symmetric convention $Q(\boldsymbol{k}, M, z)$ must be divided by $(2\pi)^{3/2}$.

and

$$T^{\mathrm{2h}}_{Q_1Q_2Q_3Q_4}(\boldsymbol{k}_1,\boldsymbol{k}_2,\boldsymbol{k}_3,\boldsymbol{k}_4;z) = P_{\mathrm{lin}}\left(|\boldsymbol{k}_1+\boldsymbol{k}_2|,z\right)\int \mathrm{d}M'\, n(M',z)b(M',z)Q_1(\boldsymbol{k}_1,M',z)Q_2(\boldsymbol{k}_2,M',z) \times \int \mathrm{d}M\, n(M,z)b(M,z)Q_3(\boldsymbol{k}_3,M,z)Q_4(\boldsymbol{k}_4,M,z) \;+\mathrm{perms}\,. \tag{C.28}$$

In these expressions, $n(M,z)$ is the halo mass function, and $b(M,z)$ is the large-scale halo bias; these are explained in more detail in sections 1.6.2 and 1.6.3, respectively. We evaluate them from functional forms and parameters fit to simulations: the mass function of Ref. [479], and the bias of Ref. [480], as implemented in the publicly-available code `hmvec`[3].

Be it because we want to investigate contributions from halos in a certain mass range, or for reasons of computational feasibility, our mass integrals will be carried out within some limits, $M_{\mathrm{min}} \leq M \leq M_{\mathrm{max}}$, rather than $0 \leq M \leq \infty$. Consequently, the consistency relation in equation (1.101) will not be satisfied strictly. This can lead to problems with many-halo terms: for example, at the two-halo level, the halo model matter power spectrum might no longer approach $P(k\to 0) \approx P_{\mathrm{lin}}(k\to 0)$ on large scales. To get around this issue, we explicitly restore the large-scale behaviour by replacing, in the two-halo expressions above,

$$\mathcal{I}(M_{\mathrm{min}},M_{\mathrm{max}};k) \to \mathcal{I}(M_{\mathrm{min}},M_{\mathrm{max}};k) - \mathcal{I}(M_{\mathrm{min}},M_{\mathrm{max}};k\to 0) + \mathcal{I}(0,\infty;k\to 0)\,, \tag{C.29}$$

where

$$\mathcal{I}(M_{\mathrm{lower}},M_{\mathrm{upper}};k) \equiv \int_{M_{\mathrm{lower}}}^{M_{\mathrm{upper}}} \mathrm{d}M\, n(M,z)b(M,z)Q(k,M,z)\,, \tag{C.30}$$

and similarly for terms involving two different $Q(k,M,z)$ factors in the integrand.

Finally, in order to ensure that the one-halo term does not contribute to the large-scale power, we 'soften' the emission profiles when calculating the one-halo contribution; see equation (1.125) and the discussion around it.

In the next two sections, explicit expressions are provided for the equal-redshift bispectra and trispectra we consider in this work.

[3]The code `hmvec`, which is based on the work of Ref. [448], can be found at `https://github.com/simonsobs/hmvec` .

C.5 Halo-model calculations for the primary bispectrum bias

We can calculate the relevant matter-tSZ-tSZ bispectrum by following the prescriptions of section 1.6.5, but replacing dark matter density profiles with their 3D Compton-y equivalent where needed — that is, $uM/\bar{\rho} \to y_{\rm 3D}$. We find

$$B^{\rm 1h}_{\phi yy}(\boldsymbol{k}_1, \boldsymbol{k}_2, \boldsymbol{k}_3; z) = \int \mathrm{d}M\, n(M,z) \frac{M}{\bar{\rho}} u(k_1, M, z) y_{\rm 3D}(k_2, M, z) y_{\rm 3D}(k_3, M, z)\,, \quad \text{(C.31)}$$

and

$$\begin{aligned} B^{\rm 2h}_{\phi yy}(\boldsymbol{k}_1, \boldsymbol{k}_2, \boldsymbol{k}_3; z) = P_{\rm lin}\left(|\boldsymbol{k}_1|, z\right) \int \mathrm{d}M'\, n(M', z) b(M', z) \frac{M}{\bar{\rho}} u(k_1, M', z) \\ \times \int \mathrm{d}M\, n(M,z) b(M,z) y_{\rm 3D}(k_2, M, z) y_{\rm 3D}(k_3, M, z)\,, \end{aligned} \quad \text{(C.32)}$$

where we have defined $\bar{\rho} \equiv \rho_{\rm m}(z)$. Everywhere in this work, $u(k, M, z)$ refers to the Fourier-transformed NFW profile, normalised as prescribed by equation (1.109), and with concentration $c(M, z)$ obtained from the fitting function of Ref. [119]; see equation (1.106) and the discussion around it for details. The subscript notation we have adopted is intended to denote the role of the higher-point function upon projection.

When writing down bispectra and trispectra of the CIB, we will follow the prescriptions of sections 1.6.7 and 1.6.6. In particular, we will use equation (1.140) (proved in appendix C.1) to relate the factorial moments of the total number of galaxies in a halo to those of satellites and centrals, which can trivially be translated to expressions in terms of $f^{\rm cen}$ and $f^{\rm sat}$. These tools suggest a one-halo contribution of the form

$$\begin{aligned} B^{\rm 1h}_{\phi I_\nu I_\nu}(\boldsymbol{k}_1, \boldsymbol{k}_2, \boldsymbol{k}_3; z) = \int \mathrm{d}M\, n(M,z) \frac{M}{\bar{\rho}} u(k_1, M, z) u(k_2, M, z) u(k_3, M, z) \\ \times \frac{f^{\rm sat}_\nu(M,z)}{f^{\rm cen}_\nu(M,z)} \left[2 f^{\rm cen}_\nu(M,z) + f^{\rm sat}_\nu(M,z)\right]\,, \end{aligned} \quad \text{(C.33)}$$

and a two-halo term

$$B^{\rm 2h}_{\phi I_\nu I_\nu}(\boldsymbol{k}_1,\boldsymbol{k}_2,\boldsymbol{k}_3;z) = P_{\rm lin}\left(|\boldsymbol{k}_1|,z\right)\int {\rm d}M'\, n(M',z)b(M',z)\frac{M}{\bar{\rho}}u(k_1,M',z) \\ \times\int {\rm d}M\, n(M,z)b(M,z)u(k_2,M,z)u(k_3,M,z) \\ \times\frac{f^{\rm sat}_\nu(M,z)}{f^{\rm cen}_\nu(M,z)}\left[2f^{\rm cen}_\nu(M,z)+f^{\rm sat}_\nu(M,z)\right]\,. \tag{C.34}$$

Note that, in this and subsequent expressions, we assume that the same CIB frequency (143 GHz) is probed by the various legs of the higher-point function. As is common in the literature, we have also assumed that the spatial distribution of galaxies in a host halo follows an NFW profile.

For the mixed biases involving both tSZ and CIB legs, we implement

$$B^{\rm 1h}_{\phi I_\nu y}(\boldsymbol{k}_1,\boldsymbol{k}_2,\boldsymbol{k}_3;z) = \int {\rm d}M\, n(M,z)\frac{M}{\bar{\rho}}u(k_1,M,z)u(k_2,M,z)y_{\rm 3D}(k_3,M,z) \\ \times\left[f^{\rm cen}_\nu(M,z)+f^{\rm sat}_\nu(M,z)\right]\,, \tag{C.35}$$

and

$$B^{\rm 2h}_{\phi I_\nu y}(\boldsymbol{k}_1,\boldsymbol{k}_2,\boldsymbol{k}_3;z) = P_{\rm lin}\left(|\boldsymbol{k}_1|,z\right)\int {\rm d}M'\, n(M',z)b(M',z)\frac{M}{\bar{\rho}}u(k_1,M',z) \\ \times\int {\rm d}M\, n(M,z)b(M,z)u(k_2,M,z)y_{\rm 3D}(k_3,M,z) \\ \times\left[f^{\rm cen}_\nu(M,z)+f^{\rm sat}_\nu(M,z)\right]\,. \tag{C.36}$$

When calculating the primary bispectrum bias as in equation (5.10), this contribution will carry an additional permutation factor of 2.

C.6 Halo-model calculations for the trispectrum bias

For the pure-tSZ trispectrum, we implement a one-halo contribution

$$T^{\rm 1h}_{yyyy}(\boldsymbol{k}_1,\boldsymbol{k}_2,\boldsymbol{k}_3,\boldsymbol{k}_4;z) \\ = \int {\rm d}M\, n(M,z)y_{\rm 3D}(k_1,M,z)y_{\rm 3D}(k_2,M,z)y_{\rm 3D}(k_3,M,z)y_{\rm 3D}(k_4,M,z)\,, \tag{C.37}$$

and a two-halo contribution

$$\begin{aligned} T^{\mathrm{2h}}_{yyyy}(\boldsymbol{k}_1, \boldsymbol{k}_2, \boldsymbol{k}_3, \boldsymbol{k}_4; z) \\ = P_{\mathrm{lin}}\left(|\boldsymbol{k}_1 + \boldsymbol{k}_2|, z\right) \int \mathrm{d}M'\, n(M', z) b(M', z) y_{\mathrm{3D}}(k_1, M', z) y_{\mathrm{3D}}(k_2, M', z) \\ \times \int \mathrm{d}M\, n(M, z) b(M, z) y_{\mathrm{3D}}(k_3, M, z) y_{\mathrm{3D}}(k_4, M, z)\,. \end{aligned} \tag{C.38}$$

For the CIB-only case, we calculate a one-halo term

$$\begin{aligned} T^{\mathrm{1h}}_{I_\nu I_\nu I_\nu I_\nu}(\boldsymbol{k}_1, \boldsymbol{k}_2, \boldsymbol{k}_3, \boldsymbol{k}_4; z) \\ = \int \mathrm{d}M\, n(M, z) u(k_1, M, z) u(k_2, M, z) u(k_3, M, z) u(k_4, M, z) \\ \times \left(\frac{f^{\mathrm{sat}}_\nu(M, z)}{f^{\mathrm{cen}}_\nu(M, z)}\right)^3 \left[4 f^{\mathrm{cen}}_\nu(M, z) + f^{\mathrm{sat}}_\nu(M, z)\right], \end{aligned} \tag{C.39}$$

and a two-halo term

$$\begin{aligned} T^{\mathrm{2h}}_{I_\nu I_\nu I_\nu I_\nu}(\boldsymbol{k}_1, \boldsymbol{k}_2, \boldsymbol{k}_3, \boldsymbol{k}_4; z) \\ = P_{\mathrm{lin}}\left(|\boldsymbol{k}_1 + \boldsymbol{k}_2|, z\right) \int \mathrm{d}M'\, n(M', z) b(M', z) u(k_1, M', z) u(k_2, M', z) \\ \times \frac{f^{\mathrm{sat}}_\nu(M', z)}{f^{\mathrm{cen}}_\nu(M', z)} \left[2 f^{\mathrm{cen}}_\nu(M', z) + f^{\mathrm{sat}}_\nu(M', z)\right] \\ \times \int \mathrm{d}M\, n(M, z) b(M, z) u(k_3, M, z) u(k_4, M, z) \\ \times \frac{f^{\mathrm{sat}}_\nu(M, z)}{f^{\mathrm{cen}}_\nu(M, z)} \left[2 f^{\mathrm{cen}}_\nu(M, z) + f^{\mathrm{sat}}_\nu(M, z)\right]. \end{aligned} \tag{C.40}$$

For the mixed biases involving both tSZ and CIB emission, we implement several couplings. The first has a one-halo term of the form

$$\begin{aligned} T^{\mathrm{1h}}_{I_\nu yyy}(\boldsymbol{k}_1, \boldsymbol{k}_2, \boldsymbol{k}_3, \boldsymbol{k}_4; z) \\ = \int \mathrm{d}M\, n(M, z) u(k_1, M, z) y_{\mathrm{3D}}(k_2, M, z) y_{\mathrm{3D}}(k_3, M, z) y_{\mathrm{3D}}(k_4, M, z) \\ \times \left[f^{\mathrm{cen}}_\nu(M, z) + f^{\mathrm{sat}}_\nu(M, z)\right], \end{aligned} \tag{C.41}$$

and a two-halo term

$$\begin{aligned} T^{\mathrm{2h}}_{I_\nu yyy}(\boldsymbol{k}_1, \boldsymbol{k}_2, \boldsymbol{k}_3, \boldsymbol{k}_4; z) \\ = P_{\mathrm{lin}}\left(|\boldsymbol{k}_1 + \boldsymbol{k}_2|, z\right) \int \mathrm{d}M'\, n(M', z) b(M', z) u(k_1, M', z) y_{\mathrm{3D}}(k_2, M', z) \\ \times \left[f^{\mathrm{cen}}_\nu(M', z) + f^{\mathrm{sat}}_\nu(M', z) \right] \\ \times \int \mathrm{d}M\, n(M, z) b(M, z) y_{\mathrm{3D}}(k_3, M, z) y_{\mathrm{3D}}(k_4, M, z)\,. \end{aligned} \tag{C.42}$$

In the calculation of the trispectrum bias, equation (5.15), this contribution features with a permutation factor of 4.

Another coupling is

$$\begin{aligned} T^{\mathrm{1h}}_{I_\nu I_\nu yy}(\boldsymbol{k}_1, \boldsymbol{k}_2, \boldsymbol{k}_3, \boldsymbol{k}_4; z) \\ = \int \mathrm{d}M\, n(M, z) u(k_1, M, z) u(k_2, M, z) y_{\mathrm{3D}}(k_3, M, z) y_{\mathrm{3D}}(k_4, M, z) \\ \times \frac{f^{\mathrm{sat}}_\nu(M, z)}{f^{\mathrm{cen}}_\nu(M, z)} \left[2 f^{\mathrm{cen}}_\nu(M, z) + f^{\mathrm{sat}}_\nu(M, z) \right], \end{aligned} \tag{C.43}$$

with a two-halo contribution

$$\begin{aligned} T^{\mathrm{2h}}_{I_\nu I_\nu yy}(\boldsymbol{k}_1, \boldsymbol{k}_2, \boldsymbol{k}_3, \boldsymbol{k}_4; z) \\ = P_{\mathrm{lin}}\left(|\boldsymbol{k}_1 + \boldsymbol{k}_2|, z\right) \int \mathrm{d}M'\, n(M', z) b(M', z) u(k_1, M', z) u(k_2, M', z) \\ \times \frac{f^{\mathrm{sat}}_\nu(M', z)}{f^{\mathrm{cen}}_\nu(M', z)} \left[2 f^{\mathrm{cen}}_\nu(M', z) + f^{\mathrm{sat}}_\nu(M', z) \right] \\ \times \int \mathrm{d}M\, n(M, z) b(M, z) y_{\mathrm{3D}}(k_3, M, z) y_{\mathrm{3D}}(k_4, M, z)\,. \end{aligned} \tag{C.44}$$

These contribute to the trispectrum bias with a permutation factor of 2.

Also,

$$\begin{aligned} T^{\mathrm{1h}}_{I_\nu y I_\nu y}(\boldsymbol{k}_1, \boldsymbol{k}_2, \boldsymbol{k}_3, \boldsymbol{k}_4; z) \\ = \int \mathrm{d}M\, n(M, z) u(k_1, M, z) y_{\mathrm{3D}}(k_2, M, z) u(k_3, M, z) y_{\mathrm{3D}}(k_4, M, z) \\ \times \frac{f^{\mathrm{sat}}_\nu(M, z)}{f^{\mathrm{cen}}_\nu(M, z)} \left[2 f^{\mathrm{cen}}_\nu(M, z) + f^{\mathrm{sat}}_\nu(M, z) \right], \end{aligned} \tag{C.45}$$

and

$$
\begin{aligned}
&T^{\mathrm{2h}}_{I_\nu y I_\nu y}(\boldsymbol{k}_1, \boldsymbol{k}_2, \boldsymbol{k}_3, \boldsymbol{k}_4; z) \\
&\quad = P_{\mathrm{lin}}\left(|\boldsymbol{k}_1 + \boldsymbol{k}_2|, z\right) \int \mathrm{d}M'\, n(M', z) b(M', z) u(k_1, M', z) y_{\mathrm{3D}}(k_2, M', z) \\
&\qquad\qquad \times \left[f^{\mathrm{cen}}_\nu(M', z) + f^{\mathrm{sat}}_\nu(M', z) \right] \\
&\qquad \times \int \mathrm{d}M\, n(M, z) b(M, z) u(k_3, M, z) y_{\mathrm{3D}}(k_4, M, z) \\
&\qquad\qquad \times \left[f^{\mathrm{cen}}_\nu(M, z) + f^{\mathrm{sat}}_\nu(M, z) \right] ,
\end{aligned} \tag{C.46}
$$

with a permutation factor of 4.

Finally, we have

$$
\begin{aligned}
&T^{\mathrm{1h}}_{y I_\nu I_\nu I_\nu}(\boldsymbol{k}_1, \boldsymbol{k}_2, \boldsymbol{k}_3, \boldsymbol{k}_4; z) \\
&\quad = \int \mathrm{d}M\, n(M, z) u(k_1, M, z) y_{\mathrm{3D}}(k_2, M, z) u(k_3, M, z) y_{\mathrm{3D}}(k_4, M, z) \\
&\qquad \times \left(\frac{f^{\mathrm{sat}}_\nu(M, z)}{f^{\mathrm{cen}}_\nu(M, z)} \right)^2 \left[3 f^{\mathrm{cen}}_\nu(M, z) + f^{\mathrm{sat}}_\nu(M, z) \right] ,
\end{aligned} \tag{C.47}
$$

and

$$
\begin{aligned}
&T^{\mathrm{2h}}_{y I_\nu I_\nu I_\nu}(\boldsymbol{k}_1, \boldsymbol{k}_2, \boldsymbol{k}_3, \boldsymbol{k}_4; z) \\
&\quad = P_{\mathrm{lin}}\left(|\boldsymbol{k}_1 + \boldsymbol{k}_2|, z\right) \int \mathrm{d}M'\, n(M', z) b(M', z) u(k_1, M', z) y_{\mathrm{3D}}(k_2, M', z) \\
&\qquad\qquad \times \left[f^{\mathrm{cen}}_\nu(M', z) + f^{\mathrm{sat}}_\nu(M', z) \right] \\
&\qquad \times \int \mathrm{d}M\, n(M, z) b(M, z) u(k_3, M, z) u(k_4, M, z) \\
&\qquad\qquad \times \frac{f^{\mathrm{sat}}_\nu(M, z)}{f^{\mathrm{cen}}_\nu(M, z)} \left[2 f^{\mathrm{cen}}_\nu(M, z) + f^{\mathrm{sat}}_\nu(M, z) \right] ,
\end{aligned} \tag{C.48}
$$

which ultimately feature in the bias calculation with a permutation factor of 4.

References

[1] Abazajian et al. (2019). CMB-S4 Science Case, Reference Design, and Project Plan. *arXiv e-prints*, page arXiv:1907.04473.

[2] Abitbol, M. H. et al. (2020). The Simons Observatory: Bandpass and polarization-angle calibration requirements for B-mode searches.

[3] Abramowitz, M. (1974). *Handbook of Mathematical Functions, With Formulas, Graphs, and Mathematical Tables,*. Dover Publications, Inc., USA.

[4] Addison, G. E., Dunkley, J., and Spergel, D. N. (2012). Modelling the correlation between the thermal Sunyaev Zel'dovich effect and the cosmic infrared background. *Mon. Not. R. Astron. Soc.* , 427(2):1741–1754.

[5] Albrecht, A. and Steinhardt, P. J. (1982). Cosmology for grand unified theories with radiatively induced symmetry breaking. *Phys. Rev. Lett.*, 48:1220–1223.

[6] Allgood, B., Flores, R. A., Primack, J. R., Kravtsov, A. V., Wechsler, R. H., Faltenbacher, A., and Bullock, J. S. (2006). The shape of dark matter haloes: dependence on mass, redshift, radius and formation. *Mon. Not. R. Astron. Soc.* , 367(4):1781–1796.

[7] Allison, R. and ACT Collaboration (2015). The Atacama Cosmology Telescope: measuring radio galaxy bias through cross-correlation with lensing. *Mon. Not. R. Astron. Soc.* , 451(1):849–858.

[8] Allison, R., Caucal, P., Calabrese, E., Dunkley, J., and Louis, T. (2015). Towards a cosmological neutrino mass detection. *Phys. Rev. D* , 92(12):123535.

[9] Alonso, D., Dunkley, J., Thorne, B., and Næss, S. (2017). Simulated forecasts for primordial B-mode searches in ground-based experiments. *Phys. Rev. D* , 95(4):043504.

[10] Alonso, D., Sanchez, J., Slosar, A., and LSST Dark Energy Science Collaboration (2019). A unified pseudo-C_ℓ framework. *Mon. Not. R. Astron. Soc.* , 484(3):4127–4151.

[11] Alpher, R. A. (1948). A Neutron-Capture Theory of the Formation and Relative Abundance of the Elements. *Physical Review*, 74(11):1577–1589.

[12] Amblard, A. et al. (2011). Submillimetre galaxies reside in dark matter haloes with masses greater than $3{\times}10^{11}$ solar masses. *Nature (London)* , 470(7335):510–512.

[13] Amblard, A., Vale, C., and White, M. (2004). Weak lensing of the CMB by large-scale structure. *New Astronomy*, 9(8):687–704.

[14] Anderes, E., Wandelt, B., and Lavaux, G. (2015). Bayesian inference of CMB gravitational lensing. *Astrophys. J.*, 808(2):152.

[15] Andersson, B. G., Lazarian, A., and Vaillancourt, J. E. (2015). Interstellar Dust Grain Alignment. *Ann. Rev. Astron. Astrophys.* , 53:501–539.

[16] Arnaud, M., Pratt, G. W., Piffaretti, R., Böhringer, H., Croston, J. H., and Pointecouteau, E. (2010). The universal galaxy cluster pressure profile from a representative sample of nearby systems (REXCESS) and the Y_{SZ} - M_{500} relation. *Astron. Astrophys.* , 517:A92.

[17] Baleato Lizancos, A., Challinor, A., and Carron, J. (2020). Impact of internal-delensing biases on searches for primordial B-modes of CMB polarisation. *arXiv e-prints*, page arXiv:2007.01622.

[18] Baleato Lizancos, A., Challinor, A., and Carron, J. (2021a). Limitations of CMB B -mode template delensing. *Phys. Rev. D* , 103(2):023518.

[19] Baleato Lizancos, A., Challinor, A., Sherwin, B. D., and Namikawa, T. (2021b). Delensing the CMB with the cosmic infrared background: the impact of foregrounds. *arXiv e-prints*, page arXiv:2102.01045.

[20] Bardeen, J. M. (1980). Gauge-invariant cosmological perturbations. *Phys. Rev. D* , 22(8):1882–1905.

[21] Bardeen, J. M., Bond, J. R., Kaiser, N., and Szalay, A. S. (1986). The Statistics of Peaks of Gaussian Random Fields. *Astrophys. J.* , 304:15.

[22] Bardeen, J. M., Steinhardt, P. J., and Turner, M. S. (1983). Spontaneous creation of almost scale-free density perturbations in an inflationary universe. *Phys. Rev. D* , 28(4):679–693.

[23] Barron, D. et al. (2018). Optimization study for the experimental configuration of CMB-S4. *J. Cosmol. Astropart. Phys.* , 2018(2):009.

[24] Bartelmann, M. and Schneider, P. (2001). Weak gravitational lensing. *Phys. Rep.* , 340(4-5):291–472.

[25] Bartolo, N., Matarrese, S., and Riotto, A. (2010). Non-Gaussianity and the Cosmic Microwave Background Anisotropies. *Advances in Astronomy*, 2010:157079.

[26] Battaglia, N., Bond, J. R., Pfrommer, C., and Sievers, J. L. (2012). On the Cluster Physics of Sunyaev-Zel'dovich and X-Ray Surveys. II. Deconstructing the Thermal SZ Power Spectrum. *Astrophys. J.* , 758(2):75.

[27] Baumann, D. (2009). TASI Lectures on Inflation. *arXiv e-prints*, page arXiv:0907.5424.

[28] Baumann, D. et al. (2009). Probing Inflation with CMB Polarization. In Dodelson, S. et al., editors, *CMB Polarization Workshop: Theory and Foregrounds: CMBPol Mission Concept Study*, volume 1141 of *American Institute of Physics Conference Series*, pages 10–120.

[29] Baxter, E. J., SPT Collaboration, and ACT Collaboration (2018). A measurement of CMB cluster lensing with SPT and DES year 1 data. *Mon. Not. R. Astron. Soc.* , 476(2):2674–2688.

[30] Beck, D., Errard, J., and Stompor, R. (2020). Impact of polarized galactic foreground emission on CMB lensing reconstruction and delensing of B-modes. *J. Cosmol. Astropart. Phys.* , 2020(6):030.

[31] Beck, D., Fabbian, G., and Errard, J. (2018). Lensing reconstruction in post-Born cosmic microwave background weak lensing. *Phys. Rev. D* , 98(4):043512.

[32] Belokurov, V. (2013). Galactic Archaeology: The dwarfs that survived and perished. *New Astronomy Reviews*, 57(3-4):100–121.

[33] Benabed, K. and Bernardeau, F. (2000). Cosmic string lens effects on CMB polarization patterns. *Phys. Rev. D* , 61(12):123510.

[34] Bennett, C. L. et al. (1992). Preliminary Separation of Galactic and Cosmic Microwave Emission for the COBE Differential Microwave Radiometers. *ApJL*, 396:L7.

[35] Benoit-Lévy, A., Déchelette, T., Benabed, K., Cardoso, J. F., Hanson, D., and Prunet, S. (2013). Full-sky CMB lensing reconstruction in presence of sky-cuts. *Astron. Astrophys.* , 555:A37.

[36] Benoit-Lévy, A., Smith, K. M., and Hu, W. (2012). Non-Gaussian structure of the lensed CMB power spectra covariance matrix. *Phys. Rev. D* , 86:123008.

[37] Benson, A. J., Bower, R. G., Frenk, C. S., Lacey, C. G., Baugh, C. M., and Cole, S. (2003). What Shapes the Luminosity Function of Galaxies? *Astrophys. J.* , 599(1):38–49.

[38] Berlind, A. A. et al. (2003). The Halo Occupation Distribution and the Physics of Galaxy Formation. *Astrophys. J.* , 593(1):1–25.

[39] Bernardeau, F. (1997). Weak lensing detection in CMB maps. *Astron. Astrophys.* , 324:15–26.

[40] Bernardeau, F. (1998). Lens distortion effects on CMB maps. *Astron. Astrophys.* , 338:767–776.

[41] Bernardeau, F., Colombi, S., Gaztañaga, E., and Scoccimarro, R. (2002). Large-scale structure of the Universe and cosmological perturbation theory. *Phys. Rep.* , 367(1-3):1–248.

[42] Bertschinger, E. (1985). Self-similar secondary infall and accretion in an Einstein-de Sitter universe. *ApJS*, 58:39–65.

[43] Béthermin, M., Dole, H., Lagache, G., Le Borgne, D., and Penin, A. (2011). Modeling the evolution of infrared galaxies: a parametric backward evolution model. *Astron. Astrophys.* , 529:A4.

[44] Béthermin, M. and HerMES Collaboration (2012). HerMES: deep number counts at 250 μm, 350 μm and 500 μm in the COSMOS and GOODS-N fields and the build-up of the cosmic infrared background. *Astron. Astrophys.* , 542:A58.

[45] Bhattacharya, S., Habib, S., Heitmann, K., and Vikhlinin, A. (2013). Dark Matter Halo Profiles of Massive Clusters: Theory versus Observations. *Astrophys. J.* , 766(1):32.

[46] Bianchini, F. et al. (2015). Cross-correlation between the CMB Lensing Potential Measured by Planck and High-z Submillimeter Galaxies Detected by the Herschel-Atlas Survey. *Astrophys. J.* , 802(1):64.

[47] BICEP2 Collaboration (2014). Detection of B-Mode Polarization at Degree Angular Scales by BICEP2. *Phys. Rev. Lett.* , 112:241101.

[48] BICEP2/Keck Array Collaboration (2018). Constraints on Primordial Gravitational Waves Using Planck, WMAP, and New BICEP2/Keck Observations through the 2015 Season. *Phys. Rev. Lett.* , 121(22):221301.

[49] BICEP2/Keck Array Collaboration and Planck Collaboration (2015). Joint Analysis of BICEP2/Keck Array and Planck Data. *Phys. Rev. Lett.* , 114:101301.

[50] BICEP2/Keck Array Collaboration (2016). BICEP2 / Keck Array VIII: Measurement of gravitational lensing from large-scale B-mode polarization. *Astrophys. J.*, 833(2):228.

[51] BICEP/Keck Collaboration and SPTpol Collaboration (2021). A demonstration of improved constraints on primordial gravitational waves with delensing. *Phys. Rev. D* , 103(2):022004.

[52] Blanchard, A. and Schneider, J. (1987). Gravitational lensing effect on the fluctuations of the cosmic background radiation. *Astron. Astrophys.* , 184(1-2):1–6.

[53] Bleem, L. E. et al. (2015). Galaxy Clusters Discovered via the Sunyaev-Zel'dovich Effect in the 2500-square-degree SPT-SZ survey. *Astrophys. J. Suppl.*, 216(2):27.

[54] Bleem, L. E. and SPT Collaboration (2012). A Measurement of the Correlation of Galaxy Surveys with CMB Lensing Convergence Maps from the South Pole Telescope. *ApJL*, 753(1):L9.

[55] Blumenthal, G. R., Faber, S. M., Primack, J. R., and Rees, M. J. (1984). Formation of galaxies and large-scale structure with cold dark matter. *Nature (London)* , 311:517–525.

[56] Bocquet, S., Heitmann, K., Habib, S., Lawrence, E., Uram, T., Frontiere, N., Pope, A., and Finkel, H. (2020). The Mira-Titan Universe. III. Emulation of the Halo Mass Function. *Astrophys. J.* , 901(1):5.

[57] Bocquet, S., Saro, A., Dolag, K., and Mohr, J. J. (2016). Halo mass function: baryon impact, fitting formulae, and implications for cluster cosmology. *Mon. Not. R. Astron. Soc.* , 456(3):2361–2373.

[58] Böhm, V., Schmittfull, M., and Sherwin, B. D. (2016). Bias to CMB lensing measurements from the bispectrum of large-scale structure. *Phys. Rev. D* , 94(4):043519.

[59] Böhm, V., Sherwin, B. D., Liu, J., Hill, J. C., Schmittfull, M., and Namikawa, T. (2018). Effect of non-Gaussian lensing deflections on CMB lensing measurements. *Phys. Rev. D* , 98(12):123510.

[60] Bond, J. R., Cole, S., Efstathiou, G., and Kaiser, N. (1991). Excursion Set Mass Functions for Hierarchical Gaussian Fluctuations. *Astrophys. J.* , 379:440.

[61] Bond, J. R. and Efstathiou, G. (1984). Cosmic background radiation anisotropies in universes dominated by nonbaryonic dark matter. *ApJL*, 285:L45–L48.

[62] Bond, J. R. and Efstathiou, G. (1987). The statistics of cosmic background radiation fluctuations. *Mon. Not. R. Astron. Soc.* , 226:655–687.

[63] Bouché, N. et al. (2010). The Impact of Cold Gas Accretion Above a Mass Floor on Galaxy Scaling Relations. *Astrophys. J.* , 718(2):1001–1018.

[64] Bouchet, F. R., Colombi, S., Hivon, E., and Juszkiewicz, R. (1995). Perturbative Lagrangian approach to gravitational instability. *Astron. Astrophys.* , 296:575.

[65] Bryan, G. L. and Norman, M. L. (1998). Statistical Properties of X-Ray Clusters: Analytic and Numerical Comparisons. *Astrophys. J.* , 495(1):80–99.

[66] Buchalter, A., Kamionkowski, M., and Jaffe, A. H. (2000). The Angular Three-Point Correlation Function in the Quasi-linear Regime. *Astrophys. J.* , 530(1):36–52.

[67] Bucher, M., Carvalho, C. S., Moodley, K., and Remazeilles, M. (2012). CMB lensing reconstruction in real space. *Phys. Rev. D* , 85(4):043016.

[68] Bullock, J. S., Kolatt, T. S., Sigad, Y., Somerville, R. S., Kravtsov, A. V., Klypin, A. A., Primack, J. R., and Dekel, A. (2001). Profiles of dark haloes: evolution, scatter and environment. *Mon. Not. R. Astron. Soc.* , 321(3):559–575.

[69] Bunn, E. F., Zaldarriaga, M., Tegmark, M., and de Oliveira-Costa, A. (2003). E/B decomposition of finite pixelized CMB maps. *Phys. Rev. D* , 67(2):023501.

[70] Burigana, C., Danese, L., and de Zotti, G. (1991). Formation and evolution of early distortions of the microwave background spectrum - A numerical study. *Astron. Astrophys.* , 246(1):49–58.

[71] Calabrese, E., Slosar, A., Melchiorri, A., Smoot, G. F., and Zahn, O. (2008). Cosmic microwave weak lensing data as a test for the dark universe. *Phys. Rev. D* , 77(12):123531.

[72] Cardoso, J.-F., Le Jeune, M., Delabrouille, J., Betoule, M., and Patanchon, G. (2008). Component Separation With Flexible Models—Application to Multichannel Astrophysical Observations. *IEEE Journal of Selected Topics in Signal Processing*, 2(5):735–746.

[73] Carlstrom, J. E., Holder, G. P., and Reese, E. D. (2002). Cosmology with the Sunyaev-Zel'dovich Effect. *Ann. Rev. Astron. Astrophys.* , 40:643–680.

[74] Carron, J. and Lewis, A. (2017a). Maximum a posteriori CMB lensing reconstruction. *Phys. Rev. D* , 96(6):063510.

[75] Carron, J. and Lewis, A. (2017b). Maximum a posteriori CMB lensing reconstruction. *Phys. Rev. D* , 96:063510.

[76] Carron, J., Lewis, A., and Challinor, A. (2017). Internal delensing of Planck CMB temperature and polarization. *Journal of Cosmology and Astro-Particle Physics*, 2017:035.

[77] Casas-Miranda, R., Mo, H. J., Sheth, R. K., and Boerner, G. (2002). On the distribution of haloes, galaxies and mass. *Mon. Not. R. Astron. Soc.* , 333(4):730–738.

[78] Castorina, E., Sefusatti, E., Sheth, R. K., Villaescusa-Navarro, F., and Viel, M. (2014). Cosmology with massive neutrinos II: on the universality of the halo mass function and bias. *J. Cosmol. Astropart. Phys.* , 2014(2):049.

[79] Catelan, P., Lucchin, F., Matarrese, S., and Porciani, C. (1998). The bias field of dark matter haloes. *Mon. Not. R. Astron. Soc.* , 297(3):692–712.

[80] Challinor, A. (2016). Advanced Cosmology Lecture Notes. *Part III of the Mathematical Tripos — University of Cambridge*.

[81] Challinor, A. and Chon, G. (2002). Geometry of weak lensing of CMB polarization. *Phys. Rev. D* , 66:127301.

[82] Challinor, A. and CORE Collaboration (2018). Exploring cosmic origins with CORE: Gravitational lensing of the CMB. *J. Cosmol. Astropart. Phys.* , 2018(4):018.

[83] Challinor, A. and Lasenby, A. (1998). Relativistic Corrections to the Sunyaev-Zeldovich Effect. *Astrophys. J.* , 499(1):1–6.

[84] Challinor, A. and Lewis, A. (2005). Lensed CMB power spectra from all-sky correlation functions. *Phys. Rev. D* , 71(10):103010.

[85] Chen, A. Y. and Afshordi, N. (2020). Amending the halo model to satisfy cosmological conservation laws. *Phys. Rev. D* , 101(10):103522.

[86] Choi, S. K. and ACT Collaboration (2020). The Atacama Cosmology Telescope: a measurement of the Cosmic Microwave Background power spectra at 98 and 150 GHz. *J. Cosmol. Astropart. Phys.* , 2020(12):045.

[87] Clark, S. E., Hill, J. C., Peek, J. E. G., Putman, M. E., and Babler, B. L. (2015). Neutral Hydrogen Structures Trace Dust Polarization Angle: Implications for Cosmic Microwave Background Foregrounds. *Phys. Rev. Lett.* , 115(24):241302.

[88] Clark, S. E., Kim, C.-G., Hill, J. C., and Hensley, B. S. (2021). The Origin of Parity Violation in Polarized Dust Emission and Implications for Cosmic Birefringence. *arXiv e-prints*, page arXiv:2105.00120.

[89] Clark, S. E., Peek, J. E. G., and Putman, M. E. (2014). Magnetically Aligned H I Fibers and the Rolling Hough Transform. *Astrophys. J.* , 789(1):82.

[90] CMB-S4 collaboration (2016). CMB-S4 Science Book, First Edition. *ArXiv e-prints*, page arXiv:1610.02743.

[91] Codis, S., Jindal, A., Chisari, N. E., Vibert, D., Dubois, Y., Pichon, C., and Devriendt, J. (2018). Galaxy orientation with the cosmic web across cosmic time. *Mon. Not. R. Astron. Soc.* , 481(4):4753–4774.

[92] Cole, S. and Efstathiou, G. (1989). Gravitational lensing of fluctuations in the microwave background radiation. *Mon. Not. R. Astron. Soc.* , 239:195–200.

[93] Coles, P. (1993). Galaxy formation with a local bias. *Mon. Not. R. Astron. Soc.* , 262(4):1065–1075.

[94] Cooray, A., Kamionkowski, M., and Caldwell, R. R. (2005). Cosmic shear of the microwave background: The curl diagnostic. *Phys. Rev. D* , 71(12):123527.

[95] Cooray, A. and Kesden, M. (2003). Weak lensing of the CMB: extraction of lensing information from the trispectrum. *New Astronomy*, 8:231–253.

[96] Cooray, A. and Sheth, R. (2002). Halo models of large scale structure. *Phys. Rep.* , 372(1):1–129.

[97] Coupon, J. et al. (2012). Galaxy clustering in the CFHTLS-Wide: the changing relationship between galaxies and haloes since z $\sim$1.2$\star$. *Astron. Astrophys.* , 542:A5.

[98] Crawford, T. M. et al. (2014). A Measurement of the Secondary-CMB and Millimeter-wave-foreground Bispectrum using 800 deg^2 of South Pole Telescope Data. *Astrophys. J.* , 784(2):143.

[99] Croton, D. J. et al. (2006). The many lives of active galactic nuclei: cooling flows, black holes and the luminosities and colours of galaxies. *Mon. Not. R. Astron. Soc.* , 365(1):11–28.

[100] Dalal, N., Doré, O., Huterer, D., and Shirokov, A. (2008). Imprints of primordial non-Gaussianities on large-scale structure: Scale-dependent bias and abundance of virialized objects. *Phys. Rev. D* , 77(12):123514.

[101] Darwish, O. and ACT Collaboration (2021). The Atacama Cosmology Telescope: a CMB lensing mass map over 2100 square degrees of sky and its cross-correlation with BOSS-CMASS galaxies. *Mon. Not. R. Astron. Soc.* , 500(2):2250–2263.

[102] Das, S., Errard, J., and Spergel, D. (2013). Can CMB Lensing Help Cosmic Shear Surveys? *arXiv e-prints*, page arXiv:1311.2338.

[103] Das, S. et al. (2011). Detection of the Power Spectrum of Cosmic Microwave Background Lensing by the Atacama Cosmology Telescope. *Phys. Rev. Lett.*, 107:021301.

[104] Davis, M., Efstathiou, G., Frenk, C. S., and White, S. D. M. (1985). The evolution of large-scale structure in a universe dominated by cold dark matter. *Astrophys. J.* , 292:371–394.

[105] de Belsunce, R., Gratton, S., Coulton, W., and Efstathiou, G. (2021). Inference of the optical depth to reionization from low multipole temperature and polarisation Planck data. *arXiv e-prints*, page arXiv:2103.14378.

[106] de Bernardis, P. et al. (2000). A flat Universe from high-resolution maps of the cosmic microwave background radiation. *Nature (London)* , 404(6781):955–959.

[107] de Graaff, A., Cai, Y.-C., Heymans, C., and Peacock, J. A. (2019). Probing the missing baryons with the Sunyaev-Zel'dovich effect from filaments. *Astron. Astrophys.* , 624:A48.

[108] Delabrouille, J., Cardoso, J. F., Le Jeune, M., Betoule, M., Fay, G., and Guilloux, F. (2009). A full sky, low foreground, high resolution CMB map from WMAP. *Astron. Astrophys.* , 493(3):835–857.

[109] Desjacques, V., Jeong, D., and Schmidt, F. (2018). Large-scale galaxy bias. *Phys. Rep.* , 733:1–193.

[110] Dicke, R. H., Peebles, P. J. E., Roll, P. G., and Wilkinson, D. T. (1965). Cosmic Black-Body Radiation. *Astrophys. J.* , 142:414–419.

[111] Diego-Palazuelos, P., Vielva, P., Martínez-González, E., and Barreiro, R. B. (2020). Comparison of delensing methodologies and assessment of the delensing capabilities of future experiments. *arXiv e-prints*, page arXiv:2006.12935.

[112] Diemer, B. and Joyce, M. (2019). An Accurate Physical Model for Halo Concentrations. *Astrophys. J.* , 871(2):168.

[113] Diemer, B. and Kravtsov, A. V. (2015). A Universal Model for Halo Concentrations. *Astrophys. J.* , 799(1):108.

[114] Dodelson, S. (2003a). Coherent Phase Argument for Inflation. In Nieves, J. F. and Volkas, R. R., editors, *Neutrinos, Flavor Physics, and Precision Cosmology*, volume 689 of *American Institute of Physics Conference Series*, pages 184–196.

[115] Dodelson, S. (2003b). *Modern cosmology*.

[116] Dodelson, S. (2017). *Gravitational Lensing*.

[117] Dodelson, S., Rozo, E., and Stebbins, A. (2003). Primordial Gravity Waves and Weak Lensing. *Phys. Rev. Lett.* , 91(2):021301.

[118] Doroshkevich, A. G. and Novikov, I. D. (1964). Mean Density of Radiation in the Metagalaxy and Certain Problems in Relativistic Cosmology. *Soviet Physics Doklady*, 9:111.

[119] Duffy, A. R., Schaye, J., Kay, S. T., and Dalla Vecchia, C. (2008). Dark matter halo concentrations in the Wilkinson Microwave Anisotropy Probe year 5 cosmology. *Mon. Not. R. Astron. Soc.* , 390(1):L64–L68.

[120] Dunkley, J. et al. (2011). The Atacama Cosmology Telescope: Cosmological Parameters from the 2008 Power Spectrum. *Astrophys. J.* , 739(1):52.

[121] Dvorkin, C., Hu, W., and Smith, K. M. (2009). B-mode CMB polarization from patchy screening during reionization. *Phys. Rev. D* , 79(10):107302.

[122] Dyson, F. W., Eddington, A. S., and Davidson, C. (1920). A Determination of the Deflection of Light by the Sun's Gravitational Field, from Observations Made at the Total Eclipse of May 29, 1919. *Philosophical Transactions of the Royal Society of London Series A*, 220:291–333.

[123] Efstathiou, G. (2016). The Physics of Cosmology. *Part II of the Astrophysical Tripos — University of Cambridge*.

[124] Efstathiou, G. and Bond, J. R. (1999). Cosmic confusion: degeneracies among cosmological parameters derived from measurements of microwave background anisotropies. *Mon. Not. R. Astron. Soc.* , 304(1):75–97.

[125] Efstathiou, G., Frenk, C. S., White, S. D. M., and Davis, M. (1988). Gravitational clustering from scale-free initial conditions. *Mon. Not. R. Astron. Soc.* , 235:715–748.

[126] Efstathiou, G. and Gratton, S. (2020). The evidence for a spatially flat Universe. *Mon. Not. R. Astron. Soc.* , 496(1):L91–L95.

[127] Efstathiou, G., Sutherland, W. J., and Maddox, S. J. (1990). The cosmological constant and cold dark matter. *Nature (London)* , 348(6303):705–707.

[128] Einasto, J. (1965). On the Construction of a Composite Model for the Galaxy and on the Determination of the System of Galactic Parameters. *Trudy Astrofizicheskogo Instituta Alma-Ata*, 5:87–100.

[129] Einasto, J., Kaasik, A., and Saar, E. (1974). Dynamic evidence on massive coronas of galaxies. *Nature (London)* , 250(5464):309–310.

[130] Einstein, A. (1916). Die Grundlage der allgemeinen Relativitätstheorie. *Annalen der Physik*, 354(7):769–822.

[131] Eisenstein, D. J. et al. (2005). Detection of the Baryon Acoustic Peak in the Large-Scale Correlation Function of SDSS Luminous Red Galaxies. *Astrophys. J.* , 633(2):560–574.

[132] Ellis, G. F. R., Bassett, B. A. C. C., and Dunsby, P. K. S. (1998). Lensing and caustic effects on cosmological distances. *Classical and Quantum Gravity*, 15:2345–2361.

[133] Eriksen, H. K. et al. (2006). Cosmic Microwave Background Component Separation by Parameter Estimation. *Astrophys. J.* , 641(2):665–682.

[134] Errard, J., Feeney, S. M., Peiris, H. V., and Jaffe, A. H. (2016). Robust forecasts on fundamental physics from the foreground-obscured, gravitationally-lensed CMB polarization. *J. Cosmol. Astropart. Phys.* , 2016(3):052.

[135] Evrard, A. E. et al. (2002). Galaxy Clusters in Hubble Volume Simulations: Cosmological Constraints from Sky Survey Populations. *Astrophys. J.* , 573(1):7–36.

[136] Fabbian, G., Lewis, A., and Beck, D. (2019). CMB lensing reconstruction biases in cross-correlation with large-scale structure probes. *J. Cosmol. Astropart. Phys.* , 2019(10):057.

[137] Fabbian, G. and Peloton, J. (2021). Simulating instrumental systematics of Cosmic Microwave Background experiments with s4cmb. *arXiv e-prints*, page arXiv:2104.11816.

[138] Fantaye, Y., Baccigalupi, C., Leach, S. M., and Yadav, A. P. S. (2012). CMB lensing reconstruction in the presence of diffuse polarized foregrounds. *J. Cosmol. Astropart. Phys.* , 2012(12):017.

[139] Faris, W. G. (2008). Radial functions and the fourier transform.

[140] Feng, C. and Holder, G. (2020). Polarization of the Cosmic Infrared Background Fluctuations. *Astrophys. J.* , 897(2):140.

[141] Ferraro, S. and Hill, J. C. (2018). Bias to CMB lensing reconstruction from temperature anisotropies due to large-scale galaxy motions. *Phys. Rev. D* , 97(2):023512.

[142] Fillmore, J. A. and Goldreich, P. (1984). Self-similar gravitational collapse in an expanding universe. *Astrophys. J.* , 281:1–8.

[143] Fixsen, D. J. (2009). The Temperature of the Cosmic Microwave Background. *Astrophys. J.* , 707(2):916–920.

[144] Frenk, C. S., White, S. D. M., Davis, M., and Efstathiou, G. (1988). The Formation of Dark Halos in a Universe Dominated by Cold Dark Matter. *Astrophys. J.* , 327:507.

[145] Gamow, G. (1948). The Evolution of the Universe. *Nature (London)* , 162(4122):680–682.

[146] Geach, J. E. et al. (2013). A Direct Measurement of the Linear Bias of Mid-infrared-selected Quasars at z $\approx$ 1 Using Cosmic Microwave Background Lensing. *ApJL*, 776(2):L41.

[147] George, E. M. and SPT Collaboration (2015). A Measurement of Secondary Cosmic Microwave Background Anisotropies from the 2500 Square-degree SPT-SZ Survey. *Astrophys. J.* , 799(2):177.

[148] Gerbino, M. et al. (2020). Likelihood methods for CMB experiments. *Frontiers in Physics*, 8:15.

[149] Gerbino, M., Lattanzi, M., Migliaccio, M., Pagano, L., Salvati, L., Colombo, L., Gruppuso, A., Natoli, P., and Polenta, G. (2019). Likelihood methods for CMB experiments. *arXiv e-prints*, page arXiv:1909.09375.

[150] Ghigna, S., Moore, B., Governato, F., Lake, G., Quinn, T., and Stadel, J. (2000). Density Profiles and Substructure of Dark Matter Halos: Converging Results at Ultra-High Numerical Resolution. *Astrophys. J.* , 544(2):616–628.

[151] Giannantonio, T., Fosalba, P., et al. (2016). CMB lensing tomography with the DES Science Verification galaxies. *Mon. Not. R. Astron. Soc.* , 456(3):3213–3244.

[152] Greco, J. P., Hill, J. C., Spergel, D. N., and Battaglia, N. (2015). The Stacked Thermal Sunyaev-Zel'dovich Signal of Locally Brightest Galaxies in Planck Full Mission Data: Evidence for Galaxy Feedback? *Astrophys. J.* , 808(2):151.

[153] Green, D., Meyers, J., and van Engelen, A. (2017). CMB delensing beyond the B modes. *J. Cosmol. Astropart. Phys.* , 2017(12):005.

[154] Grishchuk, L. P. (1975). Amplification of gravitational waves in an isotropic universe. *Soviet Journal of Experimental and Theoretical Physics*, 40:409.

[155] Gunn, J. E. and Gott, J. Richard, I. (1972). On the Infall of Matter Into Clusters of Galaxies and Some Effects on Their Evolution. *Astrophys. J.* , 176:1.

[156] Guth, A. H. (1981). Inflationary universe: A possible solution to the horizon and flatness problems. *Phys. Rev. D* , 23(2):347–356.

[157] Guth, A. H. and Pi, S. Y. (1982). Fluctuations in the New Inflationary Universe. *Phys. Rev. Lett.* , 49(15):1110–1113.

[158] Guzik, J. and Seljak, U. (2002). Virial masses of galactic haloes from galaxy-galaxy lensing: theoretical modelling and application to Sloan Digital Sky Survey data. *Mon. Not. R. Astron. Soc.* , 335(2):311–324.

[159] Hahn, T. (2005). CUBA—a library for multidimensional numerical integration. *Computer Physics Communications*, 168(2):78–95.

[160] Haiman, Z. and Knox, L. (2000). Correlations in the Far-Infrared Background. *Astrophys. J.* , 530(1):124–132.

[161] Hall, N. R. and SPT Collaboration (2010). Angular Power Spectra of the Millimeter-wavelength Background Light from Dusty Star-forming Galaxies with the South Pole Telescope. *Astrophys. J.* , 718(2):632–646.

[162] Hamilton, A. J. S. (2000). Uncorrelated modes of the non-linear power spectrum. *Mon. Not. R. Astron. Soc.* , 312(2):257–284.

[163] Hamimeche, S. and Lewis, A. (2008). Likelihood analysis of CMB temperature and polarization power spectra. *Phys. Rev. D* , 77:103013.

[164] Han, D. and ACT Collaboration (2021). The Atacama Cosmology Telescope: delensed power spectra and parameters. *J. Cosmol. Astropart. Phys.* , 2021(1):031.

[165] Hanany, S. et al. (2000). MAXIMA-1: A Measurement of the Cosmic Microwave Background Anisotropy on Angular Scales of 10'-5°. *ApJL*, 545(1):L5–L9.

[166] Hanany, S. et al. (2019). PICO: Probe of Inflation and Cosmic Origins. *arXiv e-prints*, page arXiv:1902.10541.

[167] Hand, N. et al. (2015). First measurement of the cross-correlation of CMB lensing and galaxy lensing. *Phys. Rev. D* , 91(6):062001.

[168] Hansen, S. M., Sheldon, E. S., Wechsler, R. H., and Koester, B. P. (2009). The Galaxy Content of SDSS Clusters and Groups. *Astrophys. J.* , 699(2):1333–1353.

[169] Hanson, D., Challinor, A., Efstathiou, G., and Bielewicz, P. (2011). CMB temperature lensing power reconstruction. *Phys. Rev. D* , 83(4):043005.

[170] Hanson, D., Challinor, A., and Lewis, A. (2010). Weak lensing of the CMB. *General Relativity and Gravitation*, 42:2197–2218.

[171] Hanson, D., Rocha, G., and Górski, K. (2009). Lensing reconstruction from Planck sky maps: inhomogeneous noise. *Mon. Not. R. Astron. Soc.* , 400(4):2169–2173.

[172] Hanson, D. and SPT Collaboration (2013). Detection of B-Mode Polarization in the Cosmic Microwave Background with Data from the South Pole Telescope. *Phys. Rev. Lett.* , 111:141301.

[173] Harnois-Déraps, J., Tröster, T., Chisari, N. E., et al. (2017). KiDS-450: tomographic cross-correlation of galaxy shear with Planck lensing. *Mon. Not. R. Astron. Soc.* , 471(2):1619–1633.

[174] Harnois-Déraps, J., Tröster, T., Hojjati, A., van Waerbeke, L., Asgari, M., et al. (2016). CFHTLenS and RCSLenS cross-correlation with Planck lensing detected in fourier and configuration space. *Mon. Not. R. Astron. Soc.* , 460(1):434–457.

[175] Harnois-Déraps, J., van Waerbeke, L., Viola, M., and Heymans, C. (2015). Baryons, neutrinos, feedback and weak gravitational lensing. *Mon. Not. R. Astron. Soc.* , 450(2):1212–1223.

[176] Harrington, K. et al. (2016). The Cosmology Large Angular Scale Surveyor. In Holland, W. S. and Zmuidzinas, J., editors, *Millimeter, Submillimeter, and Far-Infrared Detectors and Instrumentation for Astronomy VIII*, volume 9914 of *Society of Photo-Optical Instrumentation Engineers (SPIE) Conference Series*, page 99141K.

[177] Harrison, E. R. (1970). Fluctuations at the Threshold of Classical Cosmology. *Phys. Rev. D* , 1(10):2726–2730.

[178] Haslam, C. G. T., Salter, C. J., Stoffel, H., and Wilson, W. E. (1982). A 408 MHz all-sky continuum survey. II. The atlas of contour maps. *A&AS*, 47:1–143.

[179] Hauser, M. G. and Dwek, E. (2001). The Cosmic Infrared Background: Measurements and Implications. *Ann. Rev. Astron. Astrophys.* , 39:249–307.

[180] Hawking, S. W. (1982). The development of irregularities in a single bubble inflationary universe. *Physics Letters B*, 115(4):295–297.

[181] Henderson, S. W. and other (2016). Advanced ACTPol Cryogenic Detector Arrays and Readout. *Journal of Low Temperature Physics*, 184(3-4):772–779.

[182] HI4PI Collaboration (2016). HI4PI: A full-sky H I survey based on EBHIS and GASS. *Astron. Astrophys.* , 594:A116.

[183] Hildebrand, R. H. (1988). Magnetic fields and stardust. *Q. J. R. Astron. Soc*, 29:327–351.

[184] Hill, C. A. et al. (2020). A cryogenic continuously rotating half-wave plate mechanism for the POLARBEAR-2b cosmic microwave background receiver. *Review of Scientific Instruments*, 91(12):124503.

[185] Hill, J. C. and Pajer, E. (2013). Cosmology from the thermal Sunyaev-Zel'dovich power spectrum: Primordial non-Gaussianity and massive neutrinos. *Phys. Rev. D* , 88(6):063526.

[186] Hill, J. C. and Spergel, D. N. (2014). Detection of thermal SZ-CMB lensing cross-correlation in Planck nominal mission data. *J. Cosmol. Astropart. Phys.* , 2014(2):030.

[187] Hilton, M. and ACT Collaboration (2021). The Atacama Cosmology Telescope: A Catalog of >4000 Sunyaev–Zel'dovich Galaxy Clusters. *ApJS*, 253(1):3.

[188] Hirata, C. M., Ho, S., Padmanabhan, N., Seljak, U., and Bahcall, N. A. (2008). Correlation of CMB with large-scale structure. II. Weak lensing. *Phys. Rev. D* , 78(4):043520.

[189] Hirata, C. M. and Seljak, U. (2003a). Analyzing weak lensing of the cosmic microwave background using the likelihood function. *Phys. Rev. D* , 67:043001.

[190] Hirata, C. M. and Seljak, U. (2003b). Reconstruction of lensing from the cosmic microwave background polarization. *Phys. Rev. D* , 68(8):083002.

[191] Hojjati, A. et al. (2017). Cross-correlating Planck tSZ with RCSLenS weak lensing: implications for cosmology and AGN feedback. *Mon. Not. R. Astron. Soc.* , 471(2):1565–1580.

[192] Holder, G. P. and SPT Collaboration (2013). A Cosmic Microwave Background Lensing Mass Map and Its Correlation with the Cosmic Infrared Background. *ApJL*, 771(1):L16.

[193] Holz, D. E. and Wald, R. M. (1998). New method for determining cumulative gravitational lensing effects in inhomogeneous universes. *Phys. Rev. D* , 58:063501.

[194] Hoyle, F. and Tayler, R. J. (1964). The Mystery of the Cosmic Helium Abundance. *Nature (London)* , 203(4950):1108–1110.

[195] Hu, W. (2000a). Reionization Revisited: Secondary Cosmic Microwave Background Anisotropies and Polarization. *Astrophys. J.* , 529(1):12–25.

[196] Hu, W. (2000b). Weak lensing of the CMB: A harmonic approach. *Phys. Rev. D* , 62:043007.

[197] Hu, W. (2001). Angular trispectrum of the cosmic microwave background. *Phys. Rev. D* , 64:083005.

[198] Hu, W. (2001). Mapping the dark matter through the CMB damping tail. *Astrophys. J.*, 557:L79–L83.

[199] Hu, W. and Cooray, A. (2001). Gravitational time delay effects on cosmic microwave background anisotropies. *Phys. Rev. D* , 63(2):023504.

[200] Hu, W., DeDeo, S., and Vale, C. (2007). Cluster mass estimators from CMB temperature and polarization lensing. *New Journal of Physics*, 9(12):441.

[201] Hu, W., Hedman, M. M., and Zaldarriaga, M. (2003). Benchmark parameters for CMB polarization experiments. *Phys. Rev. D* , 67(4):043004.

[202] Hu, W. and Okamoto, T. (2002). Mass Reconstruction with Cosmic Microwave Background Polarization. *Astrophys. J.* , 574:566–574.

[203] Hu, W. and Sugiyama, N. (1995). Anisotropies in the Cosmic Microwave Background: an Analytic Approach. *Astrophys. J.* , 444:489.

[204] Hu, W. and Sugiyama, N. (1996). Small-Scale Cosmological Perturbations: an Analytic Approach. *Astrophys. J.* , 471:542.

[205] Hu, W. and White, M. (1997). A CMB polarization primer. *New Astronomy*, 2:323–344.

[206] Hubble, E. (1929). A Relation between Distance and Radial Velocity among Extra-Galactic Nebulae. *Proceedings of the National Academy of Science*, 15(3):168–173.

[207] Hubble, E. P. (1925). Cepheids in Spiral Nebulae. *Popular Astronomy*, 33:252–255.

[208] Huterer, D. and Shafer, D. L. (2018). Dark energy two decades after: observables, probes, consistency tests. *Reports on Progress in Physics*, 81(1):016901.

[209] Itoh, N., Kohyama, Y., and Nozawa, S. (1998). Relativistic Corrections to the Sunyaev-Zeldovich Effect for Clusters of Galaxies. *Astrophys. J.* , 502(1):7–15.

[210] Ivezić, Ž. et al. (2019). LSST: From Science Drivers to Reference Design and Anticipated Data Products. *Astrophys. J.* , 873:111.

[211] Jeans, J. H. (1902). The Stability of a Spherical Nebula. *Philosophical Transactions of the Royal Society of London Series A*, 199:1–53.

[212] Jenkins, A., Frenk, C. S., White, S. D. M., Colberg, J. M., Cole, S., Evrard, A. E., Couchman, H. M. P., and Yoshida, N. (2001). The mass function of dark matter haloes. *Mon. Not. R. Astron. Soc.* , 321(2):372–384.

[213] Jing, Y. P. (1998). Accurate Fitting Formula for the Two-Point Correlation Function of Dark Matter Halos. *ApJL*, 503(1):L9–L13.

[214] Jing, Y. P. (2000). The Density Profile of Equilibrium and Nonequilibrium Dark Matter Halos. *Astrophys. J.* , 535(1):30–36.

[215] Kaiser, N. (1983). Small-angle anisotropy of the microwave background radiation in the adiabatic theory. *Mon. Not. R. Astron. Soc.* , 202:1169–1180.

[216] Kaiser, N. (1984). On the spatial correlations of Abell clusters. *ApJL*, 284:L9–L12.

[217] Kaiser, N. (1986). Evolution and clustering of rich clusters. *Mon. Not. R. Astron. Soc.* , 222:323–345.

[218] Kaiser, N. and Jaffe, A. (1997). Bending of Light by Gravity Waves. *Astrophys. J.* , 484(2):545–554.

[219] Kamionkowski, M., Kosowsky, A., and Stebbins, A. (1997). A Probe of primordial gravity waves and vorticity. *Phys. Rev. Lett.*, 78:2058–2061.

[220] Karkare, K. S. (2019). Delensing degree-scale B-mode polarization with high-redshift line intensity mapping. *Phys. Rev. D* , 100(4):043529.

[221] Kashlinsky, A. and Odenwald, S. (2000). Clustering of the Diffuse Infrared Light from the COBE DIRBE Maps. III. Power Spectrum Analysis and Excess Isotropic Component of Fluctuations. *Astrophys. J.* , 528(1):74–95.

[222] Kennicutt, Robert C., J. (1998). Star Formation in Galaxies Along the Hubble Sequence. *Ann. Rev. Astron. Astrophys.* , 36:189–232.

[223] Kesden, M., Cooray, A., and Kamionkowski, M. (2003). Lensing reconstruction with CMB temperature and polarization. *Phys. Rev. D* , 67(12):123507.

[224] Kirk, D. and DES Collaboration (2016). Cross-correlation of gravitational lensing from DES Science Verification data with SPT and Planck lensing. *Mon. Not. R. Astron. Soc.* , 459(1):21–34.

[225] Knox, L. (1995). Determination of inflationary observables by cosmic microwave background anisotropy experiments. *Phys. Rev. D* , 52:4307–4318.

[226] Knox, L., Cooray, A., Eisenstein, D., and Haiman, Z. (2001). Probing Early Structure Formation with Far-Infrared Background Correlations. *Astrophys. J.* , 550(1):7–20.

[227] Knox, L. and Song, Y.-S. (2002). A Limit on the detectability of the energy scale of inflation. *Phys. Rev. Lett.*, 89:011303.

[228] Kodama, H. and Sasaki, M. (1984). Cosmological Perturbation Theory. *Progress of Theoretical Physics Supplement*, 78:1.

[229] Kogut, A. et al. (2007). Three-Year Wilkinson Microwave Anisotropy Probe (WMAP) Observations: Foreground Polarization. *Astrophys. J.* , 665(1):355–362.

[230] Komatsu, E. et al. (2009). Five-Year Wilkinson Microwave Anisotropy Probe Observations: Cosmological Interpretation. *ApJS*, 180(2):330–376.

[231] Komatsu, E. et al. (2011). Seven-year Wilkinson Microwave Anisotropy Probe (WMAP) Observations: Cosmological Interpretation. *ApJS*, 192(2):18.

[232] Komatsu, E. and Kitayama, T. (1999). Sunyaev-Zeldovich Fluctuations from Spatial Correlations between Clusters of Galaxies. *ApJL*, 526(1):L1–L4.

[233] Komatsu, E. and Seljak, U. (2002). The Sunyaev-Zel'dovich angular power spectrum as a probe of cosmological parameters. *Mon. Not. R. Astron. Soc.* , 336(4):1256–1270.

[234] Kovac, J. M., Leitch, E. M., Pryke, C., Carlstrom, J. E., Halverson, N. W., and Holzapfel, W. L. (2002). Detection of polarization in the cosmic microwave background using DASI. *Nature (London)* , 420(6917):772–787.

[235] Krachmalnicoff, N., Baccigalupi, C., Aumont, J., Bersanelli, M., and Mennella, A. (2016). Characterization of foreground emission on degree angular scales for CMB B-mode observations . Thermal dust and synchrotron signal from Planck and WMAP data. *Astron. Astrophys.* , 588:A65.

[236] Krauss, L. M. and Turner, M. S. (1995). The cosmological constant is back. *General Relativity and Gravitation*, 27(11):1137–1144.

[237] Kravtsov, A. V., Berlind, A. A., Wechsler, R. H., Klypin, A. A., Gottlöber, S., Allgood, B., and Primack, J. R. (2004). The Dark Side of the Halo Occupation Distribution. *Astrophys. J.* , 609(1):35–49.

[238] Kravtsov, A. V. and Borgani, S. (2012). Formation of Galaxy Clusters. *Ann. Rev. Astron. Astrophys.* , 50:353–409.

[239] Krolewski, A., Ferraro, S., Schlafly, E. F., and White, M. (2020). unWISE tomography of Planck CMB lensing. *J. Cosmol. Astropart. Phys.* , 2020(5):047.

[240] Krolewski, A., Ferraro, S., and White, M. (2021). Cosmological constraints from unwise and planck cmb lensing tomography.

[241] Kusaka, A. et al. (2014). Modulation of cosmic microwave background polarization with a warm rapidly rotating half-wave plate on the Atacama B-Mode Search instrument. *Review of Scientific Instruments*, 85(2):024501.

[242] Lacasa, F., Pénin, A., and Aghanim, N. (2014). Non-Gaussianity of the cosmic infrared background anisotropies - I. Diagrammatic formalism and application to the angular bispectrum. *Mon. Not. R. Astron. Soc.* , 439(1):123–142.

[243] Lacey, C. and Cole, S. (1994). Merger Rates in Hierarchical Models of Galaxy Formation - Part Two - Comparison with N-Body Simulations. *Mon. Not. R. Astron. Soc.* , 271:676.

[244] Lagache, G., Bethermin, M., Montier, L., Serra, P., and Tucci, M. (2019). Impact of polarised extragalactic sources on the measurement of CMB B-mode anisotropies. *arXiv e-prints*, page arXiv:1911.09466.

[245] Lagache, G., Béthermin, M., Montier, L., Serra, P., and Tucci, M. (2020). Impact of polarised extragalactic sources on the measurement of CMB B-mode anisotropies. *Astron. Astrophys.* , 642:A232.

[246] Lagache, G. and Puget, J. L. (2000). Detection of the extra-Galactic background fluctuations at 170 mu m. *Astron. Astrophys.* , 355:17–22.

[247] Larsen, P., Challinor, A., Sherwin, B. D., and Mak, D. (2016). Demonstration of Cosmic Microwave Background Delensing Using the Cosmic Infrared Background. *Phys. Rev. Lett.* , 117:151102.

[248] Lemaître, G. (1927). Un Univers homogène de masse constante et de rayon croissant rendant compte de la vitesse radiale des nébuleuses extra-galactiques. *Annales de la Société Scientifique de Bruxelles*, 47:49–59.

[249] Lemos, P., Challinor, A., and Efstathiou, G. (2017). The effect of Limber and flat-sky approximations on galaxy weak lensing. *J. Cosmol. Astropart. Phys.* , 2017(5):014.

[250] Lenz, D., Doré, O., and Lagache, G. (2019). Large-scale Maps of the Cosmic Infrared Background from Planck. *Astrophys. J.* , 883(1):75.

[251] Lesgourgues, J., Liguori, M., Matarrese, S., and Riotto, A. (2005). CMB lensing extraction and primordial non-Gaussianity. *Phys. Rev. D* , 71(10):103514.

[252] Lewis, A. and Challinor, A. (2006). Weak gravitational lensing of the CMB. *Phys. Rep.* , 429:1–65.

[253] Lewis, A., Challinor, A., and Hanson, D. (2011). The shape of the CMB lensing bispectrum. *Journal of Cosmology and Astro-Particle Physics*, 2011:018.

[254] Lewis, A., Challinor, A., and Lasenby, A. (2000). Efficient Computation of Cosmic Microwave Background Anisotropies in Closed Friedmann-Robertson-Walker Models. *Astrophys. J.* , 538:473–476.

[255] Lewis, A., Challinor, A., and Turok, N. (2002). Analysis of CMB polarization on an incomplete sky. *Phys. Rev. D* , 65(2):023505.

[256] Lewis, A., Hall, A., and Challinor, A. (2017). Emission-angle and polarization-rotation effects in the lensed CMB. *J. Cosmol. Astropart. Phys.* , 2017(8):023.

[257] Lewis, A. and Pratten, G. (2016). Effect of lensing non-Gaussianity on the CMB power spectra. *J. Cosmol. Astropart. Phys.* , 2016(12):003.

[258] Li, C. and Cooray, A. (2006). Weak lensing of the cosmic microwave background by foreground gravitational waves. *Phys. Rev. D* , 74(2):023521.

[259] Li, C., Smith, T. L., and Cooray, A. (2007). Non-gaussian covariance of cmb b-modes of polarization and parameter degradation. *Phys. Rev. D* , 75:083501.

[260] Liddle, A. R., Lyth, D. H., Viana, P. T. P., and White, M. (1996). Cold dark matter models with a cosmological constant. *Mon. Not. R. Astron. Soc.* , 282:281.

[261] Lifshitz, E. M. (1946). On the gravitational stability of the expanding universe. *Zhurnal Eksperimentalnoi i Teoreticheskoi Fiziki*, 16:587–602.

[262] Limber, D. N. (1953). The Analysis of Counts of the Extragalactic Nebulae in Terms of a Fluctuating Density Field. *Astrophys. J.* , 117:134.

[263] Linde, A. (1982). A new inflationary universe scenario: A possible solution of the horizon, flatness, homogeneity, isotropy and primordial monopole problems. *Physics Letters B*, 108(6):389–393.

[264] Linde, A. (1983). Chaotic inflation. *Physics Letters B*, 129(3):177–181.

[265] Linder, E. V. (1990). Analysis of gravitationally lensed microwave background anisotropies. *Mon. Not. R. Astron. Soc.* , 243:353–361.

[266] LiteBIRD Collaboration (2019). LiteBIRD: A Satellite for the Studies of B-Mode Polarization and Inflation from Cosmic Background Radiation Detection. *Journal of Low Temperature Physics*, 194(5-6):443–452.

[267] Liu, G.-C., Sugiyama, N., Benson, A. J., Lacey, C. G., and Nusser, A. (2001). Polarization of the Cosmic Microwave Background from Nonuniform Reionization. *Astrophys. J.* , 561(2):504–516.

[268] Liu, J. and Hill, J. C. (2015). Cross-correlation of Planck CMB lensing and CFHTLenS galaxy weak lensing maps. *Phys. Rev. D* , 92(6):063517.

[269] Liu, J., Ortiz-Vazquez, A., and Hill, J. C. (2016). Constraining multiplicative bias in CFHTLenS weak lensing shear data. *Phys. Rev. D* , 93(10):103508.

[270] Longair, M. S. (2013). *The Cosmic Century.*

[271] LoVerde, M. and Afshordi, N. (2008). Extended Limber approximation. *Phys. Rev. D* , 78(12):123506.

[272] Lozanov, K. D. (2019). Lectures on Reheating after Inflation. *arXiv e-prints*, page arXiv:1907.04402.

[273] LSST Dark Energy Science Collaboration (2019). Core Cosmology Library: Precision Cosmological Predictions for LSST. *ApJS*, 242(1):2.

[274] Lyth, D. H. (1997). What Would We Learn by Detecting a Gravitational Wave Signal in the Cosmic Microwave Background Anisotropy? *Phys. Rev. Lett.* , 78:1861–1863.

[275] Lyth, D. H., Malik, K. A., and Sasaki, M. (2005). A general proof of the conservation of the curvature perturbation. *J. Cosmol. Astropart. Phys.* , 2005(5):004.

[276] Lyth, D. H. D. H. and Riotto, A. A. (1999). Particle physics models of inflation and the cosmological density perturbation. *Phys. Rep.* , 314(1-2):1–146.

[277] Ma, C.-P. and Fry, J. N. (2000). Deriving the Nonlinear Cosmological Power Spectrum and Bispectrum from Analytic Dark Matter Halo Profiles and Mass Functions. *Astrophys. J.* , 543(2):503–513.

[278] Mackay, D. J. C. (2003). *Information Theory, Inference and Learning Algorithms.*

[279] Maddox, S. J., Efstathiou, G., Sutherland, W. J., and Loveday, J. (1990). Galaxy correlations on large scales. *Mon. Not. R. Astron. Soc.* , 242:43.

[280] Madhavacheril, M. and ACT Collaboration (2015). Evidence of Lensing of the Cosmic Microwave Background by Dark Matter Halos. *Phys. Rev. Lett.* , 114(15):151302.

[281] Madhavacheril, M. S. and ACT Collaboration (2020). The Atacama Cosmology Telescope: Weighing Distant Clusters with the Most Ancient Light. *ApJL*, 903(1):L13.

[282] Madhavacheril, M. S. and Hill, J. C. (2018). Mitigating foreground biases in CMB lensing reconstruction using cleaned gradi ents. *Phys. Rev. D* , 98(2):023534.

[283] Mak, D. S. Y., Challinor, A., Efstathiou, G., and Lagache, G. (2017). Measurement of CIB power spectra over large sky areas from Planck HFI maps. *Mon. Not. R. Astron. Soc.* , 466(1):286–319.

[284] Mandelbaum, R. (2018). Weak Lensing for Precision Cosmology. *Ann. Rev. Astron. Astrophys.* , 56:393–433.

[285] Maniyar, A., Béthermin, M., and Lagache, G. (2021a). Simple halo model formalism for the cosmic infrared background and its correlation with the thermal Sunyaev-Zel'dovich effect. *Astron. Astrophys.* , 645:A40.

[286] Maniyar, A., Lagache, G., Béthermin, M., and Ilić, S. (2019). Constraining cosmology with the cosmic microwave and infrared backgrounds correlation. *Astron. Astrophys.* , 621:A32.

[287] Maniyar, A. S., Ali-Haïmoud, Y., Carron, J., Lewis, A., and Madhavacheril, M. S. (2021b). Quadratic estimators for CMB weak lensing. *arXiv e-prints*, page arXiv:2101.12193.

[288] Maniyar, A. S., Béthermin, M., and Lagache, G. (2018). Star formation history from the cosmic infrared background anisotropies. *Astron. Astrophys.* , 614:A39.

[289] Manzotti, A. (2018). Future cosmic microwave background delensing with galaxy surveys. *Phys. Rev. D* , 97(4):043527.

[290] Manzotti, A. and SPT Collaboration (2017). CMB Polarization B-mode Delensing with SPTpol and Herschel. *Astrophys. J.* , 846:45.

[291] Manzotti, A. and SPTpol Collaboration (2017). CMB Polarization B-mode Delensing with SPTpol and Herschel. *Astrophys. J.* , 846(1):45.

[292] Marian, L. and Bernstein, G. M. (2007). Detectability of CMB tensor B modes via delensing with weak lensing galaxy surveys. *Phys. Rev. D* , 76(12):123009.

[293] Marques, G. A., Liu, J., Huffenberger, K. M., and Colin Hill, J. (2020). Cross-correlation between Subaru Hyper Suprime-Cam Galaxy Weak Lensing and Planck Cosmic Microwave Background Lensing. *Astrophys. J.* , 904(2):182.

[294] Matsumoto, T., Cohen, M., Freund, M. M., Kawada, M., Lim, M., Matsuura, S., Murakami, H., Noda, M., and Tanaka, M. (2000). *Near Infrared Extragalactic Background*, volume 548, page 96.

[295] Mead, A. J., Peacock, J. A., Heymans, C., Joudaki, S., and Heavens, A. F. (2015). An accurate halo model for fitting non-linear cosmological power spectra and baryonic feedback models. *Mon. Not. R. Astron. Soc.* , 454(2):1958–1975.

[296] Merkel, P. M. and Schäfer, B. M. (2013). The interplay of CMB temperature lensing power reconstruction with primordial non-Gaussianity of local type. *Mon. Not. R. Astron. Soc.* , 429(1):444–451.

[297] Meszaros, P. (1974). The behaviour of point masses in an expanding cosmological substratum. *Astron. Astrophys.* , 37(2):225–228.

[298] Millea, M., Anderes, E., and Wandelt, B. D. (2019). Bayesian delensing of CMB temperature and polarization. *Phys. Rev. D* , 100(2):023509.

[299] Millea, M., Anderes, E., and Wandelt, B. D. (2020a). Sampling-based inference of the primordial CMB and gravitational lensing. *Phys. Rev. D* , 102(12):123542.

[300] Millea, M. et al. (2020b). Optimal CMB Lensing Reconstruction and Parameter Estimation with SPTpol Data. *arXiv e-prints*, page arXiv:2012.01709.

[301] Miller, A. D. et al. (1999). A Measurement of the Angular Power Spectrum of the Cosmic Microwave Background from L = 100 to 400. *ApJL*, 524(1):L1–L4.

[302] Mirmelstein, M., Fabbian, G., Lewis, A., and Peloton, J. (2020). Instrumental systematics biases in CMB lensing reconstruction: a simulation-based assessment. *arXiv e-prints*, page arXiv:2011.13910.

[303] Miville-Deschênes, M.-A. and Lagache, G. (2005). IRIS: A New Generation of IRAS Maps. *ApJS*, 157(2):302–323.

[304] Miyatake, H., Madhavacheril, M. S., Sehgal, N., Slosar, A., Spergel, D. N., Sherwin, B., and van Engelen, A. (2017). Measurement of a Cosmographic Distance Ratio with Galaxy and Cosmic Microwave Background Lensing. *Phys. Rev. Lett.* , 118(16):161301.

[305] Mo, H., van den Bosch, F. C., and White, S. (2010). *Galaxy Formation and Evolution*.

[306] Mo, H. J., Jing, Y. P., and White, S. D. M. (1997). High-order correlations of peaks and haloes: a step towards understanding galaxy biasing. *Mon. Not. R. Astron. Soc.* , 284(1):189–201.

[307] Mo, H. J. and White, S. D. M. (1996). An analytic model for the spatial clustering of dark matter haloes. *Mon. Not. R. Astron. Soc.* , 282(2):347–361.

[308] Mroczkowski, T. et al. (2019). Astrophysics with the Spatially and Spectrally Resolved -Zeldovich Effects. A Millimetre/Submillimetre Probe of the Warm and Hot Universe. *Space Sci. Rev.*, 215(1):17.

[309] Mukherjee, S., Paul, S., and Choudhury, T. R. (2019). Is patchy reionization an obstacle in detecting the primordial gravitational wave signal? *Mon. Not. R. Astron. Soc.* , 486(2):2042–2049.

[310] Murakami, H. et al. (1994). The Infrared Telescope in Space (IRTS). *Astrophys. J.* , 428:354.

[311] Nagata, R. and Namikawa, T. (2021). A numerical study of observational systematic errors in lensing analysis of CMB polarization. *arXiv e-prints*, page arXiv:2102.00133.

[312] Namikawa, T. (2017). CMB internal delensing with general optimal estimator for higher-order correlations. *Phys. Rev. D* , 95:103514.

[313] Namikawa, T., Baleato Lizancos, A., Robertson, N., Challinor, A., and Sherwin, B. (2021). Constraining Primordial Gravitational Waves by Delensing B-modes with the Simons Observatory. in preparation.

[314] Namikawa, T., Hanson, D., and Takahashi, R. (2013a). Bias-hardened CMB lensing. *Mon. Not. R. Astron. Soc.* , 431(1):609–620.

[315] Namikawa, T., Hanson, D., and Takahashi, R. (2013b). Bias-hardened CMB lensing. *Mon. Not. R. Astron. Soc.* , 431:609–620.

[316] Namikawa, T. and Nagata, R. (2014). Lensing reconstruction from a patchwork of polarization maps. *Journal of Cosmology and Astro-Particle Physics*, 2014:009.

[317] Namikawa, T. and Nagata, R. (2015). Non-Gaussian structure of B-mode polarization after delensing. *Journal of Cosmology and Astro-Particle Physics*, 2015:004.

[318] Namikawa, T., POLARBEAR Collaboration, and SUBARU HSC SSP Collaboration (2019). Evidence for the Cross-correlation between Cosmic Microwave Background Polarization Lensing from Polarbear and Cosmic Shear from Subaru Hyper Suprime-Cam. *Astrophys. J.* , 882(1):62.

[319] Namikawa, T. and Takahashi, R. (2019). Impact of nonlinear growth of the large-scale structure on CMB B -mode delensing. *Phys. Rev. D* , 99(2):023530.

[320] Namikawa, T., Yamauchi, D., Sherwin, B., and Nagata, R. (2016). Delensing cosmic microwave background B modes with the Square Kilometre Array Radio Continuum Survey. *Phys. Rev. D* , 93(4):043527.

[321] Namikawa, T., Yamauchi, D., and Taruya, A. (2012). Full-sky lensing reconstruction of gradient and curl modes from CMB maps. *J. Cosmol. Astropart. Phys.* , 2012(1):007.

[322] Navarro, J. F., Frenk, C. S., and White, S. D. M. (1996). The Structure of Cold Dark Matter Halos. *Astrophys. J.* , 462:563.

[323] Navarro, J. F., Frenk, C. S., and White, S. D. M. (1997). A Universal Density Profile from Hierarchical Clustering. *Astrophys. J.* , 490(2):493–508.

[324] Navarro, J. F., Hayashi, E., Power, C., Jenkins, A. R., Frenk, C. S., White, S. D. M., Springel, V., Stadel, J., and Quinn, T. R. (2004). The inner structure of ΛCDM haloes - III. Universality and asymptotic slopes. *Mon. Not. R. Astron. Soc.* , 349(3):1039–1051.

[325] Nelson, K., Lau, E. T., and Nagai, D. (2014). Hydrodynamic Simulation of Non-thermal Pressure Profiles of Galaxy Clusters. *Astrophys. J.* , 792(1):25.

[326] Neto, A. F., Gao, L., Bett, P., Cole, S., Navarro, J. F., Frenk, C. S., White, S. D. M., Springel, V., and Jenkins, A. (2007). The statistics of Λ CDM halo concentrations. *Mon. Not. R. Astron. Soc.* , 381(4):1450–1462.

[327] Newman, E. T. and Penrose, R. (1966). Note on the Bondi-Metzner-Sachs Group. *Journal of Mathematical Physics*, 7(5):863–870.

[328] Neyman, J. and Scott, E. L. (1952). A Theory of the Spatial Distribution of Galaxies. *Astrophys. J.* , 116:144.

[329] Nozawa, S., Itoh, N., Suda, Y., and Ohhata, Y. (2006). An improved formula for the relativistic corrections to the kinematical Sunyaev-Zeldovich effect for clusters of galaxies. *Nuovo Cimento B Serie*, 121(5):487–500.

[330] O'Dea, D., Challinor, A., and Johnson, B. R. (2007). Systematic errors in cosmic microwave background polarization measurements. *Mon. Not. R. Astron. Soc.* , 376(4):1767–1783.

[331] Okamoto, T. and Hu, W. (2003). Cosmic microwave background lensing reconstruction on the full sky. *Phys. Rev. D* , 67:083002.

[332] Omori, Y., DES Collaboration, and SPT Collaboration (2019a). Dark Energy Survey Year 1 Results: Cross-correlation between Dark Energy Survey Y1 galaxy weak lensing and South Pole Telescope+Planck CMB weak lensing. *Phys. Rev. D* , 100(4):043517.

[333] Omori, Y., DES Collaboration, and SPT Collaboration (2019b). Dark Energy Survey Year 1 Results: Tomographic cross-correlations between Dark Energy Survey galaxies and CMB lensing from South Pole Telescope +Planck. *Phys. Rev. D* , 100(4):043501.

[334] Omori, Y. et al. (2017). A 2500 square-degree CMB lensing map from combined South Pole Telescope and Planck data.

[335] Osborne, S. J., Hanson, D., and Doré, O. (2014). Extragalactic foreground contamination in temperature-based CMB lens reconstruction. *J. Cosmol. Astropart. Phys.* , 2014(3):024.

[336] Ostriker, J. P., Peebles, P. J. E., and Yahil, A. (1974). The Size and Mass of Galaxies, and the Mass of the Universe. *ApJL*, 193:L1.

[337] Ostriker, J. P. and Steinhardt, P. J. (1995). The observational case for a low-density Universe with a non-zero cosmological constant. *Nature (London)* , 377(6550):600–602.

[338] Ostriker, J. P. and Vishniac, E. T. (1986). Generation of Microwave Background Fluctuations from Nonlinear Perturbations at the ERA of Galaxy Formation. *ApJL*, 306:L51.

[339] Pajer, E., Pimentel, G. L., and van Wijck, J. V. S. (2017). The conformal limit of inflation in the era of CMB polarimetry. *Journal of Cosmology and Astro-Particle Physics*, 2017:009.

[340] Pan, Z., Anderes, E., and Knox, L. (2018). Approximate Likelihood Approaches for Detecting the Influence of Primordial Gravitational Waves in Cosmic Microwave Background Polarization. *Phys. Rev.*, D97(10):103512.

[341] Peacock, J. A. and Bilicki, M. (2018). Wide-area tomography of CMB lensing and the growth of cosmological density fluctuations. *Mon. Not. R. Astron. Soc.* , 481(1):1133–1148.

[342] Peacock, J. A. and Smith, R. E. (2000). Halo occupation numbers and galaxy bias. *Mon. Not. R. Astron. Soc.* , 318(4):1144–1156.

[343] Peebles, P. J. E. (1980). *The large-scale structure of the universe*.

[344] Peebles, P. J. E. (1982). Large-scale background temperature and mass fluctuations due to scale-invariant primeval perturbations. *ApJL*, 263:L1–L5.

[345] Peebles, P. J. E. (1993). *Principles of Physical Cosmology*.

[346] Peebles, P. J. E. and Yu, J. T. (1970). Primeval Adiabatic Perturbation in an Expanding Universe. *Astrophys. J.* , 162:815.

[347] Peloton, J., Schmittfull, M., Lewis, A., Carron, J., and Zahn, O. (2017). Full covariance of CMB and lensing reconstruction power spectra. *Phys. Rev. D* , 95:043508.

[348] Penzias, A. A. and Wilson, R. W. (1965). A Measurement of Excess Antenna Temperature at 4080 Mc/s. *Astrophys. J.* , 142:419–421.

[349] Perlmutter, S. et al. (1999). Measurements of Ω and Λ from 42 High-Redshift Supernovae. *Astrophys. J.* , 517(2):565–586.

[350] Piras, D., Joachimi, B., Schäfer, B. M., Bonamigo, M., Hilbert, S., and van Uitert, E. (2018). The mass dependence of dark matter halo alignments with large-scale structure. *Mon. Not. R. Astron. Soc.* , 474(1):1165–1175.

[351] Planck Collaboration (2011). Planck early results. XVIII. The power spectrum of cosmic infrared background anisotropies. *Astron. Astrophys.* , 536:A18.

[352] Planck Collaboration (2013). Planck intermediate results. V. Pressure profiles of galaxy clusters from the Sunyaev-Zeldovich effect. *Astron. Astrophys.* , 550:A131.

[353] Planck Collaboration (2014a). Planck 2013 results. IX. HFI spectral response. *Astron. Astrophys.* , 571:A9.

[354] Planck Collaboration (2014b). Planck 2013 results. XVI. Cosmological parameters. *Astron. Astrophys.* , 571:A16.

[355] Planck Collaboration (2014c). Planck 2013 results. XVIII. The gravitational lensing-infrared background correlation. *Astron. Astrophys.* , 571:A18.

[356] Planck Collaboration (2014d). Planck 2013 results. XXI. Power spectrum and high-order statistics of the Planck all-sky Compton parameter map. *Astron. Astrophys.* , 571:A21.

[357] Planck Collaboration (2014e). Planck 2013 results. XXX. Cosmic infrared background measurements and implications for star formation. *Astron. Astrophys.* , 571:A30.

[358] Planck Collaboration (2016a). Planck 2015 results. XII. Full focal plane simulations. *Astron. Astrophys.* , 594:A12.

[359] Planck Collaboration (2016b). Planck 2015 results. XV. Gravitational lensing. *Astron. Astrophys.* , 594:A15.

[360] Planck Collaboration (2016c). Planck 2015 results. XXIII. The thermal Sunyaev-Zeldovich effect-cosmic infrared background correlation. *Astron. Astrophys.* , 594:A23.

[361] Planck Collaboration (2016d). Planck 2015 results. XXIV. Cosmology from Sunyaev-Zeldovich cluster counts. *Astron. Astrophys.* , 594:A24.

[362] Planck Collaboration (2016e). Planck 2015 results. XXVI. The Second Planck Catalogue of Compact Sources. *Astron. Astrophys.* , 594:A26.

[363] Planck Collaboration (2016f). Planck 2015 results. XXVII. The second Planck catalogue of Sunyaev-Zeldovich sources. *Astron. Astrophys.* , 594:A27.

[364] Planck Collaboration (2016g). Planck intermediate results. XLIV. Structure of the Galactic magnetic field from dust polarization maps of the southern Galactic cap. *Astron. Astrophys.* , 596:A105.

[365] Planck Collaboration (2016h). Planck intermediate results. XLVIII. Disentangling Galactic dust emission and cosmic infrared background anisotropies. *Astron. Astrophys.* , 596:A109.

[366] Planck Collaboration (2018a). Planck 2018 results. I. Overview and the cosmological legacy of Planck. *arXiv e-prints*, page arXiv:1807.06205.

[367] Planck Collaboration (2018b). Planck 2018 results. XI. Polarized dust foregrounds. *arXiv e-prints*, page arXiv:1801.04945.

[368] Planck Collaboration (2018c). Planck intermediate results. LIV. The Planck multi-frequency catalogue of non-thermal sources. *Astron. Astrophys.* , 619:A94.

[369] Planck Collaboration (2020a). Planck 2018 results. IV. Diffuse component separation. *Astron. Astrophys.* , 641:A4.

[370] Planck Collaboration (2020b). Planck 2018 results. IX. Constraints on primordial non-Gaussianity. *Astron. Astrophys.* , 641:A9.

[371] Planck Collaboration (2020c). Planck 2018 results. VI. Cosmological parameters. *Astron. Astrophys.* , 641:A6.

[372] Planck Collaboration (2020d). Planck 2018 results. VIII. Gravitational lensing. *Astron. Astrophys.* , 641:A8.

[373] Planck Collaboration (2020e). Planck 2018 results. X. Constraints on inflation. *Astron. Astrophys.* , 641:A10.

[374] Planck Collaboration (2014). Planck 2013 results. XVII. Gravitational lensing by large-scale structure. *Astron. Astrophys.*, 571:A17.

[375] Poh, J. and Dodelson, S. (2017). Line-of-sight extrapolation noise in dust polarization. *Phys. Rev. D* , 95(10):103511.

[376] Pointecouteau, E. et al. (2021). PACT. II. Pressure profiles of galaxy clusters using Planck and ACT. *arXiv e-prints*, page arXiv:2105.05607.

[377] POLARBEAR Collaboration (2014a). A Measurement of the Cosmic Microwave Background B-mode Polarization Power Spectrum at Sub-degree Scales with POLARBEAR. *Astrophys. J.* , 794:171.

[378] POLARBEAR Collaboration (2014b). Measurement of the Cosmic Microwave Background Polarization Lensing Power Spectrum with the POLARBEAR Experiment. *Phys. Rev. Lett.* , 113(2):021301.

[379] POLARBEAR Collaboration (2017). A Measurement of the Cosmic Microwave Background B-mode Polarization Power Spectrum at Subdegree Scales from Two Years of polarbear Data. *Astrophys. J.* , 848(2):121.

[380] POLARBEAR Collaboration (2020). Internal Delensing of Cosmic Microwave Background Polarization B -Modes with the POLARBEAR Experiment. *Phys. Rev. Lett.* , 124(13):131301.

[381] Polnarev, A. G. (1985). Polarization and Anisotropy Induced in the Microwave Background by Cosmological Gravitational Waves. *Soviet Astronomy*, 29:607–613.

[382] Prada, F., Klypin, A. A., Cuesta, A. J., Betancort-Rijo, J. E., and Primack, J. (2012). Halo concentrations in the standard Λ cold dark matter cosmology. *Mon. Not. R. Astron. Soc.* , 423(4):3018–3030.

[383] Pratt, G. W., Arnaud, M., Biviano, A., Eckert, D., Ettori, S., Nagai, D., Okabe, N., and Reiprich, T. H. (2019). The Galaxy Cluster Mass Scale and Its Impact on Cosmological Constraints from the Cluster Population. *Space Sci. Rev.*, 215(2):25.

[384] Pratten, G. and Lewis, A. (2016). Impact of post-Born lensing on the CMB. *J. Cosmol. Astropart. Phys.* , 2016(8):047.

[385] Press, W. H. and Schechter, P. (1974). Formation of Galaxies and Clusters of Galaxies by Self-Similar Gravitational Condensation. *Astrophys. J.* , 187:425–438.

[386] Pritchard, J. R. and Kamionkowski, M. (2005). Cosmic microwave background fluctuations from gravitational waves: An analytic approach. *Annals of Physics*, 318:2–36.

[387] Puget, J. L., Abergel, A., Bernard, J. P., Boulanger, F., Burton, W. B., Desert, F. X., and Hartmann, D. (1996). Tentative detection of a cosmic far-infrared background with COBE. *Astron. Astrophys.* , 308:L5.

[388] Reed, D., Gardner, J., Quinn, T., Stadel, J., Fardal, M., Lake, G., and Governato, F. (2003). Evolution of the mass function of dark matter haloes. *Mon. Not. R. Astron. Soc.* , 346(2):565–572.

[389] Rees, M. J. (1968). Polarization and Spectrum of the Primeval Radiation in an Anisotropic Universe. *ApJL*, 153:L1.

[390] Rees, M. J. and Sciama, D. W. (1968). Large-scale Density Inhomogeneities in the Universe. *Nature (London)* , 217(5128):511–516.

[391] Reichardt, C. L. et al. (2009). High-Resolution CMB Power Spectrum from the Complete ACBAR Data Set. *Astrophys. J.* , 694(2):1200–1219.

[392] Reichardt, C. L. and SPT Collaboration (2012). A Measurement of Secondary Cosmic Microwave Background Anisotropies with Two Years of South Pole Telescope Observations. *Astrophys. J.* , 755(1):70.

[393] Reichardt, C. L. and SPTpol Collaboration (2021). An Improved Measurement of the Secondary Cosmic Microwave Background Anisotropies from the SPT-SZ + SPTpol Surveys. *Astrophys. J.* , 908(2):199.

[394] Remazeilles, M., Delabrouille, J., and Cardoso, J.-F. (2011a). CMB and SZ effect separation with constrained Internal Linear Combinations. *Mon. Not. R. Astron. Soc.* , 410(4):2481–2487.

[395] Remazeilles, M., Delabrouille, J., and Cardoso, J.-F. (2011b). Foreground component separation with generalized Internal Linear Combination. *Mon. Not. R. Astron. Soc.* , 418(1):467–476.

[396] Rephaeli, Y. (1995). Comptonization Of The Cosmic Microwave Background: The Sunyaev-Zeldovich Effect. *Ann. Rev. Astron. Astrophys.* , 33:541–580.

[397] Riess, A. G., Casertano, S., Yuan, W., Macri, L. M., and Scolnic, D. (2019). Large Magellanic Cloud Cepheid Standards Provide a 1% Foundation for the Determination of the Hubble Constant and Stronger Evidence for Physics beyond ΛCDM. *Astrophys. J.* , 876(1):85.

[398] Riess, A. G. et al. (1998). Observational Evidence from Supernovae for an Accelerating Universe and a Cosmological Constant. *Astron. J.* , 116(3):1009–1038.

[399] Roberts, M. S. and Rots, A. H. (1973). Comparison of Rotation Curves of Different Galaxy Types. *Astron. Astrophys.* , 26:483–485.

[400] Robertson, H. P. (1929). On the Foundations of Relativistic Cosmology. *Proceedings of the National Academy of Science*, 15(11):822–829.

[401] Robertson, N. C., ACT Collaboration, and KiDS Collaboration (2020). Strong detection of the CMB lensingxgalaxy weak lensingcross-correlation from ACT-DR4,PlanckLegacy and KiDS-1000. *arXiv e-prints*, page arXiv:2011.11613.

[402] Rotti, A., Bolliet, B., Chluba, J., and Remazeilles, M. (2021). Removing the giants and learning from the crowd: A new SZ power spectrum method and revised Compton y-map analysis. *Mon. Not. R. Astron. Soc.* .

[403] Roy, A., Kulkarni, G., Meerburg, P. D., Challinor, A., Baccigalupi, C., Lapi, A., and Haehnelt, M. G. (2021). Revised estimates of CMB B-mode polarization induced by patchy reionization. *J. Cosmol. Astropart. Phys.* , 2021(1):003.

[404] Rubakov, V. A., Sazhin, M. V., and Veryaskin, A. V. (1982). Graviton creation in the inflationary universe and the grand unification scale. *Physics Letters B*, 115(3):189–192.

[405] Rubin, V. C., Ford, W. K., J., and Thonnard, N. (1980). Rotational properties of 21 SC galaxies with a large range of luminosities and radii, from NGC 4605 (R=4kpc) to UGC 2885 (R=122kpc). *Astrophys. J.* , 238:471–487.

[406] Rubiño-Martín, José Alberto et al. (2013). *The cosmic microwave background : from quantum fluctuations to the present universe*. Cambridge University Press, Cambridge.

[407] Sachs, R. K. and Wolfe, A. M. (1967). Perturbations of a Cosmological Model and Angular Variations of the Microwave Background. *Astrophys. J.* , 147:73.

[408] Sailer, N., Schaan, E., and Ferraro, S. (2020). Lower bias, lower noise CMB lensing with foreground-hardened estimators. *Phys. Rev. D* , 102(6):063517.

[409] Salopek, D. S., Bond, J. R., and Bardeen, J. M. (1989). Designing density fluctuation spectra in inflation. *Phys. Rev. D* , 40(6):1753–1788.

[410] Sayers, J. et al. (2013). Sunyaev-Zel'dovich-measured Pressure Profiles from the Bolocam X-Ray/SZ Galaxy Cluster Sample. *Astrophys. J.* , 768(2):177.

[411] Sazonov, S. Y. and Sunyaev, R. A. (1999). Microwave polarization in the direction of galaxy clusters induced by the CMB quadrupole anisotropy. *Mon. Not. R. Astron. Soc.* , 310(3):765–772.

[412] Schaan, E. and Ferraro, S. (2018). Foreground-immune CMB lensing with shear-only reconstruction. *ArXiv e-prints*, page arXiv:1804.06403.

[413] Schaan, E., Ferraro, S., and Spergel, D. N. (2018). Weak lensing of intensity mapping: The cosmic infrared background. *Phys. Rev. D* , 97(12):123539.

[414] Schaan, E., Krause, E., Eifler, T., Doré, O., Miyatake, H., Rhodes, J., and Spergel, D. N. (2017). Looking through the same lens: Shear calibration for LSST, Euclid, and WFIRST with stage 4 CMB lensing. *Phys. Rev. D* , 95(12):123512.

[415] Scherrer, R. J. and Bertschinger, E. (1991). Statistics of Primordial Density Perturbations from Discrete Seed Masses. *Astrophys. J.* , 381:349.

[416] Schmittfull, M. and Seljak, U. (2018). Parameter constraints from cross-correlation of CMB lensing with galaxy clustering. *Phys. Rev. D* , 97(12):123540.

[417] Schmittfull, M. M., Challinor, A., Hanson, D., and Lewis, A. (2013). Joint analysis of CMB temperature and lensing-reconstruction power spectra. *Phys. Rev.*, D88(6):063012.

[418] Scoccimarro, R., Sheth, R. K., Hui, L., and Jain, B. (2001). How Many Galaxies Fit in a Halo? Constraints on Galaxy Formation Efficiency from Spatial Clustering. *Astrophys. J.* , 546(1):20–34.

[419] Sehgal, N., Bode, P., Das, S., Hernandez-Monteagudo, C., Huffenberger, K., Lin, Y.-T., Ostriker, J. P., and Trac, H. (2010). Simulations of the Microwave Sky. *Astrophys. J.* , 709(2):920–936.

[420] Sehgal, N., Madhavacheril, M. S., Sherwin, B., and van Engelen, A. (2017). Internal delensing of cosmic microwave background acoustic peaks. *Phys. Rev. D* , 95:103512.

[421] Sehgal, N., Trac, H., Huffenberger, K., and Bode, P. (2007). Microwave Sky Simulations and Projections for Galaxy Cluster Detection with the Atacama Cosmology Telescope. *Astrophys. J.* , 664(1):149–161.

[422] Seljak, U. (1996). Gravitational Lensing Effect on Cosmic Microwave Background Anisotropies: A Power Spectrum Approach. *Astrophys. J.* , 463:1.

[423] Seljak, U. (1997). Measuring Polarization in the Cosmic Microwave Background. *Astrophys. J.* , 482(1):6–16.

[424] Seljak, U. (2000). Analytic model for galaxy and dark matter clustering. *Mon. Not. R. Astron. Soc.* , 318(1):203–213.

[425] Seljak, U. and Hirata, C. M. (2004). Gravitational lensing as a contaminant of the gravity wave signal in CMB. *Phys. Rev.*, D69:043005.

[426] Seljak, U. and Zaldarriaga, M. (1997). Signature of gravity waves in polarization of the microwave background. *Phys. Rev. Lett.*, 78:2054–2057.

[427] Serra, P., Lagache, G., Doré, O., Pullen, A., and White, M. (2014). Cross-correlation of cosmic far-infrared background anisotropies with large scale structures. *Astron. Astrophys.* , 570:A98.

[428] Shang, C., Haiman, Z., Knox, L., and Oh, S. P. (2012). Improved models for cosmic infrared background anisotropies: new constraints on the infrared galaxy population. *Mon. Not. R. Astron. Soc.* , 421(4):2832–2845.

[429] Shaw, L. D., Nagai, D., Bhattacharya, S., and Lau, E. T. (2010). Impact of Cluster Physics on the Sunyaev-Zel'dovich Power Spectrum. *Astrophys. J.* , 725(2):1452–1465.

[430] Sherwin, B. D. and ACT Collaboration (2012). The Atacama Cosmology Telescope: Cross-correlation of cosmic microwave background lensing and quasars. *Phys. Rev. D* , 86(8):083006.

[431] Sherwin, B. D. and ACT Collaboration (2017). Two-season Atacama Cosmology Telescope polarimeter lensing power spectrum. *Phys. Rev. D* , 95(12):123529.

[432] Sherwin, B. D. and Schmittfull, M. (2015). Delensing the CMB with the cosmic infrared background. *Phys. Rev. D* , 92:043005.

[433] Sheth, R. K. and Lemson, G. (1999). Biasing and the distribution of dark matter haloes. *Mon. Not. R. Astron. Soc.* , 304(4):767–792.

[434] Sheth, R. K., Mo, H. J., and Tormen, G. (2001). Ellipsoidal collapse and an improved model for the number and spatial distribution of dark matter haloes. *Mon. Not. R. Astron. Soc.* , 323(1):1–12.

[435] Sheth, R. K. and Tormen, G. (1999). Large-scale bias and the peak background split. *Mon. Not. R. Astron. Soc.* , 308(1):119–126.

[436] Sheth, R. K. and Tormen, G. (2002). An excursion set model of hierarchical clustering: ellipsoidal collapse and the moving barrier. *Mon. Not. R. Astron. Soc.* , 329(1):61–75.

[437] Shi, X., Komatsu, E., Nagai, D., and Lau, E. T. (2016). Analytical model for non-thermal pressure in galaxy clusters - III. Removing the hydrostatic mass bias. *Mon. Not. R. Astron. Soc.* , 455(3):2936–2944.

[438] Shimon, M., Keating, B., Ponthieu, N., and Hivon, E. (2008). CMB polarization systematics due to beam asymmetry: Impact on inflationary science. *Phys. Rev. D* , 77(8):083003.

[439] Silk, J. (1968). Cosmic Black-Body Radiation and Galaxy Formation. *Astrophys. J.* , 151:459.

[440] Simard, G., Hanson, D., and Holder, G. (2015). Prospects for Delensing the Cosmic Microwave Background for Studying Inflation. *Astrophys. J.* , 807(2):166.

[441] Simons Observatory Collaboration (2019). The Simons Observatory: science goals and forecasts. *J. Cosmol. Astropart. Phys.* , 2019(2):056.

[442] Singh, S., Mandelbaum, R., Seljak, U., Rodríguez-Torres, S., and Slosar, A. (2020). Cosmological constraints from galaxy-lensing cross-correlations using BOSS galaxies with SDSS and CMB lensing. *Mon. Not. R. Astron. Soc.* , 491(1):51–68.

[443] Smith, K. M. (2006). Pseudo-C_ℓ estimators which do not mix E and B modes. *Phys. Rev. D* , 74(8):083002.

[444] Smith, K. M. et al. (2009). Gravitational Lensing. In Dodelson, S. et al., editors, *CMB Polarization Workshop: Theory and Foregrounds: CMBPol Mission Concept Study*, volume 1141 of *American Institute of Physics Conference Series*, pages 121–178.

[445] Smith, K. M., Hanson, D., LoVerde, M., Hirata, C. M., and Zahn, O. (2012). Delensing CMB polarization with external datasets. *Journal of Cosmology and Astro-Particle Physics*, 2012:014.

[446] Smith, K. M., Hu, W., and Kaplinghat, M. (2004). Weak lensing of the CMB: Sampling errors on B modes. *Phys. Rev. D* , 70:043002.

[447] Smith, K. M., Hu, W., and Kaplinghat, M. (2006a). Cosmological information from lensed CMB power spectra. *Phys. Rev. D* , 74:123002.

[448] Smith, K. M., Madhavacheril, M. S., Münchmeyer, M., Ferraro, S., Giri, U., and Johnson, M. C. (2018). KSZ tomography and the bispectrum. *arXiv e-prints*, page arXiv:1810.13423.

[449] Smith, K. M., Zahn, O., and Doré, O. (2007a). Detection of gravitational lensing in the cosmic microwave background. *Phys. Rev. D* , 76(4):043510.

[450] Smith, R. E. et al. (2003). Stable clustering, the halo model and non-linear cosmological power spectra. *Mon. Not. R. Astron. Soc.* , 341(4):1311–1332.

[451] Smith, R. E., Scoccimarro, R., and Sheth, R. K. (2007b). Scale dependence of halo and galaxy bias: Effects in real space. *Phys. Rev. D* , 75(6):063512.

[452] Smith, R. E., Sheth, R. K., and Scoccimarro, R. (2008). Analytic model for the bispectrum of galaxies in redshift space. *Phys. Rev. D* , 78(2):023523.

[453] Smith, S., Challinor, A., and Rocha, G. (2006b). What can be learned from the lensed cosmic microwave background B-mode polarization power spectrum? *Phys. Rev. D* , 73:023517.

[454] Smoot, G. F. et al. (1992). Structure in the COBE Differential Microwave Radiometer First-Year Maps. *ApJL*, 396:L1.

[455] Song, Y.-S., Cooray, A., Knox, L., and Zaldarriaga, M. (2003). The Far-Infrared Background Correlation with Cosmic Microwave Background Lensing. *Astrophys. J.* , 590(2):664–672.

[456] Spergel, D. N. et al. (2003). First-Year Wilkinson Microwave Anisotropy Probe (WMAP) Observations: Determination of Cosmological Parameters. *ApJS*, 148(1):175–194.

[457] Spergel, D. N. and Zaldarriaga, M. (1997). Cosmic Microwave Background Polarization as a Direct Test of Inflation. *Phys. Rev. Lett.* , 79(12):2180–2183.

[458] SPT-3G Collaboration (2014). SPT-3G: a next-generation cosmic microwave background polarization experiment on the South Pole telescope. In Holland, W. S. and Zmuidzinas, J., editors, *Millimeter, Submillimeter, and Far-Infrared Detectors and Instrumentation for Astronomy VII*, volume 9153 of *Society of Photo-Optical Instrumentation Engineers (SPIE) Conference Series*, page 91531P.

[459] SPTpol Collaboration (2020). Measurements of B -mode polarization of the cosmic microwave background from 500 square degrees of SPTpol data. *Phys. Rev. D* , 101(12):122003.

[460] Starobinskiĭ, A. A. (1979). Spectrum of relict gravitational radiation and the early state of the universe. *Soviet Journal of Experimental and Theoretical Physics Letters*, 30:682.

[461] Starobinsky, A. A. (1980). A new type of isotropic cosmological models without singularity. *Physics Letters B*, 91(1):99–102.

[462] Starobinsky, A. A. (1982). Dynamics of phase transition in the new inflationary universe scenario and generation of perturbations. *Physics Letters B*, 117(3-4):175–178.

[463] Stein, G., Alvarez, M. A., and Bond, J. R. (2019). The mass-Peak Patch algorithm for fast generation of deep all-sky dark matter halo catalogues and its N-body validation. *Mon. Not. R. Astron. Soc.* , 483(2):2236–2250.

[464] Stein, G., Alvarez, M. A., Bond, J. R., van Engelen, A., and Battaglia, N. (2020). The Websky extragalactic CMB simulations. *J. Cosmol. Astropart. Phys.* , 2020(10):012.

[465] Stewart, J. M. (1990). Perturbations of Friedmann-Robertson-Walker cosmological models. *Classical and Quantum Gravity*, 7(7):1169–1180.

[466] Stompor, R., Errard, J., and Poletti, D. (2016). Forecasting performance of CMB experiments in the presence of complex foreground contaminations. *Phys. Rev. D* , 94(8):083526.

[467] Stompor, R., Leach, S., Stivoli, F., and Baccigalupi, C. (2009). Maximum likelihood algorithm for parametric component separation in cosmic microwave background experiments. *Mon. Not. R. Astron. Soc.* , 392(1):216–232.

[468] Story, K. T. et al. (2015). A Measurement of the Cosmic Microwave Background Gravitational Lensing Potential from 100 Square Degrees of SPTpol Data. *Astrophys. J.*, 810(1):50.

[469] Sultan Abylkairov, Y., Darwish, O., Hill, J. C., and Sherwin, B. D. (2020). Partially Constrained Internal Linear Combination: a method for low-noise CMB foreground mitigation. *arXiv e-prints*, page arXiv:2012.04032.

[470] Sunyaev, R. A. and Zeldovich, Y. B. (1972). The Observations of Relic Radiation as a Test of the Nature of X-Ray Radiation from the Clusters of Galaxies. *Comments on Astrophysics and Space Physics*, 4:173.

[471] Sunyaev, R. A. and Zeldovich, Y. B. (1980). The velocity of clusters of galaxies relative to the microwave background - The possibility of its measurement. *Mon. Not. R. Astron. Soc.* , 190:413–420.

[472] Talman, J. D. (1978). Numerical Fourier and Bessel Transforms in Logarithmic Variables. *Journal of Computational Physics*, 29(1):35–48.

[473] Tasca, L. A. M. et al. (2015). The evolving star formation rate: M_* relation and sSFR since z = 5 from the VUDS spectroscopic survey. *Astron. Astrophys.* , 581:A54.

[474] Tassis, K. and Pavlidou, V. (2015). Searching for inflationary B modes: can dust emission properties be extrapolated from 350 GHz to 150 GHz? *Mon. Not. R. Astron. Soc.* , 451:L90–L94.

[475] Tegmark, M., de Oliveira-Costa, A., and Hamilton, A. J. (2003). High resolution foreground cleaned CMB map from WMAP. *Phys. Rev. D* , 68(12):123523.

[476] Tegmark, M. and Efstathiou, G. (1996). A method for subtracting foregrounds from multifrequency CMB sky maps**. *Mon. Not. R. Astron. Soc.* , 281(4):1297–1314.

[477] Teng, W.-H., Kuo, C.-L., and Proty Wu, J.-H. (2011). Cosmic Microwave Background Delensing Revisited: Residual Biases and a Simple Fix. *ArXiv e-prints*, page arXiv:1102.5729.

[478] Thorne, B., Dunkley, J., Alonso, D., and Næss, S. (2017). The Python Sky Model: software for simulating the Galactic microwave sky. *Mon. Not. R. Astron. Soc.* , 469(3):2821–2833.

[479] Tinker, J., Kravtsov, A. V., Klypin, A., Abazajian, K., Warren, M., Yepes, G., Gottlöber, S., and Holz, D. E. (2008). Toward a Halo Mass Function for Precision Cosmology: The Limits of Universality. *Astrophys. J.* , 688(2):709–728.

[480] Tinker, J. L., Robertson, B. E., Kravtsov, A. V., Klypin, A., Warren, M. S., Yepes, G., and Gottlöber, S. (2010a). The Large-scale Bias of Dark Matter Halos: Numerical Calibration and Model Tests. *Astrophys. J.* , 724(2):878–886.

[481] Tinker, J. L., Wechsler, R. H., and Zheng, Z. (2010b). Interpreting the Clustering of Distant Red Galaxies. *Astrophys. J.* , 709(1):67–76.

[482] Tinker, J. L. and Wetzel, A. R. (2010). What does Clustering Tell us About the Buildup of the Red Sequence? *Astrophys. J.* , 719(1):88–103.

[483] Trac, H., Bode, P., and Ostriker, J. P. (2011). Templates for the Sunyaev-Zel'dovich Angular Power Spectrum. *Astrophys. J.* , 727(2):94.

[484] Vallinotto, A. (2012). Using Cosmic Microwave Background Lensing to Constrain the Multiplicative Bias of Cosmic Shear. *Astrophys. J.* , 759(1):32.

[485] van Engelen, A. and ACT Collaboration (2015). The Atacama Cosmology Telescope: Lensing of CMB Temperature and Polarization Derived from Cosmic Infrared Background Cross-correlation. *Astrophys. J.* , 808(1):7.

[486] van Engelen, A., Bhattacharya, S., Sehgal, N., Holder, G. P., Zahn, O., and Nagai, D. (2014). CMB Lensing Power Spectrum Biases from Galaxies and Clusters Using High-angular Resolution Temperature Maps. *Astrophys. J.* , 786(1):13.

[487] van Engelen, A. et al. (2012). A measurement of gravitational lensing of the microwave background using South Pole Telescope data. *Astrophys. J.*, 756:142.

[488] van Engelen, A. et al. (2015). The Atacama Cosmology Telescope: Lensing of CMB Temperature and Polarization Derived from Cosmic Infrared Background Cross-Correlation. *Astrophys. J.*, 808(1):7.

[489] Van Waerbeke, L., Bernardeau, F., and Benabed, K. (2000). Lensing Effect on the Relative Orientation between the Cosmic Microwave Background Ellipticities and the Distant Galaxies. *Astrophys. J.* , 540(1):14–19.

[490] Van Waerbeke, L., Hinshaw, G., and Murray, N. (2014). Detection of warm and diffuse baryons in large scale structure from the cross correlation of gravitational lensing and the thermal Sunyaev-Zeldovich effect. *Phys. Rev. D* , 89(2):023508.

[491] Vansyngel, F., Boulanger, F., Ghosh, T., Wandelt, B., Aumont, J., Bracco, A., Levrier, F., Martin, P. G., and Montier, L. (2017). Statistical simulations of the dust foreground to cosmic microwave background polarization. *Astron. Astrophys.* , 603:A62.

[492] Verde, L., Treu, T., and Riess, A. G. (2019). Tensions between the early and late Universe. *Nature Astronomy*, 3:891–895.

[493] Viero, M. P. and HerMES Collaboration (2013a). HerMES: Cosmic Infrared Background Anisotropies and the Clustering of Dusty Star-forming Galaxies. *Astrophys. J.* , 772(1):77.

[494] Viero, M. P. and HerMES Collaboration (2013b). HerMES: The Contribution to the Cosmic Infrared Background from Galaxies Selected by Mass and Redshift. *Astrophys. J.* , 779(1):32.

[495] Voit, G. M. (2005). Tracing cosmic evolution with clusters of galaxies. *Reviews of Modern Physics*, 77(1):207–258.

[496] Wagoner, R. V., Fowler, W. A., and Hoyle, F. (1967). On the Synthesis of Elements at Very High Temperatures. *Astrophys. J.* , 148:3.

[497] Walsh, D., Carswell, R. F., and Weymann, R. J. (1979). 0957+561 A, B: twin quasistellar objects or gravitational lens? *Nature (London)* , 279:381–384.

[498] Wang, L. et al. (2013). Connecting stellar mass and star-formation rate to dark matter halo mass out to z ∼ 2. *Mon. Not. R. Astron. Soc.* , 431(1):648–661.

[499] Wang, Y., Yang, X., Mo, H. J., van den Bosch, F. C., and Chu, Y. (2004). The three-point correlation function of galaxies: comparing halo occupation models with observations. *Mon. Not. R. Astron. Soc.* , 353(1):287–300.

[500] Warren, M. S., Abazajian, K., Holz, D. E., and Teodoro, L. (2006). Precision Determination of the Mass Function of Dark Matter Halos. *Astrophys. J.* , 646(2):881–885.

[501] Watanabe, Y. and Komatsu, E. (2006). Improved calculation of the primordial gravitational wave spectrum in the standard model. *Phys. Rev. D* , 73(12):123515.

[502] Wechsler, R. H., Bullock, J. S., Primack, J. R., Kravtsov, A. V., and Dekel, A. (2002). Concentrations of Dark Halos from Their Assembly Histories. *Astrophys. J.* , 568(1):52–70.

[503] Wechsler, R. H. and Tinker, J. L. (2018). The Connection Between Galaxies and Their Dark Matter Halos. *Ann. Rev. Astron. Astrophys.* , 56:435–487.

[504] Weinberg, D. H., Mortonson, M. J., Eisenstein, D. J., Hirata, C., Riess, A. G., and Rozo, E. (2013). Observational probes of cosmic acceleration. *Phys. Rep.* , 530(2):87–255.

[505] Weinberg, S. (1972). *Gravitation and Cosmology: Principles and Applications of the General Theory of Relativity*.

[506] Weinberg, S. (2002). Cosmological Fluctuations of Small Wavelength. *Astrophys. J.* , 581(2):810–816.

[507] Weinberg, S. (2008). *Cosmology*.

[508] Weller, J. (1999). Inhomogeneous Reionization and the Polarization of the Cosmic Microwave Background. *ApJL*, 527(1):L1–L4.

[509] White, S. D. M. and Frenk, C. S. (1991). Galaxy Formation through Hierarchical Clustering. *Astrophys. J.* , 379:52.

[510] White, S. D. M. and Rees, M. J. (1978). Core condensation in heavy halos: a two-stage theory for galaxy formation and clustering. *Mon. Not. R. Astron. Soc.* , 183:341–358.

[511] Wilson, M. J. et al. (2012). Atacama Cosmology Telescope: A measurement of the thermal Sunyaev-Zel'dovich effect using the skewness of the CMB temperature distribution. *Phys. Rev. D* , 86(12):122005.

[512] Wilson, M. J. and White, M. (2019). Cosmology with dropout selection: straw-man surveys & CMB lensing. *J. Cosmol. Astropart. Phys.* , 2019(10):015.

[513] Wu, W. L. K., Errard, J., Dvorkin, C., Kuo, C. L., Lee, A. T., McDonald, P., Slosar, A., and Zahn, O. (2014). A Guide to Designing Future Ground-based Cosmic Microwave Background Experiments. *Astrophys. J.* , 788(2):138.

[514] Wu, W. L. K. and SPTPol Collaboration (2019). A Measurement of the Cosmic Microwave Background Lensing Potential and Power Spectrum from 500 $\deg^2$ of SPTpol Temperature and Polarization Data. *Astrophys. J.* , 884(1):70.

[515] Wu, X.-P. (2004). Weak lensing of the Sunyaev-Zel'dovich sky. *Mon. Not. R. Astron. Soc.* , 349(3):816–820.

[516] Yamauchi, D., Namikawa, T., and Taruya, A. (2012). Weak lensing generated by vector perturbations and detectability of cosmic strings. *J. Cosmol. Astropart. Phys.* , 2012(10):030.

[517] Yu, B., Hill, J. C., and Sherwin, B. D. (2017). Multitracer CMB delensing maps from Planck and WISE data. *Phys. Rev. D* , 96(12):123511.

[518] Yu, B., Knight, R. Z., Sherwin, B. D., Ferraro, S., Knox, L., and Schmittfull, M. (2018). Towards Neutrino Mass from Cosmology without Optical Depth Information. *arXiv e-prints*, page arXiv:1809.02120.

[519] Zaldarriaga, M. and Harari, D. D. (1995). Analytic approach to the polarization of the cosmic microwave background in flat and open universes. *Phys. Rev. D* , 52(6):3276–3287.

[520] Zaldarriaga, M. and Seljak, U. (1998). Gravitational lensing effect on cosmic microwave background polarization. *Phys. Rev. D* , 58:023003.

[521] Zaldarriaga, M. and Seljak, U. (1999). Reconstructing projected matter density power spectrum from cosmic microwave background. *Phys. Rev. D* , 59(12):123507.

[522] Zehavi, I. et al. (2004). On Departures from a Power Law in the Galaxy Correlation Function. *Astrophys. J.* , 608(1):16–24.

[523] Zeldovich, Y. B. (1972). A hypothesis, unifying the structure and the entropy of the Universe. *Mon. Not. R. Astron. Soc.* , 160:1P.

[524] Zhao, D. H., Jing, Y. P., Mo, H. J., and Börner, G. (2009). Accurate Universal Models for the Mass Accretion Histories and Concentrations of Dark Matter Halos. *Astrophys. J.* , 707(1):354–369.

[525] Zheng, Z., Berlind, A. A., Weinberg, D. H., Benson, A. J., Baugh, C. M., Cole, S., Davé, R., Frenk, C. S., Katz, N., and Lacey, C. G. (2005). Theoretical Models of the Halo Occupation Distribution: Separating Central and Satellite Galaxies. *Astrophys. J.* , 633(2):791–809.

[526] Zubeldia, Í. and Challinor, A. (2019). Cosmological constraints from Planck galaxy clusters with CMB lensing mass bias calibration. *Mon. Not. R. Astron. Soc.* , 489(1):401–419.

[527] Zwicky, F. (1933). Die Rotverschiebung von extragalaktischen Nebeln. *Helvetica Physica Acta*, 6:110–127.